APPLICATION OF SATELLITE ALTIMETRY IN MARINE GEODESY AND GEOPHYSICS

EDITED BY: Jinyun Guo, Xiaoli Deng and Cheinway Hwang

PUBLISHED IN: Frontiers in Earth Science and Frontiers in Environmental Science

frontiers Research Topics

ISSN 1664-8714
ISBN 978-2-88976-250-7
DOI 10.3389/978-2-88976-250-7

About Frontiers

Frontiers is more than just an open-access publisher of scholarly articles: it is a pioneering approach to the world of academia, radically improving the way scholarly research is managed. The grand vision of Frontiers is a world where all people have an equal opportunity to seek, share and generate knowledge. Frontiers provides immediate and permanent online open access to all its publications, but this alone is not enough to realize our grand goals.

Frontiers Journal Series

The Frontiers Journal Series is a multi-tier and interdisciplinary set of open-access, online journals, promising a paradigm shift from the current review, selection and dissemination processes in academic publishing. All Frontiers journals are driven by researchers for researchers; therefore, they constitute a service to the scholarly community. At the same time, the Frontiers Journal Series operates on a revolutionary invention, the tiered publishing system, initially addressing specific communities of scholars, and gradually climbing up to broader public understanding, thus serving the interests of the lay society, too.

Dedication to Quality

Each Frontiers article is a landmark of the highest quality, thanks to genuinely collaborative interactions between authors and review editors, who include some of the world's best academicians. Research must be certified by peers before entering a stream of knowledge that may eventually reach the public - and shape society; therefore, Frontiers only applies the most rigorous and unbiased reviews.
Frontiers revolutionizes research publishing by freely delivering the most outstanding research, evaluated with no bias from both the academic and social point of view. By applying the most advanced information technologies, Frontiers is catapulting scholarly publishing into a new generation.

What are Frontiers Research Topics?

Frontiers Research Topics are very popular trademarks of the Frontiers Journals Series: they are collections of at least ten articles, all centered on a particular subject. With their unique mix of varied contributions from Original Research to Review Articles, Frontiers Research Topics unify the most influential researchers, the latest key findings and historical advances in a hot research area! Find out more on how to host your own Frontiers Research Topic or contribute to one as an author by contacting the Frontiers Editorial Office: frontiersin.org/about/contact

APPLICATION OF SATELLITE ALTIMETRY IN MARINE GEODESY AND GEOPHYSICS

Topic Editors:
Jinyun Guo, Shandong University of Science and Technology, China
Xiaoli Deng, The University of Newcastle, Australia
Cheinway Hwang, National Chiao Tung University, Taiwan

Citation: Guo, J., Deng, X., Hwang, C., eds. (2022). Application of Satellite Altimetry in Marine Geodesy and Geophysics. Lausanne: Frontiers Media SA. doi: 10.3389/978-2-88976-250-7

Table of Contents

frontiers | Frontiers in Earth Science

EDITORIAL
published: 09 May 2022
doi: 10.3389/feart.2022.910562

Editorial: Application of Satellite Altimetry in Marine Geodesy and Geophysics

Jinyun Guo[1]*, *Cheinway Hwang*[2] and *Xiaoli Deng*[3]

[1]College of Geodesy and Geomatics, Shandong University of Science and Technology, Qingdao, China, [2]Department of Civil Engineering, National Yang Ming Chiao Tung University, Hsinchu, Taiwan, [3]School of Engineering, The University of Newcastle, Callaghan, NSW, Australia

Keywords: satellite altimetry, marine geodesy, marine geophysics, marine gravity field, sea surface height, marine bathymetry, sea level change, GNSS-R

Editorial on the Research Topic

Application of Satellite Altimetry in Marine Geodesy and Geophysics

The satellite altimetry concept was first proposed in 1969. Since then, many satellite altimetry missions have been implemented. With the development of the satellite altimetry technique, altimetry modes have been created for ocean and land observations, such as the traditional pulse-limited radar, the synthetic aperture radar (SAR), the laser mode, the three-dimensional imaging mode, and the global navigation satellite system refection (GNSS-R) mode. **Figure 1** gives an overview of all satellite altimetry missions. China also developed the ocean dynamic environment satellite missions, HY-2A/2B/2C/2D. These three missions (HY-2B/2C/2D) are currently simultaneously collecting global marine information and monitoring changes in ocean states.

Altimeter data quality may be affected by an error in instruments, atmospheric delay, sea state bias, geophysical environment correction (e.g., solid earth tide correction, ocean tide correction, inverse barometric effect, etc.), and precise orbit determination, The coastal waveforms may be seriously contaminated by the land and seabed. Therefore, these systematic errors should be corrected and presented in geophysical data records (GDRs). Researchers can then apply alternative correction models and new waveform retracking algorithms to further improve the quality of satellite altimetry data.

Radar altimetry missions include the exact repeat mission (ERM) and the geodetic mission (GM). The oceanic environment can be continuously monitored with ERM data. The GM data are mainly used to study marine geodesy and geophysics. Laser altimeter, SAR altimeter, and three-dimensional imaging altimeter collect massive ocean data. Once fused, multi-source altimeter data can provide high-resolution and precise ocean information. In marine geodesy, geophysics, and oceanography, altimeter data have been used in several studies including marine gravity, geoid, mean sea surface, mean dynamic topography, sea levels rising, ocean currents, geostrophic, sea wind, and wave, bathymetry, and seabed tectonics.

This Research Topic includes 17 papers in the field of satellite altimeter data processing, exploring applications to marine geodesy and geophysics. A summary of these papers is given below.

CALIBRATION OF SATELLITE ALTIMETER DATA

HY-2A mission was successfully implemented in 2011, which is the first altimetry satellite of the marine dynamic environment satellite series of China. HY-2B (the follow up to HY-2A) was

OPEN ACCESS

Edited and reviewed by:
Susana Barbosa,
University of Porto, Portugal

***Correspondence:**
Jinyun Guo
jinyunguo1@126.com

Specialty section:
This article was submitted to Environmental Informatics and Remote Sensing, a section of the journal Frontiers in Earth Science

Received: *01 April 2022*
Accepted: *08 April 2022*
Published: *09 May 2022*

Citation:
Guo J, Hwang C and Deng X (2022) Editorial: Application of Satellite Altimetry in Marine Geodesy and Geophysics. Front. Earth Sci. 10:910562. doi: 10.3389/feart.2022.910562

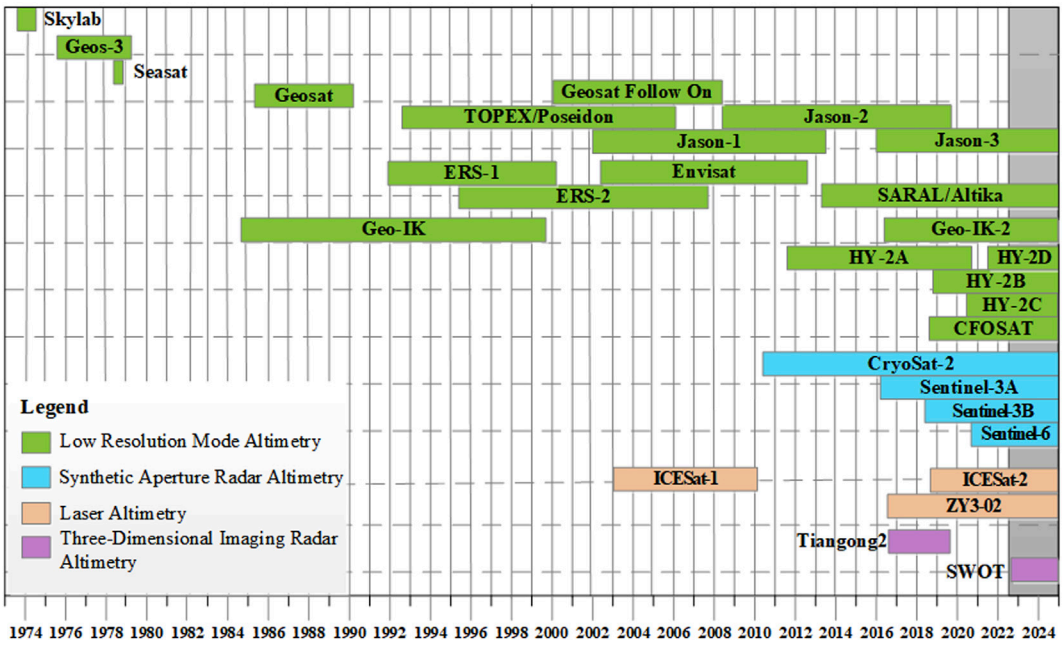

FIGURE 1 | Overview of satellite altimetry missions.

launched in 2018, and HY-2C and HY-2D were implemented in 2020, and 2021, respectively. Now, HY-2B, HY-2C, and HY-2D are simultaneously running global ocean observation. Wang J. et al. 2021 compared HY-2B GDR data and Jason-3 GDR data based on sea level anomalies, backscatter coefficient, sea state bias, wet tropospheric delay, and ionospheric delay. The cross-calibration performed in this study enables an evaluation of the performance of HY-2B for marine geodesy, geophysics, and oceanography.

WAVEFORM RETRACKING FOR THE IMPROVEMENT OF SATELLITE ALTIMETER DATA

Satellite altimeter data in the coastal seas are seriously degraded because of waveform contamination. Coastal altimetry exploits seamless satellite altimetry datasets from open oceans to coasts, so that the altimeter data quality can satisfy the requirement of coastal geodesy, geophysics, and oceanography. Many waveform retracking methods have been developed to improve the coastal data quality to some extent, such as OCOG, threshold algorithm, β-parameter algorithm, function fitting method, multi-leading-edge method, X-track, and ALES. Wang and Huang, 2021b combined a novel realignment algorithm and a gate-wise outlier detector to make waveform decontamination over coastal seas and then used the threshold method and ICE1 to retrack the decontaminated waveforms. The case study of Jason-2 data indicated that the upgraded waveform decontamination strategy can provide a promising solution for coastal altimetry applications.

WAVE ANISOTROPIC FEATURE OF BACKSCATTER COEFFICIENT DETERMINED BY SATELLITE ALTIMETER

Satellite altimeters have collected large amounts of marine information, including sea surface heights, wind speeds, wave heights, and backscatter coefficients. Satellite altimetry modes mainly include the compressed radar pulse mode, low resolution mode, SAR, SARIn (synthetic aperture interferometric mode), wide swath mode, and laser pulse mode, which can affect the backscatter coefficients over the ocean surface. Xu et al. 2021 analyzed the sigma0 data from Sentinel-3A, Cryosat-2, and Jason-3 and found the anisotropic features for different ocean wave modes.

REGIONAL MSS AND MDT DETERMINED FROM SATELLITE ALTIMETER DATA

The mean sea surface (MSS) and the mean dynamic topography (MDT) are the basic geographical information of oceans. Hamden et al. 2021 processed 27 years of along-track altimeter data from multiple satellite altimetry missions and established the Universiti Technologi Malaysia 2020 Mean Sea Surface (UTM20 MSS) model with a grid of 1.5′×1.5′ by considering the 19-years moving average technique (Yuan et al., 2021). The latest altimeter data are used (i.e., Sentinel-3A). The UTM20 MDT model is derived with a pointwise approach from the differences between UTM20 MSS and the local gravimetric geoid of Malaysia. The MDT yielded significant

improvement compared to the precious regional models developed by the Universiti Technologi Malaysia.

Sun W. et al. 2021 constructed a mean sea surface model of the Antarctic Ocean by integrating the Technical University of Denmark 2018 MSS (DTU18 MSS) with 6-years ERM and GM data from HY-2A, the first ocean dynamic environment satellite from China. The power spectral density shows the model errors with different sea surface wave bands.

MARINE GRAVITY INVERSION FROM ALTIMETER DATA AND ITS ASSESSMENT

Ice, cloud, and land Elevation Satellite 2 (ICESat-2) uses a synchronized multi-beam photon-counting method to collect data from three pairs of synchronous ground tracks. ATLAS loaded on ICESat-2 uses a 523-nm laser to actively map surface elevations, including the ice sheet height, sea-ice thickness, and sea surface height. Che et al. 2021 processed ICESat-2 data to estimate the deflections of the vertical (DOV) and marine gravity anomalies over the South China Sea. They found that the combination of along-track and cross-track data can improve the precision of deflections of the vertical and gravity anomalies.

Since 1969, many altimetry missions have been implemented. The altimeter can collect ocean information with limited-wide depressed pulse mode, low resolution mode, SAR/SARIn, laser, or wide swath mode. Marine gravity field models can be derived with the inverse Stokes formula, inverse Vening-Meinesz (IVM) formula, least squares collocation method, and the Laplace equation. Many marine gravity models have been constructed using massive datasets from exact repeat missions and geodetic missions. The S&S series from the Scripps Institution of Oceanography, University of California San Diego, United States, and the DTU series from the Technical University of Denmark are typical representatives. Recently the space geodetic group of Shandong University of Science and Technology, China, has developed a global marine gravity field model ($1'\times1'$) with IVM from multi-source satellite altimeter data (Zhu et al., 2020). Li et al., 2021) use ship-borne gravity data to evaluate the S&S and DTU models over the offshore and coastal seas of China and discuss the contribution of Jason-2, SARAL, and Cryosat-2.

The precise global geopotential model (GGM) can supply abundant information about the Earth's gravity field. High-degree GGMs have been constructed using multi-source geodetic data, such as EGM 2008, GECO, SGG-UGM-1, EIGEN-6C4, GOCO05C, XGM 2016, and XGM 2019. Multi-satellite altimeter data have played an important role in constructing these high-degree GGMs, especially over oceans. These GGMs are widely applied in marine geodesy, geophysics, and oceanography. Wu Y. et al. 2021 assessed the updated high-degree GGMs over the South China Sea with heterogenous geodetic observations (e.g., airborne and ship-borne gravity data) and synthetic ocean reanalysis data (e.g., CNES-CLS13MDT, SODA3, ECMWF, and ORAS5). The choice of a precise GGM is crucial for oceanography, and these synthetic ocean data are very useful in regional oceans were good quality geodetic and geophysical data are lacking.

Global or regional marine gravity anomalies can be inversed from multi-source satellite altimeter data with the inverse Stokes formula, the inverse Vening Meinesz formula, and the least squares collocation method, respectively. The precision of marine gravity anomalies inversed from multi-satellite altimeter data are generally affected by the density of altimeter tracks, number of observations, precision of sea surface heights, and footprint position of satellite altimeters. Liu S. et al. 2021 used the altimetry data from Geosat, ERS-1/2, TOPEX/Poseidon, Envisat, Jason-1/2/3, Cryosat-2, HY-2A, SARAL, and Sentinel-3A to analyze the influence of altimeter data quality on the precision of marine gravity anomalies inversed from multi-source altimetry data. Their results show that an effective combination of multi-source satellite altimeter data can improve the precision and the spatial resolution of global/regional marine gravity derived from the satellite altimetry technique.

BATHYMETRY AND SEABED DENSITY CONTRAST

High-resolution marine gravity data can be determined from multi-source satellite altimeter data. Then the marine gravity data can be used to predict bathymetry based on the frequency relation between the depth of density interface and gravity anomalies in the frequency domain. Therefore, the mass density contrast is one important parameter for bathymetry. Wan et al. 2021 used the gravity geological method to study the density contrast over the Atlantic Ocean from the altimetry-derived gravity data and the ship-borne depth data.

Ocean depth plays a very important role in marine geodesy, geophysics, geology and oceanography, and studies of earth plate tectonics, ocean currents, tide, and marine navigation. Gravity-induced bathymetry is one of the main techniques to determine the seabed topography over large oceans. The gravity-geologic method, admittance function method, and least-squares collocation method are three main methods to estimate the seafloor depth from marine gravity data determined by satellite altimetry technique. Wei et al. 2021 constructed the marine gravity anomalies using HY-2A/GM data and predicted bathy bathymetry accordingly over the South China Sea. Their results suggest that the GGM can be widely applied to bathymetry prediction and HY-2A/GM-derived gravity data are feasible with good results for determining seabed topography.

APPLICATIONS TO LAND AND INLAND LAKE

Ice gaps over the Antarctic and Greenland and terrestrial glaciers are gradually melting due to global warming. The temporal gravity data of GRACE and GRACE-Follow On are generally used to study the global or regional mass changes and height variations. Chen et al., 2021) processed the SARIn data and low-

resolution data of Cryosat-2, as well as the airborne topographic mapper data over the Greenland ice sheet. The elevation change rate is -11.83 ± 1.14 cm/year, corresponding to the volume change rate of -200.22 ± 18.26 km3/year.

The satellite altimetry technique can collect massive data reflecting from the sea surface and terrestrial surface, including inland lake surface. The lake level change can also be monitored with the radar altimeter, laser altimeter, and/or SAR/SARIn altimeter. The high-altitude lakes over the Tibetan Plateau are extremely sensitive to global climate change, and therefore the lake level evolution is very important for hydrological and climate change analysis. Sun M. et al. 2021 robustly processed the altimetry data from TOPEX/Poseidon and Jason-1/2/3 to construct the lake level series over lake Zhari Namco, and analyze the lake level variations, The results improve our understanding of inland water budget and the effects of climate change over the Tibetan Plateau.

GNSS-R ALTIMETRY

GNSS-R technique is an emerging remote sensing technology for sea surface altimetry to retrieve the sea surface height by measuring the time delay between direct GNSS signal and reflected signal. Several satellite missions (e.g., TechDemoSat-1, CYGNSS, and Bufeng-1) have been executed to step the GNSS-R technique into a new stage of collecting global sea surface information, like sea surface height, sea surface wind speed, sea ice, and so on. Wang Q. et al. 2021 integrated one machine learning fusion model and feature optimization to extract precise sea surface height.

Wu F. et al. 2021 studied the reflected sea surface model for GNSS-R signals. The mean dynamic topography (MDT) is different from the instantaneous sea surface and its normal is not along the vertical. The actual direct and reflected signals of ship-borne GNSS were processed and the MDT correction and the vertical correction can improve the precision of specular point positioning.

Liu Z. et al. 2021 analyzed the performance of airborne interferometric global navigation satellite system reflectometry (iGNSS-R) for sea surface altimetry and showed the relation between the altimetric data quality and the along-track spatial resolution. Yan et al. 2022 studied the atmospheric delay on sea surface altimetry with airborne and spaceborne GNSS-R techniques. Their results will provide a scientific reference for future spaceborne iGNSS-R altimetry missions.

AUTHOR CONTRIBUTIONS

JG, CH and XD make the contribution of topic management, manuscript review, writing and editing.

ACKNOWLEDGMENTS

We thank the responsible editor for handling and editing all manuscripts. We thank all reviewers for their valuable comments and proposals, which improved the quality of these manuscripts.

REFERENCES

Che, D., Li, H., Zhang, S., and Ma, B. (2021). Calculation of Deflection of Vertical and Gravity Anomalies over the South China Sea Derived from ICESat-2 Data. *Front. Earth Sci.* 9, 670256. doi:10.3389/feart.2021.670256

Chen, G., Zhang, S., Liang, S., and Zhu, J. (2021). Elevation and Volume Changes in Greenland Ice Sheet from 2010 to 2019 Derived from Altimetry Data. *Front. Earth Sci.* 9, 674983. doi:10.3389/feart.2021.674983

Hamden, M. H., Yusoff, M. Y. M., Pa'suya, M. F., Wijaya, D. D., and Pa'suya, M. F. (2021). Regional Mean Sea Surface and Mean Dynamic Topography Models Around Malaysian Seas Developed from 27 Years of Along-Track Multi-Mission Satellite Altimetry Data. *Front. Earth Sci.* 9, 665876. doi:10.3389/feart.2021.665876

Li, Q., Bao, L., and Wang, Y. (2021). Accuracy Evaluation of Altimeter-Derived Gravity Field Models in Offshore and Coastal Regions of China. *Front. Earth Sci.* 9, 722019. doi:10.3389/feart.2021.722019

Liu, S., Li, Y., Sun, Q., Wan, J., Jiao, Y., and Jiang, J. (2021a). Evaluation of Marine Gravity Anomaly Calculation Accuracy by Multi-Source Satellite Altimetry Data. *Front. Earth Sci.* 9, 730777. doi:10.3389/feart.2021.730777

Liu, Z., Zheng, W., Wu, F., Kang, G., Sun, X., and Wang, Q. (2021b). Relationship between Altimetric Quality and Along-Track Spatial Resolution for iGNSS-R Sea Surface Altimetry: Example for the Airborne Experiment. *Front. Earth Sci.* 9, 730513. doi:10.3389/feart.2021.730513

Sun, M., Guo, J., Yuan, J., Liu, X., Wang, H., and Li, C. (2021b). Detecting Lake Level Change from 1992 to 2019 of Zhari Namco in Tibet Using Altimetry Data of TOPEX/Poseidon and Jason-1/2/3 Missions. *Front. Earth Sci.* 9, 640553. doi:10.3389/feart.2021.640553

Sun, W., Zhou, X., Yang, L., Zhou, D., and Li, F. (2021a). Construction of the Mean Sea Surface Model Combined HY-2A with DTU18 MSS in the Antarctic Ocean. *Front. Environ. Sci.* 9, 697111. doi:10.3389/fenvs.2021.697111

Wan, X., Han, W., Ran, J., Ma, W., Annan, R. F., and Li, B. (2021). Seafloor Density Contrast Derived from Gravity and Shipborne Depth Observations: A Case Study in a Local Area of Atlantic Ocean. *Front. Earth Sci.* 9, 668863. doi:10.3389/feart.2021.668863

Wang, H., and Huang, Z. (2021b). Waveform Decontamination for Improving Satellite Radar Altimeter Data over Nearshore Area: Upgraded Algorithm and Validation. *Front. Earth Sci.* 9, 748401. doi:10.3389/feart.2021.748401

Wang, J., Xu, H., Yang, L., Song, Q., and Ma, C. (2021a). Cross-Calibrations of the HY-2B Altimeter Using Jason-3 Satellite during the Period of April 2019-September 2020. *Front. Earth Sci.* 9, 647583. doi:10.3389/feart.2021.647583

Wang, Q., Zheng, W., Wu, F., Xu, A., Zhu, H., and Liu, Z. (2021c). A New GNSS-R Altimetry Algorithm Based on Machine Learning Fusion Model and Feature Optimization to Improve the Precision of Sea Surface Height Retrieval. *Front. Earth Sci.* 9, 730565. doi:10.3389/feart.2021.730565

Wei, Z., Guo, J., Zhu, C., Yuan, J., Chang, X., and Ji, B. (2021). Evaluating Accuracy of HY-2a/gm-Derived Gravity Data with the Gravity-Geologic Method to Predict Bathymetry. *Front. Earth Sci.* 9, 636246. doi:10.3389/feart.2021.636246

Wu, F., Zheng, W., Liu, Z., and Sun, X. (2021b). Improving the Specular Point Positioning Accuracy of Ship-Borne GNSS-R Observations in China Seas Based on Comprehensive Geophysical Correction. *Front. Earth Sci.* 9, 720470. doi:10.3389/feart.2021.720470

Wu, Y., He, X., Luo, Z., and Shi, H. (2021a). An Assessment of Recently Released High-Degree Global Geopotential Models Based on Heterogeneous Geodetic and Ocean Data. *Front. Earth Sci.* 9, 749611. doi:10.3389/feart.2021.749611

Xu, X.-Y., Xu, K., Jiang, M., Geng, B., and Shi, L. (2021). Investigation of the Anisotropic Patterns in the Altimeter Backscatter Measurements over Ocean Wave Surfaces. *Front. Earth Sci.* 9, 731610. doi:10.3389/feart.2021.731610

Yan, Z., Zheng, W., Wu, F., Wang, C., Zhu, H., and Xu, A. (2022). Correction of Atmospheric Delay Error of Airborne and Spaceborne GNSS-R Sea Surface Altimetry. *Front. Earth Sci.* 10, 730551. doi:10.3389/feart.2022.730551

Yuan, J., Guo, J., Zhu, C., Hwang, C., Yu, D., Sun, M., et al. (2021). High-resolution Sea Level Change Around China Seas Revealed through Multi-Satellite Altimeter Data. *Int. J. Appl. Earth Observation Geoinformation* 102, 102433. doi:10.1016/j.jag.2021.102433

Zhu, C., Guo, J., Gao, J., Liu, X., Hwang, C., Yu, S., et al. (2020). Marine Gravity Determined from Multi-Satellite GM/ERM Altimeter Data over the South China Sea: SCSGA V1.0. *J. Geod.* 94 (5), 50. doi:10.1007/s00190-020-01378-4

Conflict of Interest: The authors declare that the research was conducted in the absence of any commercial or financial relationships that could be construed as a potential conflict of interest.

Publisher's Note: All claims expressed in this article are solely those of the authors and do not necessarily represent those of their affiliated organizations, or those of the publisher, the editors and the reviewers. Any product that may be evaluated in this article, or claim that may be made by its manufacturer, is not guaranteed or endorsed by the publisher.

frontiers in Earth Science

ORIGINAL RESEARCH
published: 29 March 2021
doi: 10.3389/feart.2021.640553

Detecting Lake Level Change From 1992 to 2019 of Zhari Namco in Tibet Using Altimetry Data of TOPEX/Poseidon and Jason-1/2/3 Missions

Mingzhi Sun[1], Jinyun Guo[1], Jiajia Yuan[1], Xin Liu[1], Haihong Wang[2] and Chengming Li[3]**

[1] College of Geodesy and Geomatics, Shandong University of Science and Technology, Qingdao, China, [2] School of Geodesy and Geomatics, Wuhan University, Wuhan, China, [3] Chinese Academy of Surveying and Mapping, Beijing, China

Zhari Namco, a large lake in the Tibetan Plateau (TP), is sensitive to climate and environmental change. However, it is difficult to retrieve accurate and continuous lake levels for Zhari Namco. A robust strategy, including atmospheric delay correction, waveform retracking, outlier deletion, and inter-satellite adjustment, is proposed to generate a long-term series of lake levels for Zhari Namco through multi-altimeter data. Apparent biases are found in troposphere delay correction from different altimeter products and adjusted using an identical model. The threshold (20%) algorithm is employed for waveform retracking. The two-step method combining a sliding median filter and 2σ criterion is used to eliminate outliers. Tandem mission data of altimeters are used to estimate inter-satellite bias. Finally, a 27-year-long lake level time series of Zhari Namco are constructed using the TOPEX/Poseidon-Jason1/2/3 (T/P-Jason1/2/3) altimeter data from 1992 to 2019, resulting in an accuracy of 10.1 cm for T/P-Jason1/2/3. Temperature, precipitation, lake area, equivalent water height, and *in situ* gauge data are used for validation. The correlation coefficient more than 0.90 can be observed between this result and *in situ* gauge data. Compared with previous studies and existing database products, our method yields sequences with the best observational quality and the longest continuous monitoring in Zhari Namco. The time series indicates that the lake level in Zhari Namco has increased by ∼ 5.7 m, with an overall trend of 0.14 ± 0.01 m/yr, showing a fluctuating rate (1992–1999: −0.25 ± 0.05 m/yr, 2000–2008: 0.26 ± 0.04 m/yr, 2009–2016: −0.05 ± 0.03 m/yr, 2017–2019: 1.34 ± 0.34 m/yr). These findings will enhance the understanding of water budget and the effect of climate change in the TP.

Keywords: satellite altimetry, TOPEX/Poseidon, Jason1/2/3, Zhari Namco, lake level

OPEN ACCESS

Edited by:
Peng Liu,
Institute of Remote Sensing and Digital Earth (CAS), China

Reviewed by:
Guoqing Zhang,
Institute of Tibetan Plateau Research (CAS), China
Xiangjun Liu,
Northwest Normal University, China

****Correspondence:***
Jinyun Guo
guojy@sdust.edu.cn;
jinyunguo1@126.com
Chengming Li
cmli@casm.ac.cn

Specialty section:
This article was submitted to Environmental Informatics and Remote Sensing, a section of the journal Frontiers in Earth Science

Received: *11 December 2020*
Accepted: *10 March 2021*
Published: *29 March 2021*

Citation:
Sun M, Guo J, Yuan J, Liu X, Wang H and Li C (2021) Detecting Lake Level Change From 1992 to 2019 of Zhari Namco in Tibet Using Altimetry Data of TOPEX/Poseidon and Jason-1/2/3 Missions. Front. Earth Sci. 9:640553. doi: 10.3389/feart.2021.640553

INTRODUCTION

There are ∼1400 lakes greater than 1 km^2 over the Tibetan Plateau (TP), most of which are closed and rarely disturbed by human activities (Ma et al., 2010). These high-altitude lakes are extremely sensitive to global climate change, and digesting their evolution is important for both hydrological and climatic analysis (Song et al., 2014). In practice, due to rugged topography

and harsh environment of the TP, few *in situ* gauge observations can be used for lake level monitoring. Remote sensing has become the most feasible means to monitor the lake level change of high-altitude lakes.

Altimeter observations can be used to monitor changes in lake level. The accuracy of lake level provided by the geoscience laser altimeter system (GLAS) on the Ice, Cloud, and Land Elevation Satellite (ICESat) mission has reached the decimeter level (Zhang et al., 2011; Phan et al., 2012). The laser satellite's ground footprint is 70 m in diameter, which allows GLAS to explore more lake levels in alpine lakes. The changes of lake level in 111 lakes on the TP are successfully extracted by ICESat/ICESat-2, and it is found that the lake level has a significant upward trend (Zhang et al., 2011, 2019a; Phan et al., 2012). GLAS data are used to detect seasonal and abrupt changes in lake level of 105 closed lakes and categorized the changes for understanding their temporal evolution patterns based on cluster analysis (Song et al., 2014). SAR Interferometry (SARIn), a new sort of satellite altimetry (e.g., CryoSat-2), can also gather worthwhile data for monitoring lake level changes on the TP (Kleinherenbrink et al., 2015; Jiang et al., 2017). Both ICESat/ICESat-2 and CryoSat-2 use non-repetitive orbits. The revisit period of ICESat/ICESat-2 is 91 days, while that of CryoSat-2 is 369 days, resulting in a sparse temporal sampling. This feature makes them improper for detecting periodic lake level alteration.

Compared with laser altimetry and SARIn altimetry, traditional radar altimetry can provide lake levels with dense sampling time. The TOPEX/Poseidon-Jason1/2/3 (T/P-Jason1/2/3) missions, revisiting the same site every 10 days, have collected lake level data from October 1992 to the present. Lake levels above the TP are monitored by T/P-Jason1/2/3, e.g., Khanka, La'nga Co, Ngangzi Co, Qinghai Lake, and Ngoring. The specifics of their lake levels are described and the response of lake levels to climate is analyzed (Hwang et al., 2005; Guo et al., 2011; Lee et al., 2011). The lake level sequences of plateau lakes are extracted from T/P altimeter data and the main factors of lake level change are discussed from the perspective of water balance (Gao et al., 2013; Hwang et al., 2016). Although there are altimetry satellite observations in some lakes, the data are intensely noisy because of the influence of steep lakeshore or lofty mountains. Due to the large footprint of radar altimeter, e.g., ∼2.2 km for T/P-Jason1/2/3 altimeters, the data reaped by altimeter are inconsistent with nominal data in terms of accuracy and quantity, resulting in loss of some data, because of the complex and rugged plateau terrain. There are several global datasets for inland lakes based on multiple satellite altimeters, such as, the Global Reservoir and Lake Monitor (G-REALM), the Hydroweb database, and the High-temporal-resolution water level data sets for lakes (HTRWLD). But the data processing method cannot be optimal in a single lake. The lake levels of Zhari Namco in these data sets are noisy and data in some periods are lacking. New data processing methods, such as waveform retracking and data filtering, can be used to procure the lake levels more accurately.

The objective of this paper is to show a technique for computing lake level changes in Zhari Namco from T/P-Jason1/2/3 altimeters. We study a range of problems, such as atmospheric path delay corrections, waveform retracking, outlier detection and bias adjustment. Other lake level products (G-REALM, HTRWLD, Hydroweb, and *in situ* gauge data), precipitation, temperature, lake area, and equivalent water height (EWH) data are used to further confirm the results of altimeter-derived lake levels over Zhari Namco. Our long-term altimeter result over Zhari Namco will provide important information for exploring this basin.

STUDY AREA AND DATA

Study Area

Zhari Namco (alias Chi-jih) a large lake in the TP (Zhang, 2019), is located at 30°44′–31°05′ N and 85°19′–85°54′ E. The depth of the lake averages 3.6 m with a maximum depth of 71.55 m (Wang et al., 2010). Shoreline stretches 183 km, with a narrow north-south shoreline and an open east-west shoreline (Wang et al., 2010). The eastern shore of the lake is covered with swamps about 20 km. There are 10 ancient lake shorelines on the north and west banks, with the highest level 100 m higher than current flats, and there are three terraces in the southeast lakeside area. The lake is fed by snow and ice meltwater of the Cuoqin River and the Dalong River. **Figure 1** shows the study area and satellite ground tracks passing through Zhari Namco. Lake basin boundaries are delineated using Shuttle Radar Topography Mission Digital Elevation Model (SRTM DEM).

T/P-Jason1/2/3 Altimetry Data

The altimeter data of T/P-Jason1/2/3 are free to download from the Archiving, Validation, and Interpretation of Satellite Oceanographic (AVISO)[1]. T/P satellite was launched on August 10, 1992, with a repetition period of 10 days. It is the first altimetry satellite of T/P-Jason1/2/3 series missions. T/P Geophysical Data Records (GDRs) are observed along the orbit. Jason-1, as the successor satellite of T/P, was launched in December 2001. Jason-2 was launched in 2008 and Jason-3 in 2016. As the next generation of satellites, their main characteristics (orbit, instrument, observation accuracy, etc.) are consistent with T/P. T/P-Jason1/2/3 missions share the ground track, which can be used to correct inter-satellite bias (Hwang et al., 2016). The Sensor Geophysical Data Record (SGDR) of Jason1/2/3 satellite contains 20 Hz along with orbit sampling data, and also includes waveform data composed of 104 waveform gates with a preset waveform gate of 32.5. Waveform retracking algorithm is used to correct the range of altimeter. The data of overlapped parts between two adjacent satellites are used to adjust the bias between satellites. The altimeter data used in this paper are shown in **Table 1**.

ECMWF Data

Surface pressure and vertical integral of water vapor from ERA-Interim are published by the European Centre for Medium-Range Weather Forecasts (ECMWF)[2]. The two sets of data, with

[1]https://www.aviso.altimetry.fr/

[2]https://www.ecmwf.int/

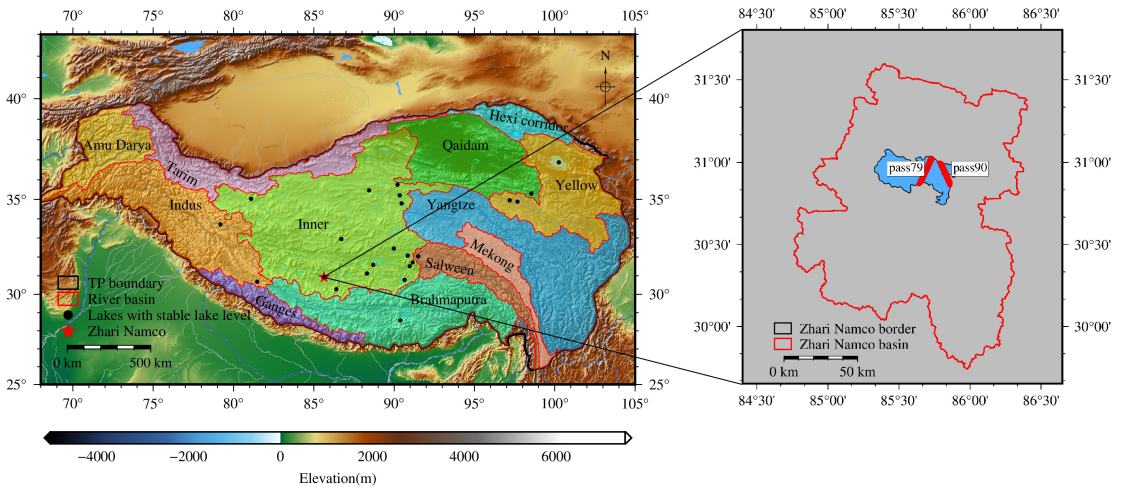

FIGURE 1 | Study area and satellite ground tracks trough Zhari Namco.

a time resolution of 24 h and 6 h, are used to calculate dry troposphere correction (DTC) and wet troposphere correction (WTC), respectively (Wang et al., 2019). Since T/P GDR data do not include WTC in inland areas, the ERA-Interim data should be used to calculate this correction. The data are divided into grids of 0.75°. The geophysical correction for the location of the footprint is calculated using bilinear interpolation.

In situ Gauge Lake Level Data

The lake level observation of Zhari Namco from 2010 to 2017 (Lei et al., 2018) released by the national Tibetan Plateau Data Center (TPDC)[3] is used as a reference to verify the lake level changes of other data sources. Since there is no clear datum, local benchmarks are used (Lei et al., 2017). The lake level is secured by a HOBO level gauge (U20-001-01) installed on the strand, then corrected using the barometer installed on the shore or pressure data of nearby weather stations, and then the real lake level changes are obtained, with the accuracy of less than 0.5 cm. Lake level data are obtained once a day except during glaciation.

G-REALM Lake Levels

Data from other products are compared with observations extracted by the method in this paper. We have searched these databases and found results over Zhari Namco in Global Reservoir and Lake Monitor (G-REALM)[4]. The University of Maryland, are routinely monitoring lake and reservoir height variations for many large lakes around the world (Schwatke et al., 2015). This comprises T/P (1992–2002), Jason-1 (2002–2008), Jason-2 (2008–2016), and Jason-3 (2016 to present). Nowadays, Jason-3 IGDR data are being used for near real-time operational monitoring at a 10-day resolution. ENVISAT products will be extended in time with data from the historical ERS and SARAL missions, and they will be appended with Sentinel-3A measurements which will provide near real-time monitoring at 27-day resolution.

[3]http://data.tpdc.ac.cn/

[4]https://ipad.fas.usda.gov/

TABLE 1 | Statistics of satellite altimeter data used in this study.

Satellite	T/P	Jason-1	Jason-2-	Jason-3
Type	GDR	SGDR	SGDR	SGDR
Cycle name	1–364	1–371	1–327	1–156
Number of cycles	344	350	324	152
Tandem	2002.2.17-2002.7.6	2009.2.8-2012-1.30		2016.6.8-2017.5.6

Hydroweb Lake Levels

Hydroweb is a database built by Laboratoire d'Etudes en Géophysique et Océanographie Spatiales/Equipe Géodesie, Océanographie et Hydrologie Spatiales (Legos/GOHS) in France. The data are publicly available on their web site (http://hydroweb.theia-land.fr/hydroweb), free to use. The Zhari Namco lake levels (1992 to present) are based on data from a combination of satellites: SARAL, T/P, Jason-2/3, ICESat/ICESat-2, and Sentinel-3A. Gravity Recover and Climate Experiment (GRACE) Gravity Model 02 is the datum for Hydroweb lake levels (Crétaux et al., 2011). The lake level accuracy of Zhari Namco in Hydroweb is ∼10 cm.

High-Temporal-Resolution Water Level Data Sets

High-temporal-resolution water level data sets for lakes (HTRWLD) on the Tibetan Plateau (2000–2017) (Li et al., 2019b) are provided free of charge by TPDC (see text footnote 3). This developed data set provides lake level, hypsometric curves, and lake storage changes for 52 large lakes across the TP from 2000 to 2017. *In situ* gauge experiments agree with the theoretical analysis that the uncertainty of the optical water level is 0.1–0.2 m, comparable with that of altimetry water level. Among them, the water level time series of Zhari Namco is from June 10, 2001, to August 28, 2018. The databases are synthesized

from Landsat, ENVISAT, CryoSat-2, and Jason-1/2/3, with elevation benchmarked EGM96 (Li et al., 2019a).

Precipitation and Temperature Data

In section "Water Reserves Inversion," the response of lake level to climate change is further explored by using the "Climate Prediction Center (CPC) Global Unified Gauge-Based Analysis of Daily Precipitation" and "CPC Global Daily Temperature" in the lake basin. CPC Global data are provided free of charge by NOAA/OAR/ESRL PSL, Boulder, CO, United States[5]. This precipitation data set is part of products suite from the CPC Unified Precipitation Project that is underway at NOAA CPC (Chen et al., 2008). This temperature data set is used for verification by NOAA/CPC. The Shepard algorithm is used to grid the data into 0.5°. The daily average temperature can be generated from max and min.

Lake Area

The lakes larger than 1 km^2 in Tibetan Plateau (V2.0) (1970s–2018) data (Zhang, 2019) are publicly released by TPDC (see text footnote 3). Lakes with area greater than 1 km^2 are delineated from Landsat MSS/TM/ETM+/OLI data for the 1970s (1972–1976), but mostly ∼1990, ∼1995, ∼2000, ∼2005, ∼2010, and 2013–2018. The lake boundaries in the 1970s, ∼1990, ∼2000, and ∼2010 are derived from a study that employed visual interpretation (Zhang et al., 2014). To ensure that each lake boundary is precisely delineated, visual checking against the original Landsat images and manual editing of incorrect lake boundaries are also employed (Zhang et al., 2019b).

Equivalent Water Heights

The relationship between high water level and lake water storage is verified. EWH data from the Center for Space Research of the University of Texas[6] RL06M.MSCNv02 EWH data product based on GRACE is distributed to verify the change of water reserves in the region from April 2002 to August 2019 (Watkins et al., 2015). The half-wavelength resolution of GRACE is 3°, and the range of 500 km is delineated to calculate the EWH of Zhari Namco.

Wind Speed Data

China Meteorological Forcing Dataset (CMFD) (1979–2018) (Kun and He, 2019) is a high spatial-temporal resolution gridded near-surface meteorological dataset downloaded from the TPDC (see text footnote 3). Its record starts from January 1979 and keeps extending (currently up to December 2018) with a temporal resolution of 3 h and a spatial resolution of 0.1°. Near-surface meteorological elements are provided in CMFD, including surface pressure, specific humidity, 10-m wind speed, downward shortwave radiation, downward longwave radiation, and precipitation rate (Yang et al., 2010; He et al., 2020).

SRTM DEM

Shuttle radar topography mission digital elevation model on the Tibetan Plateau (2012) (CIAT, 2015) obtained by TPDC (see text footnote 3) are used to extract lake watershed boundaries. This data set is mainly the SRTM terrain data obtained by International Center for Tropical Agriculture (CIAT)with the interpolation algorithm, which better fills the data void of SRTM 90.

River Basins Map Over the TP

The dataset of river basins map over the TP (2016) obtained by TPDC (see text footnote 3) is produced based on the SRTM DEM collected by Space Shuttle Radar terrain mission. There are 12 sub-basins over the Tibet Plateau (**Figure 1**), including Amu Darya, Brahmaputra, Ganges, Hexi Corridor, Indus, Inner, Mekong, Qaidam, Salween, Tarim, Yangtze, and Yellow. The outer boundary is based on the 2500-m contour line (Zhang et al., 2013; Zhang, 2016).

MATERIALS AND METHODS

According to the principle of satellite altimetry, the lake level can be expressed as (e.g., Guo et al., 2010; Hwang et al., 2016),

$$LL = Sat_{Alt} - H_{Alt} - V - N \quad (1)$$

where, LL is lake level, *Sat_Alt* is the altitude of the satellite above the reference ellipsoid, H_ Alt is the range measurement of altimeter after instrument corrections, V is the sum of the corrections, and N is the geoid height at the nadir point derived from a geoid model [EGM2008 in this study (Pavlis et al., 2012; Watkins et al., 2015)]. The corrections in Eq. 1 are shown as,

$$V = \left(WTC + DTC + IC + Set + Pol + RC\right) \quad (2)$$

where, *WTC* is wet troposphere correction; *DTC* is dry troposphere correction; *IC* is ionosphere correction; *Set* is solid earth tide; *Pol* is pole tide, and RC is the range correction from waveform retracking. Solid earth tide and polar tide corrections can be accurately modeled using simulated values. The effects of *RC*, *WTC*, *DTC*, and *IC* on the altimeter range will be further addressed in section "Atmosphere Path Daly Corrections." Compared with the above correction, other geophysical terms (e.g., hydrostatic variations, lake tide, thermal, wind piling-up effect, expansion) have less impact on altimeter range, so they can be ignored when calculating lake level. The observation processing flow of lake level generated by altimeter is shown in **Figure 2**.

Atmosphere Path Daly Corrections

Bias, caused by the use of unsuitable models when combining multiple altimeter observations, is avoided, and atmospheric path delay corrections used in each altimeter product are checked. **Figure 3** shows the atmosphere path delay corrections in the T/P (GDR), Jason-1 (SGDR), Jason-2 (SGDR), and Jason-3 (SGDR) in the Zhari Namco.

Dry troposphere correction is usually calculated from model-assimilated weather data from ECMWF. The standard deviation (STD) of DTC retrieved by T/P (DGR) is 0.017 cm, while that of Jason1/2/3 is 0.011 cm. The DTC of T/P has more noise than

[5]https://psl.noaa.gov/

[6]http://www2.csr.utexas.edu/grace/

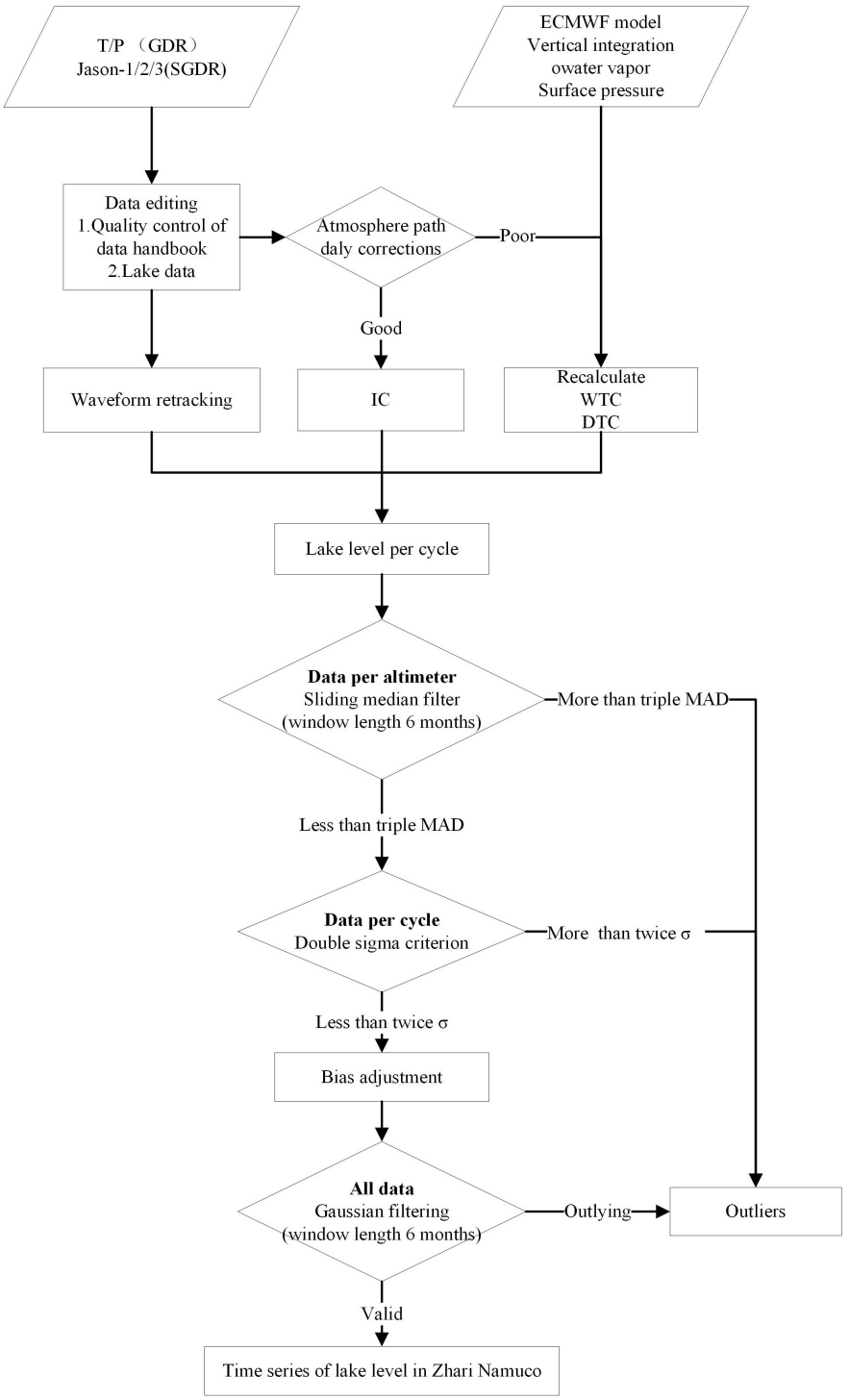

FIGURE 2 | Satellite altimetry processing flow.

that of Jason (**Figure 3A**). The DTC in T/P GDR uses sea level pressure instead of surface pressure, so it has a deviation of 1.06 m compared with Jason (Crétaux et al., 2008). The DTC in Jason-1 SGDR drops by 2.6 cm in 2006, due to the surface pressure deviation correction in the ECMWF model. Based on the above analysis, the ECMWF model is used to recalculate the DTC of T/P (Guo et al., 2012; Gao et al., 2014), which shows excellent consistency.

Radiometer measurements are contaminated by land, so WTC for inland must be recalculated using a numerical weather model.

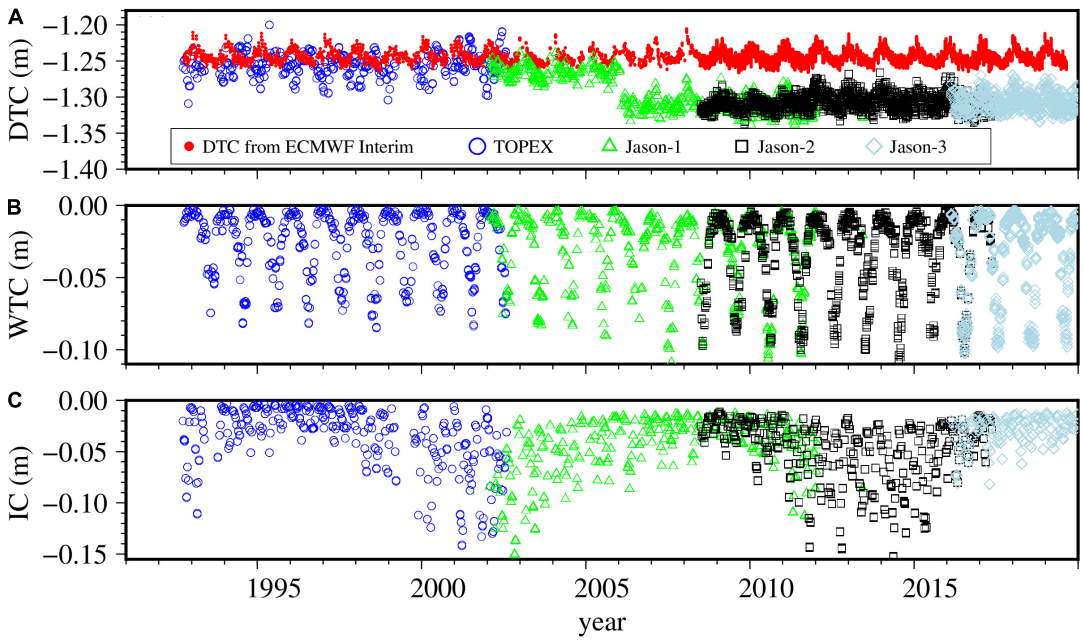

FIGURE 3 | Atmospheric path delay correction of T/P-Jason1/2/3. **(A)** Dry troposphere correction (DTC). **(B)** Wet troposphere correction (WTC). **(C)** Ionosphere correction (IC).

In Jason1/2/3 SGDR, WTC is calculated by ECMWF, but T/P is not given in this zone, which can be recalculated by,

$$\Delta R_{vap} \approx \frac{\beta'_{vap}}{T_{eff}} \int_0^R \rho_{vap}(z)\, dz \approx 6.19 \int_0^R \rho(z)\, dz \qquad (3)$$

where, $\rho_{vap}(z)$ is water vapor density at altitude Z; and R is the maximum height (Hwang et al., 2005). The recalculated WTC in **Figure 3B** shows excellent consistency in the area. In mid-latitude region, the constant $T_{eff} = 6.19\left(cm^3g^{-1}\right)$ is taken based on the empirical value, where $\beta'_{vap} = 1720.6\left(Kcm^3g^{-1}\right)$, $T_{eff} = 278K$, and the integral of $\rho_{vap}(z)$ comes from ECMWF.

The model values derived from the total electron content of the ionospheric correction (IC) are presented in **Figure 3C**. They are extracted from altimeter data products. T/P mission adopts a climatologic model (Bent model), and Global Ionospheric Maps (GIM) for Jason1/2/3 (Ho et al., 1997). Rosy consistency in both models, the IC gathered from the dataset can be used directly.

Waveform Retracking

In addition to geophysical corrections, survey quality is contaminated by land reflection waveforms. These land reflection waveforms cause the failure of the onboard tracker to exploit the accurate distance between the satellite and the bottom surface (Gao et al., 2014). **Figure 4A** shows the Jason-2 waveforms in 2010 over Zhari Namco. These waveforms are complex and seasonal. In winter, the waveforms with an extremely narrow trailing edge are dominant (**Figure 4B**). In summer, the waveforms are more complex, and some waveforms are similar to the ocean waveforms of the Brown model (Ho et al., 1997). In most cases, waveforms are contaminated by land, resulting in an abnormal peak at the trailing edge (**Figure 4C**). Calm lake surface will lead to a mirror wave in summer, and the wave amplitude is larger in winter due to high reflectivity of ice surface.

The wave reflection on the lake deviates from the Brown model, necessitating the retracking of the waveform. In the threshold waveform retracking algorithm, the threshold selection has a significant impact on the result of waveform reset. The commonly used thresholds are 10%, 20%, and 50%. It is found that different thresholds are chosen depending on the reflection conditions in the study area. When the volume scattering plays a dominant role in the waveform shape (e.g., land, ice sheet, etc.), the threshold value is 10%; when the waveform is mainly affected by surface scattering (such as vast water), the 50% threshold can better represent the average surface elevation of radar wave footprint; when volume scattering and surface scattering play a leading role (such as inland lakes, wetlands, and offshore areas), the 20% threshold should be used as a compromise between the two extreme cases (Li et al., 2020). Zhari Namco is an inland lake with an average water depth of 3.6 m (Wang et al., 2010) so Threshold (20%) of waveform weight tracking method is used.

Outlier Detection and Mean Lake Level

TOPEX/Poseidon (GDR) is a product with a sampling frequency of 1 Hz that has three observations per cycle of Zhari Namco. Jason-1/2/3 (SGDR) is a product with a sampling frequency of 20 Hz, with more lake level observations in each cycle. Taking Jason-2 as an example, after eliminating the outliers, the average number of observations per cycle is 36.

Even after waveform retracking and geophysical correction are applied, the lake level is still noisy, so outliers should be eliminated before calculating the mean lake level of each cycle.

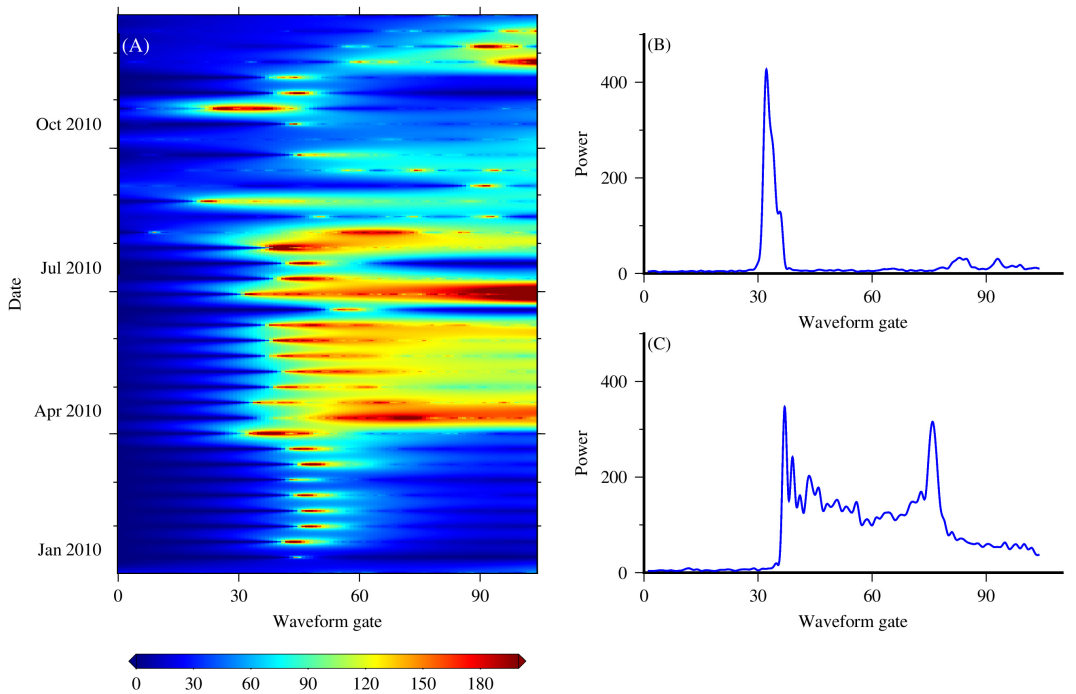

FIGURE 4 | Waveform of Jason-2 altimeter in 2010. **(A)** The annual waveform. **(B)** Typical winter waveform. **(C)** Typical summer waveform.

It is arduous to eliminate all outliers by using a specific method. A two-step outlier detection method based on a sliding median filter and 2σ criterion is used (Okeowo et al., 2017). Here Jason-2 is taken as an example (**Figure 5**). Firstly, a sliding method for determining outliers is repeated for all periods until no more outliers are found. Observations are rejected as outliers, which are greater than three local median absolute deviations (MAD) from the local median over a 6-month-wide window. MAD is defined as,

$$MAD = median(\left|LL_i - median(\mathrm{LL}_i)\right|),\ for\ i = 1,\ 2, \cdots, N \tag{4}$$

where, N is the total number of observations in the window. To obtain accurate lake levels, the second step is to adopt a more strict outliers detection standard. The 2σ criterion is repeatedly used in the observation of each cycle, i.e., the lake level more than twice the root mean square (RMS) error in each cycle is determined as the outlier and removed. The lake level STD of 83% cycles (**Figure 5**) is less than 0.15 m. The rejected outliers account for 37% of the total Jason-2 data, of which 78% can be eliminated by moving MAD. After eliminating outliers, the mean lake level is estimated for each cycle to construct the sequence.

Bias Adjustment

Bias adjustment refers to the systematic deviation between altimeters. In the fusion process of multiple altimeters, the observation data of each altimeter cannot be connected accurately, which needs to be adjusted to form a continuous time series. The bias adjustment is of great significance to the construction of time series with multi-mission data (Vu et al., 2018). Assuming that a lake is a wide plain, the lake height LL_j^A observed by altimeter A should be equal to the lake height LL_j^B observed by altimeter B at the same epoch t_j. However, their difference,

$$\Delta_j = LL_j^A - LL_j^B,\ for\ j = 1, 2, \cdots, N \tag{5}$$

is not equal to zero due to the bias and noise. N is the observations numbers of paired samples in the overlapping cycle of two missions. The bias can be determined by using synchronous data between two missions. Usually, two satellites do not overfly the lake at the same time. Interpolation is needed for the compute of differences, which may lead to interpolation error. The change of lake surface in a short period can be ignored in tandem missions (a flight mode for two satellites) setup of T/P-Jason1/2/3. The difference can be calculated directly.

The tandem flight of T/P-Jason1/2/3 missions makes overlapping observations between two sequential satellites for inter-satellite calibration (Gao et al., 2014). Due to the lack of overlapping data, the bias between T/P and Jason-1 uses observations at intervals of less than 30 days. The adjustment of the bias between Jason-1/2/3 uses lake level data with a time interval between the two altimeters of less than 5 days. Over the Zhari Namco, 10 paired-sample observations are found in the overlap between T/P and Jason-1. For Jason-1 and Jason-2, 57 paired-sample observations are retrieved. For Jason-2 and Jason-3, 20 paired-sample observations are searched.

The bias of Jason-1 with respect to T/P is 66.1 cm. Jason-2 has a mean lake level bias of 19.4 cm with respect to Jason-1. The bias of Jason-3 with respect to Jason-2 is −16.9 cm. Finally, all biases of Jason-1/2/3 with respect to T/P are tabulated in **Table 2**.

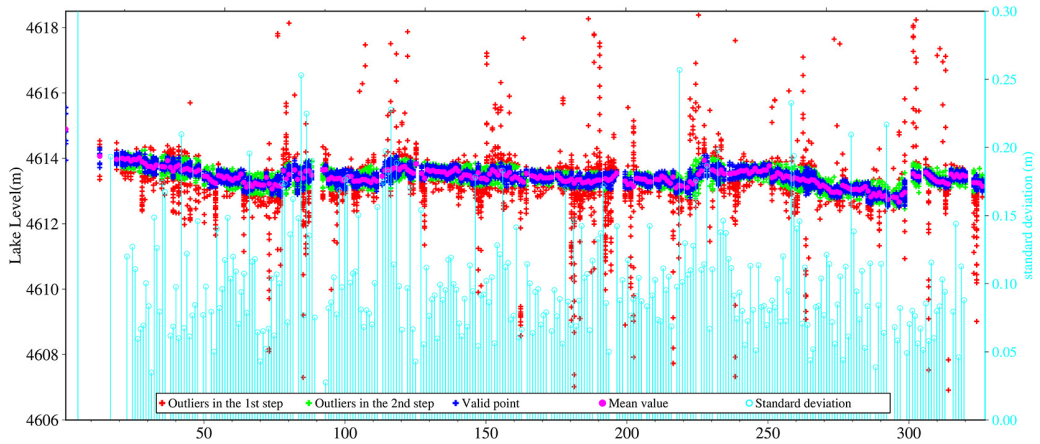

FIGURE 5 | Example of outlier detection in the case of Jason-2 observations over Zhari Namco.

RESULTS AND ANALYSIS

For the T/P-Jason1/2/3 missions from October 1992 to August 2019, the consistency of atmosphere path delay correction of each altimeter data is checked, and the corrections are recalculated. According to the waveform combined with the surface type, waveform corrections are calculated. From Eq. 1, abnormal lake levels are eliminated by a two-step method, then the average value of lake level in each cycle is obtained. After adjusting the bias between altimeters, the 27-year time series of lake level in Zhari Namco is generated with Gaussian filtering. Zhari Namco's lake level rose by $\sim$ 5.7 m from 1992 to 2019, with an overall trend of 0.13 ± 0.02 m/yr, showing a fluctuating rate (1992–1999: -0.25 ± 0.05 m/yr, 2000–2008: 0.26 ± 0.04 m/yr, 2009–2016: -0.05 ± 0.03 m/yr, 2017–2019: 1.34 ± 0.34 m/yr). In this section, temperature, precipitation, EWH, and lake area are used to further confirm the change of lake levels.

Altimeter-Derived Lake Level Accuracy

Figure 6A shows the lake levels derived from T/P, Jason-1, Jason-2, and Jason-3. Jason-2, with effective observation in 285 cycles in Zhari Namco, is the altimeter with the most data extracted from four satellites. Jason-2 has an average of 36 observations per cycle. The average STD of each Jason-2 cycle is 10.8 cm. 284 of Jason-2's 285 cycles have an STD of less than 30.0 cm, so 30.0 cm is used as the threshold of other altimeters data. T/P data are more unstable, and the maximum STD reaches nearly 90.0 cm. The reason is that T/P data have not been retracked and the amount of GDRs is relatively small. **Figures 6B–E** shows the distribution of STD for T/P-Jason1/2/3 altimeters, and it can be found that these STDs are normally distributed. They expectation (μ) and standard deviation (σ) are stable.

Wind speed (when the altimeter track passed) and the STD of lake levels are plotted in **Figure 6F**. In theory, wind can control water waves on lake surface, and further influence the lake level precisely. The correlation coefficient (CC) between wind speed and water level STD is -0.045, hence there is no significant correlation between them. The possible reasons are as follows: Surface wave field and wind surface roughness are approximately homogeneous within the proper satellite footprint (Fu and Cazenave, 2001). The lake level is obtained from the average distance measured by an altimeter in the footprint (Diameter $\sim$2.2 km). Besides, waveform retracking weakens the influence of complex waveforms. The effect of wind speed is small and hence ignored.

The results show that the accuracy of lake level in summer is lower than that in winter. In particular, the average STD of Jason-2 is 10.6 cm in July and August, and 10.2 cm in January and February. First of all, the complex shape of summer waveform reduces the accuracy of waveform retracking, and a more accurate waveform purification algorithm [automatically identify altimetry measurements corresponding to open water, ice and transition (Ziyad et al., 2020)] can improve the quality. Secondly, the change of lake boundary is not taken into account in the data screening process. A static coastline is used in the screening process, and some land observations are extracted, especially when lake level is low (e.g., T/P altimeter). The reduction of the lake area also makes satellite observations noisier, which is one of the reasons for the poor quality of T/P data. The establishment of a time-varying lakeshore model is strenuous, which requires satellite images and other sources. Therefore, a process for outlier removal is often used, instead of using dynamic shorelines.

TABLE 2 | Biases of Jason-1/2/3 with respect to T/P.

Satellite	Jason-1	Jason-2	Jason-3
Number of paired-samples	10	57	20
Bias (m)	0.534	0.728	0.559

Time Series of Lake Level

Before generating the time series of lake level, there are still some abnormal values and the time interval is inconsistent. Firstly, the remote observations larger than 2σ are removed from the observations after the bias adjustment, and then the missing

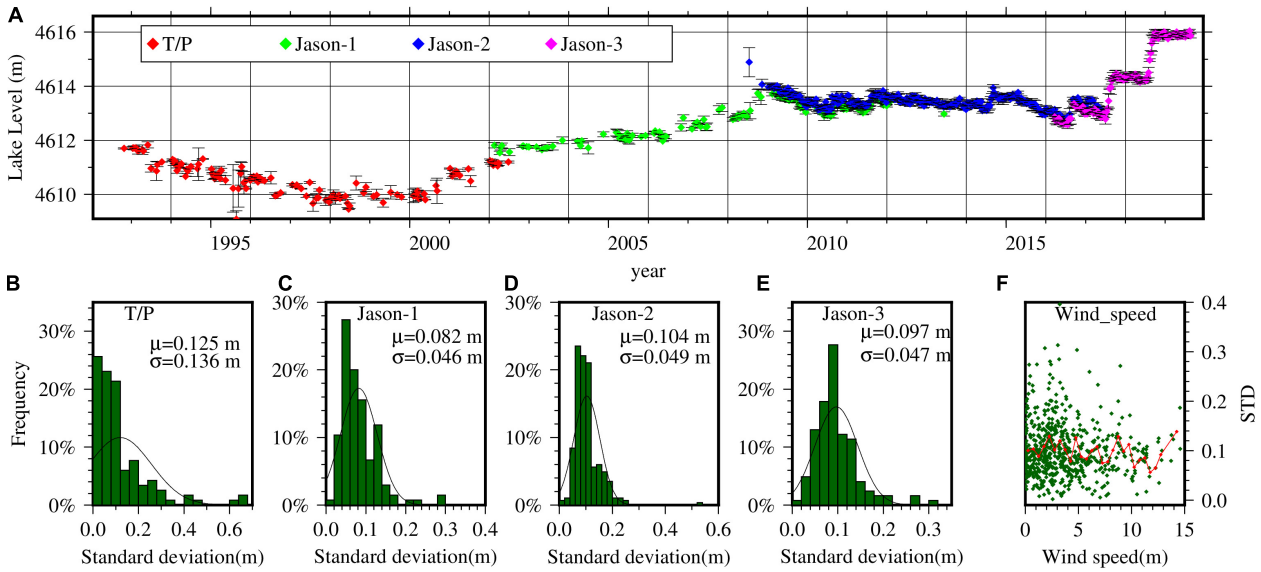

FIGURE 6 | Mean lake level derived from various satellites and histograms of their STDs. **(A)** Mean lake level; **(B)** TOPEX/Poseidon; **(C)** Jason-1; **(D)** Jason-2; **(E)** Jason-3; **(F)** The relationship between wind speed and STD.

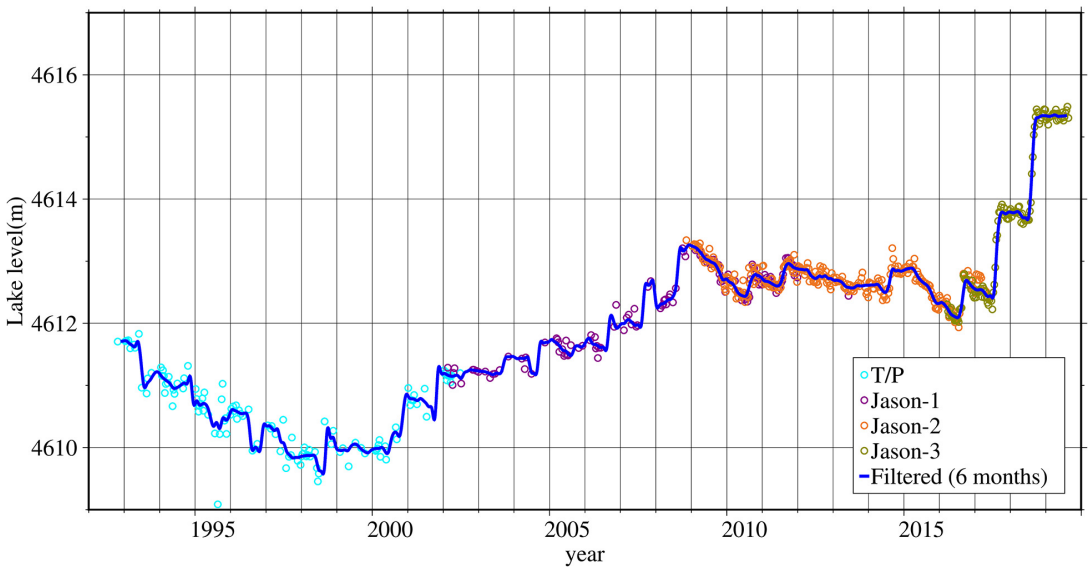

FIGURE 7 | Time series of lake level in Zhari Namco.

data are linearly interpolated. Gaussian filtering is performed to generate a uniform and continuous sequence. The time series filtered with a 12-month window is too smooth, with intra-annual amplitudes dramatically attenuated. The results with a 3-month and a 6-month window length are rather similar, both keep in energy very well. Relatively, the former has more small spikes than the latter (Wang et al., 2019). Therefore, the 6-month-wide filter window is used.

According to the time series (see **Figure 7**), the lake level in Zhari Namco decreased before 1999, showing a negative growth trend of −0.25 m/yr, and continued to rise after 1999. After December 2008, the rising trend changed, and the lake level continued to decline slowly in the next 8 years. It is worth noting that the lake level rose by 1.3 m and 1.6 m, respectively, from June to November 2017 and July to November 2018. In the 20 years from 1999 to 2019, the lake level in Zhari Namco rose by ∼ 5.7 m. The average rising rate of lake level is 0.14 m/yr in the 27 years from 1992 to 2019.

Comparison With Other Databases

Figure 8 shows lake level changes in this study, G-REALM, HTRWLD, Hydroweb, and *in situ* gauge data. In the Jason-1

period, about 60% of the data in HTRWLD come from Landsat and ENVISAT. More valid values are collected by our method in the Jason-1 observation, while G-REALM has rarely valid values in the same task.

The data of other lake level products and *in situ* gauge data in the corresponding period (May 2010 – July 2017) are intercepted. The altimeter-derived lake level is discontinuous due to the elimination of outliers, and *in situ* gauge data show vacancy during the icing period. In the first step, the relative lake level is obtained by subtracting the average value of each data. In the second step, the 30-day series is obtained by linear interpolation. In the third step, Gaussian filtering with a window length of 6 months is carried out for each database, and the results are shown in **Figure 9**. **Table 3** tabulates the statistical results. In order to prove that the lake level change of Zhari Namco in this study can best represent the real lake level change, we regard the *in situ* gauge lake level as the true value. Max, min, STD, RMS, and CC are calculated when comparing the quality of lake level data from different databases. The difference between this study and *in situ* gauge is the most stable (STD is the smallest), the deviation from the true value is the smallest (RMS is the smallest), and our data have the highest correlation with real lake level

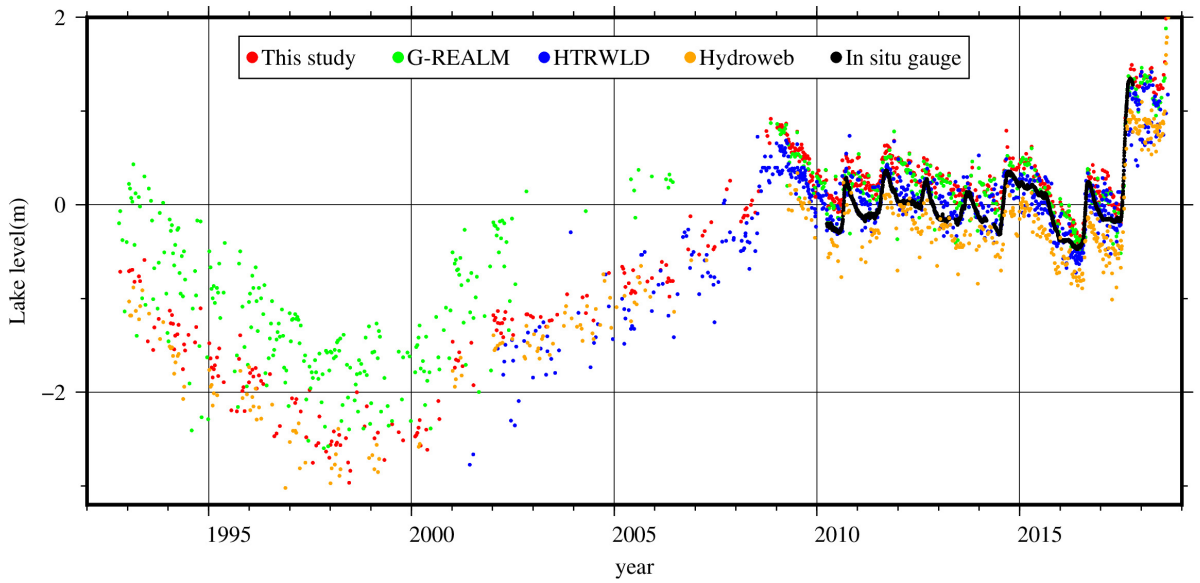

FIGURE 8 | Lake level time series of Zhari Namco from this study, G-REALM, HTRWLD, Hydroweb, and *in situ* gauge data.

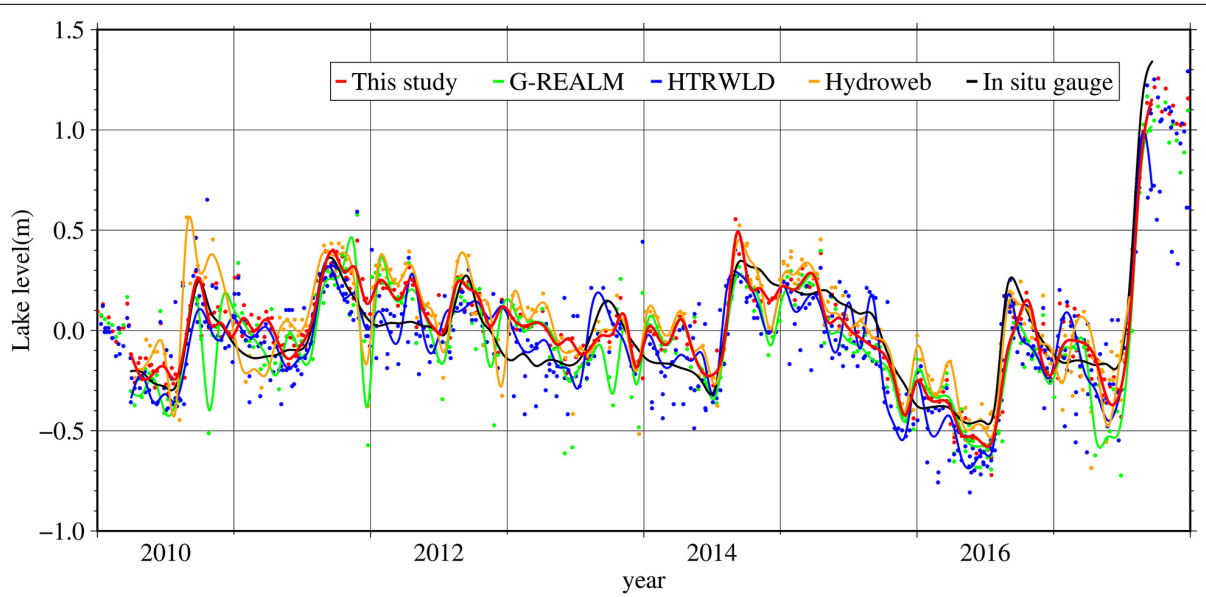

FIGURE 9 | Lake level changes of the four databases corresponding to *in situ* gauge data.

TABLE 3 | Comparative statistics of lake level in Zhari Namco from different databases.

Product	Max (cm)	Min (cm)	Mean (cm)	STD (cm)	RMS (cm)	CC
In situ gauge – this study	24.4	−31.8	−1.6	11.9	12.0	0.90
In situ gauge – G-REALM	27.1	−50.5	−4.7	17.2	17.8	0.80
In situ gauge – HTRWLD	23.9	−63.0	−4.7	13.4	14.2	0.87
In situ gauge – Hydroweb	54.4	−134	−2.9	24.7	24.9	0.79

changes (CC is the largest). Our strategy yields the most plausible sequence of lake levels.

Water Reserves Inversion

Figure 10 shows the EWH time series of Zhari Namco detected by GRACE within 500 km from April 2002 to August 2019. EWH rose sharply in 2018, and the lake level also rose about 1.6 m in the same period. EWH has increased at a rate of 0.42 ± 0.10 cm/yr, and the rising rate of altimeter-derived lake level in Zhari Namco is 14.7 ± 0.03 cm/yr since 2002. The deviation between lake level and EWH is caused by different resolutions. Hence, the relationship between water volume and lake level monitored by GRACE needs to be further analyzed in combination with multi-source satellite data and hydrological model in the future (Guo et al., 2016).

Lake Area

The lake area of Zhari Namco has increased from 961.3 km^2 in 1995 to 1046.3 km^2 in 2018 owing to increased lake level (**Figure 11**; Zhang et al., 2019b). This is in accord with the change of lake level observed by altimetry. Due to the influence of the replenishing river, the slope of the west side of the lake is slow, and lake shoreline changes obviously. In 1995, the east lakeshore had an obvious inward zigzag coastline, flooded by water and moving outward in 2010. The lake area is consistent with the change of lake level. When the water level rose sharply in 2017 and 2018, the lake area also surged. It is enough to confirm the changing pattern of lake level.

Temperature and Precipitation Associated With Lake Level Tendency

The annual mean air temperature between 1992 and 2018 obtained from CPC on the Zhari Namco basin is 0.049°C, in accord with the average temperature change in the TP (Zhang et al., 2020). Overall, the accelerated warming in the TP has led to rapid glacier retreat, snowmelt, and permafrost degradation (Bolch et al., 2019), affecting the water resources of TP. However, the relation between temperature and water reserves is complex. Warming and wetting since 1998 have created a more volatile atmosphere, triggering more deep convection and hence more precipitation (Yang et al., 2012).

Precipitation can plausibly explain the long-term trend of lake evolution and spatial patterns. Water balance of the Inner-TP lake is evaluated Inner-TP, and the results show that increased precipitation contributes to the dominant fraction of lake volume increase (∼74%), followed by glacier mass loss (∼13%), and permafrost thawing (∼12%) (Zhang et al., 2020). **Figure 11** is the precipitation data of Zhari Namco basin, which shows that the increase of precipitation is the main reason for the rise of lake level after 1998. Nearby weather stations have also recorded increased precipitation in the area since late 1990 (Zhang et al., 2017; Du et al., 2019). The lake level from 2010 to 2015 is quite stable, which is also evident in Qinghai Lake

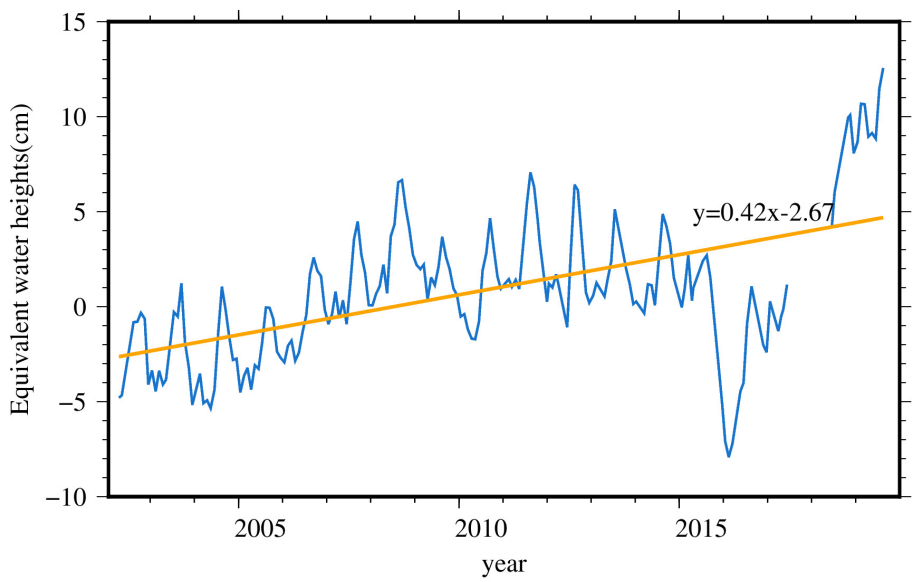

FIGURE 10 | EWH time series.

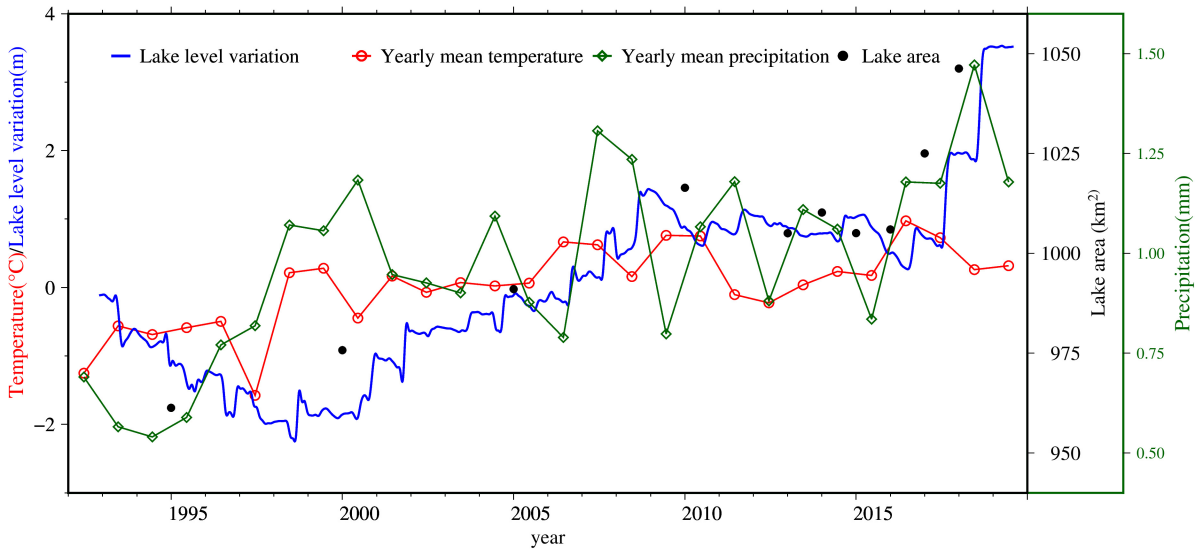

FIGURE 11 | Variation of temperature, precipitation, lake level and area in Zhari Namco.

(Zhang et al., 2019a) and other lakes (**Figure 1**) within TP (Zhang et al., 2020). These lakes are mainly located at the edges of the inner TP. During this period, there is no strong El Niño (Lei et al., 2019) and precipitation is stable. The clear inflection of lake level changes that occurred in 2015/2016 can be attributed to strong El Niño events (Zhang et al., 2020). There is a time lag between lake level change and precipitation (Lei et al., 2019). While precipitation increased in 2016, the lake level did not rise significantly until 2017.

According to the *in situ* gauge data, Dagze Co, located about 180 km away in the northeast of Zhari Namco, decreases by 2 m from 1976 to 1999 and increased by 8.2 m from 1999 to 2010 (Lei et al., 2014). The results are consistent with the lake level changes retrieved by the altimeter in Zhari Namco. The super El Niño event in 2015/2016 may lead to an abnormal change of lake level in the TP. After the end of the El Niño event, the inland lakes of the TP expanded rapidly. Especially in 2017, the lake rise was rare for many years. It is found that the seasonal fluctuation of lake level is between 0.3 and 0.6 m in normal years in Zhari Namco. However, in summer 2015, the lake level did not rise, but on the contrary, decreased slightly. Even so, the lake water rose 0.6 m in summer 2016 after El Niño and rose sharply to 1.6 m in 2017 (Lei et al., 2019), which is consistent with the trend in lake level retrieved by satellites in this study. Although the seasonal variations of precipitation, temperature, lake level, and lake area are consistent, the quantitative relationship between each factor and the water budget needs further survey.

CONCLUSION

Zhari Namco is one of the few Tibetan lakes which have been continually monitored by satellite altimeters for more than 25 years. Due to the rugged terrain and changeable environment, it is more difficult for altimeter to monitor its lake level. A robust strategy is used to generate the time series of lake levels using multi-mission data. Before merging multiple altimeters data, the consistency of geophysical corrections should be examined. For dry troposphere correction, there is a variance of about 1 m in TOPEX/Poseidon (T/P) and 2.6 cm in Jason-1. The surface pressure data from ECMWF are used to recalculate DTC. The reflection waveforms of the lake are polluted by land, and the front edge of the waveform deviates from the theoretical tracking point seriously. The threshold 20% algorithm is used for waveform retracking. The method of moving median filter and 2σ criterion is used to remove outliers. This method has good performance without any prior information. Bias adjustment is an essential step in the fusion of multi-source altimeters. Bias is estimated by paired observation samples, such as T/P and Jason-1, Jason-2, and Jason-3.

TOPEX/Poseidon-Jason1/2/3 observations are used to extract lake level time series from 1992 to 2019. During the 27 years, the average rising speed of lake level is 0.14 ± 0.01 m/yr. The mean standard deviation (STD) of observations from TOPEX/Poseidon-Jason1/2/3 (T/P-Jason1/2/3) is 10.1 cm. Compared with previous studies and existing database products, our method yields sequences with the best observational quality and the longest continuous monitoring. Continuous lake level can be provided by the running Jason-3 and the upcoming follow-up task Jason- CS. Precipitation is the main factor affecting the variation of lake level, and the future climate is predicted to be even warmer and moister, hence it is predicted that lake area and level in Zhari Namco will continue to rise in the near term.

DATA AVAILABILITY STATEMENT

The datasets presented in this study can be found in online repositories. The names of the repository/repositories

and accession number(s) can be found in the article/ supplementary material.

AUTHOR CONTRIBUTIONS

XL and JG: the study design. MS: data processing and manuscript writing. JG, XL, JY, HW, and CL: data collection and scientific analysis. All authors contributed to the article and approved the submitted version.

FUNDING

This study was supported by the National Natural Science Foundation of China (Grant Nos. 41774001 and 41374009), Autonomous and Controllable Special Project for Surveying and Mapping of China (Grant No. 816-517), and the SDUST Research Fund (Grant No. 2014TDJH101).

ACKNOWLEDGMENTS

We would like to acknowledge the Archiving, Validation, and Interpretation of Satellite Oceanographic (AVISO) providing the T/P Geophysical Data Record (GDRs) and the Jason-1/2/3 sensor data record (SGDR) (https://www.aviso.altimetry.fr/), and European Centre for Medium-Range Weather Forecasts (ECMWF) providing for surface pressure and vertical integral of water vapor data (https://apps.ecmwf.int/datasets/data/interim-full-daily/levtype=sfc/), the National Tibetan Plateau Data Center (TPDC) (https://data.tpdc.ac.cn/) providing for China Meteorological Forcing Dataset (CMFD) (1979–2018), SRTM DEM data on the Tibetan Plateau (2012), dataset of river basins map over the TP (2016), high-temporal-resolution water level data sets for lakes (HTRWLD) on the Tibetan Plateau during (2000–2017), and the lake surface area dynamics on the Tibetan Plateau (Version 1.0) (1984–2016). The United States Department of Agriculture's Foreign Agricultural Service (USDA-FAS) providing for Global Reservoir and Lake Monitor (G-REALM) data (https://ipad.fas.usda.gov/cropexplorer/global_reservoir/gr_regional_chart.aspx?regionid=che&reservoir_name=Cha-jih), Hydroweb data from LEGOS/GOHS are obtained at http://hydroweb.theia-land.fr/hydroweb. The CPC Global Unified Gauge-Based Analysis of Daily Precipitation and CPC Global Daily Temperature data provided by the NOAA/OAR/ESRL PSL, Boulder, CO, United States (https://psl.noaa.gov/data/gridded/), the Center for Space Research of the University of Texas providing for the RL06M.MSCNv02 equivalent water height data (http://www2.csr.utexas.edu/grace/RL06_mascons.html).

REFERENCES

Bolch, T., Shea, J. M., Liu, S., Azam, F. M., Gao, Y., Gruber, S., et al. (2019). *Status and Change of the Cryospherein the Extended Hindu Kush HimalayaRegion*. The Salmon Tower Building, NY: Springer International Publishing.

Chen, M., Shi, W., Xie, P., Silva, V. B. S., Kousky, V. E., Wayne, H. R., et al. (2008). Assessing objective techniques for gauge-based analyses of global daily precipitation. *J. Geophys. Res.* 113:D04001. doi: 10.1029/2007jd009132

CIAT (2015). *SRTM DEM data on the Tibetan Plateau (2012)*. Cali: CIAT. doi: 10.11888/Geogra.tpdc.270486

Crétaux, J. F., Arsen, A., Calmant, S., Kouraev, A., Vuglinski, V., Bergé-Nguyen, M., et al. (2011). SOLS: a lake database to monitor in the Near Real Time water level and storage variations from remote sensing data. *Adv. Space Res.* 47, 1497–1507. doi: 10.1016/j.asr.2011.01.004

Crétaux, J.-F., Calmant, S., Romanovski, V., Shabunin, A., Lyard, F., Bergé-Nguyen, M., et al. (2008). An absolute calibration site for radar altimeters in the continental domain: Lake Issykkul in Central Asia. *J. Geod.* 83, 723–735. doi: 10.1007/s00190-008-0289-7

Du, W., Liu, X., Guo, J., Shen, Y., Li, W., and Chang, X. (2019). Analysis of the melting glaciers in Southeast Tibet by ALOS-PALSAR data. *Terrestr. Atmosph. Ocean. Sci.* 30, 7–19. doi: 10.3319/tao.2018.07.09.03

Fu, L.-L., and Cazenave, A. (2001). *Satellite Altimetry and Earth Sciences: A Handbook of Techniques and Applications*. Magarpatta: A Harcourk Science and Technology Company.

Gao, L., Hao, L., and Chen, X. (2014). Evaluation of ERA-interim monthly temperature data over the Tibetan Plateau. *J. Mount. Sci.* 11, 1154–1168. doi: 10.1007/s11629-014-3013-5

Gao, L., Liao, J., and Shen, G. (2013). Monitoring lake-level changes in the Qinghai-Tibetan Plateau using radar altimeter data (2002-2012). *J. Appl. Remote Sens.* 7:073470. doi: 10.1117/1.Jrs.7.073470

Guo, J., Mu, D., Liu, X., Yan, H., Sun, Z., and Guo, B. (2016). Water storage changes over the tibetan plateau revealed by GRACE mission. *Acta Geophys.* 64, 463–476. doi: 10.1515/acgeo-2016-0003

Guo, J., Sun, J., Chang, X., Guo, S., and Liu, X. (2011). Correlation analysis of NINO3.4 SST and inland lake level variations monitored with satellite altimetry: case studies of lakes hongze, Khanka, La-ang, Ulungur, Issyk-kul and Baikal. *Terrestr. Atmosph. Ocean. Sci.* 22, 203–213. doi: 10.3319/TAO.2010.09.17.01(TibXS)

Guo, J., Sun, J., Chang, X., and Liu, X. (2010). Water level variation of bosten lake monitored with TOPEX/poseidon and Its correlation with NINO3 SST. *Acta Geodaet. Cartogr. Sin.* 39, 221–226. doi: 10.1051/jphyscol:1989560

Guo, J., Yang, L., Liu, X., Hwang, C., and Yang, H. (2012). On temporal-spatial distribution of backscatter coefficients over China determined by TOPEX/Poseidon mission. *Sci. China Earth Sci.* 55, 2068–2083. doi: 10.1007/s11430-012-4524-y

He, J., Yang, K., Tang, W., Lu, H., Qin, J., Chen, Y., et al. (2020). The first high-resolution meteorological forcing dataset for land process studies over China. *Sci. Data* 7, 25–35. doi: 10.1038/s41597-020-0369-y

Ho, C. M., Wilson, B. D., Mannucci, A. J., Lindqwister, U. J., and Yuan, D. N. (1997). A comparative study of ionospheric total electron content measurements using global ionospheric maps of GPS, TOPEX radar and the bent model. *Radio Sci.* 32, 1499–1512. doi: 10.1029/97rs00580

Hwang, C., Cheng, Y.-S., Han, J., Kao, R., Huang, C.-Y., Wei, S.-H., et al. (2016). Multi-decadal monitoring of lake level changes in the Qinghai-tibet plateau by the TOPEX/poseidon-family altimeters: climate implication. *Rem. Sens.* 8, 446–467. doi: 10.3390/rs8060446

Hwang, C., Peng, M.-F., Ning, J., Luo, J., and Sui, C.-H. (2005). Lake level variations in China from TOPEX/Poseidon altimetry: data quality assessment and links to precipitation and ENSO. *Geophys. J. Int.* 161, 1–11. doi: 10.1111/j.1365-246X.2005.02518.x

Jiang, L., Nielsen, K., Andersen, O., and Bauer-Gottwein, P. (2017). Monitoring recent lake level variations on the Tibetan Plateau using CryoSat-2 SARIn mode data. *J. Hydrol.* 544, 109–124. doi: 10.1016/j.jhydrol.2016.11.024

Kleinherenbrink, M., Lindenbergh, R., and Ditmar, P. (2015). Monitoring of lake level changes on the Tibetan Plateau and Tian Shan by retracking Cryosat SARIn waveforms. *J. Hydrol.* 521, 119–131. doi: 10.1016/j.jhydrol.2014.11.063

Kun, Y., and He, J. (2019). *China Meteorological Forcing Dataset (1979-2018)*. Beijing: National Tibetan Plateau Data Center. doi: 10.11888/AtmosphericPhysics.tpe.249369.file

Lee, H., Shum, C., Tseng, K., Guo, J., and Kuo, C. (2011). Present-day lake level variation from envisat altimetry over the northeastern qinghai-tibetan plateau:

links with precipitation and temperature. *Terrestr. Atmospher. Ocean. Sci.* 22, 169–175. doi: 10.3319/TAO.2010.08.09.01(TibXS)

Lei, Y., Yang, K., Wang, B., Sheng, Y., Bird, B. W., Zhang, G., et al. (2014). Response of inland lake dynamics over the Tibetan Plateau to climate change. *Clim. Change* 125, 281–290. doi: 10.1007/s10584-014-1175-3

Lei, Y., Yao, T., and Yang, K. (2018). *The Water Level Observation of Lakes on the Tibetan Plateau (2010-2017)*. Beijing: National Tibetan Plateau Data Center. doi: 10.11888/Hydrology.tpe.249464.db

Lei, Y., Yao, T., Yang, K., Sheng, Y., Kleinherenbrink, M., Yi, S., et al. (2017). Lake seasonality across the Tibetan Plateau and their varying relationship with regional mass changes and local hydrology. *Geophys. Res. Lett.* 44, 892–900. doi: 10.1002/2016gl072062

Lei, Y., Zhu, Y., Wang, B., Yao, T., Yang, K., Zhang, X., et al. (2019). Extreme lake level changes on the tibetan plateau associated with the 2015/2016 El Niño. *Geophys. Res. Lett.* 46, 5889–5898. doi: 10.1029/2019gl081946

Li, X., Long, D., Huang, Q., Han, P., Zhao, F., and Wada, Y. (2019a). High-temporal-resolution water level and storage change data sets for lakes on the Tibetan Plateau during 2000-2017 using multiple altimetric missions and Landsat-derived lake shoreline positions. *Earth Syst. Sci. Data* 11, 1603–1627. doi: 10.5194/essd-11-1603-2019

Li, X., Long, D., Huang, Q., Han, P., Zhao, F., and Wada, Y. (2019b). *High-Temporal-Resolution Water Level and Storage Change Data Sets For Lakes on the Tibetan Plateau During 2000-2017*. London: PANGAEA. doi: 10.1594/PANGAEA.898411

Li, Z., Liu, X., Guo, J., Yuan, J., Niu, Y., and Ji, B. (2020). A new method of satellite radar altimeter waveform retracking based on waveform derivative. *Rev. Int. Métodos Numér. Para Cálculo Dis. Ingen.* 36, 1–4. doi: 10.23967/j.rimni.2020.10.002

Ma, R., Yang, G., Duan, H., Jiang, J., Wang, S., Feng, X., et al. (2010). China's lakes at present: number, area and spatial distribution. *Sci. China Earth Sci.* 54, 283–289. doi: 10.1007/s11430-010-4052-6

Okeowo, M., Lee, H., Hossain, F., and Getirana, A. (2017). Automated generation of lakes and reservoirs water elevation changes from satellite radar altimetry. *Ieee J. Select. Topics Appl. Earth Observat. Remote Sens.* 10, 3465–3481. doi: 10.1109/jstars.2017.2684081

Pavlis, N. K., Holmes, S. A., Kenyon, S. C., and Factor, J. K. (2012). The development and evaluation of the Earth gravitational model 2008 (EGM2008). *J. Geophys. Res. Solid Earth* 117:B04406. doi: 10.1029/2011jb008916

Phan, V., Lindenbergh, R., and Menenti, M. (2012). ICESat derived elevation changes of Tibetan lakes between 2003 and 2009. *Int. J. Appl. Earth Observat. Geoinform.* 17, 12–22. doi: 10.1016/j.jag.2011.09.015

Schwatke, C., Dettmering, D., Bosch, W., and Seitz, F. (2015). DAHITI – an innovative approach for estimating water level time series over inland waters using multi-mission satellite altimetry. *Hydrol. Earth Syst. Sci.* 19, 4345–4364. doi: 10.5194/hess-19-4345-2015

Song, C., Huang, B., Ke, L., and Richards, K. (2014). Seasonal and abrupt changes in the water level of closed lakes on the Tibetan Plateau and implications for climate impacts. *J. Hydrol.* 514, 131–144. doi: 10.1016/j.jhydrol.2014.04.018

Vu, P., Frappart, F., Darrozes, J., Marieu, V., Blarel, F., Ramillien, G., et al. (2018). Multi-Satellite altimeter validation along the french atlantic coast in the southern bay of biscay from ERS-2 to SARAL. *Remote Sens.* 10, 93–125. doi: 10.3390/rs10010093

Wang, H., Chu, Y., Huang, Z., Hwang, C., and Chao, N. (2019). Robust, long-term lake level change from multiple satellite altimeters in tibet: observing the rapid rise of ngangzi co over a New Wetland. *Remote Sens.* 11:558. doi: 10.3390/rs11050558

Wang, J., Peng, P., Ma, Q., and Zhu, L. (2010). Modem limnological features of Tangra Yumco and Zhari Namco, Tibetan Plateau. *J. Lake Sci.* 22, 629–632. doi: 10.18307/2010.0422

Watkins, M. M., Wiese, D. N., Yuan, D.-N., Boening, C., and Landerer, F. W. (2015). Improved methods for observing Earth's time variable mass distribution with GRACE using spherical cap mascons. *J. Geophys. Res. Solid Earth* 120, 2648–2671. doi: 10.1002/2014jb011547

Yang, K., Ding, B., Qin, J., Tang, W., Lu, N., and Lin, C. (2012). Can aerosol loading explain the solar dimming over the Tibetan Plateau? *Geophys. Res. Lett.* 39:L20710. doi: 10.1029/2012gl053733

Yang, K., He, J., Tang, W., Qin, J., and Cheng, C. C. K. (2010). On downward shortwave and longwave radiations over high altitude regions: observation and modeling in the Tibetan Plateau. *Agricult. Forest Meteorol.* 150, 38–46. doi: 10.1016/j.agrformet.2009.08.004

Zhang, G. (2016). *Dataset of River Basins Map Over the TP(2016)*. Beijing: National Tibetan Plateau Data Center. doi: 10.11888/BaseGeography.tpe.249465.file

Zhang, G. (2019). *The Lakes Larger Than 1km^2 in Tibetan Plateau (V2.0) (1970s-2018)*. Beijing: National Tibetan Plateau Data Center. doi: 10.11888/Hydro.tpdc.270303

Zhang, G., Chen, W., and Xie, H. (2019a). Tibetan Plateau's Lake level and volume changes from NASA's ICESat/ICESat−2 and landsat missions. *Geophys. Res. Lett.* 46, 13107–13118. doi: 10.1029/2019gl085032

Zhang, G., Luo, W., Chen, W., and Zheng, G. (2019b). A robust but variable lake expansion on the Tibetan Plateau. *Sci. Bull.* 64, 1306–1309. doi: 10.1016/j.scib.2019.07.018

Zhang, G., Xie, H., Kang, S., Yi, D., and Ackley, S. F. (2011). Monitoring lake level changes on the Tibetan Plateau using ICESat altimetry data (2003–2009). *Remote Sens. Environ.* 115, 1733–1742. doi: 10.1016/j.rse.2011.03.005

Zhang, G., Yao, T., Piao, S., Bolch, T., Xie, H., Chen, D., et al. (2017). Extensive and drastically different alpine lake changes on Asia's high plateaus during the past four decades. *Geophys. Res. Lett.* 44, 252–260. doi: 10.1002/2016gl072033

Zhang, G., Yao, T., Xie, H., Kang, S., and Lei, Y. (2013). Increased mass over the Tibetan Plateau: from lakes or glaciers? *Geophys. Res. Lett.* 40, 2125–2130. doi: 10.1002/grl.50462

Zhang, G., Yao, T., Xie, H., Yang, K., Zhu, L., Shum, C. K., et al. (2020). Response of tibetan plateau lakes to climate change: trends, patterns, and mechanisms. *Earth Sci. Rev.* 208, 103269–103291. doi: 10.1016/j.earscirev.2020.103269

Zhang, G., Yao, T., Xie, H., Zhang, K., and Zhu, F. (2014). Lakes' state and abundance across the Tibetan Plateau. *Chin. Sci. Bull.* 59, 3010–3021. doi: 10.1007/s11434-014-0258-x

Ziyad, J., Goïta, K., Magagi, R., Blarel, F., and Frappart, F. (2020). Improving the estimation of water level over freshwater ice cover using altimetry satellite active and passive observations. *Remote Sens.* 12, 967–992. doi: 10.3390/rs12060967

Conflict of Interest: The authors declare that the research was conducted in the absence of any commercial or financial relationships that could be construed as a potential conflict of interest.

frontiers in Earth Science

ORIGINAL RESEARCH
published: 21 April 2021
doi: 10.3389/feart.2021.636246

Evaluating Accuracy of HY-2A/GM-Derived Gravity Data With the Gravity-Geologic Method to Predict Bathymetry

Zhijie Wei[1], Jinyun Guo[1], Chengcheng Zhu[1], Jiajia Yuan[1], Xiaotao Chang[2] and Bing Ji[3]*

[1] College of Geodesy and Geomatics, Shandong University of Science and Technology, Qingdao, China, [2] Land Satellite Remote Sensing Application Center of MNR, Beijing, China, [3] Department of Navigation Engineering, Naval University of Engineering, Wuhan, China

For the first time, HY-2A/GM-derived gravity anomalies determined with the least-squares collocation method and ship-borne bathymetry released from the National Centers for Environmental Information (NCEI) are used to predict bathymetry with the gravity-geologic method (GGM) over three test areas located in the South China Sea (105–122°E, 2–26°N). The iterative method is used to determine density contrasts (1.4, 1.5, and 1.6 g/cm^3) between seawater and ocean bottom topography, improving the accuracy of GGM bathymetry. The results show that GGM bathymetry is the closest to ship-borne bathymetry at check points, followed by SRTM15+V2.0 model and GEBCO 2020 model. It is found that in a certain range, the relative accuracy of GGM bathymetry tends to improve with the increase of depth. Different geological structures affect the accuracy of GGM bathymetry. In addition, the influences of gravity anomalies and data processing method on GGM bathymetry are analyzed. Our assessment result suggests that GGM can be widely applied to bathymetry prediction and that HY-2A/GM-derived gravity data are feasible with good results in calculating ocean depth.

Keywords: gravity-geologic method, marine gravity anomalies, South China Sea, density contrast, ocean depth, geological structure

OPEN ACCESS

Edited by:
Takashi Nakagawa,
University of Leeds, United Kingdom

Reviewed by:
Toshiya Fujiwara,
Japan Agency for Marine-Earth Science and Technology (JAMSTEC), Japan
Adili Abulaitijiang,
DTU Space – National Space Institute, Denmark

****Correspondence:***
Jinyun Guo
jinyunguo1@126.com

Specialty section:
This article was submitted to Solid Earth Geophysics, a section of the journal Frontiers in Earth Science

Received: *01 December 2020*
Accepted: *25 March 2021*
Published: *21 April 2021*

Citation:
Wei Z, Guo J, Zhu C, Yuan J, Chang X and Ji B (2021) Evaluating Accuracy of HY-2A/GM-Derived Gravity Data With the Gravity-Geologic Method to Predict Bathymetry. Front. Earth Sci. 9:636246. doi: 10.3389/feart.2021.636246

INTRODUCTION

Ocean depth plays a very important role in marine geology, geophysics and geodesy, such as the study of earth's plate tectonics, changes of ocean currents and tides, and navigation of ships. Bathymetry prediction mainly includes satellite remote sensing, sonar images and satellite altimetry gravity anomalies.

Although satellite remote sensing (Jay and Guillaume, 2014) has advantages in economy and flexibility, its accuracy needs to be improved. High-resolution seafloor topography prediction of sonar images is achieved with the shape from shaping (Coiras et al., 2007), which needs to be constrained by external bathymetry. In the past 50 years, great progress has been made the technical performance of satellite altimetry technology (e.g., Born et al., 1979; Cheney et al., 1986; Francis et al., 1995; Hwang et al., 2002; Guo et al., 2014, 2015, 2016), and its measurement accuracy and resolution (Hsiao et al., 2016) have been greatly improved. The technology has made a significant contribution to the satellite altimetry-derived ocean gravity field

(e.g., Sandwell and Smith, 1997, 2009; Hwang et al., 2006, 2014; Guo et al., 2010; Zhu et al., 2019, 2020; Li et al., 2020) and to the study of bathymetry prediction (e.g., Calmant and Baudry, 1996; Luo et al., 2002).

Gravity prediction of bathymetry mainly includes the gravity-geologic method (GGM) (Ibrahim and Hinze, 1972; Adams and Hinze, 1990), admittance function method (Dorman and Lewis, 1970; Watts, 1978) and least-squares collocation method (Hwang, 1999). The ship-borne bathymetry data is relatively sparse (Smith and Sandwell, 1994). Compared with the other two methods, GGM has the advantage of using sparse ship-borne bathymetry to obtain depth model. A comparison with Smith and Sandwell model shows that GGM has an advantage with short wavelength components ($\leq$12 km) which are sensitive to bathymetry variations (Kim et al., 2010).

Gravity-geologic method has been used to predict bathymetry in southern Greenland, southern Alaska (Hsiao et al., 2011), the southern Western Pacific Emperor Seamount (Hu et al., 2012) and the central South China Sea (Ouyang et al., 2014). The density contrast between seawater and ocean bottom topography has a large impact on the accuracy of bathymetry prediction. Although the accuracy of GGM bathymetry using the density contrast obtained with the downward continuation method (Hwang, 1999; Kim et al., 2010, 2011) reaches 40 m (Kim et al., 2010), the density contrast is quite different from the theoretical value of 1.64 g/cm^3 and therefore loses its physical significance. The density contrast obtained with the iterative method (Silva et al., 2006; Kim et al., 2010; Hu et al., 2012) is close to the theoretical value, achieving good test results.

At present, bathymetry prediction is generally based on existing gravity anomalies, or the gravity anomalies obtained by combining multi-satellite data. There are relatively few researches on the application of HY-2A/GM-derived gravity anomalies in bathymetry prediction. The objective of this study is to apply GGM to estimation of the bathymetry of the test areas in the South China Sea with HY-2A/GM-derived gravity anomalies. In this paper, differences are analyzed among GGM bathymetry, ship-borne bathymetry and other depth models (e.g., SRTM15+V2.0 model and GEBCO 2020 model). Geological structures, gravity anomalies and other factors affecting the accuracy of GGM bathymetry are discussed, and the relationship is studied between relative accuracy of GGM bathymetry and variation of depth. The results show that HY-2A/GM-derived gravity anomalies can be used to predict bathymetry, and GGM can be effectively applied to areas with sparse ship-borne bathymetry.

THE GRAVITY-GEOLOGIC METHOD

The gravity-geologic method (GGM) is originally proposed by Ibrahim and Hinze (1972). Because the density difference between seawater and ocean bottom topography is large, GGM is suitable for predicting bathymetry with gravity anomalies. The estimation of ocean bottom topography from gravity has the single contact restoration problem (Grant and West, 1965). Therefore, a simple Bouguer correction formula (linearized contact restoration problem) is adopted. The ambiguity involves the choice of depth, D. To minimize the ambiguity, the control points data are used. However, in a linearized contact surface problem, D happens to be the mean depth. In data processing, the gravity anomaly is linearized into the residual gravity field produced by local bedrock variations and the regional gravity field generated by deeper mass variations. Then, the residual gravity field is used to predict the final depth. The calculation process is as follows.

Gravity anomalies are divided into the residual gravity anomaly and the regional gravity anomaly, i.e.:

$$g_{inv} = g_{reg} + g_{res} \tag{1}$$

where g_{inv} means gravity anomaly, and g_{res} and g_{reg} denote residual gravity anomaly and regional gravity anomaly, respectively.

The residual gravity anomaly (g^j_{res}) can be presented as:

$$g^j_{res} = 2\pi G\Delta\rho\ (H_j - D) \tag{2}$$

where g^j_{res} denotes the residual gravity anomaly at the point j; G is the gravitational constant, and $\Delta\rho$ is the optimal density contrast between seawater and ocean bottom topographic mass, called density contrast.H_j is the control point j and D is the reference depth, which is usually referenced to the deepest depth of the control points.

Furthermore, the residual gravity anomaly (g^j_{res}) can be subtracted from the gravity anomaly (g^j_{inv}) to obtain the regional gravity anomaly (g^j_{reg}) at the point j. It can be given by:

$$g^j_{reg} = g^j_{inv} - g^j_{res} \tag{3}$$

After that, the regional gravity anomaly (g^j_{reg}) is gridded to create a reference gravity anomaly grid (g_{reg}) and the regional gravity anomaly is obtained by cubic spline interpolation at the check points (g^i_{reg}). Then, the residual gravity anomaly (g^i_{res}) is obtained by:

$$g^i_{res} = g^i_{inv} - g^i_{reg} \tag{4}$$

Finally, bathymetry is calculated by:

$$H_i = \frac{g^i_{res}}{2\pi G\Delta\rho} + D \tag{5}$$

Figure 1 shows the flow chart of GGM operation steps and the iterative method to solve density contrast. First, initialized value of the density contrast is given, and ocean depth is obtained with GGM. Then, the control points depth is obtained with cubic spline interpolation. And the standard deviation and the correlation coefficient are compared between the GGM bathymetry and the ship-borne bathymetry difference at control points. Finally, if the difference is not judged to be the smallest, the assignment continues to be performed; Otherwise, the value is the suitable density contrast.

Test Area

The South China Sea (SCS), as the western marginal sea of the Pacific Ocean, lies among the Eurasian plate, the Pacific plate and

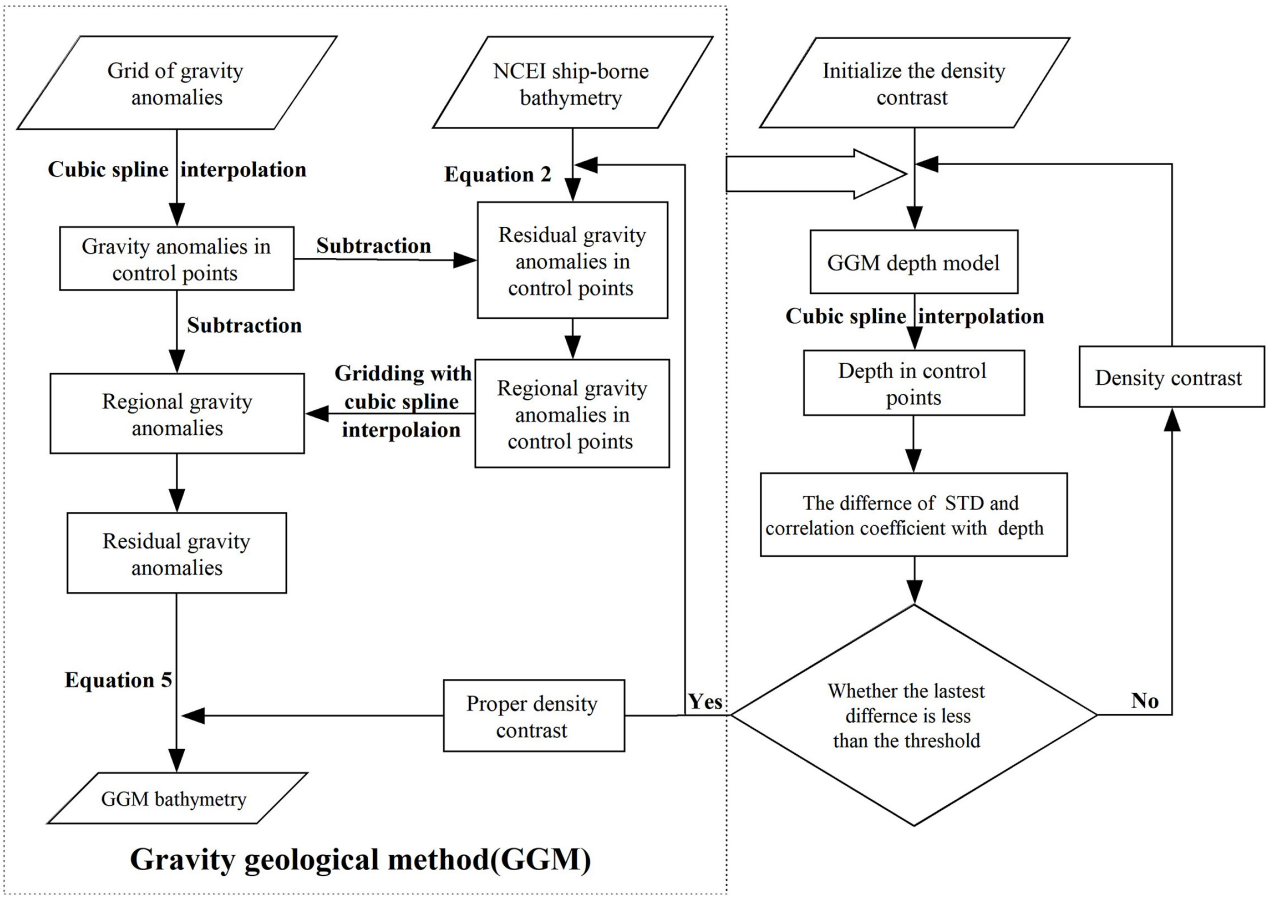

FIGURE 1 | Flow chart of the gravity-geologic method (GGM) and iterative method.

the Indian Ocean plate. Its geological structures and topography are complex. The overall topography inclines from the periphery to the center, with continental shelf, continental slope, abyssal basin and other landform types transitioning from shallow to deep (Qiu et al., 2016). Different topography and landforms constitute the basic features of the SCS geology.

The SCS is taken as the research area, and the characteristics of GGM bathymetry prediction under different geological structures can be well analyzed. The three test areas of A (112–119°E, 16–20°N), B (111–118°E, 12–15°N) and C (109–115°E, 6–10°N). **Figure 2** shows the locations of the test areas.

DATA

HY-2A/GM-derived Gravity Anomaly

The gravity anomalies on $1' \times 1'$ grids in the SCS (105–122°E, 2–26°N) are obtained from altimetry data of geodetic mission (GM) of HY-2A (which is China's first satellite altimeter mission launched in August 2011). The GM of HY-2A was carried out after the orbit modification on March 30, 2016. The cycle of GM increases from 14 d to 168 days and its working range is 81°S-81°N. The HY-2A/GM altimeter data of Level 2 Plus (L2P) products [Centre National d'Etudes Spatiales (CNES), 2017] sampled at a frequency of 1 Hz from March 30, 2016 to August 22, 2018 are selected as the research data. First, sea surface heights (SSHs) of HY-2A/GM are pre-processed by correction and gross error elimination. Then pre-processed SSHs are used to calculate along-track geoid gradients, from which residual geoid gradients can be obtained by removing geoid gradients of EGM2008. Finally, residual gravity anomalies on $1' \times 1'$ grids are derived from residual geoid gradients with the least-squares collocation method whose calculation window radius is 0.5°. The final gravity anomaly model (Zhu et al., 2019) is obtained from residual gravity anomalies by restoring gravity anomalies of EGM2008, as is shown in **Figure 3**.

Ship-Borne Bathymetry

The ship-borne bathymetry is provided by the National Centers for Environmental Information (NCEI) from the National Oceanic and Atmospheric Administration of the United States (NOAA,[1]). The time span of the data is from 1960 to 2016. NCEI

[1]http://www.noaa.gov

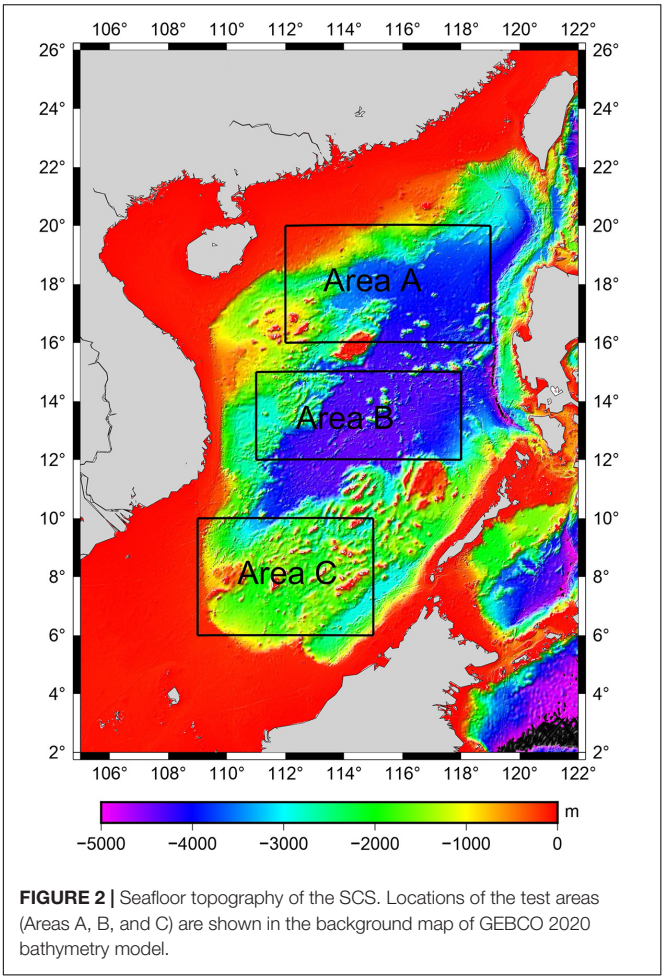

FIGURE 2 | Seafloor topography of the SCS. Locations of the test areas (Areas A, B, and C) are shown in the background map of GEBCO 2020 bathymetry model.

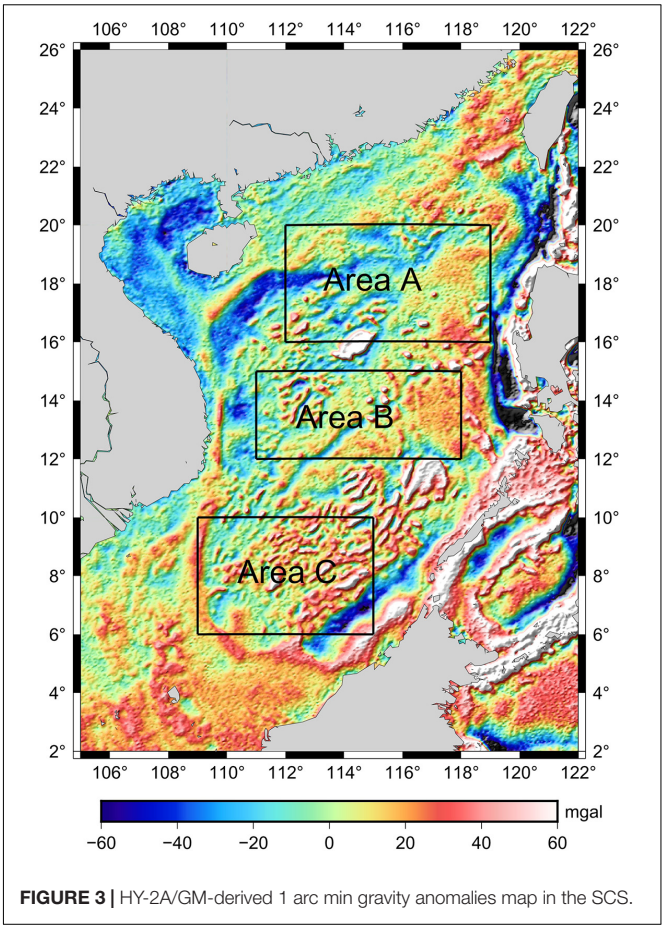

FIGURE 3 | HY-2A/GM-derived 1 arc min gravity anomalies map in the SCS.

controls data quality and gathers qualified data into a database. Although the overall data quality is accurate and reliable, some data have large measurement errors in the early stage, and it is necessary to find these errors. After eliminating ship-borne bathymetry errors, there are 24,386 control points and 12,192 check points in Area A, 27,693 control points and 13,846 check points in Area B, and 9,463 control points and 4,731 check points in Area C. The ratio of control points and check points is 2:1 in each test area. **Figure 4** shows the distribution of control points and check points for the test areas.

SRTM15+V2.0 Model and GEBCO 2020 Model

Ship-borne bathymetry data has high-precision but does not give uniform coverage, and satellite altimetry data can act as an interpolation to extend bathymetry information beyond ship tracks to the entire chosen region. Satellite altimetry technology improves the resolution and efficiency of various depth models which are built on the basis of ship-borne bathymetry data.

SRTM15+V2.0 model is a global bathymetry and topography grid, and its interval is 15 s. The model is produced by combining ship-borne bathymetry and depth predicted with altimeter-derived gravity. The multibeam and singlebeam measurements data are provided by several institutions, which are Scripps Institution of Oceanography (SIO), the National Geospatial-Intelligence Agency (NGA), Japan Agency for Marine-Earth Science and Technology (JAMSTEC), Center for Coastal and Ocean Mapping (CCOM) and Geoscience Australia (GA). The uncertainty of depth estimation is between −150 and 150 m in the deep ocean (Tozer et al., 2019). In the experiment, for the convenience of comparison, we abbreviated it as SRTM15 model. SRTM15 model can be downloaded from the website: https://figshare.com/articles/online_resource/Tozer_et_al_2019_SRTM15_GMT_Grids/7979780.

The GEBCO 2020 model is a global bathymetry and topography grid, and its interval is 15 s. which is released by the General Bathymetric Chart of the Oceans (GEBCO). the model is built based on SRTM15+V2.0 (Tozer et al., 2019). The data is fused by prediction seabed topography and land topography (GEBCO Bathymetric Compilation Group 2020, 2020). In the experiment, for the convenience of comparison, we abbreviated it as GEBCO model. GEBCO model can be downloaded from the website: https://www.gebco.net/data_and_products/gridded_bathymetry_data/gebco_2020/.

Determining the Density Contrast

To make GGM bathymetry values closer to real values, it is necessary to accurately estimate the density contrast of the SCS.

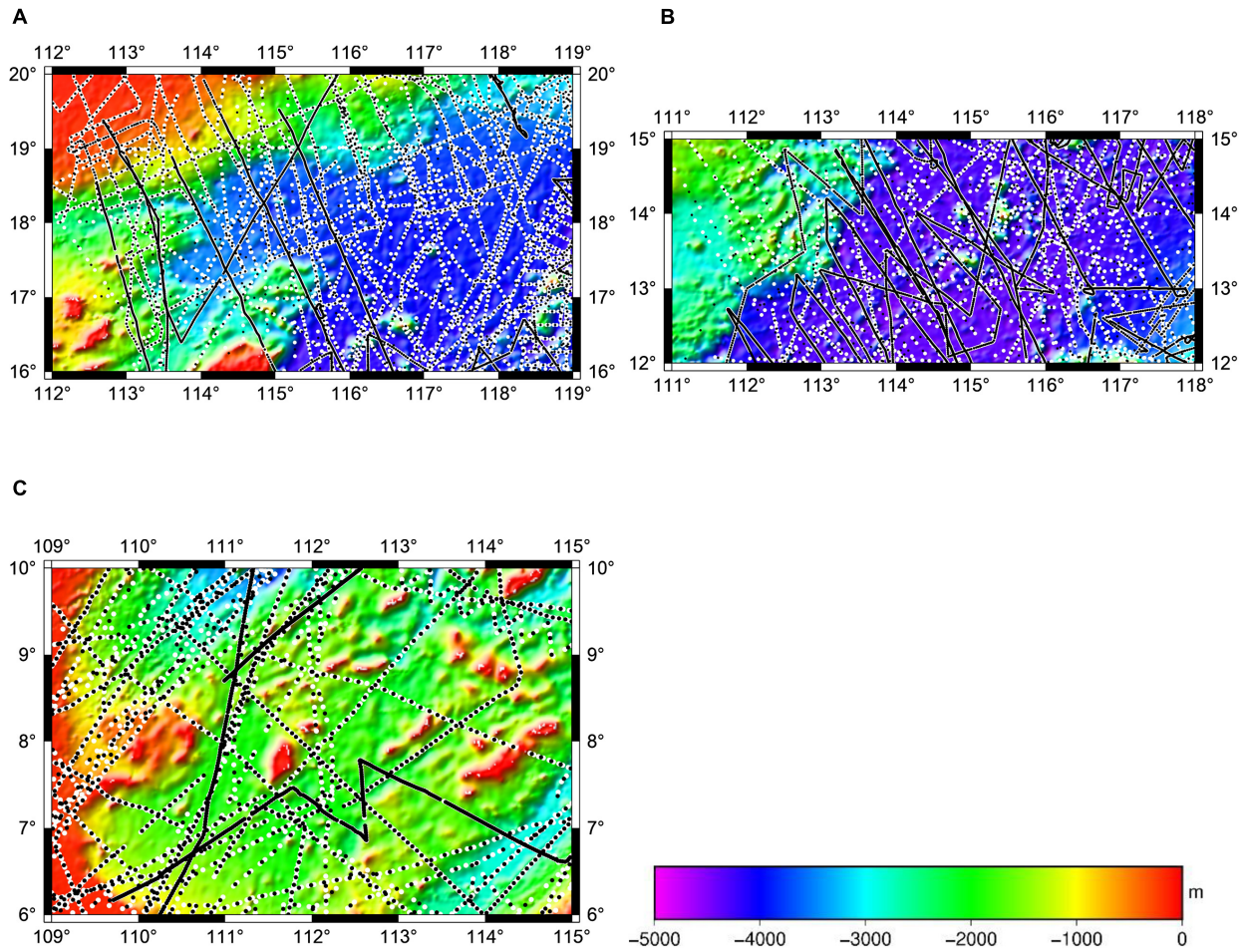

FIGURE 4 | Distribution of ship-borne bathymetry tracks for the test areas of the SCS. **(A)** Ship-borne bathymetry tracks in test area A. **(B)** Ship-borne bathymetry tracks in test area B. **(C)** Ship-borne bathymetry tracks in test area C. By considering the similarity of tomograms, the density of ship track data in each of these regions is evaluated through digital image processing-based metrics. Control points are represented by black points, and check points are represented by white points.

First, GGM bathymetry is calculated through the control points under different density contrasts. Then, the depths of check points are obtained with interpolation. Finally, the correlation coefficient and the standard deviation (STD) are obtained by comparing GGM bathymetry with the ship-borne bathymetry. The density contrast is obtained, and gravity anomalies are used to predict bathymetry with GGM (**Figure 1**).

The reference depths of the test areas are 4,756, 4,903, and 3,921 m by the deepest depth value through control points, respectively. When the correlation coefficient and the standard deviation have extreme points under the same density contrast, the density contrast is appropriate. Based on this principle, with the increase in density contrast, outliers appear in correlation coefficients and standard deviations of the test areas. The density contrasts of the test areas are 1.4, 1.5, and 1.6 g/cm^3, respectively; correlation coefficients are 0.999, 0.993, and 0.998, and standard deviations are 53.8, 64.0, and 49.3 m, respectively. **Figure 5** shows the trend of correlation coefficients and standard deviations with the density contrast, in the test areas.

RESULTS AND ANALYSIS

Statistics of ship-borne bathymetry, GGM bathymetry, GEBCO model and SRTM15 model at the check points are listed in **Table 1**. Based on ship-borne bathymetry, the mean depths of the test areas are that A is less than B and greater than C. It can be seen from the mean depths that GGM data are closest to NCEI data in the test areas, while GEBCO data are closest to SRTM15 data in various statistical indicators.

Table 2 denotes bathymetry differences between the GGM, NCEI, GEBCO and SRTM15 data, and the results of statistical accuracy at check points. The standard deviations of NCEI-GGM data are 53.8, 64.0, and 49.3 m at the check points, and these mean values of NCEI-GGM data are not more than 0.2 m. The standard deviations of GEBCO-SRTM15 data are 4.5, 3.9, and 16.2 m, respectively, which are smaller than other standard deviations, and the two data have similarity in the statistical data at the check points.

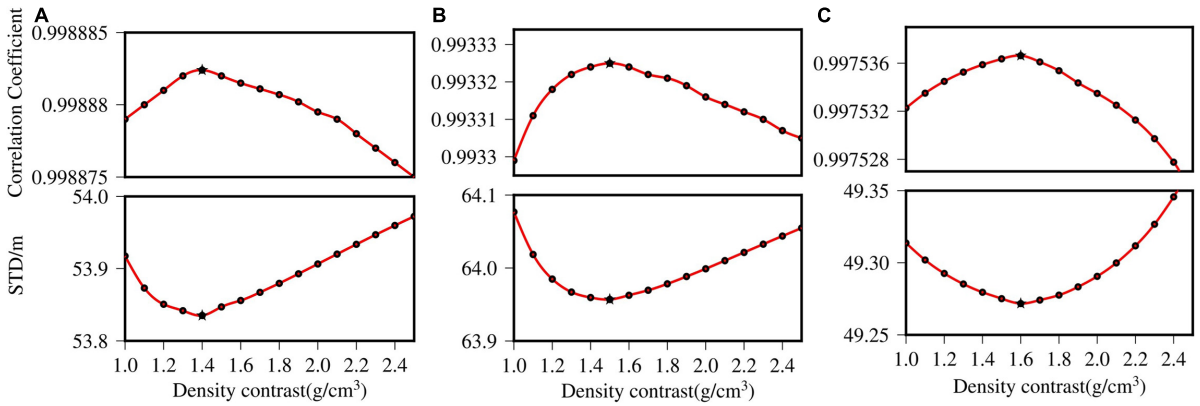

FIGURE 5 | Outliers diagrams for determining density contrast. **(A)** Determination of $\Delta\rho$ in test area A. **(B)** Determination of $\Delta\rho$ in test area B. **(C)** Determination of $\Delta\rho$ in test area C. The variation of correlation coefficient and standard deviation with $\Delta\rho$ in the test areas, and the extreme points are represented by pentagrams. Finally, it is determined that $\Delta\rho$ is 1.4, 1.5, and 1.6 g/cm^3 in each of the test areas.

Table 3 shows the difference of NCEI-GGM with depth in the test areas. The calculation equation of relative accuracy is as follows:

$$Relative\ accuracy = \frac{1}{n}\sum_{i=1}^{n}\left|1-\frac{|H_i-h_i|}{H_i}\right|*100\% \qquad (6)$$

Where H_i denotes ship-borne bathymetry, h_i means the depth calculated by GGMs, n is number of ship-borne points. The results denote that the relative accuracy improves with the increase of depth value in each test area. With the increase of depth, the STD and RMS of each area tend to decrease except for area A ranging from −3,000 to −2,000 m (STD is 56.6 m and RMS is 56.8 m).

Figure 6 presents the histogram of the difference between NCEI and GGM-derived bathymetry predictions. The percentage of error points decreases from the middle to both sides. **Table 4** shows the statistical results of error in different ranges, and the errors of GGM bathymetry are concentrated within 50 m data, accounting for 91.65, 87.73, and 87.95% respectively.

TABLE 1 | Statistics of NCEI ship-borne bathymetry, the GGM bathymetry, GEBCO model, and SRTM15 model in the test areas (unit: m).

Area	Data	Min	Max	Mean	STD	RMS
A	NCEI	−4,278	−93.3	−2,948.3	1,138.8	3,160.6
	GGM	−4,371.4	−94.2	−2,948.1	1,137.1	3,159.8
	GEBCO	−4,275.3	−91.3	−2,941.6	1,143.1	3,155.9
	SRTM15	−4,275.3	−91.3	−2,941.5	1,143.1	3,155.8
B	NCEI	−4,894	−499	−4,007.4	554.4	4,045.6
	GGM	−4,634.8	−503.5	−4,007.5	549.9	4,045.0
	GEBCO	−4,670.1	−499.3	−4,009.5	555.8	4,047.8
	SRTM15	−4,670.1	−499.3	−4,009.5	555.8	4,047.8
C	NCEI	−3,878.6	−65.0	−1,755.2	702.3	1,890.5
	GGM	−3,937.1	−63.7	−1,755.1	699.6	1,889.4
	GEBCO	−3,862.3	−22.8	−1,749.5	703.5	1,885.6
	SRTM15	−3,862.3	−22.8	−1,749.8	703.4	1,885.9

Figure 7 shows the positions of the points where the error is greater than 250 m (black points) at the check points. In **Figure 7A**, the rectangular I (112.7–116.5°E, 16–18.5°N) has poor accuracy. In **Figure 7B**, rectangular II (111.85–113.8°E, 13.2–15°N) is the area where the error distribution is concentrated. Rectangular III (113.9–116.6°E, 12.7–15°N) shows that bathymetry of GGM prediction is poor in the area of chain seamounts and linear seamounts. The complex geological structure with great change lead to more error points in these areas. The error points shown in **Figure 7C** are relatively dispersed, and its error is relatively small.

Based on the geological structures of the SCS (Qiu et al., 2016) and GGM bathymetry result (**Figure 7**), the shape of

TABLE 2 | Statistics of differences among the NCEI bathymetry, the GGM bathymetry, GEBCO model and SRTM15 model in the check points (unit: m).

Area/check point	Data comparison	Min	Max	Mean	STD	RMS
A 12192	NCEI-GGM	−1,325.7	1,244.9	−0.2	53.8	53.8
	NCEI- GEBCO	−1,614.0	1,491.9	−6.8	96.7	97.0
	NCEI- SRTM15	−1,614.0	1,491.9	−6.8	96.6	96.9
	GEBCO-GGM	−915.9	1,615.0	6.5	97.9	98.1
	SRTM15-GGM	−915.9	1,615.0	6.6	97.8	98.1
	GEBCO-SRTM15	−189.6	215.2	0.1	4.5	4.5
B 13846	NCEI-GGM	−1,609.1	1,355.5	0.1	64.0	64.0
	NCEI- GEBCO	−1,581.3	1,852.5	2.1	76.4	76.4
	NCEI- SRTM15	−1,581.3	1,852.5	2.1	76.3	76.3
	GEBCO-GGM	−1,281.1	1,352.1	−2.0	77.8	77.8
	SRTM15-GGM	−1,281.1	1,352.1	−2.0	77.6	77.6
	GEBCO-SRTM15	−151.8	190.7	−0.1	3.9	3.9
C 4731	NCEI-GGM	−381.8	1,065.2	−0.1	49.3	49.3
	NCEI- GEBCO	−1,311.8	1,120.6	−5.7	67.8	68.0
	NCEI- SRTM15	−1,311.8	1,120.6	−5.3	67.5	67.7
	GEBCO-GGM	−698.1	13,113	5.6	70.9	71.1
	SRTM15-GGM	−803.2	13,113	5.2	70.9	71.1
	GEBCO-SRTM15	−832.5	100.3	−0.4	16.2	16.3

TABLE 3 | Statistics of different depths between the NCEI bathymetry and the GGM bathymetry in the check points (unit: m).

Area	Different depths	Check points	Min	Max	Mean	STD	RMS	Relative accuracy
A	−1,000 000	961	−202.9	1,244.9	4.1	61.5	61.7	97.62%
	−2,000 −1,000	1,827	−793.8	738.7	4.7	56.6	56.8	98.63%
	−3,000 −2,000	2,123	−1,325.7	1,159.3	2.0	76.2	76.3	98.77%
	−4,000 −3,000	5,642	−1,178.1	599.0	−1.8	45.0	45.1	99.56%
	<−4,000	1,639	−720.6	183.4	−5.8	34.4	34.8	99.68%
	Entire area	12,192	−1,325.7	1,244.9	−0.2	53.8	53.8	99.15%
B	−2,000 000	155	−390.5	898.7	88.4	168.5	190.3	91.68%
	−3,000 −2,000	896	−810.9	1,355.5	7.0	143.1	143.3	97.22%
	−4,000 −3,000	2,880	−1,609.1	1,214.6	6.2	80.4	80.6	99.06%
	<−4,000	9,915	−941.6	294.9	−3.7	37.3	37.3	99.64%
	Entire area	13,846	−1,609.1	1,355.5	0.1	64.0	64.0	99.27%
C	−1,000 000	576	−346.9	380.9	6.8	54.6	55.0	94.22%
	−2,000 −1,000	2,782	−261.9	1,065.2	0.8	49.3	49.3	98.64%
	−3,000 −2,000	1,214	−381.8	283.4	−4.6	46.7	46.9	99.07%
	<−3,000	159	−217.4	178.9	−7.9	43.7	44.4	99.20%
	Entire area	4,731	−381.8	1,065.2	−0.1	49.3	49.3	98.23%

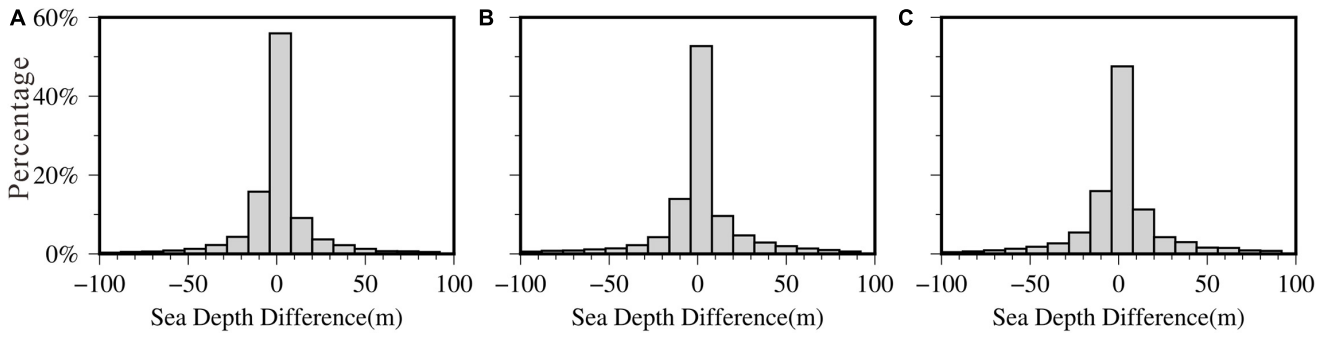

FIGURE 6 | Histograms of the differences between NCEI bathymetry and GGM-derived bathymetry in the check points. **(A)** Error statistics of test area A. **(B)** Error statistics of test area B. **(C)** Error statistics of test area C.

TABLE 4 | Statistics of GGM error range in the check points.

Error range	Area A		Area B		Area C	
	Number	Percentage	Number	Percentage	Number	Percentage
0–10 m	8,171	67.02%	8,514	61.49%	2,753	58.19%
10–20 m	1,554	12.75%	1,702	12.29%	723	15.28%
20–30 m	710	5.82%	954	6.89%	319	6.74%
30–40 m	452	3.71%	559	4.04%	230	4.86%
40–50 m	287	2.35%	418	3.02%	136	2.87%
>50 m	1,018	8.35%	1,699	12.27%	570	12.05%

the SCS basin is an irregular rhombus, and the terrain inclines from the periphery to the center. From the periphery to the center, the large landform units are continental shelf, continental slope and marginal sea basin in the SCS. The terrain of the continental shelf and abyssal basin is relatively gentle, and the terrain of the continental slope is steep. The topography of the continental slope and island slope are rugged, making it the most complex area in the SCS. In this terrain, the accuracy of GGM bathymetry is poor, and its bathymetry accuracy needs to be improved. The abyssal plain is dominated by plain landforms, generally speaking, its terrain is relatively flat, and the accuracy of GGM bathymetry is relatively high. However, when there are chain seamounts and linear seamounts (**Figure 7B**, rectangular II), the accuracy of GGM bathymetry is relatively poor. The test area C is the southern part of the SCS. Its topography fluctuates little and changes gently. The mean depth is approximately −1,755 m (**Table 1**), and STD of NCEI-GGM data can reach 49.3m (**Table 2**) in area C. Through the above analysis, different

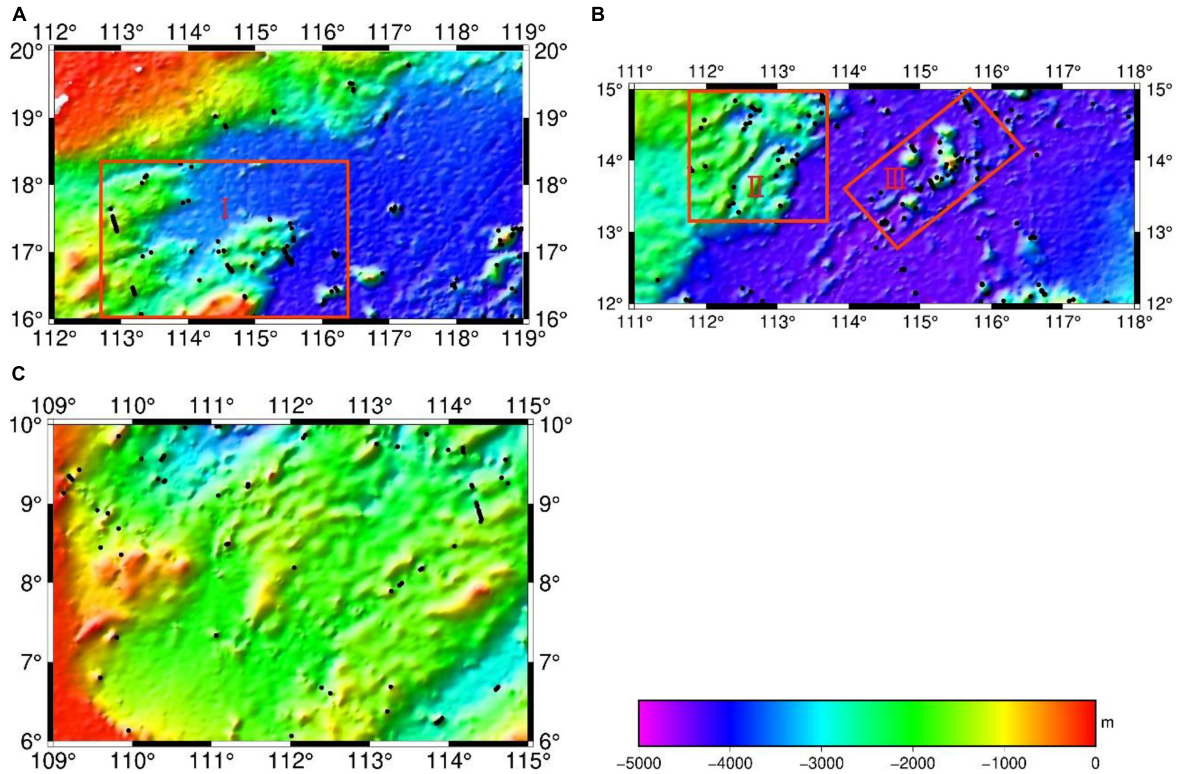

FIGURE 7 | Distribution of differences between NCEI bathymetry and GGM bathymetry in the test areas. **(A)** Error points distributionin test area A. **(B)** Error points distributionin test area B. **(C)** Error points distributionin test area C. The black spot represents the distribution of depth errors greater than 250 m. the red rectangles represents the area with large error, and the background map is GGM bathymetry prediction.

topography also has an impact on GGM bathymetry. The accuracy of GGM bathymetry is relatively poor in areas with large terrain change, while in areas with gentle change, the accuracy is relatively high.

Some other factors affect the accuracy of GGM bathymetry. The gravity anomalies affect the accuracy of GGM bathymetry.

TABLE 5 | Statistics of differences among NCEI data, $GGM_{Sandwell}$ data, and GGM_{HY-2A} data in the check points (unit: m).

Area	Data comparison	Min	Max	Mean	STD	RMS
A	NCEI-$GGM_{Sandwell}$	−1,324.0	1,254.6	−0.3	53.3	53.3
	NCEI-GGM_{HY-2A}	−1,325.7	1,244.9	−0.2	53.8	53.8
B	NCEI-$GGM_{Sandwell}$	−1,608.1	1,355.5	0.1	63.2	63.2
	NCEI-GGM_{HY-2A}	−1,609.1	1,355.5	0.1	64.0	64.0
C	NCEI-$GGM_{Sandwell}$	−440.3	1,024.2	−0.3	49.1	49.1
	NCEI-GGM_{HY-2A}	−381.8	1,065.2	−0.1	49.3	49.3

TABLE 6 | Statistics results of difference between NCEI data and bathymetry calculated by bilinear interpolation and cubic spline interpolation in area A (unit: m).

Method	Min	Max	Mean	STD	RMS
NCEI-$GGM_{bilinear}$	−1,299.7	1,246.0	−0.3	55.2	55.2
NCEI-GGM_{spline}	−1,325.7	1,244.9	−0.2	53.8	53.8

We compare HY-2A/GM-derived gravity anomalies with Sandwell model (it is V29.1 gravity anomalies and is released by Scripps Institution of Oceanography), and the statistical results are shown in **Table 5**. In test areas, Mean, STD and RMS of $GGM_{Sandwell}$ and GGM_{HY-2A} are very close to each other by comparing with NCEI data, and the accuracy of $GGM_{Sandwell}$ is slightly higher than that of GGM_{HY-2A}, which is acceptable. Because Sandwell model combines multiple satellite altimetry data, so it is better than HY-2A/GM-derived gravity anomalies in accuracy. The comparison results in **Table 5** indicate that it is feasible to use HY-2A/GM-derived gravity to predict bathymetry with GGM, and the gravity anomaly data of HY-2A/GM-derived gravity anomalies are reliable. The interpolation method used to calculate depth with GGM can affect bathymetry accuracy. The comparison results of bathymetry calculated with bilinear interpolation and cubic spline interpolation are shown in **Table 6**. The results of the cubic spline interpolation used in this paper are better than bilinear interpolation. The accuracy of GGM bathymetry is directly affected with interpolation method, which cannot be neglected.

CONCLUSION

It is feasible to apply HY-2A/GM-derived marine gravity anomalies to predict bathymetry with GGM in the South China

Sea. The density contrasts are determined with the iterative method, which improve the accuracy of GGM bathymetry prediction. The comparison with other depth data illustrates that GGM bathymetry is closer to ship-borne bathymetry than those of SRTM15 model and GEBCO model. Moreover, GGM can be applied to areas with sparse ship-borne bathymetry.

The accuracy of GGM bathymetry is analyzed under different geological structures. The accuracy is high in flat terrain, but reduces in complex terrains.

Other factors affecting the accuracy of GGM bathymetry are discussed. Within a certain depth range, as the depth increases, the relative accuracy of GGM bathymetry tends to improve. Based on the ship-borne bathymetry, bathymetry obtained HY-2A/GM-derived gravity anomalies and Sandwell model are compared, and it is concluded that the accuracy of gravity anomalies is also one of the factors affecting bathymetry prediction. In addition, the interpolation method has influence on the result of GGM bathymetry.

If gravity anomalies derived from various satellites and ship-borne are combined to establish a comprehensive gravity field model in the SCS, GGM bathymetry accuracy may be improved. In addition, if GGM bathymetry and other models are assigned different weights, a comprehensive terrain model can be established in the SCS, which may be helpful for the study of geological structure and marine resources.

DATA AVAILABILITY STATEMENT

The raw data supporting the conclusions of this article will be made available by the authors, without undue reservation.

AUTHOR CONTRIBUTIONS

ZW: scientific analysis and manuscript writing. JG: data quality control. CZ and JY: scientific analysis. XC and BJ: data collection. All authors contributed to the article and approved the submitted version.

FUNDING

This study is supported by the National Natural Science Foundation of China (grant Nos. 41774001, 41374009, 41774021, and 41874091), and the SDUST Research Fund (grant No. 2014TDJH101).

ACKNOWLEDGMENTS

We would like to thank NCEI for providing the ship-borne bathymetry data. We would also like to thank Cheinway Hwang and Yu-Shen Hsiao.

REFERENCES

Adams, J. M., and Hinze, W. J. (1990). The gravity-geologic technique of mapping buried bedrock topography. *Geotech. Environ. Geophys.* 3, 99–106. doi: 10.1190/1.9781560802785.3

Born, G. H., Dunne, J. A., and Lame, D. B. (1979). Seasat mission overview. *Science* 204, 1405–1406. doi: 10.1126/science.204.4400.1405

Calmant, S., and Baudry, N. (1996). Modelling bathymetry by inverting satellite altimetry data: a review. *Mainer Geophys. Res.* 18, 123–135. doi: 10.1007/BF00286073

Centre National d'Etudes Spatiales (CNES) (2017). *Along-track level-2+ (L2P) SLA product handbook.SALP-MU-P-EA-23150-CLS, Issue 1.0*. Available online at: https://www.aviso.altimetry.fr/fileadmin/documents/data/tools/hdbk_L2P_all_missions_except_S3.pdf (accessed October 11, 2019)

Cheney, R., Douglas, B., Green, R., Miller, L., Milbert, D., and Porter, D. (1986). The GEOSAT altimeter mission: a milestone in satellite oceanography. *EOS Trans. Am. Geophys. Union* 67, 1354–1355. doi: 10.1029/EO067i048p01354

Coiras, E., Petillot, Y., and David, M. L. (2007). Multiresolution 3-D reconstruction from side-scan sonar images. *IEEE Trans. Image Process.* 16, 382–390. doi: 10.1109/TIP.2006.888337

Dorman, L. M., and Lewis, B. T. R. (1970). Experimental isostasy: 1. theory of the determination of the earth's isostatic response to a concentrated load. *J. Geophys. Res.* 75, 3357–3365. doi: 10.1029/JB075i017p03357

Francis, C. R., Graf, G., Edwards, P. G., McCraig, M., McCarthy, C., Lefebvre, A., et al. (1995). The ERS-2 spacecraft and its payload. *Eur. Space Agency Bull.* 83, 13–31.

GEBCO Bathymetric Compilation Group 2020 (2020). *The GEBCO_2020 Grid–A Continuous Terrain Model of the Global Oceans and Land*. Liverpool: British Oceanographic Data Centre, National Oceanography Centre, NERC, doi: 10.5285/a29c5465-b138-234d-e053-6c86abc040b9

Grant, F. S., and West, G. F. (1965). *Interpretation Theory In Applied Geophysics*. New York, NY: McGraw-Hill Book.

Guo, J., Gao, Y., Hwang, C., and Sun, J. (2010). A multi-subwaveform parametric retracker of the radar satellite altimetric waveform and recovery of gravity anomalies over coastal oceans. *Sci. China Earth Sci.* 53, 610–616. doi: 10.1007/s11430-009-0171-3

Guo, J., Liu, X., Chen, Y., Wang, J., and Li, C. (2014). Local normal height connection across sea with ship-borne gravimetry and GNSS techniques. *Mar. Geophys. Res.* 35, 141–148. doi: 10.1007/s11001-014-9216-x

Guo, J., Shen, Y., Zhang, K., Liu, X., Kong, Q., and Xie, F. (2016). Temporal-spatial distribution of oceanic vertical deflections determined by TOPEX/Poseidon and Jason-1/2 missions. *Earth Sci. Res. J.* 20, 1–5. doi: 10.15446/esrj.v20n2.54402

Guo, J. Y., Wang, J. B., Hu, Z. B., Hwang, C. W., Chen, C. F., and Gao, Y. G. (2015). Temporal-spatial variations of sea level over China seas derived from altimeter data of TOPEX/Poseidon, Jason-1 and Jason-2 from 1993 to 2012. *Chin. J. Geophys.* 58, 3103–3120. doi: 10.6038/cjg20150908

Hsiao, Y. S., Hwang, C., Cheng, Y., Chen, L., Hsu, H., Tsai, J., et al. (2016). High-resolution depth and coastline over major atolls of South China Sea from satellite altimetry and imagery. *Remote Sens. Environ.* 176, 69–83. doi: 10.1016/j.rse.2016.01.016

Hsiao, Y. S., Kim, J. W., Kim, K. B., Lee, B. Y., and Hwang, C. (2011). Bathymetry estimation using the gravity-geologic method: an investigation of density contrast predicted by the downward continuation method. *Terr. Atmos. Ocean. Sci.* 22, 347–358. doi: 10.3319/TAO.2010.10.13.01

Hu, M. Z., Li, J. C., and Jin, T. Y. (2012). Bathymetry inversion with gravity-geological gethod in emperor seamount. *Geomatics Inform. Sci. Wuhan Univ.* 37, 610–612. doi: 10.13203/j.whugis2012.05.008

Hwang, C. (1999). A bathymetry model for the South China Sea from satellite altimetry and depth data. *Mar. Geod.* 22, 37–51. doi: 10.1080/014904199273597

Hwang, C., Guo, J., Deng, X., Hsu, H. Y., and Liu, Y. (2006). Coastal gravity anomaly from retracked Geosat/GM altimetry: improvement, limitation and the role of airborne gravity data. *J. Geod.* 80, 204–216. doi: 10.1007/s00190-006-0052-x

Hwang, C., Hsu, H. J., Chang, E. T. Y., Featherstone, W. E., Tenzer, R., Lien, T., et al. (2014). New free-air and Bouguer gravity fields of Taiwan from multiple platforms and sensors. *Tectonophysics* 611, 83–93. doi: 10.1016/j.tecto.2013.11.027

Hwang, C., Hsu, H. Y., and Jang, R. J. (2002). Global mean sea surface and marine gravity anomaly from multi-satellite altimetry: applications of deflection-geoidand inverse Vening Meinesz formulae. *J. Geod.* 76, 407–418. doi: 10.1007/s00190-002-0265-6

Ibrahim, A., and Hinze, W. J. (1972). Mapping buried bedrock topography with gravity. *Ground Water* 10, 18–23. doi: 10.1111/j.1745-6584.1972.tb02921.x

Jay, S., and Guillaume, M. (2014). A novel maximum likelihood based method for mapping depth and water quality from hyperspectral remote-sensing data. *Remote Sens. Environ.* 147, 121–132. doi: 10.1016/j.rse.2014.01.026

Kim, J. W., Frese, R. R. B., Frese, V., Lee, B. Y., Roman, D. R., and Doh, S. J. (2011). Altimetry-derived gravity predictions of bathymetry by the gravity-geologic method. *Pure Appl. Geophys.* 168, 815–826. doi: 10.1007/s00024-010-0170-5

Kim, K. B., Hsiao, Y. S., Kim, J. W., Lee, B. Y., Kwon, Y. K., and Kim, C. H. (2010). Bathymetry enhancement by altimetry-derived gravity anomalies in the East Sea (Sea of Japan). *Mar. Geophys. Res.* 31, 285–298. doi: 10.1007/s11001-010-9110-0

Li, Z., Liu, X., Guo, J., Zhu, C., Yuan, J., Gao, J., et al. (2020). Performance of Jason-2/GM altimeter in deriving marine gravity with the waveform derivative retracking method: a case study in the South China Sea. *Arab. J. Geosci.* 13:939. doi: 10.1007/s12517-020-05960-0

Luo, J., Li, J. C., and Jiang, W. P. (2002). Bathymetry prediction of South China Sea from satellite data. *Geomatics Inform. Sci. Wuhan Univ.* 27, 256–260. doi: 10.13203/j.whugis2002.03.006

Ouyang, M. D., Sun, Z. M., and Zhai, Z. H. (2014). Predicting bathymetry in South China Sea using the gravity-geologic method. *Chin. J. Geophys.* 57, 2756–2765. doi: 10.6038/cjg20140903

Qiu, Y., Wang, J., Yan, P., Huang, W. K., Zhu, B. D., and Wang, Y. L. (2016). Characteristics of the crustal structure in the South China Sea and their tectonic significance. *Geol. Study S. China Sea* 1, 1–39.

Sandwell, D. T., and Smith, W. H. F. (1997). Marine gravity anomaly from Geosat and ERS-1 satellite altimetry. *J. Geophys. Res.* 102, 10039–10054. doi: 10.1029/96JB03223

Sandwell, D. T., and Smith, W. H. F. (2009). Global marine gravity from retracked Geosat and ERS-1 altimetry: ridge segmentation versus spreading rate. *J. Geophys. Res.* 114:B01411. doi: 10.1029/2008JB006008

Silva, J. B., Costa, D. C., and Barbosa, V. C. (2006). Gravity inversion of basement relief and estimation of density contrast variation with depth. *Geophysics* 71, 51–58. doi: 10.1190/1.2236383

Smith, W. H. F., and Sandwell, D. T. (1994). Bathymetry prediction from dense satellite altimetry and sparse ship-borne bathymetry. *J. Geophys. Res.* 99, 21803–21824. doi: 10.1029/94JB00988

Tozer, B., Sandwell, D. T., Smith, W. H. F., Olson, C., Beale, J. R., and Wessel, P. (2019). Global bathymetry and topography at 15 arc sec: SRTM15+. *Earth Space Sci.* 6, 1847–1864. doi: 10.1029/2019ea000658

Watts, A. B. (1978). An analysis of isostasy in the world's oceans 1: Hawaiian-Emperor seamount chain. *J. Geophys. Res.* 83, 5989–6004. doi: 10.1029/JB083iB12p05989

Zhu, C., Guo, J., Gao, J., Liu, X., Hwang, C., Yu, S., et al. (2020). Marine gravity determined from multi-satellite-GM/ERM altimeter data over the South China Sea: SCSGA V1.0. *J. Geod.* 94:50. doi: 10.1007/s00190-020-01378-4

Zhu, C., Guo, J., Hwang, C., Gao, J., Yuan, J., and Liu, X. (2019). How HY-2A/GM altimeter performs in marine gravity derivation: assessment in the South China Sea. *Geophys. J. Int.* 219, 1056–1064. doi: 10.1093/gji/ggz330

Conflict of Interest: The authors declare that the research was conducted in the absence of any commercial or financial relationships that could be construed as a potential conflict of interest.

frontiers in Earth Science

ORIGINAL RESEARCH
published: 21 April 2021
doi: 10.3389/feart.2021.647583

Cross-Calibrations of the HY-2B Altimeter Using Jason-3 Satellite During the Period of April 2019–September 2020

Jianbo Wang[1,2,3], Huan Xu[1,2,3], Lei Yang[4], Qingjun Song[5] and Chaofei Ma[5]*

[1] Jiangsu Key Laboratory of Marine Bioresources and Environment/Jiangsu Key Laboratory of Marine Biotechnology, Jiangsu Ocean University, Lianyungang, China, [2] School of Marine Technology and Geomatics/Ocean Remote Sensing Big Data Applications Center, Jiangsu Ocean University, Lianyungang, China, [3] Co-Innovation Center of Jiangsu Marine Bio-industry Technology, Jiangsu Ocean University, Lianyungang, China, [4] Marine Survey Research Center, First Institute of Oceanography, Ministry of Natural Resources, Qingdao, China, [5] National Satellite Ocean Application Service, Beijing, China

OPEN ACCESS

Edited by:
Cheinway Hwang, National Chiao Tung University, Taiwan

Reviewed by:
Tianhai Cheng, Institute of Remote Sensing and Digital Earth (CAS), China
Mukesh Gupta, Catholic University of Louvain, Belgium

***Correspondence:**
Lei Yang
leiyang@fio.org.cn

Specialty section:
This article was submitted to Environmental Informatics and Remote Sensing, a section of the journal Frontiers in Earth Science

Received: *30 December 2020*
Accepted: *10 March 2021*
Published: *21 April 2021*

Citation:
Wang J, Xu H, Yang L, Song Q and Ma C (2021) Cross-Calibrations of the HY-2B Altimeter Using Jason-3 Satellite During the Period of April 2019–September 2020. Front. Earth Sci. 9:647583. doi: 10.3389/feart.2021.647583

In 2018, the Haiyang-2B (HY-2B) satellite altimeter was sent to orbit as a follow-up mission of the HY-2A satellite altimeter. The performance of the HY-2B system over the global oceans is considered to be critical. However, its performance is not fully known at the present time. In the present study, the first global quality assessment of the HY-2B Geophysical Data Record (GDR) was presented using comparison and crossover analysis processes of the main parameters and sea level anomalies (SLAs) with Jason-3 GDR data. This study's assessment results demonstrated that the editing proportion of unqualified data for the HY-2B was 2.67%, which was at a similar level as the Jason-3 (2.86%). In addition, this study's assessment results of the HY-2B key parameters (mainly the backscatter coefficients, significant wave heights, sea state bias, wet troposphere delays, and ionosphere delays) showed good agreement with the Jason-3, and there were no abnormal trends observed. The mean and standard deviations (STDs) were determined to be (0.21 ± 6.70) cm and (−3.4 ± 6.25) cm for the SLA differences at the self-crossover points of the HY-2B and dual-crossover points between the HY-2B and Jason-3 satellites, respectively. In addition, the SLA crossover analysis results indicated that the accuracy of the sea surface heights for the HY-2B was close to that of the Jason-3 satellite. The spatial distributions of the SLA differences showed no significant errors in the geographic characteristics. The SLA measurements were assessed using a wavenumber spectra method. The obtained results suggested that the power spectrum of the SLAs of the HY-2B satellite followed the regular patterns of the traditional Jason-3 altimeter. Furthermore, based on the spectrum analysis results, it was revealed that the noise level of the HY-2B was lower than that of the Jason-3, indicating a good overall performance of the HY-2B.

Keywords: GDR quality assessment, main HY-2B altimeter parameters, daily mean analysis, crossover analysis, wavenumber spectra of the SLA

INTRODUCTION

Satellite altimeters have been providing global sea surface height (SSH) measurements since the 1970s, which has greatly improved oceanography, geodesy, and polar scientific knowledge, as well as many other Earth sciences (Chelton et al., 2001; Yang et al., 2020; Yuan et al., 2020). In 2011, China launched the Haiyang-2A (HY-2A), which was the first satellite altimeter of the Chinese Marine Dynamic Environment Satellite series (Lin and Jiang, 2014; Mertikas et al., 2015b). The Haiyang-2B (HY-2B) satellite altimeter was launched in 2018 as a follow-up to the HY-2A. The HY-2A satellite altimeter was sent to nearly the same orbit as HY-2A in order to fulfill an oceanographic mission (Jiang C. F. et al., 2019). In the near future, more satellite altimeters will be launched by China as follow-ups to the HY-2A. As a result, given the satellite series-specific orbits and hardware designs, a satellite altimetric network will be formed, which will be a major contribution to the oceanic altimetry community (Lin and Jiang, 2014).

Calibration and validation (cal/val) activities are the key processes for detecting any biases and trends in satellite observations. The results ensure the long-term consistency and continuity of measurements obtained from different missions (Chelton et al., 2001; Fu and Haines, 2013). At the present time, there are two commonly used cal/val methods: absolute calibrations by dedicated sites and cross-calibrations between different satellite altimeters. The absolute calibrations of the SSHs are based on four principal long-running sites around the world (Christensen et al., 1995; Bonnefond et al., 2003; Watson et al., 2003; Mertikas et al., 2015a), as well as other auxiliary sites operated by academic institutes or universities (Crétaux et al., 2008; Babu et al., 2015; Yang et al., 2017). All of the calibration results of these sites provide valuable SSHs bias for the satellite altimeters. However, the maintenance of these dedicated sites requires continuous economic cost and logistic resources. In addition, the dedicated sites do not have the abilities to reveal the global statistic performance results of satellite altimetric measurements. Alternatively, the cross-calibration approaches based on crossover analysis methods have the potential to provide a global view of the system's performances and offer important complementary resources for the absolute calibrations at individual sites (Ablain et al., 2010; Dettmering and Bosch, 2010; Dettmering et al., 2015; Prandi et al., 2015; Passaro et al., 2016; Yang et al., 2019). Following the release of the Chinese HY-2A data, the cross-calibrations with the Jason-2 satellite altimeter were successfully carried out. The performance of the HY-2A altimetry system was assessed (Bao et al., 2015; Yang et al., 2016), which improved the reprocessing of the HY-2A data and further enhanced the data quality. However, the cross-calibrations of the HY-2B GDR data have still not been reported since the data were released last year (2019). Therefore, although the knowledge of the performance level of the new Chinese satellite altimeter system over the global oceans is critical, it is not fully known at the present time.

The focus of this study was to provide the first exhaustive quality assessment of the HY-2B mission data. The assessment was performed using a global analysis of the HY-2B main parameters and SLAs at self-crossover points and the dual-crossover points with the Jason-3 satellite. This study's layout is as follows: section "Introduction" includes this study's introduction; section "Data and Methods" provides descriptions of the HY-2B and Jason-3 altimeter data and the methods used in this study; section "Missing and Edited Measurements" details the missing and edited measurements of the HY-2B and Jason-3 missions; section "Analysis of the Main Parameters" highlights the HY-2B satellite's main parameter data and daily mean analysis results; section "SLA Analysis" provides the SLAs analysis results from the HY-2B satellite, including the analysis of the daily mean SLAs, analysis of SLA differences at the self-crossover and dual-crossover points with Jason-3 satellite, and the wave-number spectra analysis of the SLAs from both the HY-2B and Jason-3 satellites; section "Results and Discussion" is the study's discussion; and this study's conclusions are summarized in the section "Conclusions."

DATA AND METHODS

HY-2B Altimetric GDR Data

The HY-2B satellite was successfully launched in October 25, 2018 as the successor to the HY-2A satellite, which had shifted to a geodetic orbit in 2016, and ceased operation as of June 10, 2020. The HY-2B satellite carries three main microwave instruments on board, including a nadir-looking altimeter, scanning microwave radiometer, and the microwave scatter-o-meter. The HY-2B altimetric instrument is a dual-frequency (Ku- and C-bands) nadir-looking radar altimeter, which has the ability to provide the range data between the Earth's surface and the satellite. The radiometer also provides wet tropospheric corrections for the range measurements. Since the microwave scatter-o-meter measures the ocean winds and wave fields and has no connection with the altimeter, it was not discussed in this study. The HY-2B satellite has adopted a sun synchronous orbit at a height of 970 km and an inclination of 99.34°, which enables observations over high latitude areas as far as 81° N/S. The repeat cycle for the HY-2B satellite is 14 days, with a theoretical 386 tracks per cycle. The HY-2B level 2 products include Interim Geophysical Data Records (IGDR), Sensor Geophysical Data Records (SGDR), and Geophysical Data Records (GDR). The data versions are of "T," "c," and "d," respectively. In addition, the data of the GDR version "c" from April 1, 2019 to September 14, 2020 (533 days) were used to assess the HY-2B altimetric data quality and accuracy levels. The GDR product included the raw 20-Hz altimetry data and the 1-Hz geophysical corrections. The Ku-band data, which is considered to be more accurate than the C-bands, were utilized in this study.

Jason-3 Satellite Altimeter Data

The Jason-3 satellite is an international cooperative satellite altimetry mission satellite that was cooperatively launched by the National Aeronautics and Space Administration (NASA), National Oceanic and Atmospheric Administration (NOAA), European Organization for the Exploitation of Meteorological

Satellites (EUMETSAT), and Center National d'Etudes Spatiales (CNES; Yang et al., 2019). Since the Jason-3 data have been widely validated and calibrated, it was adopted as the comparison data set for the new HY-2B data in the current research investigation. In order to carry out an accurate assessment between the two different satellite altimeters, the used Jason-3 GDR data (cycles 115–169) are from the same time span as the examined HY-2B data in this study.

Experimental Methods

This study's global statistical assessment of the HY-2B satellite's performance was conducted by monitoring the main parameters and SLAs through a detailed comparison with the Jason-3 satellite's data. The main parameters examined in this study included the backscattering coefficients (Sigma0), significant wave heights (SWH), sea state bias (SSB), wet tropospheric corrections, and the ionospheric corrections. The parameter analysis mainly included data availability, accuracy, and stability. The accuracy of the SSHs, which is considered to be the most important measurements, was assessed using the crossover differences and the wavenumber spectra of the SLAs between the HY-2B and Jason-3 satellites. The SLA was computed using the following equations (Yang et al., 2019):

$$H_{SSH} = H_O - R - \sum Corr \quad (1)$$

$$H_{SLA} = H_{SSH} - H_{MSS} \quad (2)$$

where H_O represents the altitude of the satellite orbit; R is the altimeter ranging value; and ΣCorr is the sum of corrections, including the dry tropospheric corrections, wet tropospheric corrections, ionospheric corrections, SSB corrections, ocean tides, solid earth tides, polar tides, and adverse atmospheric pressure levels; H_{SSH} is the sea surface height; and H_{MSS} means mean sea surface height.

The availability of the altimeter's main parameters was assessed through the analysis of the lost track numbers and a comparison of the main parameter editing proportions of the HY-2B and Jason-3 altimeters. **Table 1** details this study's comparison of the main correction standards, which were applied to the SSHs (SLAs) for the HY-2B and Jason-3 satellites. The majority of the geophysical corrections was found to be similar between the HY-2B and the Jason-3, with the exception of the dry tropospheric corrections and inverse barometer corrections, which had adopted different weather models. The editing criteria (Watson et al., 2003) for the HY-2B and Jason-3 satellites had been recommended by the National Ocean Satellite Application Service (NSOAS, China) and CNES (France) (Bao et al., 2015). The data that had not met the constraint criteria were filtered out, and the data editing proportions were calculated by counting the filtered data with respect to the total data. In other words, the lower the editing proportion was, the better the satellite's mission performance would be.

In addition, this study calculated the daily mean values of the main HY-2B altimeter parameters and the SLA differences at the self-crossover points of the intrinsic mono-mission of the HY-2B, as well as at the dual-crossover points between the HY-2B and Jason-3 mission, in order to assess the mission performance level. The self-crossover points were estimated using the ascending and descending tracks within the same cycle. The dual-crossovers between the HY-2B and Jason-3 satellites were calculated using tracks within the same time span. This study's spatial distribution sketch map of the cross-points is shown in **Figure 1**. In order to reduce the impacts of the temporal variations in the marine environments in the crossover analysis, the altimetric data were compared with time differences less than 3 days. In addition, in order to obtain reliable results in the crossover analysis, the editing of the parameters using the established editing criteria (Bao et al., 2015) were conducted in the ocean areas between the latitude bounds of $\pm 50°$ for all of the altimetry missions and in a bathymetry $\leq -1{,}000$ m in the ocean areas.

This study adopted a wavenumber spectrum for assessing the HY-2B system's performance in regard to the SSH measurements. This wavenumber spectrum, presented as the power spectrum density in cycles per unit distance, was able to accurately reflect the internal structures of the oceans' dynamic signals. Subsequently, using the aforementioned spectrum, the system noise of the altimeters could also be assessed. In this study, the wavenumber spectrum of the SLAs along the HY-2B and Jason-3 satellite tracks was determined using a Fast Fourier Transform (FFT) method.

TABLE 1 | Main geophysical correction standards applied to sea surface heights (SSHs) [sea level anomalies (SLAs)] for the HY-2B and Jason-3 satellite altimeters.

Parameters	HY-2B	Jason-3
Dry troposphere	Model, National Centers for Environmental Prediction (NCEP; Jiang X. et al., 2019)	Model, European Center for Medium-Range Weather Forecasts (ECMWF; Jiang X. et al., 2019)
Wet troposphere	Radiometer	Radiometer
Ionosphere	Dual frequency	Dual frequency
Ocean tide	GOT 4.10c	GOT 4.8
Pole tide	Wahr, 1985	Wahr, 1985
Solid Earth tide	Cartwright and Taylor (Cartwright and Edden, 1973)	Cartwright and Taylor (Cartwright and Edden, 1973)
Sea surface bias	Empirical models	Empirical models
Mean sea surface	CLS15MSS model	CLS15MSS model
Inverse barometer	Model, NCEP	Model, ECMWF

MISSING AND EDITED MEASUREMENTS

In order to assess the data availability of the HY-2B satellite's main parameters, this study first calculated the number of lost tracks per cycle, and then the average of the number of the 20 Hz range measurements, and the average of the root mean squares (RMS) of the 20-Hz range measurements (results shown in **Figure 2**). The integrity of the altimeter track data was considered to be one of the most important features of the data availability. The editing proportions of the main parameters were analyzed cycle by cycle. In addition, the main chosen

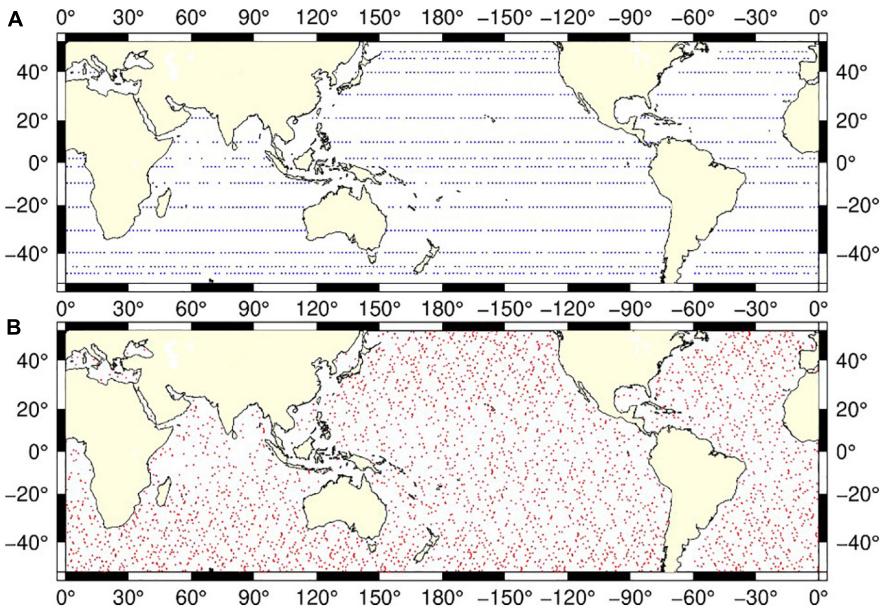

FIGURE 1 | The spatial distribution sketch map of crossover points for **(A)** self-crossover points of HY-2B (blue) and **(B)** dual-crossover points between HY-2B and Jason-3 (red).

parameters of the satellite altimeter data set were the range, SSB corrections, radiometer wet tropospheric corrections, dual-frequency ionospheric corrections, SWH, and the Sigma0. This was due to the fact that those parameters presented the primary parameters in the altimetry scientific community. The editing criteria proposed in the study conducted by Bao et al. (2015) were adopted in this study, and only the Ku-band parameters of the HY-2B and Jason-3 satellites were selected for examination.

Some of the satellite tracks may not be recorded due to such reasons as problems in the ground receiving stations or abnormal data transmissions (Zaouche et al., 2010) (especially during the processes of satellite mission mode adjustments). **Figure 2A** shows the lost passes for the HY-2B and Jason-3 missions. It can be seen in the figure that the HY-2B mission lost 17 passes during the 16th cycle, 27 tracks during the 17th cycle, 16 tracks during the 21st and 30th cycles, 66 tracks during the 22nd cycle, 19 tracks during the 35th cycle, 15 tracks during the 40th cycle, and 81, 193, 228, 256 tracks during 46th–49th cycles. However, major improvements were observed when compared to its predecessor HY-2A (Yang et al., 2016). With regard to the Jason-3 satellite, the tracks from pass 108 to pass 245 were found to be completely missing in the 116th cycle, which was attributed to changes in the safe hold mode (SHM) of the satellite (Michaud et al., 2019); due to SHM, there are only 153 passes in cycle 146, cycle 147 has only 31 passes, and 86 passes in cycle 160 are missing as detailed in **Figure 2A**.

The qualified number and RMS of the 20 Hz range measurements of the HY-2B satellite system was compared to those of the Jason-3 in order to analyze the performance of the high frequency range measurements. The statistical results for those two parameters are shown in **Figures 2B,C**. The numbers of the 20 Hz range measurements are indicators of the present data quality of the range measurements. The average of the qualified numbers of the 20-Hz range measurements were determined to range between 19.70 and 19.90 for the HY-2B mission and between 19.53 and 19.59 for the Jason-3 mission. These finding indicated that the high frequency data of the HY-2B and the Jason-3 were all of good quality. The RMS of the 20-Hz range measurements is a parameter that indicates the variability of the SSH over 20 points in 1 s. Since the 1-Hz SSH data were smoothed from the 20 Hz data, the lower the RMS of the 20-Hz data results was, the better the data quality for the 1-Hz data would be. The average of the RMS of 20 Hz range measurements was determined to be 2.52 cm in all of the cycles for the HY-2B, which was significantly smaller than that of the Jason-3 (7.96 cm).

As shown in **Figure 3**, based on the editing criteria in Bao et al. (2015), a time series of the editing proportions of the main parameters for HY-2B and Jason-3 was established. **Figures 3A,B** show the editing proportion of altimetry parameters over oceans for HY-2B and Jason-3; **Figures 3C,D** show the editing proportion of altimetry parameters in the ocean areas with water depths ($\leq -1{,}000$ m) and latitude bounds ($\pm 50°$) constraints for HY-2B and Jason-3. The statistical results are presented in **Tables 2A,B**. The results, shown in **Figures 3A,B** and **Table 2A**, demonstrated that the HY-2B satellite's average editing proportions over oceans for the parameters of wet tropospheric corrections, ionospheric corrections, and SWH were stable and <0.4%. The largest HY-2B editing proportion was due to the SSB corrections, which were determined to be 3.18% on average. The Jason-3 editing proportions of the ionospheric corrections, SWH, and SSB corrections over oceans were determined to be <0.6%. The variations in the Jason-3 editing proportions for all of the parameters were observed to be <3%, with the exception of the wet tropospheric

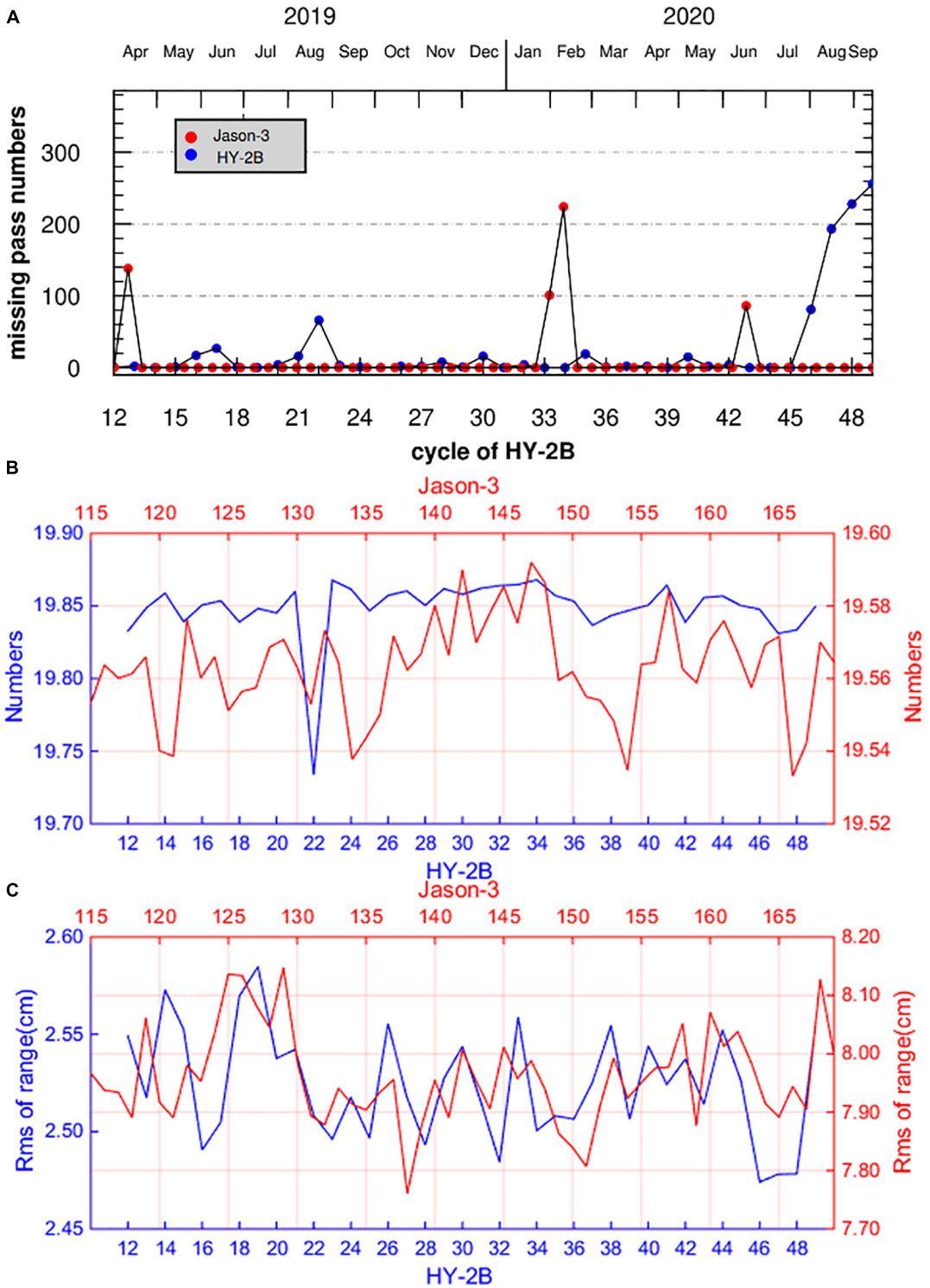

FIGURE 2 | Missing and edited measurements for HY-2B mission (blue) from cycles 12 to 49 and Jason-3 mission (red) from cycles 115–169. Cycle by cycle of **(A)** the number of lost tracks, **(B)** the average of the qualified number, and **(C)** the average of root mean square (RMS) of 20 Hz range measurements.

corrections (4.52%). However, it was found that from this study's comparison results that the editing proportions of the wet tropospheric corrections were significantly smaller for the HY-2B (2.98×10^{-2}%) when compared with the Jason-3 (2.36%). This suggested that the performance of the HY-2B satellite's radiometer may have displayed a superior

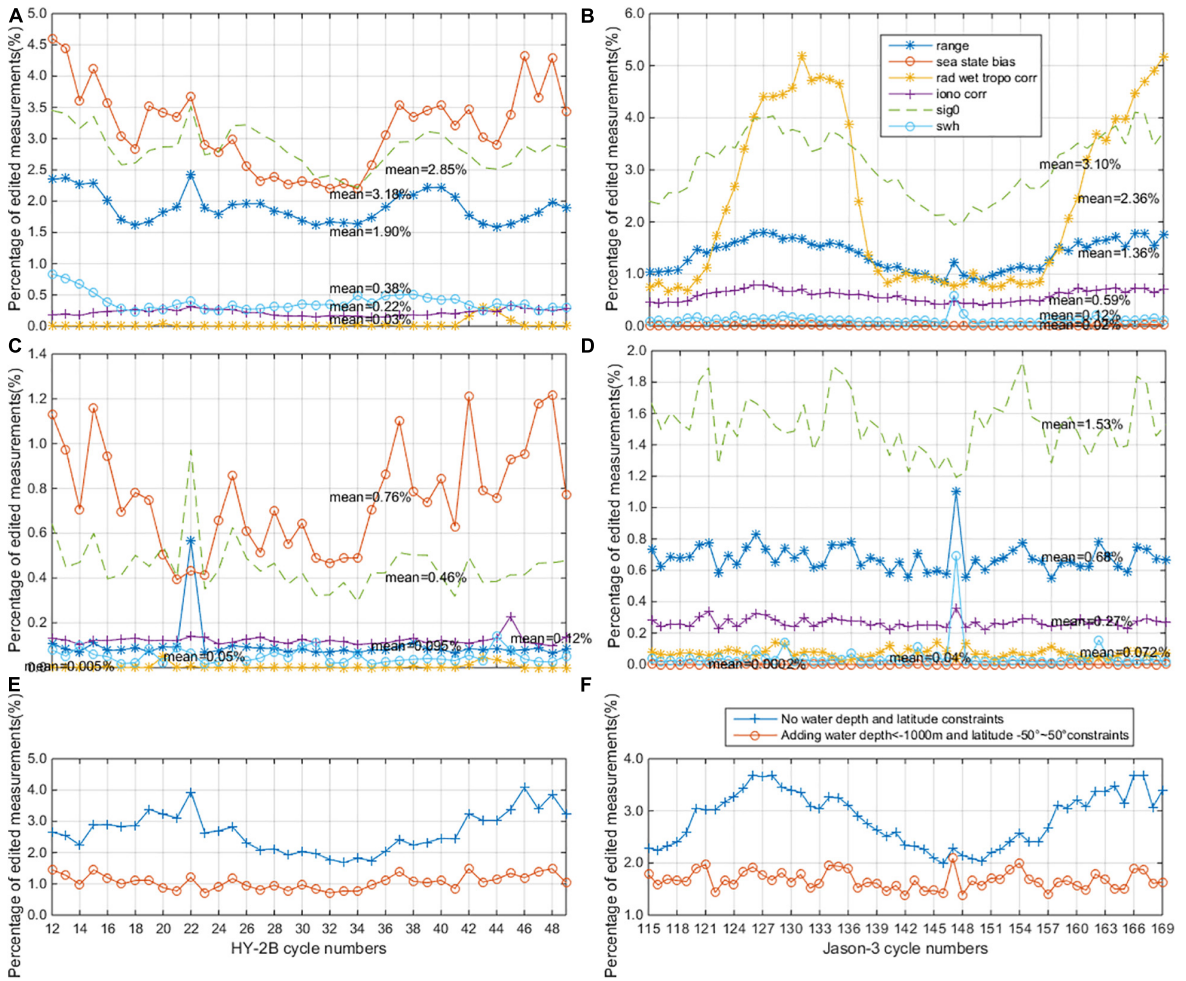

FIGURE 3 | Panels **(A,B)** are the editing proportion of altimetry parameters over oceans, in which Panel **(A)** is HY-2B and Panel **(B)** is Jason-3; Panels **(C,D)** are the editing proportion of altimetry parameters with water depths (≤−1,000 m) and latitude bounds (±50°) constraints, in which Panel **(C)** is HY-2B and Panel **(D)** is Jason-3; Panels **(E,F)** are the editing proportion of altimetry data constraints by the editing criteria of total parameters in Bao et al. (2015), in which Panel **(E)** is HY-2B and Panel **(F)** is Jason-3.

performance in that regard. To be more specific, the ocean depths and latitudes were constrained in order to obtain better data quality. This was due to the fact that satellite altimeters tend to have high data editing proportions in shallow water and high-latitude areas as a result of the influences of ocean dynamic environments near the shore and over the high latitude seas. **Figures 3C,D** and **Table 2B** show that the editing proportions of the HY-2B and Jason-3 satellites had decreased significantly when the constrained data over the deep ocean areas (bathymetry ≤−1,000 m) and between the latitude bounds of ±50° were the focus.

Generally speaking, altimetric data editing is performed through a combination of all the key parameters. Therefore, this study estimated the editing proportions by considering all of the parameters, as well as taking the impacts of the ocean depths and latitudes into consideration, and the results are shown in **Table 3** and **Figures 3E,F**. The results indicated that the editing proportions of the HY-2B and Jason-3 satellites had decreased significantly when the constrained data over the deep ocean areas (bathymetry ≤−1,000 m) and between the latitude bounds of ±50° were the focus. The average editing proportions for all the cycles were determined to be 2.86 and 1.67% for the Jason-3 mission and 2.67 and 1.07% for the HY-2B mission, with respect to no water depths and latitude constraints and water depths and between the latitude bounds of ±50° constraints. The data availability analysis results demonstrated that the HY-2B satellite mission had achieved a good performance levels similar to that of the Jason-3 satellite.

ANALYSIS OF THE MAIN PARAMETERS

The daily mean values of the main altimeter parameters for the HY-2B and Jason-3 mission were calculated and compared in this study. The statistics of the correlation coefficients and

TABLE 2A | Statistics of the editing proportions of the altimetry parameters for the HY-2B and Jason-3 satellite altimeters over the global oceans.

Mission	Parameters	Minimum (%)/cycle	Maximum (%)/cycle	Average (%)	Variation (%)
	Range	0.86/146	1.80/127	1.36	0.94
	SSB corrections	4.06×10^{-3}/150	0.04/167	0.02	0.04
Jason-3	Wet tropospheric corrections	0.68/117	5.20/131	2.36	4.52
	Ionospheric corrections	0.41/150	0.79/126	0.59	0.38
	Sigma0	1.94/147	4.10/166	3.10	2.16
	SWH	0.05/146	0.59/147	0.12	0.54
	Range	1.59/44	2.42/22	1.90	0.83
	SSB corrections	2.19/34	4.60/12	3.18	2.41
HY-2B	Wet tropospheric corrections	3.12×10^{-3}/28	0.31/43	2.98×10^{-2}	0.31
	Ionospheric corrections	0.15/35	0.34/45	0.22	0.19
	Sigma0	2.22/34	3.52/22	2.85	1.30
	SWH	0.24/18	0.84/12	0.38	0.60

TABLE 2B | Statistics of the editing proportions of the altimetry parameters for the HY-2B and Jason-3 satellite altimeters with water depths (≤−1,000 m) and latitude bounds (±50°) constraints.

Mission	Parameters	Minimum (%) /cycle	Maximum (%)/cycle	Average (%)	Variation (%)
	Range	0.55/157	1.10/147	0.68	0.55
	SSB corrections	0/116–118	8.40×10^{-4}/134	2.00×10^{-4}	8.40×10^{-4}
Jason-3	Wet tropospheric corrections	2.55×10^{-2}/135	0.14/128	0.07	0.11
	Ionospheric corrections	0.22/150	0.36/147	0.27	0.14
	Sigma0	1.19/147	1.93/154	1.53	0.74
	SWH	1.20×10^{-2}/157	0.69/147	0.04	0.68
	Range	0.06/48	0.57/22	0.10	0.51
	SSB corrections	0.39/21	1.22/48	0.76	0.83
HY-2B	Wet tropospheric corrections	0/26,46–49	0.05/20	0.01	0.05
	Ionospheric corrections	0.10/48	0.23/45	0.12	0.13
	Sigma0	0.29/34	0.97/22	0.46	0.68
	SWH	0.01/35	0.14/44	0.05	0.13

TABLE 3 | Statistics of the editing proportions using the criteria of the total parameter constraints for the HY-2B and Jason-3 satellite altimeters.

Mission	Restriction	Minimum (%)/cycle	Maximum (%)/cycle	Average (%)
Jason-3	No water depth/latitude by default	1.99/146	3.69/126	2.86
	Water depth/latitude ±50°	1.37/142	2.09/147	1.67
HY-2B	No water depth/latitude by default	1.68/33	4.08/46	2.67
	Water depth/latitude ±50°	0.71/23	1.49/42	1.07

TABLE 4 | Correlation coefficient (Pearson) and difference statistics between the daily mean data series of the main parameters of the HY-2B and Jason-3 satellite altimeters.

Parameters	Correlation coefficient ($\times 10^{-2}$)	mean ($\times 10^{-2}$)	STD ($\times 10^{-2}$)	RMS ($\times 10^{-2}$)
Sigma0 (dB)	76.20	−1.65	10.54	10.66
SWH (m)	74.80	−3.40	5.12	6.14
SSB corrections (m)	77.10	−0.73	0.32	0.80
Wet tropospheric corrections (m)	54.90	0.29	0.41	0.50
Dual-frequency ionospheric corrections (m)	66.30	−0.48	0.21	0.52

the differences in the daily mean main altimeter parameters data series between the HY-2B and Jason-3 satellites are shown in **Table 4**. **Figure 4** shows the results of the comparison of the daily mean of Sigma0, SWH, and SSB for the HY-2B and Jason-3 missions.

Backscattering Coefficients

The backscattering coefficients are acquired using the amplitudes of the radar altimeter echo signals with respect to the maximum emission amplitude of the radar echo wave energy. The backscatter coefficients are related to the wind speeds and the

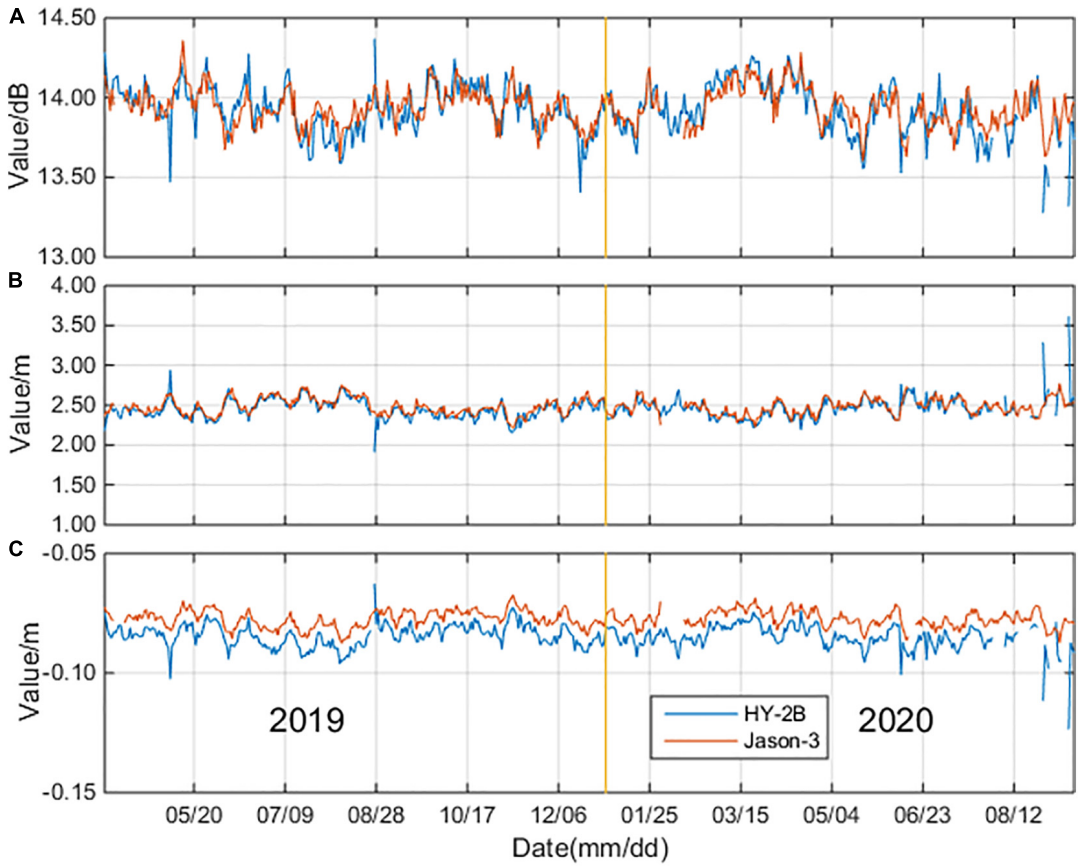

FIGURE 4 | Comparison of the daily mean of **(A)** Sigma0, **(B)** SWH, and **(C)** SSB for HY-2B and Jason-3.

sea states. The daily means of Sigma0 for the HY-2B and Jason-3 missions were compared, and the results are detailed in **Figure 4A**. It can be seen in the figure that the backscattering coefficients had displayed no obvious trends. The averages of the daily mean series of Sigma0 for the HY-2B and Jason-3 satellites, in **Figure 4A**, were 13.9243 and 13.9415 dB, respectively, with only a very small difference observed (−0.0172 dB). The maximum absolute value of the difference between the daily mean series of the parameter Sigma0 from the HY-2B and Jason-3 satellites was determined to be 0.517 dB, which occurred on September 11, 2020. The average and standard deviation of the differences between the daily mean series of the parameter Sigma0 from the HY-2B and Jason-3 data was determined (-0.0165 ± 0.1054) dB. The correlation coefficient of the Sigma0 between the HY-2B and Jason-3 satellites was 0.762, and these results had confirmed that the backscattering coefficients of the HY-2B and Jason-3 satellites were very consistent.

Significant Wave Heights

The SWH are calculated from the slopes of the altimeter echo waveforms. SWHs are approximately equal to one-third of the height of the highest wave within a period of time over a certain sea area. In addition, SWHs are related to the wind speeds, sea surface backscattering coefficients, and the SSB. **Figure 4B** shows the daily mean series of the SWHs for the HY-2B and Jason-3 satellites. The statistics of the correlation coefficients and the differences between the daily mean SWH data series from the HY-2B and Jason-3 satellites are detailed in **Table 4**. The statistical analysis results showed that the correlation coefficient between the daily mean series of the SWHs from the HY-2B and Jason-3 satellites was 0.748, which indicated that the variations in the daily means of the SWHs for the HY-2B and Jason-3 satellites were consistent. The average and standard deviation of the differences between the daily mean series of SWHs from the HY-2B and Jason-3 satellites was determined to be (-3.40 ± 5.12) cm. The results demonstrated the high accuracy of the SWHs, which had been calculated by the HY-2B satellite system.

Sea State Bias Corrections

The SSB is one of the main errors that tend to result in the deterioration of SSHs in altimetric measurements (Tran et al., 2010). The SSB is aroused due to the waves (Liu, 2014). The differences in the SSB corrections between the HY-2B and Jason-3 satellites were considered to have direct impacts on the accuracy of the height measurements. **Figure 4C** shows the daily mean series of the SSB corrections for the HY-2B and Jason-3 satellite systems. The statistics of the correlation coefficient and the differences between daily mean data series of the SSB corrections

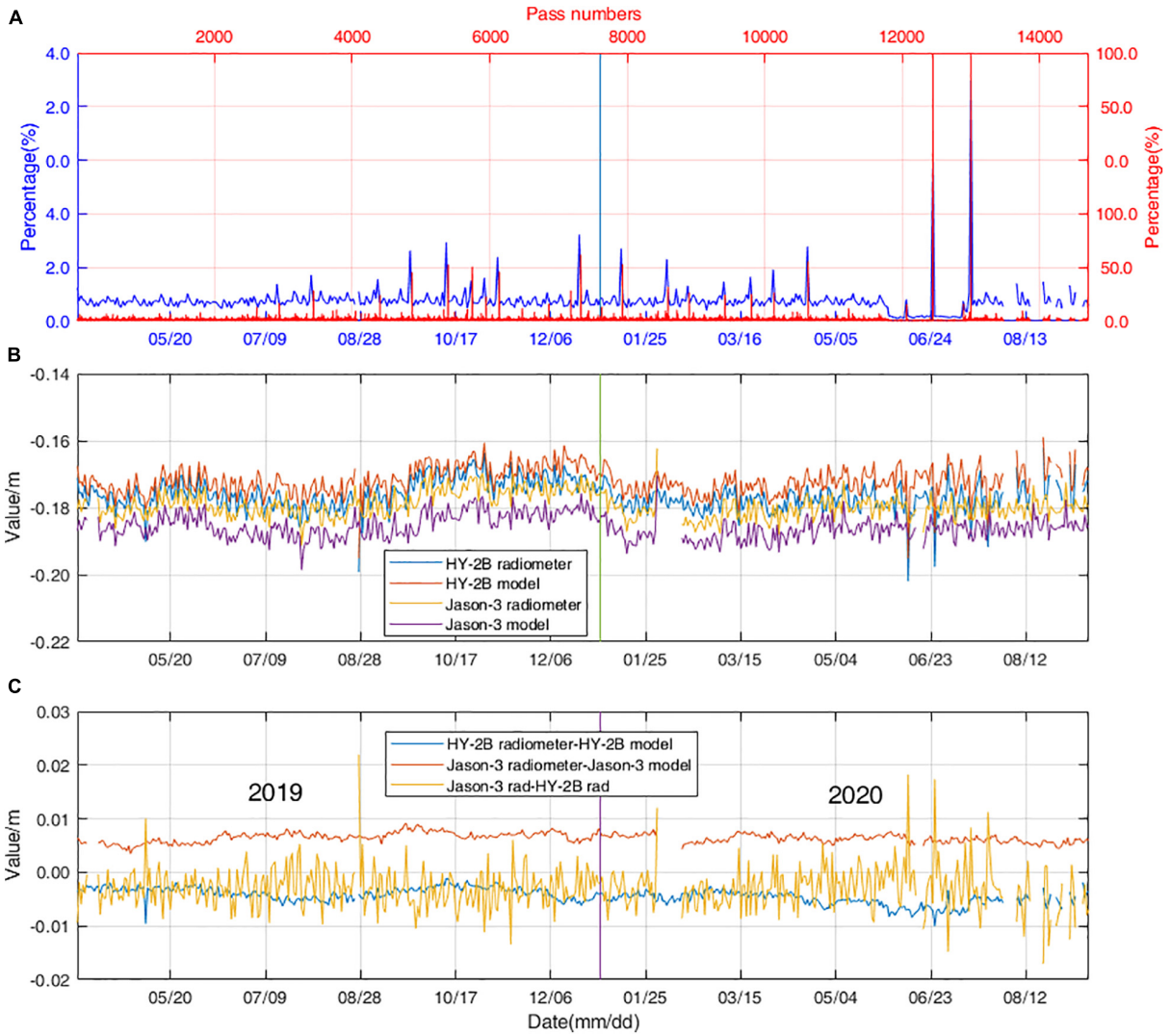

FIGURE 5 | Wet tropospheric corrections for Panel **(A)** is the proportion of null value of HY-2B collected by pass (red) and by day (blue); Panel **(B)** is the daily mean of wet tropospheric corrections time series of radiometer values and model values of HY-2B and Jason-3; Panel **(C)** is the differences between radiometer wet tropospheric corrections from HY-2B and Jason-3 and the differences between wet tropospheric corrections from radiometer and model for HY-2B and Jason-3, respectively.

from the HY-2B and Jason-3 satellites are shown in **Table 4**. The correlation coefficient between the daily mean series of the SWH from the HY-2B and Jason-3 satellites was determined to be 0.771. The maximum absolute value of the difference between the SSB corrections from the HY-2B and Jason-3 satellites was 4.46 cm. The average and standard deviation of the difference between the SSB corrections from the HY-2B and Jason-3 satellites was (-7.30 ± 3.20) mm. The comparison results indicated that the accuracy of the SSB corrections of the HY-2B satellite system was very high.

Wet Tropospheric Corrections

Wet tropospheric path delays are caused by the water vapor and cloud liquid water in the atmosphere, which tends to change significantly with the weather conditions. Wet tropospheric corrections are usually conducted using atmospheric models (such as ECMWF) or by using the brightness temperatures observed by satellite-borne microwave radiometers. The atmospheric model corrections can be utilized, while the radiometer observation data are invalid (or null values) in special circumstances. Wet tropospheric corrections are analyzed by the proportions of the null values and the comparison of the daily mean time series between HY-2B and Jason-3 missions, and the results are shown in **Figure 5**. The proportions of the null values of the wet tropospheric corrections of the HY-2B observation data were analyzed by daily time frames and cycle passes, and the results are shown in **Figure 5A**. It can be seen in the figure that the proportions of the null data from the radiometers were small during the majority of the examined days, with the exception of December 21, 2019, June 24, 2020, and July 14, 2020. In

was observed that the proportions of the null wet tropospheric correction data were 1.61, 3.17, and 4.67% on December 21, 2019, June 24, 2020, and July 14, 2020, respectively. The statistics of the null wet tropospheric corrections by pass showed that there were three passes (cycle 30, pass 330; cycle 44, pass 047; and cycle 45, pass 216) with high null wet tropospheric corrections proportions (they are 24.7, 99.8, and 100%, respectively), which caused large proportions of null wet tropospheric corrections during the three aforementioned days.

The daily mean time series of wet tropospheric corrections of the HY-2B and Jason-3 missions are shown in **Figures 5B,C**. **Figure 5B** shows the wet tropospheric corrections estimated from the model and from the HY-2B and Jason-3 radiometers. **Figure 5C** details the differences between the wet tropospheric corrections from the model and the radiometers of both the HY-2B and Jason-3 satellites. In addition, the differences between radiometer wet tropospheric corrections from the HY-2B and Jason-3 satellites are clearly shown. The statistics of the correlation coefficient and the differences between the daily mean data series of the radiometer corrections from the HY-2B and Jason-3 satellites are shown in **Table 4**. The statistics revealed that the correlation coefficient of the wet tropospheric corrections between the radiometer corrections and the model corrections for the HY-2B and Jason-3 satellites were 0.953 and 0.974, respectively. The mean value and STD of the differences between the corrections from radiometers and the model for the HY-2B and Jason-3 satellites were (-4.40 ± 1.40) mm and (6.40 ± 1.40) mm, respectively. The results demonstrated that there were only small differences between model values and radiometer corrections for the HY-2B satellite. The bias between the model values and radiometer corrections were observed to be small for HY-2B when compared with those of the Jason-3 satellite. The mean value and STD of the differences between the wet tropospheric corrections from Jason-3 and HY-2B was determined to be (2.90 ± 4.10) mm. The daily mean analysis of the wet tropospheric corrections showed no obvious trends or drifts within the examined period. Therefore, it was indicated that the HY-2B radiometer had displayed good stability and accuracy in its performance.

Ionospheric Corrections

The ionospheric corrections were estimated using a dual-frequency observation method of the Ku- and C-bands for the HY-2B and Jason-3 satellites. The global ionosphere maps (GIM) model values of the ionospheric corrections were also provided in the GDR dataset. **Figure 6A** shows this study's comparison of the daily mean series of the ionospheric corrections; **Figure 6B** details the differences between the daily mean series of the dual-frequency ionospheric corrections from the HY-2B and Jason-3 satellites and the differences between daily mean series of the ionospheric corrections retrieved from the dual-frequency corrections and model corrections for the HY-2B and Jason-3, respectively. The statistics of correlation coefficient and the differences between the daily mean series of the dual-frequency ionospheric corrections from the HY-2B and Jason-3 satellites are shown in **Table 4**. The statistical analysis results revealed that the correlation coefficient between the ionospheric corrections from the dual-frequency and GIM model values were 0.968 and 0.991 for the HY-2B and Jason-3 satellites, respectively. The mean and standard deviation of the difference between dual-frequency corrections and GIM model corrections for the HY-2B and Jason-3 satellites were (1.50 ± 0.85) mm and (7.40 ± 0.76) mm, respectively, which indicated good performance results for the ionospheric corrections of the HY-2B satellite. The mean and standard deviation of the difference between the dual-frequency corrections from the Jason-3 and HY-2B satellites was (4.80 ± 2.10) mm. These results demonstrated a systematic bias of 4.80 mm, and there were no obvious trends or drifts observed in the ionospheric corrections of the HY-2B system.

SLA ANALYSIS

The sea level anomalies, which can be estimated using Eqs 1 and 2, are generally used to study the variations in the SSHs and to monitor the long-term performance of an altimeter. SLAs were computed by the restrictions of the deep ocean areas (bathymetry $\leq -1{,}000$ m) and latitude bounds of $\pm 50°$. The accuracy of the daily mean SLAs derived from the HY-2B system was assessed in this study using by comparing them with those derived from the Jason-3 system. The crossover analysis results of the SLAs were adopted to provide a global view of the system performance of the HY-2B satellite. The SLA differences were analyzed at the self-crossover points of the HY-2B mono-mission and at dual-crossover points between the HY-2B and Jason-3 satellites. In addition, in order to reduce the impacts of the temporal variations of the marine environments, the SLAs computed at the crossover points were compared within a measurement time difference of <3 days. It was assumed that the SLAs at the crossover points with measurement differences of <3 days should be consistent. The editing criteria in Bao et al. (2015) was used in this study.

SLAs Daily Mean Analysis

The statistical analysis results showed that three times of the standard deviation of the daily mean of the SLAs are no more than 2 m. Therefore, the daily mean SLAs over 2 m were assumed as gross errors and were excluded from the results. The averages of the daily mean SLAs for the HY-2B and Jason-3 satellites were 0.75 and 4.02 cm, respectively. The average and STD of the difference between the daily mean of the SLAs from the HY-2B and Jason-3 satellites was confirmed to be (-3.24 ± 1.07) cm. As can be seen in **Figure 7**, the SLAs of the HY-2B and Jason-3 satellites both had displayed slight descending trends, which was 0.37 mm/a for the Jason-3 satellite and 5.90 mm/a for the HY-2B satellite.

SLAs Crossover Analysis

A cross-calibration method (Cheng and Andersen, 2014; Peng, 2015) was used in this study to verify the accuracy and performance of the HY-2B satellite system. During this study's examinations, differences over 1 m at the self-crossover points were excluded from the results. The results of SLA difference at

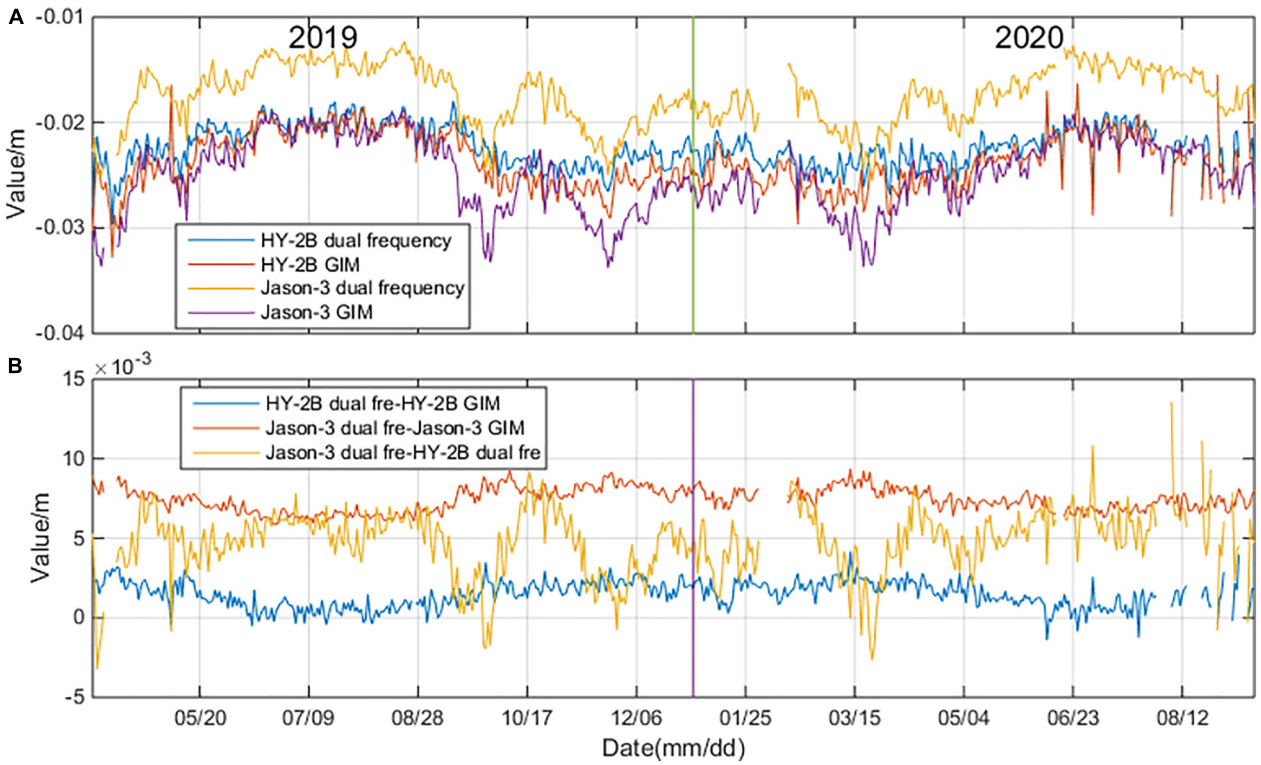

FIGURE 6 | The daily mean of ionospheric corrections time series of **(A)** dual-frequency corrections and GIM model corrections for HY-2B and Jason-3; **(B)** the difference between ionospheric corrections from dual-frequency corrections and GIM corrections for HY-2B and Jason-3 respectively, and the difference between dual-frequency ionospheric corrections from Jason-3 and HY-2B.

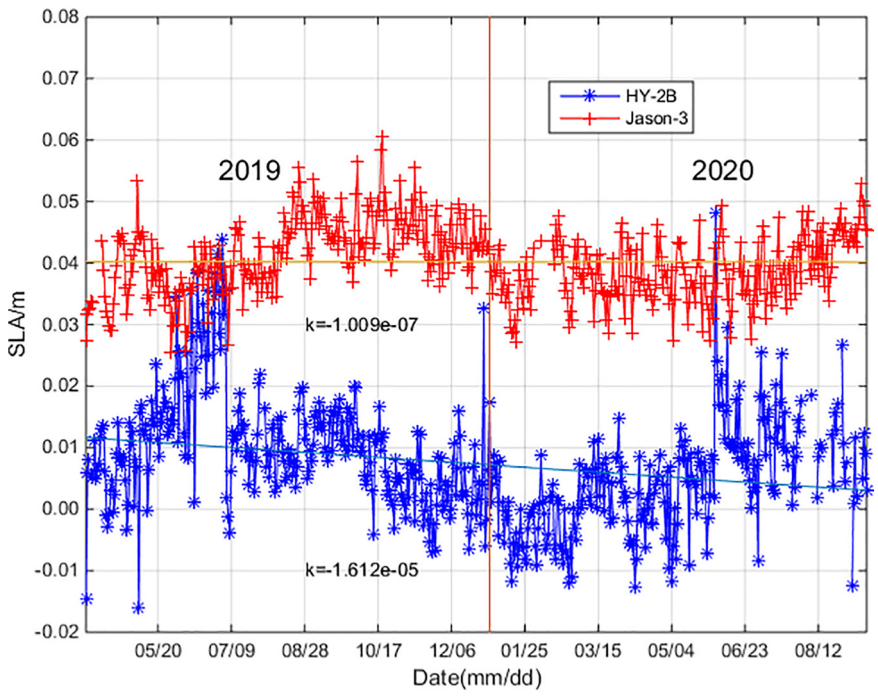

FIGURE 7 | The daily mean SLAs of HY-2B and Jason-3.

self-crossover points of the intrinsic mono-mission of the HY-2B are shown in **Figure 8**. The series of differences between the SLAs of the HY-2B satellite at self-crossover points are shown in **Figure 8A**. As can be seen in **Figure 8A**, with the exception of a few large individual errors in the SLAs, the majority of SLA differences at the self-crossover points were relatively stable and had fluctuated within a small range of scope. The mean and STD of the differences between SLAs at the self-crossover points of the HY-2B satellite was (0.19 ± 8.48) cm. The main scope range for the differences in the SLAs was between -0.06 and 0.06 m. **Figures 8B,C** shows the mean and STD of differences between the SLAs of the HY-2B satellite at self-crossover points as computed cycle by cycle. In cycles 15–18, 31, and 32, the standard deviation of the differences between the SLAs at self-crossover points were observed to be relatively larger. The SLA differences greater than three times the standard deviation of SLA differences at the crossovers were assumed to be gross errors and were removed from the SLAs series. Then, the mean and standard deviation of the differences between SLAs was determined to be (0.21 ± 6.70) cm. The statistical analysis results indicated that the data quality was relatively stable. The percentage of excluded data for the differences of the SLAs was 1.81%. **Figure 8D** details the differences in SLAs at crossovers, which were found to have a normal distribution after filtering at three times the standard deviation. This had clearly demonstrated the characteristics of a normal distribution. Then, the spatial distribution of the SLA differences of the HY-2B satellite at the self-crossovers were further analyzed. **Figure 8E** shows cycle 28 as an example of the distribution of the SSH differences at the crossovers, which were found to be relatively uniform and not affected by the marine environments.

The SLA differences at the dual-crossover points between the HY-2B and Jason-3 satellites were also calculated in this study. The crossover differences with values greater than three times of the STD were assumed to be gross error and removed, which accounted for approximately 0.87%. Then, the mean and STD

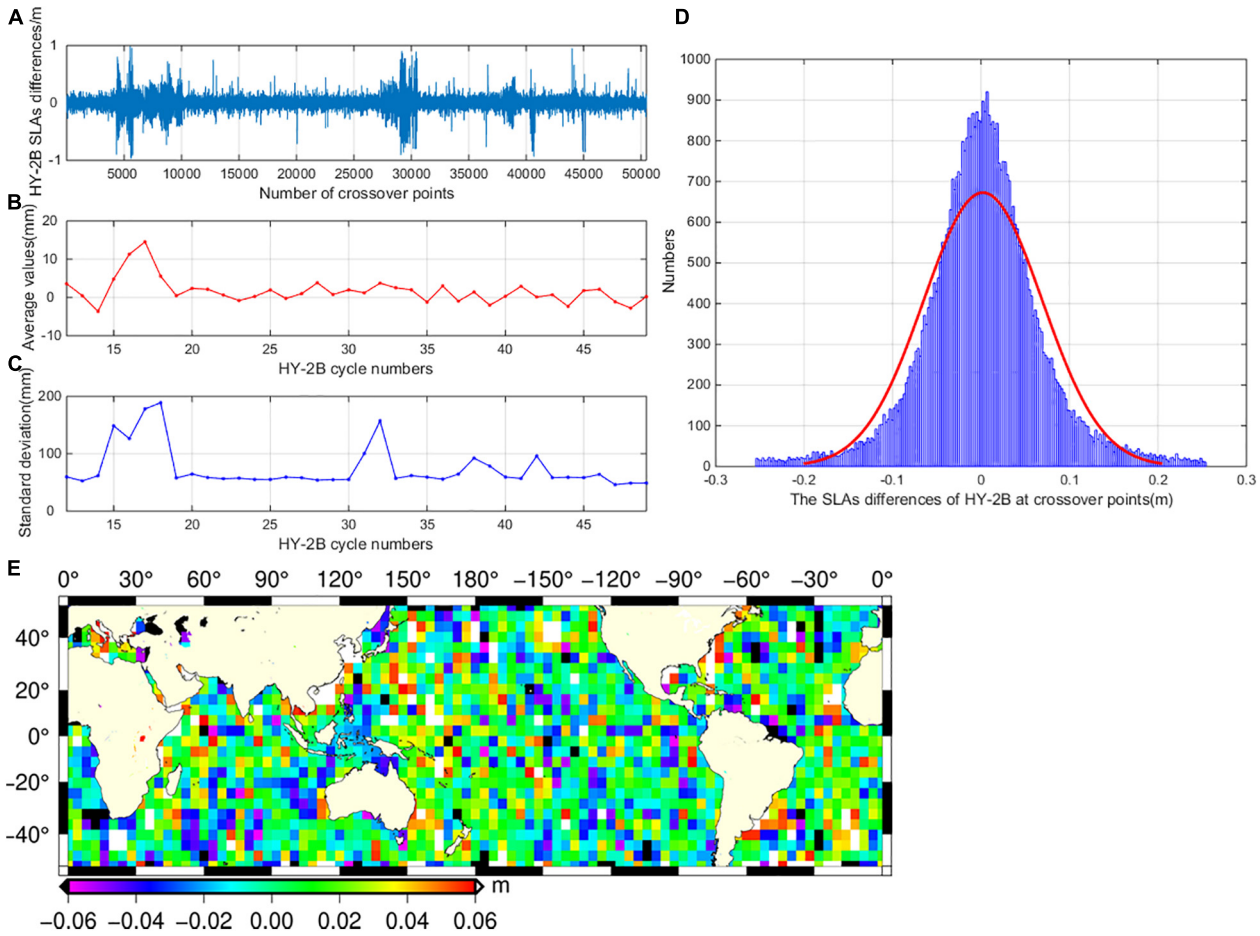

FIGURE 8 | The results of SLAs difference at self-crossover points of the intrinsic mono-mission of the HY-2B: Panel **(A)** is the differences series of HY-2B SLAs at self-crossover points (time differences larger than 3 days were removed); Panels **(B,C)** are cycle by cycle average and standard deviation of SLAs differences at self-crossover points, respectively; Panel **(D)** is the histogram of the differences between SLAs at self-crossover points of HY-2B (differences greater than three times of standard deviation were removed); Panel **(E)** is the spatial distribution of the differences between SSHs at self-crossover points of HY-2B with a grid of 4° × 4° in cycle 28.

of the differences of the SLAs at the dual-crossover points was determined to be (−3.40 ± 6.25) cm. **Figure 9** shows this study's comparison of the SLAs and the histogram of the differences between the SLAs at the dual-crossover points of the HY-2B and Jason-3 satellites. It can be seen in the figure that the SLA difference followed the normal distribution perfectly, and the slope of the linear regression of the parameters was almost equal to 1. These results confirmed the consistency of the SLAs between the HY-2B and Jason-3 satellites.

Wavenumber Spectra Analysis of the SLAs

The wavenumber spectra of the SLAs of the HY-2B satellite were computed and compared with that of the Jason-3 satellite. Then, the SLAs of the global oceans were used for this study's wavenumber spectra analysis in order to detect the noise levels of the satellite altimeters. The global SLA power spectra over the Jason-3 satellite (cycle 115) and the HY-2B satellite (cycle 12) are shown in **Figure 10**. In the coverage of the wavelengths larger than 100 km, the overall wavenumber spectra of the SLAs from the HY-2B satellite were found to almost be the same as that of the Jason-3, in which both followed specific power low between k^{-3} to k^{-4}, which meant that the signals were dominated by large scales (Bao et al., 2015). For the wavelengths smaller than 100 km, the signals of noise for both altimeters turned gradually toward dominance and the slopes became flatter, which was slightly lower for the HY-2B satellite when compared to the Jason-3. These results indicated that the HY-2B measured SLAs were as accurate as those obtained by the Jason-3 satellite over the wavelengths >100 km and were slightly better than the Jason-3 results over the wavelengths <100 km.

RESULTS AND DISCUSSION

In the present study, the main altimetry parameters and SLAs of the HY-2B satellite were analyzed and compared with the data obtained from the Jason-3 satellite mission in order to reveal the HY-2B satellites performance accuracy and consistency achievements. The statistical results confirmed the high quality and reliability of the HY-2B satellite's data. The main satellite altimetric parameters showed that the total editing proportion was 2.67% on average for the HY-2B satellite, which was slightly better than that achieved by the Jason-3 satellite (2.86%). It was found that while the data were constrained over the deep water and low altitude ocean areas, the total editing proportion had decreased to under 2% (1.07%) for the HY-2B satellite, which was slightly better than that of the Jason-3 satellite (1.67%). Five key parameters (Sigma0, SWH, SSB, wet troposphere delays, and ionospheric delays) of the HY-2B satellite were analyzed through a comparison with the Jason-3 satellite. The results showed that the Sigma0, SWH, and SSB had strong correlation coefficients between the HY-2B and Jason-3 satellites with correlation coefficients of 0.762, 0.748, and 0.771, respectively. In regard to the other two parameters, the correlation coefficient performances were slightly lower but still remained higher than 0.5. The system biases for the main parameters between the HY-2B and Jason-3 satellites were also calculated in this study. The

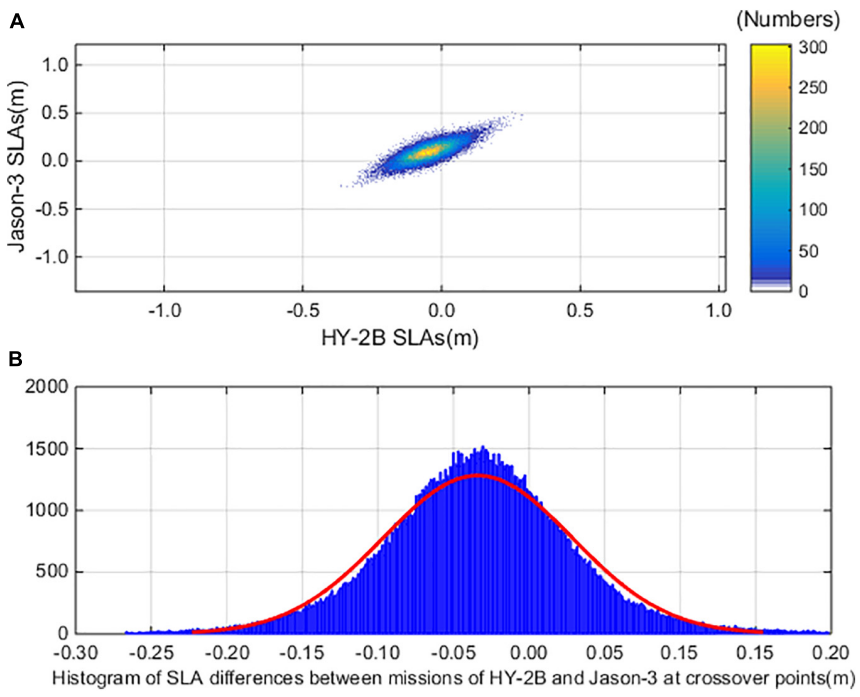

FIGURE 9 | SLA series for Panel **(A)** is the comparison between SLAs from HY-2B and Jason-3, and for Panel **(B)** is the histogram of the differences between SLAs at dual-crossover points of HY-2B and Jason-3 (differences greater than three times of standard deviation were removed).

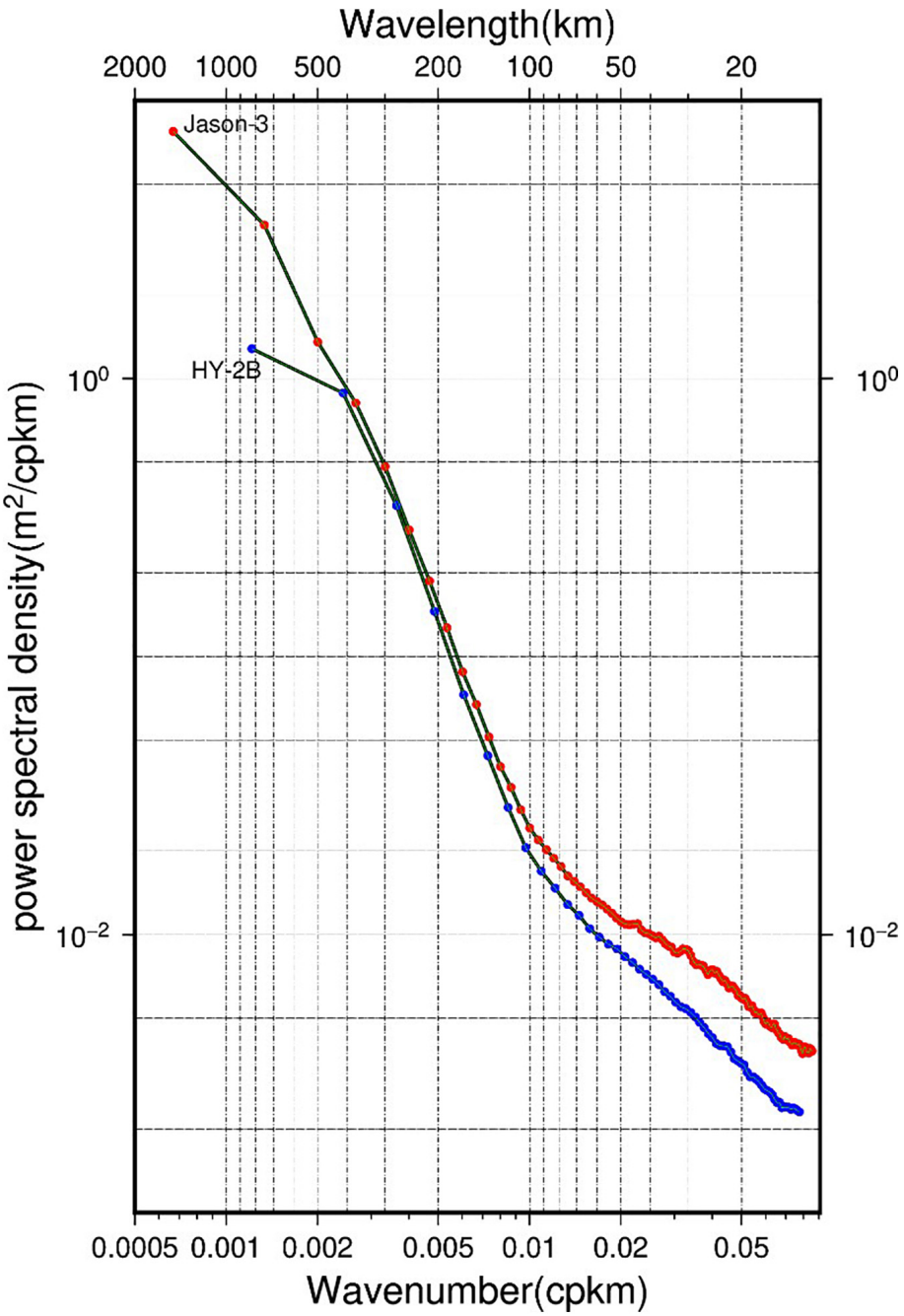

FIGURE 10 | Wavenumber spectra of SLAs computed using Jason-3 cycle 115 and HY-2B cycle 12 over global ocean.

mean and STD of differences between the daily mean series of parameters Sigma0, SWH, and SSB from the HY-2B and Jason-3 satellites were determined to be (−0.0165 ± 0.1054) dB, (−3.40 ± 5.12) cm, and (−7.30 ± 3.20) mm, respectively. In addition, for the radiometer wet tropospheric corrections and the dual-frequency ionospheric corrections, the system biases between the Jason-3 and HY-2B satellites were (2.90 ± 4.10) mm and (4.80 ± 2.10) mm, respectively. These results confirmed that the radiometer and the dual-frequency altimeter of the HY-2B had performed well and had achieved accuracy levels similar to the Jason-3 satellite. The analysis results of the time series of the wet tropospheric delays showed no system drifts within the study period, which indicated that good stability and accurate performances had been achieved by the HY-2B radiometer.

The SLAs and SSHs of the HY-2B system were calculated and compared with the Jason-3 satellite. The daily mean of the SLA time series showed similar trends for both of the

satellites, which may have been related to the seasonal sea level changes. The accuracy of the SLAs for the HY-2B satellite was up to the subcentimeter level when compared to the Jason-3 mission results. The SLA differences at the crossover points between the HY-2B and Jason-3 satellites were determined to be (-3.40 ± 6.25) cm, which indicated that the system bias was small. This study also estimated that the SLA difference at the HY-2B self-crossover points was (0.21 ± 6.70) cm. The distribution of the SSH differences at the HY-2B self-crossover points were observed to be relatively uniform, indicating that no geographically correlated errors had occurred. The mean value of the HY-2B SLA differences was close to 0 cm, which demonstrated that the HY-2B satellite's internal agreement was excellent. The STD of the SLA differences was determined to be approximately 6 cm, which confirmed that the accuracy of the SSH measurements of HY-2B system had satisfied the requirements of the design.

Through this study's SLA wavenumber analysis process, it was found that the HY-2B and Jason-3 satellites were in good agreement in wavelengths >100 km. Furthermore, it was observed that for the wavelengths <100 km, the instrumental noise levels of the HY-2B satellite were slightly lower than those of the Jason-3 satellite.

CONCLUSION

The HY-2B satellite has been operating in its orbit for more than 2 years. However, few studies have focused on the data quality and system performance of the HY-2B mission to date. Therefore, this research study focused on providing the first exhaustive statistical evaluation and quality assessment of the HY-2B altimetric GDR data set. A continuous 38 cycles of the mission, along with the widely validated and calibrated data sets of the Jason-3 satellite during the same time span, were used to perform a comprehensive quality assessment of the HY-2B system's performance. The conclusions reached in this study were as follows:

(1) When compared with HY-2A satellite system, the parameter of editing proportions of the HY-2B satellite were found to be significantly improved. It was found that the editing proportions were at a level similar to those of the Jason-3 satellite, indicating that the data availability was high for the HY-2B system.
(2) The correlation coefficient between the daily mean series of the five main examined parameters (Sigma0, SSB corrections, SWH, ionospheric corrections, and wet tropospheric corrections) from the HY-2B and Jason-3 missions were all determined to be larger than 0.5. This was particularly true in regard to the parameters of Sigma, SWH, and SSB corrections, which were all larger than 0.7. The daily mean analysis results of the five main parameters revealed that there were no obvious trends or systematic bias (drifts), which further confirmed that the HY-2B satellite had achieved consistency and accuracy levels similar to the Jason-3 satellite.
(3) The mean and standard deviation of the differences of the daily mean of the SLAs from the HY-2B and Jason-3 satellites was determined to be (-3.24 ± 1.07) cm. The standard deviations of the difference between SLAs at the self-crossover points of the HY-2B satellite and at the dual-crossover points of the HY-2B and Jason-3 satellites were determined to be 6.70 and 6.25 cm, respectively, after the points with time differences larger than 3 days were removed. These results further demonstrated the high stability and reliability of the HY-2B mission and that the accuracy of SLAs for the HY-2B had achieved a subcentimeter level.
(4) The wavenumber spectra of the SLAs estimated by the HY-2B and Jason-3 satellite systems over the global oceans indicated that the HY-2B satellite's SLA measurements were as accurate as those of the Jason-3 satellite over the wavelengths >100 km and slightly better than the Jason-3 system for the wavelengths <100 km.

In summary, the results obtained in this study showed that the HY-2B satellite system had achieved very good performance and data accuracy levels. However, the radar altimeters of HY-2B and Jason-3 satellites are typical traditional radar altimeters, altimeters' noise level are limited to a spatial resolution of 100 km or more, and the spatial resolution of individual satellites still does not allow for submesoscale observations. Combining observations from different families of on-orbit altimeter satellites (e.g., the recently launched Sentinel-6 MF and HY-2C, which launched in November 2020 and in September 2020, respectively) can improve the resolution problem. In addition, the upcoming interferometric radar altimeters [such as surface water and ocean topography (SWOT)] will also contribute significantly to the spatial resolution. Since the time span in this study were just 1.5 years, the long-term bias or drift could not be detected in this investigation. Therefore, further data validation and calibration research will be carried out for the long-term monitoring of parameters and SLAs in order to determine the long-term bias. In addition, absolute calibrations with tidal gauge observations will still be required in order to investigate the HY-2B satellite's total accuracy performance. Combined with absolute calibrations, HY-2B data can be used for the inspections and calibrations of other altimeter satellites.

DATA AVAILABILITY STATEMENT

The original contributions presented in the study are included in the article/supplementary material, further inquiries can be directed to the corresponding author/s.

AUTHOR CONTRIBUTIONS

JW: methodology, formal analysis, writing – original draft, writing – editing, and funding acquisition. LY: methodology, review and editing, formal analysis, and validation. HX: formal analysis, software, and validation. CM: data curation and resource. QS:

conceptualization, investigation, and methodology. All authors have read and agreed to the published version of the manuscript.

FUNDING

This project was funded by the Priority Academic Program Development of Jiangsu Higher Education Institutions (PAPD), the National Natural Science Foundation of China (Grant Nos. 41776029 and 41806214), and the Key Research and Development Program of Jiangsu Province under Contract No. BE2018676.

ACKNOWLEDGMENTS

We thank the National Satellite Ocean Application Service for providing the HY-2B geophysical data records (GDRs) products. We also thank the Archiving, Validation, and Interpretation of Satellite Oceanographic Data (AVISO) for providing Jason-3 geophysical data records (GDR) products. The GDR data of HY-2B now is freely available to the public through the Ocean Satellite Data Distribution System (https://osdds.nsoas.org.cn). We thank Nicholas Angiers from transwings, transwings Group China (www.gbtranswins.com), for editing the English text of a draft of this manuscript.

REFERENCES

Ablain, M., Philipps, S., Picot, N., and Bronner, E. (2010). Jason-2 global statistical assessment and cross-calibration with jason-1. *Mar. Geod.* 33 (Supp. 1), 162–185. doi: 10.1080/01490419.2010.487805

Babu, K. N., Shukla, A. K., Suchandra, A. B., Kumar, S. V. V. A., Bonnefond, P., Testut, L., et al. (2015). Absolute calibration of SARAL/AltiKa in kavaratti during its initial calibration-validation phase. *Mar. Geod.* 38 (Suppl. 1), 156–170. doi: 10.1080/01490419.2015.1045639

Bao, L. F., Gao, P., Peng, H. L., Jia, Y., Shum, C. K., Lin, M. S., et al. (2015). First accuracy assessment of the HY-2A altimeter sea surface height observations: cross-calibration results. *Adv. Space Res.* 55, 90–105. doi: 10.1016/j.asr.2014.09.034

Bonnefond, P., Exertier, P., Laurain, O., Ménard, Y., Orsoni, A., Jan, G., et al. (2003). Absolute calibration of jason-1 and TOPEX/poseidon altimeters in corsica special issue: jason-1 calibration/validation. *Mar. Geod.* 26, 261–284. doi: 10.1080/714044521

Cartwright, D. E., and Edden, A. C. (1973). Corrected tables of tidal harmonics. *Geophys. J. Int.* 33, 253–264. doi: 10.1111/j.1365-246X.1973.tb03420.x

Chelton, D., Ries, J., Haines, B., Fu, L., and Callahan, P. (2001). *Satellite Altimetry and Earth Sciences: A Handbook of Techniques and Applications*, Vol. 69, eds Fu L-L and A. Cazenave (California, CA: Academic Press).

Cheng, Y. C., and Andersen, O. B. (2014). "HY-2A satellite altimetric data evaluation in the arctic ocean," in *Proceedings of the 2014 IEEE Geoscience and Remote Sensing Symposium*, (Quebec City, QC: IEEE).

Christensen, E. J., Haines, B. J., Keihm, S. J., Morris, C. S., Norman, R. A., Purcell, G. H., et al. (1995). Calibration of TOPEX/POSEIDON at Platform Harvest. *J. Geophys. Re. Oceans* 99, 24465–24485. doi: 10.1029/94JC01641

Crétaux, J. F., Calmant, S., Romanovski, V., Shabunin, A., Lyard, F., Bergé-Nguyen, M., et al. (2008). An absolute calibration site for radar altimeters in the continental domain: lake issykkul in Central Asia. *J. Geod.* 83, 723–735. doi: 10.1007/s00190-008-0289-7

Dettmering, D., and Bosch, W. (2010). Global calibration of jason-2 by multi-mission crossover analysis. *Mar. Geod.* 33(Suppl. 1), 150–161. doi: 10.1080/01490419.2010.487779

Dettmering, D., Schwatke, C., and Bosch, W. (2015). Global calibration of SARAL/AltiKa using multi-mission sea surface height crossovers. *Mar. Geod.* 38(Suppl. 1), 206–218. doi: 10.1080/01490419.2014.988832

Fu, L. L., and Haines, B. J. (2013). The challenges in long-term altimetry calibration for addressing the problem of global sea level change. *Adv. Space Res.* 51, 1284–1300. doi: 10.1016/j.asr.2012.06.005

Jiang, C. F., Lin, M. S., and Wei, H. (2019). A study of the technology used to distinguish sea ice and seawater on the haiyang-2A/B (HY-2A/B) altimeter data. *Remote Sens.* 11:1490. doi: 10.3390/rs11121490

Jiang, X., Jia, Y., and Zhang, Y. (2019). Measurement analyses and evaluations of sea-level heights using the HY-2A satellite's radar altimeter. *Acta Oceanol. Sin.* 38, 134–139. doi: 10.1007/s13131-019-1503-6

Lin, M. S., and Jiang, X. W. (2014). "HY-2 ocean dynamic environment mission and payloads," in *Proceedings of the 2014 IEEE Geoscience and Remote Sensing Symposium*, (Quebec City, QC: IEEE), 5167–5170.

Liu, Y. Y. (2014). *Calibration Technology for HY-2 Radar Altimeter Sea Surface Height*. Master's thesis (in Chinese). Qingdao: Ocean University of China.

Mertikas, S. P., Daskalakis, A., Tziavos, I. N., Vergos, G., Fratzis, X., and Tripolitsiotis, A. (2015a). First calibration results for the SARAL/AltiKa altimetric mission using the gavdos permanent facilities. *Mar. Geod.* 1, 249–259. doi: 10.1080/01490419.2015.1030052

Mertikas, S. P., Zhou, X. H., Qiao, F. L., Daskalakis, A., Lin, M. S., Peng, H. L., et al. (2015b). First preliminary results for the absolute calibration of the chinese HY-2 altimetric mission using the CRS1 calibration facilities in west crete, Greece. *Adv. Space Res.* 57, 78–95. doi: 10.1016/j.asr.2015.10.016

Michaud, L., Roinard, H., Labroue, S., and Piras, F. (2019). *Jason-3 GDR Quality Assessment Report Cycle 116. SALP-RP-JALT3-EX-23103-CLS116 (Edition 01.0)*. Available online at: ftp://avisoftp.cnes.fr/Niveau0/AVISO/pub/jason-3/gdr_d_validation_report (accessed December 29, 2020).

Passaro, M., Dinardo, S., Quartly, G. D., Snaith, H. M., Benveniste, J., Cipollini, P., et al. (2016). Cross-calibrating ALES envisat and CryoSat-2 delay-doppler: a coastal altimetry study in the indonesian seas. *Adv. Space Res.* 58, 289–303. doi: 10.1016/j.asr.2016.04.011

Peng, H. L. (2015). *Research on Key Technology of HY-2A Satellite Radar Calibration*. Master's thesis (in Chinese). Qingdao: Ocean University of China.

Prandi, P., Philipps, S., Pignot, V., and Picot, N. (2015). SARAL/AltiKa global statistical assessment and cross-calibration with jason-2. *Mar. Geod.* 38(Suppl. 1), 297–312. doi: 10.1080/01490419.2014.995840

Tran, N., Labroue, S., Philipps, S., Bronner, E., and Picot, N. (2010). Overview and update of the sea state bias corrections for the jason-2, Jason-1 and TOPEX missions. *Mar. Geod.* 33(Suppl. 1), 348–362. doi: 10.1080/01490419.2010.487788

Wahr, J. M. (1985). Deformation induced by polar motion. *J. Geophys. Res. Solid Earth* 90, 9363–9368. doi: 10.1029/JB090iB11p09363

Watson, C., Coleman, R., White, N., Church, J., and Govind, R. (2003). Absolute calibration of topex/poseidon and jason-1 using GPS buoys in bass strait. australia special issue: jason-1 calibration/validation. *Mar. Geod.* 26, 285–304. doi: 10.1080/714044522

Yang, J. G., Zhang, J., and Wang, C. Y. (2019). Sentinel-3A SRAL global statistical assessment and cross-calibration with jason-3. *Rem. Sens.* 11:1573. doi: 10.3390/rs11131573

Yang, L., Xu, Y. S., Zhou, X. H., Zhu, L., Jiang, Q. F., Sun, H. W., et al. (2020). Calibration of an airborne interferometric radar altimeter over the qingdao Coast Sea, China. *Rem. Sens.* 12:1651. doi: 10.3390/rs12101651

Yang, L., Zhou, X. H., Lin, M. S., Lei, N., Mu, B., and Zhu, L. (2016). Global Statistical assessment of HY-2A altimeter IGDR data. *Progr. Geophys (in Chinese)* 31, 0629–0636. doi: 10.6038/pg20160216

Yang, L., Zhou, X. H., Mertikas, S. P., Lin, Z., Long, Y., and Ning, L. (2017). First Calibration results of jason-2 and Saral/AltiKa Satellite altimeters from

the qianliyan permanent facilities. *Adv. Space Res.* 59, 2831–2842. doi: 10.1016/j.asr.2017.02.044

Yuan, J. J., Guo, J. Y., Liu, X., Zhu, C. C., Niu, Y. P., Li, Z., et al. (2020). Mean Sea surface model over china seas and its adjacent ocean established with the 19-year moving average method from multi-satellite altimeter data. *Contin. Shelf Res.* 192:104009. doi: 10.1016/j.csr.2019.104009

Zaouche, G., Perbos, J., Lafon, T., Couderc, V., Lambin, J., Desjonqueres, D., et al. (2010). OSTM/jason-2: assessment of the system performances (ocean surface topography mission: OSTM). *Mar. Geod.* 33(Suppl. 1), 26–52. doi: 10.1080/01490419.2010.488978

Conflict of Interest: The authors declare that the research was conducted in the absence of any commercial or financial relationships that could be construed as a potential conflict of interest.

frontiers in Earth Science

ORIGINAL RESEARCH
published: 30 April 2021
doi: 10.3389/feart.2021.668863

Seafloor Density Contrast Derived From Gravity and Shipborne Depth Observations: A Case Study in a Local Area of Atlantic Ocean

Xiaoyun Wan[1], Weipeng Han[2], Jiangjun Ran[3], Wenjie Ma[1], Richard Fiifi Annan[1] and Bing Li[4]*

[1] School of Land Science and Technology, China University of Geosciences (Beijing), Beijing, China, [2] College of Geological Engineering and Surveying, Chang'an University, Xi'an, China, [3] Department of Earth and Space Sciences, Southern University of Science and Technology, Shenzhen, China, [4] First Institute of Oceanography, Ministry of Nature Resources, Qingdao, China

OPEN ACCESS

Edited by:
Jinyun Guo, Shandong University of Science and Technology, China

Reviewed by:
Zhicai Luo, Huazhong University of Science and Technology, China
Min Zhong, Institute of Geodesy and Geophysics (CAS), China

****Correspondence:***
Xiaoyun Wan
wanxy@cugb.edu.cn

Specialty section:
This article was submitted to Environmental Informatics and Remote Sensing, a section of the journal Frontiers in Earth Science

Received: *17 February 2021*
Accepted: *08 April 2021*
Published: *30 April 2021*

Citation:
Wan X, Han W, Ran J, Ma W, Annan RF and Li B (2021) Seafloor Density Contrast Derived From Gravity and Shipborne Depth Observations: A Case Study in a Local Area of Atlantic Ocean. Front. Earth Sci. 9:668863. doi: 10.3389/feart.2021.668863

Marine gravity data from altimetry satellites are often used to derive bathymetry; however, the seafloor density contrast must be known. Therefore, if the ocean water depths are known, the density contrast can be derived. This study experimented the total least squares algorithm to derive seafloor density contrast using satellite derived gravity and shipborne depth observations. Numerical tests are conducted in a local area of the Atlantic Ocean, i.e., 34°∼32°W, 3.5°∼4.5°N, and the derived results are compared with CRUST1.0 values. The results show that large differences exist if the gravity and shipborne depth data are used directly, with mean difference exceeding 0.4 g/cm^3. However, with a band-pass filtering applied to the gravity and shipborne depths to ensure a high correlation between the two data sets, the differences between the derived results and those of CRUST1.0 are reduced largely and the mean difference is smaller than 0.12 g/cm^3. Since the spatial resolution of CRUST1.0 is not high and in many ocean areas the shipborne depths and gravity anomalies are much denser, the method of this study can be an alternative method for providing seafloor density variation information.

Keywords: density contrast, seafloor, bathymetry, gravity anomaly, total least squares

INTRODUCTION

Shallow seabed density information plays an important role in understanding submarine structure, mineral exploration, military activity, and scientific research (Nagendra et al., 1996; Felix et al., 2002; Hsiao et al., 2011; Sandwell et al., 2014a). For a local ocean area, the shipborne equipment can be used for the detection. However, for the global ocean area, it is very difficult to detect and retrieve the shallow seabed density distribution with high resolution and high precision using shipborne observations.

Currently, there are mainly two methods for the study of the Earth's internal structure, including the density contrast of the seabed, i.e., the density difference between the seawater and the upper crust. One is based on seismic wave data and the other is based on gravity data. For the former, scholars have carried out a lot of investigations. For example, Soller et al. (1982) derived a global

crustal thickness model with resolution of 2° × 2° based on seismic data; Nataf and Ricard (1996) combined geothermal and seismic data to invert the density structure of the global and upper mantle; Mooney et al. (1998) published a global crustal model crush with a spatial resolution of 5° × 5°. Based on seismic, ice sheet and sedimentary datasets, Bassin (2000) derived the crustal model CRUST2.0 with a resolution of 2° × 2° and Laske et al. (2013) released the crustal model CRUST1.0 with a spatial resolution of 1° × 1° based on CRUST5.1 and CRUST2.0. The above models provide not only the thickness information of each layer, including water layer, ice layer, soft sedimentary layer, hard sedimentary layer, upper crust, middle and lower crust, but also the density information. These models play a significant role in the study of the Earth's internal structure.

However, the above models cannot fully meet all the application requirements. For example, the spatial resolution of the global model published only reaches 100 km, which is obviously insufficient for studying many local problems. In addition, the models mentioned above have great uncertainties in many regions, mainly because of the uneven distribution of seismic observation stations, and thus there are no or few seismic observations in some regions. Therefore, if one wants to retrieve the density distribution of the Earth's interior with higher spatial resolution using information from seismic data, a densification of current network of seismic stations is needed. It would involve a lot of financial and material resources.

Another method is to use gravity field data for density inversion. Many algorithms for inversion of the Earth's internal structure or density distribution using gravity data have been proposed and adopted. Parker (1972) gave the Fourier relationship between the depth of density interface and gravity anomaly in frequency domain. According to the relationship, the depth of density interface can be deduced from gravity anomaly. The related formula has been widely used in inversion of Moho surface depth and seafloor topography, such as Jiang et al. (2015); Hu et al. (2015), and Sandwell et al. (2014a), etc. Indeed, the formula is based on the premise that there is a density anomaly and the density contrast is known. Conversely, if the depth of the density interface is known, the formula can also be used to derive the density contrast. In recent years, with the emergence of new altimetry technologies and the release of new altimetry satellite products, Sandwell et al. (2014a) studied the submarine structure, especially using the gravity gradient data to find and confirm the position of the plate boundary on the seabed, which can also be regarded as a density interface.

Definitely, gravity data can be used to detect the density distribution of the Earth's interior. However, some problems exist in the study of the Earth's interior structure (including the density contrast of the seabed) using gravity data. For example, the inversion results are usually not unique. The fundamental reason is that many sources of gravity anomaly information exist, including not only the seabed density contrast, but also the depth of the density interface (that is, the ocean depth). Therefore, if we can combine the ocean gravity field and the ocean depth information well, it is possible to retrieve the seabed density contrast information with high accuracy.

Indeed, in the inversion of seafloor topography, many methods have been proposed for density contrast determination, such as the iterative search method (Kim et al., 2011; Ouyang et al., 2014; Xiang et al., 2017). However, the density contrast derived in the bathymetry inversion usually have no physical meaning (Annan and Wan, 2020), since the purpose of these researches is to inverse bathymetry. The idea of this study is to take the density contrasts of the seabed as the inversion product while the water depths are known.

With the advances in space technology, highly accurate marine gravity anomaly products (Hwang et al., 2002; Andersen et al., 2010; Hwang and Chang, 2014; Sandwell et al., 2014b; Zhu et al., 2020) with resolution of 1′ × 1′ have been derived using satellite altimetry observations. Besides gravity field data, a large amount of shipborne depths have been obtained by many years of ship sounding observations. It is roughly estimated that NOAA (National Oceanic and Atmospheric Administration) has collected more than 50 million shipborne depth observations. Therefore, it is possible to achieve good results by making full use of the shipborne sounding data and gravity data to jointly invert the seabed density contrast. This study presents a case study. Section "Materials and Methods" introduces the inversion algorithm. Study area and data are described in section "Study Area and Data. Results and analysis are presented in section "Results and Analysis" and conclusions are derived finally in section "Conclusion."

MATERIALS AND METHODS

Function Model

According to principle of the gravity geological method (GGM) (Ibrahim and Hinze, 1972), we have:

$$\hat{g}_i = 2\pi G \Delta\hat{\rho}(H - \hat{h}_i) + \hat{g}_l \tag{1}$$

where $\hat{g}_i$ denotes the gravity anomaly observation at the ith point; $\hat{g}_l$ denotes the long wavelength part of the gravity anomaly; G means the gravitational constant; $\Delta\rho$ represents the density contrast; H is the depth datum and $\hat{h}_i$ denotes the water depths at the ith points. Definitely, the gravity anomaly observations have a linear relationship with $(H - \hat{h})$. In a local small area, the long wavelength part of gravity anomaly $\hat{g}_l$ and density contrast $\Delta\hat{\rho}$ can be seen as constants. Hence, Equation 1 can be rewritten as:

$$\hat{g}_i = \begin{bmatrix} \hat{g}_1 \\ \hat{g}_2 \\ \hat{g}_3 \\ \vdots \\ \hat{g}_n \end{bmatrix} = \begin{bmatrix} 1 & 2\pi G(H - \hat{h}_1) \\ 1 & 2\pi G(H - \hat{h}_2) \\ 1 & 2\pi G(H - \hat{h}_3) \\ \vdots & \vdots \\ 1 & 2\pi G(H - \hat{h}_n) \end{bmatrix} \begin{bmatrix} \hat{g}_l \\ \Delta\hat{\rho} \end{bmatrix} \tag{2}$$

Because both gravity anomaly and water depth datasets contain noises, two types of data error should be considered in the determination of the density contrast $\Delta\hat{\rho}$ and long wavelength of gravity anomaly $\hat{g}_l$. Ordinary least squares method only considers the error of dependent variable, i.e., gravity anomaly errors and

ignores the error of bathymetric data measured by ships. Hence, the inversion result by traditional least squares method based on Equation 2 would be not accurate enough. Instead, the total least squares (TLS) (Golub and van Loan, 1980; Xu et al., 2012) method was adopted in this study. Considering the two types of observation errors, the following equation can be constructed:

$$\hat{g}_i + v_{gi} = 2\pi G\Delta\hat{\rho}(H - h_i - v_{hi}) + \hat{g}_l \tag{3}$$

In which, v_{gi} and v_{hi} are the noises of gravity anomaly and shipborne depths respectively. Changing Equation 3 into the form of EIV (error in variables) model results in:

$$(A + E_A)\,x = L + E_L \tag{4}$$

where A is the coefficient matrix; E_A,E_L are the errors of matrices of A and observation vector L; x is the parameter to be estimated, i.e.,

$$A = \begin{bmatrix} 1 & H - h_1 \\ 1 & H - h_2 \\ \vdots & \vdots \\ 1 & H - h_3 \end{bmatrix} E_A = \begin{bmatrix} 0 & v_{h1} \\ 0 & v_{h2} \\ \vdots & \vdots \\ 0 & v_{h3} \end{bmatrix}$$

$$x = \begin{bmatrix} \hat{g}_l \\ 2\pi G\Delta\hat{\rho} \end{bmatrix} L = \begin{bmatrix} g_1 \\ g_2 \\ \vdots \\ g_n \end{bmatrix} E_L = \begin{bmatrix} v_{g1} \\ v_{g2} \\ \vdots \\ v_{gn} \end{bmatrix} \tag{5}$$

The final solution can be derived by the following rule.

$$v_s v_s^{\mathrm{T}} = \sum_{i=1}^{n} v_{hi}^2 + \sum_{i=1}^{n} v_{gi}^2 = \min \tag{6}$$

Solution of TLS

Solution of the TLS can be derived by Singular Value Decomposition (SVD) (Golub and van Loan, 1980). Firstly, augmented matrix C is defined as:

$$C = [A \;\; L] = \begin{bmatrix} 1 & H - h_1 & g_1 \\ 1 & H - h_2 & g_2 \\ \vdots & \vdots & \vdots \\ 1 & H - h_n & g_n \end{bmatrix} \tag{7}$$

And then Orthogonal Trigonometric (QR) decomposition is conducted on matrix C, in which Q is the orthogonal matrix as follows:

$$C = QR \tag{8}$$

$$R = Q^{-1}C = Q^{\mathrm{T}}C = \begin{bmatrix} R_{11} & R_{12} & R_{1l} \\ 0 & R_{22} & R_{2l} \end{bmatrix} \begin{matrix} n \\ n-m \end{matrix} \tag{9}$$

Based on the singular value decomposition of R-part of matrix C_R, the solution of TLS is obtained as Equation 10:

$$C_R = [R_{22} \;\; R_{2l}] = U \bullet \sum \bullet V^{\mathrm{T}} \tag{10}$$

where $\sum = diag(\delta_1, \delta_2)$ with singular values $\delta_1 \geq \delta_2 \geq 0$. And thus, the estimated parameters can be derived by the following equation.

$$\begin{bmatrix} \hat{a} \\ \hat{b} \end{bmatrix} = \begin{bmatrix} 2\pi G\Delta\hat{\rho} \\ g_l \end{bmatrix} = \left(AA^{\mathrm{T}} - \delta_2^2 \begin{bmatrix} 0 & 0 \\ 0 & 1 \end{bmatrix}\right)^{-1} A^{\mathrm{T}} l \tag{11}$$

Finally, we have:

$$\Delta\hat{\rho} = \frac{\hat{a}}{2\pi G} \tag{12}$$

The accuracy of TLS solution is evaluated by standard deviation of unit weight (SDUW) as follows:

$$\delta_{tls} = \sqrt{\frac{v_s v_s^{\mathrm{T}}}{n-2}} \tag{13}$$

where $v_s v_s^T = v_x v_x^T + v_y v_y^T$.

Filtering Method

In order to test the sensitive band of gravity anomaly to the seafloor topography, which is the basis for deriving the density contrast, band filtering with different pass bands was experimented and the correlation analysis was conducted correspondingly. The band-pass filters proposed by Smith and Sandwell (1994), which is indeed a filter by combining a Gaussian high-pass filter and a Wiener low-pass filter was used. According to Smith and Sandwell (1994), the high-pass filter is defined as Equation 14:

$$w_1(k) = 1 - e^{-2(\pi k s)^2} \tag{14}$$

where $k = \frac{1}{\lambda}$,λ denotes the wavelength; s is a parameter of the filter which can be derived by $w_l(k) = 0.5$ at the cutoff wavelength (denoted as λ_h):

$$s = \frac{\lambda_h\sqrt{2\ln 2}}{2\pi} \tag{15}$$

The low-pass filter is defined as Equation 16:

$$w_l(k) = \left(1 + \mathrm{A}k^4 e^{4\pi k d}\right)^{-1} \tag{16}$$

where d is the mean depth of the study area; A is parameter of the filter, which can be derived by $w_l(k) = 0.5$ at the cutoff wavelength (denoted as λ_l) as:

$$A = \lambda_l^4 e^{-\frac{4\pi d}{\lambda_l}} \tag{17}$$

Finally, the bandpass filter is obtained as:

$$w = w_h(k)^* w_l(k) \tag{18}$$

STUDY AREA AND DATA

Study Area and Observation Data

The study area is a local region in the Atlantic Ocean, i.e., 326°E-328°E, 3.5°N–4.5°N. The bathymetric data from ship survey

were provided by First Institute of Oceanography, Ministry of Nature Resources, and 498,501 shipborne depths are obtained by multibeam echo-sounding with high accuracy. The gravity data used is DTU13 version of gravity anomaly model released by Technical University of Denmark[1]. DTU13 is derived based on DTU10 by adding more satellite observations, such as Cryosat-2 (Andersen et al., 2014). The resolution of DTU13 is $1' \times 1'$ and its precision is better than four mGal (Andersen, 2010; Andersen et al., 2014).

The whole study area is divided into eight small areas, denoted as A, B, C, D, E, F, G, and H with at a size of $30' \times 30'$, as shown in **Figure 1**, in which water depths are shown by different colors. The three-dimensional distributions of gravity anomaly and shipborne depths are shown in **Figure 2**. According to this figure, the two maps show very similar characteristics which denote the high correlation between the two types of datasets.

Density Contrast From CRUST 1.0

CRUST1.0, the latest crustal model with a resolution of $1^\circ \times 1^\circ$,is used for comparisons. It provides density information of seven layers, including water layer, ice layer, soft sedimentary layer, hard sedimentary layer, upper crust, middle crust, and lower crust. In this model, the Earth is divided into 64,800 units and each unit has a size of $1^\circ \times 1^\circ$. Sea water depth, crustal thickness, and density are derived by the average data in each unit.

Considering that the spatial resolution of CRUST1.0 is $1^\circ \times 1^\circ$ and the size of the study area is $1^\circ \times 2^\circ$, only four density contrasts were derived using CRUST1.0 in the study area, for four regions defined as a, b, c, and d corresponding to A and B, C and D, E and F, and G and H shown in **Figure 1** respectively. Parameters of CRUST1.0 in each region are presented in **Table 1**, in which the density contrast $\Delta\bar{\rho}_0$ is the difference between sea water and the upper crust. It is found that the four density contrasts are almost same except in area CD. According to **Table 1**, the thickness of the upper crust in region CD is largest compared to other regions. This may cause the differences in the density contrasts with other region, which would be investigated in future research.

It needs to be noted that the effects of sediments are not considered in the results of $\Delta\bar{\rho}_0$, but the results derived by the TLS contain the whole signals, including sediments. Hence, it is not accurate to ignore the sediments in the calculation of density contrasts using CRUST1.0 information, especially when the thickness of the sediments is large. In addition, the thickness of the sediments and the upper crust would also lead to the differences with TLS. In order to solve these issues, new density contrasts are derived as follows,

$$\Delta\bar{\rho} = \frac{\rho_{sed} H_{sed} + \rho_{c1} H_{c1}}{H_{sed} + H_{c1}} - \rho_w \tag{19}$$

in which, ρ_{sed}, ρ_{c1} are respectively, the densities of the sediment layer and the upper crust; H_{sed}, H_{c1} are the thicknesses of the sediment layer and the upper crust respectively; ρ_w is the density of the sea water. The newly derived results for each region are also given in **Table 1**.

RESULTS AND ANALYSIS

Initial Results From TLS

Figure 3 shows the fitting results of TLS for each region, in which the x- and y-axis denote $(H - \hat{h}_i)$ and $\Delta\hat{g}_i$ respectively. Please note, because the resolution of shipborne depths is much higher than DTU13, the shipborne depths are interpolated to the gird points of DTU13 before the TLS processing in order to make the two datasets have consistent resolution. It is found that the gravity anomalies show linear positive correlations with water depths (i.e.,$H - \hat{h}_i$) in each subregion. For example, the larger the water depth, the larger the gravity anomaly. However, the slopes and

[1]https://ftp.space.dtu.dk/pub/DTU13/1_MIN/

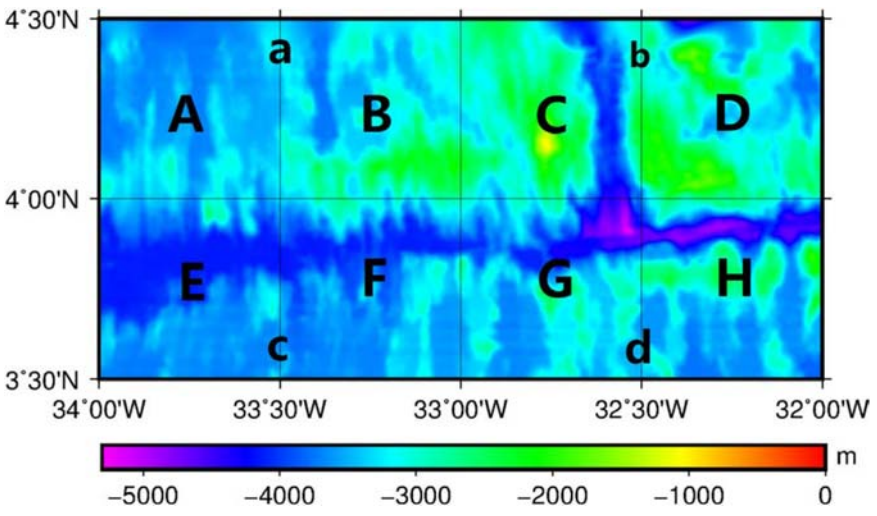

FIGURE 1 | Bathymetry of study area.

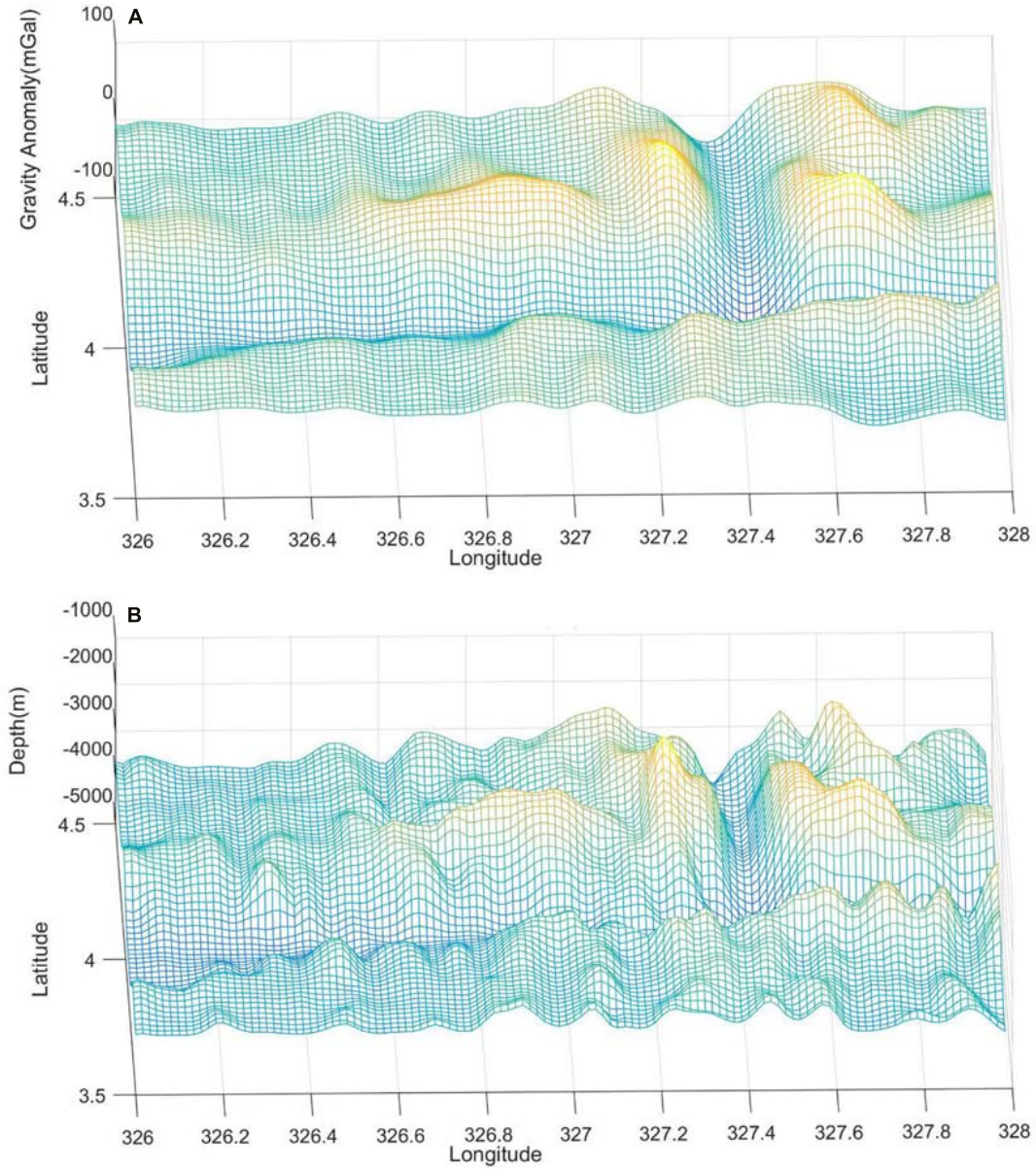

FIGURE 2 | Three-dimensional distribution of gravity anomaly **(A)** and shipborne depths **(B)**.

intercepts of the fitting lines in each region are not the same. It can be inferred that this is caused by the complexity of the seabed geological structures.

The derived density results are shown in **Table 2**. It is found that the density contrasts of area A-H are in the range of 0.599–1.173 g/cm^3, and the density contrasts are different due to the unique geological structure in each region. According to the SDUW, the fitting error in area A is the best, and that in area H is the worst. The accuracy of the whole area is between 6.124 and 14.493 mGal, among which the accuracy of area D and G is the closest, which indicates that the submarine geological structures in these two areas are similar. The SDUW of areas A and B have the largest difference in the adjacent areas, which may be caused by the large differences in the complicated seafloor geological structures between the two areas.

Compared to **Table 1**, the results from TLS are quite different from $\Delta\bar{\rho}_0$ and $\Delta\bar{\rho}_1$. Mean values of the whole study area are given in **Table 3**. It can be seen from the above table that the density contrasts obtained by CRUST1.0 model are much larger than that obtained by total least squares algorithm. The density contrast obtained by the weighted average method is closer to the result of TLS than that obtained by CRUST1.0 initial results, i.e., $\Delta\bar{\rho}_0$. Even so, the difference between the result of weighted average method and that obtained by total least squares is -0.374 g/cm^3. If the values from CRUST1.0 are true values, the relative error exceed 25%. This indicates that the derived results are not very

TABLE 1 | Density contrasts from CRUST1.0.

Region	Layer type	Density (g/cm^3)	Thickness (km)	DC0 (g/cm^3)	DC1 (g/cm^3)
AB (4.5, −33.5)	Sea water	1.02	3.35	1.53	1.4364
	Sediments	1.82	0.1		
	The upper crust	2.55	0.68		
CD (4.5, −32.5)	Sea water	1.02	2.97	1.38	1.3752
	Sediments	1.82	0.01		
	The upper crust	2.4	1.21		
EF (3.5, −33.5)	Sea water	1.02	3.64	1.53	1.4364
	Sediments	1.82	0.1		
	The upper crust	2.55	0.68		
GH (3.5, −32.5)	Sea water	1.02	3.41	1.53	1.5196
	Sediments	1.82	0.01		
	The upper crust	2.55	0.69		

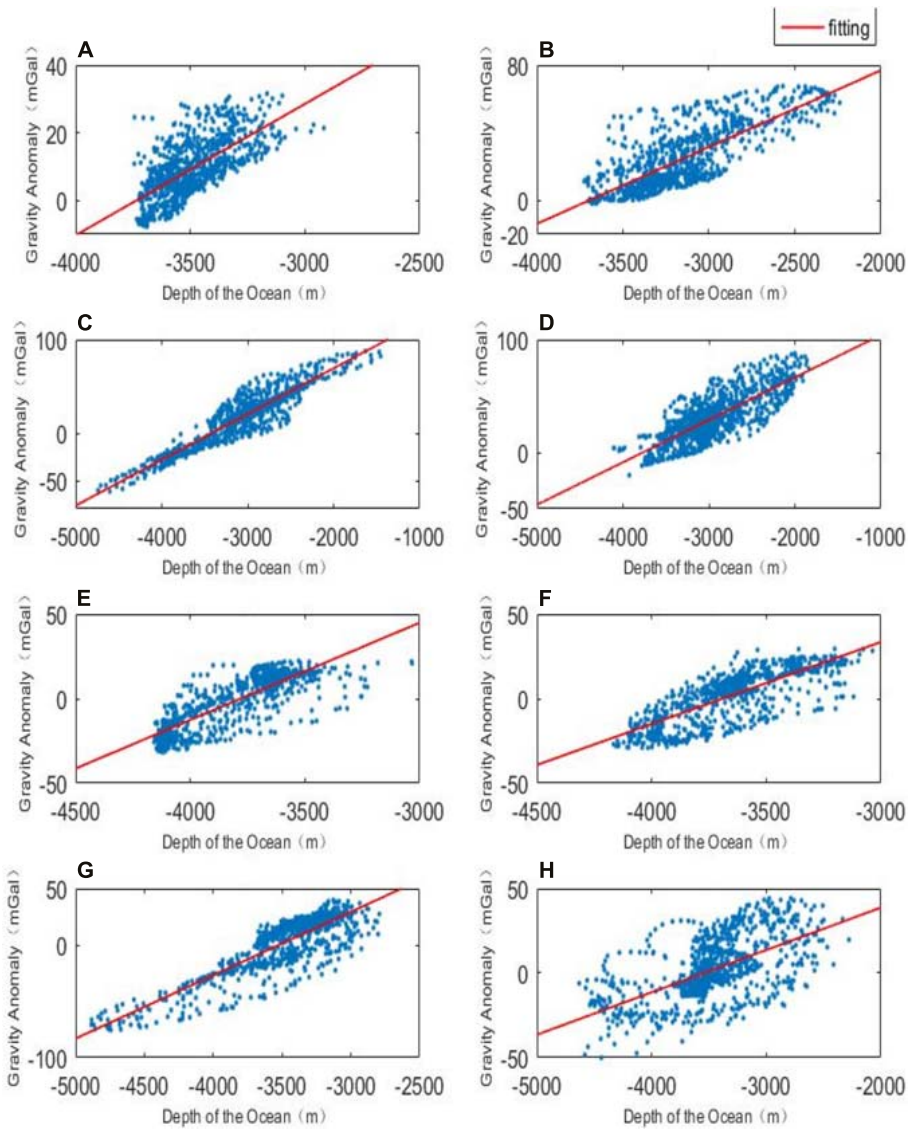

FIGURE 3 | Lines of fit for each region. **(A–H)** represent the related regions defined in **Figure 1**.

TABLE 2 | Density results derived from TLS.

Region	Mean depth (m)	Deepest depth (m)	Density contrast (g/cm^3)	Shipborne depths quantity	SDUW (mGal)
A	3,492.9	3,744.3	0.928	900	6.124
B	3,143.6	3,724.9	1.083	900	11.322
C	3,076.9	4,739.5	1.162	900	10.148
D	2,928.0	4,107.1	0.898	900	13.113
E	3,791.9	4,158.2	1.373	900	8.782
F	3,647.9	4,166.1	1.157	900	9.075
G	3,497.1	4,885.2	1.341	900	13.185
H	3,471.7	4,631.2	0.599	900	14.493

TABLE 3 | Density contrast for the whole study area.

Method	Value (g/cm^3)
TLS	1.068
CRUST1.0 Initial Result	1.493
CRUST1.0 Weighted Average Result $\Delta\tilde{\rho}$	1.442

reliable. This conclusion is consistent with the fact that the density contrast derived in the GGM for bathymetry usually has no physical meaning (Annan and Wan, 2020).

However, it should be noticed that the marine gravity anomalies are correlated with the information of the seafloor topography, including its depth and density contrast. In theory, if the density is known, the depths can be derived; if depths are known, the density can be derived. The possible reason why the large differences exist between the derived results with CRUST1.0 is that gravity anomalies have high correlations with seafloor topography only in a limited wave bandwidth (Marks and Smith, 2012; Wan et al., 2019). Although this issue has been considered in the derivation of bathymetry using GGM by modeling and removing the long wavelength gravity anomaly, the errors of the modeling would certainly cause some errors in the derivation of density contrast. In order to solve this issue, a filtering processing was added both to the gravity anomalies and shipborne depths and the new results are obtained in the next section.

New Results

Filtering Processing

The pass bands are designed by referring to studies about bathymetry, such as Smith and Sandwell (1994); Marks and Smith (2012). The sensitive band for bathymetry inversion is usually in the range of 20 ∼ 200 km (Hwang, 1999; Marks and Smith, 2012). This is also true for the density contrast inversion, because the mathematical function relationship is same as that used in bathymetry inversion, i.e., Equation 1. In order to reduce the effect from the non-sensitive bands, we decrease the band width which is usually used for bathymetry inversion and two pass bands are experimented, i.e., (30–100) km and (50–100) km.

As to why 100 km is selected as the maximum cutoff wavelength of the filtering pass-band, it is because the size of the study region is 1° × 2°; and thus, it is difficult to present signals with wavelength larger than 100 km due to the limited size, at least in the latitude direction. It is also because the spatial resolution of CRUST1.0 is 1° × 1°, corresponding to approximately 100 km × 100 km in spatial domain. As for the minimum cutoff wavelength of the pass-band, 30 and 50 km are defined as examples. Although, in bathymetry inversion, the minimum cutoff wavelengths of the pass-band are usually lower than 30 km, such as 20 or 15 km (Abulaitijiang et al., 2019), this study enlarges the minimum cut-off wavelength of the pass-band in order to ensure a higher correlation between the filtered shipborne depths and gravity anomalies. It is difficult to obtain the most sensitive band from gravity anomaly to bathymetry (Wan et al., 2019) like in gravity gradient to bathymetry. It is also true between the gravity anomaly and density contrast, since the mathematical relationship are same in bathymetry and density contrast inversions.

As an example, the filter for pass-band (30–100) km as well as the filtered data are shown in **Figures 4**, **5** respectively. In **Figure 4**, the red dotted lines denote the cutoff wavelength, i.e., 30 and 100 km. Compared to **Figure 2**, the similarity between gravity anomaly and ship-depths shown in **Figure 5** is definitely much stronger. This indicates the correlations between the two data sets are higher than that of the data shown in **Figure 2**. This point is proved further by **Table 4**, which shows the correlations between the ship-depths and gravity anomalies in each sub-region. Obviously, the correlations are improved largely by the filtering processing. Especially for the region H, the improvements in the correlations arrive at 35% compared to the initial correlations.

New Results

By band-pass filtering gravity anomalies and shipborne depths data, density contrasts are again derived using TLS and shown in **Table 5**. And the comparisons with weighted mean values of CRUST1.0 are given in **Table 6**. We named the pass-band (30–100) km as pass-band1 and the pass-band (50–100) km as pass-band2 in this study.

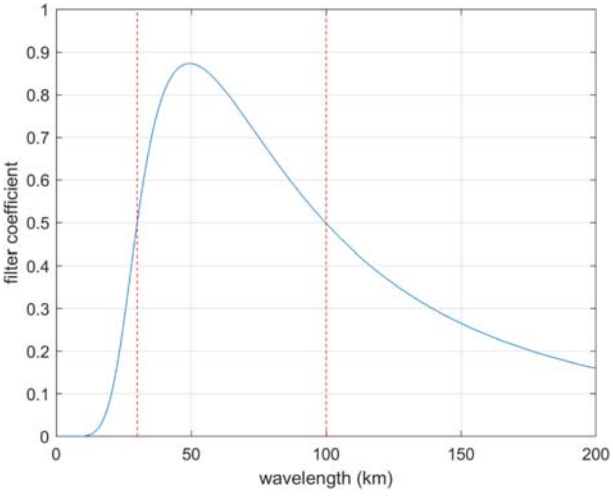

FIGURE 4 | The filter with pass-band (30–100) km.

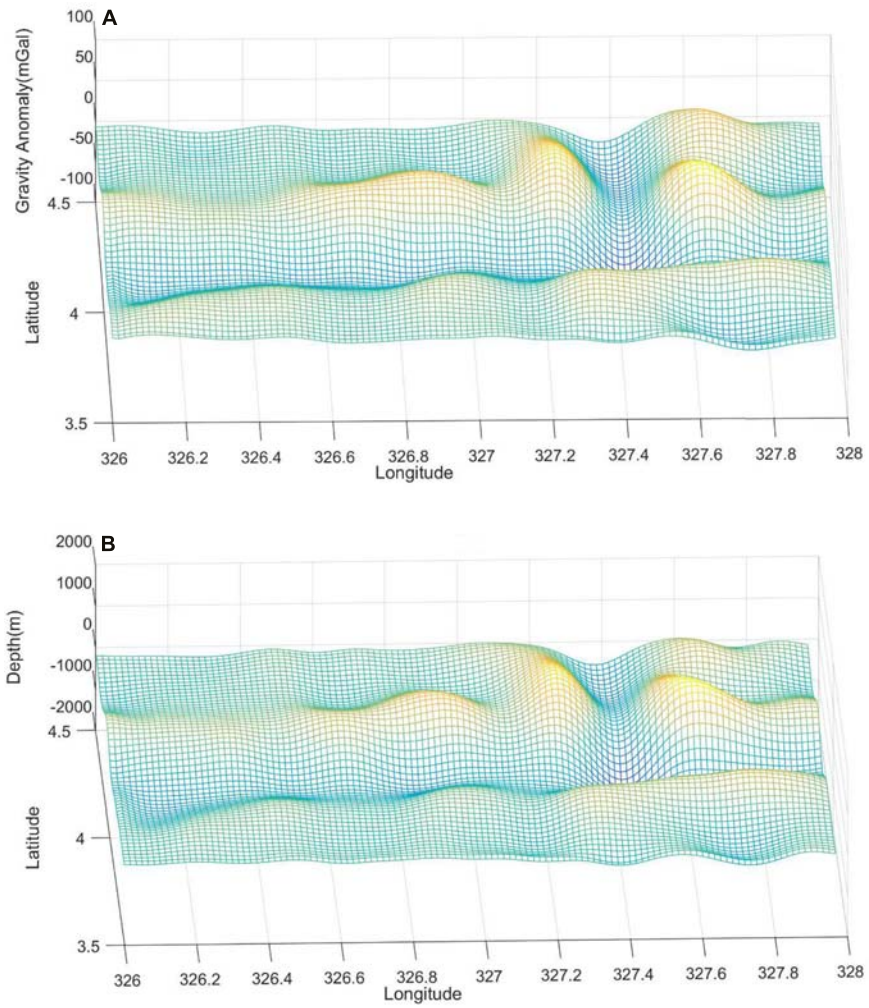

FIGURE 5 | The filtered gravity anomaly **(A)** and shipborne depths **(B)**.

Definitely, the new results are much closer to CRUST1.0 than the initial results and the differences are reduced by more than 60% in the total area. The magnitude of the differences between the new results and CRUST1.0 are smaller than 0.13 g/cm^3 and 0.03 g/cm^3 for the two pass-bands in terms of mean value of the whole area. If the CRSUT1.0's value is the true value, i.e., 1.442 g/cm^3, the relative errors of the two pass-bands are 8.46% and 1.53%, respectively. In general, in the whole area, the pass-band2, i.e., (50–100) km, yields closer results to CRUST1.0. However, in Region EF, the difference becomes larger. This may

TABLE 4 | Correlations between shipborne depths and gravity anomalies in each region.

Region	Initial	Pass band (30–100) km	Pass band (50–100) km
A	0.68	0.78	0.72
B	0.79	0.89	0.91
C	0.94	0.97	0.96
D	0.79	0.80	0.90
E	0.83	0.87	0.91
F	0.77	0.82	0.93
G	0.85	0.90	0.94
H	0.60	0.81	0.81
Mean	0.78	0.86	0.89

TABLE 5 | Density contrasts derived with TLS by adding a filtering processing (unit: g/cm^3).

Region	Initial results	Pass-band 1 results	Pass-band 2 results
A	0.928	1.177	1.058
B	1.083	1.488	1.830
C	1.162	1.297	1.310
D	0.898	1.127	1.250
E	1.373	1.507	1.533
F	1.157	1.489	1.917
G	1.341	1.492	1.785
H	0.599	0.982	1.025
Mean	1.068	1.320	1.4635

TABLE 6 | Comparisons with derived results and CRUST1.0 (unit: g/cm^3).

Region	AB	CD	EF	GH	Mean
CRUST1.0 results	1.436	1.375	1.436	1.520	1.442
Initial results (IR)	1.006	1.030	1.265	0.970	1.068
Pass-band 1 results (P1R)	1.333	1.212	1.498	1.237	1.320
Pass-band 2 results2 (P2R)	1.444	1.280	1.725	1.405	1.4635
Difference between IR and CRUST1.0	−0.43	−0.345	−0.171	−0.55	−0.374
Difference between P1R and CRUST1.0	−0.103	−0.163	0.062	−0.283	−0.122
Difference between P2R and CRUST1.0	0.008	−0.095	0.289	−0.115	0.022
Relative error of IR	29.94%	25.09%	11.91%	36.18%	25.97%
Relative error of P1R	7.17%	11.85%	4.32%	18.62%	8.46%
Relative error of P2R	0.56%	6.91%	20.13%	7.57%	1.53%

TABLE 7 | Depth statistics (unit:m).

	Initial shipborne depths			Pass-band 1 results			Pass-band 2 results		
Term	Mean	Std	Max	Mean	Std	Max	Mean	Std	Max
AB	−3,318.3	305.3	−3,744.3	68.7	171.0	−223.6	47.3	98.1	−106.9
CD	−3,002.5	509.9	−4,739.5	136.4	336.3	−1,071.1	111.5	183.5	−526.4
EF	−3,719.9	237.0	−4,166.1	−117.4	149.2	−477.4	−96.2	80.9	−289.5
GH	−3,484.4	404.8	−4,885.2	−87.8	258.3	−1,105.2	−62.6	122.5	−555.9

be due to the fact that the spatial resolution of CRUST1.0 is not enough to present the density contrast variation in local regions with size smaller than $1^\circ \times 1^\circ$. This would be investigated further in the future.

Please note, no information of CRUST1.0 is used in the inversion. Since the results are now close to CRUST1.0, it proves that marine gravity anomalies and shipborne depths can be used to derive seafloor density contrasts with a high accuracy. It also proves that the proposed method is effective. It should be emphasized that the spatial resolution of CRUST1.0 is only at 1.0 degree but it is not the case for gravity anomaly and even the shipborne depths. Hence, it is fully possible to derive the density contrast information all over the ocean with a much higher spatial resolution than CRUST1.0, because highly accurate gravity anomalies can be provided by several altimetry missions and a very large amount of shipborne depth observations have been collected by NOAA. The global inversion would be conducted in the future study.

DISCUSSION

In order to show the influence of the bathymetry undulation on density contrast inversion, the mean, deepest, and standard deviation (Std) values of the depths in each subregion are presented in **Table 7**. Comparing **Tables 6**, **7**, it is found that the deeper the water depths, the lower the inversion accuracy if the region EF is not considered. For example, in the initial shipborne depths, the absolute values of the mean and the deepest depths in GH region are all larger than regions AB and CD. Correspondingly, the inversion accuracy in region GH is much lower than those of regions AB and CD. Even after filtering, the maximum depth in region GH is still larger than those of regions AB and CD; and thus, the accuracy in region GH is still the lowest among the three regions. This phenomenon may be due to the fact: the deeper the water depth, the lower the gravity anomaly signals at the sea surface generated by density body of the seafloor. Since the gravity anomaly accuracies are almost same in the study subregions, the signal to noise ratio (SNR) must be different with different water depths. In general, the SNR of GH is lower than that of other regions. Hence, the density contrast inversion accuracy in the deep ocean area would be poorer than other areas. Because of this, in order to obtain the same inversion accuracy, the gravity anomaly should have a higher accuracy in the deep ocean regions than areas with shallower water depths.

It should be noted that the inversion results of region EF are not consistent with the above phenomenon. This may be caused by the limited spatial resolution of CRUST1.0, which is not enough to present the regional information. In order to check accuracy of CRUST1.0, we compare the sea water depths given by CRUST1.0 with shipborne depths used in this study. The statistics is given in **Table 8**, in which the differences between shipborne depths and CRUST1.0 are given and the relative error represents the ratio of the difference to shipborne depth value. According to **Table 8**, mean water depths provided by CRUST1.0 are very close to the shipborne depths and the mean differences are smaller than

TABLE 8 | Mean water depth statistics.

Region	AB	CD	EF	GH
Shipborne depths (km)	−3.32	−3.00	−3.72	−3.48
CRUST1.0 (km)	−3.35	−2.97	−3.64	−3.41
Difference (km)	0.03	0.03	0.08	0.07
Relative error	0.90%	1.00%	2.15%	2.01%

100 m. If shipborne depths are the true values, the accuracy of CRUST1.0 is poorest in Region EF. This means it is better to use other data to evaluate the inversion accuracy in Region EF. Unfortunately, this study currently could not obtain the related available data; and hence, the evaluation would be conducted in near future if other highly accurate seafloor density datasets become available.

CONCLUSION

This study presented a study for seafloor density contrast inversion using gravity anomalies and shipborne depth datasets. The inversion was achieved by a total least squares algorithm, which considers both noises from gravity anomalies and shipborne depths. The results show that if gravity anomaly and shipborne depths are used directly, the derived density contrasts contain large errors, which may be caused by the modeling error of the long wavelength part of gravity anomalies. Hence, a band pass filtering technique was proposed to resolve this issue and the final results show an obvious accuracy improvement of the derived density contrast, and thus verified the effectiveness of the method.

As for the sensitive band, in general it is the band of 20 $\sim$ 200 km. However, in density contrast inversion, it would be better to only use signals in a part of the sensitive band if it is defined as where the correlation is larger than 0.5, because the high correlation between the gravity data and shipborne depths would help improve the inversion accuracy. Therefore, we suggest that the determination of the pass-band of the filter is done by a correlation analysis between the gravity anomaly and shipborne depths, and the sensitive band can be defined as the bands with correlations larger than 0.85 or even higher between the two data sets to ensure high correlation in the pass-band.

Since various altimetry satellite missions (Hwang et al., 2002; Sandwell et al., 2014a; Wan et al., 2019; Zhu et al., 2020) have provided enough observations to derive highly accurate and dense marine gravity products and a large amount of shipborne depths data have been collected by NOAA, high accuracy and resolution of density contrasts can be derived for major areas of the global ocean by the proposed method in this study. In addition, gravity gradient products derived by some institutes (Hwang and Chang, 2014; Sandwell et al., 2014a) may also contribute a lot in the inversion.

DATA AVAILABILITY STATEMENT

Publicly available datasets were analyzed in this study. This data can be found here: The gravity data can be downloaded from the DTU space center website: https://www.space.dtu.dk/english/Research/Scientific_data_and_models/Global_Marine_Gravity_Field. CRUST1.0 is available from the website: https://igppweb.ucsd.edu/~{}gabi/crust1.html. The shipborne depths used in this study are available on the request to the corresponding author.

AUTHOR CONTRIBUTIONS

XW, WH, JR, and BL: conceptualization and investigation. XW, WH, WM, and RA: data curation and methodology. XW: funding. XW, JR, and RA: writing—original draft. XW, WH, JR, WM, RA, and BL: writing—review and editing. All authors read and approved the final manuscript.

FUNDING

This work was funded by the National Natural Science Foundation of China (Nos. 41674026 and 42074017); Fundamental Research Funds for the Central Universities (No. 2652018027); Open Research Fund of Qian Xuesen Laboratory of Space Technology, CAST (No.GZZKFJJ2020006); and China Geological Survey (No. 20191006).

ACKNOWLEDGMENTS

We would like to thank First Institute of Oceanography, Ministry of Nature Resources for providing ship sounding data and DTU for providing gravity anomaly data and Institute of Geophysics and Planetary Physics for providing CRUST1.0 data.

REFERENCES

Abulaitijiang, A., Andersen, O. B., and Sandwell, D. (2019). Improved Arctic ocean bathymetry derived from DTU17 gravity model. *Earth Space Sci.* 6, 1336–1347. doi: 10.1029/2018EA000502

Andersen, O. B. (2010). "The DTU10 gravity field and mean sea surface," in *Proceedings of the Second International Symposium of the Gravity Field of the Earth (IGFS2)* (Fairbanks, AK).

Andersen, O. B., Knudsen, P., and Berry, P. (2010). The DNSC08GRA global marine gravity field from double retracked satellite altimetry. *J. Geod.* 84, 191–199. doi: 10.1007/s00190-009-0355-9

Andersen, O. B., Knudsen, P., Kenyon, S., and Holmes, S. (2014). "Global and Arctic marine gravity field from recent satellite altimetry (DTU13)," in *Proceedings 76th EAGE Conference and Exhibition 2014* (Amsterdam), doi: 10.3997/2214-4609.20140897

Annan, R. F., and Wan, X. (2020). Mapping seafloor topography of Gulf of Guinea using an adaptive meshed gravity-geologic method. *Arab. J. Geosci.* 13:301. doi: 10.1007/s12517-020-05297-8

Bassin, C. (2000). The current limits of resolution for surface wave tomography in North America. *Eos Trans. AGU* 81:F897.

Felix, W., Regina, L., Edi, K., and Ansorge, J. (2002). High-resolution teleseismic tomography of upper-mantle structure using an a priori three-dimensional crustal model. *Geophys. J. Int.* 150, 403–414. doi: 10.1046/j.1365-246X.2002.01690.x

Golub, G. H., and van Loan, C. F. (1980). An analysis of the total least squares problem. *SIAM J. Numer. Anal.* 17, 883–893. doi: 10.1137/0717073

Hsiao, Y., Kim, J., Kim, K., Lee, B. Y., and Hwang, C. (2011). Bathymetry estimation using the gravity-geologic method: an investigation of density contrast predicted by downward continuation method. *Terr. Atmos. Ocean Sci.* 21, 347–358. doi: 10.3319/TAO.2010.10.13.01(Oc)

Hu, M., Li, J., Li, H., Shen, C. Y., and Xing, L. (2015). Predicting global seafloor topography using Multi-source data. *Mar. Geod.* 37, 176–189. doi: 10.1080/01490419.2014.934415

Hwang, C. (1999). A bathymetric model for the south China Sea from altimetry and depth data. *Mar. Geod.* 22, 37–51. doi: 10.1080/014904199273597

Hwang, C., and Chang, E. (2014). Seafloor secrets revealed. *Science* 346, 32–33. doi: 10.1126/science.1260459

Hwang, C., Hsu, H. Y., and Jang, R. J. (2002). Global mean sea surface and marine gravity anomaly from multi-satellite altimetry: applications of deflection-geoid and inverse Vening Meinesz formulae. *J. Geod.* 76, 407–418. doi: 10.1007/s00190-002-0265-6

Ibrahim, A., and Hinze, W. (1972). Mapping buried bedrock topography with gravity. *Ground Water* 10, 18–23. doi: 10.1111/j.1745-6584.1972.tb02921.x

Jiang, Y., Zhang, Y., Wang, S., Jiao, J., and Huai, Y. (2015). Inversion of Moho depth in western China considering gravity correction of deposition layer. *J. Seismol. Res.* 38, 257–261.

Kim, J., Frese, R., Lee, B., Roman, D., and Doh, S. (2011). Altimetry-derived gravity predictions of bathymetry by gravity-geologic method. *Pure Appl. Geophys.* 168, 815–826. doi: 10.1007/s00024-010-0170-5

Laske, G., Masters, G., Ma, Z., and Pasyanos, M. (2013). Update on CRUST1. 0–A 1-degree global model of earth's crust. *Geophys. Res. Abstr.* 15:20132658abstrEGU.

Marks, K. M., and Smith, W. H. F. (2012). Radially symmetric coherence between satellite gravity and multibeam bathymetry grids. *Mar. Geophys. Res.* 33, 223–227. doi: 10.1007/s11001-012-9157-1

Mooney, W. D., Laske, G., and Masters, T. G. (1998). CRUST 5.1: a global crustal model at 5° x 5°. *J. Geophys. Res. Solid Earth* 103, 727–747. doi: 10.1029/97JB02122

Nagendra, R., Prasad, P. V. S., and Bhimasankaram, V. L. S. (1996). Forward and inverse computer modeling of a gravity field resulting from a density interface using Parker-Oldenburg method. *Comput. Geosci.* 22, 227–237. doi: 10.1016/0098-3004(95)00075-5

Nataf, H. C., and Ricard, Y. (1996). 3SMAC: an a priori tomographic model of the upper mantle based on geophysical modeling. *Phys. Earth Planet. Inter.* 95, 101–122. doi: 10.1016/0031-9201(95)03105-7

Ouyang, M., Sun, A., and Zhai, Z. (2014). Predicting bathymetry in south china sea using the gravity geologic method. *Chin. J. Geophys.* 57, 2756–2765. doi: 10.6038/cjg20140903

Parker, R. L. (1972). The rapid calculation of potential anomalies. *Geophys. J. R. Astron. Soc.* 31, 447–455. doi: 10.1111/j.1365-246X.1973.tb06513.x

Sandwell, D., Carcla, E., and Smith, W. (2014b). Recent Improvements in Arctic and Antarctic Marine Gravity: Unique Contributions from CryoSat-2, Jason-1, Envisat, Geosat and ERS-1/2, Amercial General Union (AGU). (accessed November 29, 2014).

Sandwell, D., Muller, R., Smith, W., Garcia, E., and Francis, R. (2014a). New global marine gravity model from CryoSat-2 and Jason-1 reveals buried tectonic structure. *Science* 346, 65–67. doi: 10.1126/science.1258213

Smith, W. H. F., and Sandwell, D. T. (1994). Bathymetric prediction from dense satellite altimetry and sparse shipboard bathymetry. *J. Geophys. Res. Solid Earth* 99, 21803–21824. doi: 10.1029/94JB00988

Soller, D. R., Ray, D., and Brown, R. D. (1982). A new global crustal thickness map. *Tectonics* 1, 125–149. doi: 10.1029/TC001i002p00125

Wan, X., Ran, J., and Jin, S. (2019). Sensitivity analysis of gravity anomalies and vertical gravity gradient data for bathymetry inversion. *Mar. Geophys. Res.* 40, 87–96. doi: 10.1007/s11001-018-9361-8

Xiang, X., Wan, X., Zhang, R., Li, Y., Sui, X., and Wang, W. (2017). Bathymetry inversion with Gravity-Geologic Method: a study of long-wavelength gravity modeling based on adaptive mesh. *Mar. Geod.* 40, 329–340. doi: 10.1080/01490419.2017.1335257

Xu, P. L., Liu, J., and Shi, C. (2012). Total least squares adjustment in partial errors-in-variables models: algorithm and statistical analysis. *J. Geod.* 86, 661–675. doi: 10.1007/s00190-012-0552-9

Zhu, C., Guo, J., Gao, J., Liu, X., Hwang, C., Yu, S., et al. (2020). Marine gravity determined from multi-satellite GM/ERM altimeter data over the South China Sea: SCSGA V1.0. *J. Geod.* 94:50. doi: 10.1007/s00190-020-01378-4

Conflict of Interest: The authors declare that the research was conducted in the absence of any commercial or financial relationships that could be construed as a potential conflict of interest.

frontiers in Earth Science

ORIGINAL RESEARCH
published: 20 May 2021
doi: 10.3389/feart.2021.670256

Calculation of Deflection of Vertical and Gravity Anomalies Over the South China Sea Derived from ICESat-2 Data

Defu Che, Hang Li, Shengjun Zhang and Baodong Ma*

School of Resources and Civil Engineering, Northeastern University, Shenyang, China

The Ice, Cloud, and land Elevation Satellite-2 (ICESat-2) satellite uses a synchronized multi-beam photon-counting method to collect data from three pairs of synchronous ground tracks. The sampling rate along the ground tracks is designed to be ~0.7 m, much smaller than that used in conventional radar altimeters. Hence, it is reasonable to expect an improvement in marine gravity recovery over coastal zones using ICESat-2 data. ICESat-2 provides valid sea surface height (SSH) measurements and a standard data product (ATL12) over ocean areas. This led us to consider the possibility of investigating its ability to calculate the deflection of vertical (DOV) and marine gravity anomalies. We processed ATL12 data about 22 months over the South China Sea (0°–23°N, 103°–120°E) and verified the ability of ICESat-2 SSH measurements to be used in calculating directional components of DOV. The results show that the ICESat-2 SSH data have a similar centimeter-magnitude accuracy level as data from the Jason-2 satellite. Furthermore, the accuracy of cross-track deflection of vertical (CTDOV) calculations between non-identical side beams is lower. For along-track points, the difference in accuracy between the solution of the prime component and the meridional component is significantly reduced, the prime component accuracy is significantly better than the directional components of the gridded deflection of vertical (GDOV), although the enhancement is weak for the meridional component. We also implemented the inversion of the ICESat-2 single mission based on the inverse Vening Meinesz formula, and verified the capability of ICESat-2 gravity field detection using shipborne gravity measurements and XGM2019 gravity field model, and found that the accuracy is 1.35 mGal and 2.47 mGal, respectively. ICESat-2 deserves the attention of the altimetry community, and its advantages are expected to make it an alternative data source for multi-mission fusion inversion of the ocean gravity field in the future.

Keywords: icesat-2, ATL12, cross-track, deflection of vertical, gravity anomaly

OPEN ACCESS

Edited by:
Jinyun Guo,
Shandong University of Science and Technology, China

Reviewed by:
Song Li,
Wuhan University, China
Jiangjun Ran,
Southern University of Science and Technology, China

****Correspondence:***
Shengjun Zhang
zhangshengjun@mail.neu.edu.cn

Specialty section:
This article was submitted to Solid Earth Geophysics, a section of the journal Frontiers in Earth Science

Received: *20 February 2021*
Accepted: *03 May 2021*
Published: *20 May 2021*

Citation:
Che D, Li H, Zhang S and Ma B (2021) Calculation of Deflection of Vertical and Gravity Anomalies Over the South China Sea Derived from ICESat-2 Data. Front. Earth Sci. 9:670256. doi: 10.3389/feart.2021.670256

INTRODUCTION

Deflection of vertical (DOV), which can be derived from sea surface height (SSH) measurements, is an important Earth gravity field parameter. It is widely used to calculate marine gravity anomalies based on the inverse Vening Meinesz formula and a fast Fourier transform (FFT) technique (Hwang and Hsu, 2003; Wang and Lu, 2008; Zhu et al., 2020). The achieved accuracies of DOV and gravity field measurements have a mutually beneficial symbiotic relationship (Hwang et al., 1998). There are several methods for measuring DOV using satellite altimetry data (Peng and Xia, 2004), and

significant progress has been made in obtaining the directional components of DOV with higher accuracy and finer spatial resolution. However, there is still room for improvement. The accuracy of the obtained directional DOV components at gridding points is limited by the spatial distribution density of crossover points (Sandwell, 1992). Subsequently, the along-track vertical deflections solution was used to obtain gridded deflection of vertical (GDOV), but inconsistent estimated uncertainties were found between the meridional and prime components (Sandwell and Smith, 1997; Hwan et al., 2002). Previous studies have shown that the orbital inclination of the altimetry satellite will affect the accuracy of the directional component of DOV and that using a design with a low orbital inclination could help to improve the calculation of the prime component (Guo et al., 2016; Zhang et al., 2017; Wan et al., 2020a). However, the accuracy of the meridional component has still prevailed in the low-latitude sea for most cases of conventional satellite altimeter missions. Since the distribution of ground trajectories of low-orbital-inclination satellites in low-latitude waters still tends to be meridional, the sampling interval and application of observations in the cross-track direction of altimetry missions constrain the current solutions of DOV and the inversion of the ocean gravity field.

With the continuous launch of new satellites in recent years, different types of SSH observations have emerged (Zhang, 2017). Among these new types of observations, the Interferometric Radar Altimeter (InRA) model altimetry mission observations are promising for improving the accuracy of determining the prime component of the DOV. Wan et al. (2020b) used simulated data to show that, with InRA, the accuracy of the prime component solution can be consistent with the meridional component. However, these results still need to be verified practically using the National Aeronautics and Space Administration (NASA)'s Surface Water and Ocean Topography (SWOT) mission, which is due for launch in 2022. The SWOT mission will provide a new approach to solving the problem of the difference in the accuracy of the directional component.

The NASA Ice, Cloud, and Elevation Satellite-2 (often known as ICESat-2 but hereafter referred to as IS-2 for brevity), the orbital inclination is 92°, first along the flight direction using three groups of synchronous observation for reflecting surface height information. The sampling resolution of IS-2 along its trajectory is 0.7 m, which is a great improvement in the along-track spatial resolution compared with traditional radar altimetry missions (Markus et al., 2017). The simultaneous observation of three pairs in the cross-track aspect greatly reduces the influence of time-varying sea-surface topography between cross-track data, as well as the near-horizontal cross-track azimuth, so that more prime component information can be obtained. IS-2 is expected to significantly improve the accuracy of the directional components of DOV measurements.

In this study, the South China Sea (SCS; 0°–23°N, 103°–120°E) is used as the research area and IS-2 observation data is used for DOV measurements. Observation data from the Jason-2 satellite is used as a reference and 2159-order data with a spatial resolution of $2' \times 2'$ (XGM 2019e_2159; eXperimental Gravity Field Model, hereafter referred to as XGM2019) (Zingerle et al., 2019; Zingerle et al., 2020) is used as the validation model to analyze the accuracy of the sub-section results in this study. Cross-analysis is also performed for the accuracy of the IS-2 SSH. Then, the along-track and cross-track deflection of vertical (ATDOV and CTDOV) are calculated. The calculation and analysis of DOV aim to provide a reference for improving the prime component of DOV. Finally, gravity anomaly data for the SCS is obtained by inversion using the directional components of DOV, and it is compared with the XGM2019 model and shipborne gravity measurements to verify the accuracy level of the inversion.

DATA AND METHODOLOGY

Study Area

The SCS is a deep marginal sea with many coastal islands; it has an undulating topography and an average water depth of about 1,212 m (Li et al., 2001). It has been a major research area for scholars worldwide for many years (Shaw and Chao, 1994; Jilan, 2004; Huang et al., 2006; Andersen et al., 2014; Zhu et al., 2019; Li et al., 2020). However, it is known that the inversion results of global models are not ideal in coastal areas and around island groups because the quality of satellite-derived gravity data decreases close to the coast (Hwang et al., 2006; Liu et al., 2015; Zhang et al., 2017; Albayrak et al., 2020).

IS-2 Data Introduction

The IS-2 mission has provided measurements that enable to estimate of the heights of ice sheets and sea-ice thickness (Kwok and Markus, 2017; Zhu et al., 2018). Despite it not being a formal project requirement (Abdalati et al., 2010), the IS-2 project office and science team are also dedicated to providing ocean-height data that are useful to the scientific community. The main instrument onboard the IS-2 is the Advanced Topographic Laser Altimeter System (ATLAS). This instrument uses a 532 nm (green) laser to actively map surface elevations.

The mapping between the strong and weak beams of ATLAS and their relative positions on the ground depends on the orientation (yaw) of the IS-2 observatory, which changes. The ATLAS laser emits six beams and is divided into three pairs. Each pair consists of strong and weak energy beams with an energy ratio of 4:1, respectively. As IS-2 orbits the Earth, these trace out six ground tracks that are typically about 14 m wide. Six ground tracks are numbered according to the left-to-right direction of the laser spot number that generates it, with ground track 1L (GT1L),1R (GT1R), 2L (GT2L), 2R (GT2R), 3L (GT3L), and 3R (GT3R). IS-2 will orbit with a yaw angle of 2° during nominal operations, setting left/right beam separation at ~2.5 km in the along-track direction and beams within a pair by ~90 m in the cross-track direction (Smith et al., 2019). The data is organized by ground track, with ground tracks 1L and 1R forming pair one, ground tracks 2L and 2R forming pair two, and ground tracks 3L and 3R forming pair three. The pair tracks are ~3.3 km apart in the across-track direction (Neumann et al., 2019).

The yaw of IS-2 is changed twice a year to maximize the illumination of its solar panels. When the ATLAS instrument is traveling along the $+x$ coordinate in the forward orientation, the weak beam leads the strong beam, and the weak beam is located at the left edge of the beam pattern. When the ATLAS instrument is

traveling along the $-x$ coordinate in the backward orientation, the strong beam leads the weak beam, and the strong beam is located at the left edge of the beam pattern. The data book shows that ATLAS performed its first yaw flip on December 28, 2018, placing the spacecraft in the backward orientation. The exact timing of subsequent flips is shown in the datasheets, and this is crucial for reading the strong-beam data in the six beams (Morison et al., 2020).

The IS-2 mission produces along-track geophysical products over select surface types that include land ice (ATL06), sea ice (ATL07), land/vegetation (ATL08), atmosphere (ATL09), oceans (ATL12), and inland water (ATL13). The ATL03 data is a geolocated photon-cloud product that serves as the input data for each of the aforementioned higher-level data products (Neuenschwander and Pitts, 2019). The ATL12 algorithm was developed specifically for the extraction of terrain and ocean heights from the ATL03 photon clouds (Neumann et al., 2018) and the background photon rate from ATL09. The ATL12 geophysical data for one photon is generated by approximately 100 photons (segment length 70 m) according to the ATL12 adaptive algorithm. Based on the distribution of signal photons, this algorithm estimates the ground- and sea-surface elevations and then subsequently; labels the individual photons as either data or noise. Currently, the open ocean has low reflectance in the visible spectrum (Moses et al., 2015), and the ocean signal rates are 0–4 per laser shot, similar to overland.

The ATL12 data product also includes flags that can improve the interpretability of the height estimates. The ATL12 data includes dynamic atmosphere correction, which is derived from ATL09 and indicates possible scattering in the atmosphere. Furthermore, when calculating the freeboard of sea ice, the accuracy of the water-surface height can be approximated by the inter-ice water (Friedl et al., 2010). The SSH measurements take into account ocean tide correction, sea state deviation, sea breeze, and other factors.

It is worth stating that in a pure ocean region, only the strong beams are active because of the low reflectance of the open ocean in the visible spectrum. In marginal ice zones and coastal zone overlap regions, the three weak beams are also valid, and these are processed in the same way as the strong beams and exported together with the strong-beam results as part of the ATL12 ocean product (Morison et al., 2020).

Jason-2 Data Introduction

The Jason-2 calibration experiment was successfully launched on 20 June 2008 as a continuation of the TOPEX/Poseidon and Jason-1 altimeter missions, in cooperation with Centre National d'Études Spatiales, the European Organization for the Exploitation of Meteorological Satellites, NASA, and the National Oceanic and Atmospheric Administration (Fu et al., 1994; Chander et al., 2012). Data from the Jason-2 satellite is often used by international scholars for high-quality comparisons with other satellite measurements due to the outstanding quality of its sea-surface data (Yang et al., 2016; Liu et al., 2020; Sun et al., 2021).

In our analysis, we combine these indices to represent SSH, and because the study area includes both open ocean and nearshore, we do not consider strong and weak beam effects. The IS-2 data used in this study are obtained through the National Snow and Ice Data Center, 2019 and are from release 003 (Neuenschwander et al., 2020a; Neuenschwander et al., 2020b), with the time series as 2018/10/13 to 2020/07/16 (strong beam including left and right). The Jason-2 SSH data used for validation have a repeat orbital period of 10 days, with the time series 2018/10/05 to 2019/02/16 and 2019/05/22 to 2019/10/01, respectively. The ground trajectories of both sets of data in the test area are shown in **Figure 1**.

Along-Trajectory DOV

The computing methods mean sea-surface height (MSSH) and gravity anomalies in this paper use DOV as the data type. By definition, the ATDOV is the gradient of the geoid but with the opposite sign (Hwang et al., 2002). The great advantage of this method is that it is only based on geoid gradients computed along with the satellite profiles. Therefore, if there is a local bias between two arcs, it will not be affected the results, all long-wavelength errors have very small effects. As Sandwell (1992) showed, the orbit error, which is mostly of a long-wavelength nature, has a negligible effect, and no cross-over adjustment is needed.

We obtain the spherical distance s between the points p and q with the reference ellipsoid as the coordinate system according to the spherical distance formula:

$$\varepsilon = -\frac{\left(N_q - N_p\right)}{s} \tag{1}$$

where ϵ is the along-trajectory DOV and N is the geoid, which is a surface function.

Obtaining the GDOV Directional Component

Based on the correlation between the along-trajectory DOV and the directional component of the DOV (Hwang et al., 2002), the relationship between ε along the specified direction and its meridian component ξ and prime component η is:

$$\varepsilon = \xi \cos\alpha + \eta \sin\alpha \tag{2}$$

where α is the azimuth of the altimetric point along the ground track direction, which can be calculated using the position information of adjacent altimetric points according to

$$\tan\alpha = \frac{\cos\varphi_q \sin\left(\lambda_q - \lambda_p\right)}{\cos\varphi_p \sin\varphi_q - \sin\varphi_p \cos\varphi_q \cos\left(\lambda_q - \lambda_p\right)} \tag{3}$$

where φ_p, λ_p and φ_q, λ_q are the geodetic latitudes and longitudes of two adjacent points p and q, respectively, and point p is a point along the track of point q.

To calculate the GDOV components $\left(\overline{\xi} \quad \overline{\eta}\right)$ from the observation point's ATDOV ε, the observation equation is given as:

$$\varepsilon_i + v_i = \overline{\xi}\cos\alpha_i + \overline{\eta}\sin\alpha_i,\ i = 1, \cdots, n \tag{4}$$

where: n is the number of high observation points along the track in the grid and its adjacent sea area; and v_i, α_i, and ε_i are the residuals, azimuths, and DOVs along the specified direction for observation point i, respectively. This can be written in matrix form as:

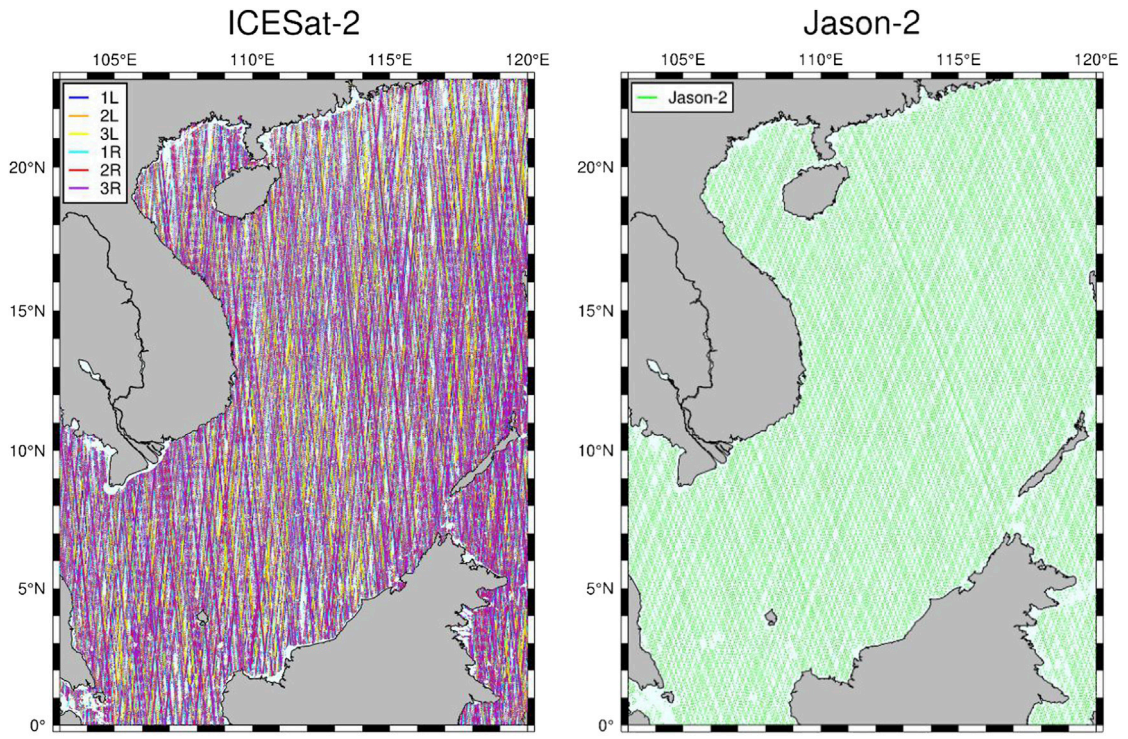

FIGURE 1 | Trajectories of IS-2 **(left)** and Jason-2 **(right)** over the SCS.

$$\mathbf{V} = \mathbf{AX} - \mathbf{L} \tag{5}$$

where $\mathbf{V} = (v_1 \cdots v_n)^{\mathrm{T}}$, $\mathbf{X} = \begin{pmatrix} \overline{\xi} \\ \overline{\eta} \end{pmatrix}$, $\mathbf{A} = \begin{bmatrix} \cos\alpha_1 & \sin\alpha_1 \\ \vdots & \vdots \\ \cos\alpha_n & \sin\alpha_n \end{bmatrix}$, and $\mathbf{L} = (\varepsilon_1 \cdots \varepsilon_n)^T$

Using the indirect leveling method, the solution to this can be obtained using:

$$\mathbf{X} = \left(\mathbf{A}^{\mathrm{T}}\mathbf{PA}\right)^{-1}\mathbf{A}^{\mathrm{T}}\mathbf{PL} \tag{6}$$

Where **p** is the weight array of observations, $P_i = 1/d_i$, where d_i is the distance from the observation point i to the grid point.

Obtaining the ATDOV Directional Components

Scholars have solved for the directional components of the DOV at the intersections or grid points (Olgiati et al., 1995; Sandwell and Smith 1997; Hwang et al., 1998). The former approximates along-track points and cross-track points as ascending and descending arcs, the latter approximates along-track points as grid points and cross-track points as points calculated within the grid. Since in the subsequent solution, we have to compare the accuracy of the ATDOV directional components with the GDOV directional component, the latter method is proposed for calculating the ATDOV directional components in this study. The GDOV formula in Section *Obtaining the GDOV Directional Component* is used as the theoretical formula, and the distance between two points and the time threshold is set as constraints. There are four methods to distinguish the number of beams being computed and the associated directions, as shown in **Figure 2**.

Obtaining Gravity Anomaly Data

The advantage of using the DOV method to obtain gravity anomaly data is that calculating the SSH difference between two points is essentially a high-pass filtering process (Wang and Wang, 2001), in which almost all the effects of long-wave errors are deducted, such as orbital errors, atmospheric propagation errors, tidal errors, the effects of sea surface steady-state topography, the effects of ocean circulation, and the effects of instrument errors, So as to reducing the requirements for pre-processing of altimetric satellite data.

Gravity anomaly data can be derived from DOV with the inverse Vening Meinesz formula (Hwang et al., 1998). Based on the grid data of the meridional component ξ and the prime component η of DOV, the formula for calculating the gravity anomaly Δg using the inverse Vening Meinesz formula method through the 1-D fast Fourier transform (FFT) technique (Haagmans, 1993) can be expressed as

$$\Delta g_{\varphi_p}(\lambda_p) = \frac{\gamma_0 \Delta\phi\Delta\lambda}{4\pi} F_1^{-1} \sum_{\phi_q=\phi_1}^{\phi_2} \begin{Bmatrix} F_1\left[H'(\Delta\lambda_{qp})\cos\alpha_{qp}\right]F_1(\xi_{\cos}) + \\ F_1\left[H'(\Delta\lambda_{qp})\sin\alpha_{qp}\right]F_1(\eta_{\cos}) \end{Bmatrix} \tag{7}$$

where: p is the "fixed" point and q is the "dummy" or "running" point; ϕ_q is the latitude of the parallel along which gravity anomalies are to be computed; φ_1 and φ_2 are the latitudes of the southernmost

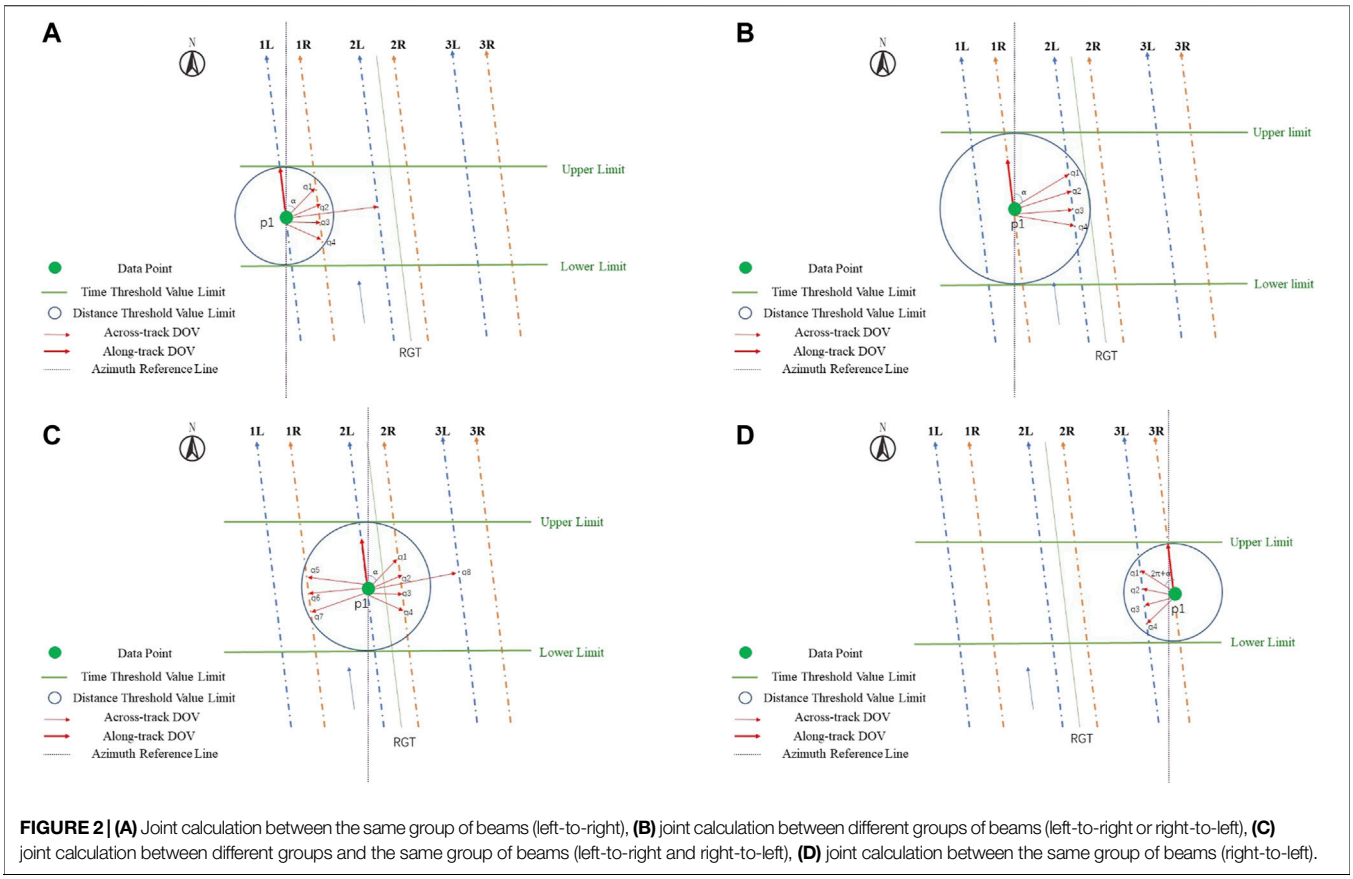

FIGURE 2 | (A) Joint calculation between the same group of beams (left-to-right), **(B)** joint calculation between different groups of beams (left-to-right or right-to-left), **(C)** joint calculation between different groups and the same group of beams (left-to-right and right-to-left), **(D)** joint calculation between the same group of beams (right-to-left).

and northernmost parallels; $\Delta\phi$ and $\Delta\lambda$ are the grid intervals in latitude and longitude; λ_{qp} is the difference in longitude; and F_1 is the 1-D FFT. We introduce a kernel function H', which is defined as

$$H' = \frac{dH}{d\psi_{pq}} = -\frac{\cos\frac{\psi_{pq}}{2}}{2\sin^2\frac{\psi_{pq}}{2}} + \frac{\cos\frac{\psi_{pq}}{2}\left(3 + 2\sin\frac{\psi_{pq}}{2}\right)}{2\sin\frac{\psi_{pq}}{2}\left(1 + \sin\frac{\psi_{pq}}{2}\right)} \tag{8}$$

where ψ_{pq} is the spherical distance between points p and q on the unit sphere, and this spherical distance can be found using

$$\sin^2\left(\frac{\psi_{pq}}{2}\right) = \sin^2\left(\frac{\Delta\varphi_{qp}}{2}\right) + \sin^2\left(\frac{\Delta\lambda_{qp}}{2}\right)\cos\varphi_q\cos\varphi_p \tag{9}$$

where $\Delta\varphi_{qp} = \varphi_q - \varphi_p$ and $\Delta\lambda_{qp} = \lambda_q - \lambda_p$. The azimuth equation is then

$$\tan\alpha_{qp} = \frac{-\cos\varphi_p\sin\left(\Delta\lambda_{qp}\right)}{-\sin\left(\varphi_q - \varphi_p\right) + 2\sin\varphi_q\cos\varphi_p\sin^2\left(\frac{\Delta\lambda_{qp}}{2}\right)} \tag{10}$$

INITIAL ASSESSMENT OF IS-2 MEASUREMENT RESULTS

In this paper, we focus on verifying the ability of the IS-2 multibeam data to enhance the accuracy level of the directional component of DOV. However, we first need to verify the data performance of IS-2. Measurements from altimetry missions are typically validated on regional to global scales using a relative calibration method based on inter-mission as well as intra-mission statistical analysis (Zhang et al., 2018). In reality, however, the smaller variations in within-mission situations indicate better stability and internal consistency, and accuracy of the airborne instruments, while the crossover variations between multiple missions are more reliable for assessing the distance accuracy between altimetry measurements (Wang and Wang, 2001). Therefore, we plan to first evaluate the performance of IS-2 by analyzing cross-differences with another typical high-accuracy mission. Inter-mission cross-differences were also considered when evaluating the intra-mission accuracy (Wang et al., 2021).

We used Jason-2 pulsed radar altimetry satellite data with a repeated orbital period of 10 days for comparison with the IS-2 laser altimetry data. The repetitive orbital period of Jason-2 is an exact integer fraction of the 91-days orbital period of IS-2. Therefore, it is possible to compare the accuracy of pulsed radar altimetry satellites and laser altimetry satellites in calculating the ocean surface height.

In this study, the IS-2 SSH data were obtained directly from the ATL12 SSH data product, and the Jason-2 SSH data were acquired by adding different geophysical corrections including dry- and wet-troposphere path delays, ionospheric corrections, ocean state bias, ocean tides, solid earth tides, polar tides, high-frequency wind effects, and inverted barometer corrections. All of these corrections were provided separately for the Jason-2 SSH

TABLE 1 | Statistical information of crossover differences under intra-mission situations.

Time limit	Jason-2 Cycle 608–644		IS-2 ATL12 (22 months)	
	NUM	STD (cm)	NUM	STD (cm)
≤10 Day	979	7.32	6,460	7.93
≤91 Day	6,345	9.70	40,088	11.61
—	12,418	13.74	150,149	14.08

data, and no additional update procedures were applied. Furthermore, the incompletely constrained time-varying effects of the ocean surface inevitably affect the internal and intermittent cross-sectional differences. Therefore, cross-differences with and without time constraints need to be considered separately in the statistical process. To ensure the overlap of measurement times, the Jason-2 dataset, which has a subordinate relationship with the IS-2 time series, was selected as the interval validation data. The IS-2/Jason-2 crossover points were determined by fitting the ground trajectories of the sample data, and the crossover points were defined as the locations where each satellite intersected its ground position. At the same time, the intermittent intersection points were defined as the locations where IS-2 and Jason-2 crossed the same sea-surface position.

The minimum, maximum, average, number of crossover points (NUM), and standard deviation (STD) were obtained by calculating the crossover differences between the corresponding ascending and descending paths on the ocean surface with and without time limits, depending on the calculated positions of the crossover points. The specific results are presented in **Tables 1**, **2** and **3**.

Taking into account the effect of time-varying sea-surface topography, to verify the overall IS-2 SSH accuracy, see **Table 1**. The orbital periods of 10 and 91 days and the unrestricted time of the two satellites are chosen as the time interval of the intersection cross difference, respectively. We can conclude from **Table 1** that: 1. IS-2 provides more information for the crossover point at the same time interval due to the synchronous observation of the six beams of IS-2. the discrepancy STD of the IS-2 SSH is somewhat larger, and this is because the wave effect, especially from wind-driven waves, is generally smoothed out at a footprint of about 2 km. For a 70-m along-track measurement (100 adjacent laser pulses), the wave effect is still significant.

The inter-mission crossover analysis was executed four times, and the resulting statistical information is listed in **Table 2**. According to the crossover analysis of the intra-mission or inter-mission situations, the IS-2 data is valid but has slightly worse performance than Jason-2. Also, the large fluctuations in the mean values of IS-2 and Jason-2 SSH are due to the different reference ellipsoids chosen by IS-2 and Jason-2 which are the WGS84 ellipsoid and T/P ellipsoid, and there is a vertical difference of about 0.7 m between the two.

We know that IS-2 completes one circle of the Earth in about 1.5 h, so there are many crossings of the same location on the ground in a single day. We assessed the accuracy of SSH measurements for each of the six beams based on the overall accuracy of the IS-2 data obtained in **Table 1**. The time intervals

TABLE 2 | Statistical information of crossover differences under intermission situation ("_A" and "_D" denote ascending and descending passes, J indicates Jason, and 1/2/3 and L/R represent the corresponding IS-2 beams).

Beam group	NUM	MAX (cm)	MIN(cm)	MEAN (cm)	STD (cm)
1L_A & J_A	9,076	2.66	−189.62	−81.64	15.01
2L_A & J_A	8,692	16.90	−180.24	−77.67	14.46
3L_A & J_A	9,008	3.24	−173.80	−79.14	14.35
1R_A & J_A	9,638	5.68	−170.96	−79.70	15.73
2R_A & J_A	9,114	8.66	−181.67	−79.09	15.59
3R_A & J_A	9,723	7.25	−214.25	−81.06	16.15
1L_A & J_D	5,232	22.85	−190.03	−81.90	15.39
2L_A & J_D	5,026	−12.08	−251.26	−77.81	14.84
3L_A & J_D	5,190	13.22	−170.86	−79.27	14.47
1R_A & J_D	5,597	20.97	−158.87	−79.92	15.59
2R_A & J_D	5,442	20.97	−228.47	−79.68	15.60
3R_A & J_D	5,654	13.12	−204.36	−81.11	16.28
1L_D & J_A	5,571	−32.27	−135.44	−79.84	16.18
2L_D & J_A	5,267	−32.13	−117.48	−78.47	18.24
3L_D & J_A	5,446	76.49	−130.34	−64.88	12.61
1R_D & J_A	5,673	8.25	−119.56	−75.09	17.79
2R_D & J_A	5,373	−38.76	−107.34	−77.75	12.41
3R_D & J_A	5,580	−31.25	−138.94	−78.83	18.67
1L_D & J_D	9,207	−18.26	−174.61	−81.44	21.73
2L_D & J_D	9,035	−6.55	−163.12	−77.46	19.02
3L_D & J_D	9,196	38.84	−171.00	−79.23	22.67
1R_D & J_D	9,608	71.46	−154.54	−77.29	15.87
2R_D & J_D	9,213	74.30	−276.74	−75.61	16.07
3R_D & J_D	9,400	76.98	−173.42	−69.72	18.19

were chosen as 1 day, 5, 10, and 91 days, respectively. Among these intervals, the purpose of the 10-days interval was to compare the SSH measurement accuracy of Jason-2 with a repeated orbital period of 10 days. The results in **Table 3** show that the accuracies of the SSH data from the six beams are similar.

The accuracy results we established to be reliable from the perspective of verifying the precision level of IS-2 in the horizontal and vertical directions of SSH by Smith et al. (2020) at Greenland Island. This validation initially implies that IS-2 is capable of investigating DOV due to its new data coverage and reliable range precision.

NUMERICAL AND EXPERIMENTAL DOV DIRECTION COMPONENT

Along Trajectories DOV

According to the solution formula for the DOV directional component given by (Hwang et al., 1998), we know that the ATDOV needs to be obtained first in the process of obtaining the DOV directional component using the SSH calculation. The validation results of the ATDOV calculations are shown in **Table 4**.

Figure 3 shows a diagram of the method used for calculating the CTDOV which includes the starting beam 1 and the calculated beam 2. The obtained CTDOV is a data point on the calculated beam 2 which will result in a large number of duplicate CTDOV points if a threshold range is not added. Therefore, in this paper, we used time and distance thresholds to limit the number of CTDOV points calculated. The CTDOV

TABLE 3 | Statistical information of crossover differences under the IS-2 six beams in the intra-mission situation ("L" and "R" denote the left and right beams, respectively).

Beam group	Time limit									
	≤1 Day		≤5 Day		≤10 Day		≤91 Day		Total	
	NUM	STD (cm)	NUM	STD (cm)	NUM	STD (cm)	NUM	STD (cm)	NUM	STD (cm)
1L&1L	73	8.16	221	8.23	328	8.29	1,669	10.27	4,083	12.96
2L&2L	71	5.38	210	6.07	310	6.69	1,555	9.29	3,811	12.50
3L&3L	73	4.06	213	4.77	310	5.62	1,642	9.42	4,008	12.75
1R&1R	74	6.57	235	7.08	339	7.86	1,639	11.50	4,491	13.75
2R&2R	70	6.03	199	7.08	272	7.24	1,431	11.68	3,916	13.67
3R&3R	85	8.34	223	8.81	359	9.66	1725	13.28	4,614	14.55

TABLE 4 | Statistical information of IS-2 ATVD.

Beam	NUM	MAX (arcsec)	MIN(arcsec)	MEAN (arcsec)	STD (arcsec)
1L	162,614	4.16	−4.16	−0.0058	1.39
2L	132,448	3.31	−3.31	−0.0069	1.10
3L	159,339	4.09	−4.10	−0.0075	1.37
1R	141,815	4.33	−4.33	−0.0049	1.44
2R	115,730	3.60	−3.60	0.0025	1.20
3R	145,194	4.53	−4.53	0.0018	1.51

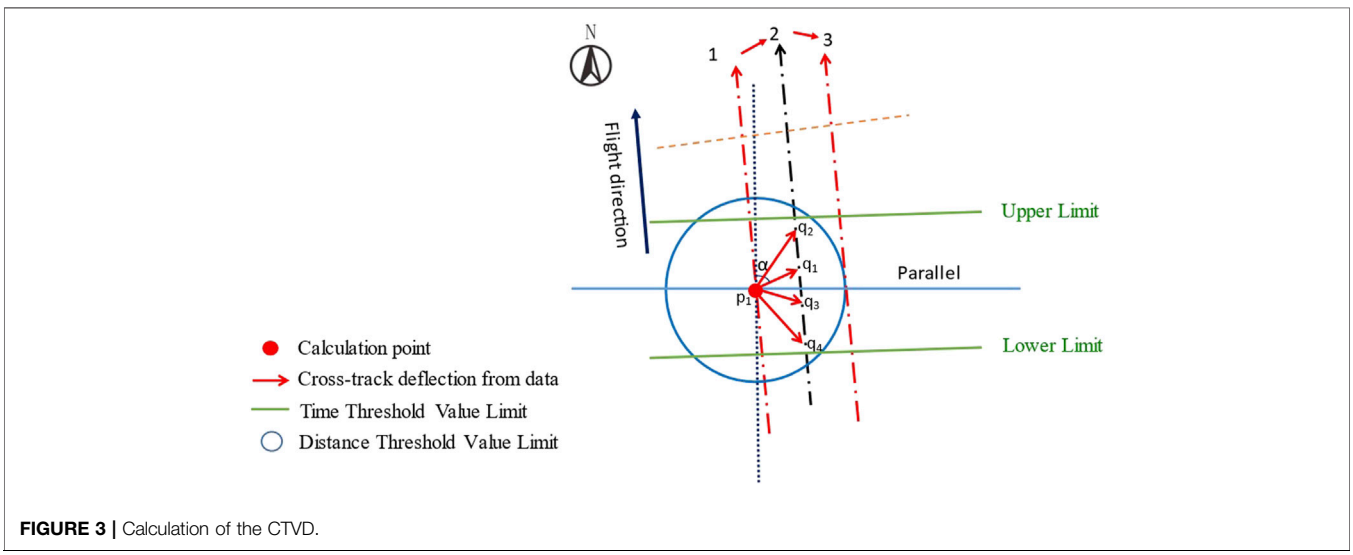

FIGURE 3 | Calculation of the CTVD.

for the coupling between the 15 groups of six beams is shown in **Table 5**.

Tables 4, **5** show the results of the calculations of ATDOV and CTDOV based on the IS-2 data. It can be seen that, during the accuracy verification of ATDOV with the XGM2019 model, the results from the middle pair are significantly better than those from the other two pairs, and the data from the other two pairs set tend to be smooth and without large fluctuations about 1.4″. For the calculation of CTDOV, to prevent a situation, in which two beams appear to be solved repeatedly, we obtained a two-by-two solution for the six beams according to the principle of calculating from left to right. From **Table 5**, we can see that the solving accuracy of the CTDOV obtained from the left and right beam solution is the worst. This is because, regardless of whether the IS-2 flight direction is forward (+x) or backward (−x), the left and right beams include strong and weak photons, and the along-track distance between these two beams far exceeds the theoretical value of 2.5 km due to the severe missing condition of the weak photons in the open sea (Morison et al., 2020). In addition, although we know that the IS-2 intermediate beam group data quality is superior, the minimum number of data points along the track has a large impact on the calculation of the CTDOV. Finally, we can draw conclusion that among the 15 sets of CTDOV data, there are six with similar accuracy to the ATDOV verification accuracy (1.4″), and most of these are values calculated from same-side beams. This confirms the reliability of the results of the CTDOV solution.

TABLE 5 | Statistical information of IS-2 CTVD.

Beam group	NUM	MAX (arcsec)	MIN (arcsec)	MEAN (arcsec)	STD (arcsec)
1L_2L	923,035	4.65	−4.65	0.78	1.55
2L_3L	746,840	4.86	−4.86	0.72	1.59
1L_3L	1,068,560	4.23	−4.23	0.68	1.41
1R_2R	630,367	5.08	−5.08	0.05	1.69
2R_3R	680,406	9.92	−9.92	0.80	3.31
1R_3R	725,181	5.80	−5.80	0.61	1.93
1L_1R	127,712	9.00	−9.00	−0.24	3.00
2L_2R	116,498	10.60	−10.60	0.90	3.53
3L_3R	127,576	12.07	−12.07	−0.05	4.03
1L_2R	110,979	7.28	−7.30	−0.35	2.43
1L_3R	117,389	6.29	−6.29	−0.09	2.10
2L_3R	114,426	6.87	−6.87	−0.67	2.29
1R_3L	108,894	5.12	−5.12	−0.14	1.71
1R_2L	123,761	6.74	−6.73	0.74	2.25
2R_3L	117,157	8.13	−8.13	−0.15	2.71

TABLE 6 | Statistical information of 2-min GVD directional component.

Beam	Meridional (arcsec)	Prime (arcsec)
1L	2.63	6.99
1R	2.58	6.03
2L	2.73	7.09
2R	2.65	6.27
3L	2.66	6.96
3R	2.48	6.39

TABLE 7 | Statistical information of ATVD directional component.

Beam	CTVD	Meridional (arcsec)	Prime (arcsec)
1L	1L_2L	2.24	5.35
2L	2L_3L	2.17	3.74
3L	1L_3L	2.25	3.73
1R	1R_2R	2.27	3.91
2R	2R_3R	2.21	6.18
3R	1R_3R	2.26	3.90

DOV Directional Component

GDOV Directional Component

In this study, the grid resolution of the GDOV is limited by the number of data points along the track and the study area. By analyzing the distance along-track of IS-2, the average along-track sampling interval of ATL12 is about 3–4 km by distance analysis, and the corresponding grid resolution is about 2 min. We, therefore, determined that the 2-min grid resolution data would be used as the comparison data for the ATDOV directional components from IS-2. **Table 6** shows the validation accuracy of the GDOV directional components of the six beams with the XGM2019 model after removing the coarse difference data by the triple standard-deviation method.

The above two sets of data make it clear that the accuracy of the prime component of DOV is lower than that of the meridional component of DOV at the grid points calculated directly from ATDOV. This provides a basis for the DOV directional-component problem we proposed in the introduction.

ATDOV Directional Component

After verifying the accuracy of the ATDOV and CTDOV, we provide a basis for solving the ATDOV directional components. Combining the calculation method for the DOV directional component at the along-track points using the joint ATDOV and CTDOV given in **Figure 2**, we examined different combinations of the six beams to calculate the DOV directional components at the along-track points. The prime and meridional components were then checked against the XGM2019 model, as shown in **Table 7**.

The comparison in **Table 7** shows that the meridional component of the six IS-2 beams is similar to the accuracy of the meridional component at the grid points, and the accuracy of the prime component is greatly improved in the solution of the directional component of ATDOV. In addition, we found anomalies in the calculated ATDOV directional component values for the IS-2 1L beam combined with the cross-track 1L_2L, and the 2R beam combined with the cross-track 2R_3R. Therefore, the data from the 1L and 2R beams needed to be recalculated. Previously, we proposed that the left and right beam solutions reduce the computational accuracy, so we neglected the accuracy of the joint approach of **Figures 2A,D** in the process of solving the CTDOV. The approach is given in **Figures 2B,C** was used in the subsequent solution (see **Table 8**). The accuracy of the recalculated 2L and 3R beams is significantly improved, and the beams with superior accuracy in the CTDOV calculation were selected as the joint calculation data.

Gravity Anomalies

In the previous section, we verified the accuracy of the GDOV directional components by using the ATDOV directional components and concluded that the accuracy of the latter component in the prime direction was improved substantially, but its meridional component was reduced. In this section, we adopt the inverse Vening Meinesz formula (1D-FFT) method introduced by Hwang et al. (1998) to calculate the gravity

TABLE 8 | Statistical information of recalculation ATVD prime components.

Beam	CT_DOV	STD (arcsec)
1L	1L_3L	3.73
2L	2L_3L	3.74
3L	1L_3L	3.73
1R	1R_3R	3.92
2R	2R_3R&1R_2R	3.68
3R	1R_3R	3.90

anomaly. Previously, we solved the gravity anomaly by using the Laplace equation method (Zhang et al., 2020), but the ICESat-2 slope data in the cross-track direction could not be reasonably applied to the calculation procedure. According to the inverse Vening Meinesz formula (1D-FFT) method, we first gridded the ATDOV directional components of the six beams into the GDOV directional component of 2 min. However, before that, it is necessary to check whether the distance-weighting method used to grid the ATDOV directional components is reliable, by matching with the XGM2019 model, to verify the GDOV directional component of 2 min, and the results are shown in **Table 9**.

In **Table 9**, we can see that the accuracy of the GDOV directional components based on the distance-weighting method is similar to that in **Table 6**, which is better than the single-beam GDOV directional component. Then, we applied the WGS84 reference ellipsoid as the marine geodetic datum and used the remove–compute–restore technique to subtract the corresponding 2190-order EGM2008 model reference geoid relief and sea-surface topography from the MSSH obtained from the satellite altimetry data so as to obtain the remaining geoid relief values. The remaining feature relief values were used as input data for inversion of the SCS gravity anomaly according to **Eqs. 1**–**7**, and the results were verified by using the National Center for Environmental Information (NCEI) shipborne gravity measurements and the XGM2019 gravity field model. A comparison of the inverse gravity anomaly with the XGM2019 model gravity anomaly is shown in **Figure 4**. In addition, we preprocessed the NCEI shipborne gravity measurements by comparing them with the EGM2008 model gravity anomalies on a line-by-line basis for systematic bias correction, and subtracted about 3.17% of the coarse deviation observations according to the robust outlier detection algorithm (RODA).

In these statistics, the STD, of which values exceeding the mean errors by three times, were removed, accounting for 6.62 and 5.52%. The screening results are shown in **Table 10**, where the screening scales, the number of remaining data points, the maximum value, the minimum value, the mean value, and the standard deviation information are given. Furthermore, to verify the performance of the IS-2 nearshore, we analyzed the points with large differences inaccuracy from the shipborne gravity measurement verification. It can be seen that, to a large extent, the data with poor quality are located in the deep sea as well as in the nearshore regions, and the sea depth has a large impact on the data accuracy (Wan et al., 2020a), but the issue of water depth is not discussed further in this paper.

The results in **Table 10** show that the validation accuracies of the SCS gravity anomaly data based on the IS-2 single mission inversion with shipborne gravity measurements and the XGM2019 field model are 1.35 mGal and 2.47 mGal, respectively. IS-2 is expected to become an alternative data source for multi-mission fusion inversion of the ocean gravity field in the future.

DISCUSSION AND CONCLUSION

The IS-2 satellite has advantages in providing simultaneous multi-beam observations with an extremely high spatial sampling rate. We used a 22-months time series from the IS-2 ATL12 product and designed a four-step numerical experiment to construct a 4-min marine gravity grid in the SCS area. The main results were summarized as follows.

Firstly, we found that the ATLAS system carried by IS-2 could obtain reliable SSH observations. Inter- and intra-mission comparisons were used to obtain the crossover differences between data from IS-2 and the traditional pulse radar mission Jason-2. The verification results showed that their SSH measurements had approximately the same level of accuracy. In addition to this, the different reference ellipsoids of IS-2 and Jason-2 caused an average value of the inter-mission measurement height difference to be in the range of 64.88–81.90 cm. In addition, considering the influence of the time-varying sea surface terrain, we designed an inter-mission accuracy evaluation of SSH at the intersections of different time intervals for the six beams. The evaluation results showed that the shortest time interval has the highest accuracy, about 5 cm, which provides reliable support for calculating the CTDOV.

Secondly, we obtained valid results in calculating ATDOV and CTDOV while verifying them with the XGM2019 model. It can be seen from **Tables 4**, **5** that although the data point amplitudes are not of the same order of magnitude, the CTDOV accuracy obtained from six of the 15 sets of solutions are similar to beams' ATDOV accuracy. The

TABLE 9 | Statistical information of ATVD directional component after gridding.

DOV direction component	NUM	MAX (arcsec)	MIN (arcsec)	MEAN (arcsec)	STD (arcsec)
Meridian	237,349	6.36	−6.36	0.21	2.12
Prime	235,397	9.74	−9.75	−0.60	3.30

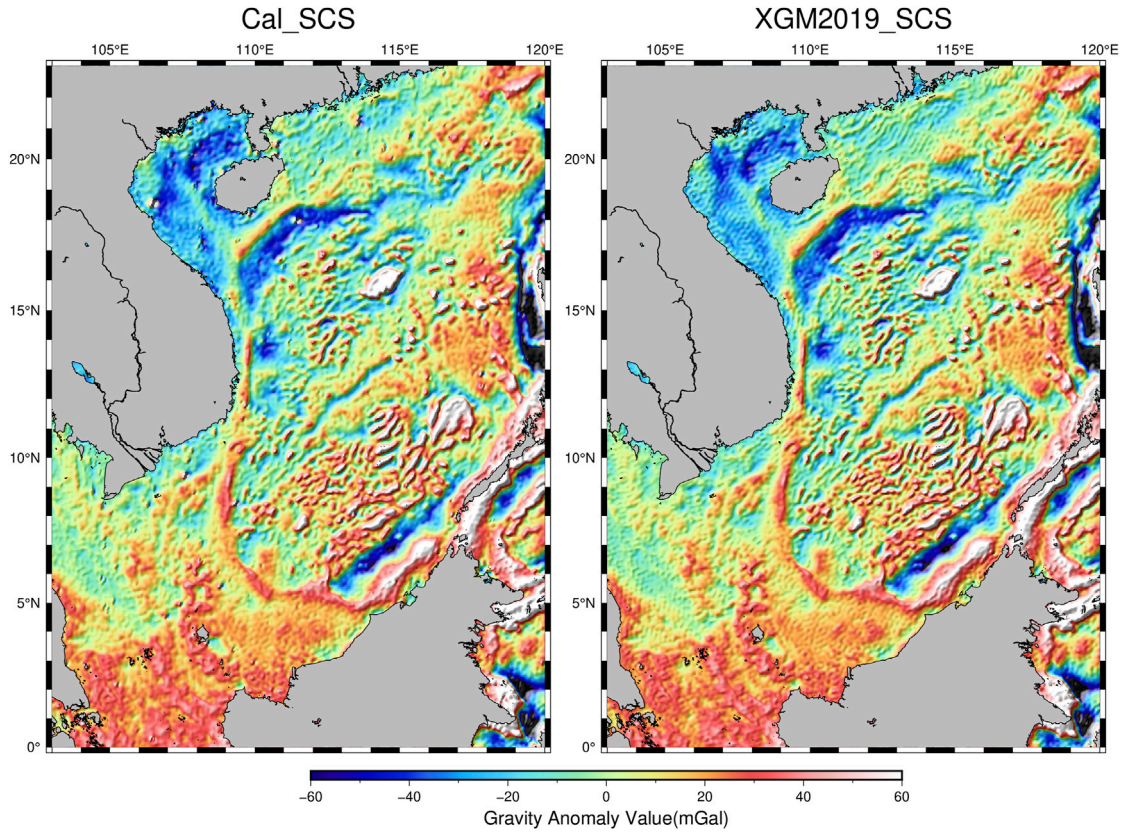

FIGURE 4 | IS-2-derived gravity anomaly over the SCS with remove–compute–restore technique **(left)** and the corresponding XGM2019 model result **(right)**.

TABLE 10 | Statistical information of compared with shipborne data and XGM2019 gravity field mod.

	Screening scales (%)	NUM	MAX (mgal)	MIN (mgal)	MEAN (mgal)	STD (mgal)
Ship-cal	6.62	129,668	4.04	−4.04	−0.02	1.35
Cal-XGM2019	5.52	235,355	7.41	−7.41	−0.12	2.47

comparison indicates that CTDOV calculation between the six beams is mutually desirable in the cross-track direction. Also, we can conclude that the ATDOV accuracy of the middle pair is better than that of the other two pairs. Furthermore, the accuracy of the CTDOV obtained by using two beams on non-identical sides is worse.

Thirdly, based on the verification of the accuracy of the ATDOV calculations, we performed calculations of the ATDOV directional components by using the joint method shown in **Figure 2**. We first found that the accuracy of the CTDOV calculations has a significant impact on the accuracy of the ATDOV directional components. It is essential to verify the accuracy of CTDOV before carrying out the calculation of the directional component of ATDOV. Further, it was determined that the methods of joint calculation between different groups of beams (**Figure 2B**) and joint calculation between different groups and the same group of beams (**Figure 2C**) are the most reliable. By the comparison with the GDOV directional component accuracy, we conclude that the accuracy of the DOV prime directional component has been significantly improved.

Finally, we gridded the ATDOV directional components of the six beams into a $2' \times 2'$ resolution GDOV directional component using a distance-weighting method, and the inverse Vening Meinesz formula (1D-FFT) was used to calculate the gravity anomalies over the SCS. It should be noted that after the six beams are uniformly gridded, the accuracy of the GDOV direction component is increased by about 8–22%, confirming the reliability of the gridding process using the distance-weighting method. The validation using NCEI shipborne gravity measurements and the XGM2019 gravity field model shows that the water depth has a large influence on the accuracy

inversion of gravity anomaly, and the accuracy decreases in both coastal areas and deep waters. Meanwhile, the accuracy inversion of gravity anomaly data using IS-2 single-mission is 1.35 mGal and 2.47 mGal, respectively.

To conclude, IS-2, as a new type of laser altimetry satellite, has improved data collection capabilities. It can use a single mission to obtain gravity anomalies with good data accuracy over the SCS and can acquire high-precision DOV prime components with a single beam. However, it does not provide a significant improvement in the accuracy of the meridional component, which only increased by ~15%. This is because, within a specified distance threshold, the amount of CTDOV data is far greater than the amount of ATDOV data, and the azimuth information is approximately horizontal. Therefore, we believe that with the increasing amount of IS-2 altimetry data and the joint solution between multiple tasks, a better determination of the DOV directional component can be expected and an accurate marine gravity field can be obtained.

DATA AVAILABILITY STATEMENT

The original contributions presented in the study are included in the article/Supplementary Material. Further inquiries can be directed to the corresponding author.

AUTHOR CONTRIBUTIONS

DC and SZ designed the research and manuscript review. HL and BM performed the data analysis, prepared all figures and led the writing of the manuscript. All the authors discussed the results and commented on the manuscript.

FUNDING

This work was jointly supported by the National Natural Science Foundation of China (grant nos. 41871310 and 41804002), Fundamental Research Funds for the Central Universities (grant number N2124005).

ACKNOWLEDGMENTS

We express our gratitude to hundreds of people at the NASA Goddard Space Flight Center and contracting partners that conceived, designed, and created the ICESat-2 Mission, the ICESat-2 Observatory, and the ATLAS instrument. We thank the NASA Earth Sciences Division, who produced the ATL12 ocean surface-height data. Meanwhile, We also thank NCEI for providing the shipborne gravity measurements and Zingerle et al. for providing the XGM2019 gravity field model.

REFERENCES

Abdalati, W., Zwally, H. J., Bindschadler, R., Csatho, B., and Webb, C. (2010). The Icesat-2 Laser Altimetry Mission. *IEEE Xplore* 98 (5), 735–751. doi:10.1109/JPROC.2009.2034765

Albayrak, M., Hirt, C., Guillaume, S., Halicioglu, K., Tevfik zlüdemir, M., and Shum, C. K. (2020). Quality Assessment of Global Gravity Field Models in Coastal Zones: A Case Study Using Astrogeodetic Vertical Deflections in Istanbul, Turkey. *Stud. Geophys. Geod.* 64, 306–329. doi:10.1007/s11200-019-0591-2

Andersen, O. B., Knudsen, P., Kenyon, S., and Holmes, S. (2014). Global and Arctic Marine Gravity Field from Recent Satellite Altimetry (Dtu13). doi:10.3997/2214-4609.20140897

Chander, S., Chauhan, P., and Ajai. (2012). Variability of Altimetric Range Correction Parameters over Indian Tropical Region Using Jason-1 & Jason-2 Radar Altimeters. *J. Indian Soc. Remote Sensing* 40 (3), 341–356. doi:10.1007/s12524-011-0171-6

Friedl, M. A., Tan, B., Schneider, A., Ramankutty, N., Sibley, A., et al. (2010). Sulla-Menashe,Modis Collection 5 Global Land Cover: Algorithm Refinements and Characterization of New Datasets. *Remote Sensing Environ.* 114 (1), 168–182. doi:10.1016/j.rse.2009.08.016

Fu, L-L., Christensen, E. J., Yamarone, C. A., Lefebvre, M., Ménard, Yves., Dorrer, M., et al. (1994). Topex/poseidon Mission Overview. *J. Geophys. Res. Oceans* 99 (C12). doi:10.1029/94JC01761

Guo, J. Y., Shen, Y., Zhang, K., Liu, X., and Xie, F. (2016). Temporal-spatial Distribution of Oceanic Vertical Deflections Determined by Topex/poseidon and Jason-1/2 Missions. *Earth Sci. Res. J.* 20 (2), H1–H5. doi:10.15446/esrj.v20n2.54402

Haagmans, R. (1993). Fast Evaluation of Convolution Integrals on the Sphere Using 1D FFT, and a Comparison with Existing Methods for Stokes?integral. *Manuscripta Geodaetica* 18, 227–241.

Huang, M.-t., Zhai, G.-j., and Ouyang, Y.-z. (2006). Recovery of Marine Gravity Field Using Integrated Data from Multi-Satellite Missions. *Sci. Surv. Mapp.* 31 (6), 37–39. doi:10.1007/s11442-006-0415-5

Hwang, C., Guo, J., Deng, X., Hsu, H. Y., and Liu, Y. (2006). Coastal gravity anomalies from retracked geosat/gm altimetry: improvement, limitation and the role of airborne gravity data. *J. Geod.* 80 (4), 204–216. doi:10.1007/s00190-006-0052-x

Hwang, C., Hsu, H. Y., and Jang, R. J. (2002). Global Mean Sea Surface and Marine Gravity Anomaly from Multi-Satellite Altimetry: Applications of Deflection-Geoid and Inverse Vening Meinesz Formulae. *J. Geodesy* 76 (8), 407–418. doi:10.1007/s00190-002-0265-6

Hwang, C., and Hsu, H. Y. (2003). Marine Gravity Anomaly from Satellite Altimetry: a Comparison of Methods over Shallow Waters, *Geophys. Oceanography*, IAG symposiumProceedings of International Workshop on Satellite Altimetry for Geodesy, 126, 59–66. doi:10.1007/978-3-642-18861-9_7

Hwang, C., Kao, E. C., and Parsons, B. (1998). Global Derivation of Marine Gravity Anomalies from Seasat, Geosat, Ers-1 and Topex/poseidon Altimeter Data. , 134(2), 449–459. doi:10.1111/j.1365-246x.1998.tb07139.x

Jilan, S. (2004). Overview of the South china Sea Circulation and its Influence on the Coastal Physical Oceanography outside the Pearl River Estuary. *Continental Shelf Res.* 24 (16), 1745–1760. doi:10.1016/j.csr.2004.06.005

Kwok, R., and Markus, T. (2017). Potential Basin-Scale Estimates of Arctic Snow Depth with Sea Ice Freeboards from Cryosat-2 and Icesat-2: an Exploratory Analysis. *Adv. Space Res.* 62 (6), 1243–1250. doi:10.1016/j.asr.2017.09.007

Li, J., Ning, J., Chen, J., and Chao, D. (2001). Determination of Gravity Anomalies over the South China Sea by Combination of TOPEX/Poseidon,ERS2 and Geosat Altimeter Data. *Acta Geodaetica et Cartographica Sinica* 3, 197–202.

Li, Z., Liu, X., Guo, J., Zhu, C., Yuan, J., Gao, J., et al. (2020). Performance of Jason-2/gm Altimeter in Deriving Marine Gravity with the Waveform Derivative Retracking Method: a Case Study in the South china Sea. *Arabian J. Geosciences* 13 (18), 1–13. doi:10.1007/s12517-020-05960-0

Liu, S. W., Jun, L. J., Wan, J. H., and Yang, J. G. (2015). Calculation of gravity anomalies over China Sea and its vicinity based on multi-generation satellite altimetry data. *Mar. Sci.* 39 (12), 130–134.

Liu, Z., Yang, J., and Zhang, J. (2020). Jason-3 Global Statistical Assessment Based on Jason-2. *Haiyang Xuebao* 42 (03), 133–143. doi:10.3969/j.issn.0253−4193.2020.03.012

Markus, T., Neumann, T., Martino, A., Abdalati, W., Brunt, K., Csatho, B., et al. (2017). The Ice, Cloud, and Land Elevation Satellite-2 (Icesat-2): Science Requirements, Concept, and Implementation. *Remote Sensing Environ.* 190, 260–273. doi:10.1016/j.rse.2016.12.029

Morison, J. H., Hancock, D., Dickinson, S., Robbins, J., Roberts, L., Kwok, R., et al. (2020). ATLAS/IS-2 L3A Ocean Surface Height, Version 3. [Indicate Subset Used]. Boulder, Colorado USA. *NASA National Snow and Ice Data Center Distributed Active Archive Center*. the IS-2 Science Team. doi:10.5067/ATLAS/ATL12.003

Moses, W., Bowles, J., and Corson, M. (2015). Expected Improvements in the Quantitative Remote Sensing of Optically Complex Waters with the Use of an Optically Fast Hyperspectral Spectrometer—A Modeling Study. *Sensors* 15 (3), 6152–6173. doi:10.3390/s150306152

National Snow and Ice Data Center (2019). Data-sets. Availableat: http://nsidc.org/data /IS-2/data-sets.

Neuenschwander, A. L., Jelley, B., Pitts, K., Popescu, S. C., Nelson, R. F., Harding, D., et al. (2020a). *ATLAS/ICESat-2 L3A Land and Vegetation Height, Version 2.NSIDC*. Boulder, Colorado USA: National Snow and Ice Data Center. doi:10.5067/ATLAS/ATL08.002

Neuenschwander, A. L., Pitts, K. L., Jelley, B. P., Robbins, J., Klotz, B., Popescu, S. C., et al. (2020b). *ATLAS/ICESat-2 L3A Land and Vegetation Height, Version 3. NASA National Snow and Ice Data Center Distributed Active Archive Center*. Boulder, Colorado, USA. doi:10.5067/ATLAS/ATL08.003accessed April, 2020)

Neuenschwander, A., and Pitts, K. (2019). The ATL08 Land and Vegetation Product for the Icesat-2 Mission. *Remote Sensing Environ.* 221, 247–259.

Neumann, T. A., Brenner, A. C., Hancock, D. W., Karbeck, K., Luthcke, S., Robbins, J., et al. (2018). Ice, Cloud, and Land Elevation Satellite-2 Project Algorithm Theoretical Basis Document for Global Geolocated Photons (ATL03). Available at: https://icesat-2.gsfc.nasa.gov/science/data-products.

Neumann, T. A., Martino, A. J., Markus, T., Bae, S., Bock, M. R., Brenner, A. C., et al. (2019). The Ice, Cloud, and Land Elevation Satellite – 2 Mission: A Global Geolocated Photon Product Derived from the Advanced Topographic Laser Altimeter System. *Remote Sensing Environ.* 233. doi:10.1016/j.rse.2019.111325

Olgiati, A., Balmino, G., Sarrailh, M., and Green, C. M. (1995). Gravity Anomalies from Satellite Altimetry: Comparison between Computation via Geoid Heights and via Deflections of the Vertical. *Bull. Géodésique* 69 (4), 252–260. doi:10.1007/BF00806737

Peng, Fuqing., and Xia, Zheren. (2004). Vertical Deflection Theorem of Satellite Altimetry. *Hydroaphic Surv. Charting* 2, 5–9.

Sandwell, D. T. (1992). Antarctic Marine Gravity Field from High-Density Satellite Altimetry. *Geophys. J. Int.* 109 (2), 437–448. doi:10.1111/j.1365-246X.1992.tb00106.x

Sandwell, D. T., and Smith, W. H. F. (1997). Marine Gravity Anomaly from Geosat and Ers 1 Satellite Altimetry. *J. Geophys. Res. Solid Earth* 102 (B5), 10039–10054. doi:10.1029/96JB03223

Shaw, P. T., and Chao, S. Y. (1994). Surface Circulation in the South china Sea. *Deep-sea Res.* 41 (11-12), 1663–1683. doi:10.1016/0967-0637(94)90067-1

Smith, B., Fricker, H. A., Gardner, A. S., Medley, B., and Zwally, H. J. (2020). Pervasive Ice Sheet Mass Loss Reflects Competing Ocean and Atmosphere Processes. *Science* 368 (6496), eaaz5845. doi:10.1126/science.aaz5845

Smith, B., Fricker, H. A., Holschuh, N., Gardner, A. S., and Siegfried, M. R. (2019). Land Ice Height-Retrieval Algorithm for Nasa's Icesat-2 Photon-Counting Laser Altimeter. *Remote Sensing Environ.* 233, 111352. doi:10.1016/j.rse.2019.111352

Sun, M., Guo, J., Yuan, J., Liu, X., Wang, H., and Li, C. (2021). Detecting Lake Level Change from 1992 to 2019 of Zhari Namco in Tibet Using Altimetry Data of TOPEX/Poseidon and Jason-1/2/3 Missions. *Front. Earth Sci.* doi:10.3389/feart.2021.640553

Wan, X., Annan, R. F., Jin, S., and Gong, X. (2020a). Vertical Deflections and Gravity Disturbances Derived from Hy-2a Data. *Remote Sensing* 12 (14), 2287. doi:10.3390/rs12142287

Wan, X., Jin, S., Liu, B., Tian, S., Kong, W., and Annan, R. F. (2020b). Effects of Interferometric Radar Altimeter Errors on Marine Gravity Field Inversion. *Sensors (Basel, Switzerland)* 20 (9). doi:10.3390/s20092465

Wang, H., and Wang, G (2001). Inversion of Gravity Anomalies from Along-Track Vertical Deflections with Satellite Altimeter Data and its Applications. *Acta Geodaetica et Cartographica Sinica* 1, 23–28. doi:10.3321/j.issn:1001-1595.2001.01.005

Wang, H., and Lu, W. Y. (2008). High Precision Vertical Deflection over china Marginal Sea and Global Sea Derived from Multi-Satellite Altimeter, 11. *Geomatics & Information Science of Wuhan University*, 289–293. doi:10.1007/s11806-008-0122-8

Wang, J., Xu, H., Yang, L., Song, Q., and Ma, C. (2021). Cross-calibrations of the HY-2B altimeter using Jason-3 satellite during the period of 2019.4~2020.9. *Front. Earth Sci.* doi:10.3389/feart.2021.647583

Yang, L., Zhou, X. H., Lin, M. S., Lei, N., Bo, M. U., and Zhu, L., (2016). Global Statistical Assessment of HY-2A Altimeter IGDR Data. *Prog. Geophys. (Chinese)* 31 (2), 0629–0636. doi:10.6038/pg20160216

Zhang, S., Sandwell, D. T., Jin, T., and Li, D. (2017). Inversion of Marine Gravity Anomalies over Southeastern china Seas from Multi-Satellite Altimeter Vertical Deflections. *J. Appl. Geophys.* 137, 128–137. doi:10.1016/j.jappgeo.2016.12.014

Zhang, S., Li, J., Jin, T., and Che, D. (2018). Hy-2a Altimeter Data Initial Assessment and Corresponding Two-Pass Waveform Retracker. *Remote Sensing* 10 (4), 507. doi:10.3390/rs10040507

Zhang, S., Li, J., and Kong, X. (2020). Inversion of Global Marine Gravity Anomalies with Vertical Deflection Method Deduced from Laplace Equation. *Acta Geodaetica et Cartographica Sinica* 49 (4), 452–460. doi:10.11947/j.AGCS.2020.20190108

Zhang, S. (2017). Research on Determination of Marine Gravity Anomalies from Multi-Satellite Altimeter Data. *Acta Geodaetica et Cartographica Sinica*. doi:10.11947/j.AGCS.2017.20170187

Zhu, C., Guo, J., Gao, J., Liu, X., Hwang, C., Yu, S., et al. (2020). Marine Gravity Determined from Multi-Satellite Gm/erm Altimeter Data over the South china Sea: Scsga v1.0. *J. Geodesy* 94 (5). doi:10.1007/s00190-020-01378-4

Zhu, C., Guo, J., Hwang, C., Gao, J., and Liu, X. (2019). How Hy-2a/gm Altimeter Performs in Marine Gravity Derivation: Assessment in the South china Sea. *Geophys. J. Int.* 219 (2), 1056–1064. doi:10.1093/gji/ggz330

Zhu, C., Zhang, S., Xiao, F., Li, J., and Zhu, T. (2018). Threshold Determination for Local Instantaneous Sea Surface Height Derivation with Icebridge Data in Beaufort Sea. doi:10.5194/isprs-archives-XLII-3-2579-2018

Zingerle, P., Pail, R., Gruber, T., and Oikonomidou, X. (2019). *The experimental gravity field model XGM2019e*. Potsdam: GFZ Data Services. doi:10.5880/ICGEM.2019.007

Zingerle, P., Pail, R., Gruber, T., and Oikonomidou, X. (2020). The combined global gravity field model xgm2019e. *J. Geod.* 94 (7). doi:10.1007/s00190-020-01398-0

Conflict of Interest: The authors declare that the research was conducted in the absence of any commercial or financial relationships that could be construed as a potential conflict of interest.

frontiers in Earth Science

ORIGINAL RESEARCH
published: 26 May 2021
doi: 10.3389/feart.2021.674983

Elevation and Volume Changes in Greenland Ice Sheet From 2010 to 2019 Derived From Altimetry Data

Guodong Chen[1]*, *Shengjun Zhang*[2]*, *Shenghao Liang*[1] and *Jiaheng Zhu*[1]

[1] School of Geography Science and Geomatics Engineering, Suzhou University of Science and Technology, Suzhou, China, [2] School of Resources and Civil Engineering, Northeastern University, Shenyang, China

Long-term altimetry data are one of the major sources to analyze the change in global ice reserves. This study focuses on the elevation and volume changes in the Greenland ice sheet (GrIS) from 2010 to 2019 derived from altimetry observations. In this study, the methods for determining surface elevation change rates are discussed, and specific strategies are designed. A new elevation difference method is proposed for CryoSat-2 synthetic aperture interferometric (SARin) mode observations. Through validation with Airborne Topographic Mapper (ATM) data, this new method is proved to be effective for slope terrains at the margins of the ice sheet. Meanwhile, a surface fit method is applied for the flat interior of the ice sheet where low resolution mode (LRM) observations are provided. The results of elevation change rates in the GrIS from 2010 to 2019 are eventually calculated by combining CryoSat-2 and ATM observations. An elevation change rate of -11.83 ± 1.14 cm·a^{-1} is revealed, corresponding to a volume change rate of -200.22 ± 18.26 km^3·a^{-1}. The results are compared with the elevation changes determined by Ice, Cloud, and Land Elevation Satellite (ICESat) from 2003 to 2009. Our results show that the overall volume change rate in the GrIS slowed down by approximately 10% during the past decade, and that the main contributor of GrIS ice loss has shifted from the southeast coast to the west margin of the ice sheet.

Keywords: altimetry, Greenland ice sheet, Arctic, volume loss, elevation change

OPEN ACCESS

Edited by:
Jinyun Guo, Shandong University of Science and Technology, China

Reviewed by:
Haihong Wang, Wuhan University, China
Wan Xiaoyun, China University of Geosciences, China

***Correspondence:**
Guodong Chen
cgdtt@126.com
Shengjun Zhang
zhangshengjun@mail.neu.edu.cn

Specialty section:
This article was submitted to Cryospheric Sciences, a section of the journal Frontiers in Earth Science

Received: *02 March 2021*
Accepted: *26 April 2021*
Published: *26 May 2021*

Citation:
Chen G, Zhang S, Liang S and Zhu J (2021) Elevation and Volume Changes in Greenland Ice Sheet From 2010 to 2019 Derived From Altimetry Data. Front. Earth Sci. 9:674983. doi: 10.3389/feart.2021.674983

INTRODUCTION

The Greenland ice sheet (GrIS), the second largest one in the world, has been undergoing a significant ablation process (Shepherd et al., 2012; The IMBIE Team, 2019; Velicogna et al., 2020) and has become an important source of global sea level rise (Zwally et al., 2005; Gardner et al., 2013; Csatho et al., 2014). The total mass loss of the GrIS was about $3{,}800 \pm 339$ Gt·a^{-1} between 1992 and 2018, which caused a mean sea level rise of about 10.6 ± 0.9 mm (The IMBIE Team, 2019). According to the modeled prediction, the total sea-level rise caused by GrIS ablation will be 50–120 mm by 2100 (Church et al., 2013). These alarming facts put forward the requirement for large-scale and long-term monitoring of ice and snow melting events in the GrIS.

The precision and accuracy of airborne and field observations are good enough for mass balance research studies on single glaciers (e.g., Muhammad and Tian, 2016; Cao et al., 2017; Wang and Holland, 2018; Muhammad et al., 2019). However, the spatial and temporal coverage of these observations are not sufficient for large-scale ice sheet mass

balance research studies. Satellite altimetry has been proved to be an effective method to study the changes in the GrIS. Both radar and laser altimeters have provided data for elevation change and mass loss monitoring of the GrIS (Thomas et al., 2008; Pritchard et al., 2009; Sørensen et al., 2011; Zwally et al., 2011; Khvorostovsky, 2012; Levinsen et al., 2015). CryoSat-2 is a new generation radar altimetry satellite launched by the European Space Agency (ESA), with a primary science objective of monitoring the changes in land and sea ice of the Earth (Nilsson et al., 2016). Based on datasets collected using CryoSat-2, researchers have made a lot of progress in this field. Helm et al. (2014) applied a threshold first-maximum retracker algorithm to CryoSat-2 Level-1b data, and found a mean volume loss of 375 $\pm$ 24 $km^3 \cdot a^{-1}$ between January 2011 and January 2014 for the GrIS. McMillan et al. (2016) applied a numerical deconvolution procedure to CryoSat-2 data to alleviate the impact of the 2012 melting event (Nilsson et al., 2015) and a mass loss of 269 $\pm$ 51 $Gt \cdot a^{-1}$ between January 2011 and December 2014 for the GrIS was found with an analysis of the combination of CryoSat-2 data and a RACMO2.3 model. Nilsson et al. (2016) applied a traditional threshold retracker algorithm to LRM data and a leading-edge maximum gradient retracker algorithm to SARin mode data, and found a volume loss of 289 $\pm$ 20 $km^3 \cdot a^{-1}$ between 2011 and 2015. By analyzing the implications of changing scattering properties on GrIS volume change, Simonsen and Sørensen (2017) found that the best results could be obtained when applying only the backscatter correction to the SARin area and only the leading edge width correction to the LRM area. They presented the result of a volume loss of 292 $\pm$ 38 $km^3 \cdot a^{-1}$ in the GrIS for the period of November 2010 to November 2014. Sørensen et al. (2018) also adopted CryoSat-2 data as an important source to build GrIS surface elevation change grids.

All the results of the studies mentioned above had shown a significant loss in volume/mass of the GrIS in the first 5 years of 2010s. However, recent studies have indicated a slowdown in GrIS mass loss rate since 2014 (Bevis et al., 2019; The IMBIE Team, 2019). Hence, it is meaningful to reevaluate the volume loss in the recent decade. Besides, although researchers have revealed reasonable results in the flat interior of the GrIS with CryoSat-2 data, the algorithm used for the ice sheet margins still needs to be improved to better cope with the impact of the slope terrains. In this study, a new elevation difference method for elevation change rate detection is proposed to acquire more reasonable results from the ice sheet margins. Then, the elevation change and volume loss in the GrIS for the period of 2010 to 2019 are determined with the combination of CryoSat-2 and ATM altimetry observations. Eventually, the results are analyzed using a drainage scale and compared with the volume loss from 2003 to 2009 calculated by Ice, Cloud, and Land Elevation Satellite (ICESat) observations.

ALTIMETRY DATA

CryoSat-2 Data

The CryoSat-2 radar altimetry mission, the first ice mission of ESA, was launched on April 8, 2010, and data collection started in July 2010. SAR interferometric radar altimeter (SIRAL), a new type of delay/Doppler radar altimeter, is the primary on-board instrument. It has three measurement modes that are specialized for different types of reflecting surfaces. It operates in two modes over the GrIS: conventional pulse limited radar altimetry mode (referred to as LRM), which is operated over the flat interior part, and SAR interferometric mode (referred to as SARin), which is operated over the complex steep terrains on the edge. From an altitude of about 717 km and reaching latitudes of 88°, CryoSat-2 provides dense observations over the entire GrIS. The full repeat cycle is 369 days with sub-cycles of around 30 days. Due to high temporal and spatial resolution in the GrIS, in this study, CryoSat-2 is the major source of data.

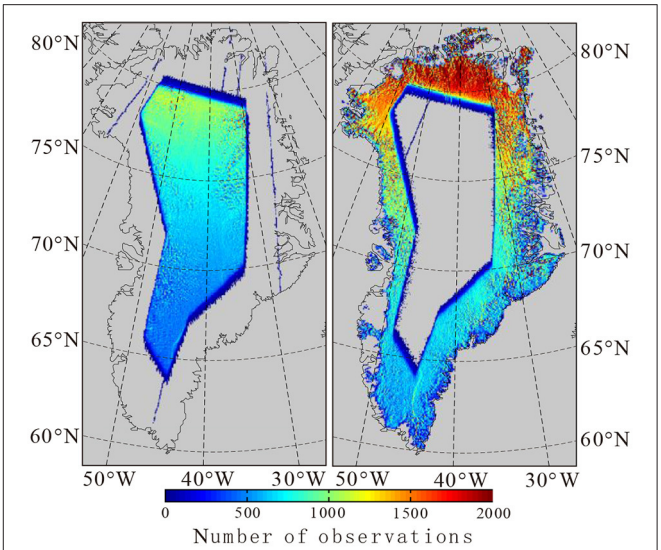

FIGURE 1 | Data distribution of CryoSat-2 LRM mode **(Left)** and SARin mode **(Right)**. Different colors stand for the number of observations for each 5-km × 5-km grid.

CryoSat-2 data products are classified into two levels and 23 types. All these products can be downloaded from the ftp server of ESA (ftp://science-pds.cryosat.esa.int/). In this study, the Level-2 GDR (Geophysical Data Record) Baseline-C product is employed. Only observations from the ice sheet, ice caps, and glaciers are required; hence a 1-km resolution Greenland surface type grid (Bamber et al., 2013) is used to discriminate CryoSat-2 data from ocean, ice-free land, and other surfaces. Observations obtained from 2010 to 2019 are used, and the number of observations for each 5-km grid is shown in **Figure 1**.

Operation IceBridge Airborne Topographic Mapper Data

The Airborne Topographic Mapper (ATM) is a scanning laser altimeter used in the Operation IceBridge airborne mission operated by the National Aeronautics and Space Administration (NASA). It can measure surface elevation changes in the polar ice of the Earth. Combined with ATM data, the record of observations started by ICESat is extended, and multi-satellite altimetry measurements are linked. The mission has been

operated every spring in Greenland since 1993. The ATM data provide a valid comparison for CryoSat-2 data, because laser altimeters generally have better accuracy than radar altimeters (Brenner et al., 2007). In this study, we use ATM observations for two purposes: to evaluate the elevation change estimation algorithm for CryoSat-2 measurements and to increase valid observations for GrIS elevation change rate determination. The ATM L4 data from 2010 to 2018, which are provided by National Snow and Ice Data Center (NSIDC) and contain surface elevation change rates derived from overlapping ATM observations, are used. Readers may refer to Studinger (2018) for further details about the ATM L4 product.

Ice, Cloud, and Land Elevation Satellite Data

The Ice, Cloud, and Land Elevation Satellite (ICESat) mission is the first low-Earth-orbit satellite with a specific laser altimeter onboard and is launched by NASA. It operated 18 33-day campaigns from 2003 to 2009 and provided important information for volume loss in the GrIS during that period. The elevation and volume changes in the GrIS between 2003 and 2009 are estimated using the ICESat data and compared with the results from between 2010 and 2019. In this study, the GLA12-release 34 products provided by NSIDC are used.

METHODS FOR ELEVATION CHANGE ESTIMATION

Elevation Difference Method for CryoSat-2 Synthetic Aperture Interferometric Mode and Airborne Topographic Mapper Data

In the existing studies, the surface fit method was widely used for surface elevation change determination from CryoSat-2 (Helm et al., 2014; McMillan et al., 2016; Nilsson et al., 2016; Simonsen and Sørensen, 2017; Sørensen et al., 2018). However, this method has limited accuracy on the margins of the ice sheet where undulating terrains appear (see section Validation for CryoSat-2 Derived Result for details). Therefore, an alternative method, referred to as the elevation difference method, is proposed to estimate the elevation change rates on the peripheries of the GrIS. This method eliminates spatially varying elevation differences before the elevation change rates are estimated, so that these two parts can be solved separately. Here, the elevation difference, $\Delta H(\Delta t)$, can be defined as

$$\Delta H(\Delta t) \;=\; H(t_j) \;-\; H(t_i) \tag{1}$$

where $H(t_i)$ and $H(t_j)$ are two elevation observations at exactly the same location obtained at different times t_i and t_j. Considering long-term and seasonal elevation changes, each elevation observation can be expressed as

$$\begin{aligned} H(t)_{SARin} \;&=\; H_0 + \frac{dH}{dt}\cdot\Delta t + s_1\cdot\sin(2\pi t) + s_2\cdot\cos(2\pi t) \\ &\quad + dBs\cdot\left(Bs(t) - \bar{Bs}\right) \end{aligned} \tag{2}$$

where dH/dt is the long-term elevation change rate, H_0 is the reference elevation at reference time t_0, and s_1 and s_2 are coefficients of the trigonometric functions used to fit the seasonal elevation change. For CryoSat-2 SARin observations, the impact of changing scattering properties of the ice sheet surface should also be considered, because changing snow penetration depth has a significant effect on radar altimetry observations (Slater et al., 2019; Otosaka et al., 2020). To alleviate this impact, a backscatter correction factor is applied following Simonsen and Sørensen (2017). Consequently, dBs in Equation (2) is the elevation variation caused by backscatter changes, $Bs(t)$ is the surface backscatter at time (t), and $\bar{Bs}$ is the mean backscatter. Considering Equations (1) and (2), the elevation difference can be written as

$$\begin{aligned} \Delta H(\Delta t)_{SARin} \;&=\; \frac{dH}{dt}\cdot(t_j - t_i) + s_1\cdot\left(\sin(2\pi t_j) - \sin(2\pi t_i)\right) \\ &\quad + s_2\cdot\left(\cos(2\pi t_j) - \cos(2\pi t_i)\right) \\ &\quad + dBs\cdot\left(Bs(t_j) - Bs(t_i)\right) \end{aligned} \tag{3}$$

In a small region, a consistent elevation change pattern is assumed (Nilsson et al., 2016), and long-term elevation change rate can be estimated by least squares estimation of Equation (3).

No slope corrections are considered in Equation (3), since elevation difference should be derived from observations at exactly the same position. Therefore, the derivation of elevation differences is crucial for this method. For SARin observations, the elevation difference determination is illustrated in **Figure 2**. Squares and black dots represent measurements from two adjacent SARin tracks, i and j, respectively. Note that the footprints of the SARin data are not necessarily located in a straight line like in conventional altimeters but may be more scattered. Then, the elevation difference is calculated as follows:

a. For observations from track i, $H_N^{\mathrm{SARin}}(t_i)$, measured at time (t_i), the nearby observations from another track (e.g., track j) within 300 m from $H_N^{\mathrm{SARin}}(t_i)$ (the gray circle in **Figure 2**) is selected for the next step, denoted as $H_1^{\mathrm{SARin}}(t_j), \cdots, H_n^{\mathrm{SARin}}(t_j)$. However, if there is less than three observations from track j within the 300-m radius search window, this track will be skipped, and observations from another nearby track will be checked.
b. At the exact same position of $H_N^{\mathrm{SARin}}(t_i)$, an interpolated elevation at time (t_j), denoted as $H_{\mathrm{int\,er}}(t_j)$, can be obtained by bilinear interpolation of the observations selected from track j [e.g., $H_1^{\mathrm{SARin}}(t_j), \cdots, H_n^{\mathrm{SARin}}(t_j)$]. To ensure reliable accuracy, interpolation is only carried out when $H_N^{\mathrm{SARin}}(t_i)$ is located inside the polygon formed by $H_1^{\mathrm{SARin}}(t_j), \cdots, H_n^{\mathrm{SARin}}(t_j)$ (i.e., dashed lines in **Figure 2**).
c. The elevation difference measurement is determined as the difference of $H_N^{\mathrm{SARin}}(t_i)$ and $H_{\mathrm{int\,er}}(t_j)$:

$$\Delta H(\Delta\, t)_{SARin} \;=\; H_{\mathrm{int\,er}}(t_j) - H_N^{\mathrm{SARin}}(t_i) \tag{4}$$

The surface elevation change rate given in the ATM L4 data is simply determined by the division of elevation difference and time difference from overlapping ATM observations (Studinger,

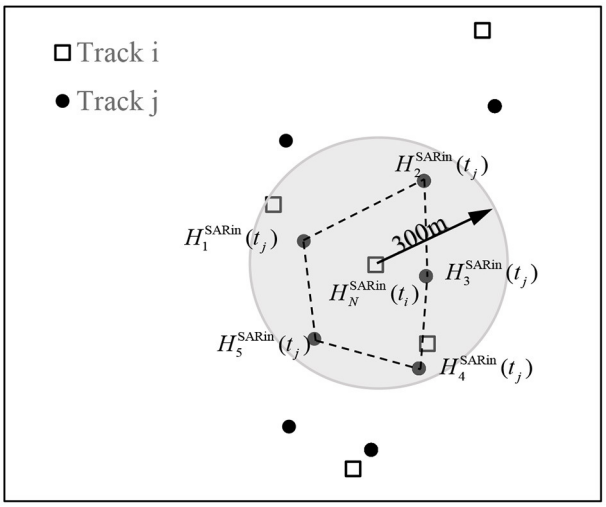

FIGURE 2 | Illustration of the elevation difference method. Squares and black dots represent measurements from track i and track j, respectively. The gray circle shows the 300-m search window and the dashed polygon shows the boundary of the interpolation area.

2018). To make the spatial resolution and time span of the ATM data consistent with CryoSat-2, the elevation change rates from ATM L4 are recalculated using the elevation difference method. The elevation difference of each pair of overlapping observations can be restored:

$$\Delta H_{ATM} = \dot{H}_{ATM} \cdot \Delta t_{ATM} \tag{5}$$

where ΔH_{ATM} is the elevation difference, and $\dot{H}_{ATM}$ and Δt_{ATM} are elevation change rate and time difference given in the ATM L4 product. Generally, no seasonal variations would be detected by ATM, because all the observations used in the L4 product were operated in spring. Snow penetration also does not need to be considered for laser altimeter like ATM. Hence, the average elevation change rate can be expressed as:

$$\Delta H(\Delta t)_{ATM} = \frac{dH}{dt} \cdot (t_j - t_i) \tag{6}$$

Equation (6) can be regarded as a special form of Equation (3). Finally, the surface elevation change rates are calculated in 5-km × 5-km grids following McMillan et al. (2016). In order to remove unreliable observations, the mean and standard deviation σ of residuals in each grid is calculated, and a 3σ iterative convergent edit is used.

Surface Fit Method for CryoSat-2 Low Resolution Mode Data

The surface fit method has been proved to be a better way for CryoSat-2 data than the crossover method used for conventional LRM observations (Nilsson et al., 2016). In this study, we apply this method for CryoSat-2 LRM data. The surface fit method is performed by fitting a linear model to the elevations as a function of time and space inside a relatively small area under the assumption that elevation changes are consistent in the area. In addition, a backscatter correction factor is applied to alleviate the impact of changing scattering properties of the ice sheet surface (Simonsen and Sørensen, 2017). Hence, CryoSat-2 measurements can be expressed as follows:

$$\begin{aligned} H(t) = {} & \frac{dH}{dt} \cdot \Delta t + s_1 \cdot \sin(2\pi t) + s_2 \cdot \cos(2\pi t) + \\ & dBs \cdot \left(Bs(t) - \bar{Bs}\right) + a_0 + a_1(x - x_0) \\ & + a_2(y - y_0) + a_3(x - x_0)^2 + a_4(y - y_0)^2 + a_5(x - x_0) \\ & (y - y_0) + a_6(x - x_0)^3 \\ & + a_7(y - y_0)^3 + a_8(x - x_0)^2(y - y_0) \\ & + a_9(x - x_0)(y - y_0)^2 \end{aligned} \tag{7}$$

In Equation (7), the ground surface is fitted by the cubic polynomial, where $a_0 \sim a_9$ are coefficients, and (x,y) and (x_0,y_0) are coordinates of measurement and center of the calculation area, respectively. Other symbols have the same meaning as those in Equations (2)–(4). The parameters can be estimated by least squares estimation. Same as the elevation difference method, elevation changes are calculated in 5-km × 5-km grids, and the 3σ iterative convergent edit is used to remove the outliers.

Elevation Change Algorithms for Ice, Cloud, and Land Elevation Satellite

To estimate the 2003–2009 surface elevation change rate of the GrIS, a repeat track analysis similar to Zwally et al. (2011) is applied for the ICESat data from 17 campaigns (L2a–L2f, L3a–L3k). The repeated tracks were divided into 500-m segments. In each segment, a reference track is selected, and measurements are interpolated to equally spaced (172 m) reference points along each track. Then, the interpolated point H_i^{ICESat} can be denoted as:

$$\begin{aligned} H_i^{ICESat} = {} & H_0 + \frac{dH}{dt} \cdot (t_i - t_0) + s_1 \cdot \sin(2\pi t_i) \\ & + s_2 \cdot \cos(2\pi t_i) + k \cdot D_i \end{aligned} \tag{8}$$

where H_0 and t_0 are elevation and observation time of the reference point, k is the surface slope at cross track direction, and D_i is the cross track distance to the reference track. The rest of the characters are similar to those in Equation (2). Further details can be found in Zwally et al. (2011) and Chen and Zhang (2019). The equations are solved in each segment and then gridded into 5-km × 5-km grids by Kriging interpolation.

VALIDATION FOR CRYOSAT-2 DERIVED RESULT

While laser altimetry data have been proved to be reliable in the GrIS (Krabill et al., 2002; Brenner et al., 2007; Schenk and Csathó, 2012; Csatho et al., 2014; Brunt et al., 2017), the elevation change rates derived from the CryoSat-2 data should be verified, and the effectiveness of the new method adopted for the SARin-covered

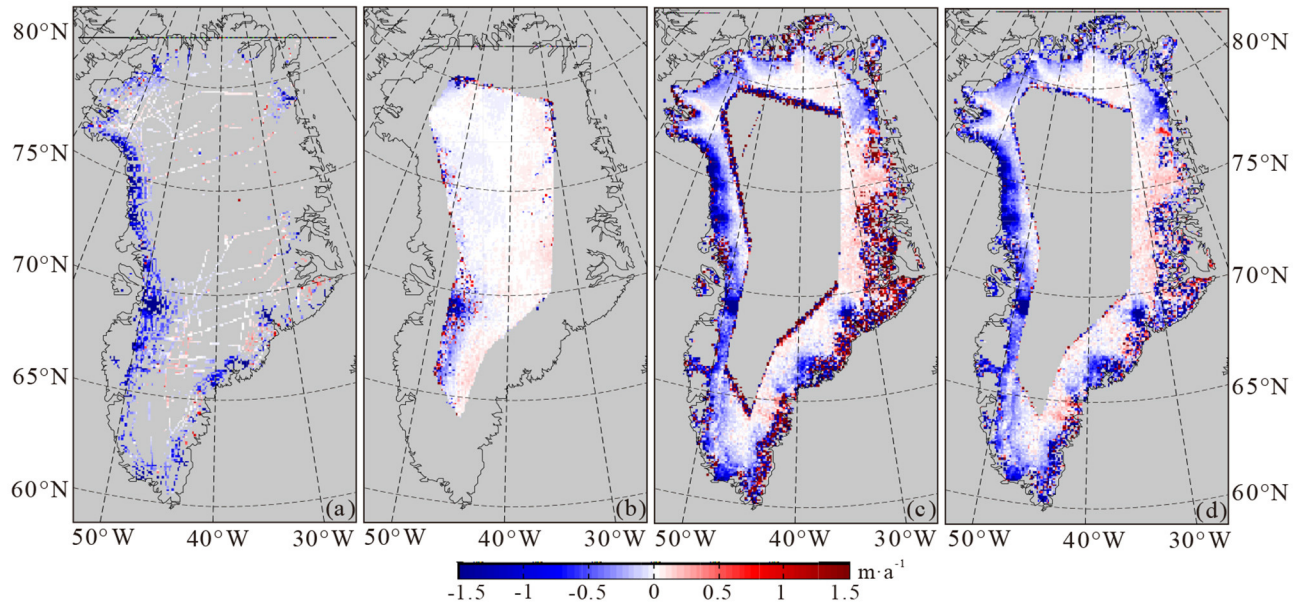

FIGURE 3 | Elevation changes in 2010–2018 derived from **(a)** ATM L4 data, **(b)** CryoSat-2 LRM data, **(c)** CryoSat-2 SARin data calculated by the surface fit method, and **(d)** CryoSat-2 SARin data calculated by the elevation difference method.

area should also be tested. In this section, the results of elevation changes derived from the CryoSat-2 data are compared with those from ATM for validation. For SARin observations, both the surface fit and elevation difference methods are investigated and compared. For LRM observations, the effectiveness of the surface fit method is tested. Since only the ATM L4 product between 2010 and 2018 is available online at the time of the study, the time range of CryoSat-2 observations used in this section is also limited from July 2010 to June 2018 to make the two datasets more comparable.

The results derived from ATM and CryoSat-2 are shown in **Figure 3**. Comparing the two methods used for the SARin-covered area (**Figures 3c,d**), similar trends are mostly found, while remarkable differences occur at the edge of the GrIS, especially over the southeast coastal region. Extensive positive elevation change rates are found using the surface-fit method in those areas, while moderate negative changes are found using the elevation difference method. However, a recent study that used the combination of Gravity Recovery and Climate Experiment (GRACE) satellite and surface mass balance data showed mass loss at the southeast margin of the GrIS (Wang et al., 2019), which is contradictory to the results of the surface fit method but consistent with those of the elevation difference method. Comparison with ATM also suggests that the elevation difference method is better than the surface fit method. The difference between elevation change rates derived from CryoSat-2 and ATM (defined as CryoSat-2—ATM) is shown in **Figure 4**. In the difference map of the surface-fit method and ATM (**Figure 4a**), the red spots at the margin of the GrIS indicate a serious underestimation of elevation decline for the CryoSat-2 result. In contrast, the difference between the elevation difference method and ATM (**Figure 4b**) shows much better results in general, and improvement in the southeast coastal area is quite obvious.

For further discussion, the differences shown in **Figure 4** are analyzed statistically. All the elevation change rate differences greater than ± 10 m·a^{-1} are considered to be outliers. By this criterion, 470 outliers are removed for the surface fit method, and 69 are removed for elevation fitting. Since the two methods reveal similar results in the flat inland area but different results in the undulating marginal area, surface slope is further considered in statistics. Therefore, an ICESat-derived digital elevation model (DEM) of the GrIS (DiMarzio, 2007) provided by NSIDC is used to determine the surface slope in each grid. For the entire SARin-covered area, about 9,500 grids are compared with ATM for both methods. The differences between the results derived from SARin and ATM are classified according to the surface slope. The mean and standard deviation (SD) of the differences and the number of grids used for statistics in each surface slope category are shown in **Table 1**. Surface slope has a great impact on the surface fit method, but it has less effect on the elevation difference method. In flat areas with a surface slope of $<0.2°$, the two methods have almost the same mean difference of about 3 cm·a^{-1} compared to ATM, with a difference of only 0.1 mm·a^{-1}. With the increase in surface slope, the average difference between the surface fit method and ATM increases rapidly and reaches 1.492 ± 3.639 m·a^{-1} when the surface slope is more than 1°. By comparison, the mean differences between the elevation difference method and ATM seem to be random with the increase in surface slope. The mean differences are generally centimeter-scale, except for the case when the surface slope is more than 1°, but the value of −0.359 is still considerably better than the case of the surface fit method. The new method also shows a lower standard deviation than that of the surface fit

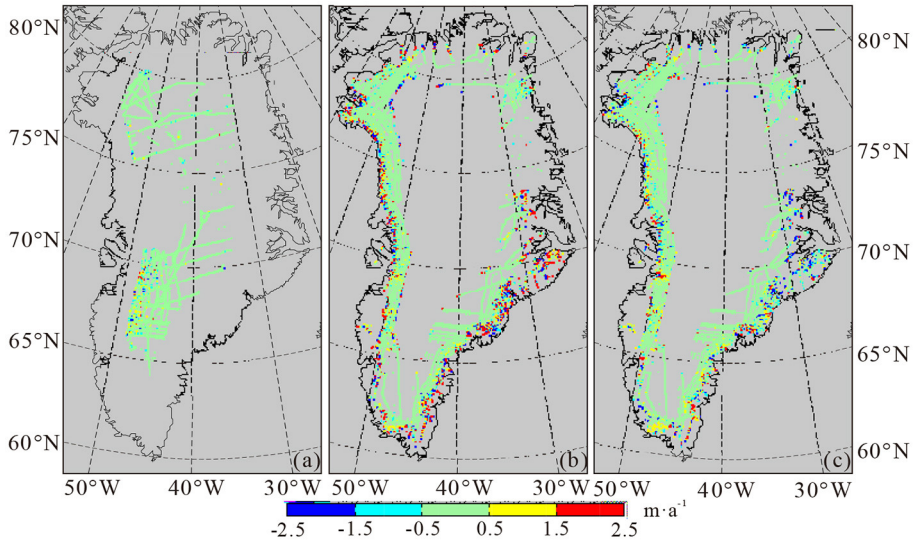

FIGURE 4 | Elevation change rate difference of **(a) Figures 3a,b**, **(b) Figures 3a–c**, and **(c) Figures 3a–d**.

method in all surface slope classifications. While the elevation difference method reveals results similar to those of ATM in the entire area with an average difference of 0.017 ± 1.128 m·a^{-1}, the surface fit method is not so reliable with an obvious bias of +25.24 cm·a^{-1} and a greater standard deviation of ±1.854 m·a^{-1}. Generally, the results shown in **Table 1** suggest that the elevation difference method is better than the surface fit method in determining the surface elevation change rate of areas with a high slope. We suggest that this discrepancy can be attributed to the different strategies used for topographic correction. The details are discussed in section Impact of Topography for the Surface Fit Method.

The results in **Table 1** also show that the surface-fit method has little difference with the elevation difference method when the surface slope is low. Hence, only the surface fit method is used for LRM data, because LRM is only operated at the flat and smooth areas in the interior of the GrIS. The elevation changes derived from LRM are shown in **Figure 3b**, and their differences with ATM are shown in **Figure 4a**. Again, the grids with elevation change rate difference greater than ±10 m·a^{-1} are removed as outliers, and 3,485 grids remain for the comparison. The mean difference of the two data sets is 0.01 m·a^{-1}, with a standard deviation of 0.878 m·a^{-1}, which indicates that the results of the LRM process are reliable.

RESULTS

Greenland Ice Sheet Elevation Change Between 2010 and 2019

Although the elevation difference method generally shows reasonable results, a small proportion of biased grids in the SARin-covered area still exists and can be distinguished, as shown in **Figure 4** (e.g., Jakobshavn Isbræ around 50°W, 69°N). Therefore, a further combination of the SARin and ATM data is adopted to improve the accuracy in the SARin-covered area based on the elevation difference method. For the LRM-covered area, the ATM data are not involved, because they are in good agreement with the LRM data. Hence, the results in this area are determined only by the LRM data with the surface fit method.

With the procedures mentioned above, the CryoSat-2 Level 2 product from July 2010 to July 2019 and the ATM L4 product from 2010 to 2018 are used for the final results. The elevation change rates are calculated in regular 5-km × 5-km grids. Grids with an root mean square (RMS) larger than 0.5 m·a^{-1} from least squares estimation are rejected as outliers. Considering the characteristics of elevation changes in the GrIS in recent decades (Nilsson et al., 2015), the grids with an elevation change rate either larger than +3 m·a^{-1} or smaller than −15 m·a^{-1} are also considered to be outliers. The blanks between altimetry tracks are filled by Kriging interpolation to cover the entire GrIS drainage systems given by Zwally et al. (2012). Following Nilsson et al. (2016), the uncertainty of the elevation change rate in each 5-km × 5-km grid is basically determined from the standard deviations of the differences between CryoSat-2 and ATM. However, different from Nilsson et al. (2016), the uncertainties used in this study are not only distinguished by observation modes (i.e., LRM and SARin) but also by surface slope according to the classification shown in **Table 1**. Our final result for the GrIS surface elevation change from 2010 to 2019 is given in **Figure 5**. The average elevation change rate for the entire GrIS is −11.83 ± 1.14 cm·a^{-1}, equivalent to a volume loss of −200.22 ± 18.26 km^3·a^{-1}. The negative numbers indicate that the GrIS is still in a state of obvious mass loss as a whole after 2010. In **Figure 5**, the boundaries of eight drainage systems (DSs 1–8) and 19 sub-drainage systems (DSs 1.1–8.2), according to Zwally et al. (2012), are shown in gray lines, and the 2,000-m elevation contour line is also presented as the black solid line.

TABLE 1 | Differences in ice sheet elevation changes obtained by CryoSat-2, SARin, and ATM observations.

Surface slope	SARin (surface fit method) -ATM			SARin (elevation difference method) –ATM		
	Number of grids	Mean ($m \cdot a^{-1}$)	SD ($m \cdot a^{-1}$)	Number of grids	Mean ($m \cdot a^{-1}$)	SD ($m \cdot a^{-1}$)
0°-0.2°	4,673	0.034	0.859	4,544	0.033	0.532
0.2°-0.5°	3,260	0.192	1.804	3,270	0.062	0.989
0.5°-1°	1,162	0.853	3.356	1,207	−0.024	1.952
>1°	419	1.492	3.639	466	−0.359	2.528
Total	9,514	0.252	1.854	9,487	0.017	1.128

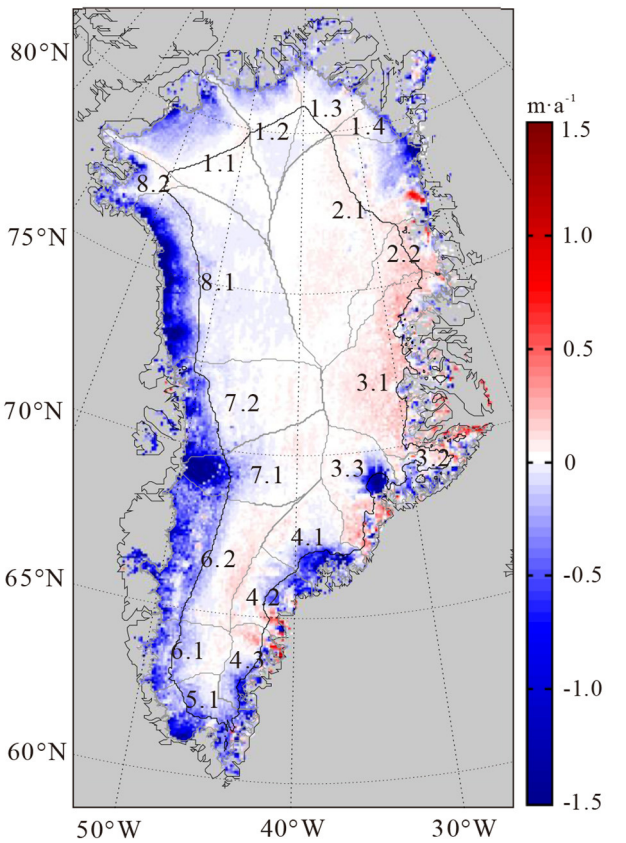

FIGURE 5 | Distribution of elevation change rates in the Greenland ice sheet from 2010 to 2019. The black solid line is the 2,000-m elevation contour. The gray lines and the numbers show the boundaries and locations of different drainages.

As shown in **Figure 5**, relatively stable conditions from 2010 to 2019 can be seen in the interior of the GrIS (i.e., above 2,000 m elevation), and rapid elevation decline can be found on the margins of the ice sheet, especially at the northwest coast in DS 8.1, Jakobshavn Isbræ in DS7.1, and several large coastal outlet glaciers in DS3.3 and DS4. Extreme elevation changes below -10 $m \cdot a^{-1}$ occur in some grids at the regions mentioned above. Areas above 2,000 m had a slight rise in elevation with a change rate of $+1.12$ $cm \cdot a^{-1}$, equivalent to a volume change rate of $+12.10$ $km^3 \cdot a^{-1}$. Elevation and volume changes in each drainage system are shown in **Table 2**.

Greenland Ice Sheet Elevation Change Comparison: 2003–2009 vs. 2010–2019

To further understand the elevation and volume changes in the GrIS, the results from 2010 to 2019 obtained from CryoSat-2 and ATM data are compared with the results derived from ICESat between 2003 and 2009. The average volume loss rate derived from ICESat is -224 ± 15 $km^3 \cdot a^{-1}$, which is a comparable result compared with existing studies (Sørensen et al., 2011; Ewert et al., 2012). The results are shown in **Figure 6**. For simplicity of expression, the two periods will be mentioned as period I (2003–2009) and period II (2010–2019) hereafter. **Figure 6b** shows the difference between the results from the two periods (periods II and I). During the period I, the glaciers in southeast Greenland were undergoing severe volume loss (Howat et al., 2008), but moderate elevation changes were found during period II (see **Figure 5**). Negative values can be found during both periods in southwest coastal areas, while the speed of elevation decline had accelerated in Period II, indicating more serious deglaciation. This fact can be confirmed by the blue zones at the southwest part of the GrIS, as shown in **Figure 6b**. On the other hand, although negative elevation change rates appear in both periods, **Figure 6b** shows remarkable red zones in DS 3 and DS 4, indicating an obvious slowdown in the speed of glacier ablation in the east coastal region during period II compared with period I. Most areas in the interior GrIS have slightly negative values as well, indicating potential ablations in high elevation areas.

Elevation and volume change rates during the two periods in each single drainage and sub-drainage systems are given in **Table 2**. The volume loss during period II is -200.22 $km^3 \cdot a^{-1}$ for the entire GrIS, about 24 $km^3 \cdot a^{-1}$ less than the value during period I, showing a remission in snow and ice loss. For both periods, DS 8 showed a sustained severe volume loss of around -60 $km^3 \cdot a^{-1}$, which was the fastest among the eight drainage systems during Period I, and the second fastest during Period II. Considering a negligible difference of only 3.6 $km^3 \cdot a^{-1}$ for the two different periods, DS 8 is regarded to be the drainage system with the most serious glacier loss. The volume change rate in DS 5 of about -17 $km^3 \cdot a^{-1}$ does not seem to be conspicuous because of the small area of this

TABLE 2 | Elevation and volume changes in each drainage system for different time periods.

Drainage system		2003–2009 (ICESat)		2010–2019 (CryoSat-2/ATM)	
		Elevation change($cm \cdot a^{-1}$)	Volume change($km^3 \cdot a^{-1}$)	Elevation change($cm \cdot a^{-1}$)	Volume change($km^3 \cdot a^{-1}$)
DS 1	1.1	−6.69	−8.42	−8.75	−11.01
	1.2	−1.4	−0.85	−7.05	−4.28
	1.3	−0.14	−0.06	−5.38	−2.35
	1.4	−5.63	−0.93	−7.03	−1.17
	Average/total	−4.16/∼	∼/−10.27	−7.62/∼	∼/−18.81
DS 2	2.1	2.33	6.18	−0.89	−2.35
	2.2	5.2	2.43	7.68	3.59
	Average/total	2.77/∼	∼/8.61	0.40/∼	∼/1.23
DS 3	3.1	−2.29	−4.1	7.48	10.71
	3.2	−27.52	−9.24	−4.44	−1.49
	3.3	−35.98	−26.47	−9.75	−7.17
	Average/total	−15.91/∼	∼/−39.81	0.82/∼	∼/2.04
DS 4	4.1	−27.03	−17.58	−21.06	−13.7
	4.2	−49.68	−24.06	−7.91	−3.83
	4.3	−62.91	−21.73	−12.32	−4.26
	Average/total	−42.8/∼	∼/−63.37	−14.72/∼	∼/−21.79
DS 5	5.1	−32.44	−17	−32.74	−17.15
DS 6	6.1	−17.07	−8.83	−16.57	−8.57
	6.2	−4.43	−6.2	−19.01	−26.65
	Average/total	−7.84/∼	∼/−15.03	−18.35/∼	∼/−35.22
DS 7	7.1	−15.89	−15.24	−32.74	−31.39
	7.2	−9.18	−11.85	−11.85	−15.28
	Average/total	−12.04/∼	∼/−27.09	−20.75/∼	∼/−46.68
DS 8	8.1	−20.84	−49.16	−24.02	−56.66
	8.2	−35.27	−11.12	−22.84	−7.2
	Average/total	−22.54/∼	∼/−60.28	−23.88/∼	∼/−63.86
GrIS average/total	−13.25/∼	∼/−224.23	−11.83/∼	∼/−200.22	

drainage, but the elevation change rate of this drainage system is eye-catching. The values are over -32 $cm \cdot a^{-1}$ in DS 5 for both periods, which is the second fastest elevation change rate during period I and the fastest during period II. DS 4 has both fastest elevation and volume change rate among the ICESat derived results, but great alleviation of about $+41.6$ $km^3 \cdot a^{-1}$ in volume change rate occurred during Period II (-63.37 $km^3 \cdot a^{-1}$ for period I vs. -21.79 $km^3 \cdot a^{-1}$ for period II). DS 3 is undergoing similar changes as DS 4, where the variation of volume change rate over time is also over $+40$ $km^3 \cdot a^{-1}$ (-39.81 $km^3 \cdot a^{-1}$ for period I vs. $+2.04$ $km^3 \cdot a^{-1}$ for period II). Howat et al. (2008) reported astonishing volume losses in DSs 3 and 4 due to mass losses in numerous marine-terminating outlet glaciers along the coast. However, as shown in **Figure 5**, no obvious volume loss can be found in DSs 3 and 4, except for the two large glaciers, Kangerdlugssuaq in DS 3.3 and Helheim in DS 4.1. The elevation and volume change rates of four other drainages (DSs 1, 2, 6, and 7) are all lower during Period II than during Period I, indicating acceleration in volume loss (DSs 1, 6, and 7) or deceleration in volume growth (DS 2).

DISCUSSION

Impact of Penetration Depth of CryoSat-2 Radar Altimetry

Variation in penetration depth into the snow surface is a typical disadvantage of the application of CryoSat-2 in the GrIS. Previous research studies have shown that the penetration depth in a dry snow zone can achieve several meters (Slater et al., 2019) and that abrupt changes were shown when an extreme melting event occurs (Nilsson et al., 2015; Slater et al., 2019; Otosaka et al., 2020). Although the actual impact of penetration on elevation observations is greatly mitigated by retracking algorithms, it might still lead to a deviation from radar altimeter-derived elevation changes (Gray et al., 2019; Otosaka et al., 2020). To assess whether the CryoSat-2 derived elevation change is affected by radar penetration, the GrIS elevation change between 2010 and 2019 was further estimated by CryoSat-2 observations from four summer months (June, July, August, and September) and compared with the result of CryoSat-2 observations from all 12 months. The difference is shown in **Figure 7**. The elevation change estimated by summer observations is considered to be

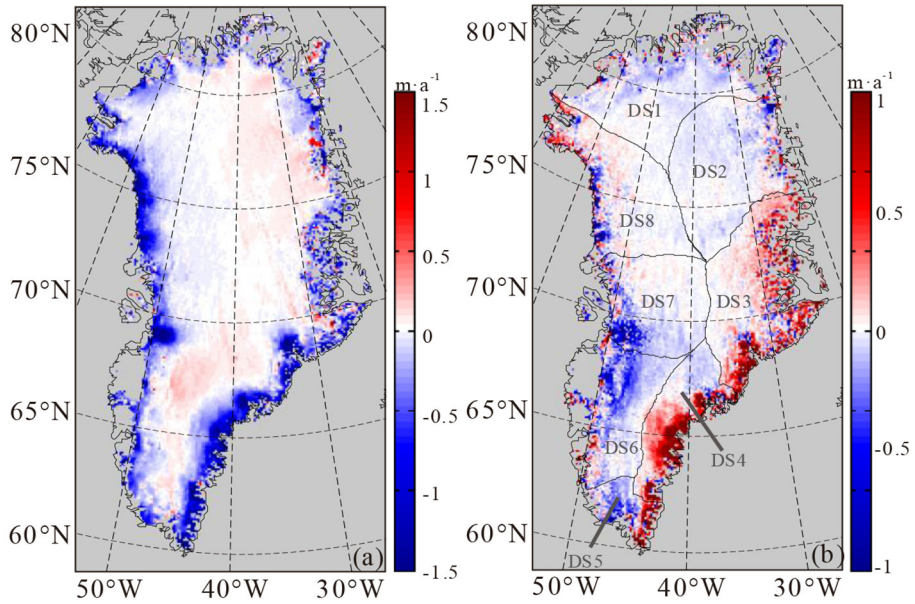

FIGURE 6 | (a) Elevation change derived from ICESat (2003–2009) and **(b)** difference between **(a)** and **Figure 5**.

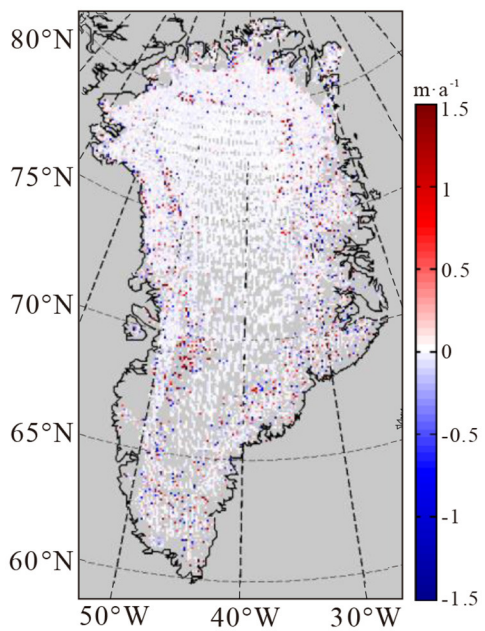

FIGURE 7 | Differences in elevation changes derived from CryoSat-2 summer (June to September) and all-year-round observations.

less affected by radar penetration, because radar returns are predominantly from the melted snow surface (Gray et al., 2019). If the snow penetration does have an obvious influence on the long-term elevation change estimation of the GrIS, the difference between the two results should be easily distinguished. However, no significant spatial pattern is shown in **Figure 7**, which means that the penetration has little impact on the estimation. The scattered random differences are more likely due to the reduced number of observations in the summer months. After removing the outliers by a 3σ edit, the average difference of the two results is -0.003 ± 0.323 m·a^{-1} for LRM and -0.003 ± 0.58 m·a^{-1} for SARin. The accordance between CryoSat-2 and ATM described in section Validation for CryoSat-2 Derived Result also suggests that reliable elevation changes can be captured by CryoSat-2. This result agrees with the conclusion of Slater et al. (2019) that the impact of snow penetration on derived elevation trend becomes negligible over a long time period.

Impact of Topography for the Surface Fit Method

In general, the elevation change results in coastal regions are poorer than the interior because the precision and accuracy of radar altimetry observations are limited by surface slope. However, the surface fit method is much more affected by surface slope than the elevation difference method, as shown in **Figure 3** and **Table 1**. Two sample 5-km × 5-km grids, located in 68°02′N, 33°48′W (referred to as sample grid 1) and 67°57′N, 50°00′W (referred to as sample grid 2) separately, were further investigated to find out why the surface fit method is so vulnerable to undulating terrains. Both grids are located on the margins of the GrIS and have a surface slope of over 1°. The distribution of observed elevations, simulated terrain according to Equation (7), the elevation residuals, and observation time are shown in **Figure 8**. For sample grid 1, it is shown that the cubic polynomial in Equation (7) failed to fit the actual topography properly, because obvious spatial patterns can still be seen in the residuals (**Figure 8c**). The results of sample grid 2 are even worse, because the simulated terrain (**Figure 8f**) is not similar

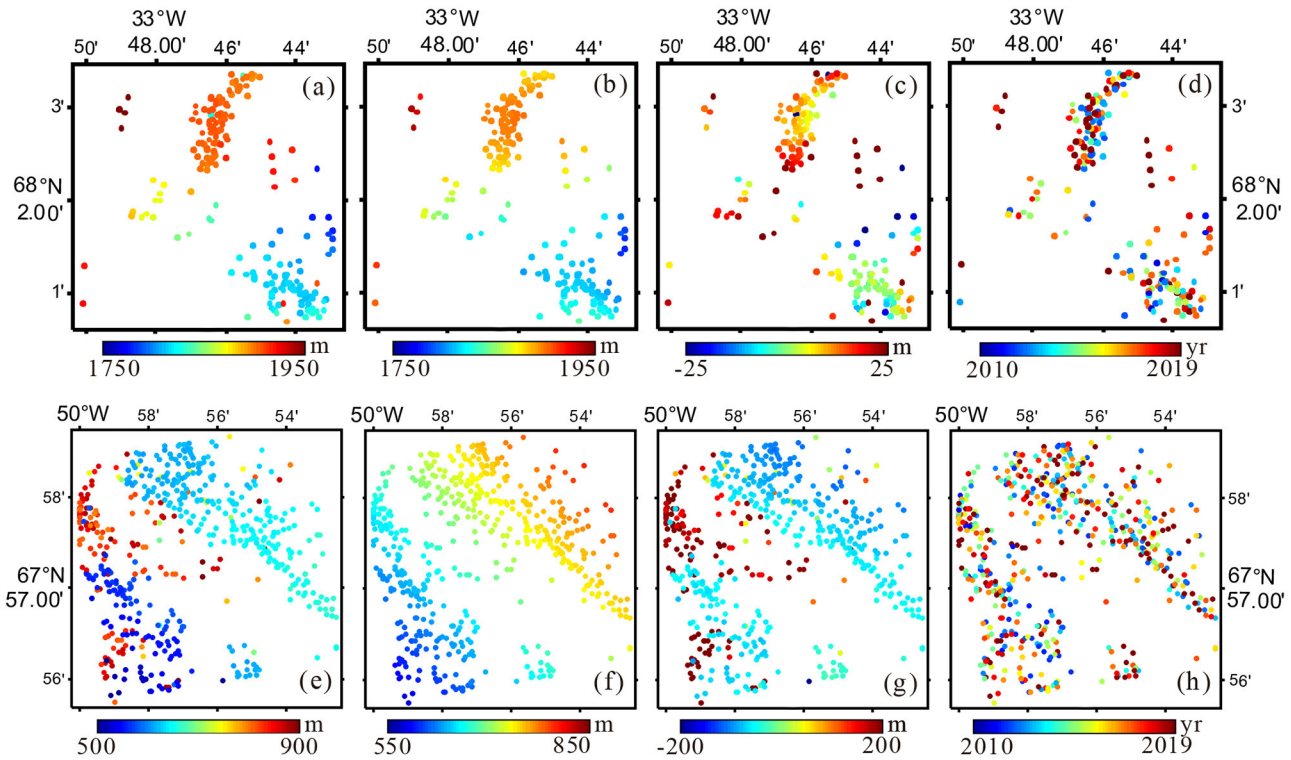

FIGURE 8 | Distribution of **(a)** observed elevations, **(b)** simulated elevations according to Equation (7), **(c)** residuals of simulated terrain, and **(d)** observation time from sample grid 1. **(e–h)** are same as **(a–d)** but from sample grid 2.

to the observed terrain (**Figure 8e**) at all, and the residual will be absorbed into the time-related elevation changes. Then, we tested different surface fitting functions for the two sample grids, from plane fit (1st-order function) to 5th-order-surface fit, and the results are shown in **Table 3**, together with the results of the elevation difference method and ATM. Considering the deviation from the ATM results, the complexity of the fitting function used in the surface fit method has limited improvement. The reason for this crucial mistake happening is probably because the time-varying elevation changes and spatially varying elevation differences are hard to be separated in Equation (7) in complex terrains. However, in both sample grids, the elevation difference method has shown much better accordance with ATM. For the elevation difference method, the impact of topography is alleviated by spatial interpolation. Hence, the elevation change can be resolved separately with reliable performance. We also divided the two sample grids into 2.5-km × 2.5-km grids to find out if a smaller region can be beneficial to the surface fit method. For sample grid 1, the results of the four smaller grids are determined to be 0, 0.612, −0.598, and −0.307 $m{\cdot}a^{-1}$. For sample grid 2, the results are 5.057, 3.872, 0.414, and 2.921 $m{\cdot}a^{-1}$. All these results did not seem to be in accordance with ATM observations. In theory, a smaller region should be easier to be fitted by polynomial functions, but we did not test a much smaller grid size, because the number of observations would also be reduced.

Abrupt Deceleration in GrIS Deglaciation

Bevis et al. (2019) reported an abrupt slowdown in deglaciation, referred to as the "2013–2014 Pause," during the period of 2013–2014 observed by the Greenland GPS Network and the GRACE satellite mission. The "Pause" was also confirmed by altimetry data. Since laser altimeters have several advantages compared with radar altimeters, the time series of ATM observations are used to study the "2013–2014 Pause." As shown in **Figures 9**, **10**, selected 5-km × 5-km grids from different drainages, named as grids a–j, generate their corresponding time series. For each grid, the elevation of 2010 is set to 0 as a reference, and the elevation difference from the ATM L4 product is used to obtain the relative elevation of the 2010 reference by the least-squares estimation. Linear trends are fitted for two stages: the pre-Pause stage from 2010 to 2013 and the post-Pause stage from 2013 to 2018. If the relative elevation of 2013 is missed because of the absence of ATM observation, the two stages are separated by the year 2014 instead. The resulting time series and linear trends are shown in **Figure 9** for each grid.

A clear slowdown can be seen by comparing the linear trends of the pre- and post-Pause stages in most of the selected grids, except for grids a and j in the northwest Greenland and grid f in the southern part, providing obvious evidence for the "2013–2014 Pause." Results from grids c, d, and e (representing DSs 3 and 4) matched well with the values shown in **Table 2** and show most evident alleviation in elevation decline. The linear trends for

TABLE 3 | Elevation change rates in the two sample grids calculated in different ways.

Grid location	Number of observations	Surface fit method (with different surface fitting functions) (m·a^{-1})					Elevation difference method (m·a^{-1})	ATM (m·a^{-1})
		1st order	2nd order	3rd order	4th order	5th order		
68°02′N, 33°48′	272	1.326	1.134	0.754	0.756	0.431	−0.150	−0.082
69°48′N, 26°46′	831	5.665	5.168	4.620	4.592	4.531	−0.825	−0.875

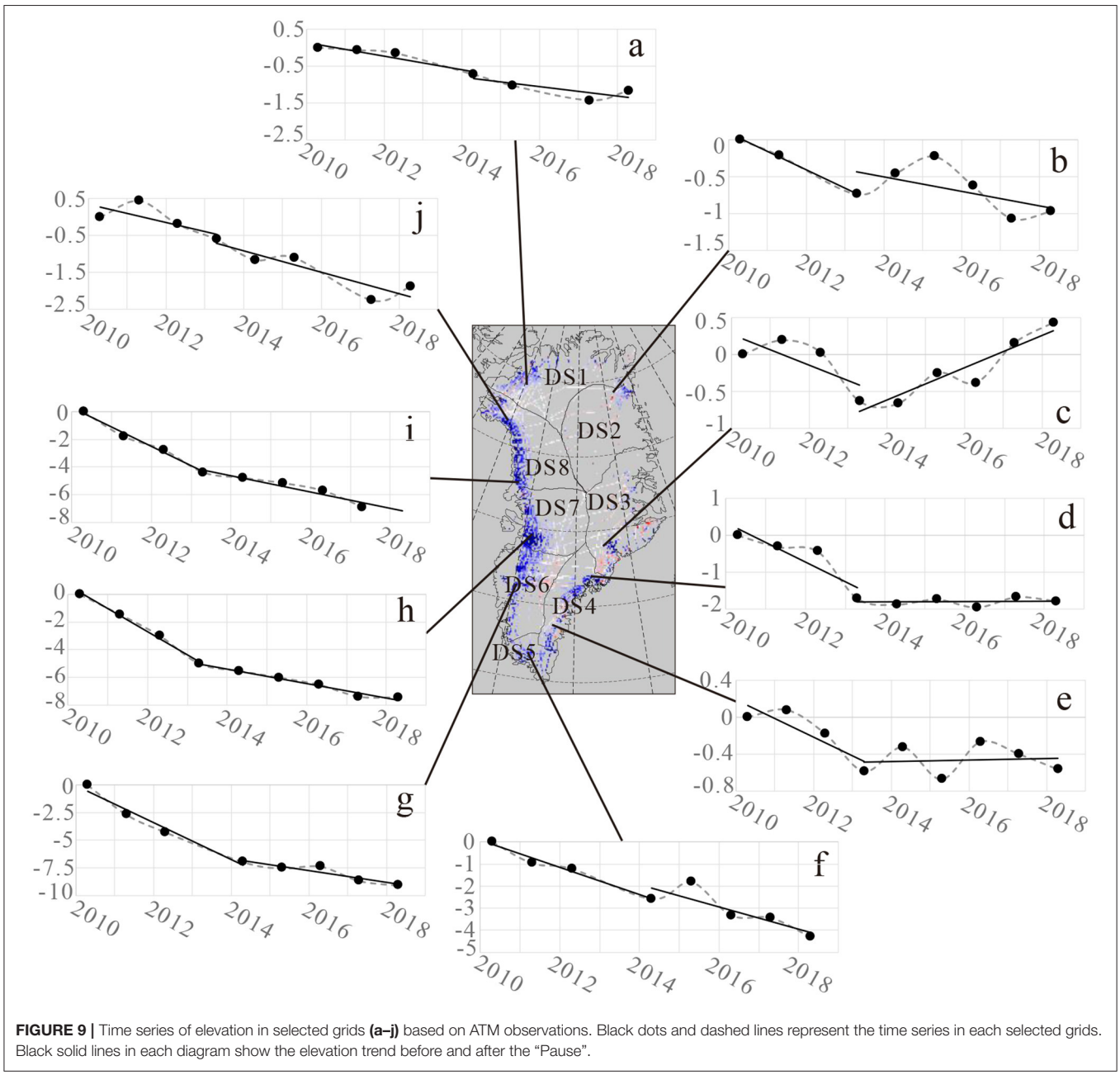

FIGURE 9 | Time series of elevation in selected grids **(a–j)** based on ATM observations. Black dots and dashed lines represent the time series in each selected grids. Black solid lines in each diagram show the elevation trend before and after the "Pause".

grids g, h, and i (representing DSs 6, 7, and the southern part of DS 8) also show alleviation in elevation decline, while the results shown in **Table 2** indicate acceleration after 2010. This seeming contradiction reflects the fact that the volume loss in this area during 2010–2014 is far more serious than the situation during 2003–2009, so that the average change rate of 2010–2019 stays

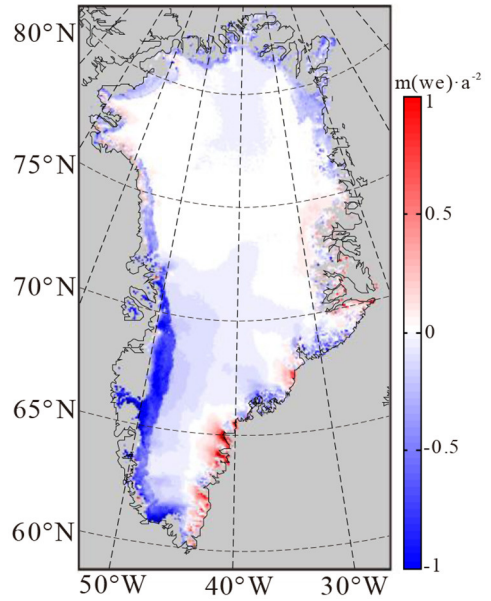

FIGURE 10 | Difference between averaged SMB of 2003–2009 and 2010–2019.

low even if deceleration happened after 2014. This conclusion can be confirmed by the volume change rate of −375 $km^3 \cdot a^{-1}$ during 2011–2014 derived from CryoSat-2 (Helm et al., 2014), which showed a considerable faster volume loss rate than the results of −224 $km^3 \cdot a^{-1}$ for 2003–2009 and −200 $km^3 \cdot a^{-1}$ for 2010–2019 given in this study. In general, grids a, g, h, i, and j, located in western Greenland, show stable trends during the post-Pause stage, while alternating elevation rise and fall take place in grids b, c, d, and e, located in the eastern part. Nevertheless, the "2013–2014 Pause" is obviously detected by ATM observations, and its effect was still continuing in 2018.

Reduced Glacier Mass Loss in Southeast GrIS

In the first decade of the twenty-first century, massive ice loss due to intensive marine-terminating outlet glaciers was found in southeast and northwest GrIS (Howat et al., 2008; Kjeldsen et al., 2013). The situation in the southeast coast shifted dramatically into a moderate elevation decline during the 2010–2019 period (see **Figure 5** and **Table 2**). As the main contributor of GrIS mass loss in recent years (Zhang et al., 2019; Sasgen et al., 2020), SMB (surface mass balance) from the regional climate model RACMO2.3p2 (Noël et al., 2019) is considered for further discussion. **Figure 10** shows the difference between the average SMB for periods I and II mentioned in section Greenland Ice Sheet Elevation Change Comparison: 2003–2009 vs. 2010–2019. For most of the areas, **Figure 10** shows similar trends compared with **Figure 6b**. Discrepancies are obviously revealed in the southeast coastal region. While the elevation decline in **Figure 6a** shows apparent attenuation in the whole area, moderate enhancements in SMB are partially detected. This discrepancy indicates that the alleviation of elevation decline in the southeast part should be attributed to the reduction in dynamic ice loss of the marine-terminating outlet glaciers. Since the ice discharge from marine-terminating outlet glaciers is greatly affected by the ocean (Bevis et al., 2019; Khazendar et al., 2019), it is a proof that the impact of oceanic force on this area is weakening. However, the alternating elevation rise and fall in grids c, d, and e after 2012, shown in **Figure 9**, reflects the complexity of the mixed impact of the oceanic and atmospheric forces. Once the oceanic force was recovered, the volume loss in the southeast part might be intense again.

CONCLUSIONS

One of the most important objectives of this study is to determine the elevation and volume change rates in the GrIS during the 2010–2019 period from altimetry data. The method of surface elevation change rate determination with CryoSat-2 data is discussed. The surface fit method is selected for LRM data, and an elevation difference method is proposed for the SARin data. Through validation with ATM data, the elevation difference method has obvious advantages in constraining the impact of undulating terrains at the margins of the ice sheet. The final result of 2010–2019 GrIS elevation changes is derived from the combination of CryoSat-2 and ATM data to achieve better accuracy. The average elevation and volume change rates are -11.83 ± 1.14 $cm \cdot a^{-1}$ and -200.22 ± 18.26 $km^3 \cdot a^{-1}$, respectively.

Another objective of this study is to compare the elevation/volume change in the GrIS for the 2010–2019 period with the results from the 2003–2009 period to investigate the trend in deglaciation in recent years. The result of -224 ± 15 $km^3 \cdot a^{-1}$ derived from ICES at laser altimetry for 2003–2009 was about 10% faster than the result from CryoSat-2 and ATM. This comparison indicated alleviation in volume loss during 2010–2019. The elevation decline in the southeast coast of the GrIS has a considerably large scale of recovery, while the situation of volume loss in the west margin is getting worse. This phenomenon indicates that the impact of the ocean on the GrIS has been weakened, and that the major source of deglaciation is transferring from the southeast coast to the west margin of the ice sheet.

Further analysis was carried out for the time series of ATM data for selected representative grids in each drainage system. The results clearly demonstrate the "2013–2014 Pause" reported by Bevis et al. (2019), and its effect did not seem to end by 2018. However, the "Pause" had different effects on different regions according to the ATM time series. In general, the west margin of the GrIS had shown stable trends after the "Pause," while complex variations had appeared on the eastern coast.

The elevation and volume changes in the GrIS in recent years seem to be complex, and further research studies are necessary for investigating the ice loss in different drainages and time periods. Better accuracy of altimetry data is, thus, required. The CryoSat-2 Level-2 GDR data used in this study still suffer from several problems, e.g., scattering properties of the reflecting surface,

phase ambiguities in the SARin data (Abulaitijiang et al., 2015), and poor accuracy in slope terrains. These problems are expected to be partly or mostly solved by adopting specialized retracking algorithms and phase ambiguity corrections on the basis of Level-1b data. In addition, the incorporation of observations from new generation altimetry missions (e.g., ICESat-2) can improve the results as well. The study on new data processing and strategy for joint calculation from multi-source data is still undergoing.

DATA AVAILABILITY STATEMENT

The raw data supporting the conclusions of this article will be made available by the authors, without undue reservation.

AUTHOR CONTRIBUTIONS

GC and SZ contributed to conception and design of the study. GC and JZ organized the database. GC and SL performed the statistical analysis. GC wrote the first draft of the manuscript. SZ wrote sections of the manuscript. All authors contributed to manuscript revision, read, and approved the submitted version.

FUNDING

This study was supported by the Basic Research Program of Jiangsu Province (No. BK20180973), the National Natural Science Foundation of China (No. 41804002), and the Open Research Foundation of the Key Laboratory of Geospace Environment and Geodesy, the Ministry of Education, Wuhan University (No. 19-01-04).

ACKNOWLEDGMENTS

The authors would like to thank Prof. Jonathan Bamber for providing the 1-km Greenland surface type grid, Prof. H. Jay Zwally for providing Greenland drainage system boundaries, and Dr. Brice Noël for providing SMB from RACMO2.3p2. The authors would also like to thank ESA for providing CryoSat-2 products, and NSIDC for providing ICESat, ICESat-2, and ATM products and Greenland DEM. The authors would also like to thank the two reviewers who provided constructive comments that helped improve the manuscript.

REFERENCES

Abulaitijiang, A., Andersen, O. B., and Stenseng, L. (2015). Coastal sea level from inland CryoSat-2 interferometric SAR altimetry. *Geophys. Res. Lett.* 42, 1841–1847. doi: 10.1002/2015GL063131

Bamber, J. L., Griggs, J. A., Hurkmans, R. T. W. L., Dowdeswell, J. A., Gogineni, S. P., Howat, I., et al. (2013). A new bed elevation dataset for Greenland. *Cryosphere* 7, 499–510. doi: 10.5194/tc-7-499-2013

Bevis, M., Harig, C., Khan, S. A., Brown, A., Simons, F. J., Willis, M., et al. (2019). Accelerating changes in ice mass within Greenland, and the ice sheet's sensitivity to atmospheric forcing. *Proc. Natl. Acad. Sci. U.S.A.* 116, 1934–1939. doi: 10.1073/pnas.1806562116

Brenner, A. C., DiMarzio, J. P., and Zwally, H. J. (2007). Precision and accuracy of satellite radar and laser altimeter data over the continental ice sheets. *IEEE Transac. Geosci. Remote Sens.* 45, 321–331. doi: 10.1109/TGRS.2006.887172

Brunt, K. M., Hawley, R. L., Lutz, E. R., Studinger, M., Sonntag, J. G., Hofton, M. A., et al. (2017). Assessment of NASA airborne laser altimetry data using ground-based GPS data near Summit Station, Greenland. *Cryosphere* 11, 681–692. doi: 10.5194/tc-11-681-2017

Cao, B., Pan, B., Guan, W., Wang, W., and Wen, Z. (2017). Changes in ice volume of the Ningchan No. 1 Glacier, China, from 1972 to 2014 as derived from *in situ* measurements. *J. Glaciol.* 63, 1025–1033. doi: 10.1017/jog.2017.70

Chen, G., and Zhang, S. (2019). Elevation and volume change determination of Greenland Ice Sheet based on icesat observations. *Chin. J. Geophys.* 62, 2417–2428. doi: 10.6038/cjg2019M0170

Church, J. A., Clark, P. U., Cazenave, A., Gregory, J. M., Jevrejeva, S., Levermann, A., et al. (2013). "Sea level change," in *Climate Change 2013: The Physical Science Basis. Contribution of Working Group I to the Fifth Assessment Report of the Intergovernmental Panel on Climate Change*, eds T. F. Stocker, D. Qin, G. K. Plattner, M. Tignor, S. K.Allen, J. Boschung, A. Nauels, Y. Xia, V. Bex, and P. M. Midgley (Cambridge: Cambridge University Press), 1137–1216. doi: 10.1017/CBO9781107415324.026

Csatho, B. M., Schenk, A. F., Veen, C. J. V. D., Babonis, G., Duncan, K., Rezvanbehbahani, S., et al. (2014). Laser altimetry reveals complex pattern of Greenland Ice Sheet dynamics. *Proc. Natl. Acad. Sci. U.S.A.* 111, 18478–18483. doi: 10.1073/pnas.1411680112

DiMarzio, J. P. (2007). *GLAS/ICESat 1 km Laser Altimetry Digital Elevation Model of Greenland*. Available online at: https://nsidc.org/data/NSIDC-0305/versions/1 (accessed May 7, 2021).

Ewert, H., Popov, S. V., Richter, A., Schwabe, J., Scheinert, M., and Dietrich, R. (2012). Precise analysis of ICESat altimetry data and assessment of the hydrostatic equilibrium for subglacial Lake Vostok, East Antarctica. *Geophys. J. Int.* 191, 557–568. doi: 10.1111/j.1365-246X.2012.05649.x

Gardner, A. S., Moholdt, G., Cogley, J. G., Wouters, B., Arendt, A. A., Wahr, J., et al. (2013). A reconciled estimate of glacier contributions to sea level rise: 2003 to 2009. *Science* 340, 852–857. doi: 10.1126/science.1234532

Gray, L., Burgess, D., Copland, L., Langley, K., Gogineni, P., Paden, J., et al. (2019). Measuring height change around the periphery of the Greenland Ice Sheet with radar altimetry. *Front. Earth Sci.* 7:146. doi: 10.3389/feart.2019.00146

Helm, V., Humbert, A., and Miller, H. (2014). Elevation and elevation change of Greenland and Antarctica derived from CryoSat-2. *Cryosphere* 8, 1539–1559. doi: 10.5194/tc-8-1539-2014

Howat, I. M., Smith, B. E., Joughin, I., and Scambos, T. A. (2008). Rates of southeast Greenland ice volume loss from combined ICESat and ASTER observations. *Geophys. Res. Lett.* 35:L17505. doi: 10.1029/2008GL034496

Khazendar, A., Fenty, I. G., Carroll, D., Gardner, A., Lee, C. M., Fukumori, I., et al. (2019). Interruption of two decades of Jakobshavn Isbræ acceleration and thinning as regional ocean cools. *Nat. Geosci.* 12, 277–283. doi: 10.1038/s41561-019-0329-3

Khvorostovsky, K. S. (2012). Merging and analysis of elevation time series over Greenland Ice Sheet from satellite radar altimetry. *IEEE Transac. Geosci. Remote Sens.* 50, 23–36. doi: 10.1109/TGRS.2011.2160071

Kjeldsen, K. K., Khan, S. A., Wahr, J., Korsgaard, N. J., Kjær, K. H., Bjørk, A. A., et al. (2013). Improved ice loss estimate of the northwestern Greenland Ice Sheet. *J. Geophys. Res. Solid Earth* 118, 698–708. doi: 10.1029/2012JB009684

Krabill, W. B., Abdalati, W., Frederick, E. B., Manizade, S. S., Martin, C. F., Sonntag, J. G., et al. (2002). Aircraft laser altimetry measurement of elevation changes of the Greenland Ice Sheet: technique and accuracy assessment. *J. Geodynam.* 34, 357–376. doi: 10.1016/S0264-3707(02)00040-6

Levinsen, J. F., Khvorostovsky, K., Ticconi, F., Shepherd, A., Forsberg, R., Sørensen, L. S., et al. (2015). ESA ice sheet CCI: derivation of the optimal method for surface elevation change detection of the Greenland Ice Sheet – round robin results. *Int. J. Remote Sens.* 36, 551–573. doi: 10.1080/01431161.2014.999385

McMillan, M., Leeson, A., Shepherd, A., Briggs, K., Armitage, T., Hogg, A., et al. (2016). A high-resolution record of Greenland mass balance. *Geophys. Res. Lett.* 43, 7002–7010. doi: 10.1002/2016GL069666

Muhammad, S., and Tian, L. (2016). Changes in the ablation zones of glaciers in the western Himalaya and the Karakoram between 1972 and 2015. *Remote Sens. Environ.* 187, 505–512. doi: 10.1016/j.rse.2016.10.034

Muhammad, S., Tian, L., and Khan, A. (2019). Early twenty-first century glacier mass losses in the Indus Basin constrained by density assumptions. *J. Hydrol.* 574, 467–475. doi: 10.1016/j.jhydrol.2019.04.057

Nilsson, J., Gardner, A., Sørensen, L. S., and Forsberg, R. (2016). Improved retrieval of land ice topography from CryoSat-2 data and its impact for volume-change estimation of the Greenland Ice Sheet. *Cryosphere* 10, 2953–2969. doi: 10.5194/tc-10-2953-2016

Nilsson, J., Vallelonga, P., Simonsen, S. B., Sørensen, L. S., Forsberg, R., Dahl-Jensen, D., et al. (2015). Greenland 2012 melt event effects on CryoSat-2 radar altimetry. *Geophys. Res. Lett.* 42, 3919–3926. doi: 10.1002/2015GL063296

Noël, B., van de Berg, W. J., Lhermitte, S., and van den Broeke, M. R. (2019). Rapid ablation zone expansion amplifies north Greenland mass loss. *Sci. Adv.* 5: eaaw0123. doi: 10.1126/sciadv.aaw0123

Otosaka, I. N., Shepherd, A., Casal, T. G., Coccia, A., Davidson, M., Di Bella, A., et al. (2020). Surface melting drives fluctuations in airborne radar penetration in West Central Greenland. *Geophys. Res. Lett.* 47: e2020GL088293. doi: 10.1029/2020GL088293

Pritchard, H. D., Arthern, R. J., Vaughan, D. G., and Edwards, L. A. (2009). Extensive dynamic thinning on the margins of the Greenland and Antarctic ice sheets. *Nature* 461, 971–975. doi: 10.1038/nature08471

Sasgen, I., Wouters, B., Gardner, A. S., King, M. D., Tedesco, M., Landerer, F. W., et al. (2020). Return to rapid ice loss in Greenland and record loss in 2019 detected by the GRACE-FO satellites. *Commun. Earth Environ.* 1:8. doi: 10.1038/s43247-020-0010-1

Schenk, T., and Csathó, B. (2012). A new methodology for detecting ice sheet surface elevation changes from laser altimetry data. *IEEE Trans. Geosci. Remote Sens.* 50, 3302–3316. doi: 10.1109/TGRS.2011.2182357

Shepherd, A., Ivins, E. R., Geruo, A., Barletta, V. R., Bentley, M. J., Bettadpur, S., et al. (2012). A reconciled estimate of ice-sheet mass balance. *Science* 338, 1183–1189. doi: 10.1126/science.1228102

Simonsen, S. B., and Sørensen, L. S. (2017). Implications of changing scattering properties on Greenland Ice Sheet volume change from Cryosat-2 altimetry. *Remote Sens. Environ.* 190, 207–216. doi: 10.1016/j.rse.2016.12.012

Slater, T., Shepherd, A., McMillan, M., Armitage, T., Otosaka, I., and Arthern, R. (2019). Compensating changes in the penetration depth of pulse-limited radar altimetry over the Greenland Ice Sheet. *IEEE Transac. Geosci. Remote Sens.* 57, 9633–9642. doi: 10.1109/TGRS.2019.2928232

Sørensen, L. S., Simonsen, S. B., Forsberg, R., Khvorostovsky, K., Meister, R., and Engdahl, M., (2018). 25 years of elevation changes of the Greenland Ice Sheet from ERS, Envisat, and CryoSat-2 radar altimetry. *Earth Planet. Sci. Lett.* 495, 234–241. doi: 10.1016/j.epsl.2018.05.015

Sørensen, L. S., Simonsen, S. B., Nielsen, K., Lucas-Picher, P., Spada, G., Adalgeirsdottir, G., et al. (2011). Mass balance of the Greenland Ice Sheet (2003–2008) from ICESat data – the impact of interpolation, sampling and firn density. *Cryosphere* 5, 173–186. doi: 10.5194/tc-5-173-2011

Studinger, M. (2018). *IceBridge ATM L4 Surface Elevation Rate of Change, Version 1*. Available online at: https://nsidc.org/data/IDHDT4/versions/1?qt-data_set_tabs=4#qt-data_set_tabs (accessed May 7, 2021).

The IMBIE Team (2019). Mass balance of the Greenland Ice Sheet from 1992 to 2018. *Nature* 579, 233–239. doi: 10.1038/s41586-019-1855-2

Thomas, R., Davis, C., Frederick, E., Krabill, W., Li, Y., Manizade, S., et al. (2008). A comparison of Greenland ice-sheet volume changes derived from altimetry measurements. *J. Glaciol.* 54, 203–212. doi: 10.3189/002214308784886225

Velicogna, I., Mohajerani, Y., Landerer, F., Mouginot, J., Noel, B., Rignot, E., et al. (2020). Continuity of Ice Sheet mass loss in greenland and antarctica from the GRACE and GRACE follow-on missions. *Geophys. Res. Lett.* 47: e2020GL087291. doi: 10.1029/2020GL087291

Wang, L., Khan, S. A., Bevis, M.,van den Broeke, M. R., Kaban, M. K., Thomas, M., et al. (2019). Downscaling GRACE predictions of the crustal response to the present-day mass changes in Greenland. *J. Geophys. Res. Solid Earth* 124, 5134–5152. doi: 10.1029/2018JB016883

Wang, X., and Holland, D. M. (2018). A method to calculate elevation-change rate of Jakobshavn Isbræ using operation icebridge airborne topographic mapper data. *IEEE Geosci. Remote Sens. Lett.* 15, 981–985. doi: 10.1109/LGRS.2018.2828417

Zhang, B., Liu, L., Khan, S. A., van Dam, T., Bjørk, A. A., Peings, Y., et al. (2019). Geodetic and model data reveal different spatio-temporal patterns of transient mass changes over Greenland from 2007 to 2017. *Earth Planet. Sci. Lett.* 515, 154–163. doi: 10.1016/j.epsl.2019.03.028

Zwally, H. J., Giovinetto, M. B., Beckley, M. A., and Saba, J. L. (2012). *Antarctic and Greenland Drainage Systems*. Available at https://earth.gsfc.nasa.gov/cryo/data/polar-altimetry/antarctic-and-greenland-drainage-systems (accessed May 7, 2021).

Zwally, H. J., Giovinetto, M. B., Li, J., Cornejo, H. G.,Beckley, M., Brenner, A. C., et al. (2005). Mass changes of the Greenland and Antarctic ice its sheets and shelves and contributions to sea-level rise: 1992–2002. *J. Glaciol.* 51, 509–527. doi: 10.3189/172756505781829007

Zwally, H. J., Li, J., Brenner, A. C., Beckley, M., Cornejo, H. G., DiMarzio, J., et al. (2011). Greenland Ice Sheet mass balance: distribution of increased mass loss with climate warming: 2003– 07 versus 1992 – 2002. *J. Glaciol.* 57, 88–102. doi: 10.3189/002214311795306682

Conflict of Interest: The authors declare that the research was conducted in the absence of any commercial or financial relationships that could be construed as a potential conflict of interest.

frontiers in Environmental Science

ORIGINAL RESEARCH
published: 21 July 2021
doi: 10.3389/fenvs.2021.697111

Construction of the Mean Sea Surface Model Combined HY-2A With DTU18 MSS in the Antarctic Ocean

Weikang Sun[1,2], *Xinghua Zhou*[1,2], *Lei Yang*[2,3]*, *Dongxu Zhou*[2] *and Feng Li*[4]

[1]College of Geodesy and Geomatics, Shandong University of Science and Technology, Qingdao, China, [2]Marine Survey Research Center, The First Institute of Oceanography, Ministry of Natural Resources, Qingdao, China, [3]Qian Xuesen Laboratory of Space Technology, Beijing, China, [4]Qingdao iSpatial Ocean Technology Co., Ltd, Qingdao, China

A new Mean Sea Surface (MSS) model called Shandong University of Science and Technology Antarctic Mean Sea Surface model (SDUST_ANT MSS) in the Antarctic Ocean is presented and validated in this paper. The SDUST_ANT MSS updates the DTU18 MSS with 6 years of Exact Repeat Mission (ERM) and Geodetic Mission (GM) data from HY-2A. Collinear adjustment was applied to all the ERM data to obtain the along-track mean sea surface height. Oceanic variability has been removed from the GM data. Crossover adjustment was applied to both the ERM and GM data. We constructed the HY-2A_MSS using HY-2A altimetry data based on optimal interpolation method. Several types of errors (such as white noise, residual effect of oceanic variability, and long wavelength bias) have been taken into account for the determination of MSS using optimal interpolation method. The SDUST_ANT MSS was constructed by mapping HY-2A_MSS onto the DTU18 MSS. The SDUST_ANT MSS was compared with DTU18 MSS and CNES_CLS15 MSS. At wavelengths below 150 km, differences between models are consistent with seafloor topographic gradient. At wavelengths above 150 km, differences are affected by the mesoscale activities and the altimetry errors in coastal areas. The errors of the three models, as indicated by their power spectral densities (PSDs), are of similar orders of magnitude. The absolute error is slightly smaller in SDUST_ANT than in CNES_CLS15 or DTU18.

Keywords: HY-2A, DTU18 MSS, sentinel-3A, validation, wavelength, absolute error, power spectral density

OPEN ACCESS

Edited by:
Xiaoli Deng,
The University of Newcastle, Australia

Reviewed by:
Mukesh Gupta,
Catholic University of Louvain, Belgium
Luis Gomez,
University of Las Palmas de Gran Canaria, Spain

***Correspondence:**
Lei Yang
leiyang@fio.org.cn

Specialty section:
This article was submitted to Environmental Informatics and Remote Sensing, a section of the journal Frontiers in Environmental Science

Received: *18 April 2021*
Accepted: *06 July 2021*
Published: *21 July 2021*

Citation:
Sun W, Zhou X, Yang L, Zhou D and Li F (2021) Construction of the Mean Sea Surface Model Combined HY-2A With DTU18 MSS in the Antarctic Ocean. Front. Environ. Sci. 9:697111. doi: 10.3389/fenvs.2021.697111

INTRODUCTION

The Mean Sea Surface (MSS) is an essential parameter in oceanography and geophysics. Geodetic and hydrographic surveys adopt the MSS or a reference surface that is related to the MSS as their datum. An accurate MSS is necessary for the analysis of oceanic variability using satellite altimetry and can be used for the calibration or validation of satellite altimetry data (Jin et al., 2016). Oceanic variabilities are dominated by seasonal variability and interannual signal, they also include sea surface anomalies caused by large scale oceanographic anomalies (such as El Nino and La Nina) occurring at specific times.

The emergence of satellite altimetry technology has changed the way that we understand and observe the Earth, especially the oceans. Substantial improvements in the spatial and temporal resolution of altimetry data have ushered global ocean system research into a new era. The satellite Skylab carried the first altimeter into space in 1973. Satellite altimetry was initially used for telemetry

TABLE 1 | Overview of recent MSS models.

	DNSC08	DTU10	DTU13	DTU15	DTU18	CLS2011	CLS2015	WHU2000	WHU2009	WHU2013
Spatial coverage	86°N to 82°S	90°N to 90°S	90°N to 90°S	90°N to 90°S	90°N to 90°S	84°N to 80°S	84°N to 80°S	82°N to 82°S	80°S to 82°N	84°N to 80°S
Spatial resolution	1′×1′	1′×1′	1′×1′	1′×1′	1′×1′	2′×2′	1′×1′	2′×2′	2′×2′	2′×2′
References period	1993–2004	1993–2009	1993–2012	1993–2014	1993–2017	1993–2008	1993–2013	1986–1999	1985–2009	1993–2012
Satellite[a]	T/P, J1, E1, E2, EN, GFO, ICESat, GeoSat	T/P, J1, J2, E1, E2, EN, GFO, ICESat, GeoSat	T/P, J1, J2, E1, E2, EN, GFO, ICESat, GeoSat, J1EOL, C2	T/P,J1, J2, E1,E2, EN, GFO, ICESat, GeoSat, J1EOL, C2	T/P, J1, J2, E1, E2, EN, SA, C2, J1EOL, S3A	T/P, E1, E2, J1, T/Pn, GFO, EN	T/P, J1, J2, E2, EN, GFO, TPn-J1n, E1, C2	T/P, E1, E2, GeoSat	T/P, J1, E1, E2, EN, GeoSat	T/P, J1, J2, E2, EN, GFO, E1, C2

[a]*Footnote: T/P for Topex/Poseidon, J1 for Jason-1, J1EOL for Jason-1 Extension of Life, J2 for Jason-2, E1 for ERS-1, E2 for ERS-2, EN for Envisat, GFO for GeoSat Follow On, C2 for CryoSat-2, S3A for Sentinel-3A, SA for SARAL.*

and has since been used to determine the structure of the sea surface and applied widely across the fields of geophysics and geodesy. Because satellite altimetry technology can repeatedly provide accurate information on the surface height of oceans throughout the world, it provides a wealth of data for studies of sea level change, the gravitational field, seafloor topography, marine lithosphere, and ocean circulation.

Since 1991, the radar altimeters onboard the European Space Agency (ESA) satellites ERS-1/2 and Envisat have been collecting data over the Southern Ocean and also over the sub-polar seas between 81.5°N and 81.5°S. In recent decades, satellite altimetry coverage has extended further towards the poles through dedicated polar missions. For example, NASA's ICESat (2003–2010) reached up to ±86 in latitude; ESA's CryoSat-2 (2010–present) reaches up to ±88 in latitude (Peacock and Laxon, 2004); NASA's ICESat-2 mission reaches ±88 in latitude and provides nearly complete coverage of the polar region. The ICESat-2 mission carries the Advanced Terrain Laser Altimeter System (ATLAS), which was launched at the end of 2018. Complementary measurements are provided by the SARAL/AltiKa (2013–present) and Sentinel-3 (2016–present) (Skourup et al., 2017).

Existing MSS models of the Antarctic Ocean are based on data from some of the altimetry missions; these models include the ERS-2 MSS (Peacock and Laxon, 2004), the ICESat–Envisat (ICEN) MSS (Farrell et al., 2012), and a CryoSat-2 MSS developed at University College London (Au Ridout, 2014). The Danish Technical University (DTU) has developed several global MSS models that cover the Antarctic Ocean; these models include the DNSC08 MSS, DTU10 MSS, DTU13 MSS, DTU15 MSS, and DTU18 MSS and use different combinations of data from ERS-1/2, Envisat, ICESat, and CryoSat-2 (Andersen and Knudsen, 2009, 2011; Andersen et al., 2010; Andersen et al., 2015; Andersen et al., 2016; Andersen et al., 2018a; Andersen et al., 2018b). The CNES_CLS global MSS models, which include the CNES_CLS11, CNES_CLS15, and CNES_CLS19 (Schaeffer et al., 2012; Schaeffer et al., 2017; Pujol et al., 2020). The WHU2000 MSS, WHU2009 MSS, and WHU2013 MSS models developed at Wuhan University in China (Jiang et al., 2002; Jin et al., 2011; Jin et al., 2016) also comprise data from multiple altimetry missions.

Spatial coverage and resolution, reference periods, and satellite altimeters for the most recent DNSC08, DTU, CNE_CLS, and WHU MSS models are summarized in **Table 1**, except for the CNES_CLS19 MSS, which has not yet been released.

The aim of this paper is to investigate a method to merge new altimetry data into conventional mean sea surface models in order to derive the next generation MSS. In this research, we show the case study of merging the Chinese HY-2A altimetry data to the present DTU18 MSS model over Antarctic ocean. It is extremely difficult to obtain information about the sea surface at high latitudes. Proximity to the poles, presence of sea ice, the strong ocean currents around the Antarctic, and the paucity of satellites have resulted in reduced quality and temporal and spatial coverage of satellite altimetry data from the high latitudes (Andersen and Knudsen, 2009). So the Antarctic ocean is the good choice to test our method. China's first satellite for the measurement of ocean dynamic and environmental parameters, such as sea surface wind field, sea surface height, significant wave height and sea surface temperature, etc. HY-2A, has been in orbit for more than 6 years and has collected a large amount of data on its Exact Repeat Mission (ERM) (2 years) and Geodetic Mission (GM) (4 years). These data will complement existing data from other sources, provide valuable information for the study of the MSS and oceanic mesoscale activities and have not yet been included in any MSS model. This paper describes the development of the Shandong University of Science and Technology Antarctic (SDUST_ANT) MSS model on the basis of the earlier DTU18 MSS model and HY-2A altimetry data.

DATA AND MODELS

Altimetry Data

HY-2A Data

The satellite HY-2A was launched on 16 August 2011, and the data were released by China's National Satellite Ocean Application Service (NSOAS). The projected orbital inclination of HY-2A is 99.34, providing a revisit time of approximately 14 days and different orientations of ground tracks during the first part of the operational life of the satellite (Zhao and Zhou,

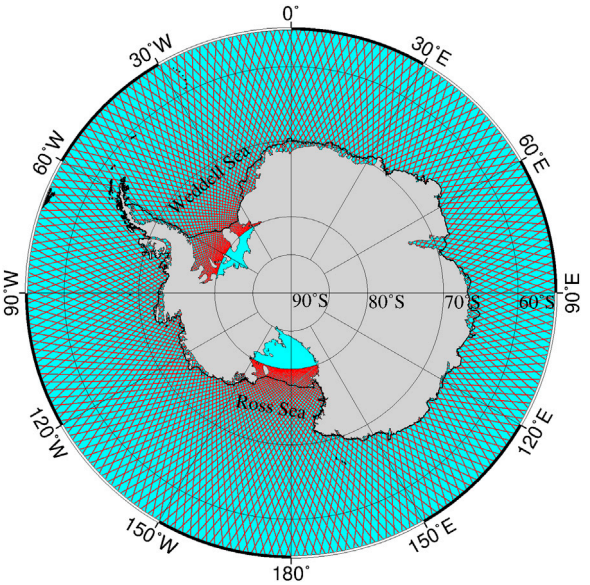

FIGURE 1 | Geographical distribution of a typical HY-2A 14-day near-repeat altimetry ground tracks.

2013). On GM phase (approximately 168 days) during the second part of its operational life, HY-2A entered into drift orbit, which increased the spatial coverage of the altimeter (Zhang et al., 2018).

The data used here are the along-track Level-2 Plus (L2P) products released by Archiving Validation and Interpretation of Satellite Oceanographic Data (AVISO). The 1 Hz HY-2A data have been adjusted to have the same reference ellipsoid and frame as TOPEX/Poseidon (T/P) data and have been corrected for instrumental errors, sea state bias, tidal effect, and atmospheric pressure.

Instrumental errors are mainly due to internal delays of the instrument, but can also be caused by attitude errors. The sea state bias is an altimeter ranging error due to the presence of ocean waves on the surface (Passaro et al., 2018). Tidal effect includes the effect brought from ocean tide, ocean tide loading, solid Earth tide, and pole tide. Ocean tide is the perturbation of the ocean free surface elevation relative to the seabed. Solid Earth tide is due to the direct attraction of the Sun and Moon on the deformable solid Earth. Ocean tide loading is the deflection of the deformable seabed by the tide-induced anomalous weight of water above it. Pole tide is the ocean response to the variation of both the solid Earth and the oceans to the centrifugal potential that is generated by small perturbations to the Earth's rotation axis. Atmospheric pressure, also known as barometric pressure (after the barometer), is the pressure within the atmosphere of the Earth.

The details of the instrumental and geophysical corrections are given in the L2P product handbook. We used the 2-year ERM data from April 2014 to March 2016 (cycle 067–117) as well as the 4-year GM data from March 2016 to March 2020 (cycle 118–281). The ground tracks of HY-2A ERM are shown in **Figure 1** and special areas are marked in **Figure 1**.

Evaluation of HY-2A Satellite Altimetry Data in the Antarctic Ocean

To assess the HY-2A satellite altimetry data in the Antarctic Ocean, we compared the distribution of SSH from SARAL/AltiKa, CryoSat-2, and HY-2A satellite altimetry data for the period between 20141206 and 20141220 (cycle 84 of HY-2A) and the period between 20140607 and 20140621 (cycle 71 of HY-2A) (Cheng and Andersen, 2014). **Figures 2**, **3** show that there is high consistency between the datasets. SSH is the lowest in the Ross Sea and the highest in the Indian Ocean. In the areas covered by sea ice, data quantity and spatial coverage are higher in summer than in winter and the quantity of observations is lower over the Ross Sea and the Weddell Sea than in other parts of the study area. **Table 2** shows that the standard deviation (STD) of the mono-mission crossover differences (SSH differences in the crossovers of descending and ascending orbits) is higher in winter than in summer. STD of the HY-2A data is higher than that of the SARAL/AltiKa data and lower than that of the CryoSat-2 data. Among the three datasets and for the same data acquisition period, data quantity is the highest for HY-2A. Combining the three datasets, data quantity is higher in summer than in winter. On the basis of our analysis of SSH values and crossover differences, we conclude that there is high consistency between the datasets, which confirms the good performance of the HY-2A altimeter. Moreover, it is possible to extend the sea level time series by combining HY-2A satellite altimetry data with other satellite altimetry datasets or MSS models for the construction of a new MSS model and the studying of sea level change and climate change.

Sentinel-3A Data

Sentinel-3A mission was launched on 16 February 2016 by ESA to an orbit of altitude 814 km. The satellite caries one altimeter radar called SRAL (SAR Radar ALtimeter), a dual-frequency SAR altimeter (Ku-band at 13.575 GHz and C-band at 5.41 GHz). 20 Hz data from Sentinel-3A was used to evaluate and validate the MSS errors. The Sentinel-3A altimeter operates in Synthetic Aperture Radar Mode, with an along-track spatial resolution of 300 m in this mode, and provides useful observations of sea level in coastal areas (EUMETSAT, 2018). The data was downloaded from Copernicus Online Data Access. Cycles 54 and 63 were selected to estimate the MSS errors.

The DTU18 Mean Sea Surface Model

The DTU18 MSS is the newest version of the global high resolution MSS released from DTU Space. The new major advance leading up to the release of DTU18 MSS is the use of the Sentinel-3A record for 3 years and an improved CryoSat-2 Low Resolution Mode record for 7 years. A new processing chain with updated editing and data correction (i.e., using FES2014 as the ocean tide model) has been implemented. The use of a consistent ocean tide model for the mean sea surface and the subsequent processing of sun-synchronous satellites have reduced the contribution of the MSS to the total error budget (Andersen, et al., 2018a). Four steps to update the DTU18 MSS. I) Retracking and reprocessing of

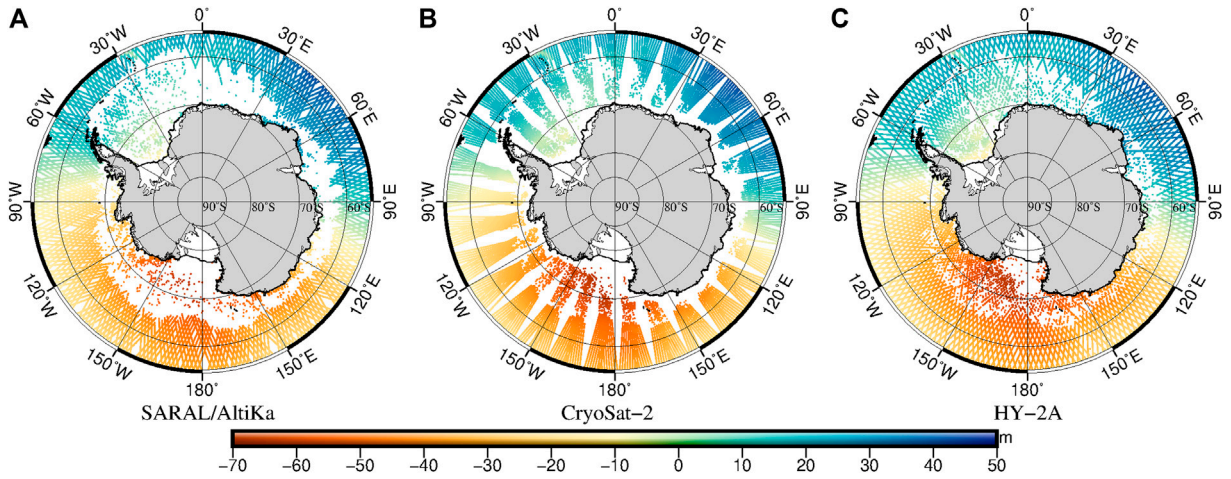

FIGURE 2 | The distribution of sea surface height observed from **(A)** SARAL/AltiKa, **(B)** CryoSat-2, and **(C)** HY-2A satellite altimetry for the same period between 20141206 and 20141220.

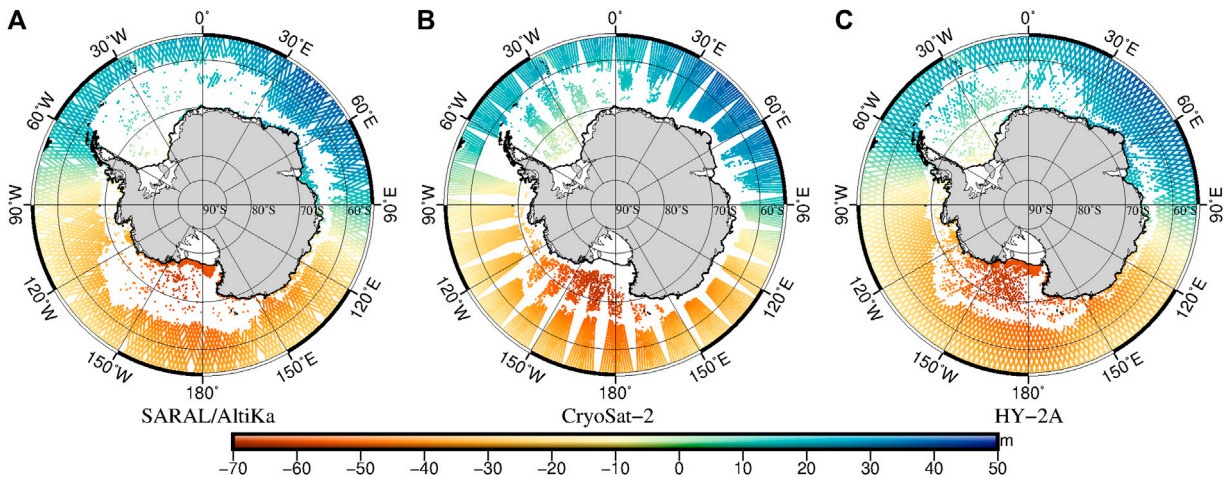

FIGURE 3 | The distribution of sea surface height observed from **(A)** SARAL/AltiKa, **(B)** CryoSat-2, and **(C)** HY-2A satellite altimetry for the same period between 20140607 and 20140621.

TABLE 2 | Comparisons of SARAL/AltiKa, CryoSat-2, and HY-2A satellite altimetry data.

	Summer			Winter		
	Al	**C2**	**HY-2A**	**Al**	**C2**	**HY-2A**
STD of mono-mission crossover differences (cm)	10.57	17.74	16.58	11.72	18.45	17.95
Total number of data	60,009	63,875	67,526	58,502	63,001	66,575

CryoSat-2 within leads. II) Long wavelength correction TP/J1/J2 mean profiles. III) Coastal zone update using Sentinel-3A and TP/J1/J2 + TDM (Tandem Phase) profiles. IV) Removing geodetic mission oceanic variability in interpolation (Andersen, et al., 2018a; Andersen, et al., 2018b).

METHODS

In general, MSS models are constructed following these steps: data selection and preprocessing, unification of temporal and spatial references, collinear adjustment of ERM data, removal of

the temporal oceanic variability from GM data, crossover adjustment, and gridding. The gridded product is combined with DTU18 MSS to construct new generation MSS.

Collinear Adjustment of HY-2A Exact Repeat Mission Data

Collinear adjustment is an effective method to reduce the time-varying effect of sea level based on the characteristics of repeated orbit design of altimetry satellites. Ground trajectories of altimetry satellites with ERM do not coincide, the 14-day Exact Repeat Orbit retraces the HY-2A ERM ground track within ±1 km. Therefore, we calculated the average trajectory and average sea level from repeat orbit altimetry data to reduce the influence of the variability of sea level with time, and especially the effects of abnormal sea level changes caused by large-scale oceanographic anomalies on the results.

The average trajectory was obtained by calculating the average between the reference and the collinear trajectories. The trajectory with stable and well-observed data in the repeated period observation data participating in the collinear was selected as the reference trajectory, and the other repetitive period observation data were interpolated into the reference trajectory. At each point along the reference trajectory, SSH was obtained using the collinear method; the difference between sea level on the reference trajectory and sea level on the collinear trajectory was calculated, and the data point was removed from the collinear trajectory if the difference exceeded 0.5 m. To ensure that annual variations in sea level are absent in the adjusted data, cycles that are shorter than one year were excluded from the collinear adjustment (Jin et al., 2011).

Oceanic Variability Correction of HY-2A Geodetic Mission Data

Removing oceanic temporal variability from the GM data was the main challenge that we encountered in the processing of HY-2A data for the MSS model. Because of the limited revisit time of the GM data, the influence of oceanic variability cannot be eliminated or reduced by averaging over multi-year data. Instead, it can be solved by daily, monthly, seasonal, and annual sea level anomaly (SLA) models that are based on simultaneous satellite data. We corrected interannual and seasonal oceanic variability of the GM data using daily gridded SLA maps provided by AVISO/ Copernicus (http://marine.copernicus.eu/) (Andersen et al., 2018a; Andersen et al., 2018b). Daily gridded SLA maps were estimated from all altimeter missions using three-dimensional optimal interpolation, which was designed to generate regular gridded SLA products by combining the measurements of various altimeters (Le Traon and Ogor., 1998b, 2003; Ducet et al., 2000; Tierney et al., 2000; Taburet et al., 2019). The reference datum of the corrected grid SLA maps is the same as the datum of the HY-2A GM data, which is the MSS_CLS_15. The corrected SSH was derived as follows (Schaeffer et al., 2012):

$$SSH_{cor}(t,\lambda,\varphi) = SSH(t,\lambda,\varphi) - \left[SLA^{i}_{(t,\lambda,\varphi)}\right] \quad (1)$$

$SSH_{cor}(t,\lambda,\varphi)$represents the corrected $SSH(t,\lambda,\varphi)$ of the satellite minus the results of the Optimal Analysis of a set of SLAs calculated from all satellites. $[SLA^{i}_{(t,\lambda,\varphi)}]$ is the interpolated value that would be corrected for oceanic variability at the spatial and temporal position.

Crossover Adjustment

Crossover adjustment is a method generally used to combine multi-mission altimetry data, including ERM and GM data, and to reduce orbit errors, residual oceanic variability, and various physical correction errors. It can weaken the long-wavelength variations of sea level, but the residual radial orbit error, the short-wavelength signal of sea surface variations, and the residual geophysical correction also influence the MSS. At the crossover point between the ascending and descending arcs, the sea level measured on the ascending arc differs from that measured on the descending arc because of the influence of the residual radial orbit error and other factors. Crossover adjustment is one of the main methods to weaken the influence of satellite radial orbit errors and other factors on altimetry data.

Crossover adjustment is used to integrate different satellite altimetry data (including ERM and GM data) or to determine the corrections that need to be applied to measurements on the basis of the difference between two observations from the same location (Huang et al., 1999; Huang et al., 2008). The classical crossover adjustment considers the radial orbit error to be one of the main sources of error affecting altimetry data and that error can be fully modeled by using either a time- or a distance-dependent polynomial (Wagner, 1985; Rummel, 1993). The classical crossover adjustment was modified and simplified by Huang et al. (Huang et al., 1999; Huang et al., 2008; Yuan et al., 2020a; Yuan et al., 2020b). Condition adjustment was applied to the crossover observation equation, and the new error model was used for least squares filtering and estimation along the satellite track. The calculation process did not involve rank deficiency and is suitable for global intersection adjustment.

Construction of HY_2A_Mean Sea Surface Using Optimal Interpolation

The HY-2A_MSS has been computed using the Optimal Interpolation method. The method is based on an optimal interpolation (Le Traon and Ogor, 1998b; Schaeffer et al., 2012):

$$\theta_{est}\left(\vec{x}\right) = \sum_{i=1}^{N}\sum_{j=1}^{N} A_{ij}^{-1} C_{xj} \Phi_{obs,j}, \quad (2)$$

where $\theta_{est}(\vec{x})$ is the estimated MSS height at the grid point x, $\Phi_{obs,j}$ is satellite observation at j, C_{xj} is the covariance/correlation function between satellite observation at j and data at x, A_{ij}^{-1} is the covariance matrix between observations and their noise budget $C(r,t)$, which is given by:

$$C(r,t) = \left[1 + ar + 1/6(ar)^2 - 1/6(ar)^3\right]\exp(-ar)\exp\left(-t^2/T^2\right), \quad (3)$$

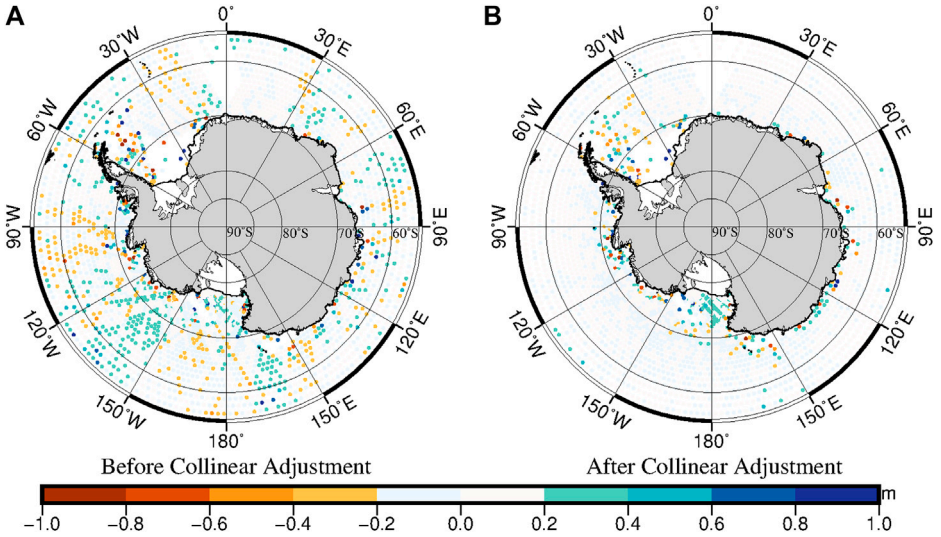

FIGURE 4 | Crossover differences before **(A)** and after **(B)** collinear adjustment.

where r is the distance between two altimetry observations. $a = 3.34/L$, L is the space correlation radius, $L$is usually 100~200 km, here is 150 km (Le Traon et al., 1998a). t is time, and $T$is the temporal correlation radius.

Various types of errors that determine the behavior of the optimal interpolation and the covariance model were taken into account. To determine the new MSS model, we calculated the error budget of altimetric heights by considering the following terms (Schaeffer et al., 2012):

- a noise budget (relating to the instrumental noise), which was expressed as white measurement noise. A white measurement noise of 3 cm was used for HY-2A data. Further details are given in Copernicus Marine Environment Monitoring Service–Sea Level Thematic Assembly Center Product User Manual (CMEMS, 2018);
- the error caused by the residual effect of the oceanic variability, which was to prescribe a spatially correlated error (at the mesoscale wavelength) without affecting the shorter wavelengths of the geophysical static field (Wessel and Smith, 1995);
- following the method proposed by Le Traon and Ogor (1998b), along-track biases are considered. By introducing this term, it is possible to reduce many of these biases caused by along-track errors. This means a better correction of residual errors, for example, geographical correlated orbit errors and imperfections of environmental corrections that may affect missions differently. This aspect is implemented when the wavelength is greater than 100 km and greatly reduces the tracking effect of the MSS grid.

Combination Method

The SDUST_ANT MSS is obtained through a two-step procedure. The HY-2A_MSS was initially mapped from the ERM and GM data using the optimal interpolation method. Then the HY-2A_MSS was subsequently used the remove-restore method to map the SDUST_ANT MSS from DTU18 MSS (Andersen and Knudsen, 2011; Schaeffer et al., 2012; Andersen et al., 2018b). The DTU18 MSS was removed from the HY-2A_MSS to obtain the remaining SSH. The remaining SSH was computed using a spherical harmonic expansion. Then the SDUST_ANT MSS was achieved through the restoration of the DTU18 MSS.

TABLE 3 | Statistics of the crossover differences before and after correction of GM observations.

	Before correction		After correction	
Absolute value range	**Number**	**Percent (%)**	**Number**	**Percent (%)**
5	7002828	31.8473	8663453	39.3994
5~10	5026731	22.8604	5988799	27.2357
10~20	5016444	22.8136	4551017	20.6970
20~30	1424187	6.4769	1059153	4.8168
30~40	753687	3.4276	391405	1.7800
40~50	315393	1.4343	214599	0.9759
50~100	928914	4.2245	553043	2.5151
>100	1520610	6.9154	567325	2.5801
Total number	219888794		219888794	
Mean (cm)	1.96		2.00	
STD (cm)	20.96		16.23	
RMS (cm)	21.05		16.35	

RESULTS AND VALIDATION

The Results of Shandong University of Science and Technology Antarctic Mean Sea Surface

Collinear adjustment was applied to the ERM data. Before collinear adjustment, the STD of crossover differences is

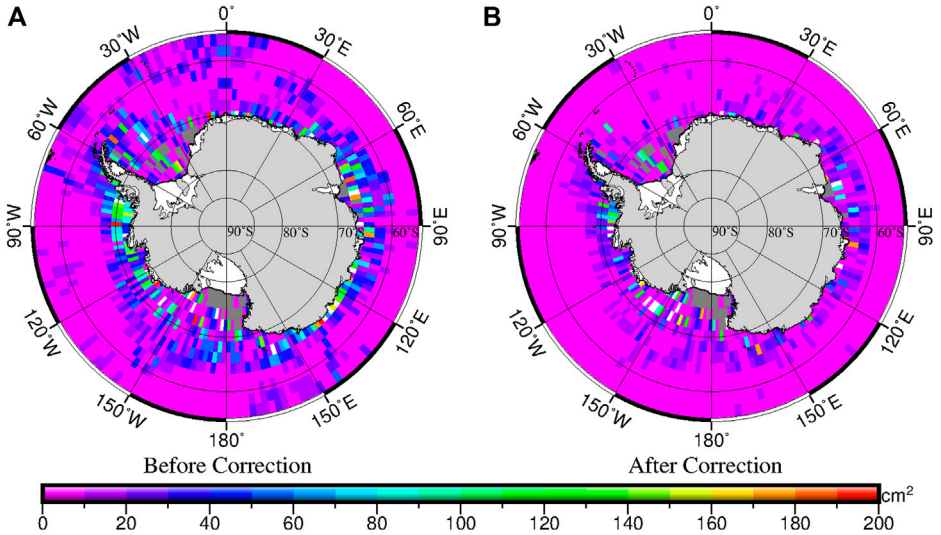

FIGURE 5 | The variance of HY-2A SLA before **(A)** and after **(B)** oceanic variability correction.

TABLE 4 | Statistical results of crossover differences of HY-2A data before and after crossover adjustment.

	Before crossover adjustment			After crossover adjustment		
	Mean (cm)	STD (cm)	RMS (cm)	Mean (cm)	STD (cm)	RMS (cm)
HY-2A/ERM	2.44	13.81	14.00	0.42	9.01	9.02
HY-2A/GM	2.00	16.23	16.35	-0.09	12.35	12.38

19.82 cm; after adjustment, the STD is 13.81 cm. After adjustment, the accuracy of the ERM data is higher, and the influence of oceanic variability on the data is reduced.

Figure 4 shows what can be achieved by collinear adjustment. **Figure 4A** shows crossover differences before the collinear adjustment and **Figure 4B** shows crossover differences after collinear adjustment. In the open ocean, especially in the Pacific Ocean, crossover differences are considerably larger after adjustment. In the offshore sea area, especially in the Weddell Sea and the Ross Sea, crossover differences remain large after adjustment.

The GM data were addressed by oceanic variability corrections and the results of crossover differences before and after the correction listed in **Table 3**, which shows that the effect of the oceanic variability on the GM data has been reduced and the accuracy of the SSH has been significantly improved. There are also fewer grid points with a crossover difference above 10 cm, and points with a crossover difference below 10 cm make up a larger proportion of the total number of grid points. The Root Mean Square (RMS) of the crossover differences is 21.05 cm before oceanic variability correction and is 16.35 cm after correction. The improvement is significant after oceanic variability correction.

Figure 5 shows the effects of oceanic variability correction. It shows the variance of the SLA signal along HY-2A tracks, before and after removing the oceanic variability (**Figures 5A,B**, respectively). Variance of SLA before correction shows mesoscale variability; it is dominant in the circumpolar current and the coastal areas and can exceed 400 cm^2. Oceanic variability correction is more effective in the open ocean and less effective in coastal sea areas. The correction has removed the bulk of the energy, although residual variability remains. Oceanic variability at wavelengths below 200 km (Copernicus Marine Environment Monitoring Service (CMEMS), 2018; Pujol et al., 2018; Taburet et al., 2019) cannot be accurately eliminated by the correction procedure because of limits imposed by the resolution of the daily gridded SLA maps.

The results of statistical analyses of the crossover differences of HY-2A altimetry data before and after crossover adjustment are shown in **Table 4**. It can be seen from **Table 4**, the RMS of crossover differences have decreased after crossover adjustment both ERM and GM data.

The SDUST_ANT MSS is obtained through the combination method and shown in **Figure 6**.

Evaluation and Validation

The accuracy of MSS models is usually verified via comparisons with other models and mean along-track altimetry observations (Andersen and Knudsen, 2009). In principle, the difference between various MSS models is determined by several factors: the dataset used in the model, the data processing method, and the gridding method. The SDUST_ANT MSS was compared and validated with the DTU18 MSS and the CNES_CLS15 MSS, which are the most widely used global MSS models.

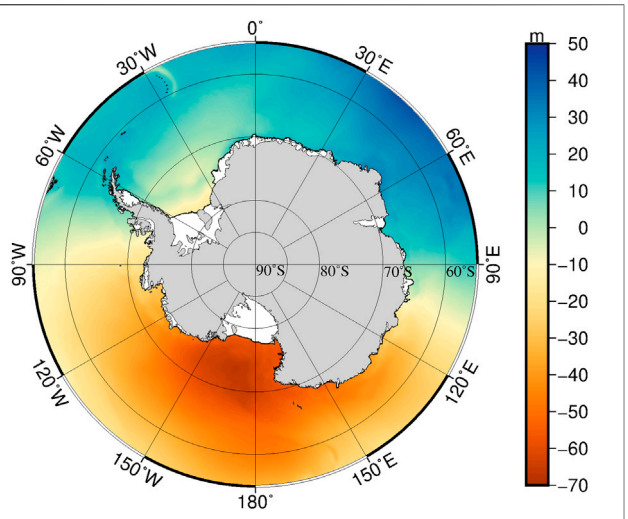

FIGURE 6 | SDUST_ANT MSS in the antarctic ocean.

TABLE 5 | Comparisons of different MSS models.

Difference	Mean (cm)	STD (cm)	RMS (cm)
SDUST_ANT-DTU18	−3.18	3.26	3.64
SDUST_ANT-CLS15	−2.41	10.94	11.08

Inter-model Comparison

In evaluating the SDUST_ANT MSS, it is worth examining the differences between SDUST_ANT MSS, DTU18 MSS and CNES_CLS15 MSS Outliers of the difference are rejected by three times STD to avoid contamination by poor observations around coastal areas and islands. The results are listed in **Table 5**. The difference between the SDUST_ANT MSS and the DTU18 MSS is smaller than the difference between the SDUST_ANT MSS and the CNES_CLS15 MSS.

The largest differences between SDUST_ANT MSS and DTU18 MSS are located in the Weddell Sea and in coastal areas (**Figure 7A**). The largest differences between SDUST_ANT MSS and CNES_CLS15 MSS are located in the Pacific Ocean–Southern Ocean, Atlantic Ocean–Southern Ocean, and in coastal areas where sea ice is present (**Figure 7B**).

A Gaussian filtered solution of the difference between the SDUST_ANT MSS and DTU18 MSS and between the SDUST_ANT MSS and CNES_CLS15 MSS in the Antarctic Ocean was adopted to compare the difference at different wavelengths. We used the tools available in the software Generic Mapping Tools (Wessel and Smith, 1995; Wessel and Smith, 1998) and calculated the differences between the models using a high-pass and low-pass Gaussian filter at the wavelength of 150 km. **Figure 8** shows the difference between the SDUST_ANT MSS and DTU18 MSS and the difference between the SDUST_ANT MSS and CNES_CLS15 MSS at short wavelengths (<150 km); the seafloor topographic gradient was calculated from the GEBCO_2020 Grid. At short wavelengths, there is no significant difference between SDUST_ANT MSS and DTU18 MSS (**Figure 8A**), while there are some differences between SDUST_ANT MSS and CNES_CLS15 MSS (**Figure 8B**), which can be mainly attributed to differences between DTU18 MSS and CNES_CLS15 MSS. Differences between SDUST_ANT MSS and CNES_CLS15 MSS or between DTU18 MSS and CNES_CLS15 MSS are related to seafloor topographic structures at medium and short wavelengths. The horizontal gradients of the geoid and the MSS are related

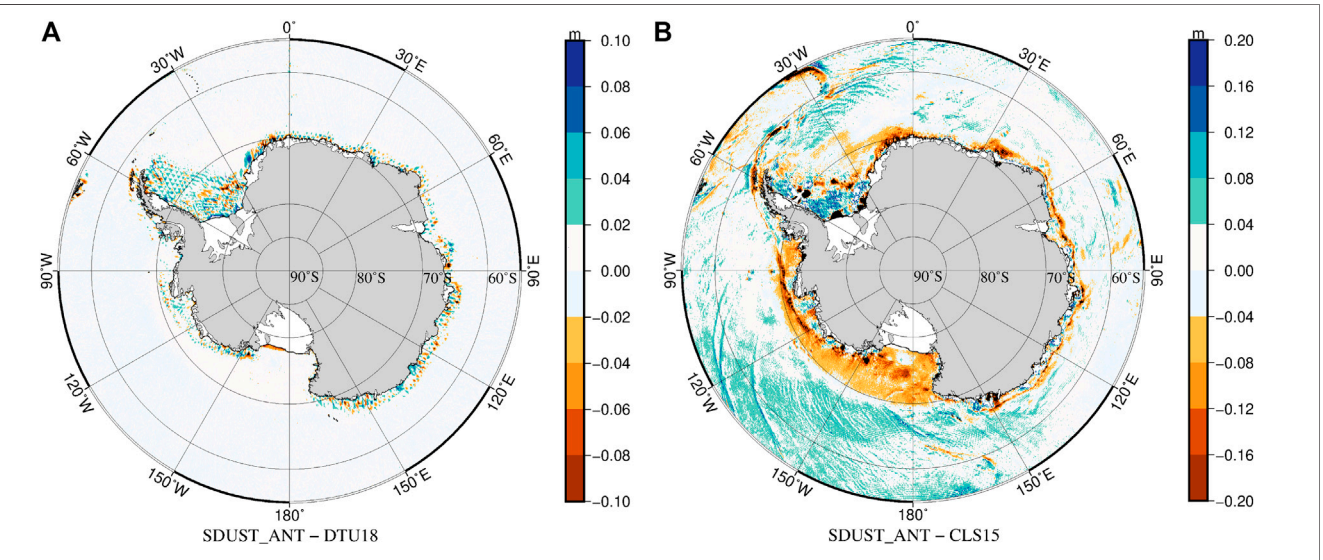

FIGURE 7 | (A) Differences between SDUST_ANT MSS and DTU18 MSS and **(B)** differences between SDUST_ANT MSS and CNES_CLS15 MSS in the Antarctic Ocean after deleting 3 times' STD error.

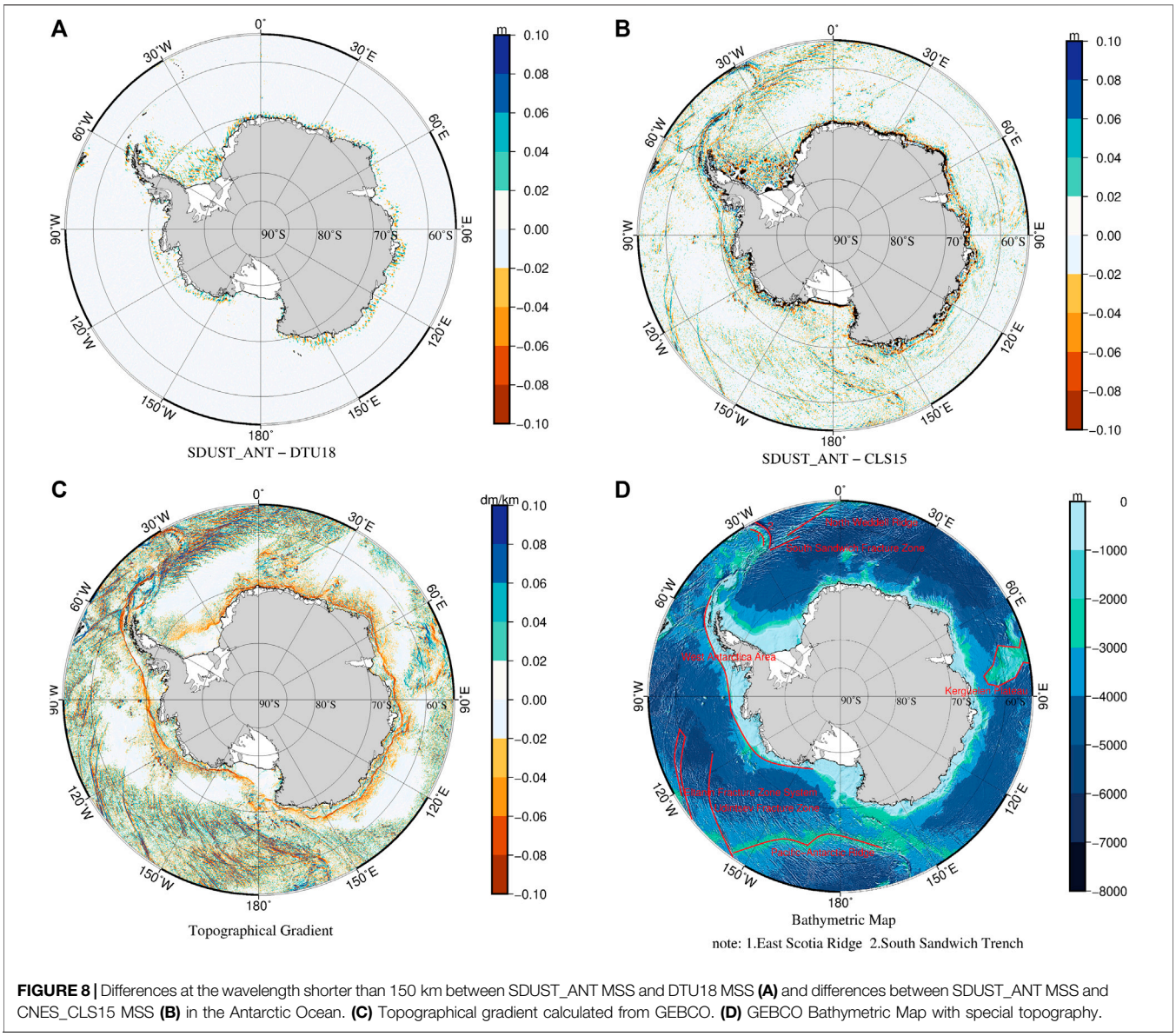

FIGURE 8 | Differences at the wavelength shorter than 150 km between SDUST_ANT MSS and DTU18 MSS **(A)** and differences between SDUST_ANT MSS and CNES_CLS15 MSS **(B)** in the Antarctic Ocean. **(C)** Topographical gradient calculated from GEBCO. **(D)** GEBCO Bathymetric Map with special topography.

to the seafloor topographic gradient (Rapp and Yi, 1997; Jimenez-Munt et al., 2008; Sandwell et al., 2014). Examination of **Figures 8B,C** reveals some correlation between MSS differences and the topographic gradient. Pearson correlation coefficient is 0.2269. Where the absolute value of the gradient is large, the MSS differences are also relatively large; this can be seen near 30°W (along the East Scotia Ridge, the South Sandwich Trench, the South Sandwich Fracture Zone, and the North Weddell Ridge), near 120°W (the Heezen Fracture zone, the Tharp Fracture zone, the Udintsev Fracture zone, and the Pacific–Antarctic Ridge), on the Kerguelen Plateau near 75°E, and in West Antarctica. These special topographic features are marked in **Figure 8D**.

At the long wavelengths (>150 km), the difference between SDUST_ANT and DTU18 (**Figure 9A**) is smaller than the difference between SDUST_ANT and CNES_CLS15 (**Figure 9B**), which still contains residuals of oceanic variability. In coastal areas, the oceanic variability in the HY-2A data has not been completely removed. The SDUST_ANT differs more from CNES_CLS15 than from DTU18 possibly because of differences in the satellite data that are included in the models and in data processing methods. Between 55°S and 60°S, the differences between SDUST_ANT and CNES_CLS15 are consistent with the spatial distribution of mesoscale activities in the Southern Ocean Antarctic Circulation (Duan et al., 2016; Cui et al., 2020).

Comparison Along Sentinel-3A Tracks Using Power Spectral Density

A sophisticated method is used to derive the absolute error of each model. The methodology is detailed in Pujol et al. (2018). The sum and difference of the SLAs from two cycles can be used to infer the absolute MSS error if the cycles are selected to

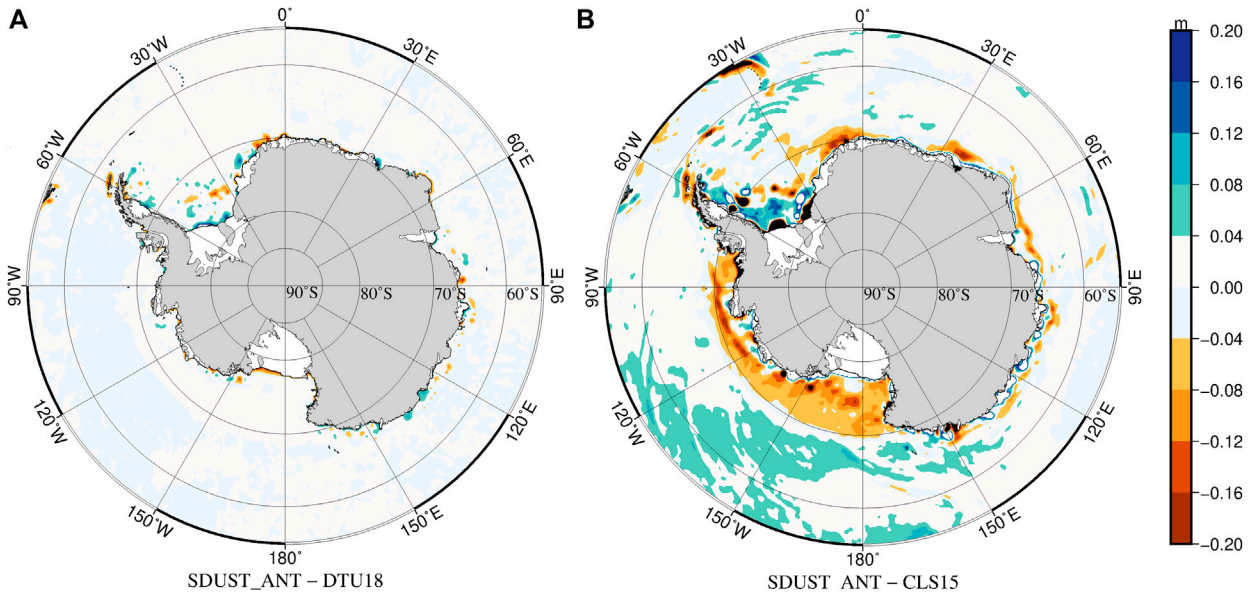

FIGURE 9 | (A) Differences between SDUST_ANT MSS and DTU18 MSS and **(B)** differences between SDUST_ANT MSS and CNES_CLS15 MSS in the Antarctic Ocean at the wavelength longer than 150 km.

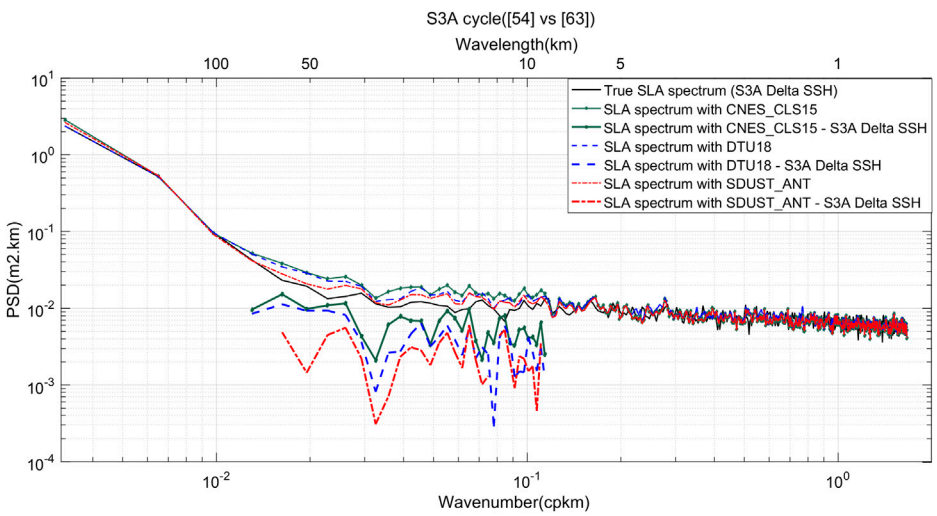

FIGURE 10 | PSD of the true SLA signal with instrumental noise (thin black line), SLA signal including the MSS error (thin color lines), MSS errors (thick color lines) with statistically significant (95% confidence threshold). SLA computed using CNES_CLS15 (green), DTU18 (bule), SDUST_ANT (red).

minimize the oceanic variability correlation. Sentinel-3A described in *Sentinel-3A Data* Section 2.1.3 was used to calculate the absolute MSS error spectrum.

Essentially, by using the difference between SLAs of the same tracks separated by several months, the true SLA PSD can be inferred, because both SLAs are decorrelated and the MSS errors cancel one another out. So it is possible to obtain the PSD of the absolute MSS error.

The thin colored lines in **Figure 10** show the PSD of the measured SLA (i.e., including the MSS error) using the three MSS models. Using the difference between the SLAs of two cycles separated by 269 days, we can deduce the thin black line which is the true PSD of the SLA signal with the instrumental noise (no more MSS error). The MSS error is stationary and has been canceled out prior to the computation of the PSD and is therefore excluded from the values indicated by the black line in **Figure 10**.

The PSD of the MSS error for the three MSS models (thick colored lines in **Figure 10**) were calculated from the difference between the PSD of the measured SLA using the

models (thin colored lines in **Figure 10**) and the true PSD of the SLA signal (thin black line in **Figure 10**). Our results are only valid for small wavelengths where the difference between two PSDs is significant (usually between approximately 8–10 km and 80–100 km). The error is the largest in the CNES_CLS15 and is the smallest in the SDUST_ANT. **Figure 10** shows that the green PSD of CNES_CS15 is 2 times larger than the red PSD of the SDUST_ANT model. The blue PSD of DTU18 is 1.5 times larger than the red PSD of the SDUST_ANT model.

DISCUSSIONS

This paper compared the altimetry data of HY-2A with the altimetry data of SARAL/AltiKa and with that of CryoSat-2 in the Antarctic Ocean and found consistency between the three datasets.

HY-2A satellite altimetry observations and DTU18 MSS were combined to establish an Antarctic MSS model named SDUST_ANT, using the mean along-track SSH of HY-2A satellite series observations spanning 2-year between 2014 and 2016 after collinear adjustment and the GM SSH spanning 4-year between 2016 and 2020 after the correction the oceanic variability.

We used the mean along-track SSH of T/P satellite series observations between 1993 and 2012 with collinear adjustment as the reference datum. Collinear adjustment was used to correct or eliminate the oceanic variability of the HY-2A ERM observations, while the daily gridded SLA maps were used to correct HY-2A GM observations. The influence of residual oceanic temporal variability and radial orbit error was eliminated by crossover adjustment. The HY-2A_MSS was computed using optimal interpolation. Using DTU18 MSS as the reference field, the SDUST_ANT MSS was created following the remove–restore method.

We calculated the differences between DTU18 MSS, CNES_CLS15 MSS, and SDUST_ANT MSS, and found that at short wavelengths (<150 km), differences between the models are consistent with the topography structure. It's shown by Pearson's correlation coefficient, there is a weak linear correlation between differences and the topographic structure. But as can be seen from **Figure 8**, it has strong correlation with the seabed topographic structure. Therefore, the nonlinear correlation between the difference at short wavelengths (<150 km) and the topographic structure needs to be further explored. At long wavelengths (>150 km), mesoscale activities are the dominant source of MSS error in the open ocean, while altimetry error (due to range and geophysical corrections) is the dominant source of error in coastal areas. We estimated the absolute error of SDUST_ANT MSS along the Sentinel-3A tracks and focused on the mesoscale. The absolute error of SDUST_ANT is slightly smaller than that of the CNES_CLS15 and that of DTU18. Therefore, under the premise of determining the temporal and spatial scales of the combined satellite altimetry data, it is feasible to integrate the data with the MSS model to improve the former MSS model.

CONCLUSION

In conclusion, the comparison results between HY-2A, SARAL, and CryoSat-2 are consistent with each other. It is possible to extend the sea level time series by combining HY-2A altimetry data with other satellite altimetry data for mean sea surface model and for climate change research.

The process of the establishment of the MSS also have been presented, including collinear adjustment of ERM data, removal of the oceanic variability from GM data, crossover adjustment and gridding. The gridding map is combined with the DTU18. After validated with DTU18 and CLS15, it can be proved, under the premise of determining the temporal and spatial scales of the combined satellite altimetry data, it is feasible to integrate the data with the MSS model to improve the existing MSS model. The combination method in the Antarctic ocean can be extended to other seas and global waters.

Future improvement in altimetric derived MSS awaits longer time series and higher data quality, particularly in coastal and polar regions, which will be the key elements to future improvement. Data from new (HY-2C, Jason-CS, Sentinel-6) and future (SWOT) satellites will provide both SAR and Ka-band altimetry data that can be used to construct higher resolution and accuracy MSS products. The oceanic variability correction procedures still need to be improved, and correction for variations at sub-mesoscale wavelengths should be developed. Improvements also need to be made to the mapping method, for example, by developing interpolation methods or data fusion or combination methods that can achieve higher accuracy.

DATA AVAILABILITY STATEMENT

The raw data supporting the conclusion of this article will be made available by the authors, without undue reservation.

AUTHOR CONTRIBUTIONS

Conceptualization, XZ and WS; methodology, WS and LY; validation, WS, LY, and DZ; data curation, XZ, WS, and FL; writing-original draft preparation, WS; writing-review and editing, WS and LY; visualization, WS and FL; supervision, XZ; project administration, XZ; funding acquisition, YL All authors have read and agreed to the published version of the manuscript.

FUNDING

This research was funded by the National Natural Science Foundation of China (grant number 41806214), the Open Research Foundation of the Qian Xuesen Laboratory of Space Technology, CAST (grant number GZZKFJJ2020005), the Natural Science Foundation of Shandong Province (grant number ZR2017QD011, ZR2020QD087), and the open foundation of Key Laboratory of Marine Environmental

Survey Technology and Application Ministry of Natural Resource (grant number MESTA-2020-B005).

ACKNOWLEDGMENTS

The author would like to thank AVISO for providing the HY-2A L2P data and CNES_CLS15 MSS (ftp://ftp-access.aviso.altimetry.fr) and Copernicus Online Data Access for providing the Sentinel-3A 20 Hz data (https://coda.eumetsat.int/#/home). The author also thankful to Andersen for providing the DTU15 MSS and DTU18 MSS. The DTU15 MSS and DTU18 MSS can be downloaded in https://ftp.space.dtu.dk/pub/. The topography name is provided in https://www.ngdc.noaa.gov/gazetteer/.

REFERENCES

Andersen, O. B., Knudsen, P., and Bondo, T. (2010). "The Mean Sea Surface DTU10MSS-Comparison with GPS and Tide Gauges," in Proceedings of ESA Living Planet Symposium, Norwey, Bergen, 28, Bergen, Norway, June–2 July 2010. Editors H. Lacoste-Francise (Paris, France).

Andersen, O. B., and Knudsen, P. (2009). DNSC08 Mean Sea Surface and Mean Dynamic Topography Models. *J. Geophys. Res. Oceans.* 114, 327–432. doi:10.1029/2008jc005179

Andersen, O. B., Knudsen, P., and Stenseng, L. (2018a). "A New DTU18 MSS Mean Sea Surface—Improvement from SAR Altimetry. 172," in Proceedings of the 25 years of progress in radar altimetry symposium, Ponta Delgada, São Miguel Island, Portugal, 24–29 September 2018. Editors J. Benveniste and F. Bonnefond (Azores Archipelago, Portugal), 172, 24–26.

Andersen, O. B., and Knudsen, P. (2011). *The DTU2010MSS Mean Sea Surface in the Arctic-For and with Cyrosat-2 DataCryoSat Validation Workshop*, Francati, Italy.

Andersen, O. B., Rose, S. K., Knudsen, P., and Stenseng, L. (2018b). "The DTU18 MSS Mean Sea Surface Improvement from SAR Altimetry," in International Symposium of Gravity, Geoid and Height Systems (GGHS) 2, The second joint meeting of the International Gravity Field Service and Commission 2 of the International Association of Geodesy, Copenhagen, Denmark, 17–21 September 2018.

Andersen, O. B., Stenseng, L., Piccioni, G., and Knudsen, P. (2016). "The DTU15 MSS (Mean Sea Surface) and DTU15LAT (Lowest Astronomical Tide) Reference Surface," in Proceedings of the ESA Living Planet Symposium, Prague, Czech Republic, 9–13 May 2016. Editors L. Ouwehand Prague, Czech Republic.

Andersen, O., Knudsen, P., and Stenseng, L. (2015). "The DTU13 MSS (Mean Sea Surface) and MDT (Mean Dynamic Topography) from 20 Years of Satellite Altimetry," in IGFS 2014: Proceedings of the 3rd International Gravity Field Service (IGFS), Shanghai, China, June 30–July 6, 2014. Editors S. Jin and R. Barzaghi (Berlin/Heidelberg, Germany: Springer), 111–121. doi:10.1007/1345_2015_182

Au Ridout, A. (2014). New Mean Sea Surface for the CryoSat-2 L2 SAR Chain (Technical Note); ESA Document No. C2-TN-UCL-BC-0003 Issue 1.0, London, UK (University College London). Retrieved from: https://earth.esa.int/documents/10174/1773005/TechNote_CryoSat_L2_MSS.

Cheng, Y., and Andersen, O. B. (2014). "HY-2A Satellite Altimetric Data Evaluation in the Arctic Ocean," in Proceedings of the IEEE International Geoscience and Remote Sensing Symposium IGARSS 2014, Quebec, Canada, July 13–18, 2014. Editors J. Lévesque, M. Bernier, E. LeDrew, and J. Garneau (Piscataway, United States: IEEE Geoscience and Remote Sensing Symposium), 5164–5166.

Copernicus Marine Environment Monitoring Service (CMEMS) (2018). Copernicus Marine Environment Monitoring Service–Sea Level Thematic Assembly Center Product User Manual. Available online at: http://marine.copernicus.eu/documents/PUM/CMEMS-SL-PUM-008-017-036.pdf (accessed July 2, 2018).

Cui, W., Wang, W., Zhang, J., and Yang, J. (2020). Identification and Census Statistics of Multicore Eddies Based on Sea Surface Height Data in Global Oceans. *Acta Oceanol. Sin.* 39, 41–51. doi:10.1007/s13131-019-1519-y

Duan, Y., Liu, H., Yu, W., and Hou, Y. (2016). Eddy Properties in the Pacific Sector of the Southern Ocean from Satellite Altimetry Data. *Acta Oceanol. Sin.* 35 (11), 28–34. doi:10.1007/s13131-016-0946-2

Ducet, N., Le Traon, P. Y., and Reverdin, G. (2000). Global High-Resolution Mapping of Ocean Circulation from TOPEX/Poseidon and ERS-1 and -2. *J. Geophys. Res.* 105, 19477–19498. doi:10.1029/2000JC900063

EUMETSAT (2018). Copernicus Online Data Access (CODA). Available at: https://coda.eumetsat.int. (accessed August 10, 2018).

Farrell, S. L., McAdoo, D. C., Laxon, S. W., Zwally, H. J., Yi, D., Ridout, A., et al. (2012). Mean Dynamic Topography of the Arctic Ocean. *Geophys. Res. Lett.* 39 (1), a–n. doi:10.1029/2011GL050052

Huang, G. Q., Mak, K. L., Zhai, G., and Ouyang, Y. (1999). Web-based Collaborative Conceptual Design. *J. Eng. Des.* 10, 183–194. doi:10.1080/014904199273452

Huang, M., Zhai, G., Ouyang, Y., Lu, X., Liu, C., and Wang, R. (2008). Integrated Data Processing for Multi-Satellite Missions and Recovery of Marine Gravity Field. *Terr. Atmos. Ocean. Sci.* 19, 103. doi:10.3319/TAO.2008.19.1-2.103

Jiang, W., Li, J., and Wang, Z. (2002). Determination of Global Mean Sea Surface WHU2000 Using Multi-Satellite Altimetric Data. *Chin. Sci Bull* 47, 1664–1668. doi:10.1007/BF03184119

Jimenez-Munt, I., Fernandez, M., Verges, J., and Platt, J. P. (2008). Lithosphere Structure underneath the Tibetan Plateau Inferred from Elevation, Gravity and Geoid Anomalies. *Earth Planet. Sci. Lett.* 267, 276–289. doi:10.1016/j.epsl.2007.11.045

Jin, T., Li, J., and Jiang, W. (2016). The Global Mean Sea Surface Model WHU2013. *Geodesy and Geodynamics* 7 (3), 202–209. doi:10.1016/j.geog.2016.04.006

Jin, T., Li, J., Jiang, W., and Wang, Z. (2011). The New Generation of Global Mean Sea Surface Height Model Based on Multi-Altimetric Data. *Acta Geod. Cartogr. Sin.* 40, 723–729. doi:10.1007/s11769-011-0446-4

Le Traon, P.-Y., and Ogor, F. (1998b). ERS-1/2 Orbit Improvement Using TOPEX/POSEIDON: The 2 Cm challenge. *J. Geophys. Res.* 103, 8045–8057. doi:10.1029/97jc01917

Le Traon, P. Y., Faugère, Y., Hernandez, F., Dorandeu, J., Mertz, F., and Ablain, M. (2003). Can We MergeGEOSAT Follow-Onwith TOPEX/Poseidon andERS-2for an Improved Description of the Ocean Circulation? *J. Atmos. Oceanic Technol.* 20, 889–895. doi:10.1175/1520-0426(2003)020<0889:cwmgfw>2.0.co;2

Le Traon, P. Y., Nadal, F., and Ducet, N. (1998a). An Improved Mapping Method of Multisatellite Altimeter Data. *J. Atmos. Ocean. Technol.* 15 (2), 522–534. doi:10.1175/1520-0426(1998)015<0522:AIMMOM>2.0.CO;2

Passaro, M., Nadzir, Z. A., and Quartly, G. D. (2018). Improving the Precision of Sea Level Data from Satellite Altimetry with High-Frequency and Regional Sea State Bias Corrections. *Remote Sensing Environ.* 218, 245–254. doi:10.1016/j.rse.2018.09.007

Peacock, N. R., and Laxon, S. W. (2004). Sea Surface Height Determination in the Arctic Ocean from ERS Altimetry. *J. Geophys. Res.* 109, C07001. doi:10.1029/2001JC001026

Pujol, M. I., Schaeffer, P., Faugere, Y., Dibarboure, G., and Picot, N. (2020). *Abstract: New CNES CLS 2019 Mean Sea Surface: First Validation*. San Diego, USA: Ocean Sciences Meeting, 16–21.

Pujol, M. I., Schaeffer, P., Faugère, Y., Raynal, M., Dibarboure, G., and Picot, N. (2018). Gauging the Improvement of Recent Mean Sea Surface Models: A New Approach for Identifying and Quantifying Their Errors. *J. Geophys. Res. Oceans* 123, 5889–5911. doi:10.1029/2017JC013503

Rapp, R. H., and Yi, Y. (1997). Role of Ocean Variability and Dynamic Ocean Topography in the Recovery of the Mean Sea Surface and Gravity Anomalies from Satellite Altimeter Data. *J. Geodesy* 71, 617–629. doi:10.1007/s001900050129

Rummel, R. (1993). "Principle of Satellite Altimetry and Elimination of Radial Orbit Errors," in *Satellite Altimetry in Geodesy and Oceanography*. Editors R. Rummel and F. Sansò (Germany: SpringerBerlin/Heidelberg), 50, 190–241.

Sandwell, D. T., Müller, R. D., Smith, W. H. F., Garcia, E., and Francis, R. (2014). New Global marine Gravity Model from CryoSat-2 and Jason-1 Reveals Buried Tectonic Structure. *Science* 346, 65–67. doi:10.1126/science.1258213

Schaeffer, P., Faugére, Y., Legeais, J. F., Ollivier, A., Guinle, T., and Picot, N. (2012). The CNES_CLS11 Global Mean Sea Surface Computed from 16 Years of Satellite Altimeter Data. *Mar. Geodesy* 35, 3–19. doi:10.1080/01490419.2012.718231

Schaeffer, P., Pujol, M. I., Faugere, Y., Guillot, A., and Picot, N. (2017). The CNES CLS 2015 Global Mean Sea Surface. Presentation OSTST (Paris, France). Available at: http://meetings.aviso.altimetry.fr/fileadmin/user_upload/tx_ausyclsseminar/files/GEO_03_Pres_OSTS T2016_MSS_CNES_CLS2015_V1_16h55.pdf(accessed on January 10, 2017).

Skourup, H., Farrell, S. L., Hendricks, S., Ricker, R., Armitage, T. W. K., Ridout, A., et al. (2017). An Assessment of State-of-the-Art Mean Sea Surface and Geoid Models of the Arctic Ocean: Implications for Sea Ice Freeboard Retrieval. *J. Geophys. Res. Oceans* 122, 8593–8613. doi:10.1002/2017JC013176

Taburet, G., Sanchez-Roman, A., Ballarotta, M., Pujol, M.-I., Legeais, J.-F., Fournier, F., et al. (2019). DUACS DT2018: 25 Years of Reprocessed Sea Level Altimetry Products. *Ocean Sci.* 15, 1207–1224. doi:10.5194/os-15-1207-2019

Tierney, C., Wahr, J., Bryan, F., and Zlotnicki, V. (2000). Short-period Oceanic Circulation: Implications for Satellite Altimetry. *Geophys. Res. Lett.* 27, 1255–1258. doi:10.1029/1999GL010507

Wagner, C. A. (1985). Radial Variations of a Satellite Orbit Due to Gravitational Errors: Implications for Satellite Altimetry. *J. Geophys. Res.* 90, 3027–3036. doi:10.1029/JB090iB04p03027

Wessel, P., and Smith, W. H. F. (1995). New Version of the Generic Mapping Tools. *Eos Trans. AGU* 76, 329. doi:10.1029/95EO00198

Wessel, P., and Smith, W. H. F. (1998). New, Improved Version of Generic Mapping Tools Released. *EOS Trans. AGU* 79, 579. doi:10.1029/98eo00426

Yuan, J., Guo, J., Niu, Y., Zhu, C., Li, Z., and Liu, X. (2020b). Denoising Effect of Jason-1 Altimeter Waveforms with Singular Spectrum Analysis: A Case Study of Modelling Mean Sea Surface Height over South China Sea. *J. Marine. Sci. Eng.* 8, 426. doi:10.3390/jmse8060426

Yuan, J., Guo, J., Niu, Y., Zhu, C., and Li, Z. (2020a). Mean Sea Surface Model over the Sea of Japan Determined from Multi-Satellite Altimeter Data and Tide Gauge Records. *Remote Sensing* 12 (24), 4168. doi:10.3390/rs12244168

Zhang, S., Li, J., Jin, T., and Che, D. (2018). HY-2A Altimeter Data Initial Assessment and Corresponding Two-Pass Waveform Retracker. *Remote Sensing* 10, 507. doi:10.3390/rs10040507

Zhao, G., Zhou, X., and Wu, B. (2013). Precise Orbit Determination of Haiyang-2 Using Satellite Laser Ranging. *Chin. Sci. Bull.* 58, 589–597. doi:10.1007/s11434-012-5564-6

Conflict of Interest: Author FL was employed by the company Qingdao iSpatial Ocean Technology Co., Ltd.

The remaining authors declare that the research was conducted in the absence of any commercial or financial relationships that could be construed as a potential conflict of interest.

frontiers in Earth Science

ORIGINAL RESEARCH
published: 23 August 2021
doi: 10.3389/feart.2021.722019

Accuracy Evaluation of Altimeter-Derived Gravity Field Models in Offshore and Coastal Regions of China

Qianqian Li[1,2], *Lifeng Bao*[1,2]* *and Yong Wang*[1,2]

[1]State Key Laboratory of Geodesy and Earth's Dynamics, Innovation Academy for Precision Measurement Science and Technology, Chinese Academy of Sciences, Wuhan, China, [2]University of the Chinese Academy of Sciences, Beijing, China

Satellite radar altimetry has made unique contributions to global and coastal gravity field recovery. This paper starts with a general introduction followed by the progress of satellite radar altimetry technology. Then, the methods of marine gravity field recovery and dominating gravity models are described briefly. Finally, typical gravity models are compared with shipboard gravity measurements to evaluate their accuracies in offshore and coastal regions of China. The root mean squares of deviations between gravity models and shipboard gravity are all more than 7 mGal in offshore regions and within the range of 9.5–10.2 mGal in coastal regions. Further analysis in coastal regions indicates that the new gravity models with new satellite missions including Jason-2, SARAL/Altika, and Envisat data have relatively higher accuracy, especially SARAL/Altika data, significantly improving the coastal gravity field. Accuracies are low in areas with strong currents, showing that tide correction is very important for altimetry-derived marine gravity recovery as well as shipboard measurements in coastal gravity field determination. Moreover, as an external check, shipboard gravity data need more operations to improve their precision, such as higher instrument accuracy and finer data processing.

Keywords: Satellite altimetry, Shipboard gravity, Marine gravity anomaly, Coastal regions of China, Accuracy evaluation

OPEN ACCESS

Edited by:
Jinyun Guo,
Shandong University of Science and Technology, China

Reviewed by:
Xu Ke,
National Space Science Center (CAS), China
Wan Xiaoyun,
China University of Geosciences, China

***Correspondence:**
Lifeng Bao
baolifeng@whigg.ac.cn

Specialty section:
This article was submitted to Solid Earth Geophysics, a section of the journal Frontiers in Earth Science

Received: *08 June 2021*
Accepted: *15 July 2021*
Published: *23 August 2021*

Citation:
Li Q, Bao L and Wang Y (2021) Accuracy Evaluation of Altimeter-Derived Gravity Field Models in Offshore and Coastal Regions of China. Front. Earth Sci. 9:722019. doi: 10.3389/feart.2021.722019

INTRODUCTION

The gravity field is one of the most important basic physical fields of the Earth, reflecting the distribution, movement, and state change of Earth's interior material. Marine gravity anomalies are important data sources to construct Earth's gravity field, as the ocean occupies approximately 70% of the Earth's surface. High accuracy marine gravity observations are essential data for seafloor bathymetry and marine geological structure and mineral resource distributions, submarine volcanoes, and global changes (Fairhead et al., 2001; Fu et al., 2001; Sandwell and Smith., 2009,2014; Hwang and Chang, 2014; Li et al., 2020; Li et al., 2021).

A variety of methods can be applied to determine the marine gravity field, at respective accuracy and spatial resolutions, using ship or airborne gravity measurements, satellite gravity, satellite altimetry, and satellite gradiometry. Marine gravity data measured onboard ships and airplanes usually have sparse data coverage, long measurement periods, and lack of repeated observations, making it impossible to obtain global marine gravity information in a relatively short time. However, their high accuracies make them important means for auxiliary measurement to

construct global marine gravity field (Forsberg and Olesen 2010). Gravity Recovery and Climate Experiment (GRACE) twin-satellite gravimetry mission can only detect Earth's mass transport signals in medium-long waves longer than 300–400 km (half-wavelength) (Tapley et al., 2004; Tapley et al., 2019). In recent decades, satellite altimetry has evolved as an effective tool for recovering the global or regional marine gravity field due to its high resolution, wide coverage, and easy access to the data (Rapp, 1979; Haxby et al., 1983; Sandwell and Smith, 1997; Andersen and Knudsen, 1998; Hwang, 1998; Sandwell et al., 2014). Satellite altimeters developed from first-generation altimeters on Geosat/GM and ERS-1/GM, through more altimeter series on TOPEX/Poseidon, Envisat, Jason-1/2, and HY-2, to the new generation, either in SAR mode (CryoSat-2 over ocean, Sentinel-3, and Sentinel-6) or in Ka band (SARAL/AltiKa, abbreviated Altika) have significantly improved the quality of altimetry range in terms of accuracy and spatial resolution (Abdalla et al., 2021; Zhang and Sandwell, 2016). Accordingly, the levels of accuracy and precision of altimetry-derived marine gravity field models, which can be derived from radar altimeter measurements of sea surface heights (Rapp, 1979; Haxby et al., 1983) or slopes (Sandwell and Smith, 1997; Andersen and Knudsen, 1998; Hwang, 1998), have greatly evolved. Until now, they have demonstrated accuracy and spatial resolution at 1–2 mGal and $1' \times 1'$ (approximately 2 km × 2 km), respectively and, as a result, have allowed many contemporary geophysical questions to be addressed (e.g., Fairhead et al., 2001; Bao et al., 2013; Sandwell et al., 2013; Sandwell et al., 2014; Sandwell et al., 2019; Hwang and Chang, 2014; Andersen et al., 2019; Li et al., 2020; Li et al., 2021).

In the early 1980s, the first global marine gravity map was produced by the Lamont Doherty geological observatory, which marked a significant step towards the study of global, high resolution, and high accuracy marine gravity field models (Zhang et al., 2020). Over the years, the theory for recovering marine gravity fields by using satellite radar altimetry has been developed. Several methods can be adopted to derive marine gravity fields using satellite altimetry observations, such as the inverse Stokes formula, inverse Vening-Meinesz formula (IVM formula), and least squares collocation method (LSC). Among them, the IVM method, based on the deflection of the vertical (DOV), can effectively suppress the radial orbit error and has evolved as the primary method. In addition, Sandwell's method is widely used to calculate high accuracy marine gravity fields, which is based on DOV, Laplace equation, and fast Fourier transform (FFT) (Sandwell and Smith, 1997). Many studies have obtained high precision and high resolution global or regional marine gravity fields based on the above methods. The S&S series from the Scripps Institution of Oceanography, University of California San Diego (SIO), and DTU series from the Technical University of Denmark (DTU) are typical representatives. They update constantly with improvements in accuracy and resolution, having more data available from CryoSat-2, Jason-1, Jason-2, and Altika in their geodetic phases. All this progress has provided a new understanding of the topography and tectonics of the deep oceans.

In this paper, we briefly introduce the evolution of satellite radar altimetry technology and the contributions it has made since the beginning. Then, the methods for constructing the global marine gravity models are summarized into four groups, which are described in detail. Accordingly, typical altimetry-derived marine gravity field models, S&S and DTU series, their area coverage, resolution, and the methods adopted are described. Finally, gravity anomalies V24.1 and V27.1 from S&S and DTU10 and DTU13 from DTU and the global Earth gravity model EGM2008 are compared with the shipborne gravity values to evaluate the accuracy in offshore and coastal regions of China.

METHODS FOR GRAVITY FIELD RECOVERY

At present, methods for marine gravity field recovery mainly include the inverse Stokes formula, IVM formula, LSC, and Laplace equation. The progress and main formulas of these methods will be introduced as follows.

Inverse Stokes Formula

The classic Stokes formula is derived from the basic equations in physical geodesy and the Bruns formula, to determine the geoidal undulation from gravity anomalies. For the solution of the inverse problem, i.e., the determination of the gravity anomaly field from the geoidal undulation, we may use a direct inverse formulation. Molodenskii first proposed a direct means for the determination of the gravity anomaly from the geoidal undulation in 1962 (Molodenskii et al., 1962). After continuous improvement, we obtain the inverse Stokes formula:

$$\Delta g = -\left(\frac{\gamma}{R} N + \frac{\gamma}{16\pi R} \iint_{\sigma} \frac{N - Np}{sin^3 \frac{\Psi}{2}} d\sigma \right), \tag{1}$$

where R is the Earth's mean radius. γ is the Earth normal gravity. N is the geoidal undulation at the computation point. Np is the geoidal undulation at the point to be computed. Ψ is the spherical distance between two points. $d\sigma$ is the unit sphere. Balmino et al. (1987) computed $1^\circ \times 1^\circ$ gravity anomalies from GEOS-3 and Seasat altimeter dataset by using the inverse Stokes formula, in which an RMS difference of ±8 mGal was found. To compute the marine gravity field by the inverse Stokes formula, only the geoidal undulation derived from altimeter measurements is needed. However, in the computation, it is necessary to divide the grid in the direction of longitude and latitude first so that **Eq. 1** can be converted into a regional summation formula, and then the global integral is carried out, which leads to a large amount of calculation and a complicated process of obtaining results; thus, it is not suitable at present.

Least Squares Collocation

In the 1960s, the LSC method was developed based on theoretical advances by Krarup (1969) and Moritz (1965) (Tscherning, 2015). Smith (1974) and Rapp (1974) proposed that the LSC method can be applied to the process of recovering gravity anomalies from satellite altimeters in the same year. Then, it was improved into the perfect method as follow:

$$\Delta\widehat{g} = C_{\Delta gh}\left(C_{hh} + D\right)^{-1}\left(h - h_{ref}\right) + \Delta g_{ref} \quad (2)$$

$$m_{\Delta g}^2 = C_{\Delta gg} - C_{\Delta gh}\left(C_{hh} + D\right)^{-1} C_{h\Delta g} \quad (3)$$

where $\Delta\widehat{g}$ is the gravity anomaly to be estimated, h is the observation of the geoidal undulation, $C_{\Delta gh}$is the covariance matrix between the gravity anomaly to be estimated and the geoidal undulation, C_{hh} is the covariance matrix of the geoidal undulation, and D is the error covariance of the measurements. $C_{\Delta g\Delta g}$ is the covariance matrix of the gravity anomaly to be estimated, h_{ref} is the reference geoidal undulation, Δg_{ref} is the reference gravity anomaly, and $m_{\Delta g}$is the standard deviation of the gravity anomaly.

Rapp (1983) and Rapp (1986) computed the gravity anomalies on a 0.125° grid in ocean areas from a combined GEOS-3/Seasat altimeter dataset using LSC. The 1° mean anomalies were compared with terrestrial data where an RMS difference of ±7 mGal was found when comparing 10,139 values. Appling the LSC method has major limitations in that one needs to know the covariance function and matrix first. In contrast, it is difficult to determine the covariance function of large sea areas. Therefore, it has only been applied to local marine gravity field computations so far.

Inverse Vening-Meinesz Formula

In the 1980s, DOV, as the initial data, began to be applied to the recovery of the marine gravity field and gradually evolved into the main effective means. For decades, the IVM formula was developed into an optimized method that needs no cross adjustment but can restrain the radial orbital error. At present, it has become the preferred method to retrieve high precision and resolution marine gravity field from altimeter data compared with others.

The inverse Vening-Meinesz formula was presented as follow:

$$\Delta g\left(P\right) = \frac{\gamma_0}{4\pi}\iint_{\sigma} H'\left(\xi_q cos\alpha_{qp} + \eta_q sin\alpha_{qp}\right)d\sigma_{qp}, \quad (4)$$

where $\Delta g(P)$ and γ_0 are the gravity anomaly and normal gravity at p, respectively. H' is the derivative of kernel function, ξ_q and η_q are the north and east components of the DOV at q (dummy index), respectively, α_{qp} is the azimuth from q to p, σ is the unit sphere, and $d\sigma_{qp}$ is the surface element.

$$H\left(\psi_{pq}\right) = \frac{1}{sin\frac{\psi_{pq}}{2}} + log\left(\frac{sin^3\frac{\psi_{pq}}{2}}{1 + sin\frac{\psi_{pq}}{2}}\right). \quad (5)$$

ψ_{pq} is the spherical distance between q and p.

In 1998, the IVM formula and FFT were employed to compute gravity anomalies over the South China Sea using deflections from Seasat, Geosat, ERS-1, and T/P satellite altimetry, and the accuracy was 9.9 mGal compared with 180297 shipborne gravity anomalies, approximately 30% better than the contemporary altimeter-derived gravity anomalies from Sandwell and Smith (1997) (Hwang, 1998). Therefore, the IVM method to compute marine gravity field not only ensures the accuracy, but also simplifies the calculation process to save time. It is very suitable for gravity field recovery in large areas and even global areas.

Laplace Equation With FFT

In 1983, Haxby et al. proposed a two-dimensional form of Laplace's equation in cartesian coordinates. Combined with the Fourier transform operation, we arrive at an algebraic equation relating the Fourier transform of the gravity anomaly to the sum of the Fourier transforms of the two components of vertical deflection. Finally, one performs inverse Fourier transforms to obtain gravity anomaly.

$$\Delta g\left(\mathbf{k}, 0\right) = \frac{ig_0}{|\mathbf{k}|}\left[k_x\eta\left(\mathbf{k}\right) + k_y\xi\left(\mathbf{k}\right)\right], \quad (6)$$

where g_0 is the average gravitational acceleration (9.81 m/s^2), $\boldsymbol{k}$ denotes (k_x, k_y), $k_x = \frac{1}{\lambda_x}$, where λ_x is wavelength; $|\mathbf{k}| = \sqrt{k_x^2 + k_y^2}$, and ξ and η are the north and east components of the DOV, respectively.

In 1997, Sandwell and Smith recovered a $2' \times 2'$ gridded global marine gravity field based on Laplace equation and FFT and ERS-1 and Geosat different phase data. A comparison with shipboard gravity measurements shows that the accuracy of the altimetry-derived gravity anomaly is about 4–7 mGal for random ship tracks. These data provide the first view of the ocean floor structures in many remote areas of the Earth. With improvements in the recent years, this method is one of the effective means for marine gravity field recovery in large areas and even global areas.

GLOBAL MARINE GRAVITY FIELD MODELS

With the development of satellite altimetry, many researchers and institutions have constructed regional or global marine gravity models. Sandwell and Smith (1997) recovered a $2' \times 2'$ gridded global marine gravity field with RMS agreements of 7 mGal compared with ship-measured gravity data. The gravity field is based on the ERS-1 and Geosat different phase data, CSR V3.0 tide model correction, the collinear average and low-pass filter to suppress the noise, and the Remove-Restore method with the 70-order JGM-3 model as a reference field. In 1998, Andersen and Knudsen (1998) applied ERS-1/GM and Geosat/GM data with denser spatial coverage, the AG95.1 tide model to correct the sea tide and load tide, and the EGM96 model as a reference field to construct the global marine gravity field with a $3.75' \times 3.75'$ resolution by using the Remove-Restore and LSC methods. The RMS of the discrepancy is superior to l0 mGal when compared with the ship-measured gravity data. Furthermore, there are also some excellent related results from other institutions and scholars. Hwang (1998) computed the global marine gravity anomalies over the area 82°S to 82°N and 0°E to 360°E on a $2' \times 2'$ grid based on Seasat, Geosat, ERS-1, and T/P altimeter data by IVM. Rapp and Bašić (1992) computed the 0.125° × 0.125° marine gravity field gridded set by LSC based on the Geos-3, Seasat, and Geosat

TABLE 1 | Introduction of partial S&S series global marine gravity field models.

Models	Year	Reference gravity field	Data	Resolution	Coverage range
V7.2	1997	JGM-3	Geosat (ERM/GM) and ERS-1 (ERM/GM) data	$2' \times 2'$	72°S ~ 72°N
V8.1	1998	EGM96	Geosat and ERS-1 data (low-pass filter parameters 2–18 km)	$1' \times 1'$	72°S ~ 72°N
V11.1	2004	EGM96	Retracked ERS-1 and Geosat data	$1' \times 1'$	72°S ~ 72°N
V16.1	2006	EGM96	Geosat, ERS-1, and T/P data	$1' \times 1'$	80.7°S ~ 80.7°N
V18.1	2009	EGM08 + MDOT	(Geosat, ERS-1, and T/P) data + biharmonic spline interpolation	$1' \times 1'$	80.7°S ~ 80.7°N
V20.1	2012	EGM08 + MDOT	Added Jason-1 and Cryosat-2 and Envisat data	$1' \times 1'$	80.7°S ~ 80.7°N
V22.1	2013	EGM08 + MDOT	(Geosat, ERS-1, Cryosat-2, Jason-1, and Envisat) data + the wavelength of low-pass filter depends on depth + slope correction	$1' \times 1'$	85°S ~ 85°N
V23.1	2014	EGM08 + MDOT	Added all of Jason-1/GM data and 9 months of Cryosat-2 data	$1' \times 1'$	85°S ~ 85°N
V24.1	2016	EGM08 + MDOT	Added 12 months of Cryosat-2 data	$1' \times 1'$	85°S ~ 85°N
V25.1	2017	EGM08 + MDOT	Added 12 months of Cryosat-2/LRM data and 31 months of Cryosat-2/SAR data and 13 months of Altika data	$1' \times 1'$	85°S ~ 85°N
V26.1	2018	EGM08 + MDOT	Added 6 months of Cryosat-2 data and 6 months of Altika data	$1' \times 1'$	85°S ~ 85°N
V27.1	2019	EGM08 + MDOT	Added 12 months of retracked Jason-2 data and 2 months of Altika data	$1' \times 1'$	85°S ~ 85°N
V28.1	2019	EGM08 + MDOT	Added more Cryosat-2 and Jason-2 and Altika data + the grid is converted to cartesian coordinates and stored as NETCDF	$1' \times 1'$	85°S ~ 85°N
V29.1	2019	EGM08 + MDOT	Added 2 years of sentinel-3A/B data	$1' \times 1'$	85°S ~ 85°N
V30.1	2020	EGM08 + MDOT	Added more Altika and Cryosat-2 and sentinel-3A/B data	$1' \times 1'$	85°S ~ 85°N

The information was retrieved from readme files of the gravity field models, which were downloaded from ftp://topex.ucsd.edu/pub/archive/grav/.

ERM data, along with $5' \times 5'$ bathymetry data. Olgiati et al. (1995) computed gravity anomalies from the geoidal undulation and DOV by inverse Stokes formula and IVM, respectively. The latter results with more continuous shortwave features were superior to the former. Hsu et al. (1999) recovered the $30' \times 30'$ gridded marine gravity anomalies in the China Sea and adjacent seas using the inverse Stokes formula and LSC, respectively, based on the gridded geoidal height from T/P and ERS-1. Li et al. (2001) and Li et al. (2003) computed the deflection of vertical and gravity anomalies based on the T/P, ERS-2, and Geosat data. The RMS agreement is 9.3 mGal compared with ship-measured gravity.

Up to now, research teams represented by Sandwell et al. and Andersen et al. have dominated in global marine gravity field model construction, as they have been continuously exploring higher-quality global marine gravity field models and performing achievements from generation to generation. Sandwell et al. published S&S series global marine gravity field models from the SIO, as shown in **Table 1** (the gravity model data can be downloaded from: ftp://topex.ucsd.edu/pub/archive/grav/). Since 1997, Sandwell and Smith constructed the global marine gravity field model V7.2, with the accumulation of new altimetry satellite data, introduction of new reference fields, emergence of waveform retracking, and improvement of data processing. Sandwell's team has successively published a series of global gravity field models. Among them, models V18.1 and V22.1 both have noteworthy improvements in data processing, which contribute to accuracy improvement. In V18.1, Sandwell and Smith retracked the raw waveforms from the ERS-1 and Geosat/GM missions to improve the range precision, used the EGM2008 global gravity model as a reference field to provide a seamless gravity transition from land to ocean, and used a biharmonic spline interpolation method to construct residual vertical deflection grids. Its accuracy precedes 4 mGal compared with shipboard gravity. In V22.1, they added Cryosat-2, Jason-1, and Envisat data and adopted a low-pass filter whose wavelength depends on depth and slope corrections to account for the offset of the footprint away from NADIR due to a high geoid slope based on former models. To date, the gravity model has evolved into V30.1, with an accuracy of 1–2 mGal in some regions.

Another important global marine gravity field model series is DTU from Andersen et al., which is shown in **Table 2** (the data can be downloaded from https://ftp.space.dtu.dk/pub/) (Andersen and Knudsen, 1998; Andersen and Knudsen, 2019; Andersen et al., 2010; Andersen et al., 2014; Andersen et al., 2015; Andersen et al., 2019; Zhang et al., 2020). Similarly, they started to calculate the global marine gravity field using satellite altimetry in the 1990s. The difference is that they started with EGM96 as reference field and the coverage range was wider. Over time, they also introduced the new Earth's gravitational field EGM2008 as a reference field and added new satellite altimetry data, which improved the accuracy and precision of gravity models. Up to now, Andersen et al. have published DTU17 and DTU18, which added new Altika data. The accuracy also achieved 1–2 mGal in some regions.

STUDY AREA AND DATA

Previous studies have verified marine gravity models by comparing different models and comparing with shipboard gravity measurements. In particular, the latter can provide a more quantitative assessment of the accuracy of gravity models. It has been confirmed that the accuracy of some current models has achieved 1–2 mGal for latitudes less than 72° and somewhat lower accuracy (2–3 mGal) at higher latitudes depending on ice cover (Sandwell et al., 2013). These validations mostly focus on the deep sea and even

TABLE 2 | Introduction of partial DTU series global marine gravity field models.

Models	Year	Reference gravity field	Data	Resolution	Coverage range
KMS96	1996	EGM96	ERS-1 and Geosat data	3.75′ × 3.75′	82°S ~ 82°N
KMS02	2002	EGM96	ERS-1/2 and Geosat data	2′ × 2′	82°S ~ 82°N
DNSC08	2008	EGM08 + DOT07A	ERS-1/2, Geosat, T/P, GFO, Jason-1, and ICESat data + double waveform retracking	1′ × 1′	90°S ~ 90°N
DTU10	2010	EGM08 + MDOT	Added Envisat data	1′ × 1′	90°S ~ 90°N
DTU13	2013	EGM08 + MDOT	Added Cryosat-2 data	1′ × 1′	90°S ~ 90°N
DTU15	2015	EGM08 + MDOT	Retracked ERS-1, Geosat, Cryosat-2, and Jason-1 data	1′ × 1′	90°S ~ 90°N
DTU17	2017	EGM08 + MDOT	7 years of Cryosat-2 and Jason-1 data and 1 year of Altika data	1′ × 1′	90°S ~ 90°N
DTU18	2018	EGM08 + MDOT	Retracked Altika data and other satellite data	1′ × 1′	90°S ~ 90°N

offshore basins. The accuracy is indeterminate in many coastal regions as the shipboard gravity is unavailable. In this paper, we collected shipboard gravity in the coastal region of China from the China Offshore Marine Comprehensive Survey and Evaluation Project (908 Project for short) and many survey lines from the NCEI (National Centers for Environmental Information), as shown in **Figure 1**. The magenta lines are the gravity measurement points from China and the black lines are from the NCEI. The former measurements were acquired by different departments in multiple time periods and distributed in different areas. To maintain data consistency, the same fine data processing is implemented, such as Eotvos correction, correction for drift, and free air correction. Moreover, the systematic error between different survey lines in different survey areas is eliminated by network adjustment and adopting a high precision gravity model as criterion (Ke et al., 2015). The gravity data were employed with a uniform benchmark and data format. As shown in **Figure 1**, the magenta shipboard gravity data covered almost the entire Chinese coastal zone, containing the Bohai Sea and the margins of the Yellow Sea, East China Sea, and South China Sea. It is an important data source to evaluate the altimeter-derived marine gravity anomalies in these areas. Based on the data distribution, the offshore and coastal regions of China within 0°–45°N, 100°–130°E were chosen as the study area.

The NCEI has 181 available survey lines in the study area, black lines in **Figure 1**. All these survey missions were conducted by different institutions in different years with different instruments. There must be systematic bias that needs to be corrected before validation. In addition, these ship-measured data inevitably contain a certain number of gross error data pieces limited to various measuring conditions. Consequently, these shipboard gravity data need extra procedures to eliminate system bias and outliers according to the preliminary evaluations with respect to EGM2008, which is described in the following text.

Marine gravity models V24.1 and V27.1 from SIO, DTU10 and DTU13 from DTU, and the Earth Gravity Field Model EGM2008 were introduced as protagonists to

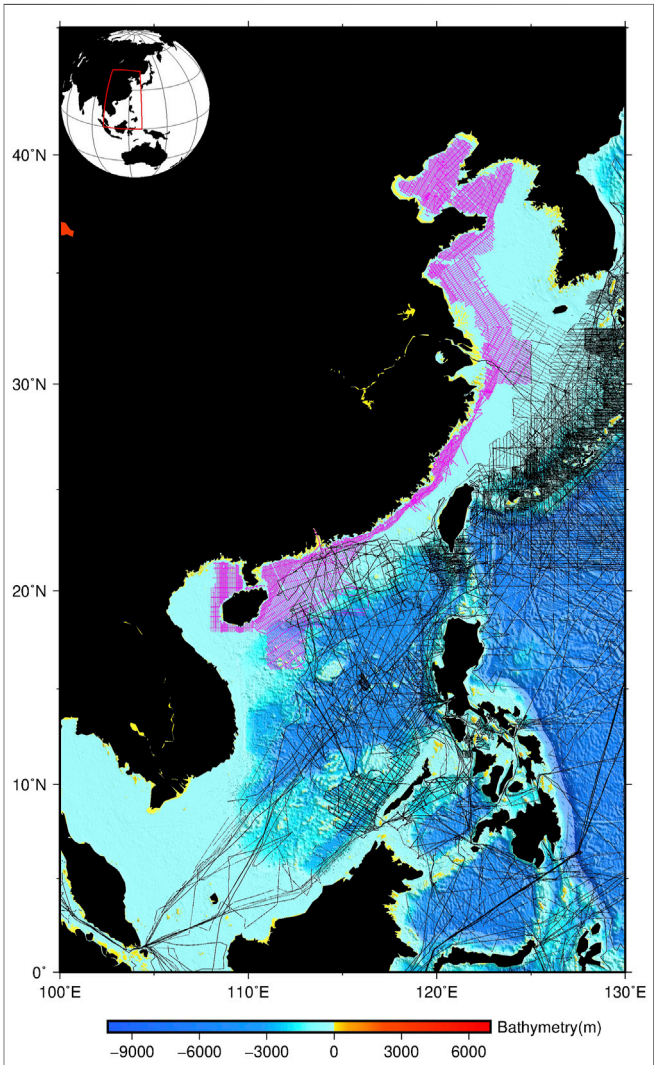

FIGURE 1 | Geographic distribution of shipboard gravity measurements in the coastal region of China. The magenta lines are from the 908 Project, and the black lines are from the NCEI. The map was created by using GMT (http://gmt.soest.hawaii.edu). The background bathymetric data is from GEBCO (https://download.gebco.net/); its spatial resolution is resampled to 1′ × 1′.

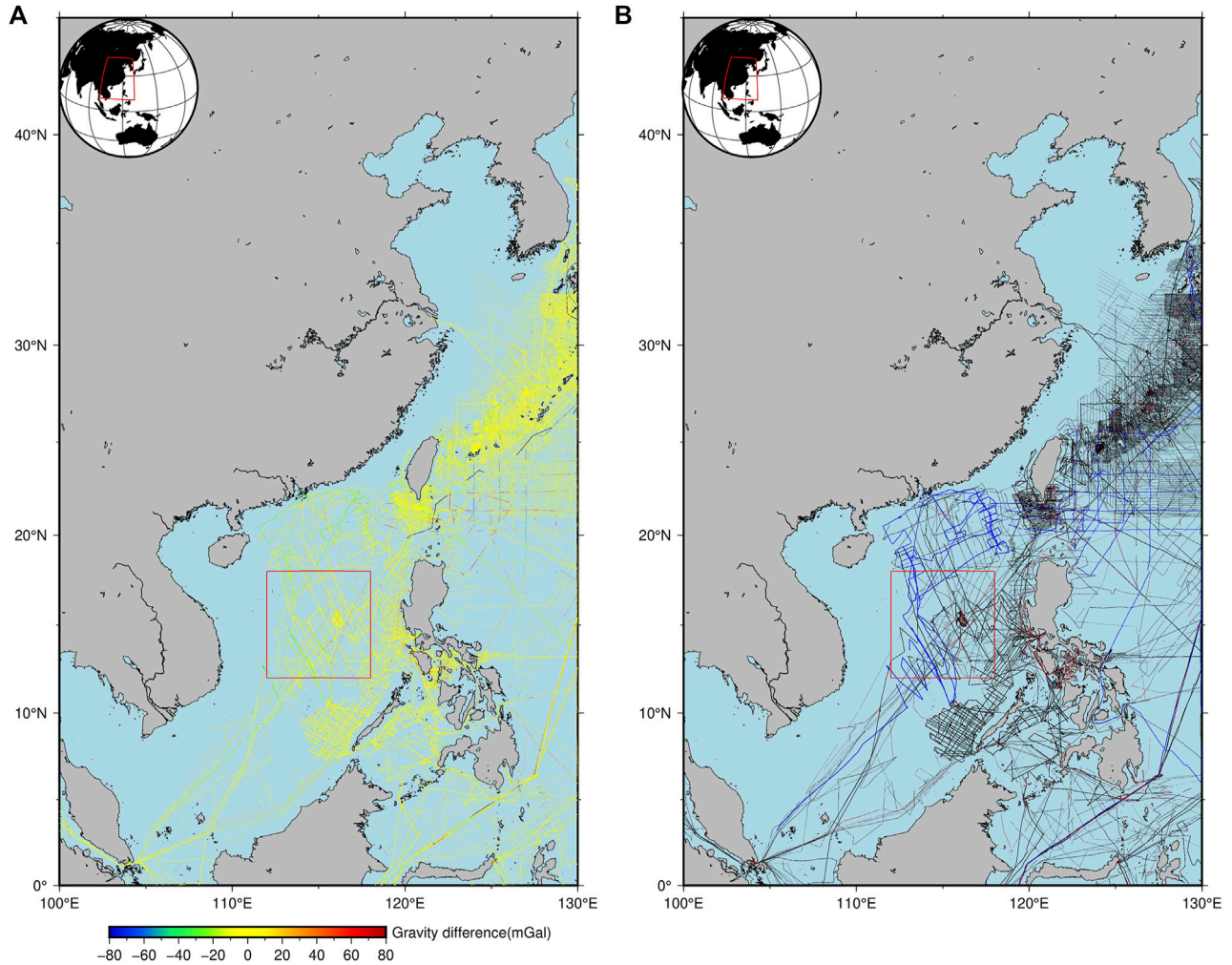

FIGURE 2 | Shipboard gravity measurements from the NCEI. **(A)** Distribution of gravity differences between EGM2008 and shipboard gravity. **(B)** The survey lines (blue) and points (red) with large discrepancies that are discarded in this study. The remaining black points are the check points for accuracy evaluation. The red rectangle is the South China Sea Basin, which is selected as a representative offshore basin to evaluate the accuracy of the gravity field models.

be verified. As shown in **Tables 1** and **2**, V24.1 employed Geosat, ERS-1, Cryosat-2, Jason-1, and Envisat data and retracking waveforms, biharmonic spline interpolation, low-pass filtering, and slope correction. V27.1 adopted the same data processing method but added more Cryosat-2, Jason-2, and Altika data. DTU10 employed Geosat, ERS-1/2, T/P, GFO, ICESat, Jason-1, and Envisat data and double waveform retracking to improve the range precision in coastal and polar regions and improved geophysical corrections. DTU13 added Cryosat-2 data on the basis of DTU10. It is widely believed that these marine gravity models have high spatial resolution and precision, even though they adopted different altimetry satellite missions and methods to recover gravity anomalies. However, accuracy assessments of these marine gravity models in the coastal region of China are absent, which is the concerned issue in this paper.

RESULTS AND ANALYSIS

Validation in Offshore Regions of China

As discussed earlier, there is a need to remove the systematic bias of the shipboard gravity measurements from the NCEI before validation. The method edits these data through comparison with EGM2008. Simple processing is applied to directly discard the survey lines and points with large errors in the offshore area as the accuracy evaluation of marine gravity field models in the coastal region of China is the focus of this paper. We calculated the discrepancies between EGM2008 and survey data by linear interpolation whose distribution is shown in **Figure 2A**. Some points with large discrepancies cover the entire survey lines, indicating that survey lines have overall large errors. These lines are 84001311 in 1984, 84003111 in 1984, JARE29L1 in 1987, POL7201 in 1972, RC2612 in 1985, RC2613 in 1985, RC2614 in 1985, and KH79 in 1979, which are discarded in

TABLE 3 | Validation results of marine gravity models with NCEI shipboard gravity data, unit: mGal.

Data	Min	Max	Mean	RMS	STD
V24.1 VS NCEI	−54.69	50.65	0.62	7.27	7.24
V27.1 VS NCEI	−49.44	80.19	0.73	7.21	7.17
DTU10 VS NCEI	−27.33	30.74	0.81	7.47	7.43
DTU13 VS NCEI	−31.46	36.14	0.82	7.34	7.30
EGM08 VS NCEI	−19.99	20.00	0.73	7.50	7.47

TABLE 4 | Validation results of marine gravity models with NCEI shipboard gravity data in South China Sea Basin.

Data	Min	Max	Mean	RMS	STD
V24.1 VS NCEI	−27.59	28.30	0.26	5.48	5.47
V27.1 VS NCEI	−24.27	25.49	0.28	5.40	5.40
DTU10 VS NCEI	−21.13	24.88	0.40	6.03	6.02
DTU13 VS NCEI	−22.04	26.05	0.38	5.69	5.68
EGM08 VS NCEI	−19.99	20.00	0.33	6.15	6.14

Unit: mGal.

this accuracy evaluation (blue lines in **Figure 2B**). First, the NCEI provides 181 tracks and 780,870 observations in the study area, which are reduced to 173 tracks and 699,355 observations after discarding the lines with large bias.

In addition, the shipboard gravity data with a discrepancy threshold of 20 mGal are regarded as outliers to be eliminated (the red points in **Figure 2B**), which leads to a total proportion of 4.39% for deleted data, and 668,662 observations remain. These deleted observations are mainly distributed around the islands and at the corners of the survey lines, which may be due to the poor precision of EGM2008 near islands or the large error introduced in the shipboard gravity measurement when the ship turns a corner.

Altimetry-derived marine gravity anomalies were compared with the shipboard gravity measurements after eliminating systematic bias and outliers. The statistical results of differences between marine gravity models and shipboard gravity values are listed in **Table 3**, which demonstrate that all marine gravity models have similar precision in the offshore area of China. Models from SIO and DTU have slightly higher accuracy than EGM2008, indicating that satellite altimetry can improve the gravity signal accuracy on a short wavelength scale on the basis of global gravity models. In addition, by observing series models from SIO and DTU, the RMS deviation improves from 7.27 mGal for V24.1 to 7.21 mGal for V27.1 and from 7.47 mGal for DTU10 to 7.34 mGal for DTU13, indicating that the new model improved slightly in accuracy, possibly due to supplementation of the latest Cryosat-2, Jason-2, and Altika data.

Considering the effects of water depths and complicated submarine topography, we selected a typical offshore basin, the South China Sea Basin, whose depth is greater than 3,000 m (red rectangle in **Figure 2**) for further analysis. The pointwise RMS differences between the marine gravity models and shipboard gravity data were computed. As shown in **Table 4**, the RMS misfit is improved to 5.48 mGal for V24.1, 5.40 mGal for V27.1, 6.03 mGal for DTU10, and 5.69 mGal for DTU13, with respect to these in the entire region. The results indicate that altimetry-derived marine gravity fields have higher accuracy in the open sea than other regions. Meanwhile, the same conclusion can be obtained in the deep sea that the marine gravity models have higher accuracy than EGM2008 and new gravity models improve the accuracy due to data supplementation of new satellite missions.

TABLE 5 | Comparison between marine gravity models and shipboard data in the coastal region of China, unit: mGal.

Data	Min	Max	Mean	RMS	STD
V24.1 VS ship	−40.25	38.01	3.32	9.80	9.22
V27.1 VS ship	−31.24	37.66	3.51	9.59	8.93
DTU10 VS ship	−36.25	40.03	2.38	10.57	10.30
DTU13 VS ship	−36.97	41.20	2.31	10.57	10.31
EGM08 VS ship	−37.82	41.00	2.27	10.71	10.46

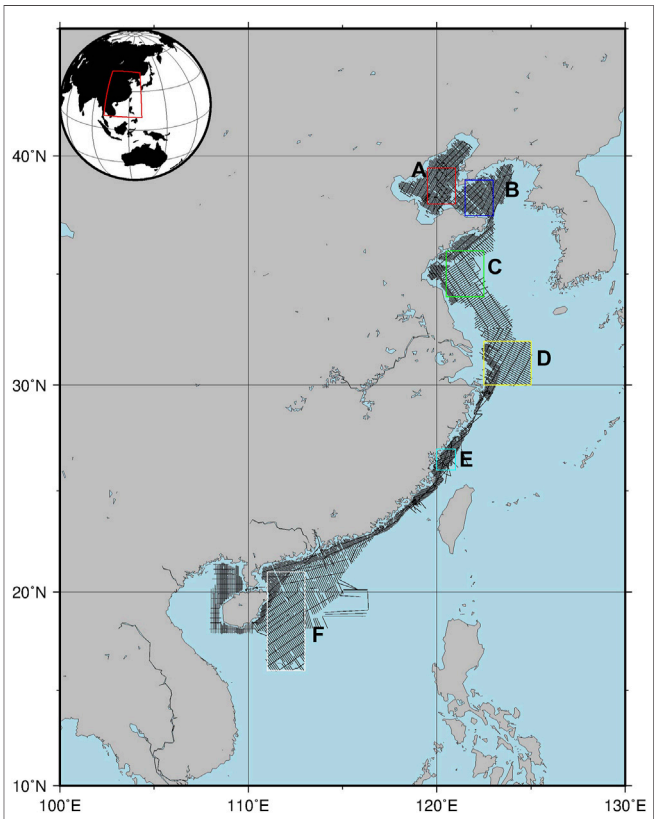

FIGURE 3 | Geographic distribution of shipboard gravity measurements from the 908 Project in the coastal regions of China. Areas A–F in different colors are selected to demonstrate the accuracies of marine gravity models in different regions.

Validation in Coastal Regions of China

Similarly, the altimetry-derived marine gravity models were compared with shipboard gravity measurements from the

TABLE 6 | Comparison between marine gravity models and shipboard data over different areas in the coastal region of China, unit: mGal.

Area	Data	Min	Max	Mean	RMS	STD
A	V24.1 VS ship	−30.95	26.95	−7.03	9.78	6.80
	V27.1 VS ship	−28.95	29.78	−6.53	9.23	6.53
	DTU10 VS ship	−36.06	40.03	−8.33	13.39	10.49
	DTU13 VS ship	−36.97	41.20	−8.40	13.53	10.61
	EGM08 VS ship	−37.82	41.00	−8.46	13.75	10.84
B	V24.1 VS ship	−30.47	17.37	−2.72	6.25	5.63
	V27.1 VS ship	−24.30	17.68	−2.54	5.77	5.18
	DTU10 VS ship	−25.29	18.56	−1.39	5.77	5.60
	DTU13 VS ship	−24.63	19.41	−1.32	5.71	5.56
	EGM08 VS ship	−24.46	19.79	−1.46	6.03	5.85
C	V24.1 VS ship	−19.17	22.51	0.09	3.15	3.14
	V27.1 VS ship	−20.22	18.75	−0.40	2.97	2.94
	DTU10 VS ship	−26.32	22.81	0.66	4.15	4.10
	DTU13 VS ship	−21.25	22.91	0.62	4.24	4.20
	EGM08 VS ship	−21.98	24.78	0.60	4.52	4.48
D	V24.1 VS ship	−14.36	38.01	13.69	14.04	3.11
	V27.1 VS ship	−10.03	37.66	13.65	13.95	2.90
	DTU10 VS ship	−22.15	36.61	13.13	13.59	3.53
	DTU13 VS ship	−21.48	36.86	13.09	13.55	3.50
	EGM08 VS ship	−22.80	36.65	13.07	13.58	3.69
E	V24.1 VS ship	−33.11	8.12	−4.51	6.31	4.41
	V27.1 VS ship	−31.24	13.80	−4.03	6.10	4.58
	DTU10 VS ship	−34.49	11.72	−4.60	7.40	5.79
	DTU13 VS ship	−34.45	11.40	−4.74	7.40	5.68
	EGM08 VS ship	−35.71	10.39	−4.83	7.59	5.85
F	V24.1 VS ship	−24.15	33.12	−0.85	3.81	3.72
	V27.1 VS ship	−24.31	31.21	−0.66	3.66	3.60
	DTU10 VS ship	−33.60	32.00	−0.10	4.81	4.81
	DTU13 VS ship	−27.97	32.00	−0.11	4.39	4.39
	EGM08 VS ship	−35.04	32.13	−0.05	5.00	5.00

China 908 Project in coastal regions of China. The statistical results are shown in **Table 5**. From that it is evident that the marine gravity models have relatively low accuracy in coastal regions of China, as the RMS difference between EGM2008 and shipboard gravity achieves 10.71 mGal. The authoritative models V24.1, V27.1, DTU10, and DTU13 have RMS differences of 9.80, 9.59, 10.57, and 10.57 mGal, respectively. This is consistent with the general understanding that satellite altimetry has poor-quality data near the coast due to the contaminated altimeter waveforms, bad tidal correction, and large sea surface variability (Wang et al., 2010).

For further analysis, six areas, A–F, are selected along the coast of China to compare marine gravity models with shipboard gravity profiles. Area A is in the Bohai Sea, China's continental sea, with a mean depth of 18 m (red rectangle in **Figure 3**). Area B is located in the northern part of the Yellow Sea, east of the Bohai Strait (blue rectangle in **Figure 3**), and area C is located in the midwestern part of the Yellow Sea (green rectangle in **Figure 3**), while the Yellow Sea is a semienclosed sea. Both the areas D (yellow rectangle in **Figure 3**) and E (cyan rectangle in **Figure 3**) are in the East China Sea; area D is near the Yangtze Estuary with a complex marine dynamic environment possibly due to river-sea interaction, and area E is near Taiwan Island. Finally, area F is located in the South China Sea, close to Hainan Island, with relatively deep water (white rectangle in **Figure 3**). The comparisons between marine gravity models and shipboard data over the above different areas are provided in **Table 6** and **Figure 4**. In **Figure 4**, the black bar is the RMS deviation between EGM2008 and shipboard gravity data in different coastal regions of China. The blue, dark green, yellow, and red bars are the RMS deviations for DTU10, DTU13, V24.1, and V27.1, respectively. From **Table 4** and **Figure 4**, EGM2008 has a larger RMS deviation than the other gravity models in almost all areas. In addition, the gravity model V27.1 has the highest accuracy among these gravity models. The reason is probably because gravity V27.1 added abundant Cryosat-2, Jason-2, and Altika data, especially the new satellite mission Altika, which functioned in Ka band, and with higher range precision, which greatly contributes to coastal ocean research.

In area A, all marine gravity models obtained dissatisfactory accuracy. The better model, V27.1, has an RMS misfit of only 9.23 mGal, while DTU13 has an RMS misfit of 13.53 mGal. This is because area A is in the Bohai Sea, an almost enclosed continental sea surrounded by land, affecting the measurement quality of satellite altimetry to a large extent. This shows that there are significant challenges to improving coastal ocean gravity field recovery by using satellite altimetry. In area B, the marine gravity models have significant improvement in accuracy, and the largest RMS misfit is 6.25 mGal for V24.1. Furthermore, the RMS deviation of V27.1 with new satellite mission Altika data improved to 5.77 mGal with respect to V24.1, which is in line with models DTU10 and DTU13. In area C, the accuracies of gravity models are further improved as the influence of land is reduced. The RMS deviation of V24.1 is only 3.15 mGal and improves to 2.97 mGal for V27.1. Gravity models DTU10, DTU13, and EGM2008 have RMS misfits of 4.15, 4.24, and 4.52 mGal, respectively.

However, in area D, the RMS misfit of gravity models is abnormally large, such as reaching 14.04 mGal for V24.1. Complex ocean dynamics may principally be responsible for this case. Area D is located near the Yangtze Estuary, with strong currents flowing through, containing the East China Sea coastal current formed by discharge from the Yangtze River and Qiantang River and the Taiwan Warm Current, a branch of the Japan Current. Altimetry-derived marine gravity models adopt different global tidal models for tide correction, which can restrain the influence of currents to a certain extent. However, tidal models have different accuracy levels in coastal areas of China and tide model errors can be potentially very large in the near-coastal zone (Stammer et al., 2014), leading to marine gravity models exhibiting errors caused by currents. Moreover, the shipboard gravity measurements from the China 908 Project do not consider ocean diversity in postdata processing. The above reasons may have resulted in a low precision over area D.

In area E, all gravity models have a relatively low precision with respect to area B. Through the analysis and comparison of the topography of the two areas, we concluded that, in addition to the influence of Taiwan Island and the mainland, the coastal currents still play an important role in precision reduction. After

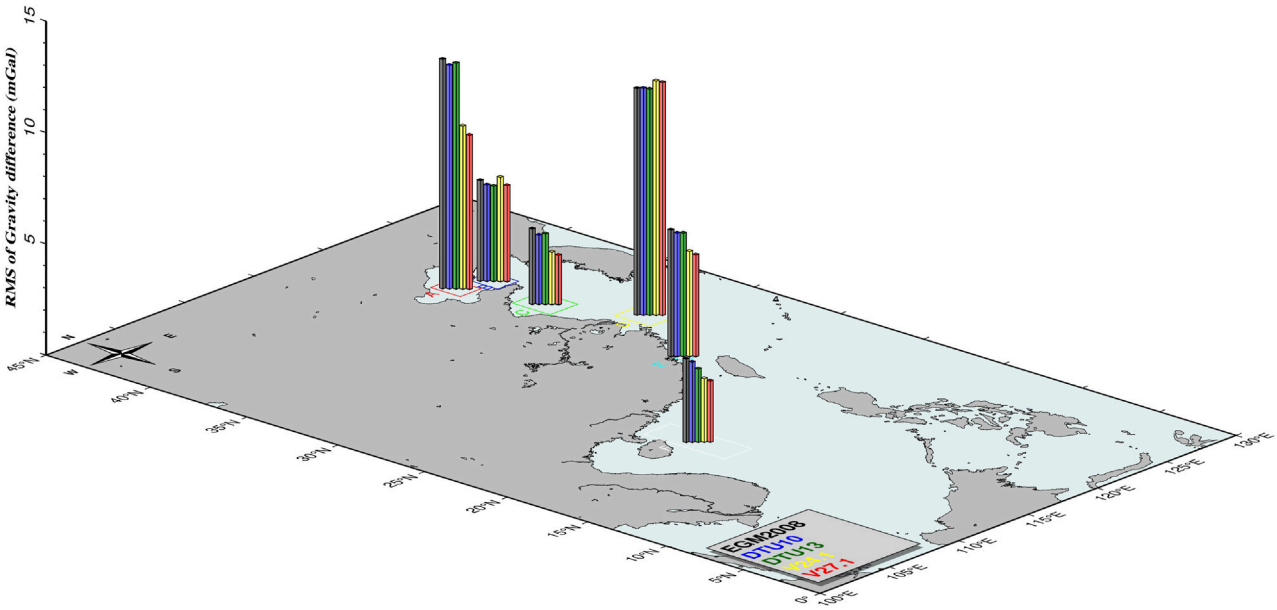

FIGURE 4 | 3D bar graph of RMSs between marine gravity models and shipboard gravity in coastal region of China. The black bar is RMS deviation between EGM2008 and shipboard gravity, and the blue, dark green, yellow, and red bar are the RMS deviation for DTU10, DTU13, V24.1, and V27.1, respectively. From north to south, the red, blue, green, yellow, cyan, and white rectangle represent the areas A–F, respectively.

all, the currents in area B are very weak. In area F, the RMS deviation is 3.81 mGal for V24.1, 3.66 mGal for V27.1, 4.81 mGal for DTU10, 4.39 mGal for DTU13, and 5.00 mGal for EGM2008, respectively.

Overall, along the coastal regions of China, the accuracies of gravity models varied greatly with region, and area C had the highest precision up to 2.97 mGal; in contrast, area D had the lowest precision of approximately 13.5 mGal. This was probably caused by a combination of surrounding topography and ocean currents, and ocean currents are a major priority. Moreover, the shipboard gravity measurements do not take the influence of currents into account, which may result in the lack of a reliable validation method in regions with strong currents. Therefore, as an external check, shipboard gravity data needs more operations to improve precision, such as higher instrument accuracy and finer data processing. Even so, these results still indicate that altimetry-derived marine gravity field models with new satellite data and advanced data processing have achieved a high accuracy level in coastal region of China.

CONCLUSION

In this paper, the methods of marine gravity determination and altimetry-derived marine gravity field recovery and the progress of satellite radar altimetry and global marine gravity field models were introduced. Typical models V24.1 and V27.1 from SIO, DTU10 and DTU13 from DTU, and EGM2008 were compared with shipboard gravity data to evaluate accuracies in offshore and coastal regions of China. The results show that the accuracies of gravity models in coastal regions are lower than those in offshore regions, and the new gravity models with new satellite missions Jason-2, Altika, and Envisat data have relatively higher accuracy, especially Altika data that brings significant improvement to coastal gravity field models. In addition, six areas are selected for further comparison and analysis, and the results show that altimetry-derived marine gravity field models with new satellite data and advanced data processing have achieved a high accuracy level. However, the accuracies are relatively low in areas with strong currents. We deduce that the reason may be related to altimetry-derived marine gravity recovery as well as shipboard gravity measurements in coastal regions. Tide correction is carried out during marine gravity model construction by using global tide models. The global tide models cannot be expected to be competitive with well-constructed local models based on high quality local bathymetric data and local tidal knowledge, whose errors can be potentially very large in the near-coastal zone (Stammer et al., 2014). On the other hand, the shipboard gravity measurements usually do not take the influence of ocean currents into account. Therefore, as an external check, shipboard gravity data need more operations to improve their precision, such as higher instrument accuracy and finer data processing.

DATA AVAILABILITY STATEMENT

The original contributions presented in the study are included in the article/Supplementary Material; further inquiries can be directed to the corresponding author.

AUTHOR CONTRIBUTIONS

LB and YW conceived the study. The data processing and the image rendering were conducted by QL. The analysis of the results was implemented by QL, LB, and YW. And the initial draft of the manuscript was written by QL with improvements and substantial edits from all authors.

FUNDING

This work is supported by the National Natural Science Foundation of China (Grant Nos. 41774022 and 41931076) and the Basic Frontier Science Research Program of Chinese Academy of Sciences (Grant No. ZDBS-LY-DQC028).

ACKNOWLEDGMENTS

The authors acknowledge David Sandwell, University of California at San Diego, and Ole Baltazar Andersen, Technical University of Denmark, for providing the radar altimeter-derived gravity models used in this study. The National Geomatics Center of China and National Centers for Environmental Information provided the shipboard gravity data in China's offshore and coastal regions.

REFERENCES

Abdalla, S., Abdeh, K. A., Adusumilli, S., Bhowmick, S., Alou, E., Amarouche, L., et al. (2021). Altimetry for the future: Building on 25 years of progress. *Adv. Space Res.* 68 (2), 319–363. doi:10.1016/j.asr.2021.01.022

Andersen, O. B., Knudsen, P., and Berry, P. A. M. (2010). The DNSC08GRA Global marine Gravity Field from Double Retracked Satellite Altimetry. *J. Geod* 84 (3), 191–199. doi:10.1007/s00190-009-0355-9

Andersen, O. B., and Knudsen, P. (1998). Global marine Gravity Field from the ERS-1 and Geosat Geodetic mission Altimetry. *J. Geophys. Res.* 103 (C4), 8129–8137. doi:10.1029/97JC02198

Andersen, O. B., Knudsen, P., Kenyon, S., Holmes, S., and Factor, J. K. (2019). "Evaluation of the Global Altimetric Marine Gravity Field DTU15: Using Marine Gravity and GOCE Satellite Gravity", in *International Symposium on Advancing Geodesy in a Changing World. International Association of Geodesy Symposia*. Editors O. B. Andersen and P. Knudsen (Cham: Springer), Vol. 149, 77–81. doi:10.1007/1345_2018_52

Andersen, O. B., Knudsen, P., Kenyon, S., and Holmes, S. (2014). "Global and Arctic Marine Gravity Field from Recent Satellite Altimetry (DTU13)", in *76th European Association of Geoscientists and Engineers Conference and Exhibition 2014: Experience the Energy - Incorporating SPE EUROPEC 2014*, 3049–3053. EAGE Publishing BV. doi:10.3997/2214-4609.20140897

Andersen, O. B., and Knudsen, P. (2019). "The DTU17 Global Marine Gravity Field: First Validation Results". in *Fiducial Reference Measurements for Altimetry. International Association of Geodesy Symposia*. Editors S. Mertikas and R. Pail, Vol. 150, 83–87. doi:10.1007/1345_2019_65

Andersen, O. B., Stenseng, L., Jain, M., and Knudsen, P. (2015). Towards the New Global Altimetric Gravity Field from Five Years of Cryosat-2 Geodetic mission Altimetry (DTU14). in EGU General Assembly 2015, Vienna, Austria, April 12–17, 2015.

Balmino, G., Moynot, B., Sarrailh, M., and Valès, N. (1987). Free Air Gravity Anomalies over the Oceans from Seasat and GEOS 3 Altimeter Data. *Eos Trans. AGU* 68, 17. doi:10.1029/EO068i002p00017

Bao, L., Xu, H., and Li, Z. (2013). Towards a 1 mGal Accuracy and 1 Min Resolution Altimetry Gravity Field. *J. Geod* 87 (10-12), 961–969. doi:10.1007/s00190-013-0660-1

Fairhead, J. D., Green, C. M., and Odegard, M. E. (2001). Satellite-derived Gravity Having an Impact on marine Exploration. *The Leading Edge* 20 (8), 873–876. doi:10.1190/1.1487298

Forsberg, R., and Olesen, A. V. (2010). *Airborne Gravity Field Determination. Sciences of Geodesy - I: Advances and Future Directions*. Berlin Heidelberg: Springer, 83–104. doi:10.1007/978-3-642-11741-1_3

Fu, L.-L., Cheng, B., and Qiu, B. (2001). 25-Day Period Large-Scale Oscillations in the Argentine Basin Revealed by the TOPEX/Poseidon Altimeter. *J. Phys. Oceanogr.* 31 (2), 506–517. doi:10.1175/1520-0485(2001)031<0506:DPLSOI>2.0

Haxby, W. F., Karner, G. D., Labrecque, J. L., and Weissel, J. K. (1983). Digital Images of Combined Oceanic and continental Data Sets and Their Use in Tectonic Studies. *Eos Trans. AGU* 64 (52), 995. doi:10.1029/EO064i052p00995

Hsu, H. T., Wang, H. Y., Lu, Y., and Wang, G. Y. (1999). GEOID UNDULATIONS AND GRAVITY ANOMALIES FROM T/P AND ERS-1 ALTIMETER DATA IN THE CHINA SEA AND VICINITY. *Chin. J. Geophys.* 42 (4), 465–471. (in Chinese with English abstract). doi:10.3321/j.issn:0001-5733.1999.04.005

Hwang, C., and Chang, E. T. Y. (2014). Seafloor Secrets Revealed. *Science* 346 (6205), 32–33. doi:10.1126/science.1260459

Hwang, C. (1998). Inverse Vening Meinesz Formula and Deflection-Geoid Formula: Applications to the Predictions of Gravity and Geoid over the South China Sea. *J. Geodesy* 72 (5), 304–312. doi:10.1007/s001900050169

Ke, B., Zhang, C., Guo, C., Wang, B., and Yang, L. (2015). System Error Correction for Shipborne Gravimetric Data from Different Regions of Offshore in China. *Geomatics Inf. Sci. Wuhan Univ.* 40 (003), 417–421. (in Chinese with English abstract). doi:10.13203/j.whugis20130299

Krarup, T. (1969). *A Contribution to the Mathematical Foundation of Physical Geodesy*. København: Geodætisk Institut. Meddelelse no. 44.

Li, J., Ning, J., Chen, J., and Chao., D. (2001). Determination of Gravity Anomalies over the South China Sea by Combination of TOPEX/Poseidon, ERS2 and Geosat Altimeter Data. *Acta Geodaetica et Cartographica Sinica* 30 (3), 197–202. (in Chinese with English abstract). doi:10.3321/j.issn:1001-1595.2001.03.003

Li, J., Ning, J., Chen, J., and Chao., D. (2003). Geoid Determination in China Sea Areas. *Acta Geodaetica et Cartographica Sinica* 32 (002), 114–119. (in Chinese with English abstract). doi:10.3321/j.issn:1001-1595.2003.02.004

Li, Q., Bao, L., and Shum, C. K. (2020). Altimeter-derived marine Gravity Variation Studies the Submarine Plate Tectonic Motions. *Chin. J. Geophys.* 63 (7), 2506–2515. (in Chinese with English abstract). doi:10.6038/cjg2020N0436

Li, Q., Bao, L., and Shum, C. K. (2021). Altimeter-derived marine Gravity Variations Reveal the Magma Mass Motions within the Subaqueous Nishinoshima Volcano, Izu-Bonin Arc, Japan. *J. Geod* 95 (5), 1–14. doi:10.1007/s00190-021-01488-7

Molodenskii, M. S., Eremeev, V. F., and Yurkina, M. I. (1962). *Methods for Study of the External Gravitational Field and Figure of the Earth*. Jurusalem: Translated from the Russian by the Israel Progr. for Sc. Transl.

Moritz, H. (1965). Schwerevorhesage und Ausgelichungsrechnung. *Z. Vermessungswesen* 90, 181–184.

Olgiati, A., Balmino, G., Sarrailh, M., and Green, C. M. (1995). Gravity Anomalies from Satellite Altimetry: Comparison between Computation via Geoid Heights and via Deflections of the Vertical. *Bull. Géodésique* 69 (4), 252–260. doi:10.1007/BF00806737

Rapp, R. (1974). *Gravity Anomaly Recovery from Satellite Altimetry Data Using Least Squares Collocation Techniques*. Dept. of Geodetic Science Report No.220. Columbus, OH: The Ohio State University.

Rapp, R. H., and Bašić, T. (1992). Oceanwide Gravity Anomalies from GEOS-3, Seasat and Geosat Altimeter Data. *Geophys. Res. Lett.* 19, 1979–1982. doi:10.1029/92GL02247

Rapp, R. H. (1979). Geos 3 Data Processing for the Recovery of Geoid Undulations and Gravity Anomalies. *J. Geophys. Res.* 84, 3784. doi:10.1029/JB084iB08p03784

Rapp, R. H., and Richard, H. (1986). Gravity Anomalies and Sea Surface Heights Derived from a Combined GEOS 3/Seasat Altimeter Data Set. *J. Geophys. Res.* 91 (B5), 4867–4876. doi:10.1029/JB091iB05p04867

Rapp, R. H. (1983). The Determination of Geoid Undulations and Gravity Anomalies from SEASAT Altimeter Data. *J. Geophys. Res.* 88, 1552–1562. doi:10.1029/JC088iC03p01552

Sandwell, D., Garcia, E., Soofi, K., Wessel, P., Chandler, M., and Smith, W. H. F. (2013). Toward 1-mGal Accuracy in Global marine Gravity from CryoSat-2, Envisat, and Jason-1. *The Leading Edge* 32, 892–899. doi:10.1190/tle32080892.1

Sandwell, D. T., Harper, H., Tozer, B., and Smith, W. H. F. (2021). Gravity Field Recovery from Geodetic Altimeter Missions. *Adv. Space Res.* 68, 1059–1072. doi:10.1016/j.asr.2019.09.011

Sandwell, D. T., Müller, R. D., Smith, W. H. F., Garcia, E., and Francis, R. (2014). New Global marine Gravity Model from CryoSat-2 and Jason-1 Reveals Buried Tectonic Structure. *Science* 346 (6205), 65–67. doi:10.1126/science.1258213

Sandwell, D. T., and Smith, W. H. F. (2009). Global marine Gravity from Retracked Geosat and ERS-1 Altimetry: Ridge Segmentation versus Spreading Rate. *J. Geophys. Res.* 114, B01411. doi:10.1029/2008JB006008

Sandwell, D. T., and Smith, W. H. F. (1997). Marine Gravity Anomaly from Geosat and ERS 1 Satellite Altimetry. *J. Geophys. Res.* 102 (B5), 10039–10054. doi:10.1029/96JB03223

Smith, G. N. (1974). *Mean Gravity Anomaly Prediction from Terrestrial Gravity Data and Satellite Altimeter Data*. Dept. of Geodetic Science Report No.214. Columbus, OH: The Ohio State University.

Stammer, D., Ray, R. D., Andersen, O. B., Arbic, B. K., Bosch, W., Carrère, L., et al. (2014). Accuracy Assessment of Global Barotropic Ocean Tide Models. *Rev. Geophys.* 52 (3), 243–282. doi:10.1002/2014RG000450

Tapley, B. D., Bettadpur, S., Ries, J. C., Thompson, P. F., and Watkins, M. M. (2004). GRACE Measurements of Mass Variability in the Earth System. *Science* 305 (5683), 503–505. doi:10.1126/science.1099192

Tscherning, C. C. (2015). "Developments in the Implementation and Use of Least-Squares Collocation," in *IAG 150 Years. International Association of Geodesy Symposia*. Editors C. Rizos and P. Willis (Cham: Springer), Vol. 143, 199–204. doi:10.1007/1345_2015_54

Wang, H., Yang, Y., Hwang, C., Chu, Y., and Ma, X. (2010). Improving Gravity Anomalies over China Marginal Sea from Retracked Geosat and ERS-1 Data. *Geo-Spatial Inf. Sci.* 13 (2), 144–149. doi:10.1007/s11806-010-0023-5

Zhang, S., and Sandwell, D. T. (2016). Retracking of SARAL/AltiKa Radar Altimetry Waveforms for Optimal Gravity Field Recovery. *Mar. Geodesy* 40 (1), 40–56. doi:10.1080/01490419.2016.1265032

Zhang, W., Zheng, W., Wu, F., Li, Z., and Liu, Z. (2020). Research Progress and prospect of Global marine Gravity Field Model. *Sci. Surv. Mapp.* 45 (No.26406), 20–34. (in Chinese with English abstract).

Conflict of Interest: The authors declare that the research was conducted in the absence of any commercial or financial relationships that could be construed as a potential conflict of interest.

frontiers in Earth Science

ORIGINAL RESEARCH
published: 25 August 2021
doi: 10.3389/feart.2021.720470

Improving the Specular Point Positioning Accuracy of Ship-Borne GNSS-R Observations in China Seas Based on Comprehensive Geophysical Correction

Fan Wu[1*†], *Wei Zheng*[1*†], *Zongqiang Liu*[1,2] *and Xuezhi Sun*[1]

[1]*Qian Xuesen Laboratory of Space Technology, China Academy of Space Technology, Beijing, China,* [2]*School of Astronautics, Nanjing University of Aeronautics and Astronautics, Nanjing, China*

OPEN ACCESS

Edited by:
Jinyun Guo,
Shandong University of Science and Technology, China

Reviewed by:
Shengjun Zhang,
Northeastern University, China
Yihao Wu,
Hohai University, China

***Correspondence:**
Fan Wu
wufan@qxslab.cn
Wei Zheng
zhengwei1@qxslab.cn

[†]*These authors have contributed equally to this work*

Specialty section:
This article was submitted to Environmental Informatics and Remote Sensing, a section of the journal Frontiers in Earth Science

Received: *04 June 2021*
Accepted: *20 July 2021*
Published: *25 August 2021*

Citation:
Wu F, Zheng W, Liu Z and Sun X (2021) Improving the Specular Point Positioning Accuracy of Ship-Borne GNSS-R Observations in China Seas Based on Comprehensive Geophysical Correction. Front. Earth Sci. 9:720470. doi: 10.3389/feart.2021.720470

The accurate modeled GNSS-R reflection delay, which is indispensable for the quantification, modeling, and correction of the GNSS-R altimetry sea-state bias, can be obtained based on the accurate modeled position of the specular point. At present, the reflection surface model of the specular point positioning still has the mean dynamic topography (MDT) error and the deviation of the vertical (DOV) error relative to the instantaneous sea surface. In this study, the following studies have been carried out. Based on the ship-borne GNSS-R observations in China seas, we introduced various elevation parameters including the MDT to correct the elevation error of the reflection surface. We introduced the DOV based on the elevation correction, and the DOV correction positioning method was proposed to correct the slope error of the reflection surface. The specular point was positioned on the instantaneous sea reflection surface. We verified the instantaneous sea reflection surface model and the specular point positioning results, analyzed the relationship between the position correction distance and the reflection incident angle, and discussed the spatial distribution characteristics of the MDT correction distance. The results showed that the reflection surface modeling and the specular point positioning were accurate. The positioning error increased to varying degrees with the increase of the reflection incident angle. The MDT correction improved the positioning by 0.91 m, and the DOV correction further improved the positioning by 0.12 m. Based on the combined application of the two kinds of correction positioning, the positioning was comprehensively improved by 0.99 m. The MDT correction of China seas gradually increased from the north to south. While in the regional sea areas, it gradually decreased from the north to south and showed randomness. The relative position between the antennas and their random changes introduced uncertainty, which can be reduced by integration. The new instantaneous sea reflection surface model and the corresponding specular point positioning method can provide accurate modeled reflection delay for the sea-state bias correction of ship-borne GNSS-R observations, and they can be extended to satellite-borne global observations.

Keywords: global navigation satellite system-reflectometry, specular point positioning, instantaneous sea reflection surface model, mean dynamic topography, deviation of the vertical, China seas, sea state bias

INTRODUCTION

GNSS-R altimetry can provide global high-coverage sea surface height (SSH) observations for research on global ocean mesoscale and sub-mesoscale processes and global climate change as an auxiliary means to traditional altimeters (Martín-Neira, 1993; Wu et al., 1998; Stammer et al., 2000; Hajj and Zuffada, 2003; Saynisch et al., 2015; Zuffada et al., 2015; Li et al., 2016; Xie et al., 2018). Due to the waves, the sea surface is rough, skewed, and rapidly changing, especially for the reflection of the GNSS signal considering the wavelength. The signal is not specularly reflected on the sea surface, which leads to the deviation of the specular point position on the reflected power waveform. This deviation introduces bias to the delay of the reflected signal relative to the direct signal, which cannot be ignored for high-precision altimetry (Hajj and Zuffada, 2003; Rius et al., 2010; Yang and Zhang, 2012). Due to the principle of GNSS-R observation and the complexity of sea surface roughness, the quantitative analysis and correction of reflection delay sea-state bias (SSB) has been one of the technical difficulties and constraints to improve the accuracy of GNSS-R altimetry. This is a key problem to be solved for highly accurate SSH retrieval in GNSS-R altimetry satellite missions (Rodriguez, 1988; Rius et al., 2010; Martín-Neira et al., 2011).

Based on the difference between the observation reflection delay and the modeled reflection delay, the SSB is expected to be quantified. The difference can be used as a prior knowledge to construct the empirical parameter model of the SSB, and thus, it can be predicted and compensated. This requires a large number of observations to suppress random errors and to obtain high coverage of the empirical model parameters. On the other hand, obtaining accurate reflection delay based on model calculation is indispensable in the quantification of the SSB. This requires correcting the specular point geometric positioning error introduced by the difference between the modeled sea surface and the instantaneous sea surface. Ship-borne observations have unique advantages for obtaining both observation delay and modeled delay. For modeled delay, the path of the direct and the reflected signals passing through the atmosphere in ship-borne scenario can be considered the same, and no additional delay is caused. The effects of hull's attitude change such as pitch and roll on observation delay and modeled delay can be considered to be the same and offset. In addition, the voyage of large research vessel (RV) is usually long and the route covers different sea areas, and this can support the study of the spatial distribution characteristics of specular point positioning correction. Based on the ship-borne GNSS-R, we conducted sea surface altimetry experiments in China seas (Gao et al., 2020) and carried out modeling and correction of delay SSB. This article focuses on the important basis for obtaining accurate modeled delay—the research on sea reflection surface modeling and specular point positioning.

The modeling of sea reflection surface has experienced the process of refinement of standard sphere, the earth ellipsoid, the geoid, and the ocean tidal surface (Wu et al., 1997; Wagner and Klokocnok, 2003; Kostelecky et al., 2005; Gleason and Gebre-Egziabher, 2009; Rius et al., 2010; Semmling et al., 2014; Jales and Unwin, 2017; Wu et al., 2019a; Wu et al., 2019b). However, the mean dynamic topography (MDT) error has not been corrected. The mean sea surface (MSS) is the average sea surface height after excluding interannual, semiannual, seasonal, and other periodic sea surface height changes over a longer period of time. The MDT is the fluctuation of the MSS relative to the geoid with a global amplitude of −2 ~2 m. The MDT is the change of sea surface height caused by the external forces of global average flow field, marine hydrological factors, atmospheric pressure, and other nontidal factors. The most important influence on the MDT is caused by the global average flow field, and its highest point is the west Pacific affected by the Kuroshio (Andersen, 2011; Liu, 2014). In this study, the ship-borne experiment's route passes through the influence area of the Taiwan warm current and the Yellow Sea warm current, tributaries of the Kuroshio. Furthermore, due to the difference of the earth's gravity field, the MSS has different slopes relative to the ellipsoid at different locations, that is, the geoid deviation of the vertical (DOV). Martín-Neira's analysis of the effect of the sea surface slope is based on the assumption that the position of the specular point remains unchanged (Martín-Neira, 1993). The resulting slope error needs to be corrected in the modeling of the sea reflection surface and the positioning of the specular point.

There are differences in the MDT of different oceans and seas. Our RV passed through the Yellow Sea, the East China Sea, and the South China Sea. These sea areas have significant sea surface topography differences (Andersen et al., 2016), which will inevitably lead to different specular point positioning corrections. Understanding the spatial distribution characteristics of the position correction distance can help develop targeted strategies of postprocessing and positioning error correction in different sea areas. This study provides a regional approach to acquire this prior knowledge, and it is expected to be extended to satellite-borne global observations.

In this study, we used ship-borne GNSS-R observations in China seas. Based on the geoid and the ocean tidal reflection surface model constructed in our previous research, we sequentially introduced the MDT and the DOV to correct the elevation error and the slope error with the corresponding specular point positioning method. The specular point is finally positioned on the instantaneous sea surface, and the positioning accuracy is improved. This study has laid the foundation for obtaining accurate modeled reflection delay and for the quantification and correction of the SSB. *Data and Model* introduces the ship-borne data and the geophysical models used, *Methodologies* introduces the reflection surface modeling and the specular point positioning methods, *Results and Discussion* discusses the results of the positioning, and *Conclusion* summarizes and prospects.

DATA AND MODEL

Ship-Borne GNSS-R Equipment and Data

We carried Xiang Yang Hong 06 RV and used GNSS-R equipment to carry out a 3-week sea surface altimetry

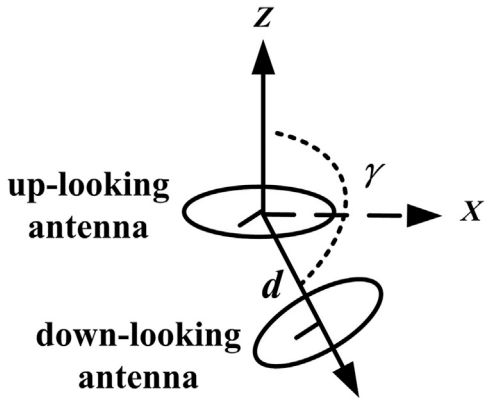

FIGURE 1 | The side-section geometry of the ship-borne GNSS-R antennas.

experiment. The route traverses most areas of China seas, including the Yellow Sea, the East China Sea, and the South China Sea. The hardware of the GNSS-R receiver system mainly included two antennas and a GNSS IF raw-data recorder. The up-looking antenna received the direct GPS/BDS signals, and the down-looking antenna received the signals reflected from the sea surface. The GNSS-R antennas are about 12 m high from the water surface. **Figure 1** shows the side-section geometry of the ship-borne GNSS-R antennas. The center line of the up-looking antenna is vertical. The down-looking antenna is installed under the direct antenna, pointing diagonally downward to the sea surface. The angle γ between the center lines of the down-looking antenna and the up-looking antenna is 150°. The distance d between the two antennas' phase centers is 0.283 m. We randomly selected 17,000 samples.

The positioning of the specular point is based on the GNSS position, the position of the GNSS-R antenna, and the reflection surface. We regarded the phase centers of the direct antenna and the reflection antenna as one same position. The position is calculated from the geodetic coordinates of the ship-borne GNSS navigation antenna combined with the relative position of the navigation antenna and the GNSS-R equipment in the hull coordinate system. The relative position of the two is calculated by their coordinates in the hull coordinate system measured by the total station. The bow direction is the ship's geodetic coordinate at the sampling time pointing to the ship's next geodetic coordinate. The GNSS position is obtained from the ephemeris file.

Geophysical Models

The instantaneous sea reflection surface model is constructed by introducing a series of geophysical parameters into the earth ellipsoid. The used geophysical models included the geoid undulation of the EGM2008 model, the ocean tidal heights of the TPXO model, and the DTU15 MDT elevations. On this basis, we introduced the DOV from the GGMPlus gravitational field to correct the sea surface slope errors.

The EGM2008 Geoid Undulation

The EGM2008 model order is up to 2,159, equivalent to a spatial resolution of about $5' \times 5'$. The commission error of the geoid undulation in the ocean area where the latitude is less than 66° is 5.8 cm. The commission error implied by EGM2008 geoid undulation. We used the highest spatial resolution product which is interpolated to a $1' \times 1'$ grid, and the difference of interpolated values from those obtained *via* harmonic synthesis does not exceed ± 1 mm (Pavlis and Saleh, 2005; Pavlis et al., 2012).

The TOPEX/POSEIDON Tidal Model (TPXO)

The TPXO tidal model has performed harmonic analysis along the track on the altimetry data of satellites and incorporates data of tide gauge and satellites in the shallow water areas. The nonlinear 1/4-period day tidal constituent has also been considered to improve the accuracy in the offshore. High-resolution regional assimilation models are developed and added to TPXO global model calculation result with a resolution of 1/6°. These regions are mainly closed and semienclosed oceans, and most of the continental parts shelve coastal areas. The resolution in China seas is 1/30°. TPXO also uses the 1′ bathymetric data in available offshore areas to improve accuracy and spatial resolution (Egbert et al., 1994; Egbert and Ray, 2000; Egbert and Erofeeva, 2002). The average deviation between TPXO and the Global Ocean Tide (GOT) Model is 0.25 cm, and the standard deviation and the RMSE are both approximately 1.5 cm (Liu, 2014). The RMSE of the main tidal constituents of TPXO in China seas is of centimeter level (Wang et al., 2010). The TPXO model is suitable for our high-resolution ship-borne experiments which were mainly carried out in offshore.

The DTU15 MDT

The DTU15 MDT is obtained from the MSS height based on the satellite data from 1993 to 2015 minus the EGM2008 geoid fluctuation, with a spatial resolution of $1' \times 1'$. In the study area, the short-wavelength residual MDT signal in the DTU15 MDT associated with EGM2008 ranges within ± 5 cm (Andersen et al., 2019). The difference between the MSS DTU15 and CNES15 models in the study area is basically within the range of ± 2 cm (Andersen et al., 2015).

The GGMplus DOV

The GGMplus model is a synthesis of GRACE and GOCE satellite gravity and EGM2008 and short-wave terrain gravity, with a spatial resolution of 0.002°, approximately 220 m. The DOV data include meridian component and prime component, and the accuracy is about one arc-second (Hirt et al., 2013).

The Ephemeris

GNSS orbital information is obtained from GNSS ephemeris files provided by the International GNSS Service (IGS) (Montenbruck et al., 2017). Unless otherwise specified, the position information used in this study is based on the ECEF WGS-84 coordinate system.

METHODOLOGIES

The modeled reflection path of GNSS-R starts from the GNSS transmitter to the specular point on the modeled reflection surface and then to the receiver's antenna. For the modeled reflection delay, the elevation and the slope of the reflection surface determine the position of the specular point and then determine the modeled reflection path. In order to obtain the modeled reflection delay without sea-state error, it is necessary to construct an ideal smooth sea surface model with the elevation and the slope close to the instantaneous sea surface at the moment and the position of the specular point. We introduced the geophysical parameters that are one order of magnitude lower than the delay SSB or more into the reflection surface modeling (see *Geophysical Models*). In the previous research, we have gradually constructed the geoid reflection surface model and the ocean tidal reflection surface model. On this basis, we further introduced the MDT and the DOV to correct the elevation and slope errors. We constructed the instantaneous sea reflection surface model and positioned the specular point on it.

MDT Correction and Positioning

The modeling of the sea reflection surface is realized in the process of specular point positioning. The specular point is initially positioned on the reference ellipsoid to obtain its initial longitude l and latitude b, and the elevation is 0 (Wu et al., 1997). In the process of transforming geodetic coordinates to space coordinates, we introduced the geophysical parameter elevation at the position and the time of the specular point (Wu et al., 2019a). The spatial coordinate of the specular point is shown in

$$\begin{bmatrix} X \\ Y \\ Z \end{bmatrix} = \begin{bmatrix} (N + H_G + H_T + H_{MDT})\cos(b)\cos(l) \\ (N + H_G + H_T + H_{MDT})\cos(b)\cos(l) \\ \left[N\left(1 - e^2\right) + H_G + H_T + H_{MDT}\right]\sin(b) \end{bmatrix} = \begin{bmatrix} N\cos(b)\cos(l) + \lambda_X + \rho_X \\ N\cos(b)\cos(l) + \lambda_Y + \rho_Y \\ N\left(1 - e^2\right)\sin(b) + \lambda_Z + \rho_Z \end{bmatrix}, \quad (1)$$

where H_G, H_T, and H_{MDT} are the geoid undulation, the ocean tidal height, and the MDT elevation of the specular point. $N = a/\sqrt{[1 - e^2\sin^2(b)]}$, where a is the long radius of the WGS-84 reference ellipsoid and e is the first eccentricity of the ellipsoid. Then, we calculated the incident angle, the emergence angle, and the geocentric angle and iterated them with weight to correct the position of the specular point (Wu et al., 1997; Wu et al., 2019a). The MDT elevation correction components ρ_X, ρ_Y, and ρ_Z of the specular reflection point in the X, Y, and Z directions at each iteration are, respectively, $H_{MDT}\cos(b)\cos(l)$, $H_{MDT}\cos(b)\sin(l)$, and $H_{MDT}\sin(b)$. And, λ_X, λ_Y, and λ_Z are the sum of the geoid and the tidal correction components. Based on the comprehensive consideration of positioning accuracy and iteration times, the iterative cutoff threshold is set to the modulo of the difference between the incident angle and the emergence angle and is less than 10^{-8} rad. When the iteration reaches this condition, the elevation correction positioning ends. The threshold is satisfied after n iteration corrections, and the total MDT correction components σ_X, σ_Y, and σ_Z are obtained as follows:

$$\begin{bmatrix} \sigma_X \\ \sigma_Y \\ \sigma_Z \end{bmatrix} = \begin{bmatrix} \sum_1^n \rho_X \\ \sum_1^n \rho_Y \\ \sum_1^n \rho_Z \end{bmatrix}. \quad (2)$$

The correction distance of the positioning accuracy of the MDT correction D_{MDT} is the distance between the specular points before and after the MDT correction, given as follows:

$$D_{MDT} = \sqrt{\sigma_X^2 + \sigma_Y^2 + \sigma_Z^2}. \quad (3)$$

DOV Correction and Positioning

The essence of the DOV correction is to use the prime component η and the meridian component ζ as the correction to correct the normal direction of the specular point successively. In the space coordinate system, we corrected the ellipsoid normal direction (x_1, y_1, z_1) to the geoid normal direction (x_2, y_2, z_2) to correct the reflection geometry and the position of the specular point. The steps are as follows:

(1) η correction: solving $|x_2'|$ and $|y_2'|$ in plane XOY.

When $\eta > 0$ and $x_1y_1 > 0$, or when $\eta < 0$ and $x_1y_1 < 0$, as shown in **Figure 2A**, there are

$$|x_2'| = |x_1|\cos(|\eta|) - |y_1|\sin(|\eta|), \quad (4)$$
$$|y_2'| = |x_1|\sin(|\eta|) + |y_1|\cos(|\eta|). \quad (5)$$

When $\eta < 0$ and $x_1y_1 > 0$, or when $\eta > 0$ and $x_1y_1 < 0$, as shown in **Figure 2B**, there are

$$|x_2'| = |y_1|\cos(|\eta|) - |x_1|\sin(|\eta|), \quad (6)$$
$$|y_2'| = |y_1|\sin(|\eta|) + |x_1|\cos(|\eta|). \quad (7)$$

(2) ζ correction: solving $|x_2|$, $|y_2|$, and $|z_2|$ in plane XOY.

When $\zeta < 0$ and $z_1 < 0$, or when $\zeta > 0$ and $z_1 > 0$, as shown in **Figure 2C**, there are

$$|Z_2| = r\cos(a + |\zeta|), \quad (8)$$
$$\alpha = \arcsin\left[(x_1, y_1, z_1)(0, 0, 1)/r\right], \quad (9)$$

where r is the modulo of the ellipsoid normal. Also,

$$r_2 = r\cos(a + |\zeta|) = r\sin(\angle\alpha)\cos(|\zeta|) + r\cos(\alpha)\sin(|\zeta|) = |z_1|\cos|\zeta| + r_1\sin|\zeta|, \quad (10)$$
$$|x_2| = (r_2/r_1)|x_2|, \quad (11)$$
$$|y_2| = (r_2/r_1)|y_2|. \quad (12)$$

When $\zeta > 0$ and $z_1 < 0$, or when $\zeta < 0$ and $z_1 > 0$, as shown in **Figure 2D**, there are

$$\beta = \pi/2 - \arcsin\left[(x_1, y_1, z_1)(0, 0, 1)/r\right], \quad (13)$$
$$|z_2| = r\cos(|\zeta| + \beta) = r\cos|\zeta|\cos(\beta) - r\sin(|\zeta|)\sin(\beta), \quad (14)$$

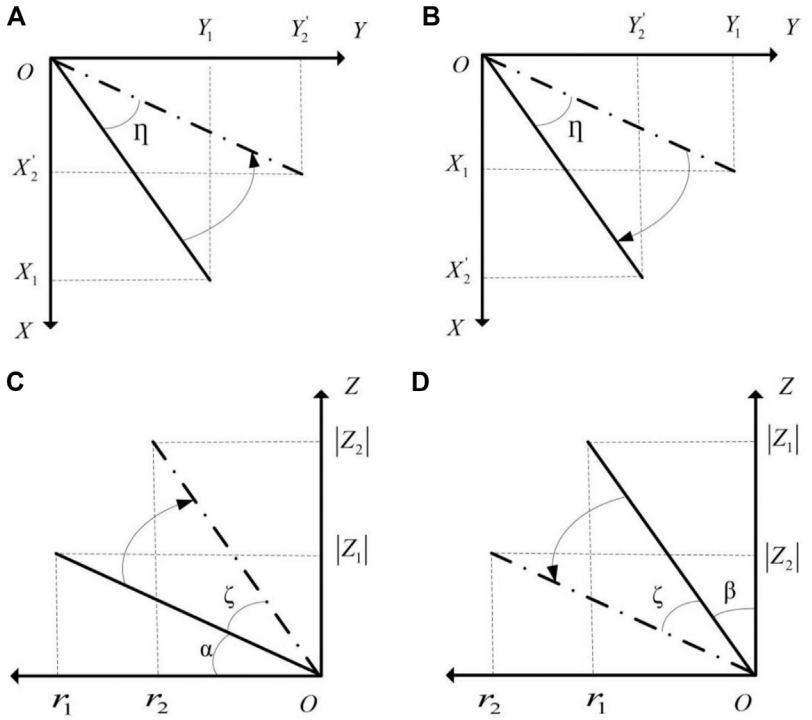

FIGURE 2 | The DOV correction geometry.

$$r_1 = r\sin(\beta), \tag{15}$$

$$r_2 = r\sin(\beta + |\zeta|) = r\sin(\beta)\cos(|\zeta|) + r\cos(\beta)\sin(|\zeta|)$$
$$= r_1\cos(|\zeta| + |z_1|\sin|\zeta|), \tag{16}$$

$$|x_2| = (r_2/r_1)(|x_2'|), \tag{17}$$

$$|y_2| = (r_2/r_1)(|y_2'|). \tag{18}$$

We obtained the geoid normal (x_2, y_2, z_2) based on the above calculation. We used the nonapproximate normal projection correction method in the following correction. By directly solving the spatial geometric relationship between the projection of the normal on the plane and the reflection path, the specular point is corrected to the vertical plane of the geoid. The positioning error caused by the radial normal difference is reduced, and the influence of approximate substitution is reduced (Wu et al., 2019a). The positioning accuracy is further improved towards normal direction.

RESULTS AND DISCUSSION

Specular Point Correction and Positioning Results

MDT Correction and Positioning

The average MDT elevation of our samples is 0.66 m, the maximum is 0.70 m, and the minimum is 0.58 m. In the space coordinate system, the correction distance is 0.91 m. The average error of the DTU15 MDT at the specular point is 2.67 cm. We calculated the difference between the specular point positions before and after adding the MDT error, and the mean value is 3.57 cm. The correction distance in the *X*, *Y*, and *Z* directions are −0.36, 0.53, and 0.18 m, respectively, and the corresponding modulus are 0.46, 0.53, and 0.39 m, respectively.

DOV Correction and Positioning

The GGMplus DOV data do not cover all the global oceans. There are 4,246 samples with DOV data. The average values of the prime components and the meridian components of the DOV are −0.0023° and 0.0012°, respectively. In the space coordinate system, the correction distance is 0.12 m. The error of the DOV model is one arc-second (Hirt et al., 2013). We calculated the difference between the positions before and after adding the one arc-second DOV error. The mean value of the difference is 1.96 cm. In the *X*, *Y*, and *Z* directions, the correction distances are −0.04, −0.03, and −0.02 m, respectively, and the moduli of the correction distance are 0.04, 0.03, and 0.04 m, respectively.

Combined Correction

We combined the MDT and DOV correction positioning, and the comprehensive positioning correction distance is the final position compared to the position without these two kinds of corrections. For the samples with the DOV data, the combined correction distance is 0.99 m in the space coordinate system. We calculated the difference between the positions of the specular points before and after adding the MDT error and the DOV error, and the mean value is 5.23 cm. In the *X*, *Y*, and *Z* directions, the

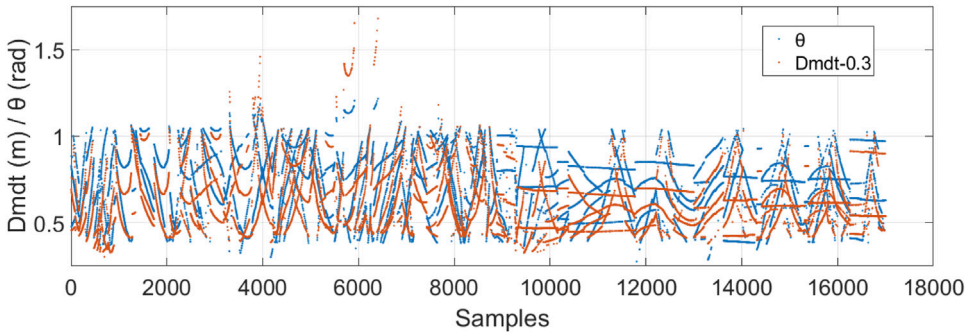

FIGURE 3 | D_{MDT} and the corresponding θ.

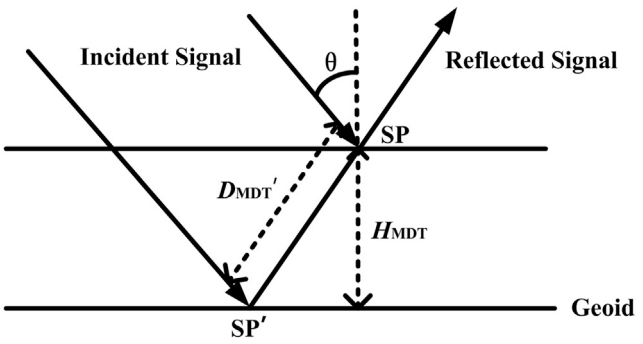

FIGURE 4 | Elevation correction geometry of the reflection surface.

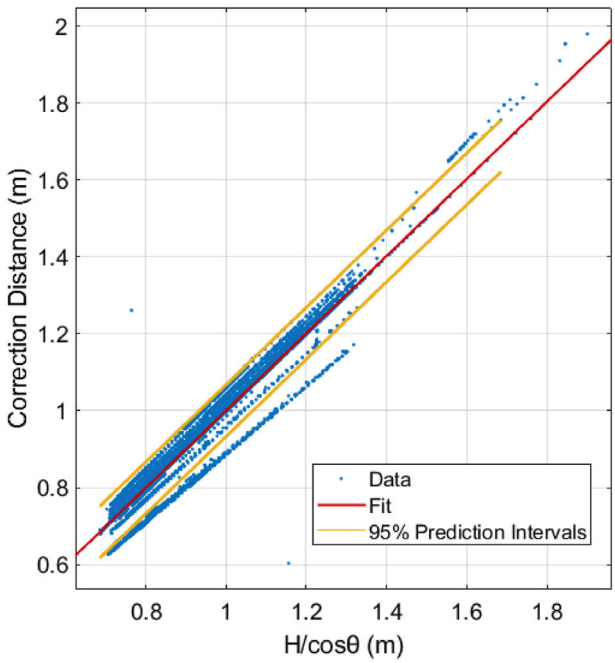

FIGURE 5 | D_{MDT}, D_{MDT}', and their fitted straight line; the *X*-axis is D_{MDT}' and the *Y*-axis is D_{MDT}.

correction distances are −0.48, 0.47, and 0.14 m, and the moduli of the correction distance are 0.57, 0.49, and 0.40 m, respectively.

Model Verification

Figure 3 shows the specular point positioning correction distance of the MDT correction D_{MDT} and the corresponding reflection incident angle θ. It can be seen that the θ of most segments changes from large to small and then to large, which is the usual process of GNSS-R equipment from being visible to invisible to a GNSS satellite. And, some of the θ changes from small to large and then to small, which is another relative motion mode. The change of D_{MDT} is very consistent with θ for almost all the segments.

In order to further verify the corrected positioning result based on the instantaneous sea reflection surface model, D_{MDT} is compared with the simulated positioning correction distance D_{MDT}'. **Figure 4** shows the elevation correction geometry of the reflection surface and we can have $D_{MDT}' = H_{MDT}/\cos\theta$. SP is the specular point before correction, and SP' is the corrected specular point. θ ranges from approximately 15° to approximately 70° in this study.

We calculated $|\Delta D_{MDT}| = |D_{MDT}' - D_{MDT}|$, and the average value is $1.09\ \text{m} \times 10^{-4}\ \text{m}$, the standard deviation is $2.29\ \text{m} \times 10^{-4}\ \text{m}$, and D_{MDT} is very close to D_{MDT}'. The correlation coefficient between D_{MDT} and D_{MDT}' is 97.66%. **Figure 5** shows the fitted straight line of D_{MDT} and D_{MDT}', the slope is 1.004 ± 0.003, SSE of the fitted straight line is 19.98, and the RMSE is 3.43×10^{-2}, which are small. The correlation does not decrease significantly with the increase of D_{MDT} or D_{MDT}'. We arranged D_{MDT} and D_{MDT}' in the ascending order of θ, and the correlation between D_{MDT} and D_{MDT}' is 99.95%. Since the two are very similar, **Figure 6** shows D_{MDT} (the blue dots) and mean $(H_{MDT})/\cos\theta$ (the red curve) in order to distinguish their trends of change. It can be seen that the changing trends of D_{MDT} and mean $(H_{MDT})/\cos\theta$ are very consistent and θ is the main influencing factor of D_{MDT}. On the far right side of Figure 6, a small number of samples have large θ, resulting in large D_{MDT}, which is consistent with the mean $(H_{MDT})/\cos\theta$ of the corresponding θ. The above results have verified the high accuracy of the MDT correction positioning.

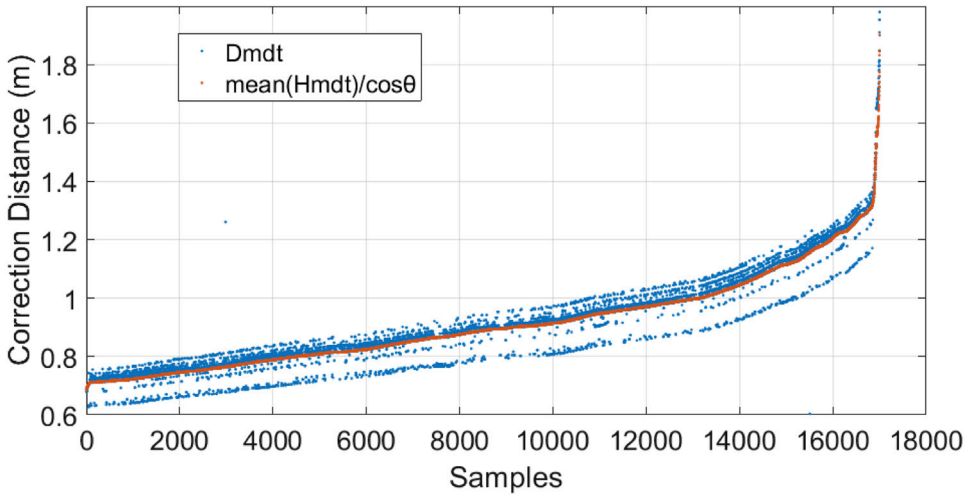

FIGURE 6 | D_{MDT} (the blue dots) and mean (H_{MDT})/cosθ arranged in the ascending order of θ.

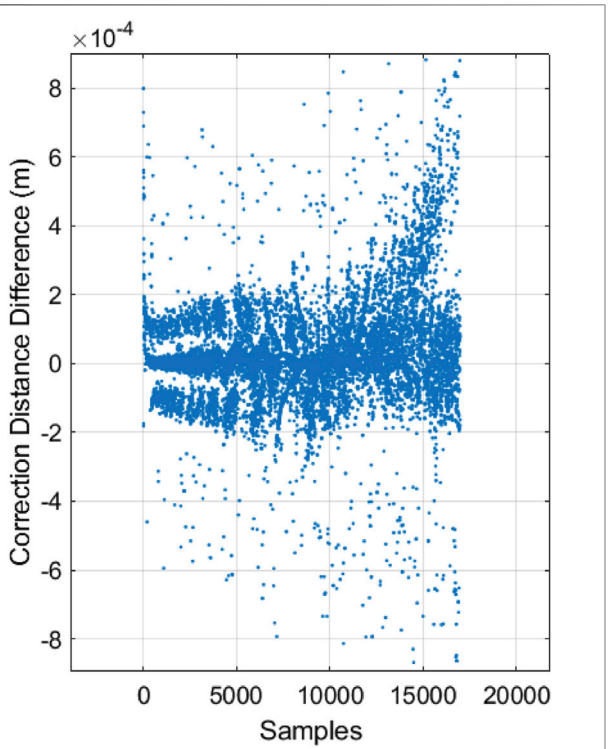

FIGURE 7 | ΔD_{MDT} arranged in the ascending order of θ.

Relationship Between the Position Correction Distance and the Reflection Incident Angle

We arranged ΔD_{MDT} in the ascending order of θ, as shown in **Figure 7**. ΔD_{MDT} is centered at 0 and has the characteristics of positive and negative symmetrical distributions. After approximately the 10,000th sample, as θ increases, ΔD_{MDT} increases. This is because as θ increases, the reflection path lengthens and hence the uncertainty introduced by the relative position between the antennas and their change increases. The symmetry feature gradually disappears after approximately the 10,000th sample; this is because large θ introduces additional increase in ΔD_{MDT}. The symmetry feature still exists after approximately the 15,000th sample, and it can be considered that this symmetrical distribution feature exists in the entire reflection incident angle range covered by the sampling. We arranged $|\Delta D_{MDT}|$ in the ascending order of θ and performed linear fitting, as shown in **Figure 8**. The trend of $|\Delta D_{MDT}|$ increases with θ. A small number of samples near the minimum and the maximum values of θ correspond to larger deviations.

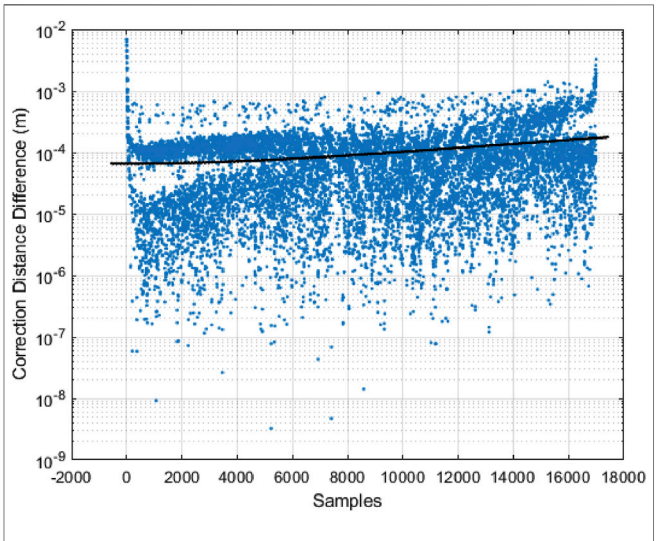

FIGURE 8 | $|\Delta D_{MDT}|$ arranged in the ascending order of θ and its linear fitting.

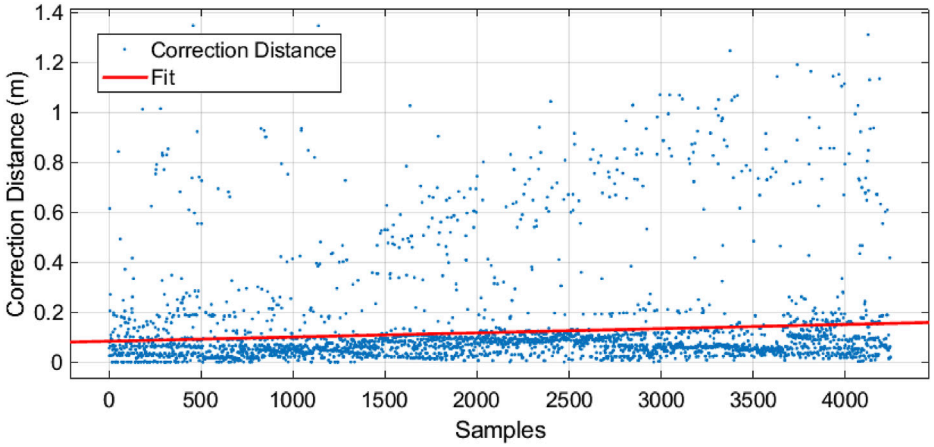

FIGURE 9 | D_{DV} arranged in the ascending order of θ and its linear fitting.

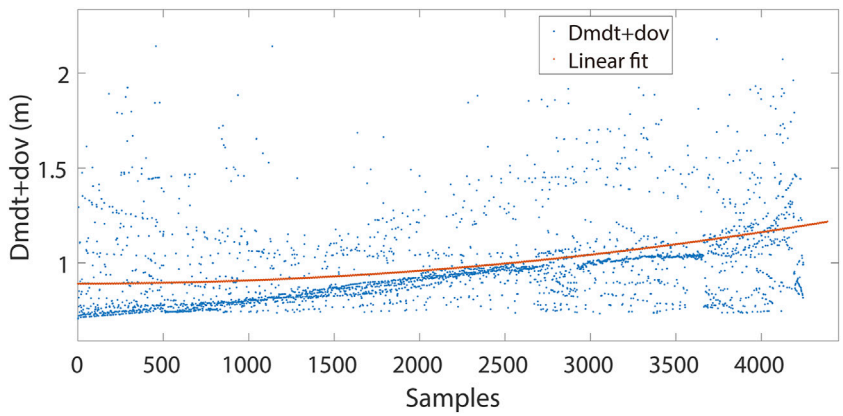

FIGURE 10 | $D_{MDT+DOV}$ arranged in the ascending order of θ and its linear fitting.

The DOV correction distance D_{DOV} is arranged in the ascending order of θ (see **Figure 9**). D_{DOV} shows an increasing trend with the increase of θ, but it is not so consistent with the change of θ like D_{MDT}. For the samples of a single track, in the incident plane, when θ increases, the increasing direction of θ is not necessarily the same as the changing direction of the normal of the incident plane. When the two directions are consistent, D_{DOV} will increase with θ; otherwise, D_{DOV} will decrease. Therefore, the change of D_{DOV} with θ has randomness. The comprehensive position correction distance $D_{MDT+DOV}$ is the distance between the specular points with and without the MDT and the DOV correction. $D_{MDT+DOV}$ is arranged in the ascending order of θ as shown in **Figure 10**. $D_{MDT+DOV}$ and θ generally have the same trend but are not completely consistent. As introduced above, the inconsistency is introduced by the randomness of D_{DOV} relative to θ.

Spatial Distribution Characteristics of the MDT Positioning Correction Distance

The H_{MDT} and D_{MDT} in China seas covered by the sampling (17°N ~ 35°N) show a gradual increase from the north to south (see **Figure 11** and **Figure 12**). For both H_{MDT} and D_{MDT}, the Yellow Sea is the lowest, the East China Sea is higher, and the South China Sea is the highest (see **Table 1**). In the two sea areas from the southern part of the Yellow Sea to the northern part of the East China Sea (32°N ~ 35°N) and the northern part of the South China Sea (17°N ~ 21°N), both H_{MDT} and D_{MDT} show a gradual decrease from the north to south. They increase near Xiamen and reach maximum in the sea area from 20°N to 21°N of the South China Sea. In the South China Sea, where the sampling coverage of latitude and longitude are both high, H_{MDT} and D_{MDT} have a tendency to gradually decrease from the northwest to southeast (away from the coast in the northwest). In the entire China seas and some regional seas, D_{MDT} is consistent with the trend of H_{MDT}.

H_{MDT} changes monotonously and smoothly in the entire China seas and the regional sea areas. Different from H_{MDT}, the partial spatial variation of D_{MDT} presents randomness. This feature is more obvious in the northern part of the South China Sea (17°N ~ 21°N) where the sampling coverage of latitudes and longitudes are both high. The randomness of the spatial distribution of D_{MDT} is due to the fact that in addition to H_{MDT}, the determinants also

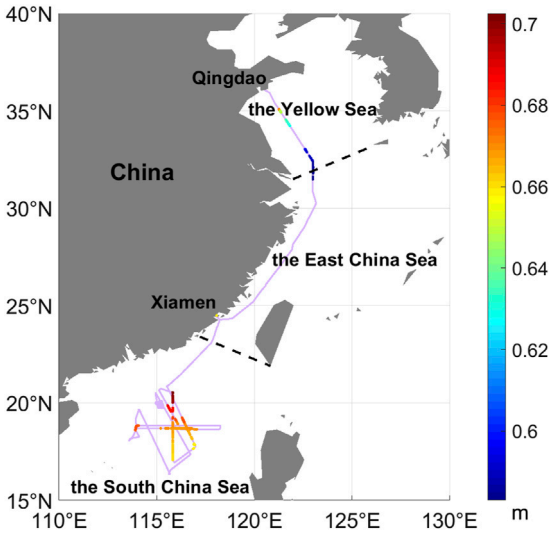

FIGURE11 | Track of Xiang Yang Hong 06 (the pink curve) and the H_{MDT} along the track.

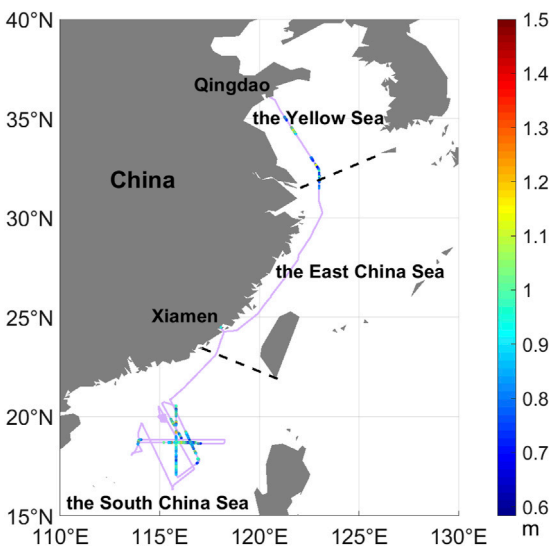

FIGURE 12 | Track of Xiang Yang Hong 06 (the pink curve) and the D_{MDT} along the track.

TABLE 1 | The average values of H_{MDT} and D_{MDT} in different sea areas in China seas.

	Mean H_{MDT} (m)	Mean D_{MDT} (m)
Yellow Sea	0.62	0.84
East China Sea	0.65	0.89
South China Sea	0.67	0.94

include the reflection incident angle, the distance between the transmitter and the specular point, and the distance between the specular point and the down-looking antenna. For a continuous sample sequence of the same GNSS satellite, the abovementioned parameters in the reflection geometry are also continuously changing, and this change will cause the D_{MDT} of the sequence to have monotonicity. The sequences with different monotonicities are intersected and connected to form the entire measurement segments along the track as shown in **Figure 12**. This makes the overall spatial variation of the segments of D_{MDT} present randomness. We believe that this feature is also present in the satellite measurement segments. In addition, there is a distance between the up-looking antenna and the down-looking antenna. The relative position of the two antennas changes with the incident plane, the incident angle, and the hull attitude. The uncertainty introduced to the model reflection geometry is estimated to be in the order of decimeters, and it introduces random errors to the correction positioning result. The impact on the MDT model near the coast may introduce errors in the correction results. In the DTU15 MDT error map, the error near Xiamen does not increase significantly compared with other parts of the study area, and the number of samples in Xiamen is small, so this will not be the main source of error.

CONCLUSION

Accurate modeled reflection delay is indispensable for quantifying and correcting GNSS-R sea-state bias. Constructing an accurate instantaneous sea reflection surface model is the key to improve the accuracy of the modeled reflection delay. The MDT and the DOV are nonnegligible errors in the reflection surface modeling and need to be corrected. Based on the geoid and the ocean-tidal reflection surface model, this study has introduced the MDT to further correct the elevation error of the reflection surface model. Then, the DOV is introduced to correct the slope error of the reflection surface model, and the corresponding specular point positioning method is proposed. The specular point is finally positioned on the instantaneous sea surface.

The MDT positioning correction distance is very consistent with the geometric simulation result, the model, and the positioning accuracy. The MDT correction improves the positioning accuracy by 0.91 m, and the DOV correction further improves the positioning accuracy by 0.12 m. Based on the combined application of the two kinds of correction, the positioning accuracy is improved by 0.99 m. The MDT correction positioning error increases with the reflection incident angle. It is presumed that the relative position between the antennas and their change introduces greater uncertainty as the reflection incident angle increases. The correlation between the DOV correction positioning error and the reflection incident angle decreased compared to the MDT correction. This is because the difference between the direction of the DOV and that of the increase in the reflection incident angle introduces randomness. The positioning correction distance by the combined application of the two kinds of correction is consistent with the overall trend of the reflection incident angle. The MDT correction distance of China seas gradually increases from the north to south, the Yellow Sea being the lowest, the East China Sea being higher, and the South China Sea being the highest. In some partial sea areas, the MDT correction distance gradually decreases from the north to south. The MDT correction distance presents randomness locally. The randomness is introduced by the intersection between measurement segments of

different GNSS satellites and the random changes of the relative position of the GNSS-R antennas. The distance between the antennas can be effectively reduced by hardware integration.

The instantaneous sea reflection surface model constructed in this study is expected to be applied to satellite GNSS-R sea surface altimetry to provide accurate modeled reflection delay for the separation, quantification, and modeling correction of sea-state bias. We hope to build a gridded global two-dimensional reflection surface model based on satellite observations, which can be directly used to position the specular points. The issues of interpolation and griding will be discussed in depth.

DATA AVAILABILITY STATEMENT

The original contributions presented in the study are included in the article/supplementary materials; further inquiries can be directed to the corresponding authors.

AUTHOR CONTRIBUTIONS

FW was responsible for the study design, data processing, scientific analysis, and manuscript writing. WZ took part in project management and manuscript modification. ZL and XS were involved in data processing. All authors contributed to the article and approved the submitted version.

FUNDING

This study was supported by the National Nature Science Foundation of China (41774014 and 41574014), the Liaoning Revitalization Talents Program (Grant XLYC2002082), the Frontier Science and Technology Innovation Project (085015) of the Central Military Commission, the Innovation Workstation Project of the Science and Technology Commission of the Central Military Commission, the Outstanding Youth Foundation of the China Academy of Space Technology, and the Independent Research and Development Start-Up Fund of Qian Xuesen Laboratory of Space Technology (Y-KC-WY-99-ZY-000-025).

ACKNOWLEDGMENTS

The ship-borne data were provided by the Institute of Space Science, Shandong University. The EGM2008 geoid undulation data is available on NGA website (http://earth-info.nga.mil/GandG/wgs84/gravitymod/egm2008/egm08_wgs84.html). The TPXO model is available on the server of Oregon State University (ftp://ftp.oce.orst.edu/pub/lana/TPXO8_atlas_30_v0/). The DTU15 model is available on the serve of National Space Institute of DTU (https://ftp.space.dtu.dk/pub/DTU15/). The GGMPlus DV data is available on the serve of Curtin University (http://ddfe.curtin.edu.au/gravitymodels/GGMplus/data/). The GNSS ephemeris is available on the IGS website (https://www.igs.org/).

REFERENCES

Andersen, B. (2011). *Range and Geophysical Corrections in Coastal Regions: And Implications for Mean Sea Surface Determination, Volume Coastal Altimetry*. Technical University of Denmark Springer, 103–146. ISBN: 978-3-642-12795-3.

Andersen, B., Stenseng, L., Piccioni, G., and Knudsen, P. (2016). *The DTU15 MSS (Mean Sea Surface) and DTU15 LAT (Lowest Astronomical Tide) Reference Surface*. Prague, Czech: ESA Living Planet Symposium.

Andersen, O. B., Knudsen, P., Kenyon, S., Holmes, S., and Factor, J. K. (2019). "Evaluation of the Global Altimetric marine Gravity Field DTU15: Using marine Gravity and GOCE Satellite Gravity," in *International Association of Geodesy Symposia*, 77–81. doi:10.1007/1345_2018_52

Andersen, O., Knudsen, P., and Stenseng, L. (2015). The DTU13 MSS (Mean Sea Surface) and MDT (Mean Dynamic Topography) from 20 Years of Satellite Altimetry. *Int. Assoc. Geodesy Symposia* 144, 111–121. doi:10.1007/1345_2015_182

Egbert, G. D., Bennett, A. F., and Foreman, M. G. G. (1994). TOPEX/Poseidon Tides Estimated Using a Global Inverse Model. *J. Geophys. Res.* 99 (C12), 24821–24852. doi:10.1029/94jc01894

Egbert, G. D., and Erofeeva, S. Y. (2002). Efficient Inverse Modeling of Barotropic Ocean Tides. *J. Atmos. Oceanic Technol.* 19 (2), 183–204. doi:10.1175/1520-0426(2002)019<0183:eimobo>2.0.co;2

Egbert, G. D., and Ray, R. D. (2000). Significant Dissipation of Tidal Energy in the Deep Ocean Inferred from Satellite Altimeter Data. *Nature* 405 (6788), 775–778. doi:10.1038/35015531

Gao, F., Xu, T., Wang, N., He, Y., and Luo, X. (2020). A Shipborne experiment Using a Dual-Antenna Reflectometry System for GPS/BDS Code Delay Measurements. *J. Geodesy* 94, 88. doi:10.1007/s00190-020-01421-4

Gleason, S., and Gebre-Egziabher, D. (2009). *GNSS Applications and Methods*. Norwood, MA, USA: Artech House, 53–71.

Hajj, G. A., and Zuffada, C. (2003). Theoretical Description of a Bistatic System for Ocean Altimetry Using the GPS Signal. *Radio Sci.* 38 (5), 1–10. doi:10.1029/2002RS002787

Hirt, C., Claessens, S., Fecher, T., Kuhn, M., Pail, R., and Rexer, M. (2013). New Ultrahigh-Resolution Picture of Earth's Gravity Field. *Geophys. Res. Lett.* 40 (16), 4279–4283. doi:10.1002/grl.50838

Jales, P., and Unwin, M. (2017). *MERRByS Product Manual—GNSS Reflectometry on TDS-1 with the SGR-ReSI*. Guildford, UK: Surrey Satellite Technology LTD.

Kostelecký, J., Klokočník, J., and Wagner, C. A. (2005). Geometry and Accuracy of Reflecting Points in Bistatic Satellite Altimetry. *J. Geodesy* 79, 421–430. doi:10.1007/s00190-005-0485-7

Li, Z., Zuffada, C., Lowe, S. T., Lee, T., and Zlotnicki, V. (2016). Analysis of GNSS-R Altimetry for Mapping Ocean Mesoscale Sea Surface Heights Using High-Resolution Model Simulations. *IEEE J. Sel. Top. Appl. Earth Observations Remote Sensing* 9 (10), 4631–4642. doi:10.1109/JSTARS.2016.2581699

Liu, Y. (2014). Calibration Technology for HY-2 Radar Atimeter Sea Surface Height. Ph.D. Thesis. Qingdao, China: Ocean University of China.

Martín-Neira, M. (1993). A Passive Reflectometry and Interferometry System (PARIS): Application to Ocean Altimetry. *ESA J.* 17, 331–355.

Martín-Neira, M., D'Addio, S., Buck, C., Floury, N., and Prieto-Cerdeira, R. (2011). The PARIS Ocean Altimeter In-Orbit Demonstrator. *IEEE Trans. Geosci. Remote Sensing* 49 (6), 2209–2237. doi:10.1109/TGRS.2010.2092431

Montenbruck, O., Steigenberger, P., Prange, L., Deng, Z., Zhao, Q., Perosanz, F., et al. (2017). The Multi-GNSS Experiment (MGEX) of the International GNSS Service (IGS) - Achievements, Prospects and Challenges. *Adv. Space Res.* 59 (7), 1671–1697. doi:10.1016/j.asr.2017.01.011

Pavlis, N. K., Holmes, S. A., Kenyon, S. C., and Factor, J. K. (2012). The Development and Evaluation of the Earth Gravitational Model 2008 (EGM2008). *J. Geophys. Res.* 117, a–n. doi:10.1029/2011JB008916

Pavlis, N. K., and Saleh, J. (2005). Error Propagation with Geographic Specificity for Very High Degree Geopotential Models. *Gravity, Geoid and Space Missions* 129, 149–154. doi:10.1007/3-540-26932-0_26

Rius, A., Cardellach, E., and Martín-Neira, M. (2010). Altimetric Analysis of the Sea-Surface GPS-Reflected Signals. *IEEE Trans. Geosci. Remote Sensing* 48 (4), 2119–2127. doi:10.1109/TGRS.2009.2036721

Rodríguez, E. (1988). Altimetry for Non-Gaussian Oceans: Height Biases and Estimation of Parameters. *J. Geophys. Res.* 93 (C11), 14107–14120. doi:10.1029/jc093ic11p14107

Saynisch, J., Semmling, M., Wickert, J., and Thomas, M. (2015). Potential of Space-Borne GNSS Reflectometry to Constrain Simulations of the Ocean Circulation. *Ocean Dyn.* 65 (11), 1441–1460. doi:10.1007/s10236-015-0886-y

Semmling, A. M., Beckheinrich, J., Wickert, J., Beyerle, G., Schön, S., Fabra, F., et al. (2014). Sea Surface Topography Retrieved from GNSS Reflectometry Phase Data of the GEOHALO Flight mission. *Geophys. Res. Lett.* 41, 954–960. doi:10.1002/2013GL058725

Stammer, D., Wunsch, C., and Ponte, R. M. (2000). De-aliasing of Global High Frequency Barotropic Motions in Altimeter Observations. *Geophys. Res. Lett.* 27 (8), 1175–1178. doi:10.1029/1999GL011263

Wagner, C., and Klokocnok, J. (2003). The Value of Ocean Reflections of GPS Signals to Enhance Satellite Altimetry: Data Distribution and Error Analysis. *J. Geodesy* 77, 128–138. doi:10.1007/s00190-002-0307-0

Wang, Y., Fang, G., Wei, Z., Wand, Y., and Wang, X. (2010). Accuracy Assessment of Global Ocean Tide Models Base on Satellite Altimetry. *J. Adv. Earth Sci.* 25 (4), 353–362. doi:10.11867/j.issn.1001-8166.2010.04.0353

Wu, F., Zheng, W., Li, Z., and Liu, Z. (2019a). Improving the GNSS-R Specular Reflection Point Positioning Accuracy Using the Gravity Field Normal Projection Reflection Reference Surface Combination Correction Method. *Remote Sensing* 11 (1), 33. doi:10.3390/rs11010033

Wu, F., Zheng, W., Li, Z., and Liu, Z. (2019b). Improving the Positioning Accuracy of Satellite-Borne GNSS-R Specular Reflection point on Sea Surface Based on the Ocean Tidal Correction Positioning Method. *Remote Sensing* 11 (13), 1626. doi:10.3390/rs11131626

Wu, S.-C., Meechan, T., and Young, L. (1997). *The Potential Use of GPS Signals as Ocean Altimetry Observation*. Santa Monica, CA, USA: the National Technical Meeting. doi:10.2118/97-05 Available at: http://hdl.handle.net/2014/21658

Wu, S. C., Romans, L. J., and Young, L. E. (1998). "A Novel GPS-Based Sensor for Ocean Altimetry," in IEEE 1998 International Geoscience and Remote Sensing Symposium (IGARSS), Seattle, WA, USA, 6-10 July 1998 (IEEE). doi:10.1109/IGARSS.1998.703723

Xie, J., Bertino, L., Cardellach, E., Semmling, M., and Wickert, J. (2018). An OSSE Evaluation of the GNSS-R Altimetry Data for the GEROS-ISS mission as a Complement to the Existing Observational Networks. *Remote Sensing Environ.* 209, 152–165. doi:10.1016/j.rse.2018.02.053

Yang, D., and Zhang, Q. (2012). *GNSS Reflected Signal Processing: Fundamentals and Applications*. Beijing, China: Publishing House of Electronics Industry. ISBN: 978-7-121-16752-2.

Zuffada, C., Li, Z., Nghiem, S. V., Lowe, S., Shah, R., Clarizia, M. P., and Cardellach, E. (2015). "The Rise of GNSS Reflectometry for Earth Remote Sensing," in IEEE 2015 International Geoscience and Remote Sensing Symposium (IGARSS), Milan, Italy, 26-31 July 2015 (IEEE), 5111–5114. doi:10.1109/IGARSS.2015.7326983

Conflict of Interest: The authors declare that the research was conducted in the absence of any commercial or financial relationships that could be construed as a potential conflict of interest.

Publisher's Note: All claims expressed in this article are solely those of the authors and do not necessarily represent those of their affiliated organizations, or those of the publisher, the editors and the reviewers. Any product that may be evaluated in this article, or claim that may be made by its manufacturer, is not guaranteed or endorsed by the publisher.

frontiers in Earth Science

ORIGINAL RESEARCH
published: 27 August 2021
doi: 10.3389/feart.2021.730565

A New GNSS-R Altimetry Algorithm Based on Machine Learning Fusion Model and Feature Optimization to Improve the Precision of Sea Surface Height Retrieval

Qiang Wang[1,2†], *Wei Zheng*[1,2,3*†], *Fan Wu*[2*†], *Aigong Xu*[1], *Huizhong Zhu*[1] and *Zongqiang Liu*[2,4]

[1]School of Geomatics, Liaoning Technical University, Fuxin, China, [2]Qian Xuesen Laboratory of Space Technology, China Academy of Space Technology, Beijing, China, [3]School of Astronautics, Taiyuan University of Technology, Jinzhong, China, [4]School of Astronautics, Nanjing University of Aeronautics and Astronautics, Nanjing, China

OPEN ACCESS

Edited by:
Jinyun Guo,
Shandong University of Science and Technology, China

Reviewed by:
Yongchao Zhu,
Hefei University of Technology, China
Konstantinos Demertzis,
International Hellenic University, Greece

***Correspondence:**
Wei Zheng
zhengwei1@qxslab.cn
Fan Wu
wufan@qxslab.cn

[†]These authors have contributed equally to this work

Specialty section:
This article was submitted to Environmental Informatics and Remote Sensing, a section of the journal Frontiers in Earth Science

Received: 25 June 2021
Accepted: 16 August 2021
Published: 27 August 2021

Citation:
Wang Q, Zheng W, Wu F, Xu A, Zhu H and Liu Z (2021) A New GNSS-R Altimetry Algorithm Based on Machine Learning Fusion Model and Feature Optimization to Improve the Precision of Sea Surface Height Retrieval. Front. Earth Sci. 9:730565. doi: 10.3389/feart.2021.730565

The global navigation satellite system reflectometer (GNSS-R) can improve the observation and inversion of mesoscale by increasing the spatial coverage of ocean surface observations. The traditional retracking method is an empirical model with lower accuracy and condenses the Delay-Doppler Map information to a single scalar metric cannot completely represent the sea surface height (SSH) information. Firstly, to use multi-dimensional inputs for SSH retrieval, this paper constructs a new machine learning weighted average fusion feature extraction method based on the machine learning fusion model and feature extraction, which takes airborne delay waveform (DW) data as input and SSH as output. R^2-Ranking method is used for weighted fusion, and the weights are distributed by the coefficient of determination of cross validation on the training set. Moreover, based on the airborne delay waveform data set, three features that are sensitive to the height of the sea surface are constructed, including the delay of the 70% peak correlation power (PCP70), the waveform leading edge peak first derivative (PFD), and the leading edge slope (LES). The effect of feature sets with varying levels of information details are analyzed as well. Secondly, the global average sea surface DTU15, which has been corrected by tides, is used to verify the reliability of the new machine learning weighted average fusion feature extraction method. The results show that the best retrieval performance can be obtained by using DW, PCP70 and PFD features. Compared with the DTU15 model, the root mean square error is about 0.23 m, and the correlation coefficient is about 0.75. Thirdly, the retrieval performance of the new machine learning weighted average fusion feature extraction method and the traditional single-point re-tracking method are compared and analyzed. The results show that the new machine learning weighted average fusion feature extraction method can effectively improve the precision of SSH retrieval, in which the mean absolute error is reduced by 63.1 and 59.2% respectively, and the root mean square error is reduced by 63.3 and 61.8% respectively; The correlation coefficient increased by 31.6 and 44.2% respectively. This

method will provide the theoretical method support for the future GNSS-R SSH altimetry verification satellite.

Keywords: GNSS-r altimetry, machine learning, wave retracking, sea surface height inversion, feature engineering, model fusion

INTRODUCTION

Sea Surface Height (SSH), as an important ocean parameter, plays an important role in establishing global ocean tide models, observing large-scale ocean circulation, and monitoring global sea level changes (Zhang et al., 2020). Traditional spaceborne mono-static radar altimeters obtain marine physical parameter information by continuously transmitting radar pulses to the earth and receiving sea surface echoes, which have the disadvantages of low coverage, long repetition period, and high cost (Bosch et al., 2014; Zawadzki and Ablain 2016; Wang et al., 2021b). GNSS-R technology is an emerging remote sensing technology in sea surface altimetry in recent years. It is used to retrieve the sea surface height by measuring the time delay between the reflected signal and the direct signal. In 1993, the concept of Passive reflectometry and interferometry system was initially proposed by Martin-Neira, proving the capability of GNSS-R to ocean altimetry (Martin-Neira 1993). GNSS-R offers several advantages over mono-static radar systems including multiple measurements over a large area, reduced cost, reduced power consumption, all-weather and highly real-time (Mashburn et al., 2020). At present, this technology has been used for the detection of sea surface height (Mashburn et al., 2016; Mashburn et al. 2018; Mashburn et al. 2020), sea surface wind speed (Ruf et al., 2015; Li et al., 2021), sea ice (Alonso-Arroyo et al., 2017; Li et al., 2017), soil moisture (Yan et al., 2019) and other parameters.

In recent years, the successful launch of TechDemoSat-1 (TDS-1) (Mashburn et al., 2018; Xu et al., 2019), cyclone global navigation satellite system (CYGNSS) (Mashburn et al., 2020) and BuFeng-1(BF-1) A/B twin satellites (Jing et al., 2019) means that GNSS-R technology has stepped into a new stage of detecting global surface parameters. As a passive remote sensing satellite-borne, GNSS-R has great prospects in the field of sea surface altimetry. However, the spaceborne GNSS-R receivers launched in the world have not dedicated for altimetry measuring purpose, which limits its high-precision research. The airborne altimetry technology is considered as a pre-research technology of spaceborne altimetry, which is being widely studied (Bai et al., 2015). According to different antenna devices, GNSS-R height measurement can be divided into a single-antenna-based auto-correlation mode and a dual-antenna-based cross-correlation interference mode. Compared with the auto-correlation mode, the interference mode does not have strict requirements on the height of the observation platform and has a wider range of application scenarios (Wang et al., 2021a). Cardellach et al. (2014) analyzed the GNSS-R airborne experimental data of CSIC-IEEC over the Finnish Baltic Sea in 2011. Both theoretical and experimental results show that the measurement accuracy of the cross-correlation interference mode is higher than that of the CA code auto-correlation mode. Based on the airborne experimental data of Monterey Bay, Mashburn et al. (2016) analyzed the measurement accuracy of three retracing methods: HALF, DER and PARA3. The results show that the HALF method produces the most precise measurements, and the biases is 1–4 m compared with the DTU13. Wang et al. (2021a) used the airborne altimetry data collected by CSIC-IEEC in the Baltic Sea on December 3, 2015 to retrieve the sea surface height. Compared to the high computational complexity of Z-V model fitting, the 7-β model is proposed to compute the delay between direct and reflected GNSS signal (Wang et al., 2021a). In previous studies, retracking methods such as HALF, DER, and FIT are usually used for GNSS-R altimetry. By analyzing the various errors involved in the inversion model, the corresponding error model is established to improve accuracy (Mashburn et al., 2016). The traditional retracking method is an empirical model for long-term observation of the sea surface, which often relies on limited scalar delay Doppler (DDM) observations. Only a part of DDM information can be used to retrieve SSH (D'Addio et al., 2014), which affects the accuracy of height estimation. Moreover, the establishment of various error models makes the inversion model more complex and difficult to realize (Mashburn et al., 2018).

Compared with the previous inversion model, the algorithm of machine learning model is easy to build, which can establish the mapping relationship between multiple observations and sea surface height. Meanwhile, the machine learning can make full use of the physical quantities related to SSH, which partly compensating the deficiency of traditional inversion methods. Machine Learning (ML) is one of the fastest growing scientific fields today, which integrates many disciplines such as computer science and statistics, is used to solve the problem of how to automatically build a calculation model through experience (Lary et al., 2016). Now machine learning algorithms have been gradually integrated into GNSS-R field and achieved excellent results. Luo et al. used the tree model algorithm in machine learning to establish a mapping model from the TDS-1 (TechDemoSat-1) observation data to the European Centre for Medium-Range Weather Foresting (ECMWF) analysis field data. The results obtained are significantly better than that of traditional GNSS-R wind speed retrieval methods (Luo et al., 2020). Liu et al. (2019) proposed the multi-hidden layer neural network (MHL-NN) for GNSS-R wind speed retrieval. The effect of DDM average, leading edge slope and incident angle features are analyzed by using simulated data and real data (Liu et al., 2019). Jia et al. (2019) used XGBoost algorithm and GNSS-R technology to retrieve soil moisture and evaluated the importance of input features such as altitude angle, signal-to-noise ratio, and receiver gain for soil moisture retrieval models.

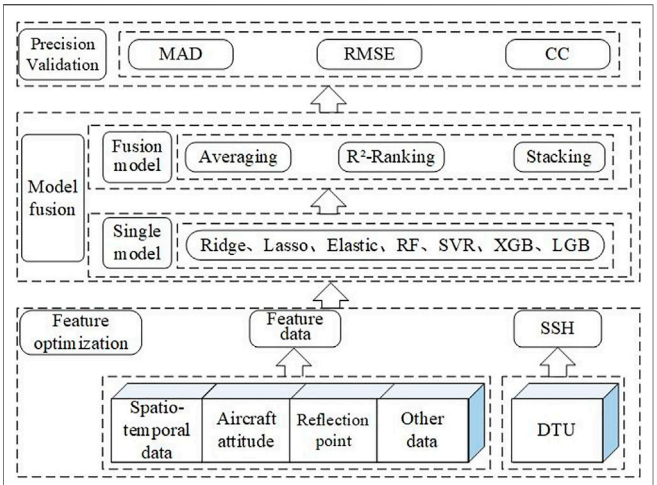

FIGURE 1 | Framework of airborne GNSS-R sea surface height retrieval.

Different from previous studies, this paper introduces the machine learning fusion model to assist GNSS-R for SSH retrieval. And the accuracy of sea surface altimetry can be improved by increasing the available information of DDM. The essence of SSH retrieval based on machine learning is a nonlinear regression problem of supervised learning. This paper first evaluates the SSH retrieval performance of regression methods commonly used in machine learning, such as linear regression model {Lasso regression (Zou 2006), Ridge regression (Hoerl and Kennard 2000), Support Vector Machine regression (Keerthi et al., 2014) (SVR) and ensembled tree regression model [XGBoost (Luo et al., 2020), LightGBM (Luo et al., 2020), Random Forests (Liu et al., 2020)]}. On this basis, Random Forests, XGBoost and Ridge models with better SSH retrieval performance and lower correlation are used for model fusion, which further improve the SSH retrieval accuracy. The fusion method adopts the R^2-Ranking method for weighted fusion, and the weights are distributed by the coefficient of determination of cross validation on the training set. In addition, to obtain a feature set that is more suitable for the SSH retrieval model, the feature construction method is used to construct three features, namely PFD, PCP70, and LES, which are sensitive to SSH changes. The effect of feature sets with varying levels of information details are analyzed as well. Two conventional single-point retracking algorithms, HALF and DER, are also implemented and their retrieval results are compared with the proposed new machine learning weighted average fusion and feature extraction method.

CONSTRUCTION OF A NEW MACHINE LEARNING WEIGHTED AVERAGE FUSION FEATURE EXTRACTION METHOD

Using machine learning algorithm to build sea surface height prediction model is a supervised learning regression problem essentially, that is, using the labeled altimetry data set as the training set to train the model, observing the performance of the trained model on the test set to optimize the model, and finally realizing the prediction of unknown data. As shown in **Figure 1**, the new machine learning weighted average fusion feature extraction method is mainly composed of feature optimization, model fusion and accuracy verification. Feature optimization refers to the use of feature engineering methods to filter and construct features related to mean sea surface (DTU) from the original airborne delay waveform (DW) data set. Model fusion mainly includes two parts, the optimization of the learner and the model fusion. First, the main machine learning regression algorithms such as Lasso, Ridge, SVR, XGB, LGB, and RF are used to invert the sea surface height. On this basis, to further improve the high inversion accuracy of the model, a single model with higher accuracy and lower correlation is selected for model fusion using three model fusion methods: Averaging, R2-Ranking, and Stacking. Precision validation is to evaluate the effectiveness of the model through Mean Absolute Difference (MAD), Root Mean Square Error (RMSE) and Pearson Correlation Coefficient (CC).

Feature Optimization

Feature optimization refers to the process of extracting features from the raw data, which can describe the data better and the performance of the model built with this feature on the unknown data can reach the best (Kim et al., 2019). In numerical data tasks, the importance of feature engineering is particularly prominent. The better the features, the greater the flexibility, and the simpler the model is, the better the performance is. Feature missing or feature redundancy will seriously affect the accuracy of the model. Due to the problems of large feature dimension, high redundancy, strong correlation between adjacent features, the poor correlation between features and the DTU15 model value, in airborne DW data. In this paper the features of airborne DW data are optimized by the methods of feature selection, feature extraction, and feature construction.

1) Feature selection: By eliminating irrelevant or redundant features, the model training time can be reduced, and the accuracy of the model can be improved. The airborne DW data is a set of high-dimensional data. It contains a lot of redundant data and unrelated features for the DTU15 model. Therefore, use the Pearson correlation coefficient method to filter the data set, and the features with correlation coefficient less than 0.1 of DTU15 are removed (Rodgers and Nicewander 1988).
2) Feature extraction: According to the high-dimensional characteristics of airborne data, principal component analysis (PCA) method is used to extract the main feature components of airborne data. PCA is a commonly used data analysis method, which transforms the original data into a group of linear independent representations of each dimension by linear transformation. It can best integrate and simplify the high-dimensional variable system based on retaining the original data information to the maximum extent, and more centrally and typically reflects the characteristics of the research object. The feature values with a cumulative contribution rate of 98% are extracted from the airborne data as training data for machine learning.

3) Feature construction: Feature construction refers to the artificial creation of new feature methods that are beneficial to model training and have certain engineering significance by analyzing raw data samples, combining practical experience of machine learning and professional knowledge in related fields. Therefore, to extract features that contain enough information, three features sensitive to SSH changes, PCP70, PFD, and LES, are constructed on the basis of the raw airborne DW data to improve the accuracy of the altimetry model. The PCP70 and PFD features are calculated from two retracking methods commonly used in GNSS-R SSH retrieval (Park et al., 2013; Clarizia et al., 2016), which can effectively reflect the changes in SSH. Leading Edge Slope (LES) is a feature that has a high correlation with sea surface roughness (Liu et al., 2019). The corresponding definition is as follows:

1) PCP70: This feature has been derived from traditional retracking methods taking the specular reflection delay at 70% of the peak correlation power. The peak correlation power is defined as (Mashburn et al., 2016):

$$\tau_{spec} = \arg\max_{\tau} \{W(\tau)\} \tag{1}$$

where, $\tau$is the time delay; $W(\tau)$is the power delay waveform related to the reflected signal.

2) PFD This feature also has been derived from traditional retracking methods taking the specular reflection delay from the maximum first derivative on the waveform leading edge. The waveform leading edge peak first derivative is defined as (Mashburn et al., 2016):

$$\tau_{spec} = \arg\max_{\tau} \left\{ \frac{dW(\tau)}{d\tau} \right\} \tag{2}$$

3) LES is often used to retrieve the effective wave height changes of ocean surface. Use the best fitted linear function slope as the leading-edge slope of the time-delayed waveform (Liu et al., 2019):

$$LES = \arg\min_{ac} \left\{ \sum_{k=1}^{2} [I(\tau k) - (\alpha \tau k + c)]^2 \right\} \tag{3}$$

4) Division of feature set: to select features that are sensitive to the sea surface height, a total of six sets of feature sets with different information details are used for model training, and their accuracy is verified on the test set, namely: Feature Set1: Use DW data only. Feature Set2: Use DW data and PCP70 features. Feature Set3: Use DW data and PFD features. Feature Set4: Use DW data and LES features. Feature Set5: Use DW data and PCP70 and PFD features. Feature Set6: Use DW data and PCP70,PFD, LES features.

Model Fusion

Model fusion is mainly divided into three parts: a single model selection and training, model hyperparameter optimization and model fusion. Single model training is mainly used for model screening and hyperparameter optimization. Model fusion refers to the use of different model fusion methods to integrate the advantages of individual learners which can achieve the goal of reducing prediction errors and optimizing overall model performance. Training process uses the five-fold cross-validation method and optimizes hyper-parameters through grid search.

TABLE 1 | Summary table of learner optimization parameters.

Learner	Optimal parameters
Lasso	L1Regularization coefficient: req_alpha
Ridge	L2Regularization coefficient: req_lambda
ElasticNet	L1Regularization coefficient: req_alpha L2Regularization coefficient: req_lambda
SVR	Penalty parameter: C
GBDT	Maximum depth of decision tree: max_depth、 Optimal number of learners: n_estimators Minimum number of samples: min_samples_split
XGBoost	Maximum depth of decision tree: max_depth、 Optimal number of learners: n_estimators
LightGBM	Optimal number of learners: n_estimators Maximum depth of decision tree: max_depth
RF	Maximum feature number of decision tree: max_features Optimal number of learners: n_estimators Minimum number of samples: min_samples_split

Selection and Training of a Single Model

The SSH retrieval mainly uses the supervised learning regression method in machine learning, and the learners in the regression method can be divided into non-integrated learners and integrated learners. This paper mainly selected Lasso Regression, Ridge Regression, ElasticNet Regression (Zeng 2020), Support Vector Regression (SVR), as the non-integrated learner, and selected Gradient Boosting Decision Tree (GBDT) (Friedman 2001), Extreme Gradient Boosting (XGBoost), Light Gradient Boosting Machine (LightGBM) and Random Forests (RF) ensembled tree model based on bagging integration thoughts (Breiman, 1996) as ensembled learner to retrieve SSH.

Model Hyper-Parameter Optimization

Hyper-parameter optimization is the key to model training. The performance of the trained model mainly depends on the algorithm of the model and the selection of hyper-parameters. A set of optimal hyper-parameters can make the trained model obtain better performance based on the inherent algorithm. In this paper, Grid search (GS) and K-fold cross validation are used to optimize the hyperparameters of each model.

K-Fold Cross Validation (CV) (Zeng 2020) is a method to continuously verify the performance of models. The basic idea is to divide the original data into K groups randomly, and make a validation set for each subset. The rest of K-1 subset as training set. K models will be obtained in this way. The final prediction performance in the validation set is averaged as the performance index of the K-fold cross-validation classifier. In this paper, we choose K = 5 (Jung 2018), that is, we use five-fold cross-validation cross to verify the model.

Grid search (GS) (Lavalle et al., 2004) is an exhaustive search method for tuning parameters. In the selection of all candidate parameters, every possibility is tried through loop traversal. The set of hyper-parameters with the highest model score is the optimal hyper-parameter. The optimization parameters of each model are shown in **Table 1** (Zeng 2020):

Model Fusion

Each machine learning algorithm has its own advantages and disadvantages, so it is difficult to fully mine the information in DW data using a single model. Model fusion refers to obtain a new model by combining the results of multiple independent learners. The purpose of model fusion is to break through the limitations of the single machine learning algorithm. Through fusion, the effect of "complementing each other's weaknesses" can be achieved. Combining the advantages of individual learners can reduce prediction errors and optimize integrated model performance. At the same time, the higher the accuracy and diversity of individual learners, the better the effect of model fusion. This paper uses three model fusion methods: Averaging, R^2-Ranking and Stacking for comparative experiments. Averaging and R^2-Ranking only merge the results of multiple models, while Stacking needs to use the sub-learner to learn the results of multiple models.

1) Averaging

The output of Average model fusion method is the simple average result of each learner (Liu et al., 2020).

2) R^2-Ranking

R^2-Ranking is a weighted average model fusion method based on the cross-validation error improvement of the learner on the training set, which is proposed in this paper. The weight is assigned by the coefficient of determination (R^2) on the training set. R^2 is a commonly used performance evaluation index in machine learning regression models, which reflects the fitting degree of the model to the input data. The closer R^2 is to 1, the better the fitting degree is. R^2-Ranking believes that under the premise of no fitting, the greater the coefficient of determination of cross-validation on the training set, the better the effect of the learner, so more weight is given. The specific calculation formula is as follows:

$$W_i = \frac{R_i^2}{\sum_{i=1}^{N} R_i^2} \tag{4}$$

$$H(x) = \sum_{i=1}^{N} W_i ML\_model_i(Featuere\_set) \tag{5}$$

Here, $H(x)$is the output result of the fusion model, ML_model_i is the different machine learning models, *Featuere_set* is the feature set divided in *Feature Optimization* Section, W_i is the weight of different machine learning models, R_i^2 is the coefficient of determination of each model on the training set, defined as (Zeng 2020):

$$R^2 = 1 - \frac{\left(T_{predict} - T_{mean}\right)^2}{\left(A - T_{predict}\right)^2} \tag{6}$$

where T is the prediction sequence of the model, T_{mean} is the sample mean, A is the SSH value verification sequence provided by the corresponding DTU15 model.

3) Stacking

Stacking is a hierarchical model integration framework. Take two layers as an example: the first layer is composed of multiple base learners whose input is the original training set; the second layer model is trained with the output of the first level basic learner as the training set, so as to obtain a complete Stacking model (Liu et al., 2020). All the training data are used in the two-layer stacking model. This paper uses the stacking model fusion method of five-fold cross-validation, and the construction process is shown in **Figure 2**:

1) Firstly, the data is divided into training set and test set, and the training set is divided into five parts: train1 ~5
2) Select the base model: selecting Model1, Model2, and Model3 as the base learners. In Model 1, train1, train2, train3, train4, and train5 are used as the verification set in turn, and the remaining four are used as the training set. Then the model is trained by 5-fold cross-validation, and the prediction is made on the test set. In this way, 5 predictions trained by the XGBoost model on the training set and 1 prediction B1 on the test set will be obtained, and then the 5 predictions will be vertically overlapped and merged to obtain A1. The Model 2 model and the Model 3 model are partially the same.
3) Select the sub-learner: after the training of the three basic models, the predicted values of the three models in the training set are taken as three "features" A1, A2 and A3 respectively, and then use the sub-learner model to train and build the model.
4) Using the trained sub-learner model predict the "feature" values (B1, B2, and B3) obtained on the test sets of the three base models, and the final prediction category or probability is obtained.

Precision Evaluation

The prediction result is compared with the sea surface height SSH provided by the DTU15 validation model, using Mean Absolute Difference (MAD), Root Mean Square Error (RMSE) and Pearson Correlation Coefficient (CC) (Garrison, 2016) evaluate the effectiveness of the model. It shows: the smaller the MAD and RMSE values are, the better the fitting degree between the predicted value and the real value is, and the smaller the error is; The closer CC is to 1, the better correlation between inversion results and DTU15 model is. The corresponding definition is (Liu et al., 2020; Zeng 2020):

$$MAD = \frac{1}{n}\sum_{i=1}^{n} |Ti - Ai| \tag{7}$$

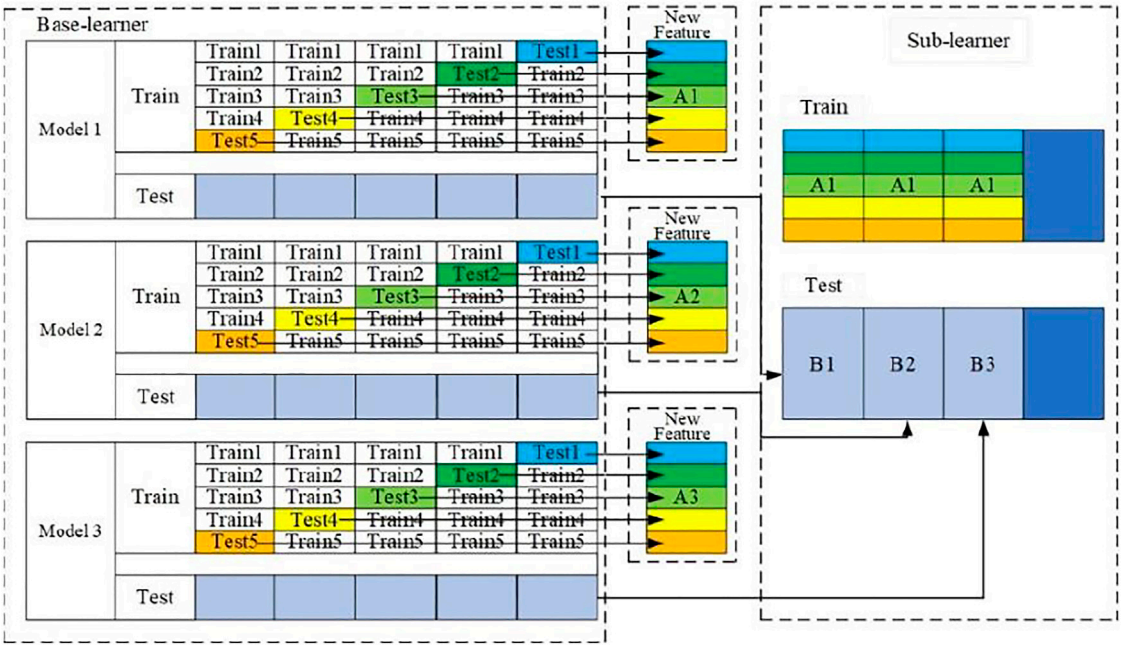

FIGURE 2 | Schematic diagram of five fold cross-validation stacking model fusion.

$$RMSE = \sqrt{\frac{1}{n} \times \sum_{i=1}^{n} (Ti - Ai)^2} \tag{8}$$

$$CC = \frac{\mathrm{Cov}(T, A)}{\sigma_T \sigma_A} \tag{9}$$

Where T is the prediction sequence of the model, where A is the SSH value verification sequence provided by the corresponding DTU15 model. Here T_i is the predicted value of the model; A_i represents the validation of the corresponding DTU15 model; n is the number of predicted values. Here$\mathrm{Cov}(T, A)$is the covariance between the predicted value and the verified value; σ_T and σ_A represent the variance of the predicted and true values, respectively.

VERIFICATION OF NEW MACHINE LEARNING WEIGHTED AVERAGE FUSION FEATURE EXTRACTION METHOD

Data Sets

Delay Waveform Data

The airborne time delay waveform data which from the airborne experiment was carried out by the IEEC of Spain on December 3, 2015 in the Baltic Sea. As the Baltic Sea is surrounded by land, it is not affected by the strong North sea tide. Under the condition of no strong wind, the sea surface is relatively stable (Wang et al., 2021a). During the experiment, there was no strong wind in the experimental area, and the sea surface was relatively stable. The direct and reflected GNSS signals were received by the 8-element antenna of RHCP (Right Handled Circular Polarization) on the top and LHCP (Left HCP) on the abdomen of the aircraft respectively, and then down converted to IF signal in 19.42 MHz by RF module for 1-bit quantization and storage. The Delay waveform (DW) data was obtained by cross-correlation interference between GPS direct signals and sea surface reflection signals (Serni et al., 2017).

As shown in **Figure 3**, the flight consisted in a set of passes between two pairs of waypoints (AD and EF). Their location was selected to have two straight flight trajectory intervals: parallel (AD) and perpendicular (EF) to the ellipsoidal height gradient of the sea surface. The flight path consisted in two perpendicular trajectories, which were travelled in both senses (A-to-D, D-to-A, E-to-F, and F-to-E). During all of them, the nominal height of the receiver was around 3 km. **Table 2** provides the most relevant information about the different flight segments and the time reference system is GPS second of the day (SoD).

In this study, 20 min of GPS L1 band observation data from 10: 52:42 to 11:21:41 on December 3, 2015 were used. To avoid the influence of aircraft steering, the data of aircraft steering is removed. Only the data of aircraft flying along a straight line is selected as the experimental analysis. Since the E-F segment is too short to be suitable for machine learning model modeling, this paper uses the D-A segment and B-C segment data as experimental data.

Validation Model

To verify the precision of airborne GNSS-R SSH retrieval, it needs to be compared with the measured sea surface data. Due to the lack of measured data, the verification model is used to verify the precision of SSH retrieval. In this paper, DTU15 (DTU mean sea

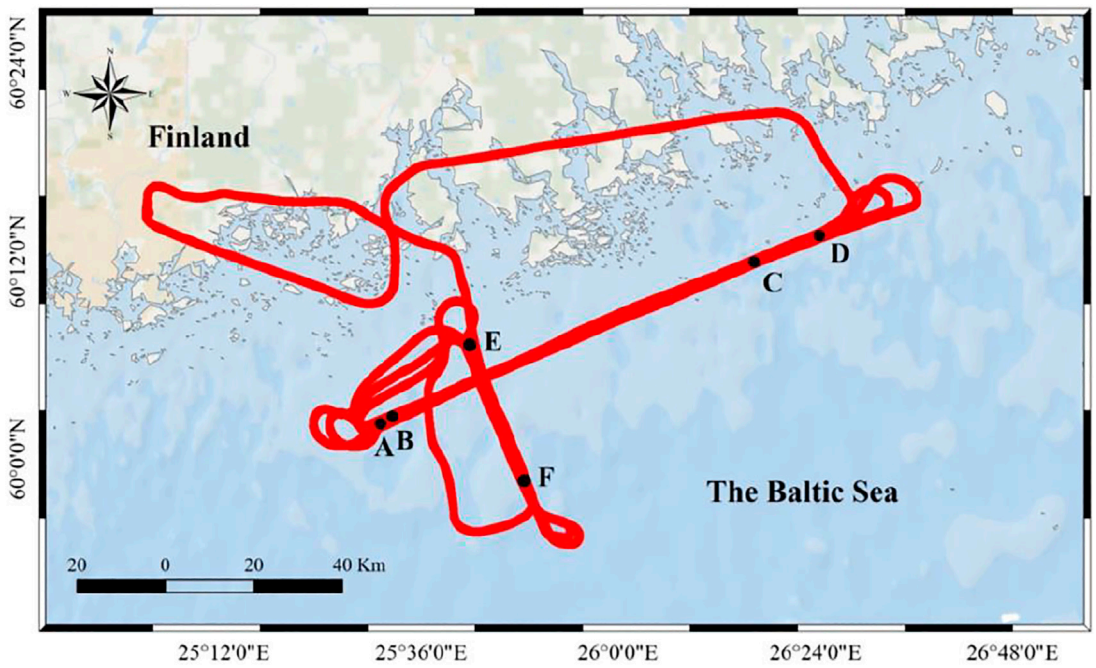

FIGURE 3 | Flight trajectory and sea surface height.

TABLE 2 | Training results of different models.

Segment label	Start time [GPS SoD]	End time [GPS SoD]	Distance [m]	Mean speed [m/s]
B-C	39,102	39,521	40.3	96.0
D-A	39,942	40,781	52.3	54.5
E-F	41,220	41,419	16.1	80.7
F-E	41,630	41,919	18.3	63.1

TABLE 3 | Training results of different models.

Learner	Optimal parameters	Optimal R^2
Lasso	req_alpha = 5.75	0.72
Ridge	req_lambda = 0.0001	0.78
Elastic	req_alpha = 0.1	0.70
	req_lambda = 0.0009	–
SVR	C = 0.3	0.77
GBDT	max_depth = 3	0.91
	n_estimators = 350	–
	min_sample_split = 5	–
XGBoost	max_depth = 1	0.95
	n_estimators = 300	–
LightGBM	max_depth = 2	0.92
	n_estimators = 500	–
	num_leaves = 16	–
RF	max_features = 24	0.93
	min_samples_split = 4	–
	n_estimators = 150	–

surface 15) (Mashburn et al., 2018) model developed by Danish University of technology and TPXO8 (Egbert and Erofeeva 2002) global ocean tide model provided by Oregon State University (OSU) are used as the validation model. The sea surface height SSH obtained from the validation model is as follows:

$$SSH = DTU15 + TPXOtide \tag{10}$$

Data Set Matching and Partition

The DW is a continuous time-varying data set, while the DTU15 is a grid data whose longitude and latitude are both 1′. Therefore, it is necessary to match the airborne DW data set with the DTU15 average sea surface model in time and space first, also extract the average sea surface value of DTU15 corresponding to the DW data, and then tide correction for the same time, latitude and longitude of the airborne time-delay waveform was calculated by the TPXO8 global ocean tide model. Finally superimpose it on the DTU15 to get the SSH value of the DTU15 verification model. The airborne delay waveform (DW) data set and the corresponding SSH value constitute the raw data set. Divide the raw data set into three parts: training set, validation set and test set, and use 80% of the second time period (GPST: 385542–386501 s) data as training data for model training; the remaining 20% of the second time period data is used as

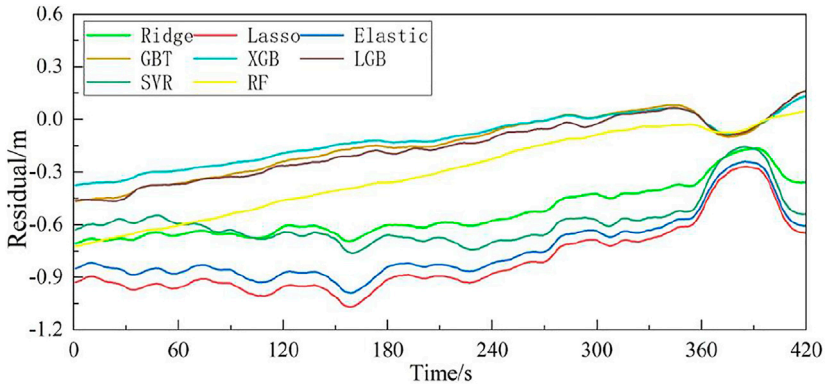

FIGURE 4 | Curves chart of forecast errors from different models.

verification data for the optimization of model hyperparameters and preliminary evaluation of model performance. The experimental data in the first time period (GPST: 384702–385121 s) is used as the test data to evaluate the generalization ability of the model.

Analysis of Height Measurement Accuracy of Different Machine Learning Models

Analysis of Training Results of Different Models

In this paper, a variety of machine learning regression algorithms are used to establish the mapping relationship between the airborne DW data and the DTU15 verification model. The hyperparameters are optimized and the performance of the model is initially evaluated through the R^2 of each machine learning model on the verification set. **Table 3** shows the training results of each machine learning model after 5-fold cross-validation training. It can be seen that the R^2 of the ensembled tree model is significantly higher than that of the non-ensembled learner, and the XGBoost model has the R^2 of 0.95, which shows that after XGBoost regression training, and the model can discover the explanatory information that explains 95% of the target factor change from the input factors. But in the non-ensembled learner, the Ridge regression model obtained the highest R^2 of 0.78, indicating that after linear regression training, the model can discover the explanatory information that explains 78% of the target factor change from the input factors.

Analysis of Generalization Ability of Different Models

Using the data in the test set to evaluate the generalization ability of the trained model in (1) to verify the final performance of the model. As is shown in **Figure 4**, the error fitted curve are obtained by making the difference between the results of each machine learning model and the SSH value provided by the DTU15 verification model.

As illustrated in **Figure 4** the overall prediction error of the ensembled tree model is relatively small, and the XGB model based on Boosting's ensembled method has the best prediction results. In the linear regression model, the Ridge model has the best estimate results. At the same time, we can see that retrieval errors of different types of models have great differences. The forecast errors of decision tree models have a significant downward bulge between 360 and 410 s on the time axis, while the linear regression errors have an obvious upward bulge. The data step is mainly due to the loss of a part of the training data (SoD: 40,781–40,842). Because the model with missing training data did not consider the information of the missing data during training, the inversion results of the model on the test set were biased. At the same time, due to the different algorithm rules of the decision tree model and the linear regression model, the two types of models have different emphasis on data information mining, which makes the prediction results different. The data step is mainly caused by the loss of some data in the training data (SOD: 40,781–40,842). Due to the lack of training data, the model does not consider the information of missing data during training, resulting in errors in the inversion results of the model on the test set. At the same time, due to the different algorithm rules of decision tree model and linear regression model, the two types of models have different emphasis on data information mining, resulting in great differences in prediction results.

Height Measurement Accuracy Analysis of Machine Learning Fusion Model

Comparative Analysis of Accuracy Between Single Model and Fusion Model

XGB, RF and ridge models with high accuracy and low correlation are used in the fusion model. Three model fusion methods are compared: Averaging, Stacking and R^2-Ranking; among them. Averaging and R^2-Ranking only combine the results of multiple models, while Stacking R^2-Ranking needs to specify sub-learner. In this paper, the base learner of the Stacking fusion model uses XGB and random forest, and the sub-learner uses Ridge, which has the best retrieval result in the linear model.

Figure 5 illustrates the retrieval results and correlation scatter of XGB, RF and ridge models. **Figure 6** illustrates the retrieval results and correlation scatter of Averaging, Stacking and R^2-Ranking fusion methods.

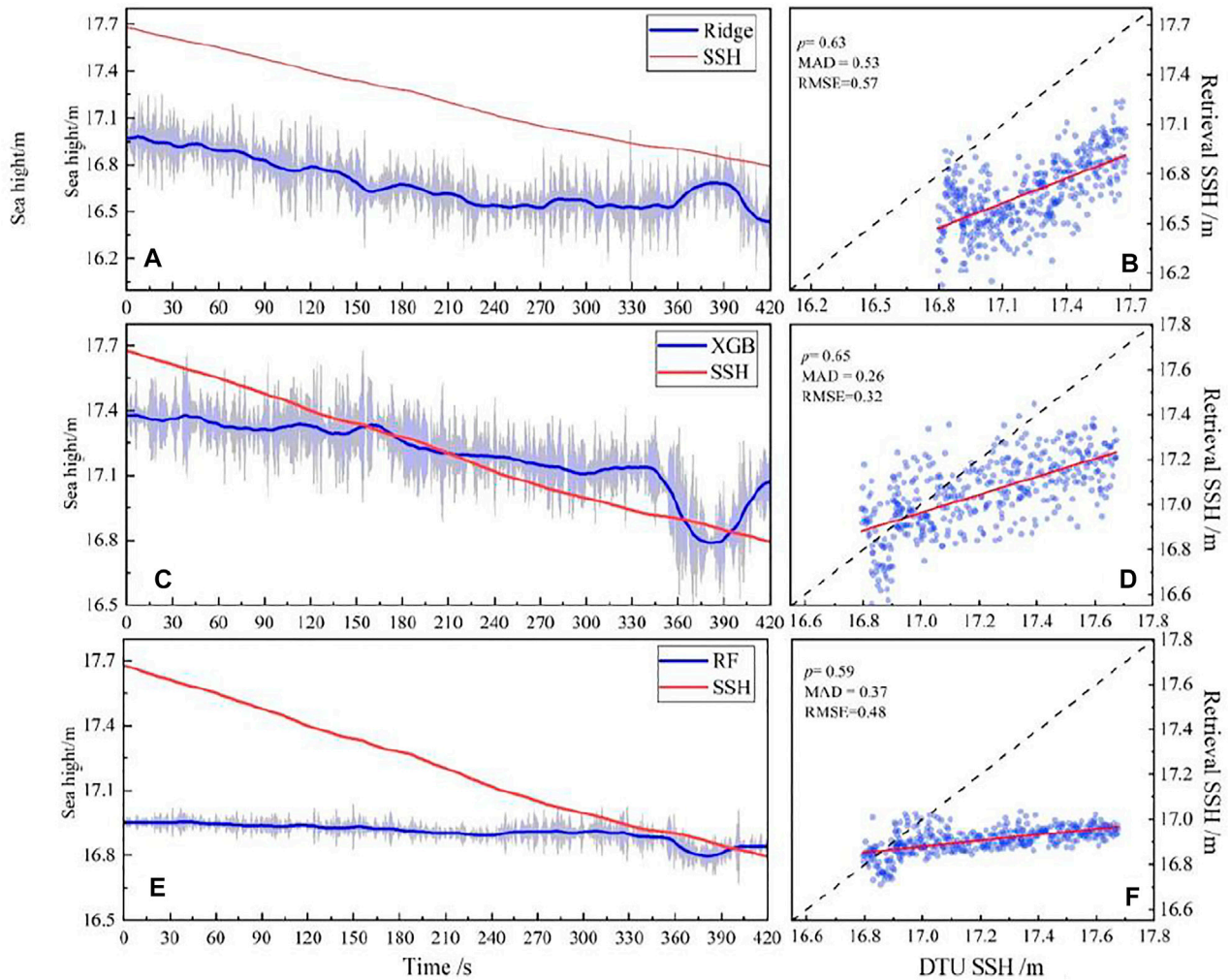

FIGURE 5 | Forecast results and correlation scatterers of single model.

It can be seen from **Figure 5** and **Figure 6** that the three fusion models show better predictions compared to single models. The predictions of R^2-Ranking and Stacking are closer to the DTU15 model, with smaller errors. The retrieval results of the R^2-Ranking and Averaging models have strong correlations with the DTU15 model, which are 0.74 and 0.75, respectively. In summary, in this paper, the R^2-Ranking fusion model has the best retrieval performance.

The number of seeds for the 5-fold cross-validation was changed three times and the experiment was repeated to verify the robustness of the fusion model. Changing the number of random seeds is equivalent to re-slicing the original data set and training the base learner again on the new data set. Finally, the performance of the three fusion methods are compared through the retrieval results still on the test set. The performance indices of different models are shown in **Table 4**. As can be seen from **Table 4** that the robustness of the three fusion models is superior. There is no obvious change in the *MAD*, *RMSE*, and *CC* of each model, and the results of the three experiments are basically consistent. The retrieval performance of Averaging, R^2-Ranking, and Stacking fusion models is almost better than that of the single model, indicating that fusion model has further improved the model performance.

The Impact of Different Features on Model Accuracy

In the field of data mining and machine learning, it is generally believed that the upper limit of machine learning is determined data and features, and the model can only approach the upper limit indefinitely. Therefore, in order to select features that are sensitive to the SSH, a total of six sets of feature sets with varying levels of information details in *Feature Optimization* are used

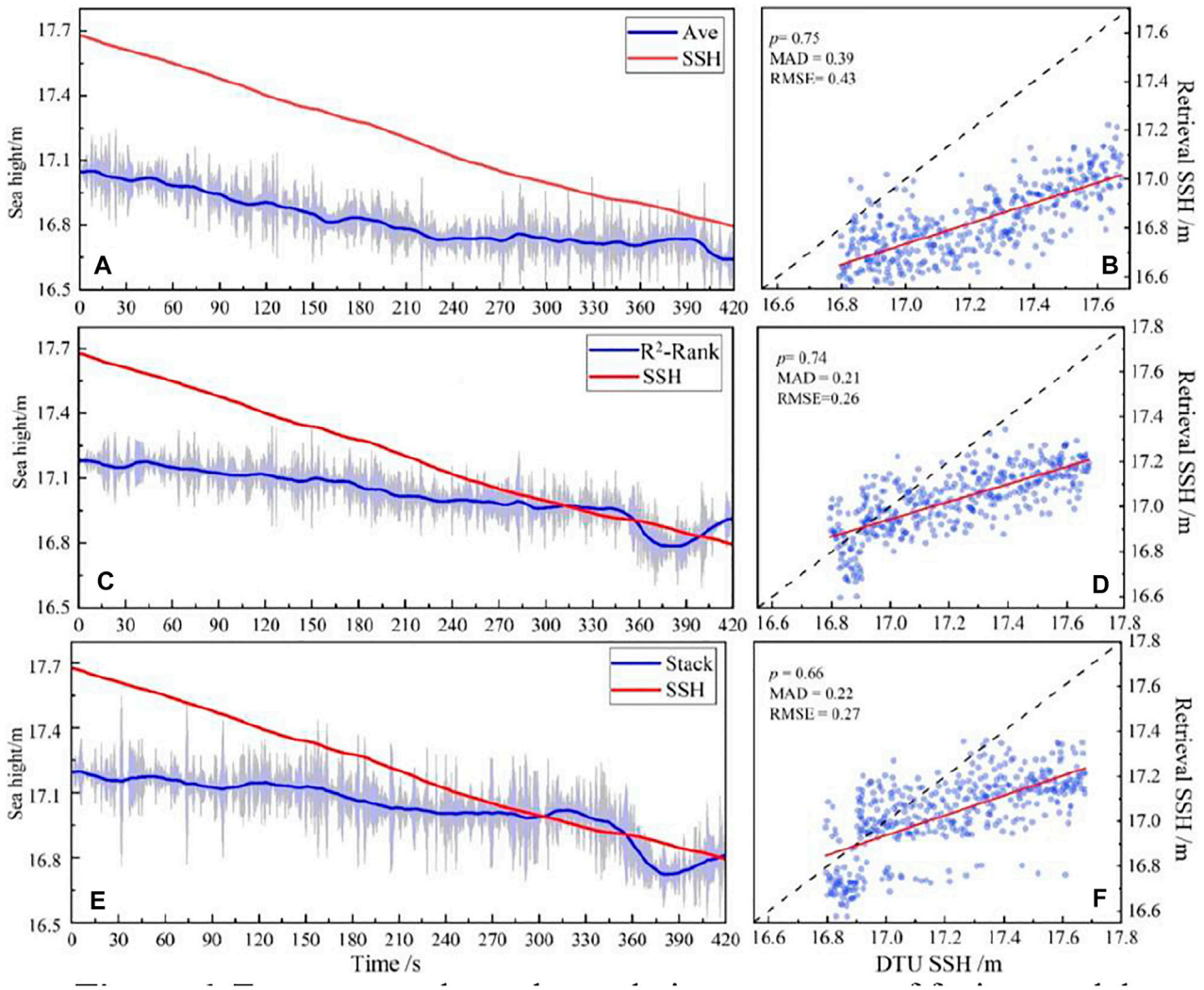

FIGURE 6 | Forecast results and correlation scatterers of fusion model.

TABLE 4 | Comparison of experimental results of different models.

Model	First			Second			Third		
	MAD	RMSE	CC	MAD	RMSE	CC	MAD	RMSE	CC
Ridge	0.53	0.57	0.63	0.56	0.59	0.64	0.55	0.55	0.64
Lasso	0.81	0.85	0.42	0.79	0.79	0.45	0.82	0.82	0.43
Elastic	0.74	0.79	0.48	0.72	0.82	0.47	0.76	0.77	0.48
SVR	0.59	0.63	0.64	0.60	0.65	0.64	0.60	0.61	0.63
KNN	0.44	0.47	0.57	0.46	0.45	0.58	0.44	0.46	0.60
GBT	0.42	0.48	0.65	0.41	0.46	0.65	0.45	0.45	0.63
XGB	0.31	0.36	0.66	0.29	0.33	0.64	0.33	0.35	0.64
LGB	0.36	0.47	0.65	0.40	0.45	0.65	0.38	0.46	0.63
RF	0.37	0.48	0.59	0.41	0.51	0.60	0.39	0.47	0.59
Ave	0.39	0.43	0.77	0.38	0.44	0.76	0.36	0.42	0.75
R2-Ranking	0.25	0.29	0.75	0.24	0.30	0.75	0.24	0.28	0.76
Stacking	0.22	0.27	0.66	0.26	0.31	0.68	0.23	0.31	0.68

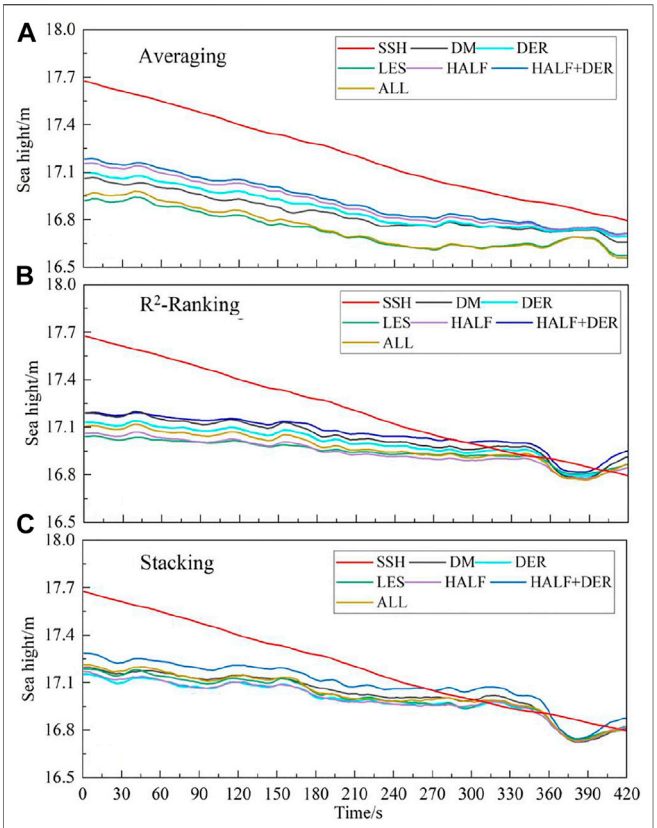

FIGURE 7 | Forecast results of three fusion model in different data sets.

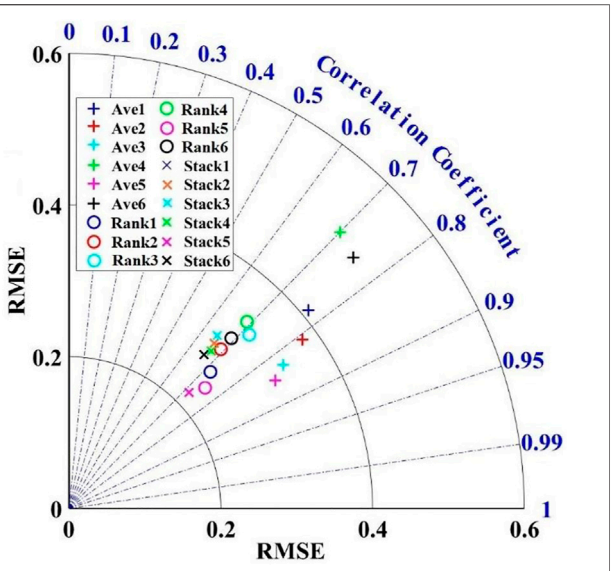

FIGURE 8 | Polar chart of prediction performance of fusion mode.

for model training, and their performance is verified on the test set.

Figure 7A–C present the comparison of the retrieval results (after fitting) of Averaging, R^2-Ranking and Stacking fusion models in six different feature sets.

It can be seen from **Figure 7** that the three fusion models do not achieve the best inversion effect in feature set 6 which contains the most feature information. But the feature set 5, which is composed of DW data, PCP70 and PFD features, shows the best. in other words, the machine learning fusion model with feature set 5 can learn the complex relationship better among the input features, so as to accurately retrieve the SSH.

As the six data sets shown in **Table 5** that both the MAD and the RMSE of the feature set 5 are the smallest in all the data sets, that is, the inversion results of the three fusion models on data set 5 are the most accurate. At the same time, the correlation between the retrieval result of data set 5 and the DTU15 model is also the best among the six data sets.

To compare the inversion accuracy of the three models more Visually on each data set, the polar coordinate system is used to visualize the experimental results, as shown in **Figure 8**.

APPLICATION OF NEW MACHINE LEARNING WEIGHTED AVERAGE FUSION FEATURE EXTRACTION METHOD

The new GNSS-R SSH retrieval model based on machine learning fusion model and feature optimization used the information of the entire delay waveform for height inversion. The traditional single-point retracking method estimate the time delay by determining the position of the characteristic points of the reflected waveform within the time delay window. The characteristic points of the waveform that have been used for sea surface altimetry include the waveform leading edge peak first derivative (DER) (Mashburn et al., 2016) and the delay of the 70%

TABLE 5 | Comparison of experimental results of different models at different Feature Set.

Set	Averaging			R^2-Ranking			Stacking		
	MAD	RMSE	CC	MAD	RMSE	CC	MAD	RMSE	CC
Set1	0.36	0.42	0.75	0.24	0.28	0.76	0.23	0.31	0.68
Set2	0.34	0.38	0.81	0.23	0.29	0.69	0.24	0.29	0.66
Set3	0.31	0.34	0.83	0.28	0.33	0.72	0.24	0.30	0.65
Set4	0.47	0.51	0.70	0.27	0.34	0.69	0.23	0.28	0.67
Set5	0.29	0.32	0.85	0.19	0.23	0.75	0.18	0.22	0.72
Set6	0.46	0.50	0.75	0.25	0.31	0.69	0.22	0.27	0.66

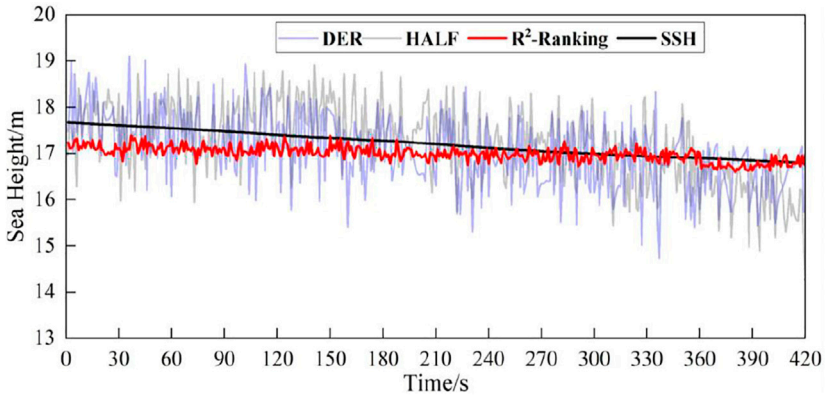

FIGURE 9 | Forecast results of R2 ranking fusion model and single point retracking method.

TABLE 6 | Comparison of SSH retrieval performance between R^2-Ranking fusion model and single point retracking methods.

Learner	MAD	RMSE	CC
HALF	0.57	0.71	0.57
DER	0.54	0.68	0.52
R2-Ranking	0.19	0.23	0.75

peak correlation power (HALF) (Mashburn et al., 2016). In order to verify the superiority of the new machine learning weighted average fusion feature extraction method, this paper compared their retrieval performance. The traditional single-point tracking method uses DER and HALF methods to estimate the time-delay of the reflected signal relative to the direct signal. The SSH retrieval algorithms in literature (Mashburn et al., 2016) is used to correct the tropospheric delay and distance error between the antennas. **Figure 9** presents the SSH estimates by the HALF, DER retracking method and the new machine learning weighted average fusion feature extraction method. It can be seen from **Figure 9** that the retrieval results of the machine learning fusion model are significantly better than the HALF and DER single-point re-tracking methods. Compared with the traditional retracking method, the prediction result of the R2-Ranking fusion model is more stable and closer to the SSH value. Moreover, the machine learning fusion model does not need to consider various error corrections in the time-delay retrieval algorithms, which partly simplifies the complexity of retrieval model.

Table 6 presents the precision index of the three models, which shows that the machine learning fusion model is obviously superior to the retracking method of HALF and DER on MAD, RMSE and CC. The application of the new machine learning weighted average fusion feature extraction method effectively improves the accuracy of SSH retrieval, in which the mean absolute error (MAD) is reduced by 63.1 and 59.2% respectively, and the root mean square error (RMSE) is reduced by 63.3 and 61.8% respectively; The correlation coefficient (CC) increased by 31.6 and 44.2% respectively.

CONCLUSION AND PROSPECT

The traditional single-point retracking method is an empirical model, which can only use a small amount of DDM information. This method will cause information waste and loss of certain inversion accuracy. In order to improve the accuracy of SSH retrieval, this paper proposed a new type of machine learning weighted average fusion feature extraction method and analyze the inversion accuracy of different models and the influence of different feature sets on the model. The specific conclusion are as follows:

1) This paper first evaluates the SSH retrieval performance of regression methods commonly used in machine learning, such as linear regression model (Lasso, Ridge) SVR and ensembled tree regression model (XGBoost, LightGBM and RF). The experimental results show that the ensembled tree regression model have an overall outstanding performance on the test set, and the effects of other models are slightly worse.
2) RF, XGBoost and Ridge models with better SSH retrieval performance and lower correlation are used for model fusion, which further improves the SSH retrieval accuracy. Three model fusion methods: Averaging, R^2-Ranking and Stacking are used for model fusion. The experimental results show that the retrieval accuracy and correlation of the SSH value fusion model compared with the DTU15 validation model are better than a single model, and the fusion further improves the effect of the model. At the same time, the R^2-Ranking fusion method proposed in this paper achieved the most accurate retrieval results, with a mean absolute error of about 0.25, a root mean square error RMSE of about 0.29, and a correlation CC of about 0.75.
3) In order to obtain a better feature set, feature engineering methods are used to screen and construct features that are highly sensitive to the sea surface. This paper uses a total of six groups of feature sets with different information details for model training and verifies its accuracy on the test set. Experimental results show that the three fusion models have the best retrieval accuracy on feature set 5 that

includes DW, PCP70 and PFD features. It shows that the machine learning fusion model with feature set of 5 can better learn the complex relationship between the original input features, so as to accurately retrieve the height.

4) By comparing the retrieval results with the commonly used DER and HALF traditional single-point tracking methods, it is concluded that the new machine learning weighted average fusion feature extraction method effectively improves the precision of SSH retrieval. The precision has been improved by 61, 61, and 44% respectively in MAD, RMSE and CC.

The new machine learning weighted average fusion feature extraction method proposed in this paper provides a new idea for the future DDM-based GNSS-R sea surface altimetry verification star height inversion. The method proposed in this paper can be extended to a wider scientific fields, such as: GNSS-R sea surface wind speed retrieval, sea ice and soil moisture detection, etc. Only need to re-optimize the features and modify the input and corresponding output data. Compared with the previous inversion models, machine learning algorithms are easier to build models, without the need to build multiple error models, and can make full use of the physical quantities related to the sea surface height, and have a good accuracy. The disadvantage is that the machine learning model requires a large number of labeled observations to train and build the model. The spaceborne GNSS-R receiver can provide massive observation data. However, the corresponding high-precision sea surface height is difficult to obtain. Meanwhile, since the GNSS-R signal is weak, how to construct features sensitive to SSH change is another main factor of SSH inversion by machine learning fusion model. In the next step, more physical parameters related to sea surface height can be extracted to improve the effect of the fusion model.

DATA AVAILABILITY STATEMENT

The original contributions presented in the study are included in the article/Supplementary Material, further inquiries can be directed to the corresponding authors.

AUTHOR CONTRIBUTIONS

QW: scientific analysis and manuscript writing. WZ and FW: experiment design, project management, review and editing. QW, WZ, and FW contributed equally to this paper. All authors contributed to the article and approved the submitted version.

FUNDING

This work was supported by the National Natural Science Foundation of China under Grant (41774014, 41574014), the Liaoning Revitalization Talents Program under Grant (XLYC2002082), the Frontier Science and Technology Innovation Project and the Innovation Workstation Project of Science and Technology Commission of the Central Military Commission under Grant (085015), the Independent Research and Development Start-up Fund of Qian Xuesen Laboratory of Space Technology (Y-KC-WY-99-ZY-000-025), and the Outstanding Youth Fund of China Academy of Space Technology.

ACKNOWLEDGMENTS

We would like to thank Institute of Space Sciences (ICE, CSIC) and Institute for Space Studies of Catalonia (IEEC) for providing the raw data processing results of the air-borne experiment.

REFERENCES

Alonso-Arroyo, A., Zavorotny, V. U., and Camps, A. (2017). Sea Ice Detection Using U.K. TDS-1 GNSS-R Data. *IEEE Trans. Geosci. Remote Sensing.* 55, 4989–5001. doi:10.1109/TGRS.2017.2699122

Bai, W., Xia, J., Wan, W., Zhao, L., Sun, Y., Meng, X., et al. (2015). A First Comprehensive Evaluation of China's GNSS-R Airborne Campaign: Part II-River Remote Sensing. *Sci. Bull.* 60, 1527–1534. doi:10.1007/s11434-015-0869-x

Bosch, W., Dettmering, D., and Schwatke, C. (2014). Multi-Mission Cross-Calibration of Satellite Altimeters: Constructing a Long-Term Data Record for Global and Regional Sea Level Change Studies. *Remote Sensing.* 6, 2255–2281. doi:10.3390/rs6032255

Breiman, L. (1996). Bagging Predictors. *Mach Learn.* 24, 123–140. doi:10.1007/bf00058655

Cardellach, E., Rius, A., Martín-Neira., M., Fabra, F., Nogues-Correig, O., Ribo, S., et al. (2014). Consolidating the Precision of Interferometric GNSS-R Ocean Altimetry Using Airborne Experimental Data. *IEEE Trans. Geosci. Remote Sensing.* 52, 4992–5004. doi:10.1109/TGRS.2013.2286257

Clarizia, M. P., Ruf, C., Cipollini, P., and Zuffada, C. (2016). First Spaceborne Observation of Sea Surface Height Using GPS-Reflectometry. *Geophys. Res. Lett.* 43, 767–774. doi:10.1002/2015GL066624

D'Addio, S., Martín-Neira, M., di Bisceglie, M., Galdi, C., and Martin Alemany, F. (2014). GNSS-R Altimeter Based on Doppler Multi-Looking. *IEEE J. Sel. Top. Appl. Earth Observations Remote Sensing.* 7, 1452–1460. doi:10.1109/JSTARS.2014.2309352

Egbert, G. D., and Erofeeva, S. Y. (2002). Efficient Inverse Modeling of Barotropic Ocean Tides. *J. Atmos. Oceanic Technol.* 19, 183–204. doi:10.1175/15200426(2002)0192.0.CO10.1175/1520-0426(2002)019<0183:eimobo>2.0.co;2

Friedman, H. (2001). Greedy Function Approximation: a Gradient Boosting Machine. *Ann. Stat.* 29, 1189–1232. doi:10.2307/269998610.1214/aos/1013203451

Garrison, J. L. (2016). A Statistical Model and Simulator for Ocean-Reflected GNSS Signals. *IEEE Trans. Geosci. Remote Sensing.* 54, 6007–6019. doi:10.1109/TGRS.2016.2579504

Hoerl, A. E., and Kennard, R. W. (1970). Ridge Regression: Biased Estimation for Nonorthogonal Problems. *Technometrics.* 12, 55–67. doi:10.1080/00401706.1970.10488634

Jia, Y., Jin, S., Savi, P., Gao, Y., Tang, J., Chen, Y., et al. (2019). GNSS-R Soil Moisture Retrieval Based on a XGboost Machine Learning Aided Method: Performance and Validation. *Remote Sensing.* 11, 1655–1779. doi:10.3390/rs11141655

Jing, C., Niu, X., Duan, C., Lu, F., Di, G., and Yang, X. (2019). Sea Surface Wind Speed Retrieval From the First Chinese GNSS-R Mission: Technique and Preliminary Results. *Remote Sensing.* 11, 3013–3025. doi:10.3390/rs1112143810.3390/rs11243013

Jung, Y. (2018). Multiple PredictingK-Fold Cross-Validation for Model Selection. *J. Nonparametric Stat.* 30, 197–215. doi:10.1080/10485252.2017.1404598

Keerthi, S. S., Shevade, S. K., Bhattacharyya, C., and Murthy, K. R. K. (2001). Improvements to Platt's SMO Algorithm for SVM Classifier Design. *Neural Comput.* 13, 637–649. doi:10.1162/089976601300014493

Kim, H., Lee, S., Lee, S., Hong, S., Kang, H., and Kim, N. (2019). Depression Prediction by Using Ecological Momentary Assessment, Actiwatch Data, and Machine Learning: Observational Study on Older Adults Living Alone. *JMIR Mhealth Uhealth.* 7, e14149–14149. doi:10.2196/14149

Lary, D. J., Alavi, A. H., Gandomi, A. H., and Walker, A. L. (2016). Machine Learning in Geosciences and Remote Sensing. *Geosci. Front.* 7, 3–10. doi:10.1016/j.gsf.2015.07.003

Lavalle, S. M., Branicky, M. S., and Lindemann, S. R. (2004). On the Relationship Between Classical Grid Search and Probabilistic Roadmaps. *Int. J. Robotics Res.* 23, 673–692. doi:10.1007/978-3-540-45058-0_510.1177/0278364904045481

Li, W., Cardellach, E., Fabra, F., Rius, A., Ribó, S., and Martín-Neira, M. (2017). First Spaceborne Phase Altimetry over Sea Ice Using TechDemoSat-1 GNSS-R Signals. *Geophys. Res. Lett.* 44, 8369–8376. doi:10.1002/2017GL074513

Li, X., Yang, D., Yang, J., Zheng, G., Han, G., Nan, Y., et al. (2021). Analysis of Coastal Wind Speed Retrieval From CYGNSS mission Using Artificial Neural Network. *Remote Sensing Environ.* 260, 112454–112466. doi:10.1016/j.rse.2021.112454

Liu, L., Sun, Y., Bai, W., and Luo, L. (2020). The Inversion of Sea Surface Wind Speed in GNSS-R Base on the Model Fusion of Data Mining. *Geomatics Inf. Sci. Wuhan Univ.* 12, 1–10. doi:10.13203/j.whugis2019038310.3390/rs12122034

Liu, Y., Collett, I., and Morton, Y. J. (2019). Application of Neural Network to GNSS-R Wind Speed Retrieval. *IEEE Trans. Geosci. Remote Sensing.* 57, 9756–9766. doi:10.1109/tgrs.2019.2929002

Luo, L., Bai, W., Sun, Y., and Xia, J. (2020). GNSS-R Sea Surface Wind Speed Inversion Based on Tree Model Machine Learning Method. *China. J. Space Sci.* 40, 595–601. doi:10.11728/cjss2020.04.595

Martin-Neira, M. (1993). A Passive Reflectometry and Interferometry System (PARIS): Application to Ocean Altimetry. *ESA J.* 17, 331–355.

Mashburn, J., Axelrad, P., Lowe, S. T., and Larson, K. M. (2018). Global Ocean Altimetry with GNSS Reflections From TechDemoSat-1. *IEEE Trans. Geosci. Remote Sensing.* 56, 4088–4097. doi:10.1109/TGRS.2018.2823316

Mashburn, J., Axelrad, P., T. Lowe, S. S., and Larson, K. M. (2016). An Assessment of the Precision and Accuracy of Altimetry Retrievals for a Monterey bay GNSS-R Experiment. *IEEE J. Sel. Top. Appl. Earth Observations Remote Sensing.* 9, 4660–4668. doi:10.1109/jstars.2016.2537698

Mashburn, J., Axelrad, P., Zuffada, C., Loria, E., O'Brien, A., and Haines, B. (2020). Improved GNSS-R Ocean Surface Altimetry With CYGNSS in the Seas of indonesia. *IEEE Trans. Geosci. Remote Sensing.* 58, 6071–6087. doi:10.1109/tgrs.2020.2973079

Park, H., Valencia, E., Camps, A., Rius, A., Ribo, S., and Martin-Neira, M. (2013). Delay Tracking in Spaceborne GNSS-R Ocean Altimetry. *IEEE Geosci. Remote Sensing Lett.* 10, 57–61. doi:10.1109/LGRS.2012.2192255

Ribó, S., Arco-Fernández, J., Cardellach, E., Fabra, F., Li, W., Nogués-Correig, O., et al. (2017). A Software-Defined GNSS Reflectometry Recording Receiver With Wide-Bandwidth, Multi-Band Capability and Digital Beam-Forming. *Remote Sensing.* 9, 450. doi:10.3390/rs9050450

Rodgers, J. L., and Nicewander, W. A. (1988). Thirteen Ways to Look at the Correlation Coefficient. *The Am. Statistician.* 42, 59–66. doi:10.2307/2685263

Ruf, C. S., Atlas, R., Chang, P. S., Clarizia, M. P., Garrison, J. L., Gleason, S., et al. (2016). New Ocean Winds Satellite Mission to Probe Hurricanes and Tropical Convection. *Bull. Am. Meteorol. Soc.* 97, 385–395. doi:10.1175/BAMS-D-14-00218.1

Wang, F., Yang, D., Zhang, G., and Zhang, B. (2021a). Measurement of Sea Surface Height Using Airborne Global Navigation Satellites System Reflectometry. *Acta Aeronautica et Astronautica Sinica.* 42, 324852. doi:10.7527/S1000-6893.2020.24852

Wang, J., Xu, H., Yang, L., Song, Q., and Ma, C. (2021b). Cross-Calibrations of the HY-2B Altimeter Using Jason-3 Satellite During the Period of April 2019-September 2020. *Front. Earth Sci.* 9, 215–231. doi:10.3389/feart.2021.647583

Xu, L., Wan, W., Chen, X., Zhu, S., Liu, B., and Hong, Y. (2019). Spaceborne GNSS-R Observation of Global lake Level: First Results from the TechDemoSat-1 Mission. *Remote Sensing.* 11, 1438–1448. doi:10.3390/rs11121438

Yan, S., Zhang, N., Chen, N., and Gong, J. (2019). Using Reflected Signal Power From the BeiDou Geostationary Satellites to Estimate Soil Moisture. *Remote Sensing Lett.* 10, 1–10. doi:10.1080/2150704X.2018.1519272

Zawadzki, L., and Ablain, M. (2016). Accuracy of the Mean Sea Level Continuous Record With Future Altimetric Missions: Jason-3 vs. Sentinel-3a. *Ocean Sci.* 12, 9–18. doi:10.5194/osd-12-1511-201510.5194/os-12-9-2016

Zeng, Z. (2020). *A Study on Alpha Strategy's Quantitative Investment (In Chinese).* Guangzhou: Jinan University.

Zhang, Y., Zhang, Y., Meng, T., and Yang, H. (2020). Research on Sea Surface Altimetry Model of Airborne GNSS Reflected Signal. *Acta Oceanologica Sinica.* 42, 149–156. doi:10.3969/j.issn

Zou, H. (2006). The Adaptive Lasso and its oracle Properties. *J. Am. Stat. Assoc.* 101, 1418–1429. doi:10.1198/016214506000000735

Conflict of Interest: The authors declare that the research was conducted in the absence of any commercial or financial relationships that could be construed as a potential conflict of interest.

Publisher's Note: All claims expressed in this article are solely those of the authors and do not necessarily represent those of their affiliated organizations, or those of the publisher, the editors and the reviewers. Any product that may be evaluated in this article, or claim that may be made by its manufacturer, is not guaranteed or endorsed by the publisher.

frontiers in Earth Science

ORIGINAL RESEARCH
published: 09 September 2021
doi: 10.3389/feart.2021.665876

Regional Mean Sea Surface and Mean Dynamic Topography Models Around Malaysian Seas Developed From 27 Years of Along-Track Multi-Mission Satellite Altimetry Data

Mohammad Hanif Hamden[1], *Ami Hassan Md Din*[1,2]*, *Dudy Darmawan Wijaya*[3], *Mohd Yunus Mohd Yusoff*[4] *and Muhammad Faiz Pa'suya*[5]

[1]Geospatial Imaging and Information Research Group (GI2RG), Faculty of Built Environment and Surveying, Universiti Teknologi Malaysia, Johor Bahru, Malaysia, [2]Geoscience and Digital Earth Centre (INSTeG), Faculty of Built Environment and Surveying, Universiti Teknologi Malaysia, Johor Bahru, Malaysia, [3]Geodesy Research Division, Faculty of Earth Science and Technology, Institute of Technology Bandung, Bandung, Indonesia, [4]Geodetic Survey Division, Department of Survey and Mapping Malaysia, Kuala Lumpur, Malaysia, [5]Environment and Climate Change Research Group, Faculty of Architecture, Planning and Surveying, Universiti Teknologi MARA, Perlis Branch, Arau Campus, Arau, Malaysia

OPEN ACCESS

Edited by:
Xiaoli Deng,
The University of Newcastle, Australia

Reviewed by:
Mukesh Gupta,
Catholic University of Louvain, Belgium
Zahra Gharineiat,
University of Southern Queensland, Australia

***Correspondence:**
Ami Hassan Md Din
amihassan@utm.my

Specialty section:
This article was submitted to Environmental Informatics and Remote Sensing, a section of the journal Frontiers in Earth Science

Received: 09 February 2021
Accepted: 26 July 2021
Published: 09 September 2021

Citation:
Hamden MH, Din AHM, Wijaya DD, Yusoff MYM and Pa'suya MF (2021) Regional Mean Sea Surface and Mean Dynamic Topography Models Around Malaysian Seas Developed From 27 Years of Along-Track Multi-Mission Satellite Altimetry Data. Front. Earth Sci. 9:665876. doi: 10.3389/feart.2021.665876

Contemporary Universiti Teknologi Malaysia 2020 Mean Sea Surface (UTM20 MSS) and Mean Dynamic Topography (UTM20 MDT) models around Malaysian seas are introduced in this study. These regional models are computed via scrutinizing along-track sea surface height (SSH) points and specific interpolation methods. A 1.5-min resolution of UTM20 MSS is established by integrating 27 years of along-track multi-mission satellite altimetry covering 1993–2019 and considering the 19-year moving average technique. The Exact Repeat Mission (ERM) collinear analysis, reduction of sea level variability of geodetic mission (GM) data, crossover adjustment, and data gridding are presented as part of the MSS computation. The UTM20 MDT is derived using a pointwise approach from the differences between UTM20 MSS and the local gravimetric geoid. UTM20 MSS and MDT reliability are validated with the latest Technical University of Denmark (DTU) and Collecte Localisation Services (CLS) models along with coastal tide gauges. The findings presented that the UTM20, CLS15, and DTU18 MSS models exhibit good agreement. Besides, UTM20 MDT is also in good agreement with CLS18 and DTU15 MDT models with an accuracy of 5.1 and 5.5 cm, respectively. The results also indicate that UTM20 MDT statistically achieves better accuracy than global models compared to tide gauges. Meanwhile, the UTM20 MSS accuracy is within 7.5 cm. These outcomes prove that UTM20 MSS and MDT models yield significant improvement compared to the previous regional models developed by UTM, denoted as MSS1 and MSS2 in this study.

Keywords: gravimetric geoid, satellite altimetry, sea level variability, regional, UTM20 MSS, UTM20 MDT

INTRODUCTION

Mean sea surface (MSS) is a term describing the average satellite-derived sea surface height (SSH) over a period of time (Andersen and Scharroo, 2011; Yuan et al., 2020). In general, MSS determination is a crucial component in supporting various scientific studies, particularly in the fields of oceanography, geoscience, and environmental science. Furthermore, the MSS model plays a crucial role in computing marine gravity anomalies (Zhu et al., 2019) and bathymetry prediction (Andersen and Knudsen, 2009) in the context of geodetic applications. In line with this notion, researchers such as Nornajihah (2017) and Astina (2017) are among those who have utilized the regional MSS model to develop a marine geoid model and to estimate bathymetry over Malaysian seas, respectively.

Theoretically, MSS, $\overline{h}$, corresponds to the geoid height, N, and the temporal mean dynamic topography, ζ, as shown in **Equation 1**. According to Woodworth et al. (2015), it will coincide with the geoid in the circumstance wherein no ocean circulation is present. Nevertheless, ocean circulation yields an additional MDT component to the MSS, with the spatial variance within ±1 m at different locations across the global ocean.

$$\overline{h} = N + \zeta. \tag{1}$$

Meanwhile, MDT is the separation value spanning the geoid and MSS. It is a significant surface for numerous oceanographic applications, and it is also a depiction of ocean mean circulation. Knowledge about MDT is of interest to oceanographers when investigating the ocean's surface currents and geodesists to unify vertical datum either globally or locally (Filmer et al., 2018). The MDT can be determined by two different approaches: geodetic and oceanic methods (Ophaug et al., 2015). The geodetic MDT is computed from the difference between MSS and the precise geoid model. Thus, the combination of good quality geoid height and altimetry MSS model is foreseen as instrumental towards enhancing the process of determining the ocean circulation (Wunsch, 1993; Andersen and Knudsen, 2009). On the other hand, the oceanic MDT is established based on numerical ocean models. In this study, MDT is computed using the geodetic approach by differentiating between regional MSS model and local precise gravimetric geoid.

In line with the above, satellite altimetry is a space-based geodetic technique that has evolved from the 1970s onwards along with the emergence of advanced space, electronics, and microwave technologies and functions to measure global SSH (Jiang et al., 2002). From 1975 onwards, many satellite altimeters have been launched, including Geos-3, Seasat, Geosat, ERS-1, TOPEX/Poseidon (denoted as T/P), ERS-2, Geosat Follow On (GFO), Jason-1, Envisat-1, Jason-2, CryoSat-2, Jason-3, SARAL/AltiKa, Sentinel-3A, Sentinel-6, and others. As a result, multiple altimetry measurements have been obtained, hence providing vital and beneficial information detailing ocean circulation, global sea-level changes, marine gravity field, and ocean topography. This has rendered the integration method for multi-mission satellite altimetry data in determining the MSS model as a consistently trendy argument.

Several MSS models have been established, such as Goddard Space Flight Centre 2000 (GSFC00.1) (Wang, 2001), Wuhan University 2000 (WHU 2000) (Jiang et al., 2002), CLS11 (Schaeffer et al., 2012), Danish National Space Centre 2008 (DNSC08) (Andersen and Knudsen, 2009), WHU 2013 (Jin et al., 2016), DTU15 (Andersen et al., 2016), CLS15 (Pujol et al., 2018), and DTU18 (Andersen et al., 2018). Currently, only two institutions are assigned to keep updating these models, namely, The Centre-National d'Etudes-Spatiales (CNES) and the Space Research Centre of the Technical University of Denmark. In particular, the CLS15 and DTU18 are the most up-to-date models, wherein they are fundamentally underpinned by the 20-year T/P series mean profile. Therefore, these models will both be implemented when validating the newly developed regional MSS model over Malaysian seas.

Universiti Teknologi Malaysia (UTM) has long since played a role in establishing several regional MSS models over Malaysian seas. It is an excellent initiative to have regional-specific models in Malaysia as this country is located in a very complex area for MSS and MDT computation. This is due to the proximity to lands and islands as well as large tidal errors in altimetry measurements. The first model was developed by Yahaya et al. (2016), in which MSS has been generated by utilizing an average of 11 years of SSH climatology data covering from 1993 to 2016. The data were deduced from seven satellite missions, namely, T/P, Jason-1, Jason-2, ERS-2, Envisat-1, CryoSat-2, and SARAL/AltiKa. Following this, the model has been subject to further enhancement by Zulkifle et al. (2019). The researchers opted for a similar methodology at this juncture but with the addition of three other satellite missions (i.e., Poseidon, Jason-3, and Sentinel-3A) and incorporate a more extended average period from 1993 to 2017. However, both of the previous MSS models have an unclear methodology in their computation. There was no proper handling in terms of removing ocean variability in ERM and GM altimetry data. Inappropriate data processing might lead to large temporal variations in SSH that could be erroneously interpreted as tides or real signals.

Accordingly, both models mentioned above have a spatial resolution of 0.25 arc degree gridded points in which the interpolation of MSS or geoid signal occurs over a region of 25 km by 25 km in size. However, this has resulted in a misfit between the first local MSS and DTU13 MSS models, which reaches up to 2 m (Yahaya et al., 2016). Such issues can be explicitly attributed to interpolation errors. For example, the northern area of Borneo Island is associated with rapidly changing geoid and MSS, up to several meters. Within the enclosed area latitude of 6°–6.5°N and longitude of 114°–114.5°E, the geoid undulation changes from approximately 33–40 m and results in a trench-like structure. Therefore, the interpolated geoid or MSS signal over a region has caused an interpolation error of roughly 2 m in the regional MSS signal when observed within a cell of 0.25 arc degree grid.

Henceforth, this work establishes a new regional Universiti Teknologi Malaysia 2020 (UTM20) MSS model to offer an enhanced version of the previous regional model by gauging

the along-track SSH points via adopting an ordinary kriging interpolation method. Here, the challenging procedure in obtaining precise filtering of the temporal sea level variability and achieving the best spatial resolution are well-known for MSS model computation. This can be overcome by integrating the ERM and GM data. Additionally, it should be noted that every inadequate elimination of any inconsistencies will lead to the striated appearance of the ground track, namely, the so-called orange skin effect (Andersen and Knudsen, 2009). In addition, the 19-year moving average method proposed by Yuan et al. (2020) is implemented in the UTM20 MSS model. This is to ensure that the residual errors of tide models can further deteriorate on the MSS model. Subsequently, the final UTM20 MSS model will be utilized for further calculation in developing a new regional MDT model, namely, the UTM20 MDT model.

This study emphasizes the establishment and validation of new regional MSS and MDT models (UTM20) over the Malaysian seas using a spatial resolution of 1.5-min grid size, encompassing a 27-year long period from 1993 to 2019. The spatial resolution of the 1.5-min grid is chosen to align with the resolution of the local gravimetric geoid, Malaysian Geoid 2017 (MyGeoid_2017) provided by the Department of Survey and Mapping Malaysia (DSMM). Then, the regional MSS and MDT models are re-interpolated into a 2-min grid for validation with the global MSS and MDT models. Therefore, this article is comprised of four sections after the introduction. The *Materials and Methods* section explains the materials and methodology for data processing. The *Results* section depicts the results and analysis obtained. The *Discussion* section verifies and discusses the UTM20 MSS and MDT models, and the *Conclusion* section concludes the study.

MATERIALS AND METHODS

Data Sources and Pre-Processing

The satellite altimetry data used in this study are the along-track SSH products extracted from Radar Altimeter Database System (RADS). The data are generated from nine satellite missions, namely, T/P, Jason-1, Jason-2, ERS-2, GFO, Envisat-1, CryoSat-2, SARAL/AltiKa, and Sentinel-3A, encompassing 27 years from 1993 to 2019. It should be noted that the ERS-1 and Geosat-3 missions are excluded in the establishment of these models as they are outdated geodetic missions and are characterized as too-low range precision (Andersen et al., 2015). Therefore, data from Jason-1 Phase C GM and CryoSat-2 are utilized to enhance the spatial resolution of the MSS model. The establishment of the MSS model involves a combination of Exact Repeat Mission (ERM) and geodetic mission (GM) data. **Supplementary Figure S1** displays each of the single satellite altimetry along-track missions and the combination of multi-mission satellite altimetry tracks. All the reference ellipsoids and frames from other satellites are adjusted to the reference of the T/P satellite. For data extraction, the geographical boundary employed ranged between 0°N ≤ latitude ≤ 14°N and 95°E ≤ longitude ≤ 126°E, including four Malaysian seas, namely, the Malacca Straits, Southern region of South China Sea, Celebes Sea, and Sulu Sea. Multi-mission satellite altimetry data selected for UTM20 MSS computation are shown in **Table 1**.

TABLE 1 | Summary of all altimetry data for MSS computation.

Satellite	Phase	Mission	Cycles	Period
TOPEX	A	ERM	012–364	Jan 10, 1993–Aug 11, 2002
	B	IM	369–481	Sep 20, 2002–Oct 08, 2005
Jason-1	A	ERM	001–260	Jan 15, 2002–Jan 26, 2009
	B	IM[a]	262–374	Feb 10, 2009–Mar 03, 2012
	C	GM	382–423	May 08, 2012–Jun 12, 2013
Jason-2	A	ERM	000–303	Jul 04, 2008–Oct 02, 2016
	B	IM[a]	305–327	Oct 13, 2016–May 17, 2017
ERS-2	A	ERM	000–169	Apr 29, 1995–Jul 04, 2011
GFO	A	ERM	037–223	Jan 07, 2000–Sep 17, 2008
Envisat-1	B	ERM	006–094	May 14, 2002–Oct 22, 2010
CryoSat-2	A	GM	011–080	Jul 14, 2010–Aug 15, 2016
SARAL/AltiKa	A	ERM	001–035	Mar 14, 2013–Jul 04, 2016
Sentinel-3A	A	ERM	001–053	Mar 01, 2016–Dec 31, 2019

[a]IM is Interleaved Mission which is considered to be ERM data in this study.

All satellite altimetry data obtained in this study are provided by the Technical University of Delft, Netherlands. They are accessible via the RADS server in UTM, thus yielding the latest information on orbits and geophysical corrections. Furthermore, the acquired data are preprocessed based on the best range and geophysical corrections in the context of the Malaysian region. This includes rendering and removing invalid data as well as generating the corresponding refined geophysical corrections. Most of the range and geophysical corrections applied for this model are underpinned and guided by user manuals and progressive experiences from previous studies (Scharroo et al., 2013; Din et al., 2014; Yahaya et al., 2016; Hamid et al., 2018; Din et al., 2019; Zulkifle et al., 2019). **Supplementary Table S1** differentiates a list of range and geophysical corrections implemented by Yahaya et al. (2016), Zulkifle et al. (2019), and UTM20 MSS. Most geophysical corrections and models applied are similar to previous regional models except for load and ocean tides. The results of ocean tide are rectified by the GOT4.10c ocean tide model for all altimetry missions (Ray, 2013).

Altimetry Data Processing Method

In most cases, the MSS model is typically determined via a temporal average method. It depends on the following processes: data selection and preprocessing, ERM mean track derivation from collinear analysis, removal of GM sea level variability, crossover minimization, and data gridding. After applying geophysical correction and removing the bias in the preprocessing section, the following action is to remove the sea level variability of ERM and GM data. **Figure 1** illustrates the general processing flow in establishing the MSS model.

Eliminating the Sea Level Variability of ERM and GM Data

The collinear analysis is the method of correcting MSS gradients by taking into account along-track gradients (Braun et al., 2004). The purpose of collinear analysis of ERM data is to eliminate the sea level variability, consisting of seasonal and inter-annual

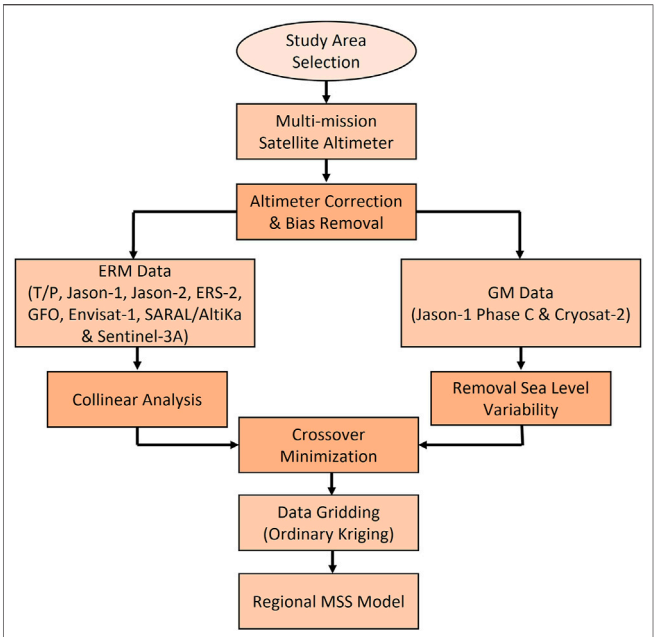

FIGURE 1 | Overall data processing flows in computing MSS model.

signals. It also strives to achieve average along-track SSH data. The average track is calculated from the selected track and corresponding collinear track. In this study, the collinear track of first cycle observations is designated to be the reference track. Subsequently, collinear analysis computes each SSH point of collinear tracks similar to the reference track (Jiang et al., 2002; Jin et al., 2016; Yuan et al., 2020).

The collinear analysis in this study is used to measure average along-track SSH. Necessary steps are taken in the process of calculating the average along-track SSH. The first is data filtering, in which the data will be discarded when the difference between SSH and MSS is greater than 1 m, and the new MSS will be re-calculated. Moving average technique is implemented to eliminate the annual and semi-annual variations in this study. The formula of the moving average technique is expressed as in **Equation 2** (Smith, 2003).

$$y(i) = \frac{1}{M} \sum_{j=0}^{M-1} x[i+j], \tag{2}$$

where $x\,[i+j\,]$ is the input signal, $y(i)$ is the output signal, and M is the number of points in the average. i is the loop for each point in the output signal and j is the index number. For instance, in a 10 point moving average filter, the index, j, can run from 0 to 11 for one side averaging or −5 to 5 for symmetrical averaging. The optimal number of points in the average (denoted as moving window) must be chosen correctly for this method to prevent over-filtering. Each satellite mission has different moving windows since they have different repeat periods.

The impact of SSH time variation for ERM can be reduced by subjecting it to time-averaging. However, unlike ERM data, SSH observations in the GM of satellite altimetry must be handled differently to minimize time variation. Time-averaging is only attributable to the GM data that not having the typical feature of the repeated period; thus, it is not suitable for the GM satellite tracks. Two methods can be implemented to remove the sea level variability from GM satellite data. The first method applies the correction based on seasonal variations fitting from the gridded sea level variation time series introduced by Andersen et al. (2006) and Andersen and Knudsen (2009). This method describes the seasonal variations are extracted using the gridded sea level variation time series, interpolated to the GM observations, and adjusted. The bias, linear trend, seasonal, and annual signals of sea level variations at each gridded point are fitted using a polynomial function. The second method is based on the interpolation of sea level anomalies (SLA) introduced by Schaeffer et al. (2012) and Jin et al. (2016). In this method, the sea level variability of GM data can be adjusted by the sea level variability of ERM data which hold as a reference at the spatial and temporal positions of GM data. Schaeffer et al. (2012) stated that the optimal analysis could be used to interpolate the SLA of one or more missions considered as a reference at the spatial and temporal position that would be adjusted for ocean variability. According to Jin et al. (2016), the correction based on the SLA interpolation showed remarkable improvement in removing the sea level variability.

Therefore, the method implemented in this study is based on the interpolation of SLA. The delayed-time Developing Use of Altimetry for Climate Studies (DUACS) Level 4 gridded SLA maps (Dibarboure et al., 2012) are used as a reference at spatial and temporal positions of the GM data. This model is obtained from the European Copernicus Marine Environment Monitoring Service (CMEMS) via https://resources.marine.copernicus.eu/. The corresponding hourly gridded SLA time series are computed to adjust the GM data listed in **Table 1** (i.e., Jason-1 Phase C, and CryoSat-2). The sea level variability of Jason-1 Phase C, and CryoSat-2 can be adjusted by the DUACS hourly gridded SLA time series to their observation duration as shown in **Table 2**.

Determination of the UTM20 Mean Sea Surface

After removing the sea level variability from ERM and GM data, it is expected that the seasonal sea level variations can be immensely eradicated. Besides, the part of radial orbit error is also expected to be reduced through the orbit calculation of ERM and GM data, adequately handled by RADS. Nevertheless, some errors such as residual orbit error and residual geophysical corrections are still present in the measurements. Thus, crossover adjustment is performed to reduce these errors. Crossover adjustment is performed due to orbital errors and inconsistencies in the satellite's orbit frame (Din et al., 2019). The crossover minimization is based on the discrepancy between two intersecting points for integrating multi-satellite altimetry data or the correction of measurements. The radial orbit error is one of the predominant factors affecting the altimetry data in the classical crossover adjustment. This error will be accurately modeled by either time-dependent or distance-dependent polynomial (Wagner, 1985; Rummel, 1993). According to Hamid et al. (2018), it is a practical approach geared towards

TABLE 2 | DUACS corresponding data used for reduction of GM sea level variability data.

GM data		Corresponding data	
Satellite	**Observation period (dd.mm.yyyy hh:mm)**	**Model**	**Observation period (dd.mm.yyyy hh:mm)**
Jason-1 (Phase C)	08.05.2012 04:03–12.06.2013 18:42	DUACS Level 4 SLA	08.05.2012 00:00–13.06.2013 00:00
CryoSat-2	18.01.2011 08:25–15.08.2016 15:47	DUACS Level 4 SLA	18.01.2011 00:00–16.08.2016 00:00

reduced orbit errors and improved multi-mission satellite altimetry measurements. Besides, it can minimize the crossover between ascending and descending height differences and concurrently limit the track errors. Since the average along-track SSH of the T/P series is used as a reference in this study, each satellite including ERS series and CryoSat-2 are calibrated to the T/P reference.

An interpolation technique is performed to create the MSS model grid after applying crossover adjustment. Based on the previous regional MSS model, both models developed by Yahaya et al. (2016) and Zulkifle et al. (2019) applied the inverse distance weighting (IDW) technique for MSS data gridding. Although Jin et al. (2016) and Yuan et al. (2020) stated that the least square collocation (LSC) is the most suitable method for gridding, this study implements ordinary kriging for the regional UTM20 MSS model. The kriging method is similar to IDW, in which it weights the surrounding measured values to compute a prediction at predicted points. The formula is expressed in **Equation 3** (Environmental Systems Research Institute, 2016a).

$$\widehat{Z}(s_0) = \sum_{i=1}^{N} \lambda_i Z(s_i), \tag{3}$$

where $Z(s_i)$ is the measured value at the ith location, λ_i is an unknown weight for the measured value at the ith location, $\widehat{Z}(s_0)$ is a predicted value, and N is the total number of measured values. In IDW, the weight is strictly based on the distance to the estimated point. Thus, the weight increases with the decreasing distance to the predicted location (Hamid et al., 2018). On the other hand, the weight in ordinary kriging relies on the model fitted to the measured points, the distance to the estimated point, and the spatial relationships between the measured values around the estimated point.

The ordinary kriging in this study use covariance function instead of semivariogram to express autocorrelation. The covariance functions quantify the assumption that the nearby measurements appear to be equal to those farther apart. It measures the strength of statistical correlation as a function of distance. The covariance function modeling method fits the covariance curve to the empirical data, in which the aim is to obtain the best fit model. Later, this model is utilized in the predictions. The covariance function of the ordinary kriging method is expressed in **Equation 4** (Environmental Systems Research Institute, 2016b).

$$C\left(s_i, s_j\right) = cov\left(Z(s_i), Z\left(s_j\right)\right), \tag{4}$$

where $C(s_i, s_j)$ is the covariogram or covariance function and cov is the covariance. $Z(s_i)$ and $Z(s_j)$ are the variables at different locations. When two points, such s_i and s_j are close to each other, it is expected that the value will be similar and the correlation is larger. Nevertheless, if two points are farther apart, the value becomes less similar, and the correlation becomes zero. Therefore, all the mean profiles of ERM tracks and corrected SSH of GM tracks are interpolated into a regular grid of 1.5-min by 1.5-min resolution.

Moving Average Technique of 19-years Interval

The moving average technique of 19-year intervals has been introduced by Yuan et al. (2020). The result showed that this technique had effectively increased the precision of the MSS model. Consequently, the moving average of the 19-year technique is also applied for the computation of the UTM20 MSS model. The satellite altimetry data from 1993 to 2019 are classified into eight groups as listed in **Supplementary Table S2**, where each group has a 19-year interval data span.

The satellite altimetry data from each group is used separately to compute the MSS model with a 1.5-min by 1.5-min grid over Malaysian seas. Thus, eight MSS models are obtained from each group. Last, the grid of eight MSS models is averaged at each grid point to obtain UTM20(G) MSS. The averaging step is expressed in **Equation 5**.

$$\overline{h}_{UTM20(G)} = \frac{\overline{h}_{G1} + \overline{h}_{G2} + \overline{h}_{G3} + \overline{h}_{G4} + \overline{h}_{G5} + \overline{h}_{G6} + \overline{h}_{G7} + \overline{h}_{G8}}{8}, \tag{5}$$

where $\overline{h}_{UTM20(G)}$ is the average of eight MSS models and $\overline{h}_{Gn}$ $(n = 1, \ldots, 8)$ is the MSS model of each group, which in this study encompass eight groups of the models.

Computation of the UTM20 Mean Dynamic Topography

The practical approach renders the process of MDT quantified from MSS and geoid model to be conceptually straightforward. In general, MDT ζ, is commonly defined as the difference between MSS and the geoid as derived in **Equation 6**.

$$\zeta = \overline{h} - N, \tag{6}$$

where $\overline{h}$ is the average sea surface height above the reference ellipsoid, and N is the geoid height. Nevertheless, several challenges should be scrutinized to produce better MDT models, where the MSS and geoid must be relative to the same reference ellipsoid and exist in the same tidal system. Regional MDT is determined from the local gravimetric geoid,

namely, MyGeoid_2017 (Jamil et al., 2017), subtracted from the regional UTM20 MSS model. MyGeoid_2017 is a newly developed precise local geoid-based vertical datum from the amalgamation of terrestrial, airborne, and satellite platforms. This local geoid model has been determined using the combined spherical harmonic model Earth Gravitational Model/Gravity Field and Steady-State Ocean Circulation Explorer (EGM/GOCE) to spherical harmonic degree N = 720, Shuttle Radar Topography Mission (SRTM) digital elevation model, DTU15 satellite altimetry-derived gravity anomalies, and flight line airborne gravity data (Jamil et al., 2017).

The UTM20 MSS is in the mean tide system, while the permanent tide system of MyGeoid_2017 is unclear. Based on Keysers et al. (2015), geoid undulations may be used in any system. However, EGMs are generally issued as both in the tide-free and zero tides. In general, most regional geoids acquired their tidal system from the EGM, but the system should be precisely specified. Thus, it is expected that MyGeoid_2017 is in tide-free system. Both models must be in the same permanent tide system in order to compute MDT precisely. Here, UTM20 MSS is converted to tide-free system by using the conversion formula (in cm) as expressed in **Equation 7** (Ekman, 1989; Keysers et al., 2015).

$$N_n = N_m + (1 + k)\left(9.9 - 29.6\,sin^2\,\phi\right), \tag{7}$$

where N_n is the tide-free system, N_m is the mean tide system, k is a variable called Love number, which depends on the mass distribution within the planet (usually taken as 0.3), and ϕ is the latitude of the point. Furthermore, thorough filtering of the differences is necessary to eliminate short-scale geoid signals and obtain an appropriate MDT estimation (Knudsen and Andersen, 2013). According to Farrell et al. (2012), this process will also reduce the presence of noise residual in the MSS field due to unmodeled tide and the ground track striation.

Spatial averaging filtering methods are likely to be more reliable and precise for regional MDT applications than spectral filtering methods (Losch et al., 2007; Knudsen and Andersen, 2013). Spatial filters with a Gaussian-like roll-off have more accurate results than those with sharp space cut-offs. 2D isotropic Gaussian function is expressed as **Equation 8** (Fisher et al., 2003).

$$G(x, y) = \frac{1}{2\pi\sigma^2} e^{-\frac{x^2+y^2}{2\sigma^2}}, \tag{8}$$

where x is the distance from the origin in the horizontal axis, y is the distance from the origin in the vertical axis, and σ is the standard deviation of the distribution, which is also defined as the filter radius. Hence, the unfiltered regional MDT is computed by differentiating the UTM20 MSS model and a local precise gravimetric geoid, MyGeoid_2017. A spatial filter is applied to smooth the unfiltered MDT. The spatial filter is an average filter at which the kernel is *nx* times *ny* matrix. Variables *nx* and *ny* are the number of kernel points in the east–west and north–south direction, respectively. An ideal sigma (σ) should be identified to preserve actual physical signal data. A larger sigma will over-filter the signal data. However, a smaller sigma will not entirely eliminate error from the signal data. Here, isotropic Gaussian smoothing kernel with a standard deviation (σ) of 6 is adopted to filter the noise in the 1.5-min gridded MDT. The smoothing is executed using the *imgaussfilt* function in MATLAB software. Finally, the final regional MDT is established by re-interpolating into a similar grid size as the UTM20 MSS model. The size of the study area for the UTM20 MDT model is reduced to follow the size of MyGeoid_2017 obtained from DSMM, which is 0°N ≤ latitude ≤ 9°N and 98°E ≤ longitude ≤ 121°E.

RESULTS

Temporal Sea Level Variability Correction

The ERM data of satellite altimetry used in this study, as listed in **Table 1**, undergo collinear analysis to eliminate seasonal variations and to obtain the average along-track SSH within the observation period. Since the GM data of satellite altimetry are involved in the MSS model, the corrections of sea level variability of the data as listed in **Table 1** are principally considered. Only two satellite missions from GM data are involved in establishing the UTM20 MSS model, namely, Jason-1 Phase C and CryoSat-2. The statistical results of crossover differences before and after the removal of seasonal variations of ERM and GM data are listed in **Table 3**. T/P series Phase A shows the highest accuracy among others, which is within 4 cm. In addition, other ERM data show significant improvement of SSH accuracy, which is better than 10 cm. It can be deduced that the impact of seasonal variations on SSH via collinear analysis has been minimized. Apart from that, the precision of ERM SSH data is considerably better than 10 cm. For GM data, the results inferred that the precision of both GM data is significantly improved after applying the correction. The crossover differences are improved within 6–7 cm.

Supplementary Figure S2 shows that the seasonal variations from ERM data are eliminated significantly. In the spatial domain of the SSH time series, the RMS of SSH before seasonal correction is 9.95 cm. After detrending the data and removing the seasonal signal, the RMS of SSH is significantly improved to 2.01 cm. The removal of seasonal variation is further analyzed by comparing the signal in the spectral domain. It signifies that after applying seasonal correction, the power spectrum of SSH frequency is lower than the signal before applying the seasonal correction.

Supplementary Figure S3 shows the achievement in correcting the seasonal variations of Jason-1 Phase C GM data. The upper map illustrates the height differences between SSH of Jason-1 Phase C GM and UTM20 MSS, where the sea level variability is induced in the measurements (**Supplementary Figure S3A**). It clearly indicates that this discrepancy is mainly prevailed by sea level variability. **Supplementary Figure S3B** shows the height differences between Jason-1 Phase C GM SSH and UTM20 MSS, where the sea level variability of GM data is removed. The RMS of Jason-1 Phase C GM data is remarkably improved from 10.27 to 6.53 cm. Therefore, it can be concluded that the sea level variability of ERM and GM data have been processed appropriately prior to computing the regional MSS model.

TABLE 3 | Statistical results of crossover difference before and after seasonal correction (units are in meters).

ERM data	Before correction			After correction		
	Mean	STD	RMS	Mean	STD	RMS
T/P, Jason-1 & Jason-2 (Phase A)	0.0047	0.1534	0.1533	–0.0064	0.0387	0.0392
T/P, Jason-1 & Jason-2 (Phase B)	0.0025	0.1598	0.1598	–0.0037	0.0477	0.0478
ERS-2	–0.0013	0.1586	0.1586	0.0061	0.0838	0.0840
GFO	–0.0058	0.1585	0.1586	–0.0082	0.0661	0.0666
Envisat-1	–0.0011	0.1504	0.1503	–0.0155	0.0644	0.0662
SARAL/AltiKa	0.0039	0.1511	0.1512	–0.0201	0.0876	0.0899
Sentinel-3A	–0.0069	0.1967	0.1968	0.0053	0.0650	0.0652
GM data	**Before correction**			**After corrections**		
	Mean	STD	RMS	Mean	STD	RMS
Jason-1 (Phase C)	–0.0029	0.1520	0.1521	–0.0024	0.0934	0.0934
CryoSat-2	–0.0038	0.1669	0.1670	–0.0072	0.0932	0.0935

TABLE 4 | Statistical results of crossover differences before and after crossover minimization (units are in meters).

Satellite	Before crossover minimization		After crossover minimization	
	Mean	RMS	Mean	RMS
T/P series (Phase B)	0.0121	0.0473	0.0000	0.0452
ERS-2	–0.0429	0.0837	0.0000	0.0716
GFO-1	–0.0255	0.0513	0.0000	0.0441
Envisat-1	–0.0107	0.0718	0.0000	0.0706
SARAL/AltiKa	–0.0917	0.1073	0.0000	0.0558
Sentinel 3A	0.0161	0.0303	0.0000	0.0257
CryoSat-2	–0.0541	0.0938	0.0000	0.0763
Jason-1 (Phase C)	–0.0478	0.0892	0.0000	0.0747

UTM20 Mean Sea Surface Model

After correcting the sea level variability of ERM and GM data, crossover minimization is performed to reduce the existing errors as mentioned in *Determination of the UTM20 Mean Sea Surface* section. Since T/P series Phase A has the highest orbit accuracy among others, it is used as the foundation for adjustment. Thus, each of the missions is adjusted towards the foundation. **Table 4** shows the statistical results before and after crossover minimization. The results show that the accuracy of crossover difference is essentially improved after crossover minimization is performed. All missions' accuracy is below 10 cm after applying crossover minimization.

A regional MSS model is successfully generated by adopting an ordinary kriging interpolation method. Two types of UTM20 MSS models are established in this study. The first model is established using the moving average technique of 19-year interval where MSS from each of the eight satellite altimetry groups is interpolated from the common average approach to form eight gridded MSS models. The average of these eight gridded MSS models is then computed to obtain UTM20(G) MSS model. The second model, namely, UTM20(F) MSS model, is established without adopting a 19-year moving average technique but by interpolating multi-mission satellite altimetry data as listed in **Table 1** from a standard average method. Since Yuan et al. (2020) have conducted the study on a 19-year moving average technique and the results showed that the model's accuracy had improved significantly; this technique is once again verified in this study within the region of the Malaysian seas. It is crucial to determine whether the moving average of the 19-year technique can significantly increase the accuracy of the regional MSS model as the study area is induced by significant tidal errors in altimetry measurements.

Figure 2 illustrates the UTM20(G) MSS model where the height of MSS increases gradually from Malacca Straits towards the Sulu Sea. All four regions of Malaysian seas incorporated in this study yield different MSS values based on the WGS84 reference ellipsoid. In particular, the Malacca Straits has the lowest MSS, which is located below the reference ellipsoid, while Celebes Sea generated the highest MSS value. It should be noted that the MSS height at the Celebes Sea and the Sulu Sea are higher than the South China Sea and Malacca Straits. Henceforth, this regional MSS model is proven essential for charting datum, observing sea-level changes and concurrently encouraging geophysical and oceanographic applications such as tidal prediction and sea-level rise study.

UTM20 Mean Dynamic Topography Model

Different MDT models utilize various geoid models in the computation of MDT, rendering it crucial to select the best geoid model. For this research, MyGeoid_2017 is adopted to

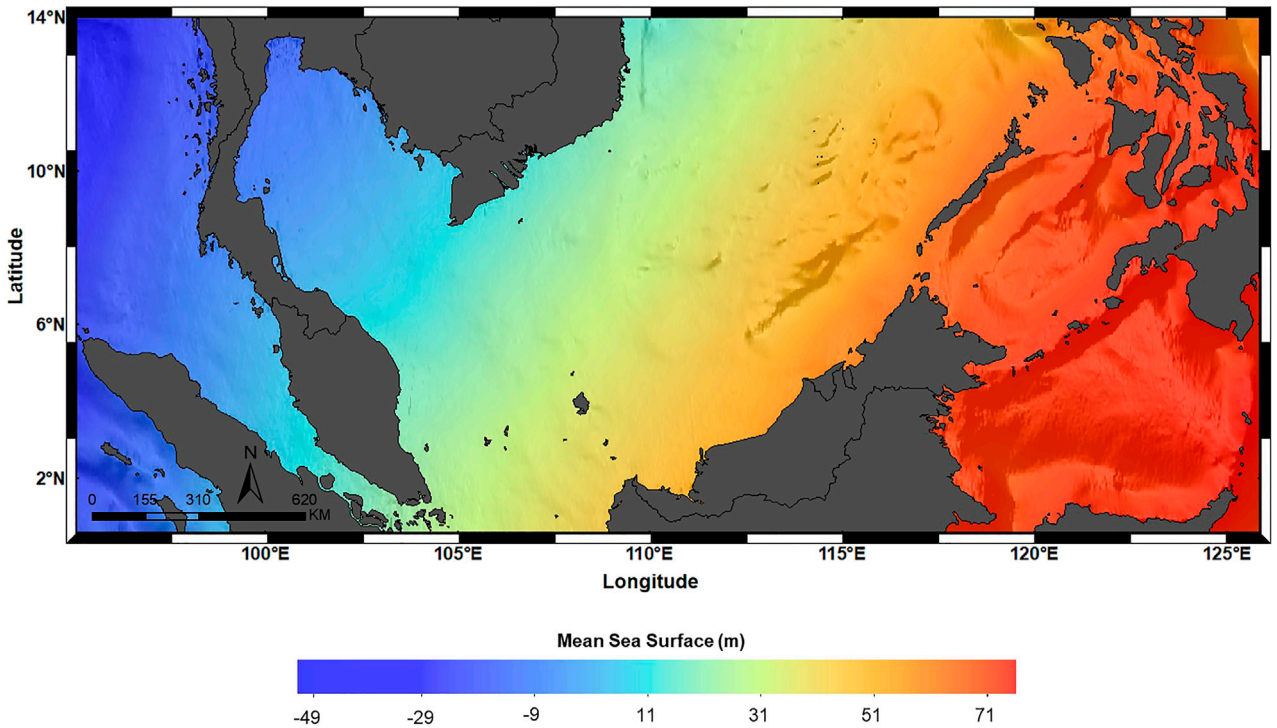

FIGURE 2 | UTM20(G) MSS model developed by using a 19-year moving average technique.

be subtracted with the UTM20 MSS model to compute the regional UTM20 MDT model. It is selected due to MyGeoid_2017, a local precise gravimetric geoid model developed by the government agency, DSMM, which is often utilized by the local surveyor community as a locally based geoid separation model for the establishment of vertical positioning aspects in surveying and work practices. The geodetic MDT is calculated using a pointwise gridded approach between the gridded MSS model and geoid height as expressed in **Equation 6**. **Figure 3A** shows the preliminary UTM20 MDT using the pointwise approach. The figure shows that the local geoid omission errors leak into the MDT due to the small scale of MSS missing from the geoid. This means that the detail is obscured by noise (gross features) due to geoid omission errors.

Bingham et al. (2008) stated that the problem of geoid omission error contaminated the MDT could be simply overwhelmed by using the spatial averaging filter to smooth the MDT. For instance, Jayne (2006) had conducted a Hamming window for spatial filtering. However, this study is utilizing a Gaussian-like roll-off filter to smooth the final regional UTM20 MDT. With few experiments, six sigma, which is approximately 70 km Gaussian filter size, is carried out to remove the scale of the short-wavelength noise and preserve mesoscale features in the study area. Not only that, but filtering can also eliminate the ground track striation, so-called the orange skin effect. **Figure 3B** shows the final UTM20 MDT computed after applying the spatial averaging Gaussian filter.

Thus, it can be concluded that the filtered regional MDT in this study preserves the spectral content with the shortest wavelength of approximately 70 km. The MDT has the highest value near the Gulf of Thailand, as shown in **Figure 3**. The pattern shows that the slope of MDT decreases from the Gulf of Thailand towards the south of Peninsular Malaysia. However, the pattern of the MDT slope decreases as it goes toward the northwest of the Malacca Straits. It can also be deduced that the South China Sea has the highest MDT values compared to the Malacca Straits, the Celebes Sea, and the Sulu Sea. Meanwhile, the Malacca Straits has the lowest MDT values among others.

DISCUSSION

This section mainly discusses the verification of the regional UTM20 MSS model and UTM20 MDT model. In general, assessing the accuracy of the MSS model developed from satellite altimetry is a very challenging process. This is due to the high accuracy of SSH determination provided by the satellite altimeter and almost all satellite altimetry data are implemented in the derivation of the MSS model. Therefore, the reliability and accuracy of the UTM20 MSS model are verified by comparing the model with two global MSS models, namely, DTU18 and CLS15 MSS. For UTM20 MDT, the model is verified with two global MDT models, namely, DTU15 and CLS18 MDT. The accuracy of both regional MSS and MDT models are also verified with Global Navigation Satellite System (GNSS) leveled tide gauges along the coast of Peninsular Malaysia.

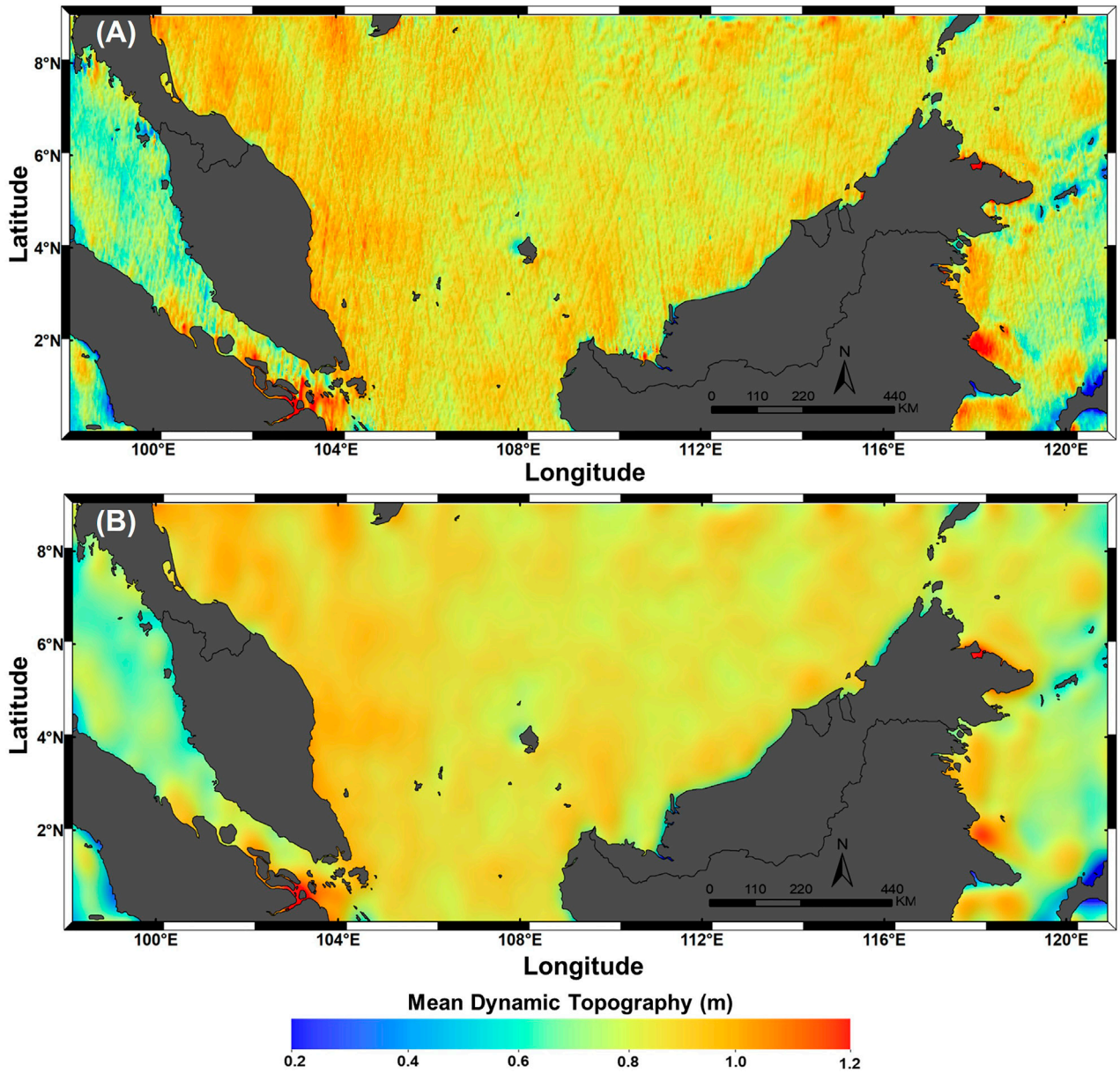

FIGURE 3 | UTM20 Mean Dynamic Topography model. **(A)** Preliminary (unfiltered) model. **(B)** Final (filtered) model.

Verification of the UTM20 MSS with the global MSS models

The discrepancy between MSS models relies on the satellite altimetry data involved in computation and processing techniques (Schaeffer et al., 2012; Yuan et al., 2020). The satellite mission of Sentinel-3A is not included in CLS15 and DTU18 models, whereas it is included in UTM20(G) and UTM20 (F). Likewise, the SARAL/AltiKa mission is involved in DTU18, UTM20(G), and UTM20(F), but not in the CLS15 model. Moreover, the regional MSS models have distinct reference periods compared to the global MSS models. The reference period for UTM20(G) and UTM20(F) spans from 1993 to 2019. Meanwhile, the reference period for CLS15 and DTU18 spans from 1993 to 2012. The data processing method also can cause the discrepancy between MSS models. This includes the pre-processing data that involve the application of range and geophysical corrections, the treatments in removing sea level variability, and the utilization of data interpolation method.

DTU18, CLS15, UTM20(G), and UTM20(F) are compared in terms of gridded MSS points as listed in **Tables 5**, **6**. **Table 5** shows the statistical result of the comparison for all points. Meanwhile, **Table 6** shows the statistical comparison results for the points where the outliers in the difference are excluded

TABLE 5 | Statistical results of the comparison between four MSS models (all points are included) (units are in meters).

Models	Max	Min	Mean	STD	RMS	Total points
UTM20(G) – CLS15	2.0669	–1.5496	0.0179	0.0717	0.0738	282,605
UTM20(F) – CLS15	2.1517	–2.0116	–0.0043	0.0741	0.0742	282,605
UTM20(G) – DTU18	5.3188	–1.4146	0.0414	0.1402	0.1462	282,605
UTM20(F) – DTU18	5.3624	–1.8766	0.0192	0.1435	0.1448	282,605
CLS15 – DTU18	5.4450	–1.6500	0.0235	0.1305	0.1326	282,605
UTM20(G) – UTM20(F)	1.0493	–1.9937	0.0222	0.0379	0.0439	282,605

TABLE 6 | Statistical results of the comparison between four MSS models (exclusion data by 3σ) (units are in meters).

Models	Max	Min	Mean	STD	RMS	Total points
UTM20(G) – CLS15	0.2149	–0.2149	0.0185	0.0426	0.0464	278,690
UTM20(F) – CLS15	0.2222	–0.2223	–0.0040	0.0443	0.0445	278,690
UTM20(G) – DTU18	0.4205	–0.4199	0.0315	0.0589	0.0668	278,690
UTM20(F) – DTU18	0.4302	–0.4286	0.0090	0.0608	0.0614	278,690
CLS15 – DTU18	0.3910	–0.3910	0.0138	0.0461	0.0481	278,690
UTM20(G) – UTM20(F)	0.1136	–0.1136	0.0224	0.0262	0.0345	278,690

TABLE 7 | Comparison of RMS misfit between regional MSS model and DTU models in Malaysian seas (units are in meters).

	MSS1 - DTU13	MSS2 - DTU15	UTM20 - DTU18
Max	7.443	12.998	5.3188
Min	–13.426	13.063	–1.4146
Mean	0.3004	–0.501	0.0414
RMSE	2.217	2.154	0.1462

by three times of standard deviation (3σ). The exclusion would prevent contamination by wrong observations around the coastal regions and islands. Both tables show that the standard deviation (denoted as STD) values for the comparison of UTM20(G) and UTM20(F) with CLS15 are lower than the comparison with DTU18. This implies that there are distinct differences between regional models and DTU18, and the best consistency is shown by the UTM20(G), UTM20(F), and CLS15 models. A total of 3,915 points have been rejected after applying three sigmas of the difference, and it shows a significant improvement of accuracy in MSS models. The distribution of rejected points is illustrated in **Supplementary Figure S4**. It clearly indicates that most of the rejected points are distributed nearshore regions. This is due to the contamination within the altimetry footprint when approaching the land, causing inaccurate observation.

These four MSS models are further verified in the offshore and coastal regions (20 km from the land). The statistical results of the differences are tabulated in **Supplementary Table S3**. All points are involved in the computation of statistical results. UTM20(F), UTM20(G), CLS15, and DTU18 are denoted as U(F), U(G), CLS, and DTU, respectively. The results show that the STDs of U(G)-DTU, U(F)-DTU, and CLS-DTU are less than 5 cm in the offshore region. However, these STDs are more prominent in the coastal region, which is within 30–33 cm. Significant differences exist between the models because of the contrasting satellite altimetry data and preprocessing techniques being executed. The STD of differences between UTM20(F) and UTM20(G) is 2.4 and 7.4 cm in the offshore and coastal regions, respectively. Moreover, UTM20(G) is remarkably more accurate than UTM20(F). This is proven where the STD of comparison between CLS15 and DTU18 models with the UTM20(F) is higher than the STD of comparison between those two models with UTM20(G). Therefore, the UTM20(G) MSS model is selected as the final regional UTM20 MSS model and further utilized for MDT computation.

The accuracy of regional MSS models developed by UTM is compared and tabulated in **Table 7**. The first model was developed by Yahaya et al. (2016) (denoted as MSS1) and then further enhanced by Muhammad (2018) and Zulkifle et al. (2019) (denoted as MSS2). Although the methodology on the computation of both MSS models is unclear, these previous regional models have computed the statistical results by comparing them with the DTU model. Thus, the root mean square error (RMSE) between previous models and DTU are compared with RMSE between UTM20 MSS and DTU model. The result shows significant improvement in accuracy for the models from 2 to 0.14 m misfit errors. This indicates that the UTM20 MSS model successfully scrutinizes the proper mean derived from along-track SSH and properly removed sea level variability and other errors in the data processing.

Verification of the UTM20 MSS With GNSS Leveled Tide Gauge

Further verification of MSS is conducted by comparing the UTM20 MSS with mean sea level (MSL) derived from *in-situ* GNSS leveled tide gauges. Eleven tide gauge stations around Peninsular Malaysia are selected for the purpose of

TABLE 8 | Statistical result of differences between tide gauges MSL and extrapolated points of satellite altimetry MSS (units are in meters).

Location	Marker name	UTM20 - TG	DTU18 - TG	CLS15 - TG
Pulau Pinang	P0379	–0.1127	–0.1132	–0.1129
Lumut	A0401	–0.1053	–0.0557	–0.1006
Tanjung Keling	M0331	–0.0796	–0.2515	–0.0570
Kukup	J5328	–0.0364	–0.1679	0.0242
Tanjung Sedili	J0888	0.0018	–0.0844	–0.1394
Pulau Tioman	C0501	–0.1042	–0.1739	–0.1257
Tanjung Gelang	C0331	0.0385	–0.0378	–0.0968
Cendering	T0283	–0.0337	–0.0282	–0.0663
Geting	D0354	–0.2444	–0.2500	–0.1212
Pulau Langkawi	K0172	–0.1601	0.1166	0.0442
Port Kelang	B0169	–0.0291	–0.0837	0.0696
Mean difference		–0.0787	–0.1027	–0.0620
Standard deviation		0.0759	0.1018	0.0707

verification. The MSL at the respective tide gauges is derived from 23 years observation period covering from 1993 to 2015 by a simple averaging method. As all tide gauge benchmarks (TGBMs) are referenced to zero tide gauge, the Tide Gauge GNSS Campaign 2019 was performed to shift the tidal measurement relative to the reference ellipsoid. The campaign was not implemented in Sabah and Sarawak-based tide gauge stations due to the lack of logistics requirements and time constraints for mobilization and demobilization in the two states. **Supplementary Figure S5** illustrates eleven DSMM tide gauge stations involved in the Tide Gauge GNSS Campaign 2019 and the relationship of various vertical surfaces towards achieving the tidal measurement with respect to the ellipsoidal surface (Azhari, 2003). The formula to obtain the MSL with respect to ellipsoid is shown in **Equation 9**.

$$h_{MSL} = h_{GPS} - \Delta H_{LEV} + \Delta H_{MSL}, \quad (9)$$

where h_{MSL} is the MSL height above the reference ellipsoid, h_{GPS} is the GNSS ellipsoidal height at TGBM, ΔH_{LEV} is the height of TGBM above zero tide gauge, and ΔH_{MSL} is the MSL height above zero tide gauge.

UTM20 MSS, CLS15 MSS, and DTU18 MSS models are extrapolated to the tide gauges location using bilinear interpolation. This interpolation method uses a distance-weighted average of the four nearest point values to estimate a new point value. These MSS models at extrapolated points are compared with MSL derived from GNSS leveled tide gauges. **Table 8** shows the statistical results of differences between MSL of GNSS leveled tide gauges and MSS of satellite altimetry models at extrapolated points. The results show that the mean height differences between tide gauges MSL and UTM20 MSS are −7.8 cm with a standard deviation of 7.5 cm. The accuracy of UTM20 and CLS15 at tide gauges location is almost similar, which is within 7 cm, while the accuracy of DTU18 is greater than both models, which is 10 cm. In addition, the height differences between the MSS models and GNSS leveled tide gauges ranging from −25 to 11 cm. This might be due to a decrease in the accuracy of altimetry observations when assessed closer to the coast. No available altimetry data or invalid value of MSS might be obtained in this study as the altimetric measurements approach within 5–10 km to the coast. According to Vignudelli et al. (2019), the altimetry sensors were not highly sufficient for the coastal region to reach precise sea levels due to the corrupted waveforms. This might also be due to a few forcing factors affecting the sea level changes in coastal areas. For instance, the SSH derived from satellite altimetry includes contributions from ocean thermal expansion and ocean circulation, water movement from land to ocean, and changes in land water storage. The larger-scale changes are covered by the sea level fluctuations from tides and coastal processes due to air pressure effects and wind setup (Woodworth et al., 2019). This resulted in the proposal to implement high-resolution coastal altimetry data and multiple retracking methods to improve SSH estimation in the coastal areas (Idris et al., 2017; How et al., 2020).

Verification of the UTM20 MDT With the Global MDT Models

Each MDT model is provided with a particular spatial resolution and time coverage. Nevertheless, a similar MDTs' characteristic is needed for consistent comparison. In this study, CLS18 MDT and DTU15 MDT are utilized for comparison with UTM20 MDT. All the models are resampled with a spatial resolution of 2-min by 2-min. The problem that arises in comparing MDT models is that each model is computed with respect to different reference surfaces, which occurred on three of the models used in this study. UTM20 MDT is computed by subtracting the UTM20 MSS with local gravimetric geoid (MyGeoid_2017). Meanwhile, DTU15 MDT is developed by subtracting the DTU15 MSS with the EIGEN-6C4 geoid model (Andersen et al., 2015), and CLS18 MDT is computed by differentiating the CLS15 MSS with the GOCO5S geoid model (Mulet et al., 2019). Finalizing Surveys For the Baltic Motorways Of The Sea FAMOS (2017) proposed that a comparison of MDT anomalies be performed to overcome this problem. It is computed by de-meaning the values for each surface. This method is simply comparing the variability of each MDT rather than its magnitude. **Figures 4A–C** show the MDT anomalies of three MDT models, which are CLS18, DTU15, and UTM20, respectively. The figures clearly indicate that all the models have a similar pattern, although UTM20 MDT anomalies

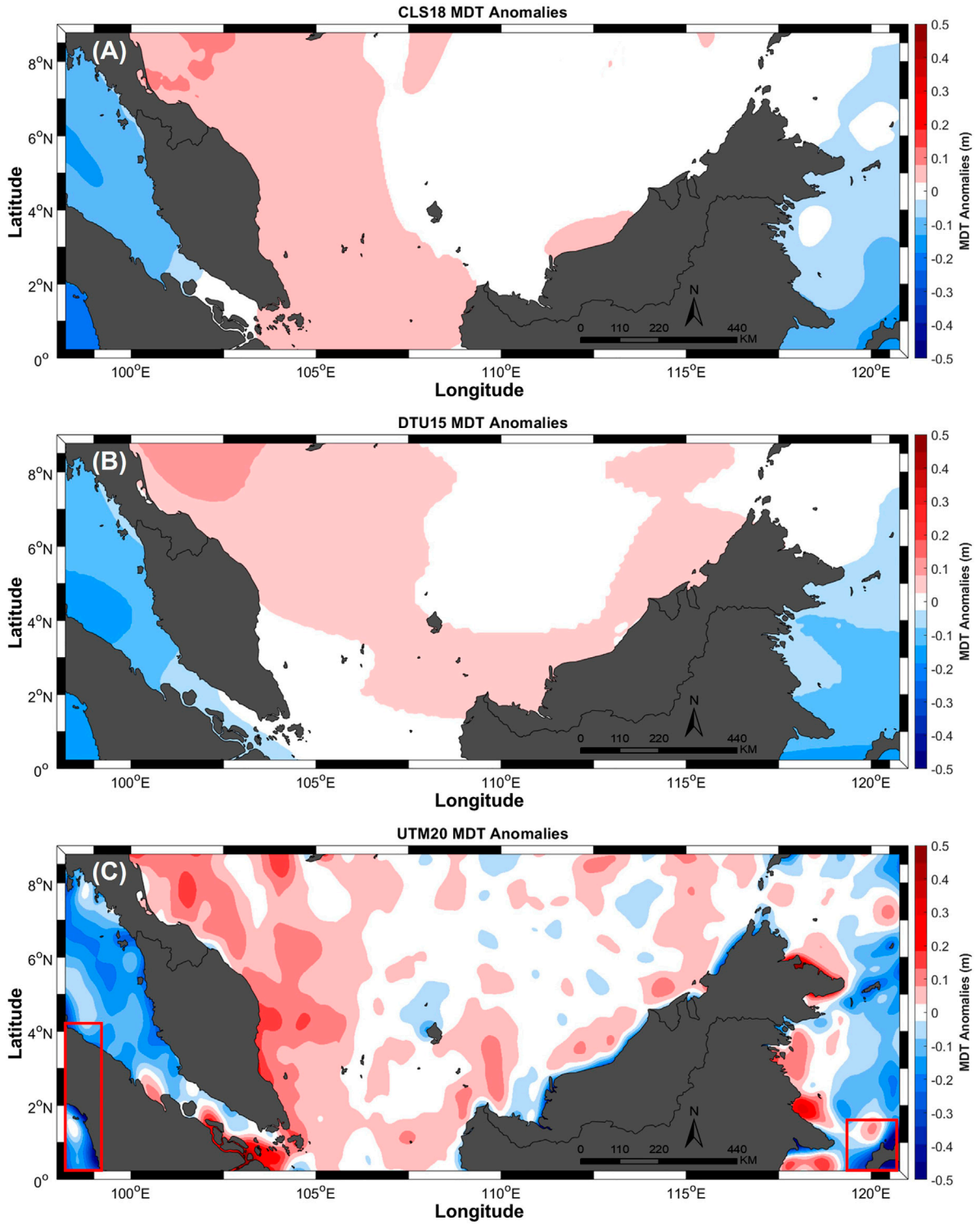

FIGURE 4 | MDT anomalies of three models: **(A)** CLS18 model; **(B)** DTU15 model; **(C)** UTM20 model.

show an unsmooth surface compared to CLS18 and DTU15, which might be due to the models' resolutions. The dark blue color that appeared at the south of Celebes Sea and the south-west Sumatra in UTM20 MDT anomalies is due to the data being near the edge of the studied area (**Figure 4C**). Therefore, smoothing and averaging techniques are inappropriate in such edge.

The statistical results of the MDT anomalies differences are compared as shown in **Table 9**. MDT anomalies between CLS18

TABLE 9 | Statistical results of the MDT anomalies differences (units are in meters).

	UTM20 - DTU15	UTM20 - CLS18	CLS18 - DTU15
Max	0.2111	0.1940	0.0548
Min	−0.2110	−0.1940	−0.0548
Mean	−0.0012	−0.0003	−0.0008
STD	0.0551	0.0507	0.0167

and DT15 show the lowest STD of the differences, which is 1.67 cm. Meanwhile, MDT anomalies between UTM20 and DTU15 show the highest STD of the differences, which is 5.5 cm. MDT anomalies between UTM20 and CLS18 have STD of 5.1 cm. Thus, it can be inferred that MDT anomalies of UTM20 have better agreement with CLS18. The discrepancy between models may be due to the differences in the epoch at which the models are estimated.

Verification of the UTM20 MDT With Tide Gauges Geodetic MDT

Although evaluating the discrepancies of MDT anomalies between regional and global models provides an opportunity for comparison, it does not clearly indicate the approximate accuracy of the model. Further verification is needed to estimate the reliability of UTM20 MDT. The efficiency of the MDT models is analyzed by comparing them with *in-situ* data from the DSMM tide gauge stations. The precise local geoid model (MyGeoid_2017) is utilized for the MDT computation at tide gauges (denoted as MDT_{TGBM}) to ensure its consistency with the computed MDT models. Also, the tide system of all measurements is set to be identical to the tide-free system. Note that no filtering is performed in the computation of MDT at tide gauge stations. The MDT models of UTM20, CLS18, and DTU15 are extrapolated to the tide gauge stations using the bilinear interpolation method. In order to simplify the comparison, the MDT values at Pulau Langkawi are arbitrarily fixed to zero. Apart from that, all MDT values at other tide gauge stations are adjusted to Pulau Langkawi.

Figure 5A depicts the comparison of the MDT models with the MDT_{TGBM}. The range of the entire MDT along the coast of Peninsular Malaysia is within 0–0.4 m, which is higher along the east coast and lower in the west coast region (refer to **Figure 4**). Also, **Figure 5B** shows the absolute differences between the MDT models with respect to MDT_{TGBM}. The absolute differences between UTM20 MDT and MDT_{TGBM} are lower in most tide

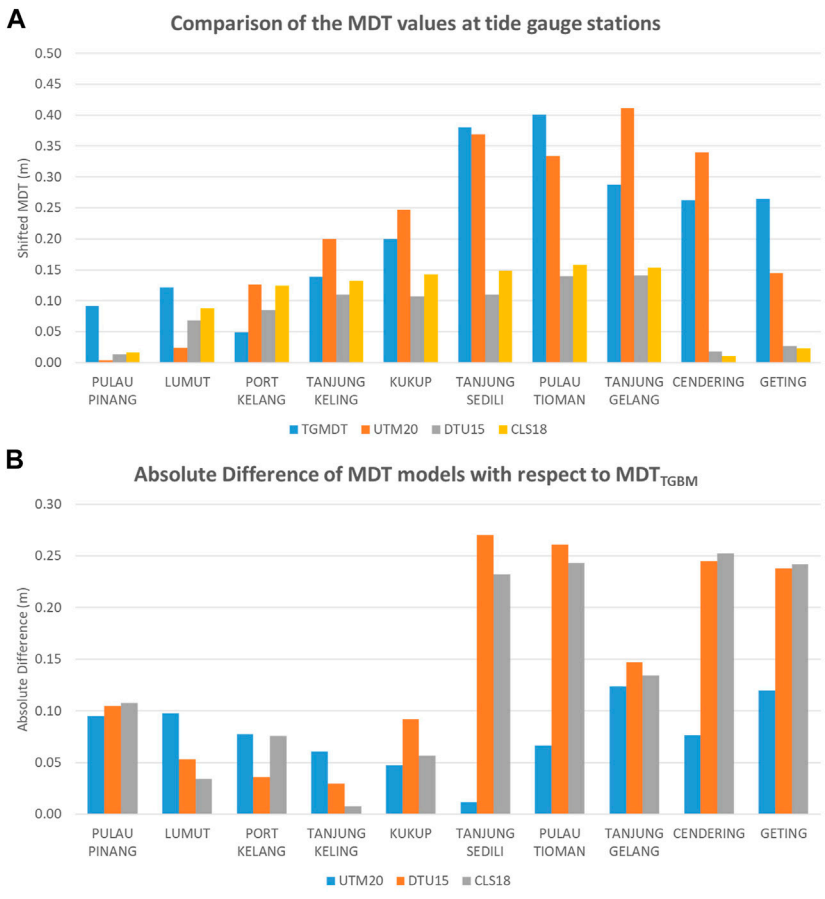

FIGURE 5 | (A) Comparison of the MDT_{TGBM} values with MDT models (UTM20, CLS18, and DTU15) at tide gauge stations. **(B)** The absolute difference of the MDT models with respect to the MDT_{TGBM} at which MDT at Pulau Langkawi is fixed to zero in all models and others are adjusted accordingly.

TABLE 10 | Statistical results of the MDT models (UTM20, CLS18, and DTU15) with respect to the tide gauge MDT (MDT_{TGBM}) (units are in meters).

Location	Marker name	UTM20 - MDT_{TGBM}	DTU15 - MDT_{TGBM}	CLS18- MDT_{TGBM}
Pulau Langkawi	K0172	0.0000	0.0000	0.0000
Pulau Pinang	P0379	0.0951	0.1045	0.1075
Lumut	A0401	0.0980	0.0534	0.0338
Port Kelang	B0169	0.0774	0.0360	0.0759
Tanjung Keling	M0331	0.0606	0.0297	0.0074
Kukup	J5328	0.0473	0.0922	0.0566
Tanjung Sedili	J0888	0.0113	0.2704	0.2319
Pulau Tioman	C0501	0.0666	0.2612	0.2429
Tanjung Gelang	C0331	0.1241	0.1471	0.1341
Cendering	T0283	0.0766	0.2448	0.2521
Geting	D0354	0.1197	0.2377	0.2419
Mean difference		0.0647	0.1343	0.1258
Standard deviation		0.0380	0.0980	0.0955

gauge stations, which display below 0.15 m compared to the CLS18 and DTU15 MDT. The highest MDT differences between UTM20 MDT and MDT_{TGBM} among all tide gauge stations are within 0.12 m, while CLS18 and DTU15 record 0.25 and 0.27 m, respectively. This figure clearly indicates that the effects of low accuracy of SSH observations from altimetry in the coastal area and interpolation method used may translate the actual shifted values.

The statistical results of the absolute differences between MDT models and MDT_{TGBM} are also computed and tabulated in **Table 10**. The UTM20 MDT has the smallest STD of 3.80 cm compared to the CLS18 MDT and DTU18 MDT, where the STD differences are 9.55 and 9.80 cm, respectively. Note that the value of MDT differences at each tide gauge station in **Table 10** is shifted to Pulau Langkawi tide gauge station. Therefore, considering the results of all tide gauge stations, it can be concluded that UTM20 MDT has a better statistical agreement with independent geodetic tide gauge MDT (MDT_{TGBM}) compared to CLS18 MDT and DTU15 MDT.

CONCLUSION

This article conclusively described the new regional UTM20 MSS and UTM20 MDT models as well as the manner in which they are established. In particular, the UTM20 MSS entailed the altimetry-averaged height of the SSH, which derived from an integration of nine satellites encompassing the period from 1993 to 2019. Two types of regional UTM20 MSS models are established, namely, UTM20(G) and UTM20(F). UTM20(G) is established by applying a 19-year moving average technique, while UTM20(F) is established using a conventional average method. Both models are compared with CLS15 MSS and DTU18 MSS in the Malaysian seas. The results show that all of the established models in this study are at par with the reference models. Apart from that, the UTM20(G) shows higher accuracy than UTM20(F), thus, indicates that the moving average technique of a 19-year interval significantly improved the accuracy of the MSS model in Malaysian seas. Consequently, the UTM20(G) has been chosen to be the final regional MSS model in this study. Carried out on a 1.5-min by 1.5-min grid, it depicted an improvement compared to the previous regional UTM MSS models by successfully measuring the proper mean derived from the along-track SSH. This has been reflected in the misfit value of 14.6 cm between UTM20 MSS and the DTU model compared to the previous model's misfit value of 2-m. Moreover, UTM20 MSS has been validated by comparing it with the MSL from GNSS leveled tide gauges, yielding the accuracy of MSS within 7 cm at all stations.

Furthermore, UTM20 MDT has been established by differentiating the local precise gravimetric geoid (MyGeoid_2017) with the UTM20 MSS model. After subtracting the MSS with the local geoid, the derived MDT undergoes Gaussian spatial filtering to smooth the unwanted noise signal. UTM20 MDT is then compared with the CLS18 MDT and DTU15 MDT models, and it is also compared with 11 tide gauges derived geodetic MDT for statistical data assessment. The findings show that UTM20 MDT is in solid agreement with global models, despite the different epoch of MSS used in each model. The verification results of MDT at tide gauge stations disclosed that the UTM20 MDT has the lowest standard deviation of MDT discrepancies, which is 3.80 cm compared to the CLS18 MDT (9.55 cm) and DTU15 MDT (9.80 cm).

In line with MSS being an essential reference for sea level variability, the UTM20 MSS model indicates relatively better accuracy than previous models. However, specific processes have not been performed in the coastal areas, which, in turn, will become the critical elements for future improvements in deriving MSS and MDT models. For instance, adopting recent radar technology such as Synthetic Aperture Radar (SAR) mode on CryoSat-2 and Sentinel-3A as well as operating high along-track sampling of SARAL/AltiKa (Ka-band altimetry) is essential to enhance the quality of the models near the coast. Indeed, the retracking of altimetry waveforms can increase the accuracy of SSH in the coastal region. Thus,

attempting the retracking process for the altimetry ranges is recommended, as it is a task that may potentially enhance the process of MSS and MDT in the future.

DATA AVAILABILITY STATEMENT

The original contributions presented in the study are included in the article/**Supplementary Material**; further inquiries can be directed to the corresponding author.

AUTHOR CONTRIBUTIONS

AD and DW provided the initial ideas and designed the experiments for this research. MH performed the designed experiments. MH and MP analyzed the outcome data. MH wrote the manuscript with contributions from AM, DW, and MY. All authors were involved in discussions throughout the development.

FUNDING

This project is funded by the Ministry of Higher Education (MOHE) under the Fundamental Research Grant Scheme (FRGS) Fund, Reference Code: FRGS/1/2020/WAB05/UTM/02/1 (UTM Vote Number: R.J130000.7852.5F374).

ACKNOWLEDGMENTS

The authors would like to express their sincere appreciation to the TU Delft, NOAA, Altimetrics LLC for providing the altimetry data through RADS server, AVISO+ through the Centre National d'Etudes Spatiales (CNES) for providing the CLS15 MSS and CLS18 MDT, the Space Research Centre of the Technical University of Denmark (DTU) for providing DTU18 MSS and DTU15 MDT, and Copernicus Marine Environment Monitoring Service (CMEMS) for providing the DUACS L4 gridded SLA. Special thanks to the Department of Surveying and Mapping Malaysia (DSMM) for kindly contributing the local precise geoid model and tidal data for this study.

SUPPLEMENTARY MATERIAL

The Supplementary Material for this article can be found online at: https://www.frontiersin.org/articles/10.3389/feart.2021.665876/full#supplementary-material

REFERENCES

Andersen, O. B., and Knudsen, P. (2009). DNSC08 Mean Sea Surface and Mean Dynamic Topography Models. *J. Geophys. Res.* 114 (11), 327–432. doi:10.1029/2008JC005179

Andersen, O. B., Knudsen, P., and Stenseng, L. (2018). A New DTU18 MSS Mean Sea Surface – Improvement from SAR Altimetry. 172." in Abstract from 25 years of progress in radar altimetry symposium, September 24–29, 2018. Portugal; Ponta Delgada. Available at: https://backend.orbit.dtu.dk/ws/files/163304443/25YPRA_Abstract_Book.pdf (Accessed October 20, 2020).

Andersen, O. B., Piccioni, G., Stenseng, L., and Knudsen, P. (2015). The DTU15 Mean Sea Surface and Mean Dynamic Topography-Focusing on Arctic Issues and Development." in Oral Presentation, in the 2015 OSTST Meeting, Virginia, USA. Editors P. Bonnefond, J. Willis, and Reston Available at: https://meetings.aviso.altimetry.fr/fileadmin/user_upload/tx_ausyclsseminar/files/OSTST2015/GEO-03-Andersen_MSSH_OSTST.pdf (Accessed October 29, 2020).

Andersen, O. B., Piccioni, G., Stenseng, L., and Knudsen, P. (2016). The DTU15 MSS (Mean Sea Surface) and DTU15LAT (Lowest Astronomical Tide) Reference Surface." in Proceedings of the ESA Living Planet Symposium 2016, May 9–13, 2016. Prague, Czech Republik. Editors L. Ouwehand Prague, J. Willis, and Reston. Available at: https://ftp.space.dtu.dk/pub/DTU15/DOCUMENTS/MSS/DTU15MSSþLAT.pdf (Accessed April 18, 2020).

Andersen, O. B., and Scharroo, R. (2011). Range and Geophysical Corrections in Coastal Regions: And Implications for Mean Sea Surface Determination. *Coastal altimetry*, 103–145. doi:10.1007/978-3-642-12796-0_5

Andersen, O. B., Vest, A. L., and Knudsen, P. (2006). The KMS04 Multi-mission Mean Sea Surface." in Proceedings of the Workshop GOCINA: Improving Modelling of Ocean Transport and Climate Prediction in the North Atlantic Region Using GOCE Gravimetry. Novotel, Luxembourg. Editors P. Knudsen 25, 103–106. Available at: http://gocinascience.spacecenter.dk/publications/4_1_kmss04-lux.pdf (Accessed May 15, 2020).

Astina, T. (2017). *Bathymetry Mapping over Malaysian Seas Using Satellite Geodetic Missions*. Skudai: MSc Thesis. Universiti Teknologi Malaysia.

Azhari, B. M. (2003). *An Investigation of the Vertical Control Network of Peninsular Malaysia Using a Combination of Levelling, Gravity, GPS and Tidal DataPhD Thesis*. Skudai: Universiti Teknologi Malaysia.

Bingham, R. J., Haines, K., and Hughes, C. W. (2008). Calculating the Ocean's Mean Dynamic Topography from a Mean Sea Surface and a Geoid. *J. Atmos. Oceanic Tech.* 25 (10), 1808–1822. doi:10.1175/2008JTECHO568.1

Braun, A., Yi, Y., and Shum, C. K. (2004). Altimeter Collinear Analysis. Satellite Altimetry and Gravimetry: Theory and Applications. Lecture Notes. Available at: https://geodesy.geology.ohio-state.edu/course/gs873.2013/lectures/alt_collinear_analysis.pdf (Accessed October 29, 2020).

Dibarboure, G., Renaudie, C., Pujol, M.-I., Labroue, S., and Picot, N. (2012). A Demonstration of the Potential of cryoSat-2 to Contribute to Mesoscale Observation. *Adv. Space Res.* 50 (8), 1046–1061. doi:10.1016/j.asr.2011.07.002

Din, A. H. M., Ses, S., Omar, K. M., Naeije, M., Yaakob, O., and Pa'suya, M. F. (2014). Derivation of Sea Level Anomaly Based on the Best Range and Geophysical Corrections for Malaysian Seas Using Radar Altimeter Database System (RADS). *Jurnal Teknologi* 71 (4), 83–91. doi:10.11113/jt.v71.3830

Din, A. H. M., Zulkifli, N. A., Hamden, M. H., and Aris, W. A. W. (2019). Sea Level Trend over Malaysian Seas from Multi-mission Satellite Altimetry and Vertical Land Motion Corrected Tidal Data. *Adv. Space Res.* 63 (11), 3452–3472. doi:10.1016/j.asr.2019.02.022

Ekman, M. (1989). Impacts of Geodynamic Phenomena on Systems for Height and Gravity. *Bull. Geodesique* 63 (3), 281–296. doi:10.1007/BF02520477

Environmental Systems Research Institute (2016b). Fitting Semivariogram and Covariance Models to the Empirical Data: Semivariogram and Covariance Functions. Available at: https://desktop.arcgis.com/en/arcmap/latest/extensions/geostatistical-analyst/semivariogram-and-covariance-functions.htm (Accessed November 1, 2020).

Environmental Systems Research Institute (2016a). Raster Interpolation Toolset Concepts: How Kriging Works. Available at https://desktop.arcgis.com/en/arcmap/10.3/tools/3d-analyst-toolbox/how-kriging-works.htm (Accessed November 1, 2020).

Farrell, S. L., McAdoo, D. C., Laxon, S. W., Zwally, H. J., Yi, D., Ridout, A., et al. (2012). Mean Dynamic Topography of the Arctic Ocean. *Geophys. Res. Lett.* 39, a–n. doi:10.1029/2011GL050052

Filmer, M. S., Hughes, C. W., Woodworth, P. L., Featherstone, W. E., and Bingham, R. J. (2018). Comparison between Geodetic and Oceanographic Approaches to Estimate Mean Dynamic Topography for Vertical Datum Unification:

Evaluation at Australian Tide Gauges. *J. Geod* 92 (12), 1413–1437. doi:10.1007/s00190-018-1131-5

Finalizing Surveys For the Baltic Motorways Of The Sea FAMOS (2017). Evaluation of MDT Models over Baltic Sea. Available at ftp://ftp.spacecenter.dk/pub/Altimetry/FAMOS/MDT2017(09A)/MDTmodels_LAST.pdf (Accessed 3 November, 2020).

Fisher, R., Perkins, S., Walker, A., and Wolfart, E. (2003). Spatial Filters – Gaussian Smoothing. Available at: https://homepages.inf.ed.ac.uk/rbf/HIPR2/gsmooth.htm (Accessed October 30, 2020). doi:10.2172/814025

Hamid, A. I. A., Din, A. H. M., Hwang, C., Khalid, N. F., Tugi, A., and Omar, K. M. (2018). Contemporary Sea Level Rise Rates Around Malaysia: Altimeter Data Optimization for Assessing Coastal Impact. *J. Asian Earth Sci.* 166 (October), 247–259. doi:10.1016/j.jseaes.2018.07.034

How, G. S., Din, A. H. M., Hamden, M. H., Uti, M. N., and Adzmi, N. H. M. (2020). Sea Level Anomaly Assessment of SARAL/Altika Mission Using High- and Low-Resolution Data. *Jurnal Teknologi* 4 (2020), 83–93. doi:10.11113/jt.v82.13882

Idris, N., Deng, X., Md Din, A., and Idris, N. (2017). CAWRES: A Waveform Retracking Fuzzy Expert System for Optimizing Coastal Sea Levels from Jason-1 and Jason-2 Satellite Altimetry Data. *Remote Sensing* 9 (6), 603. doi:10.3390/rs9060603

Jamil, H., Kadir, M., Forsberg, R., Olesen, A., Isa, M. N., Rasidi, S., et al. (2017). Airborne Geoid Mapping of Land and Sea Areas of East Malaysia. *J. Geodetic Sci.* 7 (1), 84–93. doi:10.1515/jogs-2017-0010

Jayne, S. R. (2006). Circulation of the north atlantic Ocean from Altimetry and the Gravity Recovery and Climate experiment Geoid. *J. Geophys. Res.* 111 (3), C03005 1–17. doi:10.1029/2005JC003128

Jiang, W., Li, J., and Wang, Z. (2002). Determination of Global Mean Sea Surface WHU2000 Using Multi-Satellite Altimetric Data. *Chin. Sci Bull* 47 (19), 1664–1668. doi:10.1360/02tb9365

Jin, T., Li, J., and Jiang, W. (2016). The Global Mean Sea Surface Model WHU2013. *Geodesy and Geodynamics* 7 (3), 202–209. doi:10.1360/02tb936510.1016/j.geog.2016.04.006

Keysers, J. H., Quadros, N. D., and Collier, P. A. (2015). Vertical Datum Transformations across the Australian Littoral Zone. *J. Coastal Res.* 31 (1), 119–128. doi:10.2112/JCOASTRES-D-12-00228.1

Knudsen, P., and Andersen, O. B. (2013). The DTU12MDT Global Mean Dynamic Topography and Ocean Circulation Model." in Proc. ESA Living Planet Symposium 2013" in . Edinburgh 722, 28. UK 9–13 September 2013Available at: https://ftp.space.dtu.dk/pub/Ioana/papers/s211_4knud.pdf (Accessed March 19, 20132020).

Losch, M., Snaith, H., and Siegismund, F. (2007). *GOCE User Toolbox Specification: Scientific Trade off Study and Algorithm Specification*, Proceedings of the 3rd International GOCE User Workshop, 303–310. Noordwijk: ESA Publications Division.

Muhammad, I. Z. (2018). *Determination of a Localized Mean Sea Surface Model for Malaysian Seas Using Multi-mission Satellite altimeterBachelor Engineering Thesis*. Skudai: Universiti Teknologi Malaysia.

Mulet, S., Rio, M. H., Etienne, H., Dibarboure, G., and Picot, N. (2019). The New CNES-CLS18 Mean Dynamic Topography. OceanPredict'19. Available at: https://meetings.aviso.altimetry.fr/fileadmin/user_upload/2019/GEO_03_SMulet_MDT_CNES-CLS18.pdf (Accessed November 3, 2020).

Nornajihah, Y. (2017). *Marine Geoid Determination over Malaysian Seas Using Satellite Altimeter and Gravity Missions*. Skudai: MSc ThesisUniversiti Teknologi Malaysia.

Ophaug, V., Breili, K., and Gerlach, C. (2015). A Comparative Assessment of Coastal Mean Dynamic Topography in N Orway by Geodetic and Ocean Approaches. *J. Geophys. Res. Oceans* 120 (12), 7807–7826. doi:10.1002/2015JC011145

Pujol, M. I., Schaeffer, P., Faugère, Y., Raynal, M., Dibarboure, G., and Picot, N. (2018). Gauging the Improvement of Recent Mean Sea Surface Models: A New Approach for Identifying and Quantifying Their Errors. *J. Geophys. Res. Oceans* 123, 5889–5911. doi:10.1029/2017JC013503

Ray, R. D. (2013). Precise Comparisons of Bottom-Pressure and Altimetric Ocean Tides. *J. Geophys. Res. Oceans* 118, 4570–4584. doi:10.1002/jgrc.20336

Rummel, R. (1993). "Principle of Satellite Altimetry and Elimination of Radial Orbit Errors," in *Satellite Altimetry in Geodesy and OceanographyLecture Notes in Earth Sciences*. Editors R. Rummel and F. Sansò (Berlin, Heidelberg: Springer), Vol. 50, 190–241. doi:10.1007/BFb0117929

Schaeffer, P., Faugére, Y., Legeais, J. F., Ollivier, A., Guinle, T., and Picot, N. (2012). The CNES_CLS11 Global Mean Sea Surface Computed from 16 Years of Satellite Altimeter Data. *Mar. Geodesy* 35 (Suppl. 1), 3–19. doi:10.1080/01490419.2012.718231

Scharroo, R., Leuliette, E. W., Lillibridge, J. L., Byrne, D., Naeije, M. C., and Mitchum, G. T. (2013). "RADS: Consistent Multi-mission Products." in Proc. of the Symposium on 15 Years of Progress in Radar Altimetry, Venice, September 20–28, 2012. Available at: https://www.researchgate.net/profile/Remko_Scharroo/publication/262964278_RADS_Consistent_multi-mission_products/links/0f317539b2660407c6000000/RADS-Consistent-multi-mission-products.pdf (Accessed November 3, 2020).

Smith, S. W. (2003). "CHAPTER 15 – Moving Average Filters," in *Digital Signal Processing*. Editor S. W. Smith (Elsevier Science: Newnes Press), 277–284. 9780750674447. doi:10.1016/b978-0-7506-7444-7/50052-2

Vignudelli, S., Birol, F., Benveniste, J., Fu, L.-L., Picot, N., Raynal, M., et al. (2019). Satellite Altimetry Measurements of Sea Level in the Coastal Zone. *Surv. Geophys.* 40, 1319–1349. doi:10.1007/s10712-019-09569-1

Wagner, C. A. (1985). Radial Variations of a Satellite Orbit Due to Gravitational Errors: Implications for Satellite Altimetry. *J. Geophys. Res.* 90 (B4), 3027–3036. doi:10.1029/JB090iB04p03027

Wang, Y. M. (2001). GSFC00 Mean Sea Surface, Gravity Anomaly, and Vertical Gravity Gradient from Satellite Altimeter Data. *J. Geophys. Res.* 106 (C12), 31167–31174. doi:10.1029/2000JC000470

Woodworth, P. L., Gravelle, M., Marcos, M., Wöppelmann, G., and Hughes, C. W. (2015). The Status of Measurement of the Mediterranean Mean Dynamic Topography by Geodetic Techniques. *J. Geod* 89 (8), 811–827. doi:10.1007/s00190-015-0817-1

Woodworth, P. L., Melet, A., Marcos, M., Ray, R. D., Wöppelmann, G., Sasaki, Y. N., et al. (2019). Forcing Factors Affecting Sea Level Changes at the Coast. *Surv. Geophys.* 40, 1351–1397. doi:10.1007/s10712-019-09531-1

Wunsch, C. (1993). "Physics of the Ocean Circulation," in *Geodesy and Oceanography, Lecture Notes Earth Sci*. Editors R. Rummel and F. Sanso (Heidelberg, Germany: Springer), Vol. 50, 1–99.

Yahaya, N. A. Z., Musa, T. A., Omar, K. M., Din, A. H. M., Omar, A. H., Tugi, A., et al. (2016). Mean Sea Surface (MSS) Model Determination for Malaysian Seas Using Multi-mission Satellite Altimeter. *Int. Arch. Photogramm. Remote Sens. Spat. Inf. Sci.* XLII-4/W1 (4W1), 247–252. doi:10.5194/isprs-archives-XLII-4-W1-247-2016

Yuan, J., Guo, J., Liu, X., Zhu, C., Niu, Y., Li, Z., et al. (2020). Mean Sea Surface Model over china Seas and its Adjacent Ocean Established with the 19-year Moving Average Method from Multi-Satellite Altimeter Data. *Continental Shelf Res.* 192, 104009. doi:10.1016/j.csr.2019.104009

Zhu, C., Guo, J., Hwang, C., Gao, J., Yuan, J., and Liu, X. (2019). How HY-2A/GM Altimeter Performs in marine Gravity Derivation: Assessment in the south china Sea. *Geophys. J. Int.* 219 (2), 1056–1064. doi:10.1093/gji/ggz330

Zulkifle, M. I., Din, A. H. M., Hamden, M. H., and Adzmi, N. H. M. (2019). Determination of a Localized Mean Sea Surface Model for Malaysian Seas Using Multi-mission Satellite Altimeter. *ASM Sci. J.* 12 (Special Issue 2), 81–89 Available at: https://www.akademisains.gov.my/asmsj/article/asm-sc-j-12-special-issue-2-2019-malaysia-in-space/ (Accessed January 10, 2020).

Conflict of Interest: The authors declare that the research was conducted in the absence of any commercial or financial relationships that could be construed as a potential conflict of interest.

Publisher's Note: All claims expressed in this article are solely those of the authors and do not necessarily represent those of their affiliated organizations, or those of the publisher, the editors and the reviewers. Any product that may be evaluated in this article, or claim that may be made by its manufacturer, is not guaranteed or endorsed by the publisher.

frontiers in Earth Science

ORIGINAL RESEARCH
published: 14 September 2021
doi: 10.3389/feart.2021.749611

An Assessment of Recently Released High-Degree Global Geopotential Models Based on Heterogeneous Geodetic and Ocean Data

Yihao Wu[1]*, *Xiufeng He*[1], *Zhicai Luo*[2] and *Hongkai Shi*[1]

[1]School of Earth Sciences and Engineering, Hohai University, Nanjing, China, [2]MOE Key Laboratory of Fundamental Physical Quantities Measurement, School of Physics, Huazhong University of Science and Technology, Wuhan, China

OPEN ACCESS

Edited by:
Jinyun Guo,
Shandong University of Science and Technology, China

Reviewed by:
Polina Lemenkova,
Institute of Physics of the Earth (RAS), Russia
Jinhai Yu,
University of Chinese Academy of Sciences, China

***Correspondence:**
Yihao Wu
yihaowu@hhu.edu.cn

Specialty section:
This article was submitted to Environmental Informatics and Remote Sensing, a section of the journal Frontiers in Earth Science

Received: 29 July 2021
Accepted: 31 August 2021
Published: 14 September 2021

Citation:
Wu Y, He X, Luo Z and Shi H (2021) An Assessment of Recently Released High-Degree Global Geopotential Models Based on Heterogeneous Geodetic and Ocean Data. Front. Earth Sci. 9:749611. doi: 10.3389/feart.2021.749611

The development of the global geopotential model (GGM) broadens its applications in ocean science, which emphasizes the importance for model assessment. We assess the recently released high-degree GGMs over the South China Sea through heterogeneous geodetic observations and synthetic/ocean reanalysis data. The comparisons with a high resolution (~3 km) airborne gravimetric survey over the Paracel Islands show that XGM2019e_2159 has relatively high quality, where the standard deviation (SD) of the misfits against the airborne gravity data is ~3.1 mGal. However, the comparisons with local airborne/shipborne gravity data hardly discriminate the qualities of other GGMs that have or truncated to the same expansion degree. Whereas, the comparisons with the synthetic/ocean reanalysis data demonstrate that the qualities of the values derived from different GGMs are not identical, and the ones derived from XGM2019e_2159 have better performances. The SD of the misfits between the mean dynamic topography (MDT) derived from XGM2019e_2159 and the ocean data is 2.5 cm; and this value changes to 7.1 cm/s (6.8 cm/s) when the associated zonal (meridian) geostrophic velocities are assessed. In contrast, the values derived from the other GGMs show deteriorated qualities compared to those derived from XGM2019e_2159. In particular, the contents computed from the widely used EGM2008 have relatively poor qualities, which is reduced by 3.9 cm when the MDT is assessed, and by 4.0 cm/s (5.5 cm/s) when the zonal (meridian) velocities are assessed, compared to the results derived from XGM2019e_2159. The results suggest that the choice of a GGM in oceanographic study is crucial, especially over coastal zones. Moreover, the synthetic/ocean data sets may be served as additional data sources for global/regional gravity field assessment, which are useful in regions that lack of high-quality geodetic data.

Keywords: global geopotential model, model assessment, heterogeneous gravity data, ocean reanalysis data, mean dynamic topography, geostrophic velocities

INTRODUCTION

The knowledge of a global geopotential model (GGM) enables a wealth of applications in ocean science. For instance, the combination of a GGM and satellite altimetry data allows to monitoring ocean state from space in a global scale (Bingham et al., 2011a; Knudsen et al., 2011; Volkov and Zlotnicki, 2012; Rio et al., 2014), which is beneficial for studying coastal ecosystem processes and understanding heat and energy cycles as well as water exchanges over oceanic areas. Moreover, the information of a GGM facilitates the applications of height datum unification (Rummel, 2012; Wu et al., 2016; Filmer et al., 2018), the study of oceanic lithosphere (Kaban et al., 1999; Rummel et al., 2002; Tenzer et al., 2015), and oil/gas explorations as well as other offshore activities (Braitenberg and Ebbing, 2009; Rio et al., 2011; Sampietro, 2015).

The wide applications of the global geopotential models emphasize the improvement of these models in terms of accuracy and spatial resolution. The dedicated spaceborne gravimetric missions, such as Gravity Recovery and Climate Experiment (GRACE) (e.g., Tapley et al., 2003; Tapley et al., 2005) and Gravity Field and Steady-State Ocean Circulation Explorer (GOCE) (e.g., Pail et al., 2011), significantly improve the global gravity field at long wavelength bands (Pail et al., 2010; Bruinsma et al., 2013; Brockman et al., 2014). However, the low resolution of a satellite-only GGM derived from GRACE/GOCE data remains a barrier for ocean state study at medium- and short-wavelength bands, especially for the wavelengths shorter than ~100 km (e.g., Jayne, 2006; Albertella et al., 2012). The satellite-only model can be enhanced by combining terrestrial and marine gravity data, and the enhanced solution is the so-called combined GGM, also known as the high-degree GGM. The high-degree GGM dramatically improves the accuracy and spatial resolution of global gravity field, and the widely used model like EGM2008/EIGEN-6C4 samples the global gravity field at a resolution of ~10 km (Pavlis et al., 2012, 2013; Förste et al., 2014). Consequently, the use of a high-degree GGM allows to mapping the mean ocean circulation at more detailed scales than a satellite-only model (e.g., Andersen and Knudsen, 2009; Vianna and Menezes, 2010).

However, large uncertainties were found in a high-degree GGM attempting to study the detailed mean ocean state at a regional scale, e.g., see Farrell et al. (2012). These uncertainties are attributed to two main aspects. First, the noises in observations propagated into a GGM, known as the commission errors. The properties of commission errors are heterogeneous considering different GGMs were computed with different data sets and data preprocessing strategies. Second, the use of a high-degree GGM only lacks the ability to recover the short-wavelength signals beyond its maximal expansion degree, known as the omission errors. The errors in a GGM may cause strong oscillations up to a magnitude of decimeter level, particularly in the regions that only fill-in data were used in model development. This remains a major obstacle to the use of a GGM in oceanographic studies and geophysical investigations (McAdoo et al., 2013; Fecher et al., 2017; Skourup et al., 2017). Moreover, a high-degree GGM that computed by merging altimetric gravity data over oceans suffers from the coastal problem (e.g., Huang, 2017; Wu et al., 2019, 2021); since the altimeter data contain larger errors close to coast/island than in open seas, due to the severely contaminated waveforms and deteriorated geophysical corrections (Deng and Featherstone, 2006; Andersen and Scharroo, 2011; Abulaitijiang et al., 2015).

Whereas, the development of satellite altimetry leads to the improvement of marine gravity field, and the altimetric gravity models that computed with the recent released altimetry data (e.g., CryoSat-2, Jason, SARAL/Altika) show improved accuracies compared to the ones derived from old altimeter data (e.g., Geosat and ERS-1) (Sandwell et al., 2013; Sandwell et al., 2014; Garcia et al., 2014). As a result, the GGMs that computed by using the recent altimetric gravity data may have improved qualities. In addition, the accumulation of satellite gravimetric data and the improved data preprocessing strategies as well as data weighting schemes may further contribute to improve a high-degree GGM (e.g., Fecher et al., 2017). Given the fact that the information of a GGM plays a more important role in ocean science than ever, it is crucial for evaluating the recently released GGMs before they are used for oceanographic researches; however, little attention has been paid to model assessment over oceans. This study focuses on the assessment of recently released high-degree GGMs over a local area, where no locally surveyed gravity data have been combined for computing the currently available GGMs. This study can provide an insight into the qualities of different GGMs at other oceanic areas that only fill-in or altimetric gravity data were used for model development, e.g., most regions of Asia. For model assessment, the traditionally used geodetic observations, i.e., heterogeneous gravity data are used in this study (Arabelos and Tscherning, 2010; Hirt et al., 2011). Besides, independent ocean reanalysis data sets are introduced, which were successfully applied to validating the altimeter-derived mean dynamic topography (MDT) and unifying vertical height systems (Ophaug et al., 2015; Idžanović et al., 2017; Filmer et al., 2018).

STUDY AREA AND DATA

The South China Sea (SCS) is selected as the study area, which extends from 0°N to 24°N latitude and 99°E to 121°E longitude. The SCS is a semi-enclosed marginal sea, and it connects with the East China Sea, the Pacific, and the Indian Ocean through the Taiwan Strait, the Luzon Strait, and the Strait of Malacca, respectively (e.g., Ho et al., 2000); see **Figure 1** and the background information displays the bathymetry derived from the General Bathymetric Chart of the Oceans (GEBCO) (Weatherall et al., 2015). The SCS is dominated by seasonal monsoons with active mesoscale eddies (Jia and Liu, 2004; Gan et al., 2006; Chen et al., 2011) and major water exchanges occurring at the Taiwan Strait, the Luzon Strait, and the Sunda Shelf (e.g., Hwang and Chen, 2000). The ocean state study over the SCS presents particular challenges due to the complex topography, monsoon winds, and high variability of local hydrological conditions (Wang et al., 2003; Chen et al., 2011; Xu et al., 2012). This offers a good opportunity to investigate the performances of recently published GGMs in ocean state study.

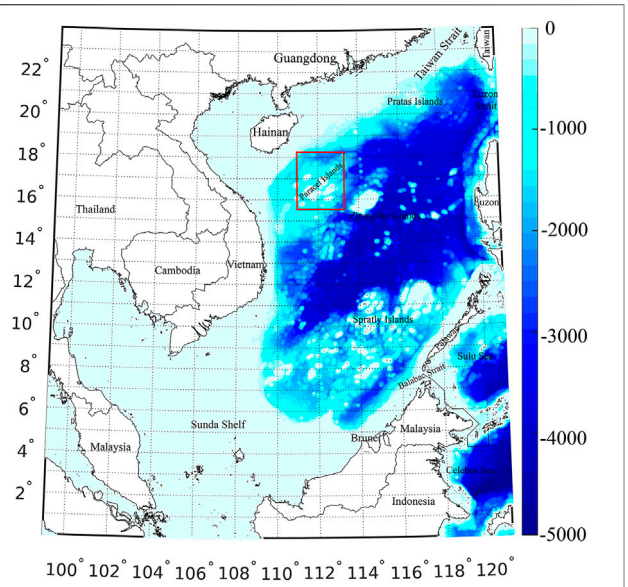

FIGURE 1 | Study area and the associated bathymetry. The region enclosed in the red rectangle represents the surveyed area of airborne gravimetry over the Paracel Islands.

In the following, the heterogeneous gravity observations and synthetic/ocean reanalysis data are introduced.

Global geopotential Models

Several recently published high-degree GGMs, i.e., EGM2008, GECO, SGG-UGM-1, EIGEN-6C4, GOCO05c, XGM2016, XGM2019, and XGM2019e_2159 are investigated in this study. The reason for choosing the models above is that these models have relatively higher spatial resolutions and better accuracies compared to most of other GGMs, see the validation results against the globally distributed GPS/levelling data in http://icgem.gfz-potsdam.de/home. These models were computed by merging satellite gravimetric data and terrestrial and marine gravity data based on spherical harmonic functions. EGM2008 has a full expansion degree and order (d/o) of (2190/2159), which was computed by merging GRACE measurements with terrestrial gravity data on the land and altimetric gravity data in the ocean. Since no GOCE data have been incorporated for developing EGM2008, and the recently published GGMs were computed by combining GOCE data, which is supposed to improve the global gravity field in the frequency bands approximately from degree 30 to 220 in spherical harmonics representation (Gruber et al., 2014). As such, several recently released GOCE-based GGMs, i.e., the GECO (d/o 2190/2159) (Gilardoni et al., 2015), SGG-UGM-1 (d/o 2159/2159) (Liang et al., 2018), EIGEN-6C4 (d/o 2190/2159) (Förste et al., 2014), GOCO05c (Fecher et al., 2017), XGM2016 (Pail et al., 2018), XGM2019, and XGM2019e_2159 (Zingerle et al., 2019), are introduced. The detailed information with respect to the data sets used in these GGMs' development is seen in **Table 1**.

An investigation of error degree variances offers an insight into the error spectra of a GGM, regarded as internal error estimates; and it supplies a rudimentary quality assessment (e.g., Pail et al., 2011). The cumulative geoid error of each GGM is calculated by using the estimated errors of Stokes' coefficients of this model, and the equations we use can be seen in, e.g., Erol et al. (2020). **Figure 2** shows the degree-wise accumulated geoid errors of different GGMs, demonstrates the error up to the maximal degree of each model. EGM2008 has relatively large error, which rises rapidly from degrees 30–220, and reaches ~7.3 cm by the degree of 220 and then increases slowly to 8.2 cm by the maximal degree. Whereas, the accumulated geoid errors of the models that have similar expansion degrees, like GECO, SGG-UGM-1, EIGEN-6C4, and XGM2019e_2159 are reduced to ~4.2, 2.7, 3.4, and 3.1 cm,

TABLE 1 | Description of global geopotenital models.

Model	Expansion degree	Data used for model development	Remarks
EGM2008	2190	GRACE data, terrestrial, altimetry-derived, and airborne gravity data	EGM2008 was computed without GOCE data. The DNSC07 data, which is the predecessor of DNSC08GRA, was used over the South China Sea Pavlis et al. (2012), Pavlis et al. (2013)
GECO	2190	GOCE-only TIM R5 (d/o 250) and EGM2008	GECO was computed by combining GOCE-only TIM R5 model into EGM2008 Gilardoni et al. (2015). GOCE-only TIM R5 was developed by using the satellite-to-satellite tracking (SST) data and GOCE satellite gravity gradiometry (SGG) data over the entire period Pail et al. (2011)
SGG-UGM-1	2159	GOCE SST and SGG data, and EGM2008	SGG-UGM-1 was developed by merging GOCE SST and SGG (d/o 220) into EGM2008 Liang et al., (2018)
EIGEN-6C4	2190	LAGEOS, GRACE RL03, GOCE SGG data, and surface gravity data	Surface data were DTU12 geoid data over oceans and EGM2008 geoid height grid over continents Förste et al. (2014)
GOCO05c	720	GOCO05S, and surface gravity anomaly data	GOCO05S (d/o 280) was developed by combining GRACE (ITGS-Grace2014s), GOCE, kinematic orbits, and satellite laser ranging (SLR) data. DTU13GRA-derived gravity data were used in oceans Fecher et al. (2017)
XGM2016	719	GOCO05S, and surface gravity grid	XGM2016 was computed by combining GOCO05S and a global 15′×15′ grid provided by National Geospatial-Intelligence Agency (NGA) Pail et al. (2018)
XGM2019/ XGM2019e_2159	760/2190	GOCO06S, and surface gravity data	XGM2019 and XGM2019e_2159 were developed using the same data, but the former was truncated to d/o 760. DTU13GRA-derived gravity data were used over oceans Zingerle et al. (2019)

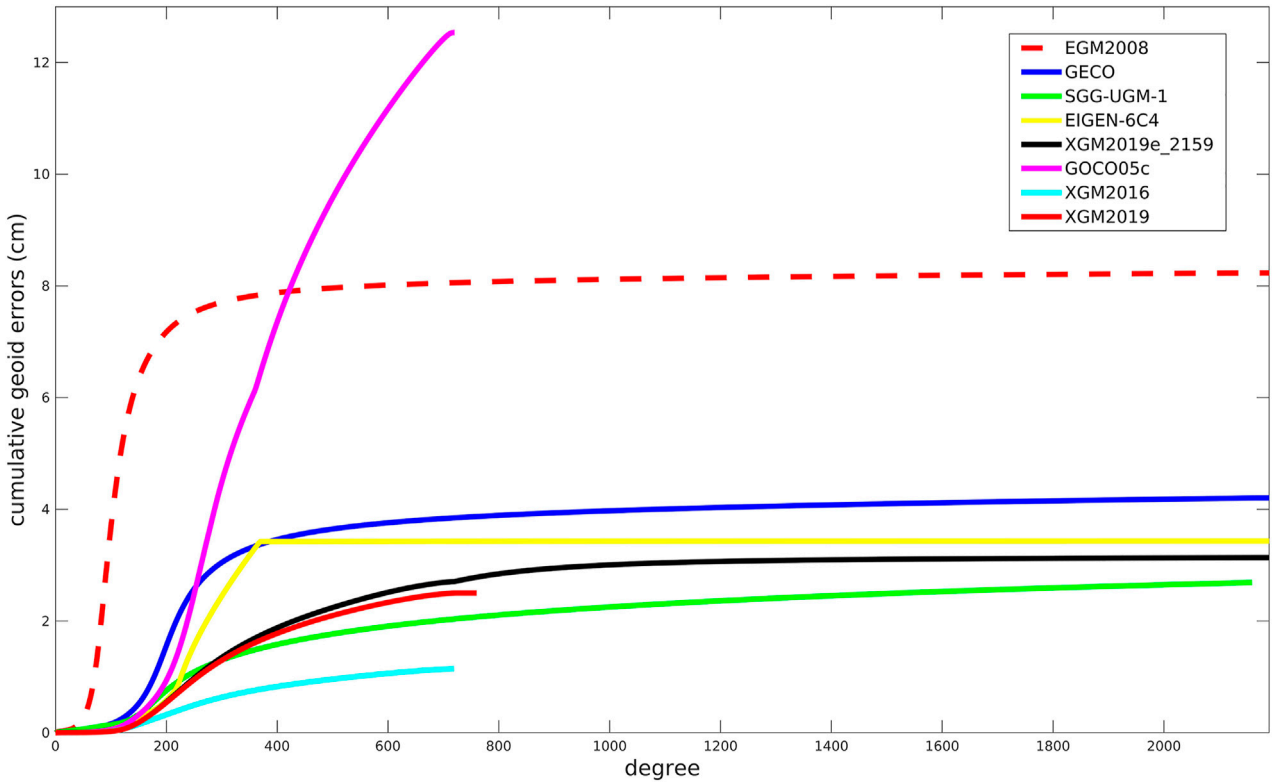

FIGURE 2 | Cumulative geoid errors of different GGMs as a function of spherical expansion degree.

respectively. The prominent error in EGM2008 at the frequency bands between degrees 30–220 is mainly due to the lack of GOCE data; and the other four models discussed above that developed with GOCE data have better qualities in this frequency bands, where GOCE data paly a dominant role in global gravity field recovery (e.g., Gruber et al., 2014). Moreover, the combination of updated altimetric gravity data may be the main reason that EIGEN-6C4/XGM2019e_2159 has smaller error than EGM2008 at short-wavelength bands. The comparisons of the GGMs that have lower truncated degrees, i.e., GOCO05C, XGM2016, and XGM2019, show that GOCO05C has the largest error, and its error increases dramatically after degree 170 and reaches 12.5 cm by the degree of 720. By comparison, the cumulative geoid error of XGM2016/XGM2019 reduces to ~1.1/2.5 cm by its maximal degree.

It is noteworthy that the correlation of errors of spherical harmonic coefficients is ignored when the (accumulated) error degree variances are computed, and the GGM's error at a specific geographic location cannot be estimated. While, a more rigorous way for internal error estimate can be implemented through the error propagation by using the full error variance-covariance matrix of spherical harmonic coefficients of a GGM (Balmino, 2009). However, considering the limited accessibility of the full error variance-covariance matrices of the high-degree GGMs and the associated huge computation load, this method may be difficult to be implemented. Moreover, the polar gap problem exists in the GGMs that developed with GOCE data, which especially affects the qualities of zonal and near-zonal coefficients (Pail et al., 2011). In total, the error degree variances only supply a global mean of internal error and cannot be regarded as the realistic error estimate.

Heterogeneous gravity Data

Airborne Gravity Disturbances

The First Geodetic Surveying Team of Ministry of Natural Resources of China conducted an airborne gravimetric survey in 2018, covered the Paracel Islands that located in the northwest SCS, see the enclosed area of the red rectangle in **Figure 1**. This area ranges from 15.5°N to 18.2°N latitude and 111.0°E to 113.3°E longitude. The airborne survey was implemented with a GT-2A gravimeter, which contained 87 flights in total to complete 61,594 line kilometers. It covered ~270 km in east-west direction and ~325 km in north-south direction, see **Figure 3**. The traverse lines were north-south oriented and spaced at 1 km, while the tie lines were east-west oriented and spaced at 5 km. The height of the flight ranged from 739 to 847 m above the mean sea level.

The GT-2A gravimeter recorded the raw data at a frequency of 18.75 Hz, and the gravity data were calculated by subtracting the GPS-derived aircraft accelerations from the inertial accelerations, which were then corrected for the Eötvös effect and compensated for the off-level corrections. The derived gravity disturbances were filtered by a low pass filter with a cut-off frequency of 0.01 Hz to reduce the high-frequency noise, which were then resampled to 2 Hz corresponding to the epoch of GPS

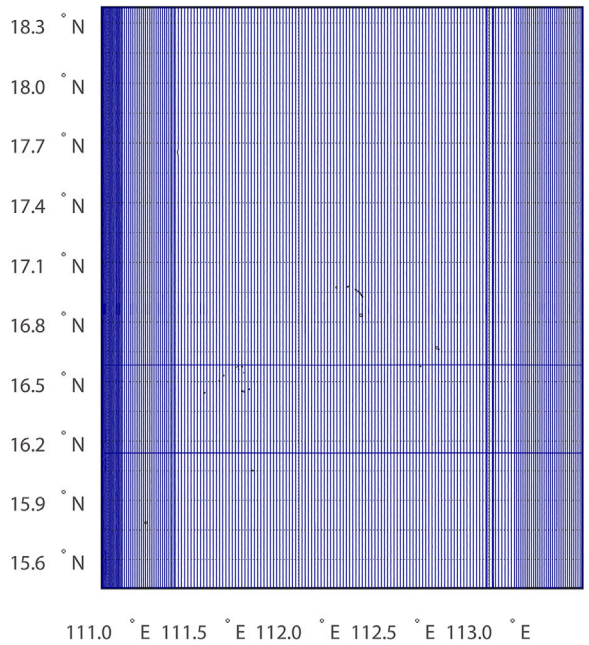

FIGURE 3 | Flight lines of airborne gravimetric survey over the Paracel Islands.

measurements. The spatial resolution of the derived airborne gravity disturbances after the filtering is ~3 km. The airborne gravity data were then referenced to the China Geodetic Coordinate System 2000 (CGCS 2000), and the geodetic coordinates were referenced to the GRS80 reference ellipsoid. Seven repeat lines were conducted for quality control, and the overall standard deviation (SD) of the variations of repeat lines was ~1.44 mGal. Moreover, the crossover measurements on transverse and tie lines offer an overview of the data quality, and the SD of the differences at crossovers was ~1.54 mGal, showing in a good agreement with the statistics of the repeat lines. This airborne survey includes ~1,854,900 point-wise data, which haven't been used for global/regional gravity field model development.

Shipborne Gravity Anomalies

The marine gravity anomalies are retrieved from the National Geophysical Data Center (NGDC) in the National Centers for environmental information (NCEI), where worldwide shipborne gravity data collected during the marine cruises from 1939 to present are available. The original gravity data suffer from the instrument errors, navigational errors, and biases stemming from the inconsistencies among different height systems as well as other systematic errors (Denker and Roland, 2005; Wu et al., 2017a). DTU17GRA is introduced to ensure the quality of the shipborne data. This model combined the 25 years of satellite altimetry data and included the recent altimeter data from Jason-1, CryoSat-2, and SARAL/Altika. The comparison with independent gravity data showed that DTU17GRA had improved precision compared with the previous versions developed at DTU space (Andersen and Knudsen, 2019). The

TABLE 2 | Statistics of the differences between the airborne gravity disturbances and quantities synthesized from different GGMs over the Paracel Islands (units: mGal).

	Degree	Max	Min	Mean	SD
EGM2008	720	53.2	−26.5	−0.9	9.0
EGM2008	2190	36.1	−18.2	−0.8	4.1
EIGEN-6C4	720	54.4	−25.2	−0.6	9.1
EIGEN-6C4	2190	35.4	−16.5	−0.4	3.9
GECO	720	54.0	−25.9	−0.7	9.0
GECO	2190	37.0	−17.2	−0.6	4.0
SGG-UGM-1	720	53.6	−25.1	−0.8	9.0
SGG-UGM-1	2159	36.6	−17.0	−0.7	4.0
XGM2019e_2159	720	53.5	−25.3	−0.7	9.0
XGM2019e_2159	2190	29.9	−16.4	−0.6	3.1
GOCO05c	720	53.4	−26.0	−0.8	9.1
XGM2016	719	53.4	−26.3	−0.7	9.0
XGM2019	760	53.7	−25.5	−0.7	9.0
XGM2019	720	53.7	−25.4	−0.7	9.0

erroneous shipborne gravity data from the NGDC are first removed through a 3-sigma rule, i.e., data are identified as blunders if the difference between the shipborne gravity data and DTU17GRA-derived value is larger than three times of the SD of all the differences. Since the shipborne gravity data originated from various epochs and systematic errors were likely to exist, we apply a crossover adjustment to reduce the systematic errors. The duplicate data are then removed and we assume a constant bias for each track. It is noteworthy that not all the systematic errors can be estimated due to the lack of track information for some cruises. The SD of the differences at the crossovers is estimated as 8.4 mGal, which is slightly smaller than the SD of the differences between DTU17GRA-derived values and shipborne gravity data before the crossover adjustment, with a value of ~9.0 mGal.

Existing MDTs and Ocean Models

The performances of different GGMs are investigated in MDT and geostrophic velocities recovery, where an existing synthetic MDT and three ocean models are introduced for comparison. The synthetic MDT is called CNES-CLS13MDT, and it covers the period of 1993–2012 at a resolution ~0.25° (~30 km). This model was estimated by using the CNES-CLS11 mean sea surface (MSS) data and EGM-DIR R4 (a satellite-only GGM) as the raw solution, which was then enhanced by *in situ* data to recover unresolved small-scale signals (Rio et al., 2011). Three ocean models, i.e., the Simple Ocean Data Assimilation, version 3 (SODA3) (Carton et al., 2018), the ocean reanalysis product of the European Centre for Medium-Range Weather Forecasts, version 5 (ECMWF ORAS5) (Zuo et al., 2017), and the Ocean Circulation and Climate Advanced Modeling Project (OCCAM) (Fox and Haines, 2003), are ocean reanalysis products provided with the field of dynamic topography. SODA3 was developed by ocean reanalysis with enhancements to model resolution, observation, forcing data, and the addition of active sea ice. This model maps the ocean state from 1980 to 2017, and it has a 0.25° horizontal resolution. ORAS5 is a recently released ocean reanalysis product from the ECMWF, which was developed

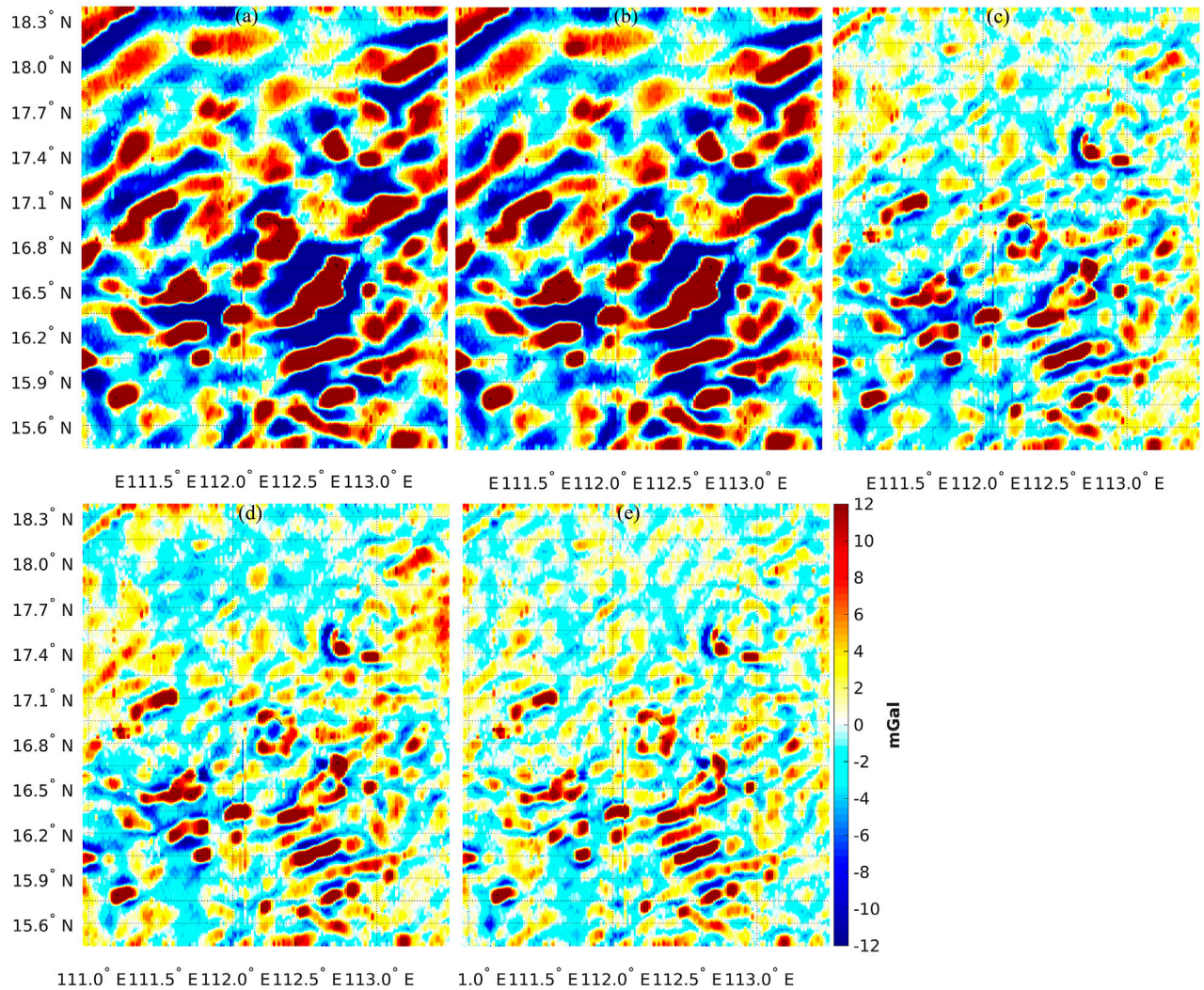

FIGURE 4 | Differences between the airborne gravity disturbances and quantities synthesized from **(A)** GOCO05c (d/o 720), **(B)** XGM2019 (d/o 760), **(C)** EGM2008 (d/o 2190), **(D)** EIGEN-6C4 (d/o 2190), and **(E)** XGM2019e_2159 (d/o 2190) over Paracel Islands.

from Ocean ReAnalysis Pilot 5 (Zuo et al., 2017) using the same ocean and sea ice model and data assimilation method. ORAS5 has a horizontal resolution of 0.25°, and it supplies monthly data from 1979 to 2018. The OCCAM MDT (0.5° horizontal resolution) maps the ocean state from 1993 to 2004, and was developed by using a hydrodynamic model forced with wind stresses from the ECMWF, hydrographic data, and surface temperature (Fox and Haines, 2003).

RESULTS AND DISCUSSION

Validation Against Airborne/Shipborne gravity Data

The maximal expansion degrees of EGM2008, EIGEN-6C4, GECO, SGG-UGM-1, and XGM2019e_2159 are higher than those of XGM2016, XGM2019, and GOCO05c. For the sake of comparison, the computations with the models that have higher expansion degrees are not only carried out up to the maximal degrees but also truncate to degree 720. **Table 2** shows the statistics of the differences between the airborne gravity disturbances and the quantities synthesized from different GGMs at the flight altitude. The statistics derived from XGM2016, GOCO05c, and GGMs that truncated to degree 720 are very close, and the SD values of the misfits against the airborne data are ~9.0 mGal. The models that truncate to degree 720 cannot recover the contents with the wavelengths shorter than ~30.4 km; and consequently, large inconsistencies against the airborne data are observed. **Figure 4** demonstrates the discrepancies between different GGMs and the airborne data (several representative models are displayed), and most significant discrepancies concentrate at regions close to islands in the Paracel Islands (see **Figure 1**). The main reason may be due to the degraded quality of altimetry data used in developing these

TABLE 3 | Statistics of the differences between the shipborne gravity anomalies retrieved from NGDC and quantities synthesized from different GGMs over South China Sea.

	Degree	Max	Min	Mean	SD
EGM2008	720	44.3	−42.0	1.1	13.3
EGM2008	2190	32.3	−28.9	1.6	9.4
EIGEN-6C4	720	44.7	−42.7	1.0	13.5
EIGEN-6C4	2190	32.6	−29.5	1.5	9.5
GECO	720	44.5	−42.4	1.1	13.4
GECO	2190	32.5	−29.3	1.6	9.5
SGG-UGM-1	720	44.4	−42.1	1.1	13.3
SGG-UGM-1	2159	32.3	−28.9	1.6	9.4
XGM2019e_2159	720	44.2	−41.9	1.1	13.3
XGM2019e_2159	2190	32.2	−28.9	1.6	9.4
GOCO05c	720	44.4	−42.1	1.2	13.3
XGM2016	719	44.2	−41.9	1.1	13.3
XGM2019	760	44.2	−41.9	1.1	13.3
XGM2019	720	44.2	−41.9	1.1	13.3

GGMs, while the airborne survey does not suffer from the problem like waveform contamination near coast/island and provides accurate observations.

The expansions of the GGMs that have higher expansion degrees to the maximal degrees recover more small-scale signals and significantly reduce the discrepancies against the airborne data; and the SD values of the misfits are reduced by a magnitude of ~5 mGal, compared to results derived from the models truncated to degree 720, see **Table 2**. However, these GGMs, i.e., with a full expansion degree of 2190 (2159), sample the gravity field at a resolution of ~10 km, which is still inferior to the mean resolution of airborne data (~3 km); and the high-frequency signals that have the wavelengths shorter than 10 km are missed in these models. As a result, the differences between these GGMs and the airborne data demonstrate as high-frequency features.

The mutual comparisons show that EGM2008, GECO, and SGG-UGM-1 have comparable qualities, with a SD value of ~4.0 mGal. GECO/SGG-UGM-1 that computed based on EGM2008 but additionally with GOCE data does not demonstrate better result than EGM2008. The possible reason is that GOCE data mainly contribute to long-wavelength bands (degrees 30–220), and the effects introduced by GOCE data are not prominent in terms of gravity disturbances since they are dominated by local short-wavelength features. EIGEN-6C4 does not show improved performance compared to EGM2008/GECO/SGG-UGM-1, although EIGEN-6C4 was computed based on an updated altimetric gravity model (DTU12 data) versus DNSC07GRA that used in developing EGM2008 (Andersen, 2010). Whereas, XGM2019e_2159 has relative high quality and the SD of the misfits reduces to ~3.1 mGal; and the discrepancies against the airborne data reduce dramatically close to islands, see **Figure 4E**. The better fit of XGM2019e_2159 with the airborne data is largely attributed to the use of updated altimetric gravity data in model development, i.e., DTU13GRA; and DTU13GRA has improved quality compared to DNSC07GRA that was used in computing EGM2008 (Andersen et al., 2013). Thus, the incorporation of the updated altimetric gravity data may be the main reason that XGM2019e_2159 has better quality than the other models that have similar expansion degrees.

The SD of the differences between the shipborne gravity anomalies retrieved from the NGDC and the quantities synthesized from different GGMs that have the maximal expansion degree of 2190 (2159) are ~9.4 mGal, see the statistics in **Table 3** and **Figure 5**. The qualities of these GGMs cannot be discriminated; and this is probably due to the limited accuracy of the shipborne gravity data, the quality of which may be questionable since some of them were collected decades ago without GPS navigation. Considering the restricted distribution of the airborne survey and suspicious quality of the shipborne data as well as the data gaps of marine surveys in the western and northern SCS, the validation against local airborne/shipborne data cannot be treated as the representative error estimate of a GGM over the SCS.

Mean Dynamic Topography Comparison

Before computing the geodetic MDT, we study the error information of different versions of MSS in order to choose an appropriate MSS. The interpolation errors of two recently released models, i.e., DTU15MSS (Andersen et al., 2016) and DTU18MSS (Andersen et al., 2018), are studied. **Figure 6** shows the errors of these models, and the root mean square (RMS) of errors of DTU15MSS and DTU18MSS are 1.95 and 1.78 cm, respectively, which indicate that DTU18MSS has better quality. DTU18MSS shows improved quality along the southern coast of Guangdong in China, the eastern coast of Vietnam and Malaysia, and the western coast of Luzon and coastal areas over Philippines. The reason that DTU18MSS outperforms DTU15MSS is mainly due to the incorporation of more high-quality altimeter data and the use of improved data pre-processing methods (Andersen et al., 2018).

MDT determined through a geodetic approach illustrates the departure of the MSS from the geoid/quasi-geoid (Bingham et al., 2011a, 2014; Griesel et al., 2012). The raw geodetic MDT is computed as the difference between DTU18MSS and quasi-geoid computed from a GGM expanded to its maximal degree. For cross validation, CNES-CLS13MDT, SODA3 MDT, ORAS5 MDT, and OCCAM MDT are introduced, where the former three models have a resolution of 0.25°, while the resolution of OCCAM is 0.5°. The raw geodetic MDT contains small-scale contents that cannot be resolved in synthetic/ocean data, and we apply a Gaussian filter with a correlation length of 30 km to the raw geodetic MDT for ensuring a spectrally consistent comparison. Different MDTs are referenced to various time periods, and we use the method suggested by Bingham and Haines (2006) to unify the time period, where all the models are adjusted to the geodetic MDT time period (1993–2018). The AVISO altimetric sea level anomaly (SLA) is used to standardize all the MDTs to the required period (e.g., Rio et al., 2011). The CNES-CLS13MDT is adjusted to the 1993–2018 period computed as CNES-CLS13MDT (93–2018) = CNES-CLS13MDT (93–2012) + MSLA (93–2018) − MSLA (93–2012), and MSLA denotes the mean value of SLA over a specific time period. For OCCAM MDT, a similar method is used

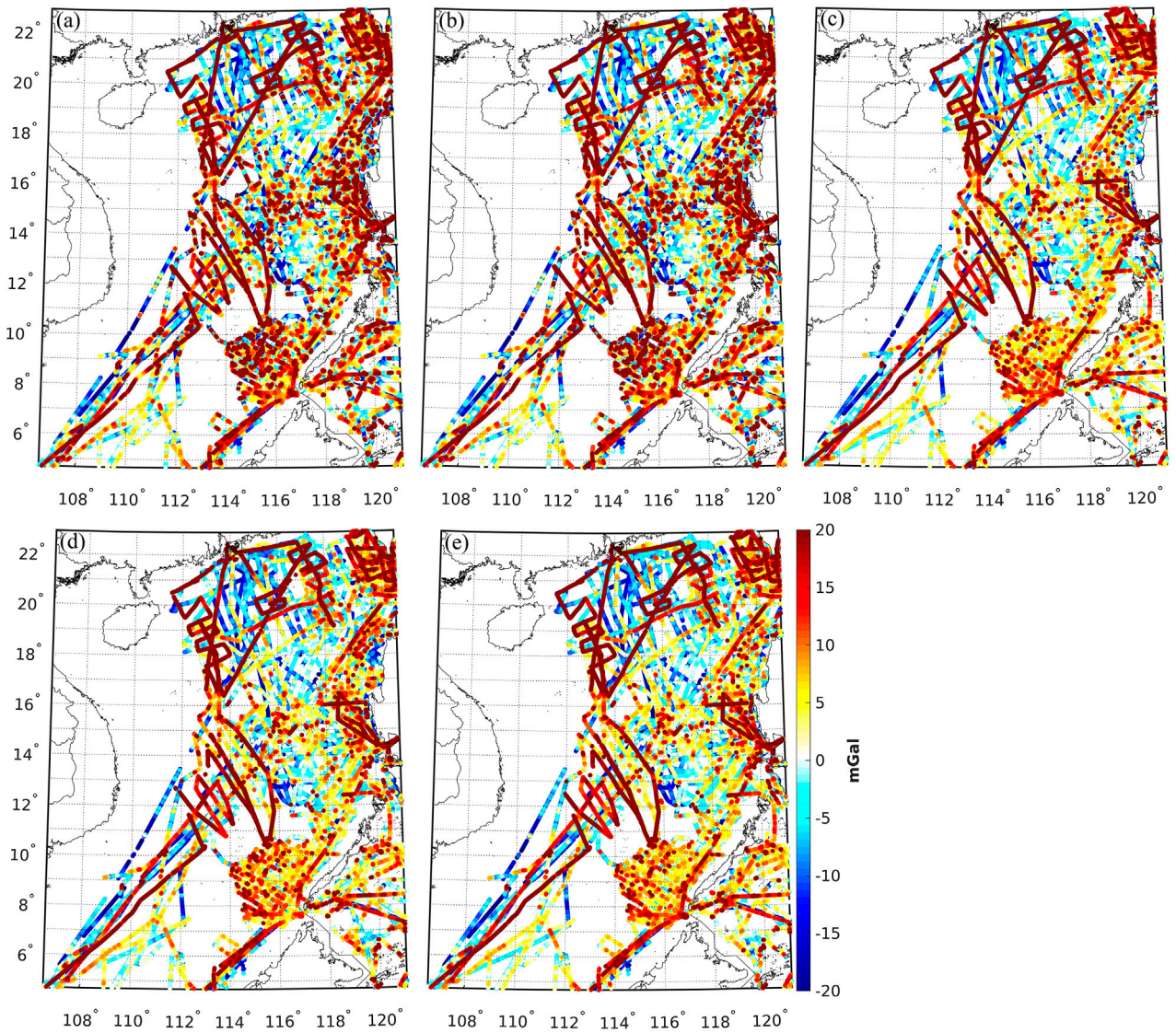

FIGURE 5 | Differences between shipborne gravity anomalies retrieved from NGDC and quantities synthesized from **(A)** GOCO05c (d/o 720), **(B)** XGM2019 (d/o 760), **(C)** EGM2008 (d/o 2190), **(D)** EIGEN-6C4 (d/o 2190), and **(E)** XGM2019e_2159 (d/o 2190) over South China Sea.

to adjust its period to 1993–2018. For SODA3, we first compute the mean SODA MDT by averaging the monthly data from 1993 to 2017, which is then adjusted to 1993–2018 by using the SLA data. For ORAS5, the associated MDT is retrieved by averaging the monthly data from 1993 to 2018.

Different MDTs generally have analogous structures, vary in a range of ~0.5 m, see **Figure 7**, where the maximum value up to 0.9 m appears around the western coast of Cambodia; while, the minimum value, roughly 0.5 m, occurs in the northern SCS. However, prominent discrepancies between the geodetic MDTs and synthetic/ocean models are observed, particularly in the northern SCS, by a magnitude up to 10 cm. The behaviors of MDTs computed from different GGMs are heterogeneous, where the signals derived from EGM2008, GECO, SGG-UGM-1, and EIGEN-6C4 have relatively significant oscillations over the southern part, compared to ones calculated from the other four GGMs. Moreover, the magnitudes of MDT signals of different synthetic/ocean models are not consistent, where CNES-CLS13MDT has smaller values over the northern SCS, while ORAS5 has larger values around the Luzon Strait.

The extreme values exist in the geodetic MDTs along the coast of Hainan, eastern coast of Vietnam, and western coast of Brunei and Malaysia. These values are identified as outliers, due to the uncorrected errors in the MSS model and errors in the quasi-geoid (Hipkin et al., 2004; Wu et al., 2017b; Wu et al., 2019). The remaining errors in the MSS model are mainly due to the orbit errors and errors in various range corrections (e.g., Andersen and Knudsen, 2009). However, these errors have been significantly reduced with the combination of recent altimeter data, even over coastal areas, see **Figure 6**. Whereas, the quasi-geoid over coastal

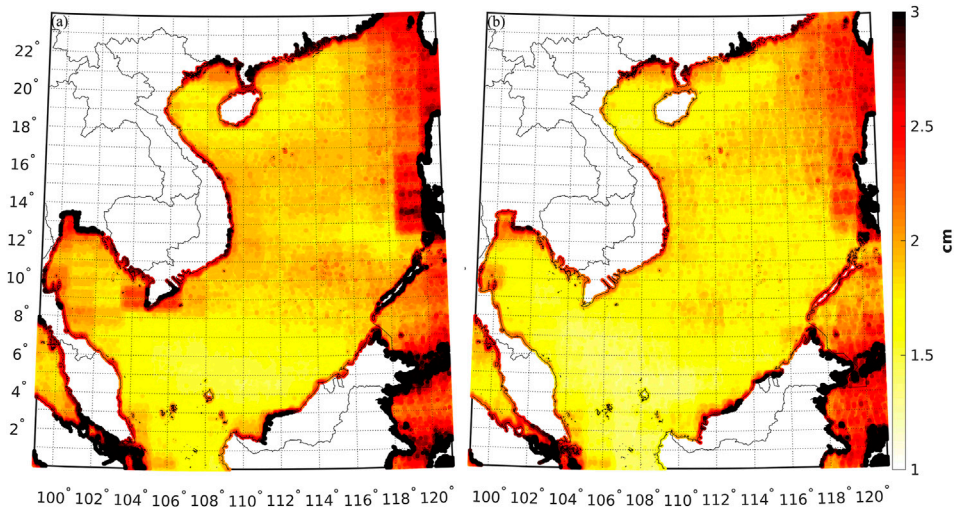

FIGURE 6 | Interpolation errors of **(A)** DTU15MSS, and **(B)** DTU18MSS over South China Sea.

regions suffers from the scarcity of surveyed gravimetric data, the degraded quality of altimetric gravity data, and the uncorrected biases/tilts among different data sets that used in computing the quasi-geoid (Huang, 2017; Wu et al., 2019). The EGM2008 commission errors, composed of the low-degree errors estimated by using a satellite-only model through error propagation and high-degree ones computed through an integral formula using surface gravity data (Pavlis et al., 2012), are seen in **Appendix A**. These errors reach decimeter level along the coastal regions over the SCS, suggesting that the computed geodetic MDTs prominently suffer from the errors in the associated GGMs, even though the application of filtering suppresses the high-frequency noises.

CNES-CLS13MDT and three ocean models are used as control data for model assessment; however, the lack of formal error of synthetic/ocean model remains an obstacle for deriving reliable results through an individual model. Thus, we not only provide the results computed from each synthetic/ocean model, but also give the statistics derived from the comparisons with the mean value of all synthetic/ocean models, which provide sufficient independence and redundancy to allow more robust comparison. **Figure 8** demonstrates the discrepancies between the MDTs computed from different GGMs and the mean of all synthetic/ocean data. The MDT derived from EGM2008 has the largest oscillations, and the maximum/minimum value is 17.9/-19.7 cm, with a SD of 6.4 cm, see **Table 4**. The significant long-wavelength errors are observed in the MDT derived from EGM2008, by a magnitude greater than 3 cm, and this is probably due to the lack of GOCE data in the computation of EGM2008. The long-wavelength errors are consequently reduced when the GGMs computed with GOCE data are applied, for instance, see the MDT derived from GECO/XGM2019e_2159 in **Figure 8**. Moreover, the coastal problem is extremely prominent in the MDT computed from EGM2008, especially around the coast of Hainan, Vietnam, Malaysia, and Brunei, where the errors reach a magnitude greater than 10 cm. This is attributed to the use of relatively low quality of altimetric gravity data in computing EGM2008 and the data voids occurred close to coast/island when EGM2008 was computed. In contrast, the MDT derived from SGG-UGM-1/GECO shows less variations and improved consistencies comparing with the synthetic/ocean data, and the SD of the misfits reduces to 3.3/4.1 cm. The incorporation of GOCE data is the main reason that these two MDTs show improved qualities at long-wavelength bands than the one computed from EGM2008. Moreover, the application of GECO/SGG-UGM-1 substantially reduces the errors of the associated MDT over coastal regions, for instance, along the coast of Hainan and Vietnam. The mutual comparison shows that the MDT derived from GECO has better quality than that computed from SGG-UGM-1, where the different methods for model development and data merging/assimilation approaches may account for these differences. The MDT derived from EIGEN-6C4 has comparable quality as that derived from GECO; however, the errors in the MDT model derived from EIGEN-6C4 are reduced over coastal regions, compared to the one derived from GECO/SGG-UGM-1. EIGEN-6C4 was computed by combining GRACE, GOCE, and EGM2008 data, but it included DTU12 geoid data over oceans; and this may be the main reason that EIGEN-6C4 has better performance in coastal MDT computation than EGM2008/GECO/SGG-UGM-1. We also notice that significant small-scale contents propagate into the MDT computed from EIGEN-6C4, particularly in the southern SCS, indicating that the use of the Gaussian filter may not be an optimal way to make a spectrally consistent fusion of the MSS and the quasi-geoid. The comparisons with local shipborne/airborne data show that these GGMs discussed above have comparable qualities; moreover, these models typically show comparable accuracies when validated against GPS/levelling data, e.g., see Featherstone et al. (2018) and Wu et al. (2018). However, this is not true when comparing with the synthetic/ocean data, where the qualities of these models can be discriminated.

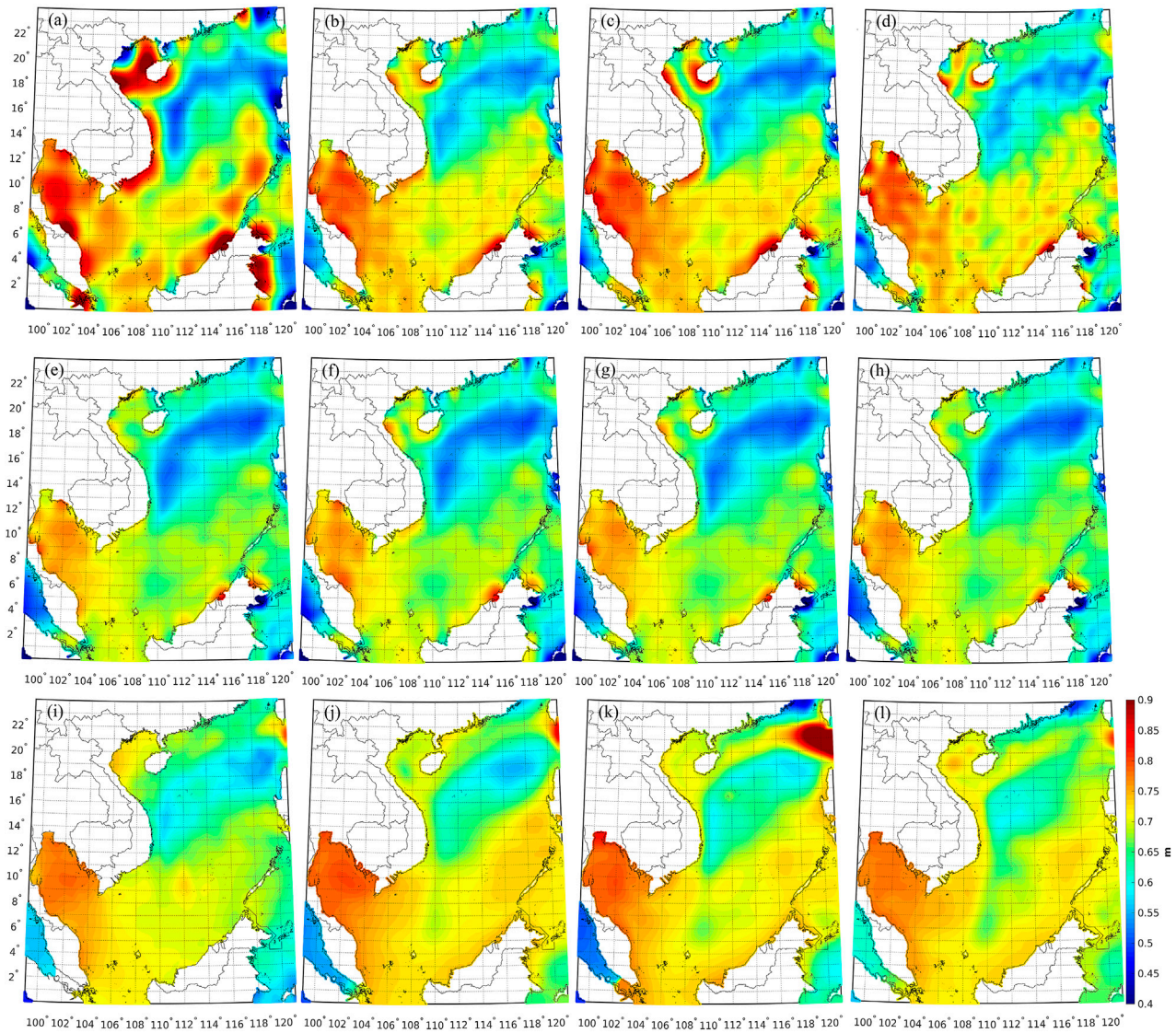

FIGURE 7 | Geodetic MDT calculated from **(A)** EGM2008, **(B)** GECO, **(C)** SGG-UGM-1, **(D)** EIGEN-6C4, **(E)** XGM2019_2159, **(F)** GOCO05c, **(G)** XGM2016, and **(H)** XGM2019; and existing synthetic/ocean models, **(I)** CNES-CLS13MDT, **(J)** SODA, **(K)** ORAS5, and **(L)** OCCAM.

The use of XGM2019e_2159 leads to a more consistent MDT with the synthetic/ocean data, which demonstrates less variations compared to the MDTs derived from the GGMs described above. The SD of the misfits between the MDT calculated from XGM2019e_2159 and the synthetic/ocean data is ~2.5 cm, with a reduction of ~0.8/0.8/1.6/3.9 cm, compared to the MDT computed from GECO/EIGEN-6C4/SGG-UGM-1/EGM2008. This is mainly attributed to the combination of recent satellite gravimetry and altimetry data in computing XGM2019e_2159, which combined a recently released GRACE/GOCE satellite-only model (GOCO06s) at long wavelength and DTU13GRA data at short-wavelength. DTU13GRA has better quality than the previous versions, e.g., DTU10GRA and DNSC07GRA, and the quasi-geoid calculated from XGM2019e_2159 was improved accordingly. This result is commensurate with the validation results against the airborne gravity data over the Paracel Islands, where XGM2019e_2159 has relatively high quality.

For the MDTs computed with the GGMs that have lower expansion degrees, the SD of the misfits between the MDT modeled from GOCO05c and the synthetic/ocean data is ~2.9 cm; while, for the MDT computed from XGM2016/XGM2019, this value is slightly better, by a magnitude of 0.3/0.4 cm XGM2016 was developed using the same methodology as GOCO05c, but the input surface data were different, where GOCO05c used DTU13GRA data, while XGM2016 combined NGA gridded data at oceans. The MDTs derived from XGM2019 and XGM2019e_2159 have almost identical features, since XGM2019 was computed using the same input data sets and modeling method as XGM2019e_2159, but truncated to degree 760.

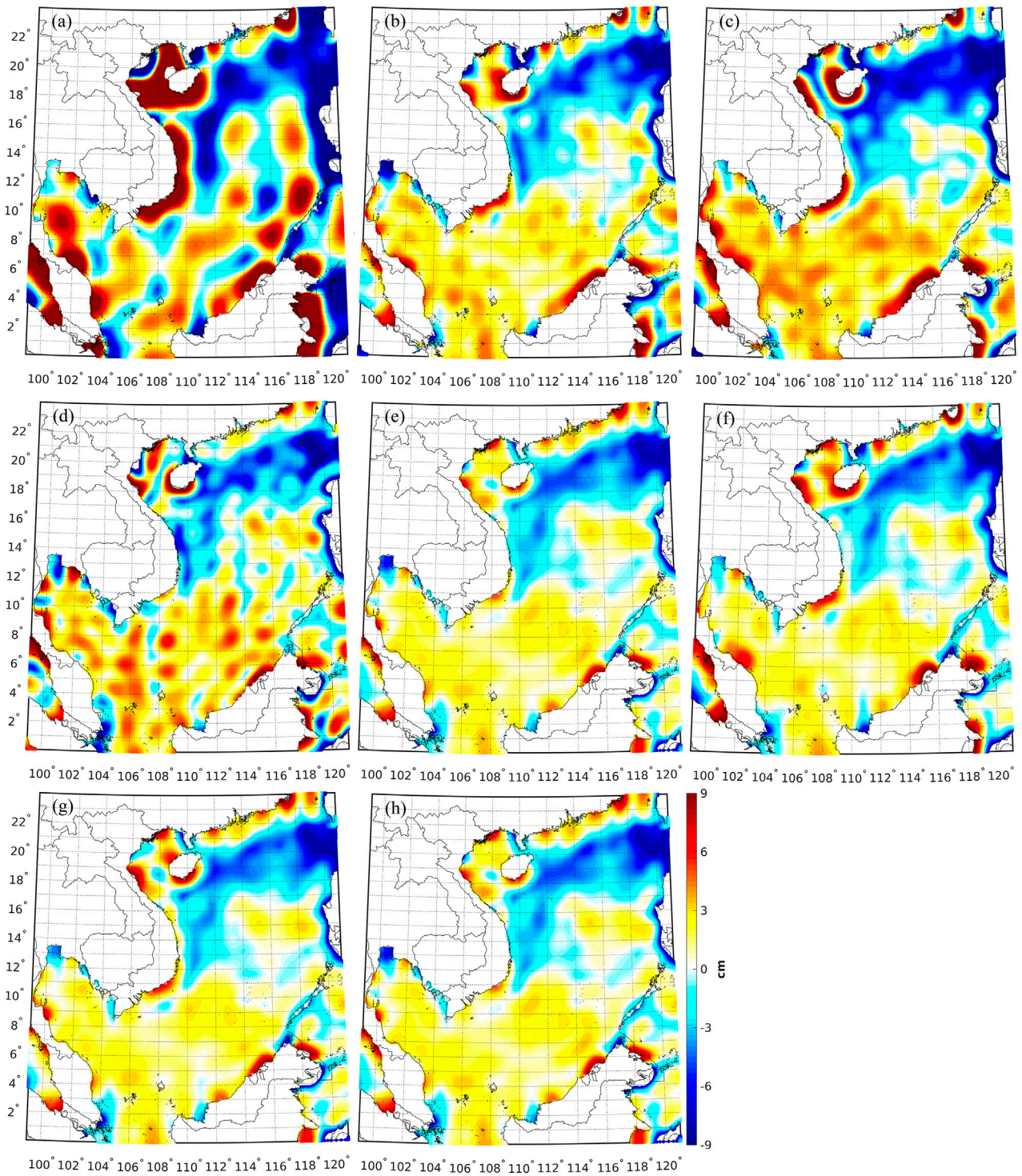

FIGURE 8 | Differences between the MDT computed from **(A)** EGM2008, **(B)** GECO, **(C)** SGG-UGM-1, **(D)** EIGEN-6C4, **(E)** XGM2019e_2159, **(F)** GOCO05c, **(G)** XGM2016, **(H)** XGM2019 and mean value of all synthetic/ocean models.

The comparison of each synthetic/ocean model and the geodetic MDTs derived from different GGMs show that CNES-CLS13MDT/SODA has smaller discrepancies against the geodetic MDTs, compared to ORAS5/OCCAM. This indicates that geodetic MDT may be used for synthetic/ocean model assessment, particularly in the regions lack of *in situ* data (e.g., buoys and hydrological profiles). However, it should be emphasized that these results are rudimentary ones since the

TABLE 4 | The standard deviation of the differences between the MDTs derived from different GGMs and synthetic/ocean model.

Geodetic MDT minus synthetic/ocean model	CNES-CLS13MDT	SODA	ORAS5	OCCAM	Mean of all synthetic/ocean models
EGM2008	6.0	6.4	7.3	6.8	6.4
GECO	2.9	3.0	3.7	4.4	3.3
SGG-UGM-1	3.7	3.7	4.5	5.1	4.1
EIGEN-6C4	3.0	3.0	3.8	4.4	3.3
XGM2019e_2159	2.4	2.4	3.0	3.7	2.5
GOCO05c	2.5	2.7	3.4	3.9	2.9
XGM2016	2.4	2.4	3.2	3.8	2.6
XGM2019	2.3	2.4	3.1	3.7	2.5

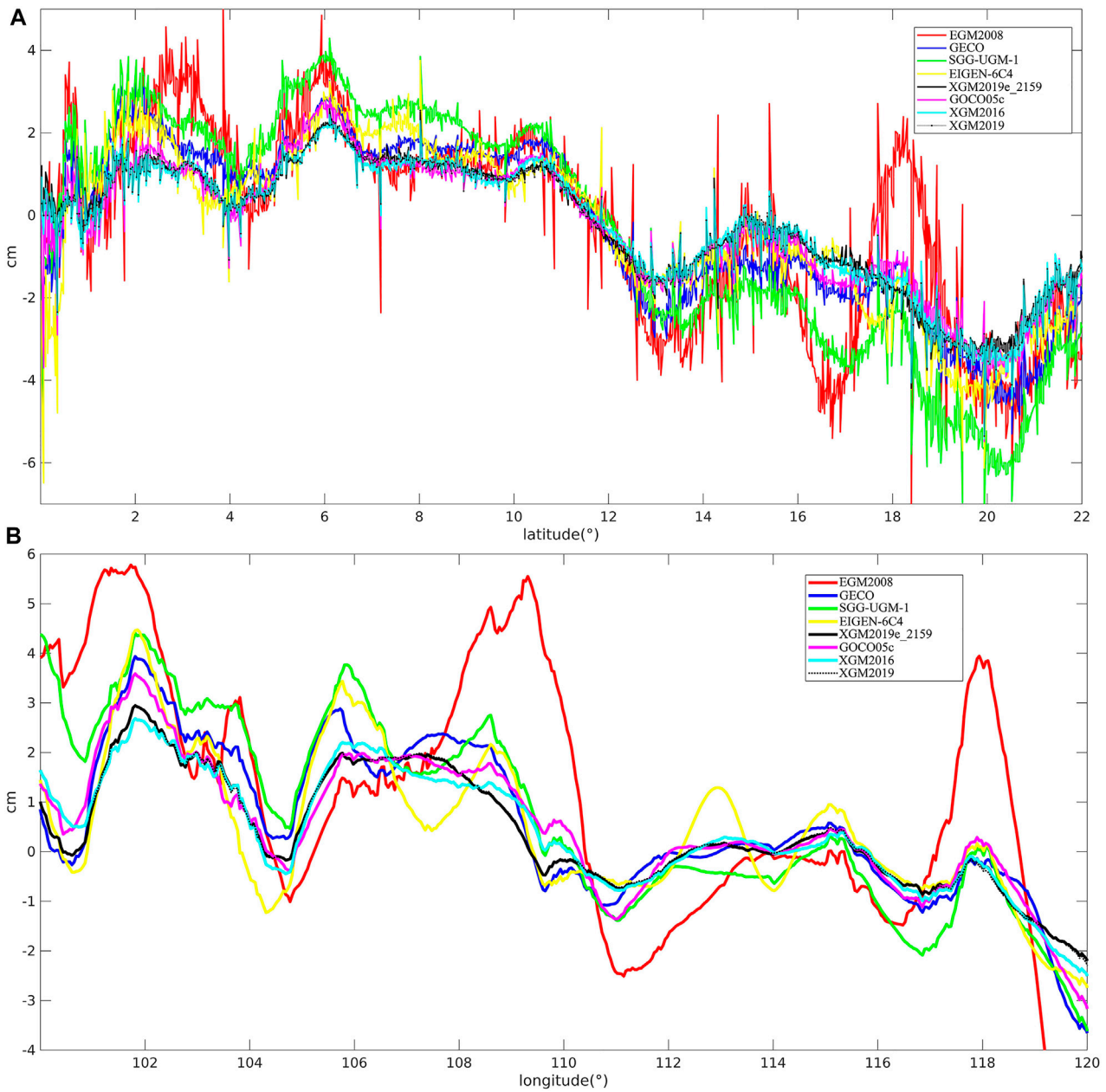

FIGURE 9 | The zonal **(A)** and meridian **(B)** mean of the misfits between the MDTs derived from different GGMs and mean of all synthetic/ocean models.

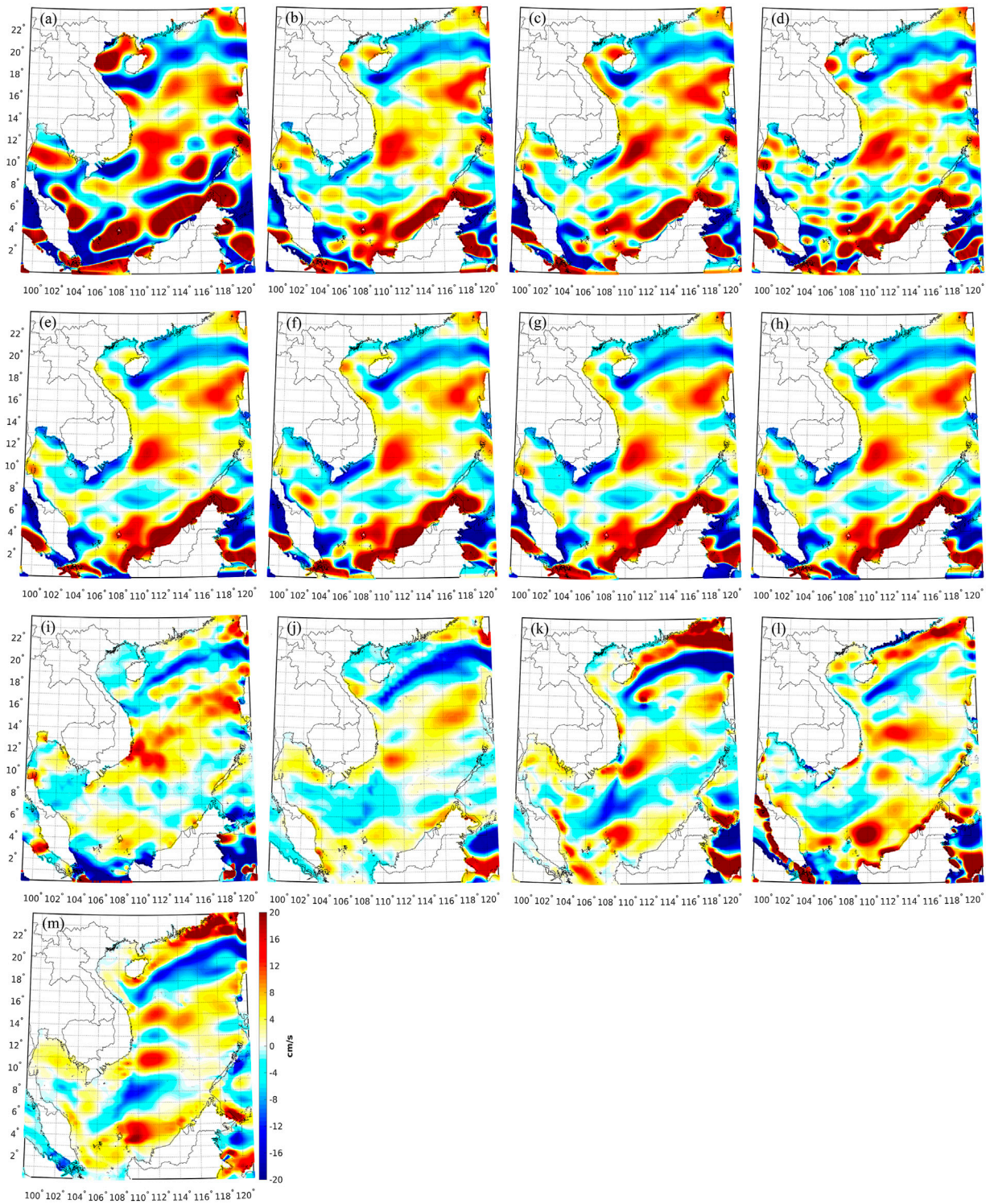

FIGURE 10 | Zonal geostrophic velocities derived from the MDT computed from **(A)** EGM2008, **(B)** GECO, **(C)** SGG-UGM-1, **(D)** EIGEN-6C4, **(E)** XGM2019_2159, **(F)** GOCO05c, **(G)** XGM2016, **(H)** XGM2019, **(I)** CNES-CLS13MDT; and zonal velocities retrieved from **(J)** SODA, **(K)** ORAS5, **(L)** OCCAM, and **(M)** AIPO.

error information of the ocean models is not available and no *in situ* data have been for evaluating the synthetic/ocean models and geodetic MDTs in this study.

In addition, the geodetic MDTs' characteristics along the zonal/meridian profile are investigated. **Figure 9A** shows the zonal mean of the misfits between different geodetic MDTs and

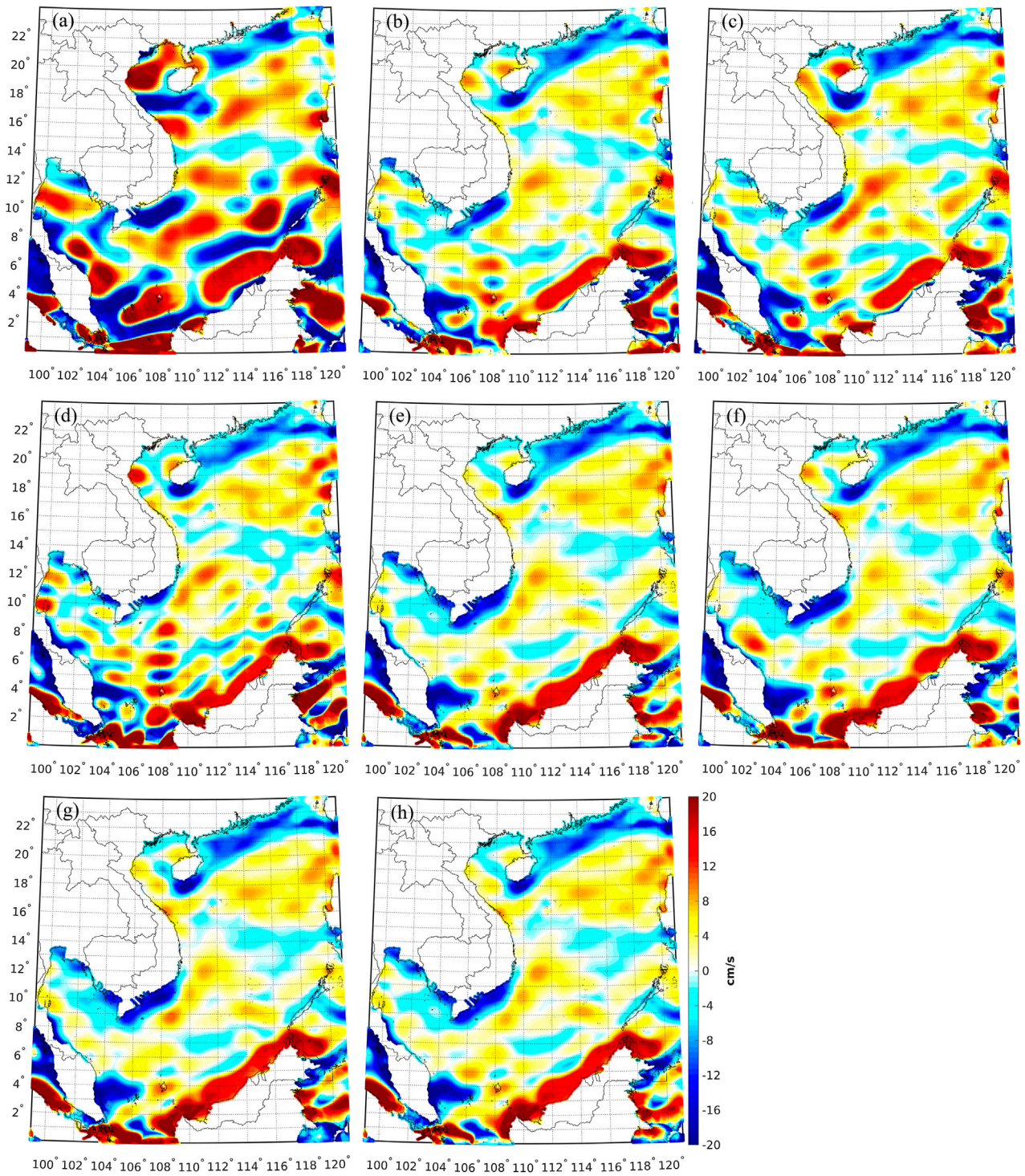

FIGURE 11 | Differences between the zonal velocities computed from the MDT computed from **(A)** EGM2008, **(B)** GECO, **(C)** SGG-UGM-1, **(D)** EIGEN-6C4, **(E)** XGM2019e_2159, **(F)** GOCO05c, **(G)** XGM2016, **(H)** XGM2019 and the mean of the zonal velocities derived from all synthetic/ocean data.

the mean of all synthetic/ocean data. The MDT derived from EGM2008 demonstrates strong oscillations, and the spike-like errors appear, by a magnitude up to 5 cm. The MDT derived from SGG-UGM-1/EIGEN-6C4 has slightly better performance; however, the spikes are still prominent. For instance, the MDT computed from SGG-UGM-1 has strong variations from 18°N to 21°N, where this profile passes through the regions around Hainan in China. This corresponds to the result that the MDT

TABLE 5 | The standard deviation of the differences between the zonal velocities synthesized from the MDTs modeled from different GGMs and those derived from synthetic/ocean data.

MDT minus synthetic/ocean model	CNES-CLS13MDT	SODA	ORAS5	OCCAM	AIPO	Mean of all synthetic/ocean models
EGM2008	11.4	11.2	13.2	12.6	11.8	11.1
GECO	7.6	7.5	8.9	8.5	8.3	7.1
SGG-UGM-1	8.0	8.0	9.6	9.1	8.9	7.7
EIGEN-6C4	8.0	8.2	9.5	9.0	9.0	7.9
XGM2019e_2159	7.7	7.4	9.0	8.2	8.3	7.1
GOCO05c	8.1	7.7	9.2	8.6	8.5	7.4
XGM2016	7.8	7.7	9.1	8.5	8.5	7.4
XGM2019	7.7	7.4	9.0	8.3	8.3	7.1

derived from SGG-UGM-1 has large errors around Hainan because of the coastal problem. In contrast, the MDTs computed from the other GGMs show improved qualities, and almost no apparent spikes are found. The MDT derived from XGM2019e_2159/XGM2019 has relatively small variations, and the discrepancies against the synthetic/ocean data are within 3 cm. The misfits between the geodetic MDTs and the ocean data are reduced along the meridian profile compared to the ones derived from the zonal profile, see **Figure 9B**. This is mainly due to the configuration of satellite orbits, which affects the error structures of the GGM-derived quantities. As the orbit of GRACE/GOCE is almost south-north oriented, the along-track data sampling is much denser than that in the across-track direction; and consequently, larger errors were found in east-west direction than in north-south direction (Balmino, 2009; Bingham et al., 2011b). Similar validation results are concluded along the meridian profile as ones derived from the zonal profile, where the signal calculated from XGM2019e_2159/XGM2019 has relatively high quality.

Geostrophic Currents Comparison

The performances of different GGMs are further assessed in terms of geostrophic velocities. Apart from the synthetic/ocean data shown in *Existing MDTs and Ocean Models*, another reanalysis data set derived from an ocean data assimilation system in Asia, the Indian Ocean, and the western Pacific Ocean (AIPO), known as AIPOcean (Yan et al., 2015), is introduced. AIPOcean data was developed based on the ensemble optimal interpolation (EnOI) method, where various types of observations including the AVISO altimetric SLA, satellite-sensed sea surface temperature, and *in situ* temperature and salinity profiles, were assimilated. AIPOcean data contains the daily averaged ocean current field from January 1, 1993 to December 31, 2006, with a horizontal resolution of 0.25°. The comparisons with independent observations and other reanalysis products show that the quality of AIPOcean data was well controlled, which provided the realistic structures of the ocean state in AIPO (Yan et al., 2015).

AIPOcean data map the ocean currents from 1993 to 2006 with a horizontal resolution of 0.25°, and the synthetic/geodetic MDT is adjusted to this time period based on AVISO SLA data, and then the geostrophic velocities are computed. Whereas, the surface currents provided in the ocean models are retrieved and averaged to map the signals over the 1993–2006 time period.

Figure 10 shows the zonal velocities computed from the geodetic MDTs and the synthetic/ocean data, which generally reconstruct the real surface circulation over the SCS. For instance, the blue strip-like features over the northern of SCS that passes through the southern of Hainan is the South China Sea Warm Current (SCSWC), playing a key role in distribution of mass, energy, and heat balances over the northern SCS (Hsueh and Zhong, 2004; Chiang et al., 2008; Yang et al., 2008). Moreover, the yellow/red signals along the Guangdong coast are known as Guangdong Coastal Current (GCC) (Hu et al., 2000; Gu et al., 2012). However, the structures of GCC are not identical in different models. For example, the intensity of GCC in CNES-CLS13MDT/SODA is not as strong as that in ORAS5/OCCAM/AIPO.

The detailed features of the zonal velocities derived from the geodetic MDTs and ocean models are heterogeneous. For signals computed from the geodetic MDTs, more scattered structures are observed in the values computed from the MDT derived from EGM2008, displaying as prominent long-wavelength patterns, especially in the southern SCS. However, these large-scale contents cannot be treated as real ocean circulation signals, since the long-wavelength contents of EGM2008 are questionable due to the lack of GOCE data. By comparison, the velocities computed from the MDTs derived from other GGMs show less variations and smoother patterns. It is noticeable that a high-degree GGM suffers from the coastal problem, where the errors in the associated MDT are magnified in the computation of geostrophic velocities, since the gradients of MDT are used to compute the geostrophic velocities. However, the coastal problem may be mitigated by using the recent altimeter data (Ophaug et al., 2015; Idžanović et al., 2017) and airborne gravimetric survey (Hwang et al., 2006; Wu et al., 2019).

CNES-CLS13MDT and SODA demonstrate smoother structures than other ocean models over the southern SCS, and significant small-scale structures are observed in CNES-CLS13MDT over the northern part. While, ORAS5, OCCAM, and AIPO have relatively intense features over the Guangdong coast, compared to CNES-CLS13MDT/SODA. Different methods and input data for model development are the main reasons for these differences. For example, CNES-CLS13MDT is a synthetic model, estimated through a geodetic method as a raw solution, which was then enhanced by *in situ* data to recover the small-scale contents. While, the ocean models are the ocean

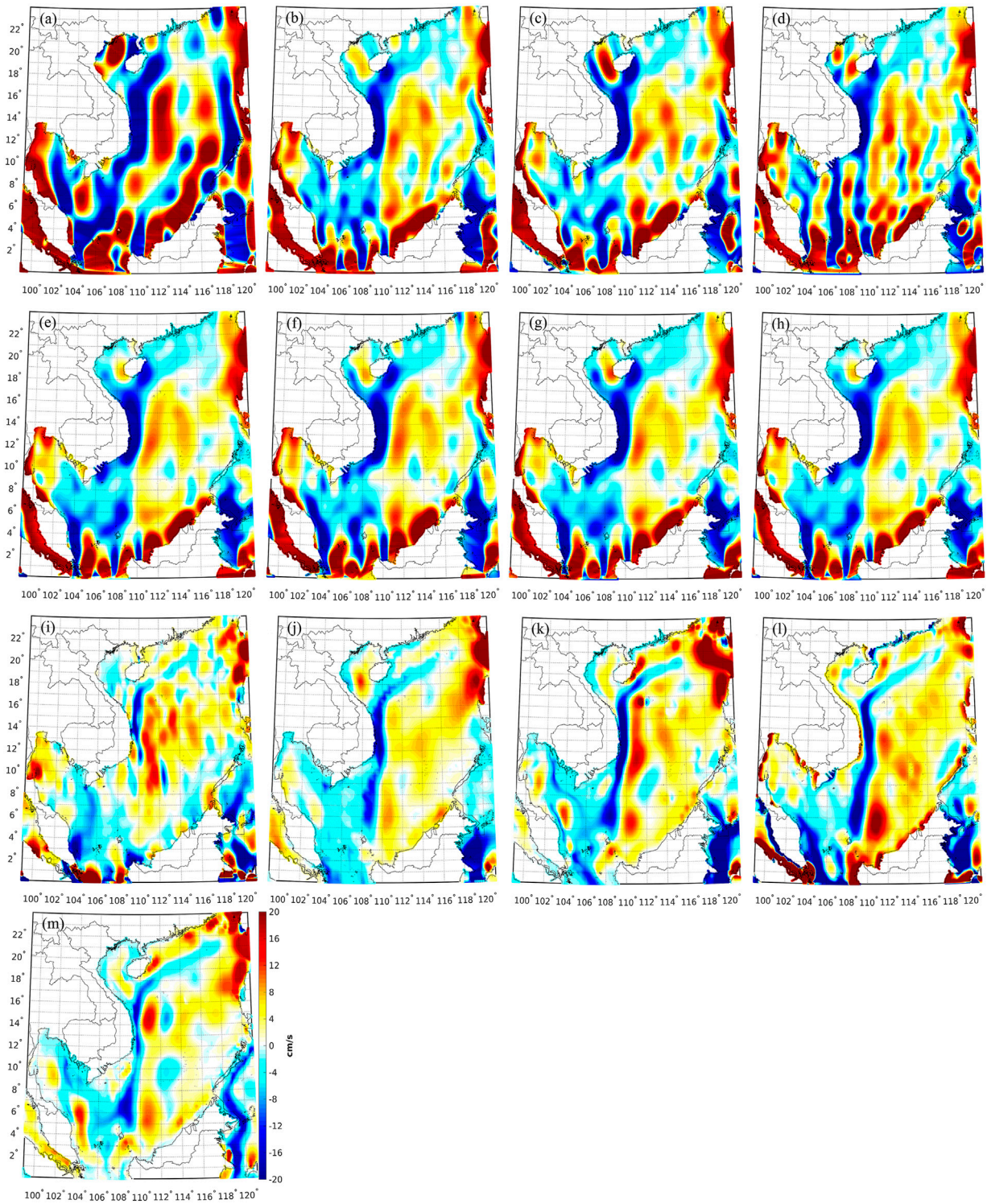

FIGURE 12 | Meridian geostrophic velocities computed from the MDT derived from **(A)** EGM2008, **(B)** GECO, **(C)** SGG-UGM-1, **(D)** EIGEN-6C4, **(E)** XGM2019_2159, **(F)** GOCO05c, **(G)** XGM2016, **(H)** XGM2019, **(I)** CNES-CLS13MDT; and meridian velocities retrieved from **(J)** SODA, **(K)** ORAS5, **(L)** OCCAM, and **(M)** AIPO.

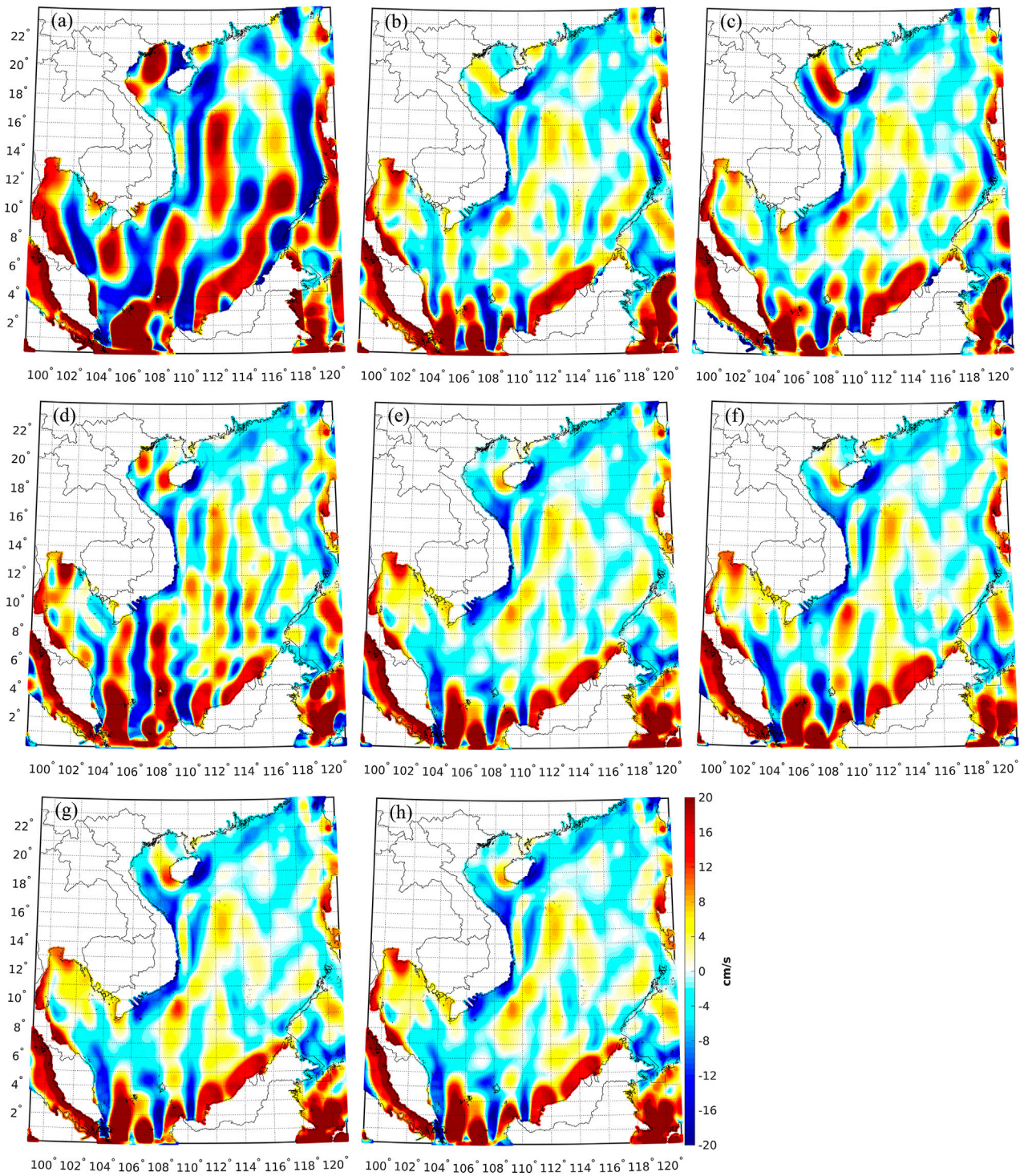

FIGURE 13 | Differences between the meridian velocities computed from the MDT derived from **(A)** EGM2008, **(B)** GECO, **(C)** SGG-UGM-1, **(D)** EIGEN-6C4, **(E)** XGM2019e_2159, **(F)** GOCO05c, **(G)** XGM2016, **(H)** XGM2019 and the mean of the meridian velocities derived from all synthetic/ocean data.

reanalysis products developed by combining ocean state data, hydrographic data, surface temperature, and so on.

Figure 11 demonstrates the discrepancies between the zonal geostrophic velocities computed from different geodetic MDTs and the mean of all synthetic/ocean data, and the associated statistics are given in **Table 5**. The performances of the velocities computed from different geodetic MDTs are heterogeneous. The zonal velocities derived from the MDT modeled with EGM2008

TABLE 6 | The standard deviation of the differences between the meridian velocities synthesized from the MDTs modeled from different GGMs and those derived from synthetic/ocean models.

MDT minus synthetic/ocean model	CNES-CLS13MDT	SODA	ORAS5	OCCAM	AIPO	Mean of all synthetic/ocean models
EGM2008	13.2	12.5	13.6	13.8	12.7	12.3
EIGEN-6C4	9.7	9.0	10.4	10.0	9.1	8.6
GECO	8.6	7.8	9.6	9.4	8.4	7.6
SGG-UGM-1	9.2	8.1	9.6	9.7	8.7	8.0
XGM2019e_2159	7.9	7.2	9.0	8.3	8.0	6.8
GOCO05c	8.8	8.1	9.8	8.9	8.4	7.7
XGM2016	8.1	7.7	9.4	8.6	8.3	7.3
XGM2019	7.8	7.2	9.0	8.3	8.0	6.9

have the largest oscillations, where the SD of the inconsistencies against the mean of synthetic/ocean data is 11.1 cm/s. The prominent discrepancies occur over the southern of SCS and along the coast of Vietnam, Malaysia and Philippines, by a magnitude up to 20 cm/s. The comparisons of EGM2008 and other models that have similar resolutions, i.e., GECO, SGG-UGM-1, EIGEN-6C4, and XGM2019e_2159, show that the zonal velocities computed from the MDTs modeled with these four models have improved qualities, and the SD values of the misfits reduce to 7.1–7.9 cm/s. The errors of the geostrophic velocities computed from these four models are significantly reduced over coastal regions, especially in the southern coast of Guangdong, north-eastern and south-eastern coast of Vietnam, western coast of Malaysia and Philippines. The mutual comparisons show that the zonal velocities derived from the MDT computed from GECO/XGM2019e_2159 have better qualities than the ones computed from the MDT modeled with SGG-UGM-1/EIGEN-6C4. This is not consistent with the results derived from the MDT comparison, where the MDT computed from GECO has lower quality than the one derived from XGM2019e_2159, but has comparable quality with the MDT derived from EIGEN-6C4. The SD of the misfits of the zonal velocities derived from the MDTs modeled with GOCO05c, XGM2016, and XGM2019 are 7.4, 7.4, and 7.1 cm/s, respectively, where the velocities derived from the MDT modeled with XGM2019 show better performances.

The meridian velocities synthesized from the geodetic MDTs and the synthetic/ocean data are seen in **Figure 12**, which represent the north-southward ocean circulation of SCS. For instance, a southward along-shelf current is seen along the coast of Vietnam, see the blue stripe-like features, which is mainly caused by local monsoon system (Hu et al., 2000; Chen et al., 2012). In addition, the red signals cross the Luzon Strait are line with the Kuroshio intrusion, e.g., see Hu et al. (2000) and Xue et al. (2004). The comparison results are seen in **Figure 13**; **Table 6**, where the velocities computed from the MDT modeled with EGM2008 have the worst performances, the SD of the misfits against the ocean data reaches 12.3 cm/s. Whereas, the SD values reduce to 7.6, 8.0, 8.6, and 6.8 cm/s, respectively, when the velocities derived from the MDTs modeled with GECO, SGG-UGM-1, EIGEN-6C4, and XGM2019e_2159 are assessed. The SD of the misfits of the meridian velocities derived from the MDTs modeled with GOCO05c, XGM2016, and XGM2019 is 7.7, 7.3, and 6.9 cm/s, respectively, where the signals derived from the MDT modeled with XGM2019 also have better performances.

CONCLUSION

The wide range of applications of the global geopotential models in ocean science emphasizes the importance for model assessment. We assess the qualities of the recently released high-degree GGMs over the South China Sea, where local airborne/shipborne gravity data and independent synthetic/ocean reanalysis data are served as the control data.

A comparison with a high resolution (~3 km) airborne gravimetric survey over the Paracel Islands shows that XGM2019e_2159 has relatively high quality, and the SD of the misfits against the airborne gravity data is ~3.1 mGal. The SD values increase to ~4.0 mGal when EGM2008, GECO, SGG-UGM-1, and EIGEN-6C4 are validated; however, the qualities of these models cannot be discriminated. Whereas, the comparisons with the shipborne gravity data that retrieved from the NGDC cannot discriminate the qualities of different GGMs that have the same expansion degree, due to the limited data precision.

The assessments with the synthetic/ocean data show that the qualities of the values derived from different GGMs are heterogeneous. The MDT computed from XGM2019e_2159 has relatively high quality, showing in an agreement with the validation results against the airborne gravity data. The SD of the differences between the MDT modeled with XGM2019e_2159 and the mean of all synthetic/ocean data is ~2.5 cm; and this value changes to 7.1 cm/s (6.8 cm/s) when the associated zonal (meridian) velocities are assessed. The assessments of the quantities modeled with EIGEN-6C4, GECO, SGG-UGM-1, GOCO05c, and XGM2016 show that they have deteriorated qualities than the ones derived from XGM2019e_2159, with a reduction of approximately 0.1–1.6 cm in terms of MDT, and of 0.3–1.8 cm/s in terms of geostrophic velocities. The values derived from EGM2008 demonstrate the worst performances, which is reduced by 3.9 cm when the MDT is assessed, and by 4.0 cm/s (5.5 cm/s) when the zonal (meridian) velocities are assessed, compared to the results derived from XGM2019e_2159. Moreover, the quantities computed from EGM2008 severely suffer from the coastal problem, which is mainly attributed to the lack of high-quality altimetric gravity data when this model was developed.

These numerical results suggest that the choice of a GGM in ocean state study is crucial, particularly in coastal regions, even though different GGMs that have the similar expansion degrees

may show comparable results when compared with local gravity data. Moreover, the use of synthetic/ocean data may be capable of distinguishing the qualities of different GGMs, indicating that these data sets may be served as additional data sources for global/regional gravity field model assessment over oceans.

DATA AVAILABILITY STATEMENT

The original contributions presented in the study are included in the article/Supplementary Material, further inquiries can be directed to the corresponding author.

AUTHOR CONTRIBUTIONS

YW initiated the study, designed the numerical experiments and wrote the manuscript. XH, ZL, and HS provided the data and gave the beneficial suggestions. YW, XH, and ZL finalized the manuscript. All authors read and approved the final manuscript.

FUNDING

This study was supported by the Natural Science Foundation of Jiangsu Province, China (No. BK20190498), the Fundamental Research Funds for the Central Universities (No. B200202019), the National Natural Science Foundation of China (No. 42004008, 41830110, 41931074), and the State Scholarship Fund from Chinese Scholarship Council (No. 201306270014).

ACKNOWLEDGMENTS

The authors gratefully acknowledge the First Geodetic Surveying Brigade of the Ministry of Natural Resources of China for kindly providing the airborne gravity data.

REFERENCES

Abulaitijiang, A., Andersen, O. B., and Stenseng, L. (2015). Coastal Sea Level from Inland CryoSat-2 Interferometric SAR Altimetry. *Geophys. Res. Lett.* 42 (6), 1841–1847. doi:10.1002/2015GL063131

Albertella, A., Savcenko, R., Janjić, T., Rummel, R., Bosch, W., and Schröter, J. (2012). High Resolution Dynamic Ocean Topography in the Southern Ocean from GOCE. *Geophys. J. Int.* 190 (2), 922–930. doi:10.1111/j.1365-246x.2012.05531.x

Andersen, O. B., and Knudsen, P. (2009). DNSC08 Mean Sea Surface and Mean Dynamic Topography Models. *J. Geophys. Res.* 114, C11001. doi:10.1029/2008JC005179

Andersen, O. B., Knudsen, P., Kenyon, S., Factor, J., and Holmes, S. A. (2013). "The DTU13 Global marine Gravity Field-First Evaluation," in *Ocean Surface Topography Science Team Meeting* Boulder, Colorado.

Andersen, O. B., Knudsen, P., and Stenseng, L. (2018). "A New DTU18 MSS Mean Sea Surface–Improvement from SAR Altimetry," in 25 years of progress in radar altimetry symposium, Portugal, 24-29 Sep 2018.

Andersen, O. B., and Knudsen, P. (2019). "The DTU17 Global Marine Gravity Field: First Validation Results," in *International Association of Geodesy Symposia* (Berlin, Heidelberg: Springer). doi:10.1007/1345_2019_65

Andersen, O. B., Piccioni, G., Knudsen, P., and Stenseng, L. (2016). "The DTU15 MSS (Mean Sea Surface) and DTU15LAT (Lowest Astronomical Tide) Reference Surface," in Paper presented at the ESA Living planet symposium 2016, Prague, Czech Republic Available at https://ftp.space.dtu.dk/pub/DTU15/DOCUMENTS/MSS/DTU15MSS+LAT.pdf (Accessed September 3, 2021).

Andersen, O. B., and Scharroo, R. (2011). "Range and Geophysical Corrections in Coastal Regions: and Implications for Mean Sea Surface Determination," in *Coastal Altimetry*. Editors S. Vignudelli, A. G. Kostianoy, P. Cipollini, and J. Benveniste (Berlin, Heidelberg: Springer). doi:10.1007/978-3-642-12796-0_5

Andersen, O. B. (2010). "The DTU10 Global Gravity Field and Mean Sea Surface – Improvements in the Arctic," in *2nd IGFS Symposium* Fairbanks, Alaska Available at http://www.space.dtu.dk/english/%20/media/Institutter/Space/English/scientific_data_and_models/global_marine_gravity_field/dtu10.ashx (Accessed September 3, 2021).

Arabelos, D. N., and Tscherning, C. C. (2010). A Comparison of Recent Earth Gravitational Models with Emphasis on Their Contribution in Refining the Gravity and Geoid at continental or Regional Scale. *J. Geod.* 84 (11), 643–660. doi:10.1007/s00190-010-0397-z

Balmino, G. (2009). Efficient Propagation of Error Covariance Matrices of Gravitational Models: Application to GRACE and GOCE. *J. Geod.* 83 (10), 989–995. doi:10.1007/s00190-009-0317-2

Bingham, R. J., Haines, K., and Lea, D. J. (2014). How Well Can We Measure the Ocean's Mean Dynamic Topography from Space? *J. Geophys. Res. Oceans* 119, 3336–3356. doi:10.1002/2013JC009354

Bingham, R. J., and Haines, K. (2006). Mean Dynamic Topography: Intercomparisons and Errors. *Phil. Trans. R. Soc. A.* 364 (1841), 903–916. doi:10.1098/rsta.2006.1745

Bingham, R. J., Knudsen, P., Andersen, O., and Pail, R. (2011a). An Initial Estimate of the North Atlantic Steady-State Geostrophic Circulation from GOCE. *Geophys. Res. Lett.* 38, L01606. doi:10.1029/2010GL045633

Bingham, R. J., Tscherning, C., and Knudsen, P. (2011b). "An Initial Investigation of the GOCE Error Variance Covariance Matrices in the Context of the GOCE User Toolbox Project," in Proceedings of 4th International GOCE User Workshop, Münich, Germany (European Space Agency), 8.

Braitenberg, C., and Ebbing, J. (2009). New Insights into the Basement Structure of the West Siberian Basin from Forward and Inverse Modeling of GRACE Satellite Gravity Data. *J. Geophys. Res.* 114, B06402. doi:10.1029/2008JB005799

Brockmann, J. M., Zehentner, N., Höck, E., Pail, R., Loth, I., Mayer-Gürr, T., et al. (2014). EGM_TIM_RL05: An Independent Geoid with Centimeter Accuracy Purely Based on the GOCE mission. *Geophys. Res. Lett.* 41, 8089–8099. doi:10.1002/2014GL061904

Bruinsma, S. L., Förste, C., Abrikosov, O., Marty, J.-C., Rio, M.-H., Mulet, S., et al. (2013). The New ESA Satellite-Only Gravity Field Model via the Direct Approach. *Geophys. Res. Lett.* 40, 3607–3612. doi:10.1002/grl.50716

Carton, J. A., Chepurin, G. A., and Chen, L. (2018). SODA3: a New Ocean Climate Reanalysis. *J. Clim.* 31, 6967–6983. doi:10.1175/JCLI-D-18-0149.1

Chen, C., Lai, Z., Beardsley, R. C., Xu, Q., Lin, H., and Viet, N. T. (2012). Current Separation and Upwelling over the Southeast Shelf of Vietnam in the South China Sea. *J. Geophys. Res.* 117, C03033. doi:10.1029/2011JC007150

Chen, G., Hou, Y., and Chu, X. (2011). Mesoscale Eddies in the South China Sea: Mean Properties, Spatiotemporal Variability, and Impact on Thermohaline Structure. *J. Geophys. Res.* 116, C06018. doi:10.1029/2010JC006716

Chiang, T.-L., Wu, C.-R., and Chao, S.-Y. (2008). Physical and Geographical Origins of the South China Sea Warm Current. *J. Geophys. Res.* 113, C08028. doi:10.1029/2008JC004794

Deng, X., and Featherstone, W. E. (2006). A Coastal Retracking System for Satellite Radar Altimeter Waveforms: Application to ERS-2 Around Australia. *J. Geophys. Res.* 111, C06012. doi:10.1029/2005JC003039

Denker, H., and Roland, M. (2005). "Compilation and Evaluation of a Consistent marine Gravity Data Set Surrounding Europe," in *A Window on the Future of Geodesy* (Berlin, Heidelberg: Springer).

Erol, B., Işık, M. S., and Erol, S. (2020). An Assessment of the GOCE High-Level Processing Facility (Hpf) Released Global Geopotential Models with Regional Test Results in turkey. *Remote Sensing* 12 (3), 586. doi:10.3390/rs12030586

Farrell, S. L., McAdoo, D. C., Laxon, S. W., Zwally, H. J., Yi, D., Ridout, A., et al. (2012). Mean Dynamic Topography of the Arctic Ocean. *Geophys. Res. Lett.* 39, L01601. doi:10.1029/2011GL050052

Featherstone, W. E., McCubbine, J. C., Brown, N. J., Claessens, S. J., Filmer, M. S., and Kirby, J. F. (2018). The First Australian Gravimetric Quasigeoid Model with Location-specific Uncertainty Estimates. *J. Geod.* 92 (2), 149–168. doi:10.1007/s00190-017-1053-7

Fecher, T., Pail, R., Pail, R., and Gruber, T. (2017). GOCO05c: A New Combined Gravity Field Model Based on Full normal Equations and Regionally Varying Weighting. *Surv. Geophys.* 38 (3), 571–590. doi:10.1007/s10712-016-9406-y

Filmer, M. S., Hughes, C. W., Woodworth, P. L., Featherstone, W. E., and Bingham, R. J. (2018). Comparison between Geodetic and Oceanographic Approaches to Estimate Mean Dynamic Topography for Vertical Datum Unification: Evaluation at Australian Tide Gauges. *J. Geod.* 92 (12), 1413–1437. doi:10.1007/s00190-018-1131-5

Förste, C., Bruinsma, S. L., Abrikosov, O., Lemoine, J. M., Schaller, T., Götze, H. J., et al. (2014). *EIGEN-6C4 the Latest Combined Global Gravity Field Model Including GOCE Data up to Degree and Order 2190 of GFZ Potsdam and GRGS Toulouse*. Potsdam, Germany: GFZ Data Services. doi:10.5880/icgem.2015.1

Fox, A. D., and Haines, K. (2003). Interpretation of Water Transformations Diagnosed from Data Assimilation. *J. Phys. Oceanogr* 33, 485–498. doi:10.1175/1520-0485(2003)033<0485:IOWMTD>2.0.CO;2

Gan, J., Li, H., Curchitser, E. N., and Haidvogel, D. B. (2006). Modeling South China Sea Circulation: Response to Seasonal Forcing Regimes. *J. Geophys. Res.* 111, C06034. doi:10.1029/2005JC003298

Garcia, E. S., Sandwell, D. T., and Smith, W. H. F. (2014). Retracking CryoSat-2, Envisat and Jason-1 Radar Altimetry Waveforms for Improved Gravity Field Recovery. *Geophys. J. Int.* 196 (3), 1402–1422. doi:10.1093/gji/ggt469

Gilardoni, M., Reguzzoni, M., and Sampietro, D. (2015). GECO: a Global Gravity Model by Locally Combining GOCE Data and EGM2008. *Stud. Geophys. Geod.* 60 (2), 228–247. doi:10.1007/s11200-015-1114-14

Griesel, A., Mazloff, M. R., and Gille, S. T. (2012). Mean Dynamic Topography in the Southern Ocean: Evaluating Antarctic Circumpolar Current Transport. *J. Geophys. Res.* 117, C01020. doi:10.1029/2011JC007573

Gruber, T., Rummel, R., Abrikosov, O., and van Hees, R. (2014). GOCE Level 2 Product Data Handbook, GO-MA-HPF-GS-0110, Issue 4.2. Available online at: https://earth.esa.int/documents/10174/1650485/GOCE_Product_Data_Handbook_Level-2 (accessed Aug 25, 2021).

Gu, Y., Pan, J., and Lin, H. (2012). Remote Sensing Observation and Numerical Modeling of an Upwelling Jet in Guangdong Coastal Water. *J. Geophys. Res.* 117, C08019. doi:10.1029/2012JC007922

Hipkin, R., Haines, K., Beggan, C., Bingley, R., Hernandez, F., Holt, J., et al. (2004). The Geoid EDIN2000 and Mean Sea Surface Topography Around the British Isles. *Geophys. J. Int.* 157 (2), 565–577. doi:10.1111/j.1365-246X.2004.01989.x

Hirt, C., Gruber, T., and Featherstone, W. E. (2011). Evaluation of the First GOCE Static Gravity Field Models Using Terrestrial Gravity, Vertical Deflections and EGM2008 Quasigeoid Heights. *J. Geod.* 85 (10), 723–740. doi:10.1007/s00190-011-0482-y

Ho, C.-R., Zheng, Q., Soong, Y. S., Kuo, N.-J., and Hu, J.-H. (2000). Seasonal Variability of Sea Surface Height in the South China Sea Observed with TOPEX/Poseidon Altimeter Data. *J. Geophys. Res.* 105 (C6), 13981–13990. doi:10.1029/2000JC900001

Hsueh, Y., and Zhong, L. (2004). A Pressure-Driven South China Sea Warm Current. *J. Geophys. Res.* 109, C09014. doi:10.1029/2004JC002374

Hu, J., Kawamura, H., Hong, H., and Qi, Y. (2000). A Review on the Currents in the South China Sea: Seasonal Circulation, South China Sea Warm Current and Kuroshio Intrusion. *J. Oceanogr.* 56 (6), 607–624. doi:10.1023/A:1011117531252

Huang, J. (2017). Determining Coastal Mean Dynamic Topography by Geodetic Methods. *Geophys. Res. Lett.* 44, 11,125–11,128. doi:10.1002/2017GL076020

Hwang, C., and Chen, S.-A. (2000). Circulations and Eddies over the South China Sea Derived from TOPEX/Poseidon Altimetry. *J. Geophys. Res.* 105 (C10), 23943–23965. doi:10.1029/2000JC900092

Hwang, C., Guo, J., Deng, X., Hsu, H.-Y., and Liu, Y. (2006). Coastal Gravity Anomalies from Retracked Geosat/GM Altimetry: Improvement, Limitation and the Role of Airborne Gravity Data. *J. Geodesy* 80 (4), 204–216. doi:10.1007/s00190-006-0052-x

Idžanović, M., Ophaug, V., and Andersen, O. B. (2017). The Coastal Mean Dynamic Topography in Norway Observed by CryoSat-2 and GOCE. *Geophys. Res. Lett.* 44 (11), 5609–5617. doi:10.1002/2017GL073777

Jayne, S. R. (2006). Circulation of the North Atlantic Ocean from Altimetry and the Gravity Recovery and Climate Experiment Geoid. *J. Geophys. Res.* 111, C03005. doi:10.1029/2005JC003128

Jia, Y., and Liu, Q. (2004). Eddy Shedding from the Kuroshio bend at Luzon Strait. *J. Oceanogr.* 60, 1063–1069. doi:10.1007/s10872-005-0014-6

Kaban, M. K., Schwintzer, P., and Tikhotsky, S. A. (1999). A Global Isostatic Gravity Model of the Earth. *Geophys. J. Int.* 136 (3), 519–536. doi:10.1046/j.1365-246x.1999.00731.x

Knudsen, P., Bingham, R., Andersen, O., and Rio, M.-H. (2011). A Global Mean Dynamic Topography and Ocean Circulation Estimation Using a Preliminary GOCE Gravity Model. *J. Geod.* 85 (11), 861–879. doi:10.1007/s00190-011-0485-8

Liang, W., Xu, X., Li, J., and Zhu, G. (2018). The Determination of an Ultra-high Gravity Field Model SGG-UGM-1 by Combining EGM2008 Gravity Anomaly and GOCE Observation Data. *Acta Geodaetica et Cartographica Sinica* 47 (4), 425–434. doi:10.11947/j.AGCS.2018.20170269

McAdoo, D. C., Farrell, S. L., Laxon, S., Ridout, A., Zwally, H. J., and Yi, D. (2013). Gravity of the Arctic Ocean from Satellite Data with Validations Using Airborne Gravimetry: Oceanographic Implications. *J. Geophys. Res. Oceans* 118, 917–930. doi:10.1002/jgrc.20080

Ophaug, V., Breili, K., and Gerlach, C. (2015). A Comparative Assessment of Coastal Mean Dynamic Topography in N Orway by Geodetic and Ocean Approaches. *J. Geophys. Res. Oceans* 120 (12), 7807–7826. doi:10.1002/2015JC011145

Pail, R., Bruinsma, S., Migliaccio, F., Förste, C., Goiginger, H., Schuh, W.-D., et al. (2011). First GOCE Gravity Field Models Derived by Three Different Approaches. *J. Geod.* 85 (11), 819–843. doi:10.1007/s00190-011-0467-x

Pail, R., Fecher, T., Barnes, D., Factor, J. F., Holmes, S. A., Gruber, T., et al. (2018). Short Note: the Experimental Geopotential Model XGM2016. *J. Geod.* 92 (4), 443–451. doi:10.1007/s00190-017-1070-6

Pail, R., Goiginger, H., Schuh, W.-D., Höck, E., Brockmann, J. M., Fecher, T., et al. (2010). Combined Satellite Gravity Field Model GOCO01S Derived from GOCE and GRACE. *Geophys. Res. Lett.* 37, L20314. doi:10.1029/2010GL044906

Pavlis, N. K., Holmes, S. A., Kenyon, S. C., and Factor, J. K. (2013). Correction to "The Development and Evaluation of the Earth Gravitational Model 2008 (EGM2008)". *J. Geophys. Res. Solid Earth* 118 (5), 2633. doi:10.1029/jgrb.5016710.1002/jgrb.50167

Pavlis, N. K., Holmes, S. A., Kenyon, S. C., and Factor, J. K. (2012). The Development and Evaluation of the Earth Gravitational Model 2008 (EGM2008). *J. Geophys. Res.* 117, B04406. doi:10.1029/2011JB008916

Rio, M.-H., Mulet, S., and Picot, N. (2014). Beyond GOCE for the Ocean Circulation Estimate: Synergetic Use of Altimetry, Gravimetry, and *In Situ* Data Provides New Insight into Geostrophic and Ekman Currents. *Geophys. Res. Lett.* 41 (24), 8918–8925. doi:10.1002/2014GL061773

Rio, M. H., Guinehut, S., and Larnicol, G. (2011). New CNES-CLS09 Global Mean Dynamic Topography Computed from the Combination of GRACE Data, Altimetry, and *In Situ* Measurements. *J. Geophys. Res.* 116, C07018. doi:10.1029/2010JC006505

Rummel, R., Balmino, G., Johannessen, J., Visser, P., and Woodworth, P. (2002). Dedicated Gravity Field Missions—Principles and Aims. *J. Geodyn.* 33 (1-2), 3–20. doi:10.1016/S0264-3707(01)00050-3

Rummel, R. (2012). Height Unification Using GOCE. *J. geodetic Sci.* 2 (4), 355–362. doi:10.2478/v10156-011-0047-2

Sampietro, D. (2015). Geological Units and Moho Depth Determination in the Western Balkans Exploiting GOCE Data. *Geophys. J. Int.* 202 (2), 1054–1063. doi:10.1093/gji/ggv212

Sandwell, D., Garcia, E., Soofi, K., Wessel, P., Chandler, M., and Smith, W. H. F. (2013). Toward 1-mGal Accuracy in Global marine Gravity from CryoSat-2, Envisat, and Jason-1. *The Leading Edge* 32 (8), 892–899. doi:10.1190/tle32080892.1

Sandwell, D. T., Müller, R. D., Smith, W. H. F., Garcia, E., and Francis, R. (2014). New Global marine Gravity Model from CryoSat-2 and Jason-1 Reveals Buried Tectonic Structure. *Science* 346 (6205), 65–67. doi:10.1126/science.1258213

Skourup, H., Farrell, S. L., Hendricks, S., Ricker, R., Armitage, T. W. K., Ridout, A., et al. (2017). An Assessment of State-of-the-Art Mean Sea Surface and Geoid Models of the Arctic Ocean: Implications for Sea Ice Freeboard Retrieval. *J. Geophys. Res. Oceans* 122, 8593–8613. doi:10.1002/2017JC013176

Tapley, B. D., Chambers, D. P., Bettadpur, S., and Ries, J. C. (2003). Large Scale Ocean Circulation from the GRACE GGM01 Geoid. *Geophys. Res. Lett.* 30 (22), 2163. doi:10.1029/2003GL018622

Tapley, B., Ries, J., Bettadpur, S., Chambers, D., Cheng, M., Condi, F., et al. (2005). GGM02 - an Improved Earth Gravity Field Model from GRACE. *J. Geodesy* 79, 467–478. doi:10.1007/s00190-005-0480-z

Tenzer, R., Chen, W., Tsoulis, D., Bagherbandi, M., Sjöberg, L. E., Novák, P., et al. (2015). Analysis of the Refined CRUST1.0 Crustal Model and its Gravity Field. *Surv. Geophys.* 36 (1), 139–165. doi:10.1007/s10712-014-9299-6

Vianna, M. L., and Menezes, V. V. (2010). Mean Mesoscale Global Ocean Currents from Geodetic Pre-GOCE MDTs with a Synthesis of the North Pacific Circulation. *J. Geophys. Res.* 115, C02016. doi:10.1029/2009jc005494

Volkov, D. L., and Zlotnicki, V. (2012). Performance of GOCE and GRACE-derived Mean Dynamic Topographies in Resolving Antarctic Circumpolar Current Fronts. *Ocean Dyn.* 62 (6), 893–905. doi:10.1007/s10236-012-0541-9

Wang, G., Su, J., and Chu, P. C. (2003). Mesoscale Eddies in the South China Sea Observed with Altimeter Data. *Geophys. Res. Lett.* 30, 2121. doi:10.1029/2003GL018532

Weatherall, P., Marks, K. M., Jakobsson, M., Schmitt, T., Tani, S., Arndt, J. E., et al. (2015). A New Digital Bathymetric Model of the World's Oceans. *Earth Space Sci.* 2, 331–345. doi:10.1002/2015EA000107

Wu, Y., Abulaitijiang, A., Andersen, O. B., He, X., Luo, Z., and Wang, H. (2021). Refinement of Mean Dynamic Topography over Island Areas Using Airborne Gravimetry and Satellite Altimetry Data in the Northwestern South China Sea. *J. Geophys. Res. Solid Earth* 126 (8). doi:10.1029/2021JB021805

Wu, Y., Abulaitijiang, A., Featherstone, W. E., McCubbine, J. C., and Andersen, O. B. (2019). Coastal Gravity Field Refinement by Combining Airborne and Ground-Based Data. *J. Geod.* 93 (12), 2569–2584. doi:10.1007/s00190-019-01320-3

Wu, Y., Luo, Z., Chen, W., and Chen, Y. (2017a). High-resolution Regional Gravity Field Recovery from Poisson Wavelets Using Heterogeneous Observational Techniques. *Earth Planets Space* 69 (34), 1–15. doi:10.1186/s40623-017-0618-2

Wu, Y., Luo, Z., Mei, X., and Lu, J. (2016). Normal Height Connection across Seas by the Geopotential-Difference Method: Case Study in Qiongzhou Strait, China. *J. Surv. Eng.* 143 (2), 05016011. doi:10.1061/(ASCE)SU.1943-5428.0000203

Wu, Y., Luo, Z., Zhong, B., and Xu, C. (2018). A Multilayer Approach and its Application to Model a Local Gravimetric Quasi-Geoid Model over the North Sea: QGNSea V1.0. *Geosci. Model. Dev.* 11, 4797–4815. doi:10.5194/gmd-11-4797-2018

Wu, Y., Zhou, H., Zhong, B., and Luo, Z. (2017b). Regional Gravity Field Recovery Using the GOCE Gravity Gradient Tensor and Heterogeneous Gravimetry and Altimetry Data. *J. Geophys. Res. Solid Earth* 122 (8), 6928–6952. doi:10.1002/2017JB014196

Xu, D., Zhu, J., Qi, Y., Li, X., and Yan, Y. (2012). The Impact of Mean Dynamic Topography on a Sea-Level Anomaly Assimilation in the South China Sea Based on an Eddy-Resolving Model. *Acta Oceanol. Sin.* 31 (5), 11–25. doi:10.1007/s13131-012-0232-x

Xue, H., Chai, F., Pettigrew, N., Xu, D., Shi, M., and Xu, J. (2004). Kuroshio Intrusion and the Circulation in the South China Sea. *J. Geophys. Res.* 109, C02017. doi:10.1029/2002JC001724

Yan, C., Zhu, J., and Xie, J. (2015). An Ocean Data Assimilation System in the Indian Ocean and West Pacific Ocean. *Adv. Atmos. Sci.* 32 (11), 1460–1472. doi:10.1007/s00376-015-4121-z

Yang, J., Wu, D., and Lin, X. (2008). On the Dynamics of the South China Sea Warm Current. *J. Geophys. Res.* 113, C08003. doi:10.1029/2007JC004427

Zingerle, P., Pail, R., Gruber, T., and Oikonomidou, X. (2019). *The Experimental Gravity Field Model XGM2019e*. Potsdam, Germany: GFZ Data Services. doi:10.5880/ICGEM.2019.007

Zuo, H., Balmaseda, M. A., and Mogensen, K. (2017). The New Eddy-Permitting ORAP5 Ocean Reanalysis: Description, Evaluation and Uncertainties in Climate Signals. *Clim. Dyn.* 49, 791–811. doi:10.1007/s00382-015-2675-1

Conflict of Interest: The authors declare that the research was conducted in the absence of any commercial or financial relationships that could be construed as a potential conflict of interest.

Publisher's Note: All claims expressed in this article are solely those of the authors and do not necessarily represent those of their affiliated organizations, or those of the publisher, the editors and the reviewers. Any product that may be evaluated in this article, or claim that may be made by its manufacturer, is not guaranteed or endorsed by the publisher.

APPENDIX A | ERROR OF EGM2008

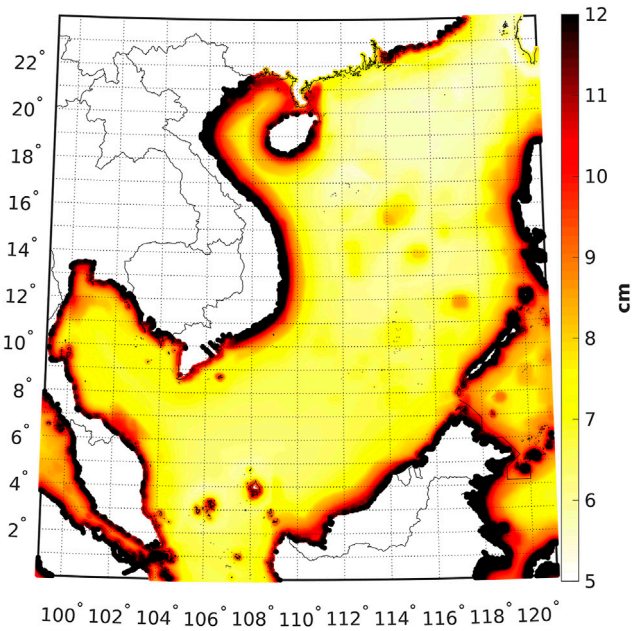

FIGURE A1 | Associated errors of EGM2008 in terms of quasi-geoid heights.

frontiers in Earth Science

ORIGINAL RESEARCH
published: 21 September 2021
doi: 10.3389/feart.2021.748401

Waveform Decontamination for Improving Satellite Radar Altimeter Data Over Nearshore Area: Upgraded Algorithm and Validation

Haihong Wang[1,2]* *and Zhengkai Huang*[3,4]

[1]School of Geodesy and Geomatics, Wuhan University, Wuhan, China, [2]Key Laboratory of Marine Environmental Survey Technology and Application, Ministry of Natural Resources, Guangzhou, China, [3]School of Civil Engineering and Architecture, East China Jiaotong University, Nanchang, China, [4]Key Laboratory of Basin Water Resources and Eco-environmental Science in Hubei Province, Yangtze River Scientific Research Institute, Wuhan, China

One of the thorniest problems in altimetry community is retrieving accurate coastal sea surface height, especially in the last several kilometers offshore. It is confirmed in previous studies that decontaminating waveforms is beneficial to improve the quality of coastal SSHs. In this article, we proposed an upgraded strategy for waveform decontamination, including a novel realignment algorithm and gate-wise outlier detector. We validated the new strategy in four test regions using Jason-2 altimeter data. In the validation process, we compared retracked SSHs by 16 retrackers, which include retrackers provided in SGDR (Sensor Geophysical Data Record), ALES (Adaptive Leading Edge Subwaveform), and PISTACH (Prototype Innovant de Système de Traitement pour les Applications Côtières et l'Hydrologie) products. Comparison results verified that retracking the waveforms decontaminated using our new method can greatly improve the SSHs in the coastal region. The 20% threshold retracker (DW-TR20) and the ICE1 retracker (DW-ICE1) based on the decontaminated waveforms outperform other retrackers, especially in 0–4 km zone offshore. DW-TR20 and DW-ICE1 can provide robust SSHs with a consistent accuracy in 0–20 km coastal band and a high correlation (>0.9) with nearby gauge data. To conclude, the upgraded waveform decontamination strategy provides a promising solution for coastal altimetry, which makes it possible to extend reliable observations to the last several kilometers offshore.

Keywords: coastal altimetry, sea surface height, waveform retracking, waveform decontamination, Jason-2

OPEN ACCESS

Edited by:
Jinyun Guo,
Shandong University of Science and Technology, China

Reviewed by:
Yihao Wu,
Hohai University, China
Shengjun Zhang,
Northeastern University, China
Nurul Hazrina Idris,
University of Technology Malaysia, Malaysia

***Correspondence:**
Haihong Wang
hhwang@sgg.whu.edu.cn

Specialty section:
This article was submitted to Environmental Informatics and Remote Sensing, a section of the journal Frontiers in Earth Science

Received: *27 July 2021*
Accepted: *23 August 2021*
Published: *21 September 2021*

Citation:
Wang H and Huang Z (2021) Waveform Decontamination for Improving Satellite Radar Altimeter Data Over Nearshore Area: Upgraded Algorithm and Validation. Front. Earth Sci. 9:748401. doi: 10.3389/feart.2021.748401

INTRODUCTION

Satellite altimetry is a mature technique for observing the global open ocean from space, providing a wealth of measurements for oceanographic, geodetic, and geophysical applications (Stammer and Cazenave, 2017; Fu and Cazenave, 2001). In the past decade, applications further extended to the coastal areas, which triggered a new discipline in the altimetry community, referred to as coastal altimetry (Vignudelli et al., 2011). It dedicates to exploit satellite altimetry from the open ocean to the coasts.

The crucial difficulty for coastal altimetry is that the altimeter data in the coastal zones are seriously degraded. In standard products, data in the coastal zone (up to tens of kilometers from the

coast) are usually flagged as bad (Cipollini et al., 2017; Vignudelli et al., 2011). It will result in no usable data over the coastal strip. Hence, the paramount work of coastal altimetry is retrieving more and better data closer to the coast. In recent years, considerable concern has arisen over this challenging topic and a dramatic effort has been made by the altimetry community of researchers. A series of reprocessed products for coastal applications were developed by some agencies, such as X-TRACK by LEGOS (Laboratoire d'Etudes en Géophysique et Océanographie Spatiales, France) (Birol et al., 2017), ALES (Adaptive Leading Edge Subwaveform) by NOC (National Oceanography Centre, United Kingdom) (Passaro et al., 2014), and PISTACH (Prototype Innovant de Système de Traitement pour l'Altimétrie Côtière et l'Hydrologie) (Mercier et al., 2010) and PEACHI (the Prototype for Expertise on Altimetry for Coastal, Hydrology and Ice) (Valladeau et al., 2015) by CNES (Centre National d'Etudes Spatiales).

The degradation of coastal altimeter data can be attributed to a couple of factors, such as contamination of the radar echoes and inadequate corrections. The most important one is the range error due to the distorted coastal waveforms. The coastal waveforms received by the altimeter will be contaminated by the reflections from land, calm water, or steep waves appearing in the radar footprint (Deng and Featherstone, 2006; Gomez-Enri et al., 2010). The contaminated waveforms depart from the open-ocean Brown model (Brown, 1977), which is routinely used for the onboard tracking system. Therefore, erroneous measurements might be derived in coastal regions. During the last few decades, a postprocessing technique referred to as waveform retracking has been extensively applied to overcome this problem. Numerous waveform retracking algorithms were developed that can be categorized into model-based and empirical retrackers (Gommenginger et al., 2011; Passaro et al., 2014). A number of studies have demonstrated the improvements in both quantity and quality of the coastal measurements when they are reprocessed using waveform retracking methods. Valid measurements after retracking have been approaching to the band of 10 km offshore from 50 km offshore. However, retrieving valid data over the last few kilometers to the coastline is still a challenge (Tseng et al., 2014; Huang et al., 2017; Vignudelli et al., 2019).

The closer to shore, the more complex the waveform is (Chaudhary et al., 2015; Idris et al., 2017, Bignalet-Cazalet et al., 2020; Sinurata et al., 2021). The traditional retrackers for processing the ocean waveform, neither model-based nor empirical, sometimes fail to retrack the waveform or misestimate parameters in coastal regions due to the severe noise in the coastal waveform. In order to depress the noise, approaches based on the subwaveform containing the leading edge are widely used (Hwang et al., 2006; Guo et al., 2010; Yang L. et al., 2012; Idris and Deng, 2012; Passaro et al., 2018). However, it is not easy to accurately extract the subwaveform since the partitioning of the waveform is inevitably disturbed by the signal from non-ocean surfaces (Yang Y. et al., 2012; Huang et al., 2017; Wang and Ichikawa, 2017). In the coastal zone, a large portion of altimetric waveforms are corrupted by peaks caused by bright targets inside the illustrated area. These peaks may lead to overestimation of the amplitude of the waveform. For these peaky waveforms, some hybrid models were introduced to refine parameter estimation, e.g., the Brown with Gaussian peak model (Halimi et al., 2013). Another strategy is removing anomalous peaks before retracking (Peng and Deng, 2018). Based on the stack of successive along-track waveforms (referred to as echogram or radar-gram), parabola traces can be observed at the trailing edge area, which are corresponding to the signals of bright targets within the altimeter footprint (Gomez-Enri et al., 2010). The parabolic feature can be applied to remove the peaky-type noise at the trailing edge caused by fixed-point bright targets (Wang and Ichikawa, 2017). In a more ordinary way, noise superimposed on the waveform can be suppressed using empirical methods. A waveform modifying procedure based on a preset criterion was proposed to mitigate anomalous peaks in coastal waveforms (0.5–7 km from coasts) (Tseng et al., 2014). This procedure was further improved by Huang et al. (2017). Abovementioned studies have consolidated a concept that cleaning the waveform prior to retracking can contribute greatly to retrieving more accurate data closer to the coast.

The purpose of this article is to upgrade the waveform decontamination technique and ascertain its effect on improving coastal altimetric data. It has been pointed out that the criteria for selecting reference waveforms and identifying outliers are still open research questions (Huang et al., 2017). In this study, an optimized algorithm for waveform decontamination is presented based on realigned waveforms. More sophisticated criteria are adopted in the new algorithm. The upgraded decontaminating technique will be more stable and robust, especially for waveforms at the last few kilometers to coasts.

DATA AND STUDY AREA

Jason-2 Sensor Geophysical Data Record (SGDR)

The altimetry satellite Jason-2 was launched on June 20, 2008. The main objective of Jason-2 is to measure ocean surface ensuring the continuity of the TOPEX/Poseidon and Jason-1 missions. Due to the improvements in the echo acquisition and tracking modes, the Poseidon-3 altimeter onboard Jason-2 maintained significantly higher data availability over land or mixed land-sea terrain in comparison with its predecessor Poseidon-2 onboard Jason-1 (Desjonquères et al., 2010). It guaranteed an additional goal of Jason-2, which is to provide measurements over coastal areas and inland waters.

For retracking, SGDR product should be used. The Jason-2 SGDR products (version d) are downloaded from Archiving, Validation, and Interpretation of Satellite Oceanography (AVISO, https://www.aviso.altimetry.fr). The dataset provides 1 and 20Hz sampling values. Waveforms contained in the dataset allow customized retracking for refining measurements. The dataset provides four kinds of ranges derived using different retracking strategies. One is the onboard operating tracker (hereafter referred to as "Raw"). The other three retrackers are MLE4 (4-parameter Maximum Likelihood Estimator), MLE3 (3-parameter), and ICE, respectively (Dumont et al., 2017).

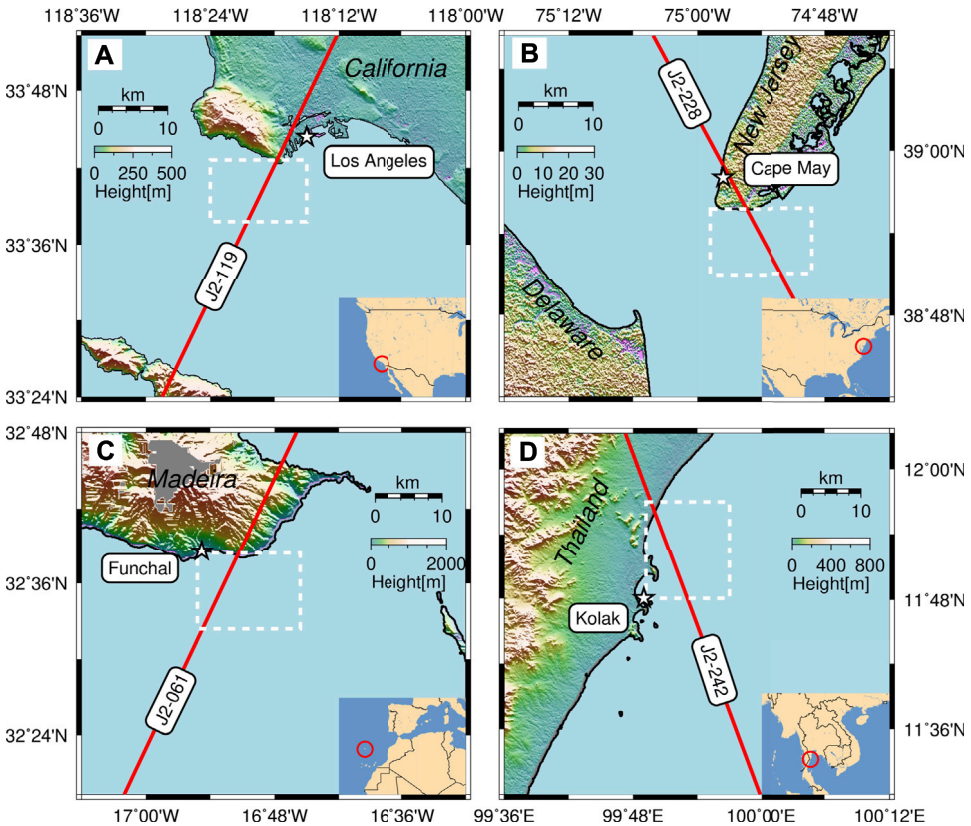

FIGURE 1 | Four areas for validation near tide gauge stations: **(A)** Los Angeles, California, United States; **(B)** Cape May, New Jersey, United States; **(C)** Funchal, Maderia Island, Portugal; **(D)** Ko Lak, Thailand. The red line denotes ground track of Jason-2. The white pentacle shows the position of tide gauge. The rectangle with white dashed line sketches the test area.

Coastal and Hydrology Altimetry (PISTACH) Products

The PISTACH products were developed by Collecte Localization Satellites (CLS) with support from CNES. PISTACH is dedicated to refining Jason-2 data over coastal regions and inland waters for coastal and hydrological applications. For this purpose, several new retracking algorithms were developed. A set of four alternative retracked ranges are provided in the PISTACH products. The four retrackers are ICE1, ICE3, RED3, and OCE3, respectively. Furthermore, the PISTACH products include several state-of-the-art geophysical corrections, e.g., wet tropospheric corrections and sea state bias corrections. More details about these retrackers are available in the PISTACH handbook (Mercier et al., 2010). These products can be accessed via AVISO ftp (ftp://ftp-access.aviso.altimetry.fr/pub/oceano/pistach).

ALES Dataset

The ALES Jason-2 dataset was produced by DGFI-TUM (Deutsches Geodätisches Forschungsinstitut Technische Universität München) and distributed via Open Altimeter Database (OpenADB, https://www.openadb.dgfi.tum.de). This dataset was a reprocessed product using the ALES retracker. This retracker selects part of each waveform by adapting its width according to the significant wave height and models the subwaveform with the classic Brown model by means of least square estimation (Passaro et al., 2014). A number of studied have validated that ALES has good performance over coastal areas (Passaro et al., 2014; Xu et al., 2018; Gómez-Enri et al., 2019; Birol et al., 2021). As well as PISTACH, the ALES product is used as a reference to evaluate the performance of the new retracking scheme proposed in this work.

Tide Gauge Data

Sea level measured by tide gauge is usually used to validate the altimeter-derived sea surface heights (SSHs). Tide gauge data used in this study are the Research Quality Data (RQD) at hourly resolution, achieved by UHSLC (University of Hawaii Sea Level Center) (Caldwell et al., 2015). The RQD is a final science-ready dataset with quality control, which can be downloaded from the ftp sever of UHSLC (ftp://ftp.soest.hawaii.edu/uhslc/rqds). Four stations equipped with float gauge were used for validation. The four stations are located at Los Angeles (United States), Cape May (United States), Funchal (Madeira Island), and Ko Lak (Thailand), respectively. The float gauge has an accuracy of several millimeters. Thus, the tide gauge data are preferred for validating altimeter-derived SSHs. However, each tide station has

TABLE 1 | General information of study areas.

Study area		Los Angeles	Cape May	Funchal	Ko Lak
Gauge information	Station location	118.27°W, 33.72°N	74.96°W, 38.97N	16.91°W, 32.64°N	99.82°E, 11.80°N
	Nearest distance to the track (km)	7.0	7.3	6.8	4.8
	Last date of gauge data	Dec 31, 2014	Dec 31, 2014	Dec 31, 2013	Dec 31, 2015
Satellite ground track		119, ascending	228, descending	061, ascending	242, descending
Bathymetry within 10 km offshore (m)		0–660	0–12	0–2200	0–23
Waveform class	Brown	70.3%	83.3%	86.7%	55.5%
	Brown + noise	19.9%	15.1%	8.9%	37.3%
	Peak	2.4%	0	2.4%	3.8%
	Peak + noise	6.2%	1.4%	1.9%	1.8%

a unique local datum, and datum information of some stations are not given. Therefore, relative validation is frequently conducted by removing their mean values.

Study Areas

Figure 1 shows four test areas chosen to validate the upgraded strategy, which are same as those in Huang et al. (2017). One Jason-2 pass (red line) accompanied by a tide gauge station (white pentacle) nearby is used for each case. Cycle 1-252 altimeter data were used in this study. In each area, the coastal topography and ocean floor are very different from each other, representing different sea state and surface reflectivity. General information of these regions are tabulated in **Table 1**. In Los Angeles, the coastal topography is a 500 m high mountain. The along-track bathymetry within 10 km offshore varies from 0 to 600 m, which has a sharp slope within 4–6 km. The terrain in Cape May is very flat and low altitude and ocean water is very shallow. While the third case is near Madeira Island, where the coast is very steep and the bathymetry sharply drops by 2000 m within 4 km. In the last case, the coast terrain is smooth and water depth is shallow. However, the satellite track is very close to the coastline, which induces a great amount of noise in altimeter waveforms. According to the classification of waveforms in PISTACH, percentages of each waveform class within 20 km offshore are listed in **Table 1**. It clearly shows that serious waveform contamination occurred in each case, especially in the Ko Lak region.

MATERIALS AND METHODS

In this section, we will introduce our new strategy for retrieving coastal SSHs based on the decontamination technique. Compared with the previous method, two significant improvements were made in the new strategy. Firstly, we proposed an algorithm to realign waveforms in the echogram before outlier detection, aiming to moderate the influence of shifting of the leading edge. Secondly, we substituted the single criterion in the old method with the gate-wise criteria for outlier detection in each echogram.

Sea Surface Height

SSH is the height of sea surface with respect to the reference ellipsoid. By altimetry, SSH can be determined by subtracting altimeter range from the altitude of the satellite. Ranges measured by the altimeter must be corrected for instrument effects, path delay in the atmosphere, and the nature of the reflecting sea surface. The resultant SSH is given by

$$h = Alt - \left(R + \Delta R_{instr} + \Delta R_{atmos} + \Delta R_{ssb} + \Delta R_{dyn} + \Delta R_{retrack}\right), \quad (1)$$

where h is the altimetry-derived SSH, Alt is the orbit altitude of the satellite, R is the altimeter range, and ΔR represents corrections for the range. The subscripts "instr," "atmos," and "ssb" indicate instrumental corrections, atmospheric corrections, and sea state bias (SSB) corrections, respectively. ΔRdyn is the correction for the dynamic response to atmospheric pressure. The last item ΔRretrack is an optional correction, which is applied only when retracking is implemented.

In general, instrumental corrections consist of the distance offset between antenna and center of gravity, USO (Ultra Stable Oscillator) frequency drift correction, internal path correction, Doppler correction, modeled instrumental errors correction, and system bias. For the Jason-2 SGDR products, all retracked ranges have been corrected for all instrumental corrections. It is noteworthy that the last three corrections are not included in raw ranges. They should be additionally counted if one makes use of the raw ranges or implements customized retracking processing. Atmospheric corrections consist of wet troposphere correction, dry troposphere correction, and ionosphere correction. Model-derived atmospheric corrections in SGDR are used in this study. The SSB and dynamic atmosphere corrections used in the study are retrieved from the PISTACH product, which is suggested in the previous study (Huang et al., 2017).

Waveform Decontamination and Retracking

The main idea of waveform decontamination is identifying and amending anomalous samples in the waveform according to some preset criteria. The criteria have to be determined based on each echogram as no other a priori information can be available. The reference waveform, which is determined by averaging whole waveforms in the echogram, plays an important role in this procedure. It is shown that the migration of the leading edge of along-track waveforms will lead to misjudgment of contaminated gates due to improper selection of the reference waveform (Huang et al., 2017). In order

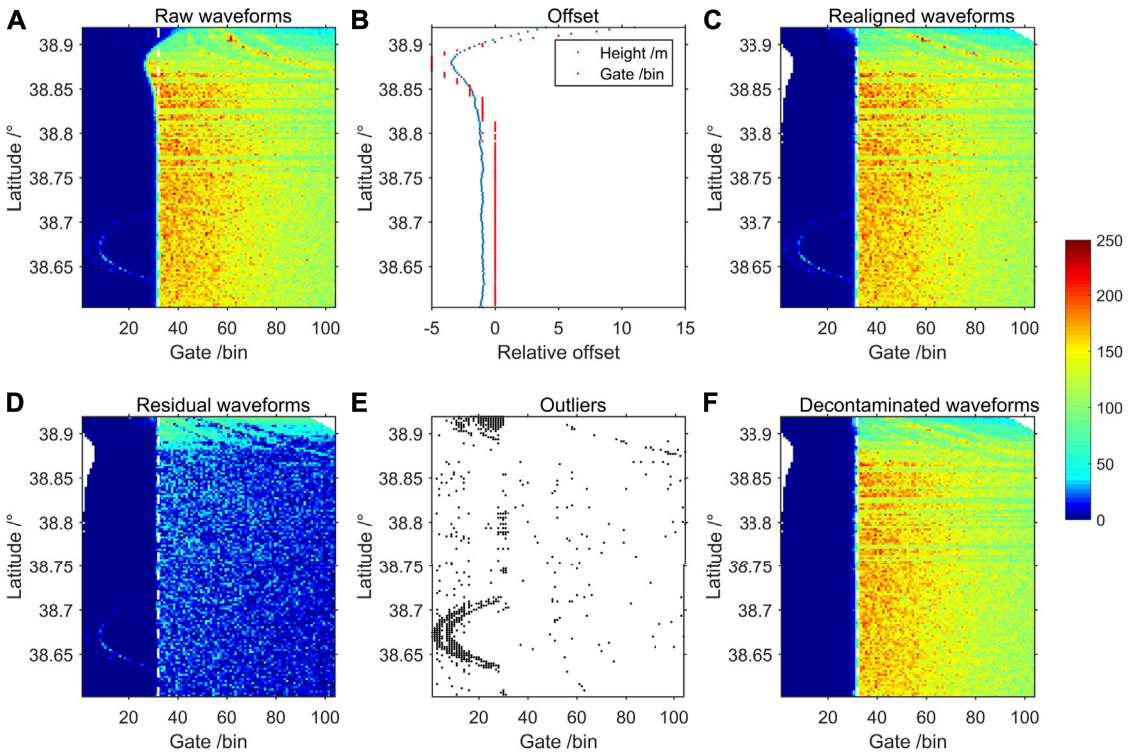

FIGURE 2 | Illustration of the waveform contamination procedure using a Jason-2 coastal track (Pass #228, cycle #225). **(A)** Raw waveforms. **(B)** Translation offsets derived from height differences. **(C)** Realigned waveforms. **(D)** Residual waveforms. **(E)** Detected outliers. **(F)** Decontaminated waveforms. The white dashed line indicates the nominal gate of Jason-2.

to reduce the effect caused by the shift of the leading edge, a method is proposed to realign waveforms in the echogram (see *Realignment of Waveforms*). In addition, new algorithms are adopted for the detection and remedy of outliers (see *Outlier Detection*).

Realignment of Waveforms

Shifts of the leading edges in the echogram can cause serious distortion of the leading edge of the reference waveform. It is better to align waveforms prior to averaging. Here, it is called realignment because the onboard tracker had tried to align the leading edges centered on a nominal gate. To do this, the offset of each waveform relative to a given waveform should be determined and then eliminated by translation along the time (or range) axis. According to the tracking principal of the altimeter, the relative offset can be estimated using the difference of surface topography by

$$\Delta G_i = \frac{\Delta h_i - \Delta N_i}{d}, \tag{2}$$

where ΔG_i is the offset of the ith waveform relative to the selected waveform (farthest to the coast in this study), Δh_i is the SSH difference derived from the raw SSHs, ΔN_i is the difference of the geoid undulations, and d is the range resolution of the altimeter (about 0.47 m for Jason-2). The offset should be rounded to the nearest whole number because waveform gates require integer values. The EGM 2008 (Pavlis et al., 2012) geoid model was used in this study. The accuracy of EGM2008 marine geoid is in centimeter level, which is much less than the range resolution of the altimeter. So, the impact of the geoid error can be ignored when estimating the relative offset.

Let the matrix $\boldsymbol{P} = \{P(i,k),\ i = 1\cdots n; k = 1\cdots 104\}$ denote raw waveforms in the echogram of a coastal track and $\overline{\boldsymbol{P}}$ denote the realigned waveforms. Each row of the matrix is a waveform; that is, the row index i is the waveform number along track and the column index k is the gate number. n is the total number of waveforms. Then, the realigned waveforms can be expressed as follows:

$$\overline{P}(i,k) = \begin{cases} P(i,k+\Delta G_i), & if\ (k+\Delta G_i) > 0\ and\ (k+\Delta G_i) \le 104 \\ null\ value, & else \end{cases}. \tag{3}$$

Figure 2 shows an example of a Jason-2 coastal track, which is a descending pass departing from the coast. Apparent shifts of the leading edges can be observed near the coast (latitude >38.8°N) in the raw waveforms (**Figure 2A**). Two parabola traces due to bright targets are notable prior to the leading edges between 38.63° and 38.7°. **Figure 2B** indicates that the height differences are closely correlated with the location of the leading edges. As observed in **Figure 2C**, shifts of the leading edges had been

efficiently reduced in the realigned waveforms based on the offsets derived from the height differences.

Outlier Detection

The realigned waveforms are averaged and used as a reference for outlier detection. The reference waveform P_{ref} for each track can be defined as follows:

$$P_{ref}(k) = \frac{1}{n}\sum_{i=1}^{n}\overline{P}(i,k). \tag{4}$$

Subtracting the reference waveform from the realigned waveforms, residuals can be derived as follows:

$$\boldsymbol{\Delta P(i,k)} = \left|\boldsymbol{\overline{P}(i,k)} - \boldsymbol{P_{ref}(k)}\right|. \tag{5}$$

Based on the residuals, the root mean square (RMS) for each gate is calculated as follows:

$$\boldsymbol{\sigma_k} = \sqrt{\frac{\sum_{i=1}^{n}\boldsymbol{\Delta P^2(i,k)}}{\boldsymbol{n-1}}}. \tag{6}$$

Pixels in the echogram are tested using the gate-wise criterion given in **Eq. 7**. If the residual on a pixel exceeds twice RMS, this pixel will be regarded as an outlier and set to a null value.

$$\Delta P(i,k) > 2\sigma_k. \tag{7}$$

Amending Outlier

Outliers are necessary to be amended before retracking. This procedure is implemented by interpolation. In the previous work (Tseng et al., 2014), a 2D linear interpolation from neighboring pixels was applied to amend outliers, which is actually a weighted mean method. Inevitably, interpolation might induce errors especially when neighboring samples are noisy. An alternative method that outliers are directly set to null value was proposed in order to avoid interpolation error (Huang et al., 2017). However, null values potentially affect parameter estimation during retracking when they appear within or near the leading edge of a waveform. Therefore, interpolation is still performed in this study but using a different method. If $\overline{P}(i,k)$ is identified as an outlier, it will be fixed using the mean value of its available neighbors or substituted directly by the value at the same gate in the reference waveform.

Figures 2D–F illustrate the efficiency of algorithms for detecting and amending outliers. Two parabola signals at the thermal noise stage and anomalous peaks in the trailing edge area were successfully identified and fixed.

Retracking Methods

Three retrackers were applied on the decontaminated waveforms. The three retrackers are 20% threshold retracker (TR20), 50% threshold retracker (TR50), and ICE1 retracker. For these retrackers, the retracked gate (also named as Epoch) can be computed using a uniform equation as follows:

$$G_i^r = G_i^{k-1} + \frac{T_i - \overline{P}(i,k-1)}{\overline{P}(i,k) - \overline{P}(i,k-1)} \cdot \left(G_i^k - G_i^{k-1}\right), \tag{8}$$

where G is the gate number, the subscript i denotes the ith waveform, the superscript r represents the retracked gate, and k is the first gate with power exceeding the threshold value T_i. The threshold value for different retrackers can be determined using

$$T_i = T_i^0 + th \cdot \left(A_i - T_i^0\right), \tag{9}$$

where T_i^0 is the thermal noise of each waveform, th is the threshold which equals to 20%, 50%, and 30% for TR20, TR50, and ICE1, respectively. A_i is the maximum waveform amplitude for TR20 and TR50 or the OCOG (Offset Center of Gravity) amplitude fot ICE1.

Since the emphasis of this study is to improve coastal SSHs, only the parameter for range correction was estimated in the retracking procedure. Finally, the retracking correction was derived by

$$\Delta R_{retrack,i} = \left(G_i^r + \Delta G_i - G_0\right) * d, \tag{10}$$

in which G_0 is the nominal gate number of the onboard tracking system. For comparison, raw waveforms were also retracked using the same retrackers. In this case, P substitutes for $\overline{P}$ in **Eq. 8** and the offset ΔG_i should be ignored in **Eq. 10**.

VALIDATION RESULTS AND DISCUSSION

For the convenience of illustration, we used the abbreviation "RW" for the raw waveform, "DW" for the decontaminated waveform by the new method developed in this article, and "MW" for the modified waveform by the previous approach given by Huang et al. (2017). Three kinds of waveforms were retracked using TR20, TR50, and ICE1, respectively. Adding retrackers provided in SGDR, ALES, and PISTACH, 16 retrackers were involved for comparison in total.

Evaluating the Variability of Along-Track SSHs

The internal variability in each cycle of the along-track SSHs with respect to the geoid can reflect the performance of various retrackers. Standard deviations (SD) of the differences between the retracked SSHs and the geoid are frequently employed to evaluate the variability (Hwang et al., 2006; Lee et al., 2010). Meanwhile, data availability is an important consideration. Generally, a good retracker should be capable to retrieve more valid data with the smaller SD. We hence introduced the ratio of the percentage of valid measurements to SD as an evaluation index (Wang et al., 2019), which is expressed as

$$PSR_i = \frac{p_i}{\sigma_i}, \tag{11}$$

where p_i is the percentage of valid measurements after retracking and the calibration procedure (a 3σ de-outlier process), σ_i is the SD (in meter) of the differences between the retracked SSHs and the geoid, and PSR_i is the ratio for each cycle. Statistical results of the tests in four regions are presented graphically in **Figure 3**. The left panels show the SDs in all cycles for each retracker in 0–10 km

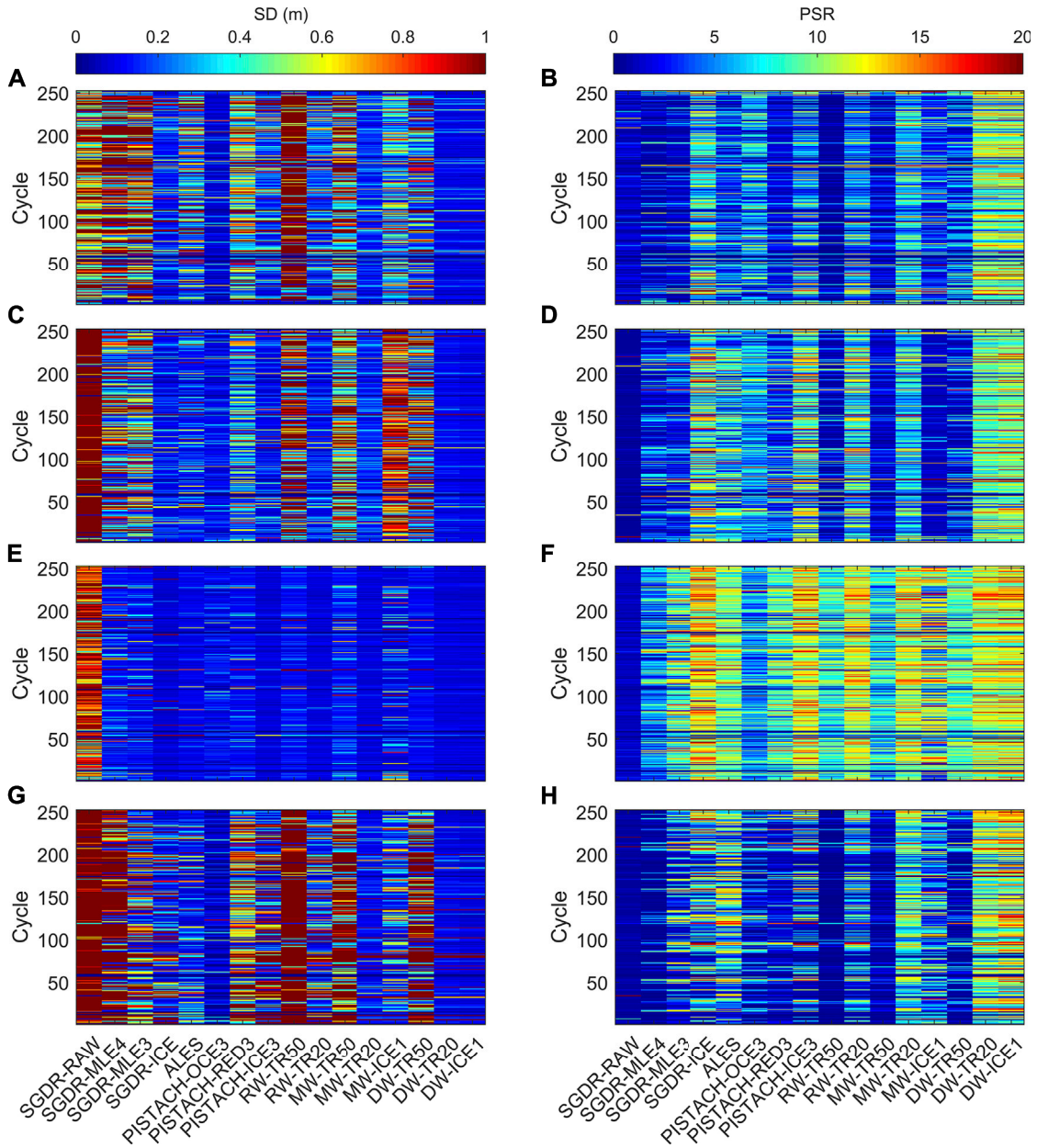

FIGURE 3 | Performance comparison of various retrackers in terms of SD **(left)** and PSR **(right)** in 0–10 km zone for each case: **(A)**–**(B)** Pass 119 near Los Angeles; **(C)**–**(D)** Pass 228 near Cape May; **(E)**–**(F)** Pass 61 near Funchal; **(G)**–**(H)** Pass 242 near Ko Lak.

zone. Corresponding PSRs are illustrated in the right panels. **Table 2** summarizes the mean values of these evaluation indices. The best performing retracker in each case is highlighted in bold.

Obviously, the nonretracked (SGDR-RAW) SSHs are of poor quality, which is a common sense in coastal altimetry community. The Brown model-based retrackers, such as MLE4 and MLE3, do not perform well because they are developed for "clean" ocean waveforms. As observed in **Figure 3**, the SDs of ICE retracker are much smaller than those of other retrackers in SGDR, and its corresponding PSRs are relatively high indicating good data availability in the coastal area. These results are consistent with those reported previous studies (Kuo et al., 2012; Tseng et al., 2014; Huang et al., 2017). Validation at Ko Lak tide gauge station performed by Idris et al. (2020) also indicated that the ICE retracker is the best in the SGDR data. Compared with SGDR-ICE, PISTACH retrackers do not seem to bring significant improvement as expected. Although OCE3 achieves good accuracy, its percentage of valid measurements is very low. ICE3 and RED3 are also not as good as ICE1 in the four test areas. On average, ALES outperforms SGDR and PISTACH.

Threshold retrackers with different threshold levels are applied to RWs, MWs, and DWs separately. TR20 achieved much better results than TR50, implying that 20% threshold level is more suitable for

TABLE 2 | Average indices of various retracked along-track SSHs in 0–10 km zone for each case.

Product-retracker	Pass 119				Pass 228			
	SD (cm)	Valid data (%)	PSR	Invalid cycles	SD (cm)	Valid data (%)	PSR	Invalid cycles
SGDR-RAW	95	99	1.0	1	193	99	0.5	1
SGDR-MLE4	106	78	0.7	2	64	85	1.3	3
SGDR-MLE3	102	97	1.0	5	57	98	1.7	2
SGDR-ICE	21	96	4.7	5	15	97	6.6	2
ALES	46	95	2.1	5	21	95	4.6	4
PISTACH-OCE3	9	42	4.5	14	13	59	4.7	5
PISTACH-RED3	63	92	1.5	7	33	92	2.8	3
PISTACH-ICE3	34	94	2.8	10	16	96	6.1	5
RW-TR50	230	97	0.4	2	143	96	0.7	4
RW-TR20	28	95	3.3	8	16	97	6.0	3
MW-TR50	94	97	1.0	5	94	95	1.0	7
MW-TR20	18	98	5.5	1	17	97	5.7	2
MW-ICE1	38	97	2.6	1	79	98	1.2	1
DW-TR50	55	95	1.7	7	88	95	1.1	7
DW-TR20	**12**	**99**	**8.2**	**1**	12	98	8.2	2
DW-ICE1	12	98	8.1	2	**11**	**98**	**9.1**	**2**

Product-retracker	Pass 061				Pass 242			
	SD (cm)	Valid data (%)	PSR	Invalid cycles	SD (cm)	Valid data (%)	PSR	Invalid cycles
SGDR-RAW	94	100	1.1	0	188	100	0.5	0
SGDR-MLE4	18	68	3.8	7	126	54	0.4	2
SGDR-MLE3	14	96	6.6	7	60	97	1.6	4
SGDR-ICE	9	97	11.0	6	52	95	1.8	7
ALES	11	97	9.0	6	22	95	4.3	6
PISTACH-OCE3	12	58	4.7	7	10	24	2.4	78
PISTACH-RED3	13	97	7.4	6	72	84	1.2	9
PISTACH-ICE3	9	99	11.4	1	95	96	1.0	3
RW-TR50	14	98	6.9	4	289	99	0.3	0
RW-TR20	9	99	10.9	1	59	95	1.6	8
MW-TR50	17	98	5.8	4	189	99	0.5	0
MW-TR20	9	99	10.6	1	17	94	5.4	12
MW-ICE1	16	96	6.0	6	32	93	2.9	11
DW-TR50	12	98	8.2	4	172	99	0.6	0
DW-TR20	**9**	**100**	**11.0**	**0**	15	96	6.3	9
DW-ICE1	**9**	**99**	**11.3**	**0**	**14**	**96**	**6.7**	**8**

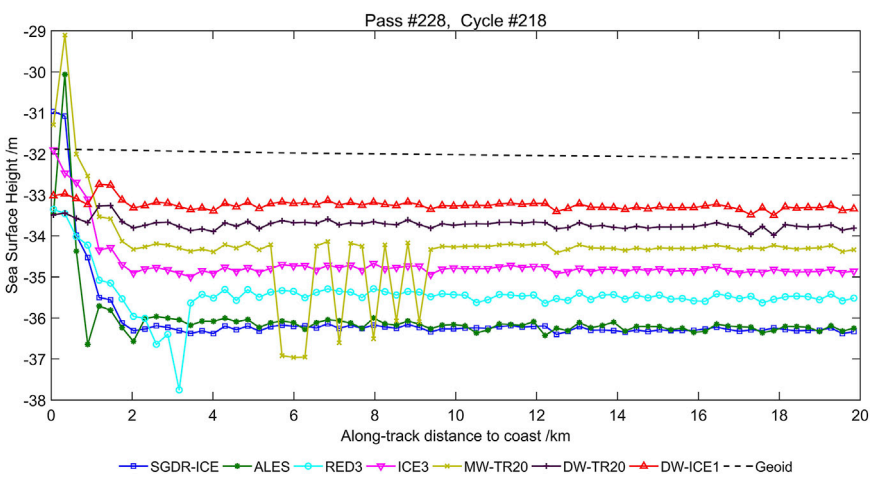

FIGURE 4 | Along-track sea surface heights retrieved by various retrackers. Arbitrary constants were added to the result of each retracker for visual clarity.

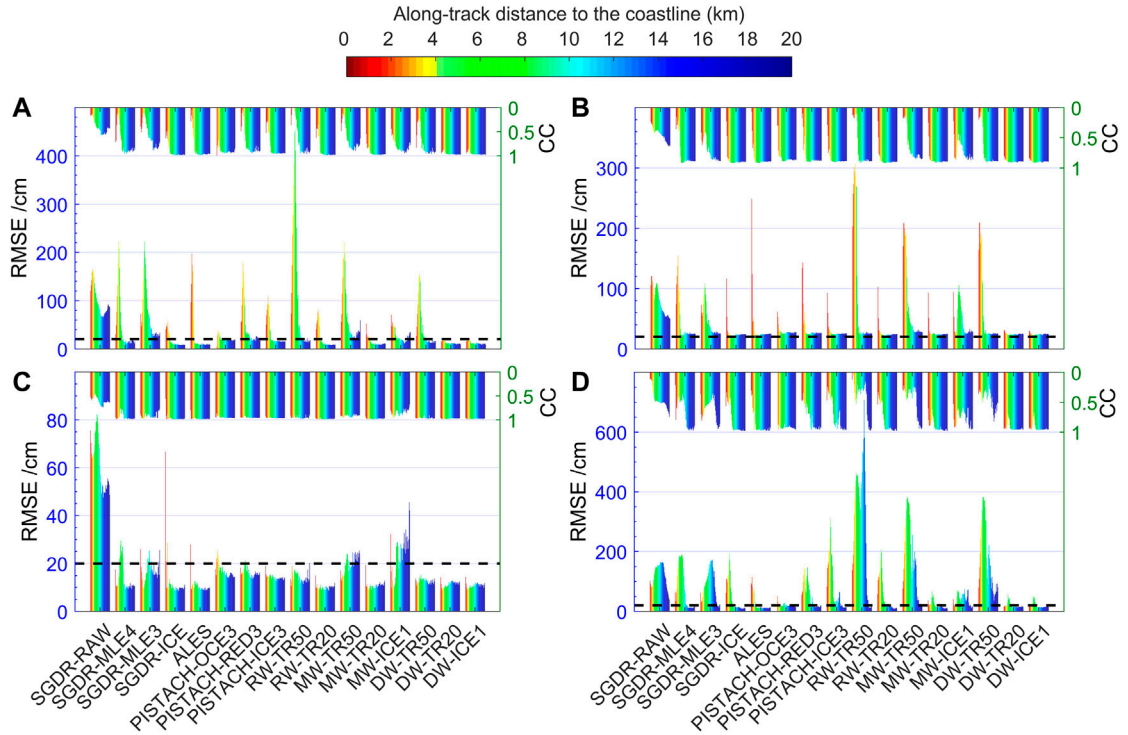

FIGURE 5 | RMSE and correlation coefficients (CCs) of retracked SSH time series within 20 km offshore w.r.t. tide gauge data in each test area. **(A)** Los Angeles; **(B)** Cape May; **(C)** Funchal; **(D)** Ko Lak. The color of the bar changes from red to blue, indicating along-track distance to the coastline rising from 0 to 20 km. The black dashed line denotes the accuracy level of 20 cm.

retrieval of coastal data. It is reasonable because peaky noise extensively appearing in coastal waveforms may lead TR50 to overestimate the epoch. On the other hand, it can be seen in **Figure 3** and **Table 2** that the performance of the same retrackers when applying to DWs is apparently superior to that when applying to RWs and MWs. Among 16 retrackers, furthermore, DW-TR20 and DW-ICE1 got the largest PSR values, as well as the smallest SDs in all cases. The results show a strike effect of our upgraded decontamination algorithm on refining the coastal SSHs.

To explore how close to the shore valid SSH data retrieved by each retracker can reach to, we plotted along-track SSHs along with the EGM2008 geoid for all tracks used in this study and made a movie for each region for easy scanning. **Figure 4** presents a plot as an example. Only the SSHs by seven retrackers with relatively high accuracy were illustrated in the plot, and arbitrary constants were added to each result for visual clarity. It shows that the DW-TR20 and DW_ICE1 retrackers can stably retrieve valid SSHs in the last 1 km stripe, while the other retrackers become unstable in 0–4 km zone. It is notable that some biased values appear in the SSHs by MW-TR20 at about 6–9 km. It might be attributable to null values in waveforms set by the old version of the decontamination algorithm (Huang et al., 2017).

Validation With Gauge Data

Tide gauge provides independent sea level observations to validate altimeter-derived SSHs. In order to compare with *in situ* sea level, tidal corrections were excluded from the SSHs. Since tide gauge stations do not locate on the satellite track, geoid gradient corrections were applied to the SSHs. To avoid possible datum bias between altimeter measurements and gauge data, the mean value of each time series was subtracted. The RMSE value was calculated to show the mean error of retracked results compared with gauge data. Correlation coefficients (CCs) between altimeter-derived SSHs and gauge data were also computed. Statistical results within 0–20 km zone offshore for each retracker in the four test regions are demonstrated in **Figure 5**. In each panel, bars at the bottom represent RMSE values and CCs are illustrated as waterfalls on the top. The color denotes along-track distance to the coastline, changing from red to blue corresponding to the increase in distance from 0 to 20 km.

Figure 5 visually depicts that the accuracy of the altimeter-derived SSHs decreases when approaching to the coast. In 10–20 km coastal zone, most retrackers perform well keeping the RMSE value below 20 cm and CC higher than 0.9. However, within 10 km, the RMSE increases rapidly and the correlation decreases correspondingly. Remarkably, two retrackers (DW-TR20 and DW-ICE1) developed in this study show very robust performance. The two retrackers can consistently yield small RMSEs in 0–20 km coastal zone. Overall, the performance of various retrackers revealed in **Figure 5** agrees well with the evaluation results in *Evaluating the Variability of Along-Track SSHs*.

Figure 6 presents an example of SSH time series within 20 km offshore near Ko Lak gauge station by several selected retrackers, which have relatively good performance in the coastal area. It is obvious that the results based on retracking denoised waveforms are

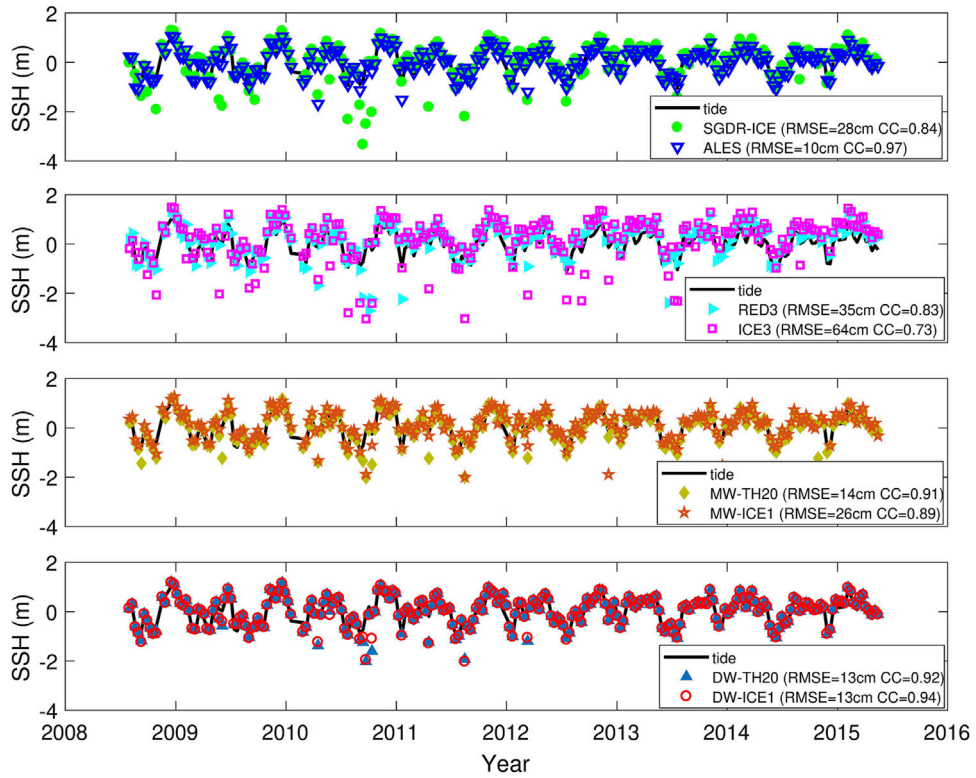

FIGURE 6 | Coastal (0–20 km) SSH time series derived by selected retrackers near Ko Lak gauge station (Pass 242). Mean value of each time series is removed to avoid possible bias.

TABLE 3 | Statistical results of retracked SSHs in 0–4 km zone offshore compared with gauge data.

Retracker	Pass 119			Pass 228			Pass 61			Pass 242		
	RMSE (cm)	CC	IMP (%)	RMSE (cm)	CC	IMP (%)	RMSE (cm)	CC	IMP (%)	RMSE (cm)	CC	IMP (%)
SGDR-RAW	138	0.20	–	96	0.35	–	62	0.55	–	76	0.26	–
SGDR-MLE4	186	0.13	–34.5	97	0.34	–0.7	13	0.97	79.2	150	0.39	–96.8
SGDR-MLE3	95	0.27	31.5	56	0.62	41.4	11	0.98	83.0	45	0.76	40.3
SGDR-ICE	34	0.67	75.4	31	0.81	67.7	9	0.87	85.7	89	0.58	–17.3
ALES	57	0.57	58.4	32	0.83	67.2	**7**	**0.99**	**88.4**	28	0.87	62.5
PISTACH-OCE3	33	0.81	75.8	29	0.83	70.1	21	0.92	66.6	18	0.91	76.7
PISTACH-RED3	80	0.35	42.2	43	0.66	55.7	15	0.96	76.4	59	0.68	21.9
PISTACH-ICE3	51	0.43	63.1	34	0.79	64.1	14	0.96	77.1	145	0.48	–90.6
RW-H50	209	–0.01	–51.7	207	0.15	–116.1	13	0.94	79.5	219	0.35	–188.0
RW-TH20	46	0.59	66.5	31	0.81	67.6	8	0.99	87.0	101	0.57	–32.4
MW-TH50	128	0.21	7.0	140	0.20	–46.0	10	0.95	83.7	166	0.42	–118.9
MW-TH20	24	0.88	82.9	30	0.83	68.5	8	0.98	86.7	20	0.93	73.9
MW-ICE1	38	0.72	72.4	34	0.78	64.4	12	0.91	80.3	19	0.90	74.9
DW-TH50	84	0.33	39.2	136	0.20	–41.9	9	0.98	85.6	172	0.46	–125.8
DW-TH20	16	0.94	88.5	26	0.89	73.2	8	0.99	87.2	15	0.96	80.4
DW-ICE1	**15**	**0.93**	**89.3**	**24**	**0.90**	**74.6**	**8**	**0.99**	**87.3**	**13**	**0.97**	**82.9**

better than those based on retracking raw waveforms. Comparing results of MW-ICE1 and DW-ICE1, we can conclude that the upgraded decontamination strategy made a great improvement. In this case, ALES achieved the smallest RMSE. The reason is due to the good efficacy of ALES in the zone beyond 7-8 km offshore. Enough high accuracy measurements in the farther zone can help to reject crude measurements in the very near coastal area by the de-outlier process during constructing the

SSH time series. However, the efficiency of ALES dramatically declines within 8 km (Huang et al., 2017; Wang and Ichikawa, 2017), which can also be verified by results in **Figure 5** and **Table 2**.

Focusing on the last several kilometers, we compared the performance of various retrackers within 4 km. The improvement percentage (IMP) was computed to assess the improvement over the nonretracked SSHs (Hwang et al., 2006). Statistical results are given in **Table 3**. We can observe that most retrackers yield large RMSE and small CC except DW-TR20 and DW-ICE1. On rare occasion, ALES has the minimum RMSE of 7 cm in the third case (Pass 61), where the percentage of Brown and Brown-like waveforms is more than 95% (see **Table 1**). However, its performance is much poorer than that of DW-TR20 or DW-ICE1 in other cases. It implies that the ALES retracker has a good ability to handle with the Brown-like waveforms, but it is not good at processing the more complicated coastal waveforms. It makes sense because the ALES retracker is based on the Brown model (Passaro et al., 2014). Evidently, the DW-TR20 and DW-ICE1 retrackers achieve the biggest improvement in accuracy in 0–4 km zone. Their IMP values are larger than 80% in all cases. It is indicated that our technique works well not only for the Brown-like waveforms but also for the extremely distorted waveforms.

Additional Comments on the Decontamination Technique

It is ideal to minimize noise interference during waveform retracking. Traditional subwaveform technique works well in many situations by extracting the clean leading edge according to partitioning waveforms (Guo et al., 2006; Guo, et al., 2010; Idris and Deng, 2012; Yang, et al., 2012a; Passaro et al., 2014). However, this passive approach gets into trouble in near coast zone where waveforms are seriously distorted. The results in **Table 2** and **Table 3** illustrate that subwaveform-based retrackers such as ALES, RED3, and ICE3 are poor performing for the complicated waveforms. It can be attributed to the difficulty for determining the noise-free leading edge in this situation.

In another way, the decontamination technique which is developed to actively reduce noise in waveform has proved to be very effective for processing complex coastal waveforms (Tseng et al., 2014; Huang et al., 2017; Wang and Ichikawa, 2017). The core of this technique is how to locate polluted sampling gates and how to fix them. The strategy proposed in the current study is easy to implement and not time-consuming. By considering the issue of shifting of the leading edge and adopting gate-wise judging criteria, the new strategy improves the outlier detection procedure. This can be verified by comparing MW- and DW-retrackers. However, there is still no other sophisticated method for amending outliers except interpolation from neighbors. Furthermore, rounding off the offset derived by **Eq. 2** during realignment might induce alignment error in individual cases, which may influence subsequent denoising. Small jaggies might appear in the along-track SSHs in this case, e.g., at 18 km in **Figure 4**. This effect can be eliminated by smoothing or downsampling into 1 Hz data.

CONCLUSIONS

In this article, we presented an upgraded strategy for decontaminating waveform, aiming to improve altimeter-derived coastal SSHs. The tests in four areas with four satellite passes validated the efficiency of the new strategy. Two retrackers (DW-TR20 and DW_ICE1) based on decontaminated waveforms show powerful performance to retrieve more and better coastal measurements, which will be beneficial to coastal applications such as coastal sea level change and geoid refining in oceanography, geodesy, and other fields.

Compared with the old decontamination strategy, one important improvement of the update method is the realignment of waveforms prior to decontamination. We proposed a novel alignment algorithm based on the raw SSH measurements. This improvement leads to a more reasonable reference waveform for the later outlier detection and remedy. Another improvement is that we adopted gate-based outlier judging criteria, which enable outlier detector to treat different parts of the waveform (e.g., thermal noise stage, leading edge, and trailing edge) with different criteria. These improvements make it possible to retrieve reliable SSHs in the last 1 km to the coast.

Although the decontamination strategy was validated only using Jason-2 data, it is appropriate to apply to the similar radar altimetry missions. In addition, only the threshold retracker and the ICE1 retracker were tested on the DWs in this work. It is worthy to explore the efficiency of other model-based retrackers such as MLE applied to the DWs. The combination of ALES and DW may be of great interest for future research.

It should be mentioned that the validation in this study focused on the new decontamination strategy. Refining coastal geophysical corrections such as wet troposphere correction and SSB was not considered. Different tidal effects between the tide gauge station and satellite nadirs were also not removed in the validation. Therefore, the accuracy of coastal SSHs can be further improved if these factors are taken into account.

DATA AVAILABILITY STATEMENT

The original contributions presented in the study are included in the article/Supplementary Material; further inquiries can be directed to the corresponding author.

AUTHOR CONTRIBUTIONS

HW designed the study and wrote the first draft. ZH performed the experiments and drew the pictures. All authors analyzed the data and wrote the final draft.

FUNDING

This work was sponsored by the National Natural Science Foundation of China (Grant No. 41974016), the Open Research Program of Key Laboratory of Marine Environmental Survey Technology and Application, Ministry of Natural Resources (Grant No. MESTA-

2020-A004), the CRSRI Open Research Program (Grant No. CKWV2019773/KY), and the Natural Science Foundation of Jiangxi Province (Grant No. 20202BABL214055).

ACKNOWLEDGMENTS

We would like to acknowledge AVISO providing the Jason-2 SGDR data and the PISTACH data (https://www.aviso.altimetry.fr/), UHSLC providing the tide gauge data (ftp://ftp.soest.hawaii.edu/uhslc/rqds), and DGFI-TUM providing the ALES data (https://www.openadb.dgfi.tum.de).

SUPPLEMENTARY MATERIAL

The Supplementary Material for this article can be found online at: https://www.frontiersin.org/articles/10.3389/feart.2021.748401/full#supplementary-material

REFERENCES

Bignalet-Cazalet, F., Urien, S., Picot, N., Couhert, A., Marechal, C., Desai, S., et al. (2020). Jason-3 Products Handbook, Version 2.0. CNES:SALP-MU-M-OP-16118-CN. Available at: https://www-cdn.eumetsat.int/files/2020-10/pdf_j3_prod_handbook.pdf.

Birol, F., Fuller, N., Lyard, F., Cancet, M., Niño, F., Delebecque, C., et al. (2017). Coastal Applications From Nadir Altimetry: Example of the X-TRACK Regional Products. *Advances Space Research.* 59 (4), 936–953. doi:10.1016/j.asr.2016.11.005

Birol, F., Léger, F., Passaro, M., Cazenave, A., Niño, F., Calafat, F. M., et al. (2021). The X-TRACK/ALES Multi-Mission Processing System: New Advances in Altimetry towards the Coast. *Adv. Space Res.* 67 (8), 2398–2415. doi:10.1016/j.asr.2021.01.049

Brown, G. (1977). The Average Impulse Response of a Rough Surface and its Applications. *IEEE Trans. Antennas Propagat.* 25 (1), 67–74. doi:10.1109/TAP.1977.1141536

Caldwell, P. C., Merrifield, M. A., and Thompson, P. R. (2015). *Sea Level Measured by Tide Gauges From Global Oceans — the Joint Archive for Sea Level Holdings (NCEI Accession 0019568), Version 5.5*. Dataset: NOAA National Centers for Environmental Information. doi:10.7289/V5V40S7W

Chaudhary, A., Basu, S., Kumar, R., Mahesh, C., and Sharma, R. (2015). Shape Classification of AltiKa 40-Hz Waveforms Using Linear Discriminant Analysis and Bayes Decision Rule in the Gujarat Coastal Region. *Mar. Geodesy.* 38, 62–72. doi:10.1080/01490419.2014.1001504

Cipollini, P., Calafat, F. M., Jevrejeva, S., Melet, A., and Prandi, P. (2017). Monitoring Sea Level in the Coastal Zone With Satellite Altimetry and Tide Gauges. *Surv. Geophys.* 38 (1SI), 33–57. doi:10.1007/s10712-016-9392-0

Deng, X., and Featherstone, W. E. (2006). A Coastal Retracking System for Satellite Radar Altimeter Waveforms: Application to ERS-2 Around Australia. *J. Geophys. Res.* 111 (C6), C6012. doi:10.1029/2005JC003039

Desjonquères, J. D., Carayon, G., Steunou, N., and Lambin, J. (2010). Poseidon-3 Radar Altimeter: New Modes and In-Flight Performances. *Mar. geodesy.* 33 (Suppl. 1), 53–79. doi:10.1080/01490419.2010.488970

Dumont, J. P., Rosmordue, V., Picot, N., Desai, S., Bonekamp, H., Figa, J., et al. (2017). OSTM/Jason-2 Products Handbook", Version 1.11, CNES:SALP-MU-M-OP-15815-cn. Available at: https://www.ospo.noaa.gov/Products/documents/hdbk_j2.pdf.

Fu, L. L., and Cazenave, A. (2001). *Satellite Altimetry and Earth Sciences: A Handbook of Techniques and Applications*. San Diego: Academic Press.

Gómez-Enri, J., González, C. J., Passaro, M., Vignudelli, S., Álvarez, O., Cipollini, P., et al. (2019). Wind-Induced Cross-Strait Sea Level Variability in the Strait of Gibraltar from Coastal Altimetry and *In-Situ* Measurements. *Remote Sensing Environ.* 221, 596–608. doi:10.1016/j.rse.2018.11.042

Gomez-Enri, J., Vignudelli, S., Quartly, G. D., Gommenginger, C. P., Cipollini, P., Challenor, P. G., et al. (2010). Modeling Envisat RA-2 Waveforms in the Coastal Zone: Case Study of Calm Water Contamination. *IEEE Geosci. Remote Sensing Lett.* 7 (3), 474–478. doi:10.1109/LGRS.2009.2039193

Gommenginger, C., Thibaut, P., Fenoglio-Marc, L., Quartly, G., Deng, X., Gómez-Enri, J., et al. (2011). "Retracking Altimeter Waveforms Near the Coasts," in *Coastal Altimetry*. Editors S. Vignudelli, A. Kostianoy, P. Cipollini, and J. Benveniste (Berlin: Springer), 61–101. doi:10.1007/978-3-642-12796-0_4

Guo, J., Gao, Y., Hwang, C., and Sun, J. (2010). A Multi-Subwaveform Parametric Retracker of the Radar Satellite Altimetric Waveform and Recovery of Gravity Anomalies Over Coastal Oceans. *Sci. China Earth Sci.* 53 (4), 610–616. doi:10.1007/s11430-009-0171-3

Halimi, A., Mailhes, C., Tourneret, J.-Y., Thibaut, P., and Boy, F. (2013). Parameter Estimation for Peaky Altimetric Waveforms. *IEEE Trans. Geosci. Remote Sensing.* 51 (3), 1568–1577. doi:10.1109/TGRS.2012.2205697

Huang, Z., Wang, H., Luo, Z., Shum, C., Tseng, K.-H., and Zhong, B. (2017). Improving Jason-2 Sea Surface Heights Within 10 Km Offshore by Retracking Decontaminated Waveforms. *Remote Sensing.* 9 (107710), 1077. doi:10.3390/rs9101077

Hwang, C., Guo, J., Deng, X., Hsu, H.-Y., and Liu, Y. (2006). Coastal Gravity Anomalies From Retracked Geosat/GM Altimetry: Improvement, Limitation and the Role of Airborne Gravity Data. *J. Geodesy.* 80, 204–216. doi:10.1007/s00190-006-0052-x

Idris, N., Deng, X., Md Din, A., and Idris, N. (2017). CAWRES: A Waveform Retracking Fuzzy Expert System for Optimizing Coastal Sea Levels From Jason-1 and Jason-2 Satellite Altimetry Data. *Remote Sensing.* 9 (603), 603–622. doi:10.3390/rs9060603

Idris, N. H., and Deng, X. (2012). The Retracking Technique on Multi-Peak and Quasi-Specular Waveforms for Jason-1 and Jason-2 Missions Near the Coast. *Mar. Geodesy.* 35 (Suppl. l), 217–237. doi:10.1080/01490419.2012.718679

Idris, N. H. (2020). Regional Validation of the Coastal Altimetry Waveform Retracking Expert System (CAWRES) Over the Largest Archipelago in Southeast Asian Seas. *Int. J. Remote Sensing.* 41 (15), 5680–5694. doi:10.1080/01431161.2019.1681605

Jinyum, G., Cheiway, H., Xiaotao, C., and Yuting, L. (2006). Improved Threshold Retracker for Satellite Altimeter Waveform Retracking over Coastal Sea. *Prog. Nat. Sci.* 16 (7), 732–738. doi:10.1080/10020070612330061

Kuo, C.-Y., Kao, H.-C., Lee, H., Cheng, K.-C., and Lin, L.-C. (2012). Assessment of Radar Waveform Retracked Jason-2 Altimetry Sea Surface Heights Near Taiwan Coastal Ocean. *Marine Geodesy.* 35 (2), 188–197. doi:10.1080/01490419.2011.637861

Lee, H., Shum, C. K., Emery, W., Calmant, S., Deng, X., Kuo, C.-Y., et al. (2010). Validation of Jason-2 Altimeter Data by Waveform Retracking Over California Coastal Ocean. *Mar. Geodesy.* 33 (Suppl. l), 304–316. doi:10.1080/01490419.2010.488982

Mercier, F., Rosmorduc, V., Carrere, L., and Thibaut, P. (2010). "Coastal and Hydrology Altimetry Product (PISTACH) Handbook", Version 1.0, CNES: CLS-DOS-NT-10-246. Available at: https://www.aviso.altimetry.fr/fileadmin/documents/data/tools/hdbk_Pistach.pdf.

Passaro, M., Cipollini, P., Vignudelli, S., Quartly, G. D., and Snaith, H. M. (2014). ALES: A Multi-Mission Adaptive SubwaveForm Retracker for Coastal and Open Ocean Altimetry. *Remote Sensing Environment.* 145, 173–189. doi:10.1016/j.rse.2014.02.008

Passaro, M., Rose, S. K., Andersen, O. B., Boergens, E., Calafat, F. M., Dettmering, D., et al. (2018). ALES+: Adapting a Homogenous Ocean Retracker for Satellite Altimetry to Sea Ice Leads, Coastal and Inland Waters. *Remote Sensing Environment.* 211, 456–471. doi:10.1016/j.rse.2018.02.074

Pavlis, N. K., Holmes, S. A., Kenyon, S. C., and Factor, J. K. (2012). The Development and Evaluation of the Earth Gravitational Model 2008 (EGM2008). *J. Geophys. Res.* 117, a–n. doi:10.1029/2011JB008916

Peng, F., and Deng, X. (2018). A New Retracking Technique for Brown Peaky Altimetric Waveforms. *Mar. Geodesy.* 41 (2), 99–125. doi:10.1080/01490419.2017.1381656

Sinurata, M. E., Nababan, B., Gaol, J. L., Manik, H. M., and Idris, N. H. (2021). Waveform classification and retracking of Jason-2 and Jason-3 in Halmahera Sea. *Jurnal Teknologi* 83, 107–117. doi:10.11113/jurnalteknologi.v83.15125

Stammer, D., and Cazenave, A. (2017). *Satellite Altimetry over Oceans and Land Surfaces*. Boca Raton: CRC Press.

Tseng, K.-H., Shum, C. K., Yi, Y., Emery, W. J., Kuo, C.-Y., Lee, H., et al. (2014). The Improved Retrieval of Coastal Sea Surface Heights by Retracking Modified Radar Altimetry Waveforms. *IEEE Trans. Geosci. Remote Sensing.* 52 (2), 991–1001. doi:10.1109/TGRS.2013.2246572

Valladeau, G., Thibaut, P., Picard, B., Poisson, J. C., Tran, N., Picot, N., et al. (2015). Using SARAL/AltiKa to Improve Ka-Band Altimeter Measurements for Coastal Zones, Hydrology and Ice: The PEACHI Prototype. *Marine Geodesy*. 38 (SI), 124–142. doi:10.1080/01490419.2015.1020176

Vignudelli, S., Birol, F., Benveniste, J., Fu, L.-L., Picot, N., Raynal, M., et al. (2019). Satellite Altimetry Measurements of Sea Level in the Coastal Zone. *Surv. Geophys.* 40 (6), 1319–1349. doi:10.1007/s10712-019-09569-1

Vignudelli, S., Kostianoy, A. G., Cipollini, P., and Jerome, B. (2011). *Coastal Altimetry*. Berlin: Springer.

Wang, H., Chu, Y., Huang, Z., Hwang, C., and Chao, N. (2019). Robust, Long-Term Lake Level Change From Multiple Satellite Altimeters in Tibet: Observing the Rapid Rise of Ngangzi Co over a New Wetland. *Remote Sensing.* 11 (5), 558. doi:10.3390/rs11050558

Wang, X., and Ichikawa, K. (2017). Coastal Waveform Retracking for Jason-2 Altimeter Data Based on Along-Track Echograms Around the Tsushima Islands in Japan. *Remote Sensing.* 9 (7), 762. doi:10.3390/rs9070762

Xu, X.-Y., Birol, F., and Cazenave, A. (2018). Addendum: Xu, X.-Y. et al. Evaluation of Coastal Sea Level Offshore Hong Kong From Jason-2 Altimetry. Remote Sens. 2018, 10, 282. *Remote Sensing.* 10 (7), 1059. doi:10.3390/rs10071059

Yang, L., Lin, M., Liu, Q., and Pan, D. (2012a). A Coastal Altimetry Retracking Strategy Based on Waveform Classification and Sub-Waveform Extraction. *Int. J. Remote Sensing.* 33 (24), 7806–7819. doi:10.1080/01431161.2012.701350

Yang, Y., Hwang, C., Hsu, H.-J., Dongchen, E., and Wang, H. (2012b). A Subwaveform Threshold Retracker for ERS-1 Altimetry: A Case Study in the Antarctic Ocean. *Comput. Geosciences.* 41, 88–98. doi:10.1016/j.cageo.2011.08.017

Conflict of Interest: The authors declare that the research was conducted in the absence of any commercial or financial relationships that could be construed as a potential conflict of interest.

frontiers in Earth Science

ORIGINAL RESEARCH
published: 21 October 2021
doi: 10.3389/feart.2021.731610

Investigation of the Anisotropic Patterns in the Altimeter Backscatter Measurements Over Ocean Wave Surfaces

Xi-Yu Xu[1]*, *Ke Xu*[1], *Maofei Jiang*[1], *Bingxu Geng*[2] and *Lingwei Shi*[1]

[1]The CAS Key Laboratory of Microwave Remote Sensing, National Space Science Center, Chinese Academy of Sciences, Beijing, China, [2]The State Key Laboratory of Tropical Oceanography (LTO), South China Sea Institute of Oceanology, Chinese Academy of Sciences, Guangzhou, China

This article attempts to analyze the influence of the anisotropic effects of the ocean wave surface on SAR altimetry backscatter coefficient (Sigma-0) measurements, which has not been intensively addressed in publications. Data of Sentinel-3A, Cryosat-2, and Jason-3 altimeters allocated by the WW3 numeric wave model were analyzed, and the patterns of Sigma-0 with respect to the wave direction were acquired under ~2 m significant wave height. The ocean waves were classified into six categories, among which the moderate swell and short win-wave cases were analyzed intensively. Swell-dominated ocean surface shows less randomness than the wind-wave-dominated ocean surface. Clear and significant sinusoid trends are found in the Sigma-0 and SSB patterns of both operational modes (SAR mode and PLRM mode) of the Sentinel-3A altimeter for the moderate swell case, indicating the sensitivity of Sigma-0 and SSB measurements to the anisotropic features of the altimeter measurements. The anisotropic pattern in the Sentinel-3A PLRM Sigma-0 is somewhat counterintuitive, but the analysis of Jason-3 altimeter data would show similar results. Additionally, by comparing the anisotropic patterns of two orthogonally polarized SAR altimeters (Sentinel-3A and Cryosat-2), we could draw the conclusion that the Sigma-0 measurements are not sensitive to the polarization mode. As for the SSHA patterns, no clear sinusoid could be identified for the moderate swell. A possible explanation is that the SSB pattern may be overwhelmed in the complicated factors that can influence the SSHA pattern.

Keywords: SAR altimetry, sentinel-3A, polarization, ocean wave direction, backscatter coefficient, sea state bias (SSB), swell, wind-wave

OPEN ACCESS

Edited by:
Jinyun Guo,
Shandong University of Science and Technology, China

Reviewed by:
Lei Yang,
First Institute of Oceanography, Ministry of Natural Resources, China
Yonggang Gao,
Fuzhou University, China

***Correspondence:**
Xi-Yu Xu
xuxiyu@mirslab.cn

Specialty section:
This article was submitted to Environmental Informatics and Remote Sensing, a section of the journal Frontiers in Earth Science

Received: *27 June 2021*
Accepted: *06 September 2021*
Published: *21 October 2021*

Citation:
Xu X-Y, Xu K, Jiang M, Geng B and Shi L (2021) Investigation of the Anisotropic Patterns in the Altimeter Backscatter Measurements Over Ocean Wave Surfaces. Front. Earth Sci. 9:731610. doi: 10.3389/feart.2021.731610

INTRODUCTION

Satellite altimetry is one of the most intriguing ocean remote sensing techniques, which has provided operational products of not only the sea level but also ocean wave and wind, for decades, and has made solid contribution in the global ocean and climate study (Chelton et al., 2001; Stammer and Cazenave, 2017).

In the late 1990s, the concept of the delay-Doppler altimeter (also called the "Synthesis Aperture Radar Altimeter (SARA)" in the altimetry community later) was proposed by Raney (Raney, 1998). SARA outperforms Conventional Radar Altimetry (CRA) in many aspects: the along-track

resolution is improved by an order of magnitude, which brings advantages in sea ice and coastal and hydrologic application; the instrument height noise is reduced by roughly a half, which improves the precision of the sea level measurement over open ocean surfaces. Payloads on Cryosat-2 and Sentinel-3 satellites have successfully demonstrated the potentials of this new technique (Wingham and Francis, 2006; Donlon et al., 2012), among which the altimeter on Jason-MF (in memory of the former NASA president Michael Freilich)/Sentinel-6 satellite is the latest (Parisot et al., 2018).

Sea state bias (SSB) is currently the largest uncertainty source in the altimetry error budget with the remarkable improvements in orbit determination technology. By definition, SSB can be derived from the three-dimension backscattering field of the radar (Elfouhaily et al., 2000),

$$SSB = \frac{\iiint z\sigma^0\left(z_x, z_y, z\right)dz_x dz_y dz}{\iiint \sigma^0\left(z_x, z_y, z\right)dz_x dz_y dz}, \quad (1)$$

where x, y, z are the three axes of the local Cartesian coordinate system (usually x is the along-track direction, y is the across-track direction, and z is the upward direction), $z_x = \frac{dz}{dx}$ and $z_y = \frac{dz}{dy}$ are the local gradients in directions x and y, respectively, and σ^0 is the Sigma-0 (or the normalized radar cross section).

Even the rationale of the SSB for CRA is not sufficient enough, and no theoretical correction method can give better results than empirical ones. The studies on the SSB for SARA can only been traced back to a few years. Bellingham et al. (2016) proposed a simplified theoretic mode and analyzed some Cryosat-2 altimeter SAR mode data, but they did not find significant error due to the swell wave period (equivalent to the square root of wavelength) and wave direction for SWH<4 m. Moreau et al. (2018a, 2018b) analyzed the noise level of SWH and range measurements of Cryosat-2 and Sentinel-3A altimeters. They found that the range and SWH noise level were weak but clearly dependent on the wave direction, and the noise level was higher for shorter swell. The studies by Morrow et al. focused on the range and SWH noise level under long swell (relatively less frequent over the ocean), while the characteristics of Sigma-0 measurements were not addressed. Pires et al. (2018) processed some Sentinel-3A altimeter data with collocated Sentinel-1 SAR mode, finding that longer swell usually corresponded to higher Sigma-0 and the eastward swells were more likely to have larger SWH and smaller Sigma-0 (this feature may be primarily due to the geographic pattern of the westerlies). This work did not present the results of PLRM mode of the Sentinel-3A altimeter, and data under various sea states were analyzed together and the high sea state regions (e. g., westerlies) may introduce additional errors. This paper attempts to analyze the influence of the anisotropic effects on SARA measurements. To the authors' knowledge, there has been no publication in this issue yet.

ALTIMETRY GEOMETRY AND OCEAN SURFACE ANISOTROPY

Altimetry Geometry

One distinction between CRA and SARA is the anisotropic observation geometry. Satellite altimeters are nadir-pointing

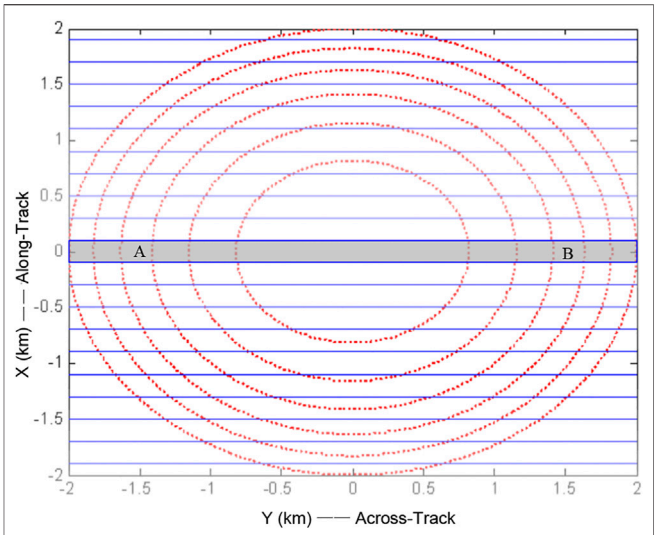

FIGURE 1 | Equal-delay and equal-Doppler lines of altimeters (Xu et al., 2010).

radars, except wide swath ones such as the primary payload of SWOT (Surface Water and Ocean Topography, Fjørtoft et al., 2014). For CRA, the resolving ability is achieved solely by the time delay (or range) bins determined by the altimeter pulse width. The equal-delay lines over a flat ocean surface are depicted in **Figure 1** (red dotted lines). The echo power of a bin in a CRA waveform is the integral along the annuli formed by neighboring equal-delay lines.

On the other hand, the SARA introduces a second resolving dimension: the Doppler domain. Theoretically, the equal-Doppler lines are hyperbolas, but in nadir geometry, they can be well approximated to straight lines in the across-track direction (see blue solid lines in **Figure 1**). The waveforms are compressed to a narrow stripe, and the echo power of a bin in a waveform is the integral along small blocks formed by neighboring equal-delay lines and neighboring equal-Doppler lines.

Intuitively, the anisotropic features (due to wave or wind directivity) of the ocean surface would not have significant influence on the measurements in CRA because the radar footprint is isotropic. On the other hand, the footprint of a SARA is highly anisotropic (the across-track resolution is roughly a magnitude larger than the along-track resolution), so the echo would be different if the ocean surface is anisotropic.

It can also be noted that the SARA has an intrinsic limitation in across-track resolving (e.g., points A and B in **Figure 1** share the same delay bin and Doppler bin, so they are unresolvable unless an across-track interferometric measurement can be provided). Therefore, it can be expected that the anisotropic effect would have a 180° ambiguity (i. e., we cannot determine the wave propagating direction from the two opposite directions).

Characteristics of Ocean Surface Anisotropy

To describe the anisotropy of the sea surface, one can adopt either the ocean wave direction or the ocean surface wind direction. The

two directions are approximately consistent when the wind-wave dominates, while for the swell-dominated sea surface, the wave direction can diverge significantly from the wind direction. The wave direction is superior to the wind direction in our analysis because the most cumbersome influence of anisotropy on the altimetry measurements is the SSB, which relies much more on ocean waves than on the ocean surface wind.

The satellite ground track is inclined, so it is the "relative wave direction", rather than the absolute wave direction that counts,

$$\boldsymbol{\varphi_{rel}} = \boldsymbol{mod}\left(\boldsymbol{\varphi_{wave}} - \boldsymbol{\beta}, 360\right), \tag{2}$$

where $\boldsymbol{\varphi_{rel}}$ is the relative wave direction $\boldsymbol{\varphi_{wave}}$ is the absolute wave direction, $\boldsymbol{\beta}$ is the direction of the satellite flight pass, and $\boldsymbol{mod}(\cdot)$ is the modulus function making sure that the relative wave direction lies in the interval of [0°, 360°]. $\boldsymbol{\beta}$ is a function of latitude and the satellite orbit inclination, but in this work, it is directly computed from the satellite altimeter position information, for it takes consideration of the orbital perturbation.

DATA

Satellite Altimetry Data

Satellite data from three altimetry missions were processed in this work: Sentinel-3A, Jason-3, and Cryosat-2. Sentinel-3 is the first altimetric mission that can provide global measurements in SAR mode, while it can also act as an equivalent CRA, generating the so-called "PLRM (pseudo low resolution mode)" data product. Jason-3 is the successor of the most recognized altimetry missions (Topex/Poseidon, Jason-1 and Jason-2) and currently the reference mission for the altimetry community. Jason-3 altimeter is a CRA, which is an ideal counterpart of Sentinel-3A SARA. Cryosat-2 is the first satellite that carries an altimeter with SAR mode, but the SAR data are only available over limited regions (Bouffard et al., 2017). Cryosat-2 is the first altimetric mission with SAR mode, the altimeter onboard that has a polarization orthogonal to that of Sentinel-3A, so it is helpful in evaluating the influence of polarization configuration on the measurements.

The data are all GDR (Geophysics Data Record) products downloaded from the official websites. The Sentinel-3A data are distributed by the Copernicus Marine Environment Monitoring Service (CMEMS), ESA (European Space Agency, https://sentinel.esa.int); the Jason-3 data are maintained by the Archiving, Validation, and Interpretation of Satellite Oceanographic Data (AVISO, http://www.aviso.altimetry.fr); the Cryosat-2 data can be downloaded from the ESA CryoSat-2 dissemination server (ftp://science-pds.cryosat.esa.int). For all the satellites, the Sigma-0, SWH (Significant Wave Height) and SSHA (Sea Surface Height Anomaly) measurements were extracted. No valid SSB parameter can be extracted from the SAR mode of CryoSat-2 altimeter GDR, so we only processed the SSB of Sentinel-3A and Jason-3. If not specifically declared, the time span of the analysis is the whole year of 2018. Some data of year 2017 were also processed to clarify if there were time-dependence features.

Numeric Wave Model Data

The numeric wave model data can provide the information of ocean wave, which can be very helpful for the investigation of the ocean surface anisotropy. WaveWatch III (WW3), consisting of hourly, 1 ° × 1 ° gridded field of ocean SWH), wavelength, wave period, and wave direction, is one of the most accredited wave modes (Rascle and Ardhuin, 2013). Some empirical SSB models adopted the wave period as a parameter. For a gravity wave, according to the dispersion theory, the wave period is proportional to the root square of the wavelength. Wavelength is more pertinent to the altimetric observation geometry, so we use wavelength as an index of the ocean wave rather than the wave period. The waves are partitioned into many (usually more than 20) components sorted from the largest wave height to the smallest wave height. In this work, we extract the parameters of the largest wave component, since the largest wave component usually accounts for a large fraction of the wave energy.

METHODOLOGY

Wave Type Identification

The ocean waves (restricted to gravity waves in this work) can be categorized into three types: wind-dominated wave, swell-dominated wave, and mixed wave (Ardhuin, 2019). Wind-waves are arisen from local winds, while swells are the waves generated by winds in remote storms. Swells usually have longer wavelength and less randomness, so they are more likely to cause bias in altimetric measurements. The radar altimeter has the advantage to measure the significant wave height (SWH) and wind speed simultaneously, from which the wave type information can be inferred. The wind/swell contribution can be roughly described by the "pseudo wave-age (Fu and Glazman, 1991),"

$$\psi = a \bullet \left(gH_{1/3}/U_{10}^2\right)^b, \tag{3}$$

where $\boldsymbol{\Psi}$ is a function of the ratio of the wave potential energy and wind kinetic energy, $\boldsymbol{a}$ and $\boldsymbol{b}$ are empirical coefficients, and $\boldsymbol{g}$ is the gravity acceleration. For a fully-developed pure wind-wave, $\boldsymbol{\Psi}$ = 1.21; a smaller wave-age infers a developing wind-wave, while a larger wave-age means a contribution of swell (for a pure swell, $\boldsymbol{\Psi} = \infty$).

The "wind_sea_fraction" parameter in the WW3 data was extracted as the indicator of the ocean wave type. The parameter is proposed by Hanson and Phillips (2001) and implemented as described in Tracy et al. (2007). The value of the "wind-sea fraction of partition (W)" is defined as

$$\mathrm{W} = \frac{\mathrm{E}\left|\ \mathrm{Up} > \mathrm{c}\right.}{\mathrm{E}},$$

where E is the total spectral energy and $E|_{Up>c}$ is the energy in the spectrum for which the projected wind speed U_p is larger than the local wave phase velocity c. For the pure wind sea, $W = 1$, while for the pure swell, $W = 0$.

TABLE 1 | Six categories of ocean wave.

Wavelength / Wind-wave fraction	L ≤ 100 m	100 m < L ≤ 400 m	L > 400 m
W < 0.3	Short swell	Moderate swell	Long swell
W > 0.7	Short wind-wave	Moderate wind-wave	Long wind-wave

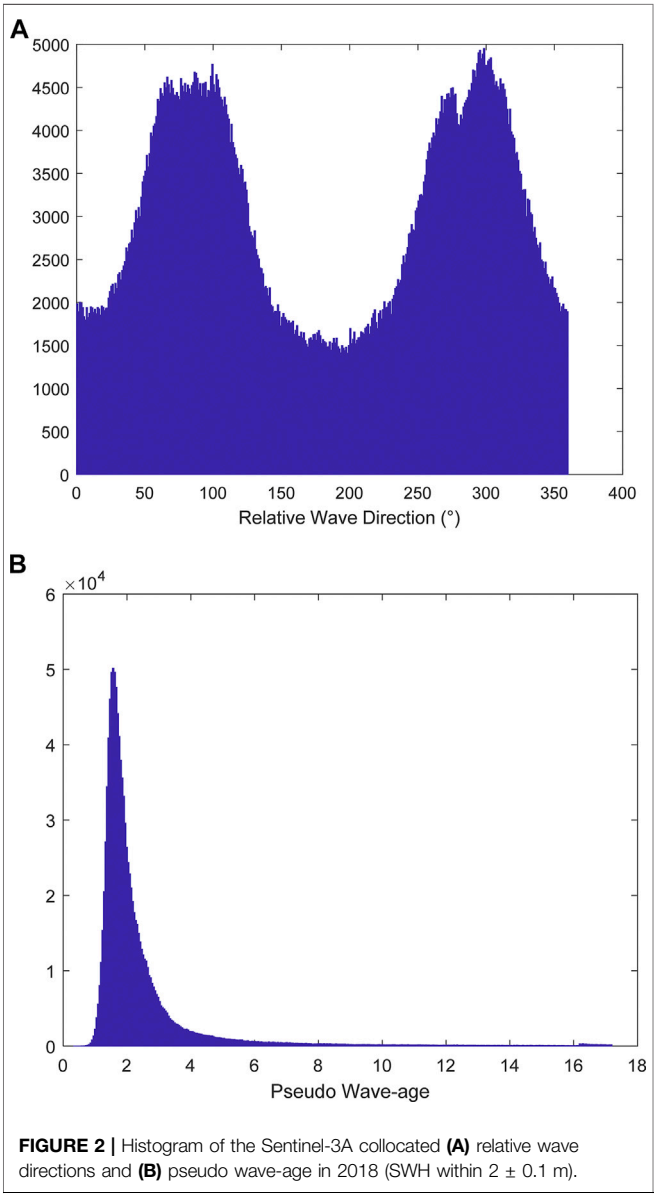

FIGURE 2 | Histogram of the Sentinel-3A collocated **(A)** relative wave directions and **(B)** pseudo wave-age in 2018 (SWH within 2 ± 0.1 m).

For wind_sea_fraction<0.3, the ocean wave is identified as swell-dominated wave (abbreviated to "swell" hereinafter); for wind_sea_fraction>0.7, the ocean wave is identified as the wind-dominated wave (abbreviated to "wind-wave" hereinafter); otherwise, the ocean wave is identified as mixed wave. The thresholds of 0.3 and 0.7 are somewhat arbitrary, while they leave enough margins to alleviate the ambiguity between wind-waves and swells. The mixed waves were not investigated in this work.

In many publications, the wind-wave and swell are distinguished according to the ocean wavelength. For instance, in Toffoli and Bitner-Gregersen. (2017), swells have a typical wavelength that is greater than 260 m (i.e., wave period larger than 13 s) up to maximum of approximately 900 m. We would find that the strategy of wave classification has a very significant influence on the anisotropic patterns, as shown in *On the Strategy of Wave Type Identification* Section.

Data Matching

The numeric wave model data are gridded data in both time and space domains, so the data must be interpolated to the time and location of the altimeter measurements. In the time domain, we just choose the time stamp closest to the altimeter measurement; this strategy can introduce a mismatching error. The mismatching time errors obey a uniform distribution in the interval of (−0.5 h, +0.5 h), and the wave characteristics are highly correlative in such a short time scale. We carried out experiments to estimate the effect of this simplification with respect to linear interpolation, showing that the difference can be safely negligible. In the space domain, because the spatial resolution of WW3 is relatively coarse, we carried out bilinear interpolations from the four closest grids,

$$X = X_{nw}W_{nw} + X_{ne}W_{ne} + X_{sw}W_{sw} + X_{se}W_{se}, \tag{4}$$

where $\boldsymbol{X}$ is a measurement (it could be wavelength, wave direction, etc.), the subscripts ***nw***, ***ne***, ***sw***, and ***se*** denote the northwest, northeast, southwest, and southeast grids around the location of the altimeter measurement respectively, and the $\boldsymbol{W}$s are the corresponding weights,

$$W_{nw} = \frac{(lon_{ne} - lon_{alt})(lat_{alt} - lat_{sw})}{(lon_{ne} - lon_{nw})(lat_{nw} - lat_{sw})}, \tag{5}$$

$$W_{ne} = \frac{(lon_{alt} - lon_{nw})(lat_{alt} - lat_{se})}{(lon_{ne} - lon_{nw})(lat_{ne} - lat_{se})}, \tag{6}$$

$$W_{sw} = \frac{(lon_{se} - lon_{alt})(lat_{nw} - lat_{alt})}{(lon_{se} - lon_{sw})(lat_{nw} - lat_{sw})}, \tag{7}$$

$$W_{se} = \frac{(lon_{alt} - lon_{sw})(lat_{ne} - lat_{alt})}{(lon_{se} - lon_{sw})(lat_{ne} - lat_{se})}, \tag{8}$$

where *lon* and *lat* are the longitude and latitude of the grid point, respectively. After the data matching, WW3 wave information (wave height, wavelength, wave direction, and wind-sea fraction) was merged into every altimeter measurement.

Data Editing Criterion

The most stringent requirement for accurate backscatter measurement is the SSB correction, which is significantly

TABLE 2 | Numbers and percentages of different wave types (Sentinel-3A, SWH within 2 ± 0.1 m, year 2018).

Wavelength region	Short (<100 m)	Moderate (100–400 m)	Long (>400 m)
Swell	244,701 (9.00%)	1384952 (50.95%)	105,320 (3.87%)
Wind-wave	806,779 (29.68%)	174,688 (6.43%)	1,628 (0.06%)

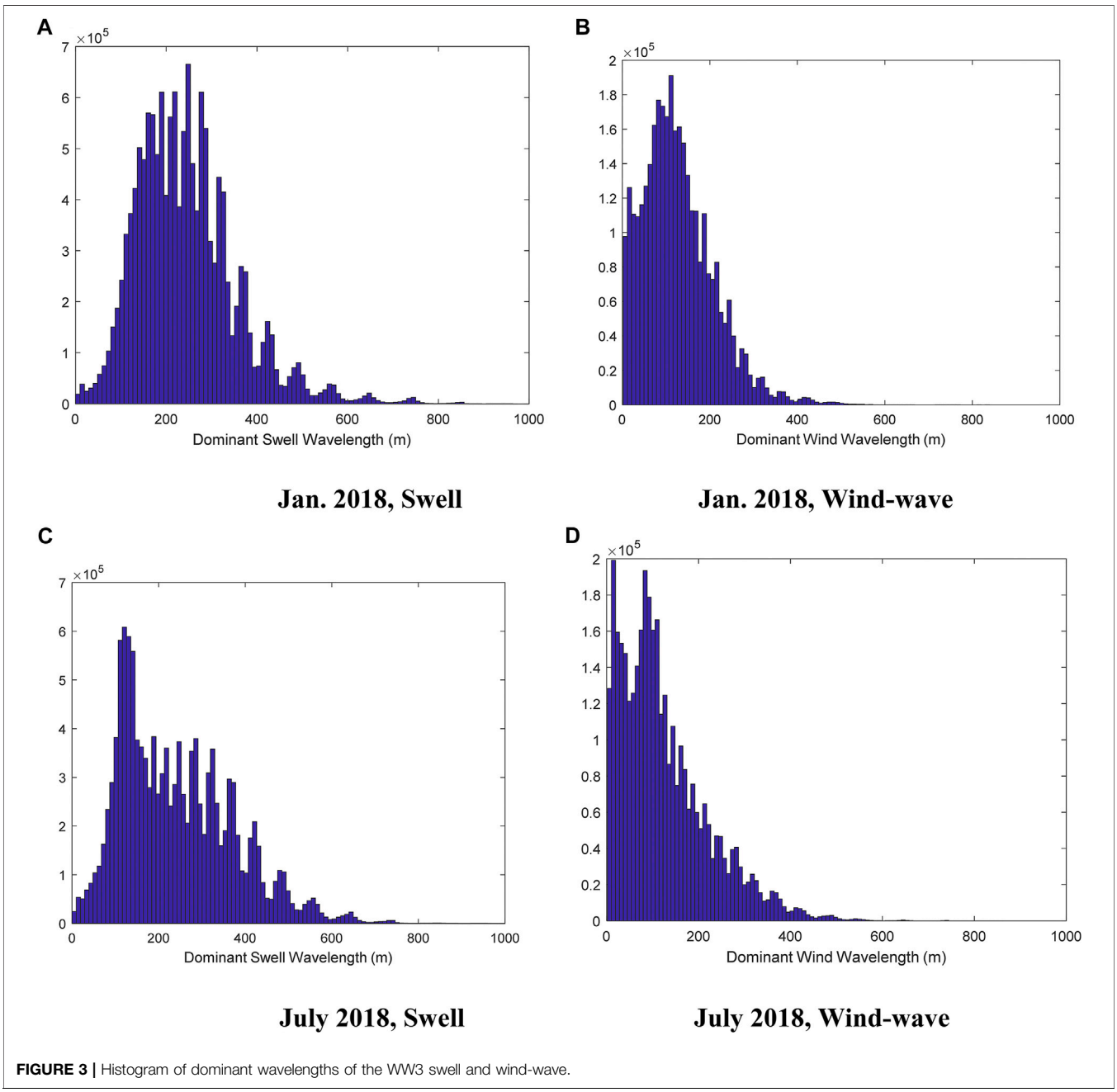

FIGURE 3 | Histogram of dominant wavelengths of the WW3 swell and wind-wave.

dependent on the quality of both the SWH and the radar backscatter coefficient (Sigma-0). To evaluate the influence of the Sigma-0 measurement on SSB, we picked out the altimetry measurements having a SWH within 2 ± 0.1 m. The measurement noise level of SWH is comparable to 0.1 m, so the SWHs are statistically indistinguishable. The data pole-ward of 50°of latitude were discarded to circumvent the influence of sea-ice because a significant portion of altimeter measurements were acquired over high-latitude zones. The rain-contaminated measurements were also discarded according to the rain flag in the data product.

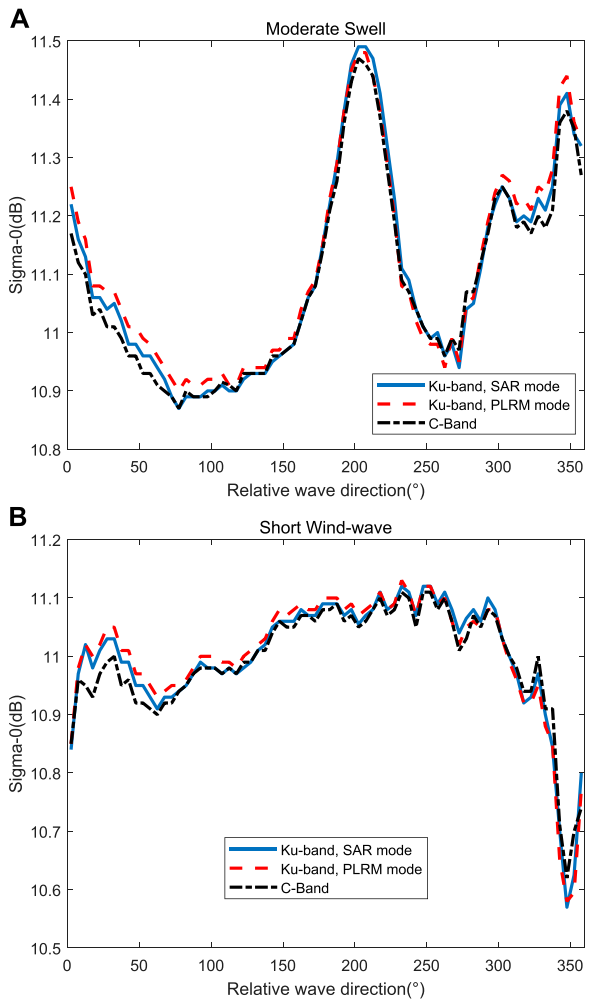

FIGURE 4 | Sentinel-3A Sigma-0 anisotropic pattern **(A)** for moderate swell; **(B)** for short wind-wave: solid blue: Ku-Band, SAR mode, dashed red: Ku-Band, PLRM mode, dot-dash black: C-Band.

The typical SARA along-track resolution is 250–300 m, so we categorized the ocean wave into three regions according to the wavelength: short wave region (wavelength less than 100 m), moderate wave region (wavelength between 100 and 400 m, comparable to the along-track resolution of SARA), and long wave region (wavelength larger than 400 m). Therefore, six types of ocean waves can be identified: 1) short swell, 2) moderate swell, 3) long swell, 4) short wind-wave, 5) moderate wind-wave, and 6) long wind-wave. The criteria for classification of the wave type are tabulated in **Table 1** (L denotes the wavelength and W denotes the wind-sea fraction).

Generation of the Anisotropic Pattern

To establish the relationship between Sigma-0 (and SSB) and the relative wave direction, we computed the relative wave directions of all the measurements. Every altimetric measurement can contain a relative wave direction (computed from the WW3 wave direction interpolation value and the satellite flight direction), and this direction is within the range of 0–360°. This angle range can be split to 72 bins with a step of 5°. We read this direction and allocate the corresponding measurements in a predefined stack. All the measurements in the first stack has a relative wave direction of 0–5°, all the measurements in the second stack has a relative wave direction of 5–10°, etc. Consequently, we have 72 stacks, each of which contains a large number of measurements (every measurement contains Sigma-0, SSB, SWH, SSHA, wavelength, wave direction, etc.). Finally, we computed the statistics of each stack as a represent of each bin and drew a curve called "pattern" from the median value of each bin of the relative wave direction. The pattern of Sigma-0, SSB, and SSHA are all generated in the same way, and they can indicate the features of the anisotropic effect.

RESULTS

Ocean Wave Characteristics

The ocean wave characteristics collocated to the altimeter measurements were analyzed, the waves showed a distinct anisotropic feature, and the east-west propagating wave dominated in the histogram (**Figure 2A**). The histogram of pseudo wave-age computed from **Eq. 3** was also depicted as **Figure 2B**. The histogram of pseudo wave-age has a long tail, indicating that swell is more popular in the ocean than wind-wave. We computed the pseudo wave-age of Sentinel-3A and Jason-3 measurements using the Topex values (in Topex altimetry, $\boldsymbol{a} = 3.24$, $\boldsymbol{b} = 0.62$), but according to the $\boldsymbol{\Psi} = 1.21$ threshold, only 3% of the waves can be identified as wind-wave, which is unrealistically low. An explanation of this situation is that the coefficients $\boldsymbol{a}$ and $\boldsymbol{b}$ (**Eq. 3**) should be estimated by individual altimeter data products, while different mission has different estimations due to the residual errors in the altimeter calibration. To circumvent the potential calibration errors, pseudo wave-age is not adopted as a wind/swell indicator. The "wind_sea_fraction" indictor is used to classify the wind-wave and swell.

The numbers and percentages of different wave type are summarized in **Table 2**. Swells are almost twice as frequent as wind-waves in the global oceans. For swells, the waves with moderate wavelength dominate (accounting for ~80%), while for wind-waves, the waves with short wavelength dominate (accounting for ~82%). Therefore, only the moderate swell case and the short wind-wave cases are presented intensively.

Histograms of the dominant wavelengths of the WW3 swell and wind-wave in different seasons are shown in **Figure 3**. Both in the north-hemisphere winter and in north-hemisphere summer, the average wavelength of the wind-wave is about half of the wavelength of the swell, which is consistent with our expectation.

Sentinel-3A Anisotropic Pattern

The Sigma-0 anisotropic pattern of Sentinel-3A for the moderate swell and short wind-wave satellite altimeter were analyzed and the results are shown in **Figure 4**. For the moderate swell, the patterns reach maximum around 0° (360°) or 180°. To investigate the influence of SAR configuration on the measurements, both SAR and PLRM modes were analyzed. Surprisingly, the anisotropic patterns of the two Ku-band modes (and the C-band) are very similar. The pattern for short wind-wave is more irregular: no distinct sinusoid feature can be identified.

TABLE 3 | Correlation coefficients of Sentinel-3A Sigma-0 anisotropic patterns between different modes (moderate swell, year 2018).

Correlation coefficient	Ku-band SAR mode	Ku-band PLRM mode	C-band
Ku-band SAR mode	1	0.9948	0.9954
Ku-band PLRM mode	0.9948	1	0.9894
C-band	0.9954	0.9819	1

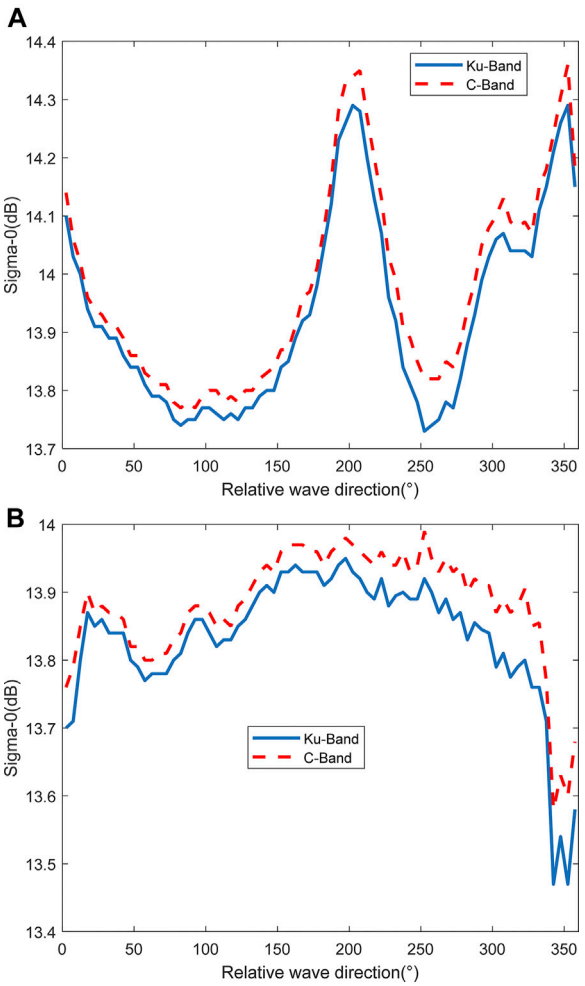

FIGURE 5 | Jason-3 Sigma-0 anisotropic pattern **(A)** for moderate swell; **(B)** for short wind-wave: solid blue: Ku-Band, dashed red: C-Band. An offset of −1.5 dB is added to the C-band Sigma-0.

To evaluate the agreement of the patterns between different modes, the correlation coefficients are tabulated in **Table 3**, **4** for the two most frequent wave types (moderate swell and short wind). All the correlation coefficients are larger than 0.97, indicating that the introduction of the SAR mode has little influence on the Sigma-0 patterns. The dynamic range of the SAR mode is 0.62 dB, only slightly larger than that of the PLRM mode (0.58 dB). The C-band Sigma-0 product may contain an uncalibrated bias: typically, the Sigma-0 of the C-band is 1~2 dB greater than that of the Ku-band (noting the −1.5 dB offset for the Jason-3 altimeter in **Figure 5**), but for Sentinel-3 altimeter, the Sigma-0 values for the two bands have little difference. Nevertheless, this bias does not change the shape of the patterns.

Jason-3 Anisotropic Pattern

The unexpected sinusoid feature for the Sentinel PLRM Sigma-0 pattern for the swell case was reinforced by the results of Jason-3. As a representative CRA, the Sigma-0 anisotropic pattern for the moderate swell and short wind-wave of Jason-3 satellite altimeter was analyzed and the results are shown in **Figure 5**. Similar sinusoid trend can be found in the swell pattern. An offset of −1.5 dB is added to the C-band Sigma-0 for a better demonstration. The patterns or the two bands also show excellent agreement. For the moderate swell condition, the correlation coefficient between two bands is 0.9977, while for the short wind-wave condition, the correlation coefficient between two bands is 0.9896.

Cryosat-2 Anisotropic Pattern

The Sigma-0 anisotropic pattern of the Cryosat-2 satellite altimeter was analyzed and the results are shown in **Figure 6** (for moderate swell). The pattern is extremely noisy, mainly due to the poor geographic distribution of Cryosat-2 SAR mode. Most measurements of SAR-mode were acquired from the polar region. In fact, the data pole-ward of 50° of latitude were discarded to circumvent the influence of sea-ice. Only few regions (e.g. the Mediterranean Sea, south to the Southern African coast and north to the Indonesian coast) have enough data, resulting in relatively large representative errors. In spite of this, the Cryosat-2 pattern also shows a roughly sinusoid trend, especially in the region of 0–180°.

DISCUSSION

On the Strategy of Wave Type Identification

As mentioned in the *Wave Type Identification* section, we use the "wind_sea_fraction" parameter of the WW3 data product as a criterion to classify the ocean wave. A larger fraction corresponds to a wind-dominated wave, while a smaller fraction corresponds to a swell-dominated wave. This strategy is somewhat different to the commonly-used strategy (e. g., Toffoli and Bitner-Gregersen, 2017), which is solely dependent on the wavelength. To investigate the influence of the wave classification strategy, we generated the patterns under different strategies and compared the corresponding patterns of swell and wind-wave. The Sigma-0 patterns for swell and wind-wave of the Sentinel-3 altimeter using different strategies are shown in **Figure 7**.

It can be seen from the figures that for the Toffoli and Bitner-Gregersen, (2017) strategy, the patterns of wind-wave and swell

TABLE 4 | Correlation coefficients of Sentinel-3A Sigma-0 anisotropic patterns between different modes (short wind-wave, year 2018).

Correlation coefficient	Ku-band SAR mode	Ku-band PLRM mode	C-band
Ku-band SAR mode	1	0.9913	0.9790
Ku-band PLRM mode	0.9913	1	0.9683
C-band	0.9790	0.9683	1

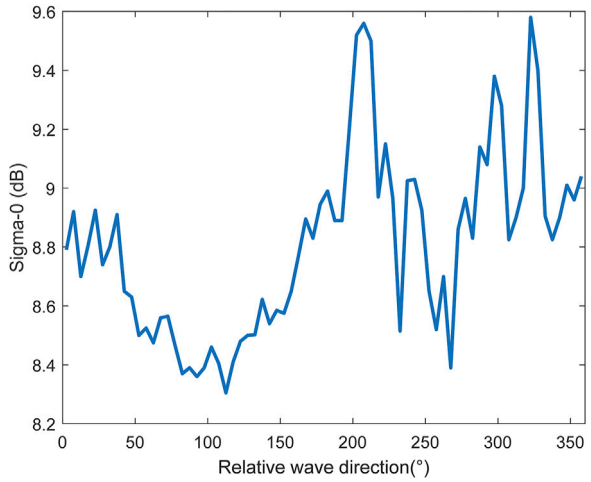

FIGURE 6 | Cryosat-2 SAR mode Sigma-0 anisotropic pattern for moderate swell.

both have clear sinusoid features with peaks around 180° (almost undistinguishable), while for our strategy, the anisotropic patterns of wind-wave and swell are very distinct: the wind-wave pattern is more like a random one. Therefore, we deem that the "wind-wave fraction" may be a better indictor to identify the wave type. Indeed, a shorter wave is more likely to be a wind-wave as shown in **Figure 3**, but it seems that the anisotropic patterns may have much less correlation with wavelength than with the wind-wave fraction parameter.

On the Temporal Consistency of the Pattern Feature

Inter-annual Variation

In order to identify the possible time-dependent effects in the anisotropic patterns, we processed the Sentinel-3A, Jason-3, and Cryosat-2 data of the year 2017 using the same approach as the year 2018. Comparisons of the Sigma-0 patterns of years 2017 and 2018 of the three satellites are shown in **Figure 8** for the moderate swell. Correlative coefficients between the patterns of the two years under the swell or wind-wave condition are always larger than 0.9 for Sentinel-3A and Jason-3. For Cryosat-2, the coefficients are relatively low (0.5821 for swell), maybe due to the relatively poor spatial distribution of Cryosat-2 SAR mode. Therefore, it can be concluded that the sinusoid feature under the swell-dominated condition is constant through time.

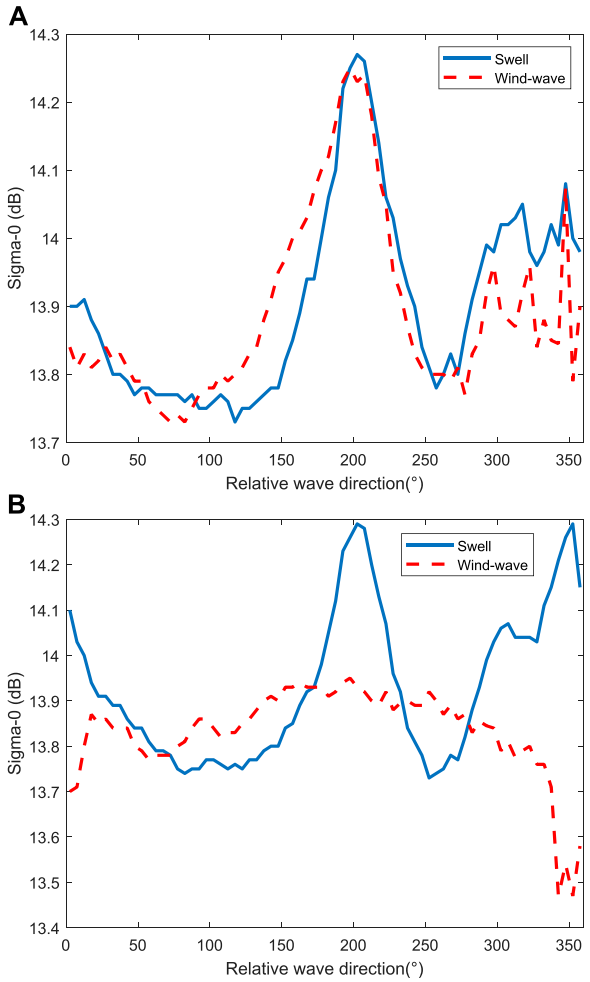

FIGURE 7 | The Sigma-0 patterns for swell (solid blue) and wind-wave (dashed red): **(A)** defined by Toffoli et al.; **(B)** defined in this work (year 2018, Sentinel-3A).

On the Seasonal Variation

The anisotropic features of different seasons were also compared. **Figure 9** depicts the Sentinel-3A Sigma-0 patters for the four quarters of 2018 (under the moderate swell condition). It can be seen that all the quarter share the similar sinusoid pattern. **Table 5** (for swell) and **Table 6** (for wind-wave) give the correlation matrix of the Sentinel-3A Sigma-0 patterns for the four quarters of 2018. Under the swell condition, the correlation coefficients between different quarters are always higher than 0.7, while for the wind-wave-

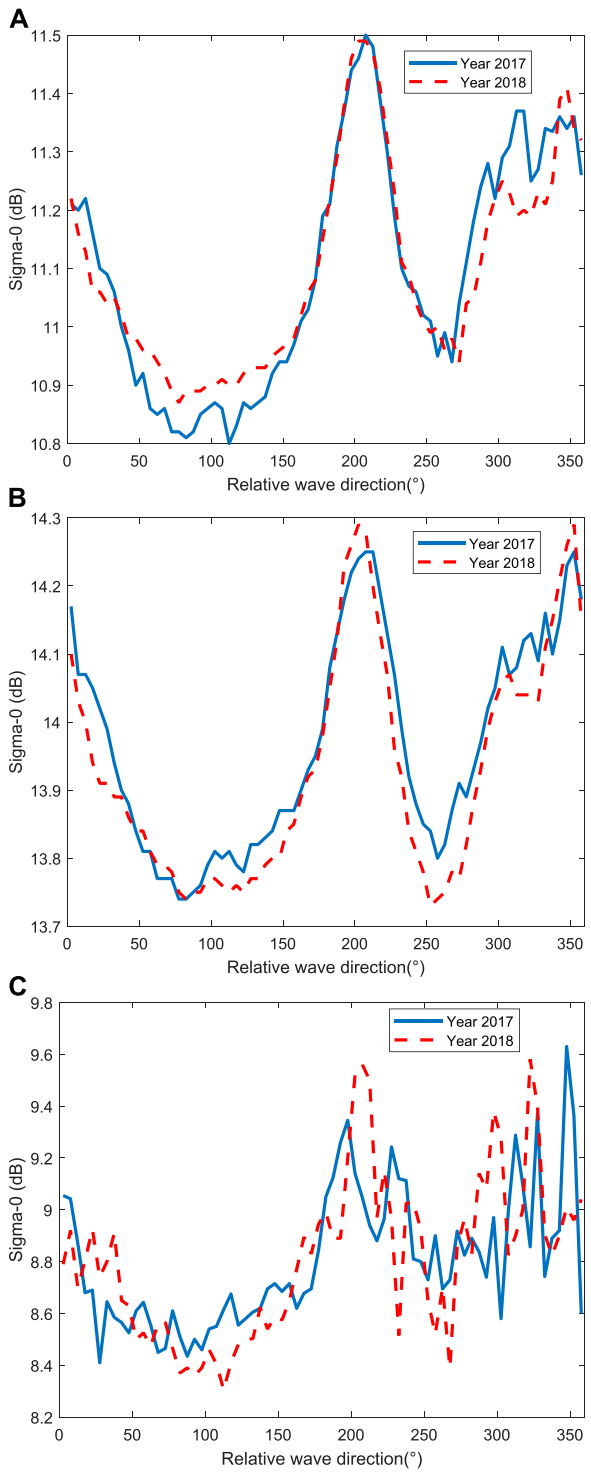

FIGURE 8 | (A) Sentinel-3A, **(B)** Jason-3 and **(C)** Cryosat-2 Sigma-0 patterns of year 2017 and year 2018 for moderate swell.

dominated case, the correlation matrix is always smaller than that of the swell case; particularly, the coefficient correlation between winter (Q1) and summer (Q3) is the lowest (~0.35),

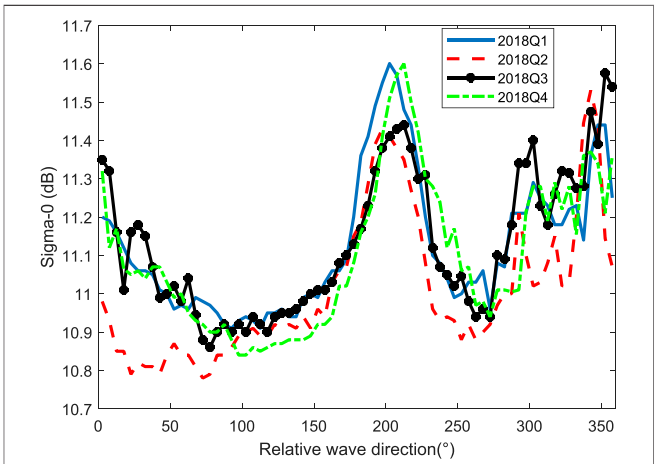

FIGURE 9 | The Sentinel-3A Sigma-0 patterns of the four quarters of year 2018 for moderate swell.

which can be explained by the effects of widespread monsoons over wind sea.

On the Relationship of Sigma-0 and SWH as well as the SWH and Wave Direction

To exclude the effects of SWH, we only deal with the data with a altimetric SWH between 1.9 and 2.1 m. So there is almost no trend in the SWH–Sigma0 or SWH–wave-direction relationships (**Figure 10**). The scattering diagrams of the SWH–Sigma0 pair and SWH–wave-direction pair of an arbitrary month (Jan. 2018) are shown as follows. The SWH extracted from WW3 has a larger dynamic (for the swell condition, mean = 1.97 m, std = 0.44 m), no trend can be found in the SWH–Sigma0 or SWH–wave-direction relationships either.

On the Geographic Sampling of the Satellite

It may be argued that the sinusoid feature in the Sigma-0 pattern could arise from the geographic sampling of the

TABLE 5 | Correlation matrix of the Sentinel-3A Sigma-0 patters for the four quarters of 2018 (moderate swell condition).

	Q1	Q2	Q3	Q4
Q1 (Jan. ~ Mar.)	1	0.8496	0.8792	0.8685
Q2 (Apr. ~ June)	0.8496	1	0.7558	0.7450
Q3 (July ~ Sept)	0.8792	0.7558	1	0.8621
Q4 (Oct. ~ Dec.)	0.8685	0.7450	0.8621	1

TABLE 6 | Correlation matrix of the Sentinel-3A Sigma-0 patters for the four quarters of 2018 (short wind-wave condition).

	Q1	Q2	Q3	Q4
Q1 (Jan. ~ Mar.)	1	0.6929	0.3724	0.6781
Q2 (Apr. ~ June)	0.6929	1	0.5539	0.6950
Q3 (July ~ Sept)	0.3724	0.5539	1	0.5236
Q4 (Oct. ~ Dec.)	0.6781	0.6950	0.5236	1

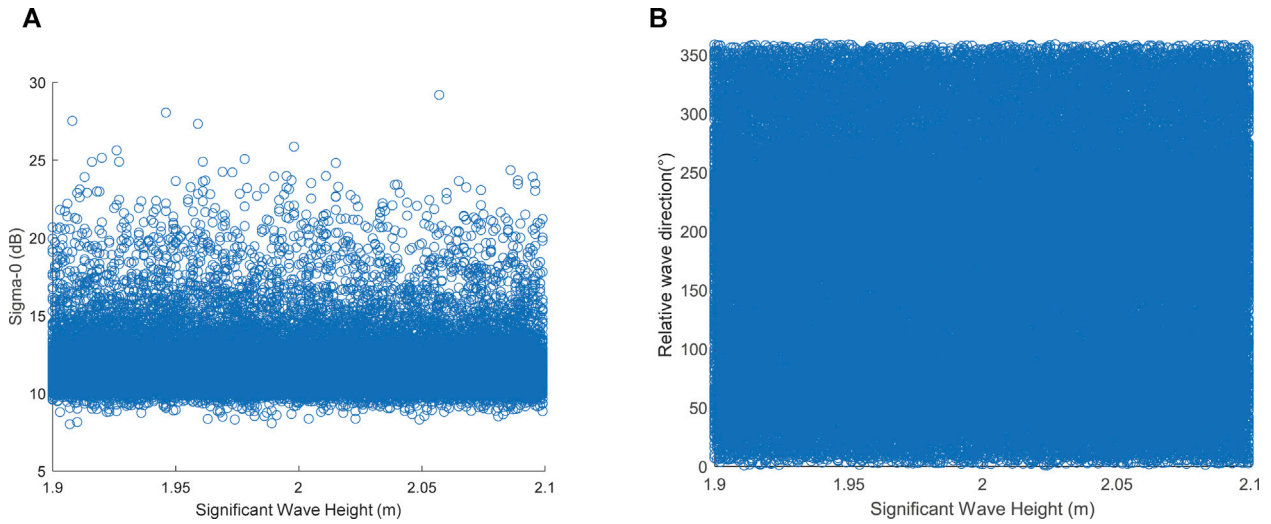

FIGURE 10 | (A) SWH-Sigma0 and **(B)** SWH-wave-direction relationships of Sentinel-3A measurements altimeter in January 2018.

satellite. We compared the Sigma-0 patterns of Jason-3, Sentinel-3A, and Cryosat-2 satellites. The orbit configuration of the three satellites is extremely different: Jason-3 is a prograde satellite with a revisiting period of 9.9156 days; Sentinel-3A is a sun-synchronous satellite with a revisiting period of 27 days; Cryosat-2 is non-repeating in one year's duration (the revisiting period is 369 days, longer than one year). The geographic distribution of Sentinel-3A and Jason-3 Sigma-0 under ~2 m SWH are shown in **Figure 11**. No significant correlations can be found between the distributions of the two missions.

The Sigma-0 patterns of the three satellites are shown in **Figure 12**. Although there are clear biases between different missions, the trends of the three patterns are very similar. The correlative coefficient between the Sigma-0 patterns of Sentinel-3A and Jason-3 is 0.9662, and the correlative coefficient between the Sigma-0 patterns of Sentinel-3A and Cryosat-2 is 0.8034 (this is high enough in consideration of the poor-sampling and noisy feature of

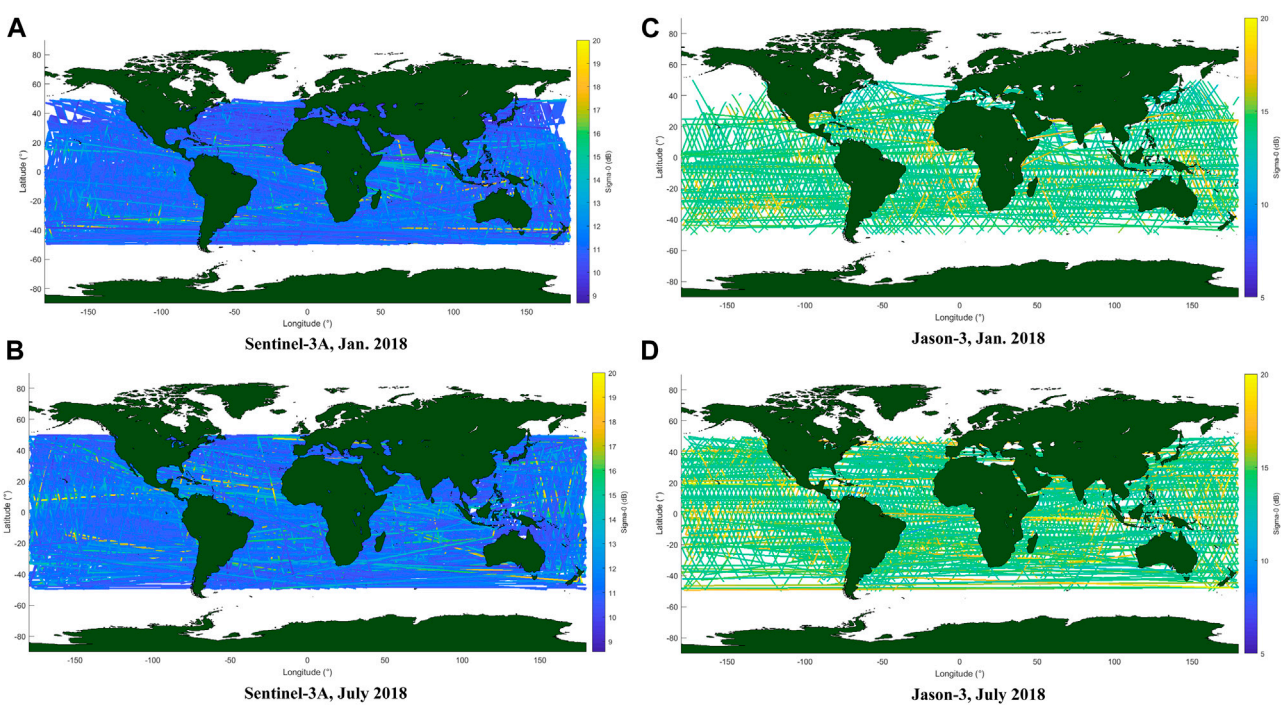

FIGURE 11 | Geographic distribution of the Sentinel-3A **(A,B)** and Jason-3 **(C,D)** Sigma-0, all the measurements have a SWH between 1.9 m and 2.1 m.

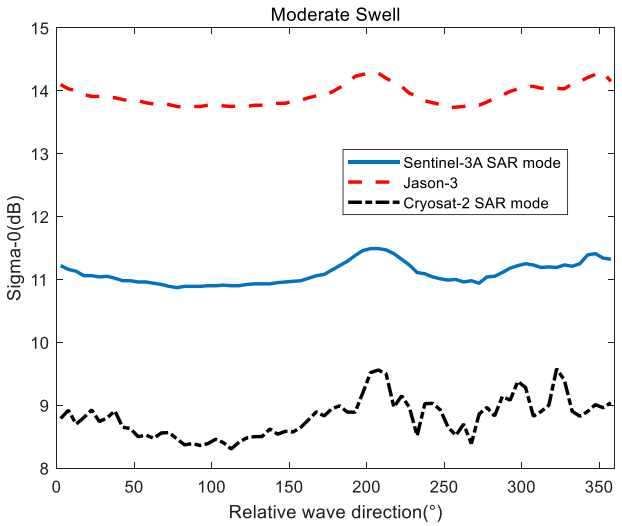

FIGURE 12 | Comparison of the Ku-Band Sigma-0 patterns of Sentinel-3A (solid blue, SAR mode), Jason-3 (dashed red) and Cryosat-2 (dot-dash black, SAR mode) for moderate swell.

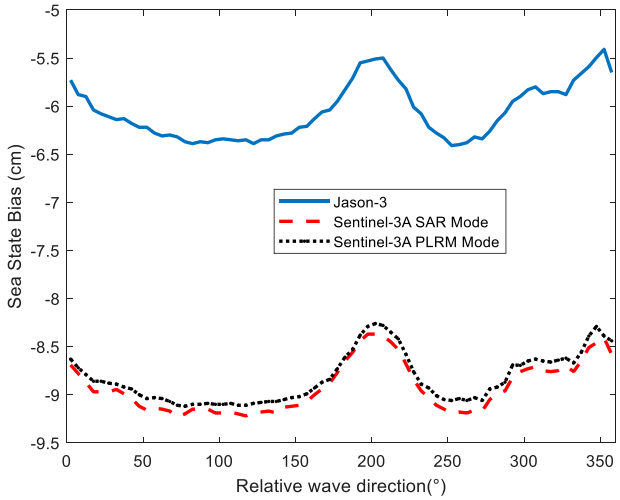

FIGURE 13 | Comparison of the Ku-Band SSB patterns of Jason-3 (solid blue), Sentinel-3A SAR mode (dashed red) and Sentinel-3A PLRM mode (dot-dash black) for moderate swell.

the Cryosat-2 pattern). It seems that the three satellites share the similar Sigma-0 pattern in spite of the distinct geographic sampling.

The Influence of Polarization Mode

Polarization is a very important feature of the microwave. Radar altimeters operate under nadir geometry, so polarization mode is not a serious issue for CRA. Tran and Chapron (2006) reported a small but clear sinusoid anisotropic feature of the Jason-1 altimeter backscatter measurements, but this feature was not discovered in the measurements of TRMM (Tropical Rainfall Measuring Mission) PR (Precipitation Radar) nadir beam (Chu and He, 2012), which is essentially equivalent to an altimeter. For SARA, the issue of polarization has not been addressed in any publication, to the authors' knowledge.

To include the polarization information, we can redefine the "relative wave direction": the reference direction should be the electric field direction of the microwave pulse transmitted by the altimeter rather than the flight direction of the satellite. To clarify the influence of the polarization mode, we can compare the Sigma-0 patters of two orthogonal polarization modes. If there were a 90° lag between the two patterns, we could make the assertion that the pattern is sensitive to the polarization. For Jason-3 and Sentinel-3A altimeters (and almost all the dual-band radar altimeters), the polarization mode of the two bands are orthogonal. However, no significant difference could be identified from the two bands for both altimeters. For Sentinel-3A, the standard deviation of the Sigma-0 difference pattern (sigma0-Ku minus sigma0-C) is 0.0187 dB for moderate swell; while for Jason-3, the standard deviation of the Sigma-0 difference pattern (sigma0-Ku minus sigma0-C) is 0.0192 dB for the moderate swell. Both values are well below the altimetric Sigma-0 measurement specification.

Because only Ku-band of the Sentinel-3A altimeter operates in SAR mode (C-band of the Sentinel-3A altimeter is a CRA), we processed the Cryosat-2A SAR mode data as a second SARA. The Cryosat-2 altimeter has an orthogonal polarization mode with respect to the Sentinel-3A Ku-band: for Cryosat-2, the flight direction of the satellite is perpendicular to the electric field vector of the microwave pulses (Rémy et al., 2012), while for Sentinel-3A, the flight direction of the satellite is parallel to the electric field vector. The Sigma-0 pattern of Cryosat-2 for the moderate swell also has a primary peak around 180°, showing no evidence of any possible 90° lag relative to that of Sentinel-3A (see **Figure 11**). Therefore, we can make the conclusion that the polarization configuration of SARA would not significantly influence the Sigma-0 (in turn, SSB) measurement.

SSB with Respect to the Anisotropic Features

The most important influence of the anisotropic pattern is on the SSB. The patterns of SSB were generated using the same approach to Sigma-0 measurements. The SSB anisotropic patterns for Jason-3, Sentinel-3A SAR mode, and Sentinel-3A PLRM mode for the moderate swell is shown in **Figure 13**. The correlation coefficient between the SSB patterns of the two modes is 0.9943 and 0.9692 for the moderate swell and short wind-wave, respectively. As the SWH is restricted to ~2 m throughout this work, the SSB pattern is highly correlative to the corresponding Sigma-0 pattern. The correlative coefficient between the SSB patterns of Sentinel-3A and Jason-3 is 0.9849.

No valid SSB value can be extracted from the Cryosat-2 SAR mode GDR, so we did not evaluate the SSB for Cryosat-2.

SSHA with Respect to the Anisotropic Features

SSHA is the primary measurement of the altimeters, so we generated the SSHA patters of Sentinel-3A for analysis. The results are shown in **Figure 14A** (for moderate swell) and

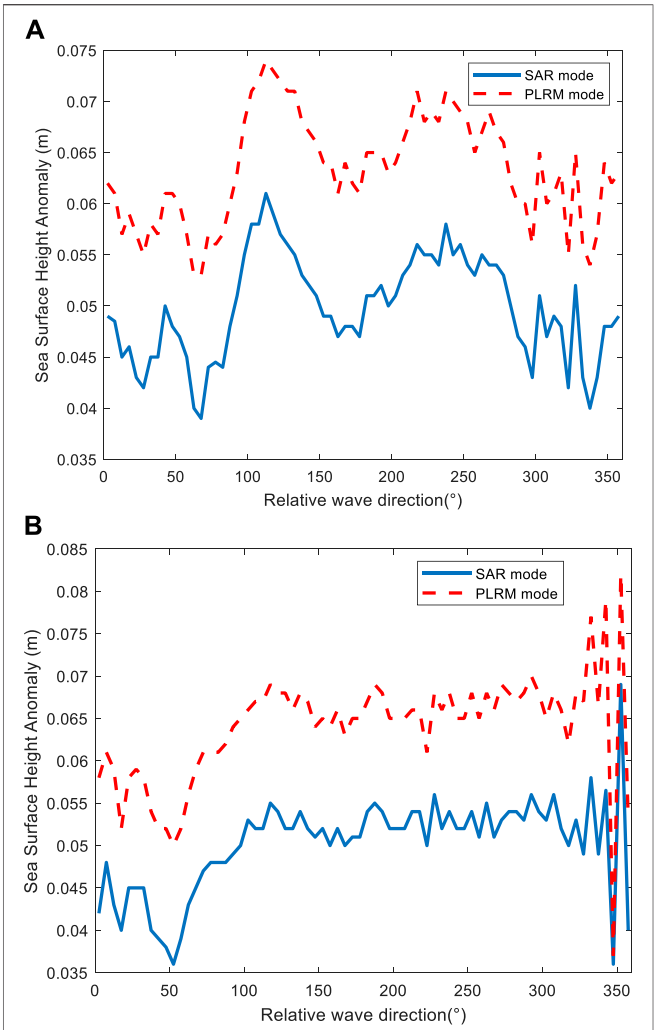

FIGURE 14 | Sentinel-3A Ku-band SSHA anisotropic pattern for **(A)** moderate swell and **(B)** short wind-wave (lower panel).

Figure 14B (for short wind-wave). There is a bias between the SSHA of the two modes (the PLRM one is ~1.4 cm higher), but the correlative coefficients between the two patterns are very high (0.9792 for the moderate swell and 0.9433 for the short wind-wave).

Somewhat surprisingly, the correlative coefficients between the SSHA and SSB are very small (−0.1719 for SAR mode and −0.1348 for PLRM mode under the moderate swell situation). If the patterns of the SSHA were dominated by SSB, the correlative coefficients would be close to −1. A possible explanation is that there are many complicated factors (noises as well as oceanographic signals) in the SSH pattern. In fact, the standard deviation of the SSHA pattern is significantly larger than that of the SSB in any case (**Table 7**), so the sinusoid trend in SSB may be overwhelmed.

CONCLUSION

In this article, the influences of ocean surface anisotropy on the backscattering measurements and sea state bias corrections of conventional and SAR altimeters were investigated. Two years' (2017 and 2018) data record of Sentinel-3A, Jason-3, and Cryosat-2 altimeters were extracted, edited, and collocated with the WW3 wave model. The anisotropic patterns of Sigma-0 and SSB were generated for moderate swell and short wind-wave cases. Several interesting phenomena were found. The main conclusions of this study were as follows:

1) As expected, the anisotropic patterns for the swell condition are much more regular than that of the wind-wave. The moderate swell patterns show a sinusoid feature with a period of roughly 180°, which is due to the 180° ambiguity of the nadir-pointing observation geometry. For the wind-wave, the pattern is less regular. Besides, the "wind-sea-fraction" (which can be extracted from the WW3 numerical model) might be more appropriate than the commonly-used "wavelength" as an indicator of wave type.
2) It is somewhat counterintuitive that the Sigma-0 and SSB patterns of CRA and SARA are almost identical. This feature has never been reported before. We compared the patterns of different time and different missions with different geographic sampling, and all the patterns have the similar clear sinusoid

TABLE 7 | Summary of the statistics properties of the Sigma-0, SSB, and SSHA of Sentinel-3A patterns.

Parameters	Mean value	Standard deviation	Dynamic range
Sigma-0 (Swell, SAR)	11.07 dB	0.18 dB	0.62 dB
Sigma-0 (Swell, PLRM)	11.08 dB	0.17 dB	0.58 dB
Sigma-0 (Wind-wave, SAR)	10.98 dB	0.10 dB	0.54 dB
Sigma-0 (Wind-wave, PLRM)	10.98 dB	0.10 dB	0.52 dB
SSB (Swell, SAR)	-8.92 cm	0.26 cm	0.86 cm
SSB (Swell, PLRM)	−8.83 cm	0.26 cm	0.86 cm
SSB (Wind-wave, SAR)	−9.04 cm	0.14 cm	0.79 cm
SSB (Wind-wave, PLRM)	−8.96 cm	0.11 cm	0.56 cm
SSHA (Swell, SAR)	4.98 cm	0.50 cm	2.20 cm
SSHA (Swell, PLRM)	6.33 cm	0.53 cm	2.10 cm
SSHA (Wind-wave, SAR)	5.01 cm	0.57 cm	3.30 cm
SSHA (Wind-wave, PLRM)	6.39 cm	0.67 cm	4.50 cm

trend for the moderate swell case. The standard deviation is about 0.18 dB for Sigma-0 and 0.26 cm for SSB, while the dynamic range could reach about 0.6 dB for Sigma-0 and 0.86 cm for SSB. This trend could bring impacts on the results in high-accuracy application. A possible explanation of this sinusoid trend is that, although for an individual pulse the footprint of the CRA is isotropic, the movement of the satellite in the along-track direction may elongate the radar footprint and introduce an extra anisotropic feature (the altimeter measurements are averaged to 1 Hz products, and the satellite travels ~7 km in one second, which is much larger than the ~2 km across-track resolution).

3) As for the SSHA patterns, no clear sinusoid could be identified for the moderate swell. The correlative coefficients between the SSHA and SSB are relatively small. A possible explanation is that the SSB pattern may be overwhelmed in the complicated factors that can influence the SSHA pattern. Nonetheless, if we correct the trend in SSHA, we may bring subtle improvements to the SSHA product. Given that SSHA is more accurate for SAR mode and the SSB of the two modes are comparable, we can expect that the absolute value of correlative coefficients between the SSHA and SSB would be larger for SAR mode, which has been verified by the analysis results.
4) We show the solid evidence demonstrating that the polarization configuration of the radar altimeter has little (if any) influence on the anisotropic patterns, even for SAR mode.

The results in this work show the complexity of the rationale of satellite altimeter measurements on the anisotropic ocean surface. Not only SARA but also CRA would suffer from the anisotropic errors both in Sigma-0 measurements and the SSB corrections. This finding supports the necessity of introducing the wave direction to the SSB correction algorithms for both CRA and SARA.

DATA AVAILABILITY STATEMENT

Publicly available datasets were analyzed in this study. This data can be found here: https://scihub.copernicus.eu/

AUTHOR CONTRIBUTIONS

XX: draft, writing – methodology, data processing and results explanation. KX: conceptualization. MJ: validation. BG: WW3 wave data preparation. LS: satellite altimetry data preparation. All authors have read and agreed to the published version of the manuscript.

FUNDING

This study is supported by the National Natural Science Foundation of China (Grant No. 41876209 and E0112002), the Pandeng Program of National Space Science Center, Chinese Academy of Sciences, the State Key Laboratory of Tropical Oceanography, South China Sea Institute of Oceanology, Chinese Academy of Sciences (Project No. LTO1908) and the Guangdong Basic and Applied Basic Research Foundation (No. 2019A1515012108) and research funds from the State Key Laboratory of Tropical Oceanography (No. LTOZZ2101).

ACKNOWLEDGMENTS

We thank the Copernicus Marine Environment Monitoring Service (CMEMS), ESA (European Space Agency) for providing the Sentinel-3A Geophysical Data Records (GDR) and the Archiving, Validation, and Interpretation of Satellite Oceanographic Data (AVISO) for providing Jason-3 GDR products. We also thank the National Center for Environmental Prediction (NCEP), NOAA (National Oceanic and Atmospheric Administration), for distributing the WW3 model data.

REFERENCES

Ardhuin, F. (2019). *Ocean Waves in Geosciences*. doi:10.13140/RG.2.2.16019.78888/5

Bouffard, J., Naeije, M., Banks, C. J., Calafat, F. M., Cipollini, P., Snaith, H. M., et al. (2018). CryoSat Ocean Product Quality Status and Future Evolution. *Adv. Space Res.* 62, 1549–1563. doi:10.1016/j.asr.2017.11.043

Chelton, D. B., Ries, J. C., Haines, B. J., Fu, L. L., and Callahan, P. S. (2001). "Satellite Altimetry," in *Satellite Altimetry and Earth Sciences:* A Handbook Of Techniques And Applications. *2000: Improved Electromagnetic*. Editors B. Chapron and D. Vandemark (San Diego, CA, USA: Academic), 1.

Chu, X., and He, Y. (2012). Asymmetry and Anisotropy of Microwave Backscatter at Low Incidence Angles. *IEEE Trans. Geosci. Remote Sensing* 50 (10), 4014–4024. doi:10.1109/tgrs.2012.2189010

Donlon, C., Berruti, B., Buongiorno, A., Ferreira, M.-H., Féménias, P., Frerick, J., et al. (2012). The Global Monitoring for Environment and Security (GMES) Sentinel-3 mission. *Remote Sensing Environ.* 120 (1), 37–57. doi:10.1016/j.rse.2011.07.024

Elfouhaily, T., Thompson, D. R., Chapron, B., and Vandemark, D. (2000). Improved Electromagnetic Bias Theory. *J. Geophys. Res.* 105, 1299–1310. doi:10.1029/1999jc900277

Fjortoft, R., Gaudin, J.-M., Pourthié, N., Lalaurie, J.-C., Mallet, A., Nouvel, J.-F., et al. (2014). Karin on SWOT: Characteristics of Near-Nadir Ka-Band Interferometric SAR Imagery. *IEEE Trans. Geosci. Remote Sensing* 52 (4), 2172–2185. doi:10.1109/tgrs.2013.2258402

Fu, L.-L., and Glazman, R. (1991). The Effect of the Degree of Wave Development on the Sea Stale Bias in Radar Altimetry Measurements. *J. Geophys. Res.* 96, 829–834. doi:10.1029/90jc02319

Hanson, J. L., and Phillips, O. M. (2001). Automated Analysis of Ocean Surface Directional Wave Spectra. *J. Atmos. Oceanic Technol.* 18, 177–193. doi:10.1175/1520-0426(2001)018<0277:aaoosd>2.0.co;2

Moreau, T., Aublanc, J., Rieu, P., Tison, C., Le Gac, S., and Boy, F. (2018b). "Innovative Coherent Processing Approach for Measuring Ocean Surface Parameters,". *Ocean Surface Topography Science Team Meeting, Ponta Delgada, São Miguel Island Azores Archipelago* (Portugal).

Moreau, T., Tran, N., Aublanc, J., Tison, C., Le Gac, S., and Boy, F. (2018a). Impact of Long Ocean Waves on Wave Height Retrieval from SAR Altimetry Data. *Adv. Space Res.* 62, 1434–1444. doi:10.1016/j.asr.2018.06.004

Parisot, F., Vaze, P., Loving, J., Tavernier, G., and Vuilleumier, P. (2018). "Sentinel-6/Jason-CS: Status of the Project,". *Ocean Surface Topography Science Team Meeting, Ponta Delgada, São Miguel Island Azores Archipelago* (Portugal).

Pires, N., Joana Fernandes, J., Gommenginger, C., and Scharroo, R. (2018). "Perspectives on Combining SAR Sentinel-1 Ocean Wave Parameters with Jason-3 and Sentinel-3 Estimations for SSB Models,". *Ocean Surface Topography Science Team Meeting, Ponta Delgada, São Miguel Island Azores Archipelago* (Portugal).

Raney, R. K. (1998). The delay/Doppler Radar Altimeter. *IEEE Trans. Geosci. Remote Sensing* 36 (5), 1578–1588. doi:10.1109/36.718861

Rascle, N., and Ardhuin, F. (2013). A Global Wave Parameter Database for Geophysical Applications. Part 2: Model Validation with Improved Source Term Parameterization. *Ocean Model.* 70, 174–188. doi:10.1016/j.ocemod.2012.12.001

Rémy, F., Flament, T., Blarel, F., and Benveniste, J. (2012). Radar Altimetry Measurements over Antarctic Ice Sheet: A Focus on Antenna Polarization and Change in Backscatter Problems. *Adv. Space Res.* 50, 998–1006. doi:10.1016/j.asr.2012.04.003

Stammer, D., and Cazenave, A. (2017). *Satellite Altimetry over Oceans and Land Surfaces*. Boca Raton: CRC Press, 1–608.

Toffoli, A., and Bitner-Gregersen, E. M. (2017). "Types of Ocean Surface Waves, Wave Classification," in *Encyclopedia of Maritime and Offshore Engineering* (Hoboken: John Wiley), 1–8. doi:10.1002/9781118476406.emoe077

Tracy, B., Devaliere, E.-M., Nicolini, T., Tolman, H. L., and Hanson, J. L. (2007). "Wind Sea and Swell Delineation for Numerical Wave Modeling," in 10th International Workshop on Wave Hindcasting and Forecasting & Coastal Hazards Symposium. JCOMM Tech. Rep. 41, WMO/TD-No. 1442. Paper P12.

Tran, N., and Chapron, B. (2006). Combined Wind Vector and Sea State Impact on Ocean Nadir-Viewing Ku- and C-Band Radar Cross-Sections. *Sensors* 6 (3), 193–207. doi:10.3390/s6030193

Wingham, D. J., Francis, C. R., Baker, S., Bouzinac, C., Brockley, D., Cullen, R., et al. (2006). CryoSat: A mission to Determine the Fluctuations in Earth's Land and marine Ice fields. *Adv. Space Res.* 37, 841–871. doi:10.1016/j.asr.2005.07.027

Xu, X. Y., Liu, H. G., and Yang, S. B. (2010). Mechanisms and System Design of Satellite Interferometric Synthetic Aperture Radar Altimeter. *ITTA-GRS Proc.* 2010, 209–211. doi:10.1109/IITA-GRS.2010.5203760

Conflict of Interest: The authors declare that the research was conducted in the absence of any commercial or financial relationships that could be construed as a potential conflict of interest.

Publisher's Note: All claims expressed in this article are solely those of the authors and do not necessarily represent those of their affiliated organizations, or those of the publisher, the editors and the reviewers. Any product that may be evaluated in this article, or claim that may be made by its manufacturer, is not guaranteed or endorsed by the publisher.

frontiers in Earth Science

ORIGINAL RESEARCH
published: 09 November 2021
doi: 10.3389/feart.2021.730777

Evaluation of Marine Gravity Anomaly Calculation Accuracy by Multi-Source Satellite Altimetry Data

Shanwei Liu[1], Yinlong Li[2], Qinting Sun[2], Jianhua Wan[1]*, Yue Jiao[1] and Jinghui Jiang[1]*

[1]College of Oceanography and Space Informatics, China University of Petroleum, Qingdao, China, [2]School of Geosciences, China University of Petroleum, Qingdao, China

OPEN ACCESS

Edited by:
Cheinway Hwang,
National Chiao Tung University, Taiwan

Reviewed by:
Luis Gomez,
University of Las Palmas de Gran Canaria, Spain
Saumitra Mukherjee,
Jawaharlal Nehru University, India
Mukesh Gupta,
Catholic University of Louvain, Belgium
Maofei Jiang,
Key Laboratory of Microwave Remote Sensing (CAS), China
Tilo Schöne,
German Research Centre for Geosciences, Helmholtz Centre Potsdam, Germany

***Correspondence:**
Jianhua Wan
wjh66310@163.com
Qinting Sun
qintingsun20200910@163.com

Specialty section:
This article was submitted to Environmental Informatics and Remote Sensing, a section of the journal Frontiers in Earth Science

Received: *25 June 2021*
Accepted: *04 October 2021*
Published: *09 November 2021*

Citation:
Liu S, Li Y, Sun Q, Wan J, Jiao Y and Jiang J (2021) Evaluation of Marine Gravity Anomaly Calculation Accuracy by Multi-Source Satellite Altimetry Data. Front. Earth Sci. 9:730777. doi: 10.3389/feart.2021.730777

The purpose of this paper is to analyze the influence of satellite altimetry data accuracy on the marine gravity anomaly accuracy. The data of 12 altimetry satellites in the research area (5°N–23°N, 105°E–118°E) were selected. These data were classified into three groups: A, B, and C, according to the track density, the accuracy of the altimetry satellites, and the differences of self-crossover. Group A contains CryoSat-2, group B includes Geosat, ERS-1, ERS-2, and Envisat, and group C comprises T/P, Jason-1/2/3, HY-2A, SARAL, and Sentinel-3A. In Experiment I, the 5′×5′ marine gravity anomalies were obtained based on the data of groups A, B, and C, respectively. Compared with the shipborne gravity data, the root mean square error (RMSE) of groups A, B, and C was 4.59 mGal, 4.61 mGal, and 4.51 mGal, respectively. The results show that high-precision satellite altimetry data can improve the calculation accuracy of gravity anomaly, and the single satellite CryoSat-2 enables achieving the same effect of multi-satellite joint processing. In Experiment II, the 2′×2′ marine gravity anomalies were acquired based on the data of groups A, A + B, and A + C, respectively. The root mean square error of the above three groups was, respectively, 4.29 mGal, 4.30 mGal, and 4.21 mGal, and the outcomes show that when the spatial resolution is satisfied, adding redundant low-precision altimetry data will add pressure to the calculation of marine gravity anomalies and will not improve the accuracy. An effective combination of multi-satellite data can improve the accuracy and spatial resolution of the marine gravity anomaly inversion.

Keywords: marine gravity anomaly, shipborne gravity data, accuracy evaluation, CryoSat-2, South China Sea and its adjacent regions

INTRODUCTION

Because the density distribution inside the actual Earth is very uneven, the actual observed gravity value always deviates from the theoretical normal gravity value, and the difference between the observed gravity field and the field of a reference model is called the gravity anomaly (Kaban et al., 2011). Altimeter satellites can periodically obtain high-resolution, all-weather, and long-term global ocean observation data except the polar region, which is of great significance to the study of gravity anomaly inversion in large-scale sea areas. Studies have shown that the error of satellite altimetry data is proportional to the inversion error of gravity anomaly (Li et al., 2015). Therefore, research on the accuracy of satellite altimetry data and the selection of suitable satellite altimetry data combination can improve the accuracy of inversion marine gravity anomaly.

Up to now, 18 altimetry satellites have been launched successively. Moreover, we have an uninterrupted satellite altimetry dataset for more than 30 years. It provides data support for the study of marine gravity anomaly inversion from multi-source satellite altimetry data fusion. After successful acquisition of satellite altimetry data such as T/P (Traon et al., 1994), Jason-1 (Dorandeu et al., 2004), Jason-2 (Ablain et al., 2010), SARAL (Prandi et al., 2015), and HY-2A (Peng et al., 2015), the launch agencies and researchers evaluated them systematically and studied the accuracy and stability of the altimetry system and so on. There are certain differences in period, spatial resolution, and altitude measurement precision among satellite altimetry data. After evaluating the new and old satellite altimetry systems, the rules of multi-source satellite altimetry data fusion can be determined for marine gravity anomaly inversion. As a whole, the accuracy of the satellite altimetry data is constantly improving. And with the increasing accuracy of satellite altimetry data, the spatial resolution and accuracy of gravity anomaly inversion can be improved by combining the newly launched satellite altimetry data.

Satellite altimetry data contain abundant high-frequency information, which provides strong support for marine gravity research. Joint multiple-source altimetry data can improve the accuracy and resolution of marine gravity anomaly inversion. At present, a host of scholars have done numerous work in the marine gravity field (Huang et al., 2001; Li et al., 2003; Sandwell et al., 2013; Sandwell et al., 2014; Liang et al., 2020; Nguyen et al., 2020; Wan et al., 2020; Wang et al., 2020). The accuracy of marine gravity anomaly inversion from satellite altimetry data has reached 4 mGal–10 mGal approximately. The main methods to retrieve marine gravity anomalies from satellite altimetry data include least-squares collocation, Stokes inverse algorithm, and inverse Vening Meinesz formula method.

The least-squares collocation method is the first method to invert marine gravity anomalies using satellite altimetry data. Hofmann-Wellenhof introduced this method in physical geodesy (Hofmann-Wellenhof, 2005) in detail, and then Sandwell (Sandwell, 1984) and Hwang (Hwang, 1989; Hwang et al., 1995) further studied and improved this method and used the improved method to invert marine gravity anomalies. This method has favorable calculation stability, especially in offshore areas. In addition, this method can fuse multiple-source gravity data to improve the accuracy of marine gravity anomaly inversion (Wang et al., 2005). However, this method has a large amount of calculation, which is only suitable for calculating marine gravity anomalies in small regions and is not suitable for the calculation of large-scale marine gravity anomalies. The Stokes inverse algorithm is evolved from the Stokes formula. Xu and others used this method to invert the $30' \times 30'$ marine gravity anomaly in offshore China (Xu et al., 1999) with an accuracy of 3.5 mGal. This method can eliminate the influence of sea surface topography, but with less robustness. The vertical deviation method is also known as the inverse Vening Meinesz formula method, and the marine gravity anomaly can be calculated by using the inverse Vening Meinesz formula with the vertical deviation as the initial value. This method is currently the main method to retrieve marine gravity anomalies with multi-source altimetry satellite data. A multitude of team scholars use this method to retrieve marine gravity anomalies, such as Sandwell (1992), Knudsen (1991), and Andersen (1998), and others invert global marine gravity anomalies by using Geosat/GM and ERS-1 altimetry data with this method. Li and others used this method to invert marine gravity anomalies in the offshore China and its adjacent areas (Wang et al., 2001).

The vertical deviation method for inversion of marine gravity anomalies is currently the most widely used method with the most effective inversion. However, in the process of joint inversion of multi-source satellite altimetry data, the method does not consider the influence of uneven accuracy of multi-source satellite altimetry data on joint inversion and does not consider whether the joint multi-source satellite altimetry data meet the data volume requirements of the inversion resolution. In this paper, we evaluate the accuracy of each satellite's altimetry data, selectively combine the altimetry satellite data, and analyze the influence of various combinations of different satellite altimetry data on the inversion of marine gravity anomaly. The most suitable combination of satellite altimetry data is also selected by evaluating the accuracy with shipborne gravity data. Finally, the $1' \times 1'$ marine gravity anomaly is obtained by combining the multi-source satellite altimetry data inversion.

DATA AND METHODS

While inverting the marine gravity anomaly with multi-source satellite altimetry data, fine processing on every satellite's altimetry data can reduce the influence of data error and improve the accuracy of the marine gravity anomaly inversion, including data screening and editing, collinear adjustment, and cross point adjustment.

Satellite Altimetry Data

Geosat, ERS-1, T/P, ERS-2, Jason-1, Envisat, Jason-2, CryoSat-2, HY-2A, SARAL, Jason-3, and Sentinel-3A satellite altimetry data were selected for joint processing in this paper, including Exact Repeat Mission (ERM) and Geodetic Mission (GM) data. T/P, Envisat, Jason-1, Jason-2, Jason-3, and SARAL satellite data can be viewed and downloaded from the AVISO website (https://www.aviso.altimetry.fr/). Geosat satellite data can be viewed and downloaded from the NOAA website (https://data.noaa.gov/dataset/dataset/data-records-derived-from-geosat-geodetic-mission-gm-and-exact-repeat-mission-erm-data-fro-19891). ERS-1, ERS-2, CryoSat-2, and Sentinel-3A satellite data can be viewed and downloaded from the ESA website (https://www.esa.int/). HY-2A satellite data can be viewed and downloaded from the NSOAS website (https://osdds.nsoas.org.cn/MarineDynamic). The details are listed in **Table 1** and **Table 2**.

Shipborne Gravity Data

The shipborne gravity data collected in this paper are derived from a special project for comprehensive survey and evaluation of China's offshore ocean and are acquired by different departments in multiple time periods of measurement, distributed in different

TABLE 1 | Information of the satellite altimetry GM data.

Altimetry data/GM	Cycle	Time span	Repeat cycle (days)	Ground track separation at equator (km)
Geosat	001–025	1985.03–1986.09	17	4
ERS-1	139–144	1994.04–1995.03	35	8
Jason-1	500–537	2012.05–2013.06	10	—
Jason-2	500–514	2017.07–2017.12	10	—
SARAL[a]	100–115	2016.07–2018.01	35	—

[a]*The satellite is in the orbit.*

TABLE 2 | Information of the satellite altimetry ERM data.

Altimetry data/ERM	Cycle	Time span	Repeat cycle (days)	Ground track separation at equator (km)
Geosat	001–043	1986.11–1988.11	17	164
ERS-1	083–100	1992.04–1993.12	35	80
	145–156	1995.03–1996.05	35	80
T/P	001–364	1992.09–2002.08	10	315
T/P (after orbit change)	369–481	2002.09–2005.10	10	315
ERS-2	001–085	1995.05–2003.07	35	80
Jason-1	001–258	2002.01–2009.01	10	315
Jason-1 (after orbit change)	263–355	2009.02–2011.08	10	315
Envisat	007–113	2002.06–2012.03	35	80
Jason-2	001–303	2008.07–2016.09	10	315
Jason-2 (after orbit change)	305–327	2016.10–2017.05	10	315
CryoSat-2[a]	002–008	2011.01–2017.12	369	7.5
HY-2A	050–075	2013.08–2014.08	14	207
SARAL[a]	001–035	2013.03–2016.07	35	80
Jason-3[a]	001–066	2016–02-2017–12	10	315
Sentinel-3A[a]	018–023	2017.05–2017.10	27	104

[a]*The satellite is in the orbit.*

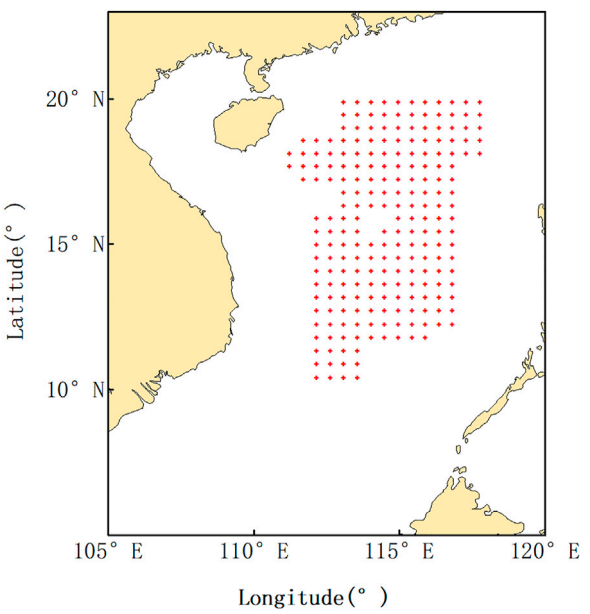

FIGURE 1 | Distribution map of shipborne gravity data. The red mark is the location of the ship gravity anomaly.

regions. The data are finely processed to obtain shipborne gravity data anomalies with a spatial resolution of about 30′ (Huang, 1990; Huang, 1993; Li et al., 2002; Liu et al., 2012; Ke et al., 2015). In this paper, shipborne gravity data from the South China Sea with low spatial resolution are used, and their distribution is shown in **Figure 1**. We take the shipborne gravity data as the real value, match the satellite gravity anomaly with the location where the shipborne data points are located, and evaluate the accuracy of the experimental results by comparing the inverse marine gravity anomaly with the shipborne gravity data.

Data Preprocessing

The data accuracy of China offshore and its vicinity was analyzed, which provides the basis for the joint rules of multiple-source satellite altimetry data. First, in order to ensure the data quality of the study area, the land, sea ice, rainfall, and other invalid or polluted observation points were deleted. Data were edited by using marking and threshold screening criteria in the altimetry satellite data handbook (Blanc et al., 1996; National Oceanic and Atmospheric Administration (NOAA), 1997; Gilbert et al., 2014; Bronner et al., 2016; Dumont et al., 2017; Picot et al., 2018; Soussi et al., 2018; Mertz et al., 2019; National Satellite Ocean

TABLE 3 | Statistical results before and after collinear and crossover adjustment.

Altimetry data	Cycle (days)	Number of intersections	Intersection point discrepancy value before collinear adjustment, RMSE (cm)	Intersection point discrepancy value after collinear adjustment, RMSE (cm)	Intersection point discrepancy value after crossover adjustment, RMSE (cm)
Geosat	17	853	21.15	16.41	12.25
ERS-1	35	1934	21.49	19.00	11.70
T/P	10	236	21.55	15.88	9.04
T/P (after orbit change)	10	233	18.14	15.97	9.65
ERS-2	35	1946	24.67	19.89	13.11
Jason-1	10	221	16.32	12.67	8.12
Jason-1 (after orbit change)	10	228	19.13	16.01	9.03
Envisat	35	2034	18.14	16.04	12.05
Envisat (after orbit change)	30	1,533	21.53	19.48	15.14
Jason-2	10	246	17.02	12.55	8.52
Jason-2 (after orbit change)	10	246	14.78	11.58	6.71
CryoSat-2	369	9,220	26.18	20.74	16.41
HY-2A	14	305	19.92	14.52	9.96
SARAL	35	2076	19.21	13.13	9.86
Jason-3	10	245	17.24	13.95	8.13
Sentinel-3A	27	971	15.21	12.38	8.82

Application Service (NSOAS), 2019; European Space Agency (ESA), 2019; Bignalet-Cazalet et al., 2021).

According to the characteristics of the repeated orbits of altimetry satellites, the ERM data of each altimetry satellite were collinearly processed, respectively (Jiang et al., 2002). The observed values on the same pass number of different cycles were adjusted to the reference orbit, so as to weaken the influence of sea surface time variation and random noise (Braun et al., 2004). The differences of self-crossover before and after collinear adjustment are described in **Table 3**.

The ERM data after collinear adjustment still contain system deviation, radial orbit error, and so on. In order to eliminate these errors as much as possible, crossover adjustment (Zhang, 2015) for the satellite altimetry data after collinear adjustment was carried out, and the differences before and after crossover adjustment are shown in **Table 3**.

It is shown that the differences of self-crossover were reduced with different degrees after collinear adjustment, and that of SARAL was reduced by 6.08 cm at most. The RMSE of CryoSat-2 after collinear adjustment was reduced less because the cycle of CryoSat-2 is 1 year and the time-varying effect of sea surface is large. The RMSEs were reduced with different degrees after crossover adjustment. Among them, those of T/P, Jason-1/2/3, HY-2A, SARAL, and Sentinel-3A were reduced to less than 10 cm; those of Geosat, ERS-1, ERS-2, and Envisat were all above 10 cm, with slightly poor accuracy; and CryoSat-2 had the largest RMSE, which is limited by its long cycle of 365 days besides its own accuracy error.

GM data have non-repeat orbits. GM data underwent crossover adjustment without collinear adjustment.

After crossover adjustment, satellite data are processed separately according to the grouping. Ellipsoid and orbit frame unification is carried out for the satellite data in the same group (Din et al., 2019), and all data are calibrated to the TP reference. Then, preprocessing satellite altimetry data were obtained through crossover adjustment between each satellite's data.

Marine Gravity Anomaly Inversion Method

In this paper, the Hwang method (Hwang et al., 1998; Hwang et al., 2002) was used to invert the vertical deviation, and then marine gravity anomaly was obtained by using the inverse Vening Meinesz formula (Hwang et al., 1996; Hwang, 1998).

The remove–restore method (Sansò et al., 2013) was used to reflect the high-frequency information in the satellite altimetry data and the long-wave advantages of the gravity field model, which improved the inversion accuracy. The remove–restore technique consists of two steps. The first step is to remove the model interpolation geoid height from the geoid height, and then the residual geoid height is obtained. The second step is to restore the effect of the model gravity field and the inner circle marine gravity field to the residual marine gravity field. The final grid marine gravity anomaly (as shown in **Figure 2**) is composed of three parts: the EGM2008 gravity field model gravity anomaly (U.S. National Geospatial-Intelligence Agency EGM Development Team, 2010), the residual marine gravity anomaly, and the inner circle marine gravity anomaly. The steps to calculate the grid point gravity anomaly are as follows:

1) The geoid height at the measurement point is obtained by subtracting the DOT2008A sea surface topography model (U.S. National Geospatial-Intelligence Agency EGM Development Team, 2010) from the preprocessing satellite altimetry data.
2) The residual geoid height is obtained by subtracting the EGM2008 model interpolation geoid height from the geoid height.
3) The residual vertical deviation along the track and the residual vertical deviation grid data is obtained by using the Hwang method.

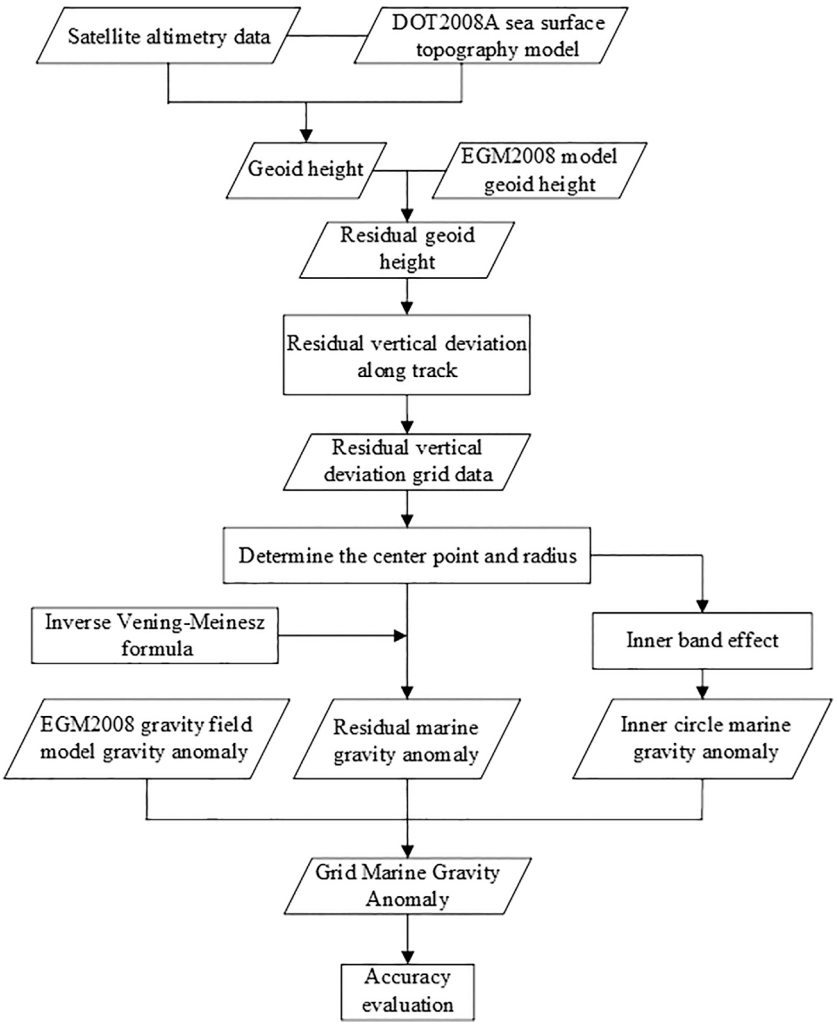

FIGURE 2 | Flowchart of gravity anomaly inversion.

4) The residual marine gravity anomaly is obtained by using the inverse Vening Meinesz formula, with an integral radius of 30′.
5) The inner circle marine gravity anomaly is obtained by using the Vening Meinesz formula.
6) The final grid marine gravity anomaly is obtained by adding the EGM2008 model marine gravity anomaly, residual marine gravity anomaly, and inner circle marine gravity anomaly.
7) The accuracy of grid marine gravity anomaly is evaluated by using shipborne gravity data as the real value. The grid marine gravity anomaly was interpolated to the shipborne data points by taking the shipborne data points as the center and 12′ as the radius of the circle. The interpolation method is the inverse distance weight (Hartmann et al., 2018). Finally, the interpolated gravity data are compared with the shipborne gravity data.

TABLE 4 | Experimental design and grouping.

Experiment number	Spatial resolution	Experimental data		
I	5′×5′	A	B	C
II	2′×2′	A	A + B	A + C

EXPERIMENTS

Experimental Setup

The experimental groups in this paper are shown in **Table 4**. All satellite altimetry data are divided into three groups according to the altimetry satellite orbit density, accuracy, and self-crossing point discrepancy. Group A contains the new CryoSat-2 single

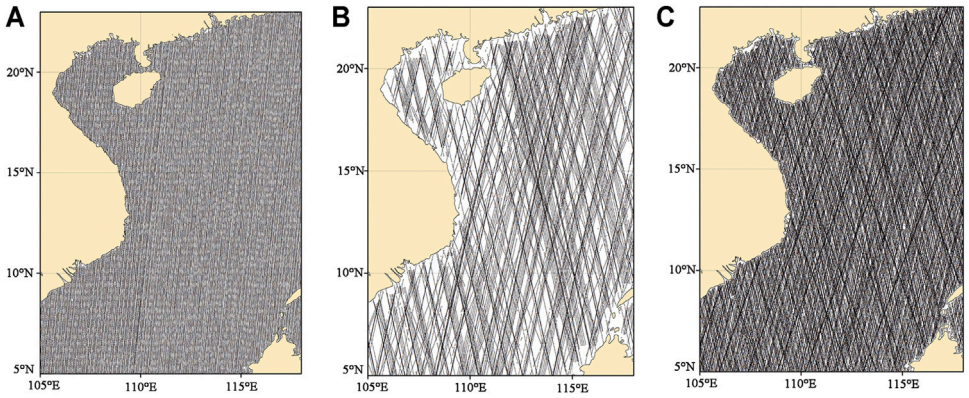

FIGURE 3 | Ground tracks corresponding to the satellite altimetry data of groups A **(A)**, B **(B)**, and C **(C)**.

satellite data, group B includes Geosat, ERS-1, ERS-2, and Envisat with lower accuracy, and group C contains T/P, Jason-1/2/3, HY-2A, SARAL, and Sentinel-3A with higher accuracy. The CryoSat-2 single satellite is added to low-precision group B to form the A + B group and to high-precision group C to form the A + C group. Firstly, $5' \times 5'$ marine gravity anomaly data were set up by using groups A, B, and C, respectively, and the accuracy results of marine gravity anomaly inversion corresponding to each group were analyzed. Then, $2' \times 2'$ marine gravity anomaly data were established by using the A, A + B, and A + C groups to test the impact of the addition of new satellites on the inversion accuracy.

According to the distribution range of shipborne gravity data, the gravity anomaly inversion study area of the experiment is set as 5°N–23°N, 105°E–118°E. The ground tracks corresponding to the satellite altimetry data of groups A, B, and C are shown in **Figure 3**.

Results and Analysis of Marine Gravity Anomaly Inversion With Different Satellite Altimetry Data Combination

The experiments were carried out according to the marine gravity anomaly inversion method with $30'$ as the integral radius, and the $5' \times 5'$ and $2' \times 2'$ marine gravity anomalies in the study area were calculated, respectively, by using the preprocessed data of each group. **Figure 4** shows the $5' \times 5'$ marine gravity anomaly results calculated from the three groups A, B, and C in Experiment I and the $2' \times 2'$ marine gravity anomaly results calculated from the three groups A, A + B, and A + C in Experiment II.

It can be seen from **Figure 4** that the inversion of the $5' \times 5'$ and $2' \times 2'$ marine gravity anomalies can clearly reflect the distribution of large gravity anomalies in the ocean, and the $2' \times 2'$ marine gravity anomaly has more details than $5' \times 5'$. Comparing the inverted six kinds of marine gravity anomaly results with the shipborne gravity data, the accuracy evaluation results are shown in **Table 5**, and the scatter plot compared with shipborne gravity data is shown in **Figure 5**.

1) Accuracy evaluation of $5' \times 5'$ marine gravity anomaly

The RMSE of group A, B, and C satellite altimetry data is 4.59 mGal, 4.61 mGal, and 4.51 mGal, respectively. The overall maintenance is around 4 mGal, and the effect is favorable. A single satellite group A inversion result is close to that of high-precision satellite group C. The CryoSat-2 single altimetry satellite can achieve the effect of multi-source satellite joint, and its accuracy is slightly higher than that of low-precision altimetry satellite joint inversion. **Figure 5A** shows a scatter plot of the comparison between the group B data and the shipborne gravity data, and Figure 5B shows the scatter plot of the comparison between the group C data and the shipborne gravity data, both of which are distributed on both sides of a straight line $y = x$. But the overall deviation of group B is larger than that of group C. The results show that high-precision altimetry data can improve the inversion accuracy of gravity anomalies.

2) Accuracy evaluation of $2' \times 2'$ marine gravity anomaly

The RMSE of group A, B, and C satellite altimetry data is 4.29 mGal, 4.30 mGal, and 4.21 mGal, respectively. Compared with the result of $5' \times 5'$ marine gravity anomaly, the RMSE has a certain reduction. **Figures 5C,D** show scatter plots of the comparison between group A + B and A + C data and shipborne gravity data, respectively. The overall deviation degree is better than that in **Figures 5A,B**. The results show that the inversion results of CryoSat-2 alone are higher than the joint inversion results of the low-precision satellite group and lower than the joint inversion results of the high-precision satellite group. On the basis of CryoSat-2 data, two groups of data B and C were added, respectively, and the calculation accuracy of gravity anomaly has been reduced and improved, respectively. It is shown that the calculation accuracy of gravity anomalies can be reduced by adding redundant data with lower accuracy when the spatial resolution is satisfied, and the effective combination of multi-source satellite altimetry data can improve the accuracy of marine gravity anomaly calculations and spatial resolution.

By comparing the results of $5' \times 5'$ and $2' \times 2'$ gravity anomalies by using the altimetry data of group A satellites, the accuracy of

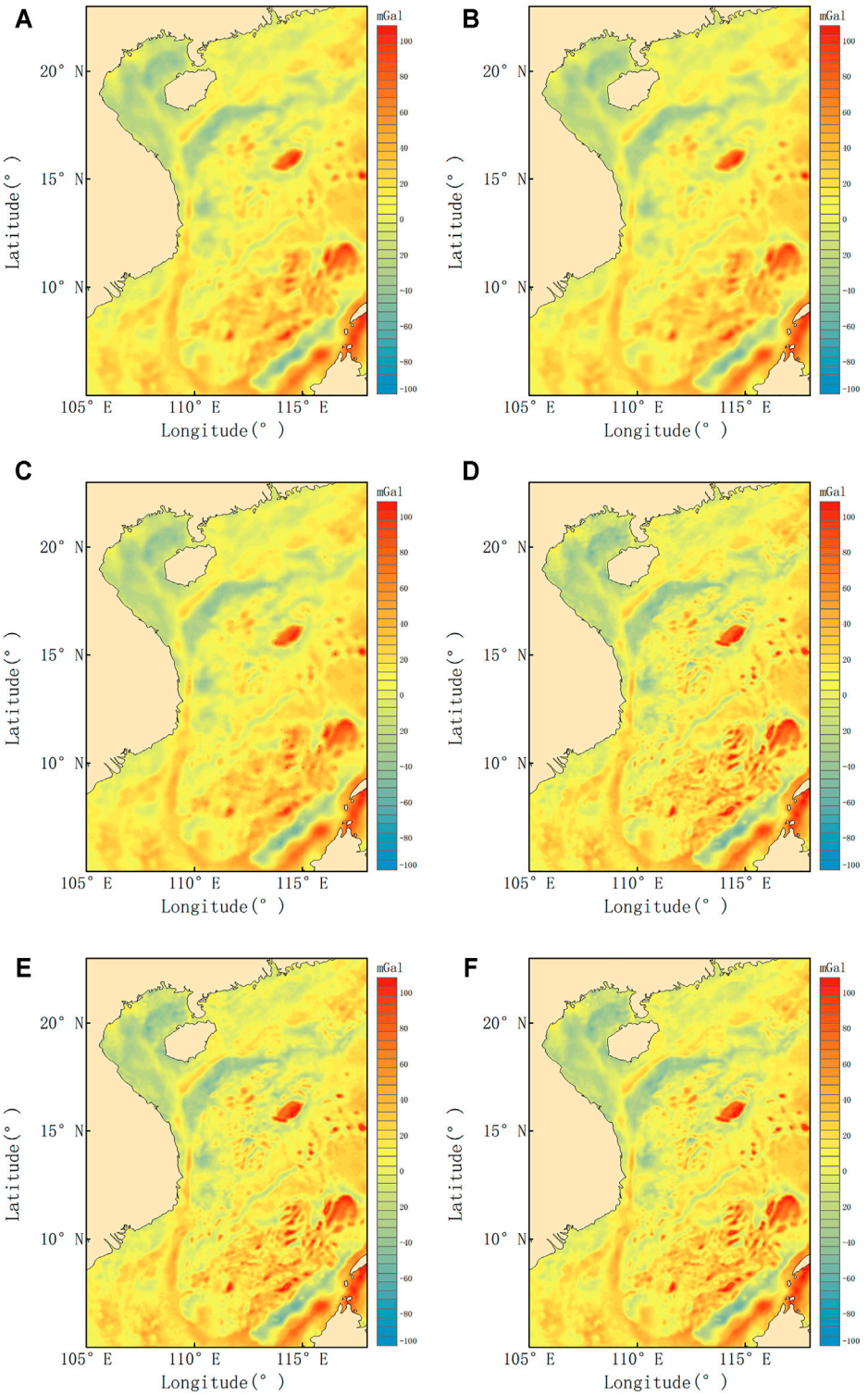

FIGURE 4 | Map of the marine gravity anomaly in the study area: 5′×5′ marine gravity anomaly results calculated by the three groups A **(A)**, B **(B)**, and C **(C)** in Experiment I and 2′×2′ marine gravity anomaly results calculated by the three groups A **(D)**, A + B **(E)**, and A + C **(F)** in Experiment II.

TABLE 5 | 5′×5′ and 2′×2′ satellite gravity inversion results compared with shipborne gravity anomaly data (unit: mGal).

Resolution	Group	Max.	Min.	Mean	RMSE
5′×5′	A	13.84	−12.49	1.89	4.59
	B	12.98	−12.71	1.87	4.61
	C	14.57	−11.97	1.94	4.51
2′×2′	A	11.98	−10.47	1.76	4.29
	A + B	12.14	−10.97	1.76	4.30
	A + C	11.62	−11.12	1.74	4.21

gravity anomaly calculation has increased by 0.30 mGal after the spatial resolution is improved. Combined with the orbit density of CryoSat-2 data, it is shown that the CryoSat-2 single satellite can satisfy the calculation requirements of 2′ × 2′ gravity anomaly.

All the mean values are above 1 mGal. Indeed, the marine gravity anomaly inversion is slightly higher than the shipborne gravity data. The accuracy of the marine gravity anomalies obtained by combining the satellites of groups A, B, and C is higher than that of the marine gravity anomalies calculated by each group individually. The highest accuracy of the marine gravity anomaly is obtained by combining CryoSat-2 with group C, which has higher accuracy, in the process of calculating the marine gravity anomaly with high spatial resolution. It indicates that the combination of multi-source satellite data can effectively improve the accuracy of gravity anomaly calculation, and the single satellite CryoSat-2 enables achieving the same effect of multi-satellite joint processing.

Multi-Source Satellite Data Inversion of 1′×1′ Marine Gravity Anomaly

According to the above analysis, the highest accuracy of marine gravity anomaly is obtained by using CryoSat-2 combined with the higher accuracy group C. The accuracy of TP series satellites in group C is higher, but the T/P, Jason-1, Jason-2, and Jason-3 satellite data have the same ground track. Therefore, TP and Jason-1 data with a relatively old time in group C are not used in this paper.

In this paper, we used CryoSat-2, SARAL/ERM, SARAL/GM, Jason-2/ERM, Jason-2/GM, Jason-3, Sentinel-3A, and HY-2A

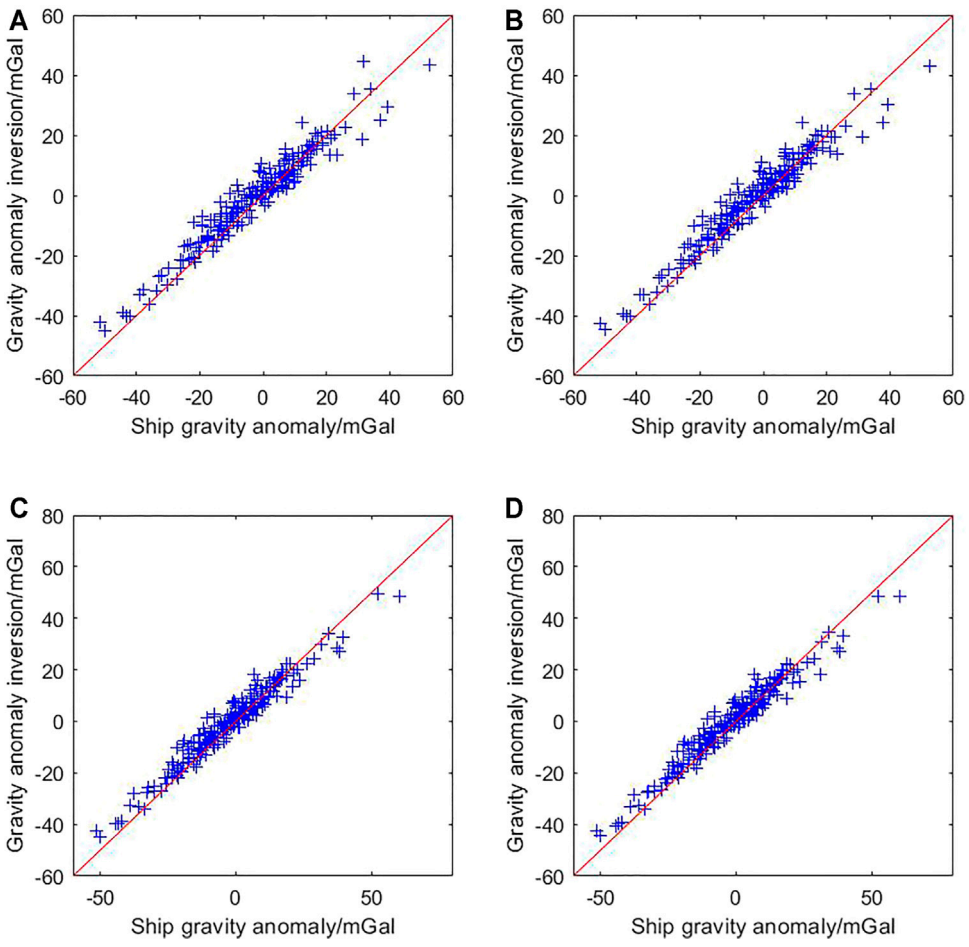

FIGURE 5 | Scatter plot image compared with shipborne gravity anomaly data. Comparison of the gravity anomaly data obtained by the B **(A)**, C **(B)**, A + B **(C)**, and A + C **(D)** satellite altimetry data inversion with the shipborne gravity anomaly data. The red line is the y = *x* straight line. The blue mark is the value corresponding to the gravity anomaly inversion data and the shipborne gravity anomaly data.

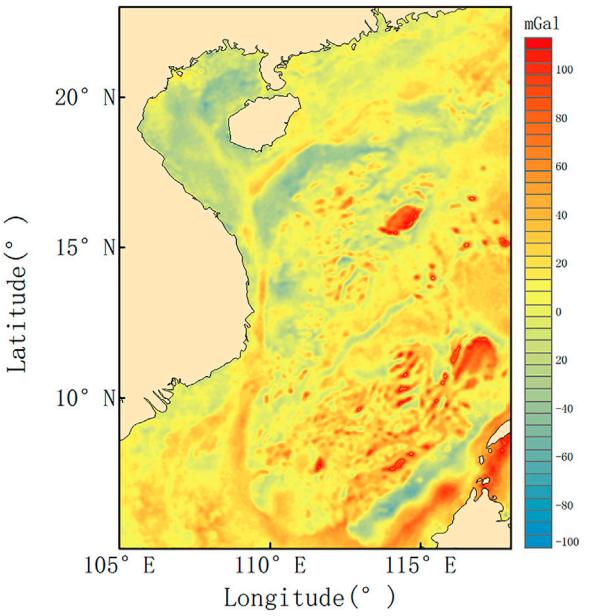

FIGURE 6 | Map of the 1′×1′ marine gravity anomaly in the study area.

TABLE 6 | Models and inversion data statistical results compared with shipborne gravity anomaly data (unit: mGal).

	Max.	Min.	Mean	RMSE
EGM2008, shipborne gravity data	12.10	−11.31	1.52	4.01
Sandwell V25.1, shipborne gravity data	11.33	−8.53	1.59	3.38
Inversion data, shipborne gravity data	11.51	−9.84	1.76	3.45

satellite altimetry data to invert the gravity anomalies. These data are evenly distributed without blind areas and meet the 1′×1′ gravity anomaly inversion accuracy. The obtained 1′×1′ marine gravity anomalies are shown in **Figure 6**.

It can be seen from Figure 6 that the 1′×1′ marine gravity anomaly can better reflect the details of gravity distribution. The internationally recognized global gravity anomaly models are the EGM2008 model and Sandwell V25.1 model, but these two models are less applicable to regional gravity anomalies. The gravity data obtained by shipboard measurements are more responsive to local gravity anomalies. Therefore, the results of the EGM2008 model gravity anomaly, the Sandwell V25.1 gravity anomaly, and the inversion data of this paper are compared with the shipborne gravity anomaly data, respectively, and the comparison results are shown in **Table 6**.

From the results, it can be seen that the overall root mean square error of the 1′×1′ gravity anomaly inversion using the remove–restore method in combination with the EGM2008 gravity field model is 3.45 mGal, which is better than the EGM2008 gravity field model comparison value of 4.01 mGal. It is comparable to the Sandwell V25.1 comparison value of 3.38 mGal.

CONCLUSION

In this paper, 12 altimetry satellites, such as CryoSat-2, Geosat, ERS-1, ERS-2, Envisat, T/P, Jason-1/2/3, HY-2A, SARAL, and Sentinel-3A, are selected to carry out gravity anomaly calculation experiments in groups. The results show the following:

1) High-precision altimetry data can improve the calculation accuracy of gravity anomalies. CryoSat-2 has a better measurement accuracy and higher orbit density. So, a single altimetry satellite can achieve the effect of multi-source altimetry satellite fusion.
2) When the spatial resolution meets the requirements, the accuracy of marine gravity anomaly has no significant impact by adding redundant low-precision altimetry data, but it will increase the calculation pressure.

DATA AVAILABILITY STATEMENT

Publicly available datasets were analyzed in this study. These data can be found here: AVISO website (https://www.aviso.altimetry.fr/), ESA (European Space Agency) (https://earth.esa.int/), National Oceanic and Atmospheric Administration (NOAA; https://www.nesdis.noaa.gov/), and NSOAS (National Satellite Ocean Application Service) (http://www.nsoas.org.cn/eng/).

AUTHOR CONTRIBUTIONS

SL and JW conceptualized and designed the study. SL was involved in data quality control. QS and YL were responsible for data collection and scientific analysis. QS, YJ, and JJ wrote the manuscript. All authors contributed to the article and approved the submitted version.

FUNDING

This research was supported by the Fundamental Research Funds for the Central Universities (17CX02071), the NSFC (61571009), and the Key R&D Program of Shandong Province (2018GHY115046).

ACKNOWLEDGMENTS

The authors would like to thank the editors and would also like to thank the AVISO website of the French Space Center (CNES) (https://www.aviso.altimetry.fr/), ESA (European Space Agency) (https://earth.esa.int/), National Oceanic and Atmospheric Administration (NOAA) https://www.nesdis.noaa.gov/), and NSOAS (National Satellite Ocean Application Service) (http://www.nsoas.org.cn/eng/) for providing the satellite altimetry data.

REFERENCES

Ablain, M., Philipps, S., Picot, N., and Bronner, E. (2010). Jason-2 Global Statistical Assessment and Cross-Calibration with Jason-1. *Mar. Geodesy* 33, 162–185. doi:10.1080/01490419.2010.487805

Andersen, O. B., and Knudsen, P. (1998). Global Marine Gravity Field from the ERS-1 and Geosat Geodetic Mission Altimetry. *J. Geophys. Res.* 103, 8129–8137. doi:10.1029/97JC02198

Bignalet-Cazalet, F., Couhert, A., Queruel, N., Urien, S., Carrere, L., Tran, N., et al. (2021). SARAL/AltiKa Products Handbook. SALP-MU-M-OP-15984-CN, Issue: 3.1. Available online at: https://www.aviso.altimetry.fr/fileadmin/documents/data/tools/SARAL_Altika_products_handbook.pdf. (Accessed August 10, 2021).

Blanc, F., Borra, M., Boudou, P., D'Alessio, S., Gaspar, P., Greenwood, N., et al. (1996). Aviso User Handbook: Merged Topex/Poseidon Products. AVI-NT-02-101-CN, Issue 3.1. Available online at: https://www.aviso.altimetry.fr/fileadmin/documents/data/tools/hdbk_tp_gdrm.pdf. (Accessed August 10, 2021).

Braun, A., Yi, Y., and Shum, C. K. (2004). Altimeter Collinear Analysis. Satellite Altimetry and Gravimetry: Theory and Applications. Lecture Notes. Available at: https://geodesy.geology.ohio-state.edu/course/gs873.2013/lectures/alt_collinear_analysis.pdf. (Accessed August 10, 2021).

Bronner, E., Picot, N., Desjonqueres, J. D., Desal, S., Hausman, L., Carrere, L., et al. (2016). Jason-1 Products Handbook. SAL-MU-M5-OP-13184-CN, Issue 3.1. Available online at: https://www.aviso.altimetry.fr/fileadmin/documents/data/tools/hdbk_j1_gdr.pdf. (Accessed August 10, 2021).

Din, A. H. M., Zulkifli, N. A., Hamden, M. H., and Aris, W. A. W. (2019). Sea Level Trend over Malaysian Seas from Multi-Mission Satellite Altimetry and Vertical Land Motion Corrected Tidal Data. *Adv. Space Res.* 63 (11), 3452–3472. doi:10.1016/j.asr.2019.02.022

Dorandeu, J., Ablain, M., FAUGèRE, Y., Mertz, F., Soussi, B., and Vincent, P. (2004). Jason-1 Global Statistical Evaluation and Performance Assessment: Calibration and Cross-Calibration Results. *Mar. Geodesy* 27, 345–372. doi:10.1080/01490410490889094

Dumont, J. P., Rosmorduc, V., Carrere, L., Picot, N., Bronner, E., Couhert, A., et al. (2017). OSTM/Jason-2 Products Handbook. SALP-MU-M-OP-15815-CN, Issue: 1.11. Available online at: https://www.aviso.altimetry.fr/fileadmin/documents/data/tools/hdbk_j2.pdf. (Accessed August 10, 2021).

European Space Agency (ESA) (2019). Sentinel-3 Altimetry Technical Guide. Available online at: https://sentinel.esa.int/web/sentinel/technical-guides/sentinel-3-altimetry/. (Accessed August 10, 2021).

Gilbert, L., Baker, S., Dolding, C., Vernier, A., Brockley, D., Martinez, B., et al. (2014). Reaper Product Handbook for ERS Altimetry Reprocessed Products. REA-UG-PHB-7003, Issue 3.1. Available online at: https://earth.esa.int/eogateway/documents/20142/37627/Reaper-Product-Handbook-3.1.pdf/bfc28740-c732-ab17-40d3-309ab65c3743.

Hartmann, K., Krois, J., and Waske, B. (2018). *E-learning Project SOGA: Statistics and Geospatial Data Analysis*. Freie Universitaet Berlin: Department of Earth Sciences. Available online at: https://www.geo.fu-berlin.de/en/v/soga/Geodata-analysis/geostatistics/Inverse-Distance-Weighting/index.html.

Hofmann-Wellenhof, B., and Moritz, H. (2005). *Physical Geodesy*. Berlin: Springer.

Huang, M. (1990). Examination, Adjustment and Precision Estimation of Half-Systematic Error in Marine Gravity Surveying. *Mar. Sci. Bull.* 9, 81–86. CNKI: SUN: HUTB.0.1990-04-012.

Huang, M. (1993). Marine Gravity Survey Line Network Adjustment. *Acta Geod. Cartogr. Sin.* 22, 103–110. CNKI:SUN:CHXB.0.1993-02-003. doi:10.1108/eb005954

Huang, M., Zhai, G., and Guan, Z. (2001). On the Recovery of Gravity Anomalies from Altimeter Data. *Acta Geod. Cartogr. Sin.* 30, 179–184. doi:10.3321/j.issn:1001-1595.2001.02.014

Hwang, C. (1989). *High Precision Gravity Anomaly and Sea Surface Height Estimation from Geos-3/Seasat Altimeter Data*, *Report No. 399*. Columbus: Dept. of Geodetic Science and Surveying, The Ohio State University.

Hwang, C., Hsu, H.-Y., and Jang, R.-J. (2002). Global Mean Sea Surface and Marine Gravity Anomaly from Multi-Satellite Altimetry: Applications of Deflection-Geoid and Inverse Vening Meinesz Formulae. *J. Geodesy* 76 (8), 407–418. doi:10.1007/s00190-002-0265-6

Hwang, C. (1998). Inverse Vening Meinesz Formula and Deflection-Geoid Formula: Applications to the Predictions of Gravity and Geoid over the South China Sea. *J. Geodesy* 72, 304–312. doi:10.1007/s001900050169

Hwang, C., Kao, E.-C., and Parsons, B. (1998). Global Derivation of Marine Gravity Anomalies from Seasat, Geosat, ERS-1 and TOPEX/POSEIDON Altimeter Data. *Geophys. J. Int.* 134 (2), 449–459. doi:10.1111/j.1365-246X.1998.tb07139.x

Hwang, C., and Parsons, B. (1996). An Optimal Procedure for Deriving Marine Gravity from Multi-Satellite Altimetry. *Geophys. J. R. Astron. Soc.* 125, 705–718. doi:10.1111/j.1365-246X.1996.tb06018.x

Hwang, C., and Parsons, B. (1995). Gravity Anomalies Derived from Seasat, Geosat, ERS-1 and TOPEX/POSEIDON Altimetry and Ship Gravity: A Case Study over the Reykjanes Ridge. *Geophys. J. Int.* 122, 551–568. doi:10.1111/j.1365-246X.1995.tb07013.x

Jiang, W., Li, J., and Wang, Z. (2002). Determination of Global Mean Sea Surface WHU2000 Using Multi-Satellite Altimetric Data. *Chin. Sci Bull* 47 (19), 1664–1668. doi:10.1360/02tb9365

Kaban, M. K. (2011). "Gravity Anomalies, Interpretation," in *Encyclopedia of Solid Earth Geophysics. Encyclopedia of Earth Sciences Series*. Editor H. K Gupta (Dordrecht: Springer), 456–461. doi:10.1007/978-90-481-8702-7_88

Ke, P., Zhang, C., Guo, C., Wang, B., and Yang, L. (2015). Research on the System Error Correction for Shipborne Gravimetric Data of Different Region in China Offshore. *Geomatics Inf. Sci. Wuhan Univ.* 40, 417–421. doi:10.13203/j.whugis20130299

Knudsen, P. (1991). Simultaneous Estimation of the Gravity Field and Sea Surface Topography from Satellite Altimeter Data by Least-Squares Collocation. *Geophys. J. Int.* 104, 307–317. doi:10.1111/j.1365-246X.1991.tb02513.x

Le Traon, P. Y., Stum, J., Dorandeu, J., Gaspar, P., and Vincent, P. (1994). Global Statistical Analysis of TOPEX and POSEIDON Data. *J. Geophys. Res.* 99, 24619–24631. doi:10.1029/94JC01110

Li, J., Ning, J., Chen, J., and Chao, D. (2003). Geoid Determination in China Sea Areas. *Acta Geod. Cartogr. Sin.* 32, 1001–1595. doi:10.3321/j.issn:1001-1595.2003.02.004

Li, M., Liu, Y., Huang, M., and Zhai, G. (2002). Three Models for Determination of Survey Line Systematic Errors in Marine Survey Net. *J. Inst. Surv. Mapp.* 19, 157–161. CNKI: SUN: JFJC.0.2002-03-000.

Li, Y., and Zhang, R. (2015). Inference of Altimeter Accuracy on Along-Track Gravity Anomaly Recovery. *Acta Geod. Cartogr. Sin.* 44, 363–369. doi:10.11947/j.AGCS.2015.20140022

Liang, W., Li, J., Xu, X., Zhang, S., and Zhao, Y. (2020). A High-Resolution Earth's Gravity Field Model SGG-UGM-2 from GOCE, GRACE, Satellite Altimetry, and EGM2008. *Engineering* 6, 860–878. doi:10.1016/j.eng.2020.05.008

Liu, Y., Li, M., and Huang, M. (2012). The Rank-Defect Adjustment Model for Survey Line Systematic Errors in Marine Survey Net. *Geomatics Inf. Sci. Wuhan Univ.* 26, 533–538. doi:10.3321/j.issn:1671-8860.2001.06.013

Mertz, F., Bouffard, J., and Féménias, P. (2019). Baseline-C CryoSat Ocean Processor Ocean Product Handbook. Issue: 4.1. Available online at: https://earth.esa.int/documents/10174/125272/CryoSat-Baseline-C-Ocean-Product-Handbook. (Accessed August 10, 2021).

National Oceanic and Atmospheric Administration (NOAA) (1997). The Geosat Altimeter JGM-3 GDRS on CD-ROM. Available online at: https://www.nodc.noaa.gov/archive/arc0024/0053056/2.2/about/userhandbook.pdf. (Accessed August 10, 2021).

National Satellite Ocean Application Service (NSOAS) (2019). HY-2B Satellite Altimeter Data Product Handbook. Available online at: https://osdds-ftp.nsoas.org.cn/main.html?download&weblink=a573def5960804423de16d7c37eabac1&lang=schinese. (Accessed August 10, 2021).

Nguyen, V.-S., Pham, V.-T., Van Nguyen, L., Andersen, O. B., Forsberg, R., and Tien Bui, D. (2020). Marine Gravity Anomaly Mapping for the Gulf of Tonkin Area (Vietnam) Using Cryosat-2 and Saral/AltiKa Satellite Altimetry Data. *Adv. Space Res.* 66, 505–519. doi:10.1016/j.asr.2020.04.051

Peng, H., Lin, M., Mu, B., and Wu, Z. (2015). Global Statistical Evaluation and Performance Analysis of HY-2A Satelite Radar Altimeter Data. *Acta Oceanol. Sin.* 37, 54–66. doi:10.3969/j.issn,0253-4193201507.006

Picot, N., Marechal, C., Couhert, A., Desai, S., Scharroo, R., and Egido, A. (2018). Jason-3 Products Handbook. SALP-MU-M-OP-16118-CN, Issue: 1.5. Available online at: https://www.aviso.altimetry.fr/fileadmin/documents/data/tools/hdbk_j3.pdf.

Prandi, P., Philipps, S., Pignot, V., and Picot, N. (2015). SARAL/AltiKa Global Statistical Assessment and Cross-Calibration with Jason-2. *Mar. Geodesy* 38, 297–312. doi:10.1080/01490419.2014.995840

Sandwell, D., Garcia, E., Soofi, K., Wessel, P., Chandler, M., and Smith, W. H. F. (2013). Toward 1-mGal Accuracy in Global Marine Gravity from CryoSat-2, ENVISAT, and Jason-1. *The Leading Edge* 32, 892–899. doi:10.1190/tle32080892.1

Sandwell, D. T. (1992). Antarctic Marine Gravity Field from High-Density Satellite Altimetry. *Geophys. J. Int.* 109, 437–448. doi:10.1111/j.1365-246X.1992.tb00106.x

Sandwell, D. T., Müller, R. D., Smith, W. H. F., Garcia, E., and Francis, R. (2014). New Global marine Gravity Model from CryoSat-2 and Jason-1 Reveals Buried Tectonic Structure. *Science* 346, 65–67. doi:10.1126/science.1258213

Sandwell, D. T. (1984). Thermomechanical Evolution of Oceanic Fracture Zones. *J. Geophys. Res.* 89, 11401–11413. doi:10.1029/JB089iB13p11401

Sansò, F., and Sideris, M. G. (2013). "Observables of Physical Geodesy and Their Analytical Representation," in *Geoid Determination. Lecture Notes in Earth System Sciences*. Editors F. Sansò and M. Sideris (Berlin, Heidelberg: Springer), 110, 73–110. doi:10.1007/978-3-540-74700-0_2

Soussi, B., Urien, S., Picard, B., Muir, A., Roca, M., and Garcia, P. (2018). ENVISAT Altimetry Level 2 Product Handbook. V2.0.CLS-ESLF-18-0003, Issue 2.0Available online at: https://earth.esa.int/eogateway/documents/20142/37627/PH_light_2rev0_ESA.pdf/711e748d-2db7-d131-1060-3deace1973b3. (Accessed August 10, 2021).

U.S. National Geospatial-Intelligence Agency EGM Development Team (2010). EGM2008 - Files & Products for Oceanographic Applications. Available at: https://earth-info.nga.mil/. (Accessed August 10, 2021).

Wan, X., Jin, S., Liu, B., Tian, S., Kong, W., and Annan, R. F. (2020). Effects of Interferometric Radar Altimeter Errors on Marine Gravity Field Inversion. *Sensors* 20, 2465. doi:10.3390/s20092465

Wang, H., and Wang, G. (2001). Inversion of Gravity Anomalies from along Track Vertical Deflections with Satellite Altimeter Data and its Applications. *Acta Geod. Cartogr. Sin.* 30, 21–26. doi:10.3321/j.issn:1001-1595.2001.01.005

Wang, H., Wang, Y., Lu, Y., and Zan, J. (2005). Inversion of Marine Gravity Anomalies by Combinating Multi Altimeter Data and Shipborne Gravimetric Data. *Crustal Deform. Earthquake* 25, 81–85. doi:10.16251/j.cnki.1009-2307.2016.06.004-en

Wang, Z., Chao, N., and Chao, D. (2020). Using Satellite Altimetry Leveling to Assess the marine Geoid. *Geodesy and Geodynamics* 11, 106–111. doi:10.1016/j.geog.2019.11.003

Xu, H., Wang, H., Lu, Y., and Wang, G. (1999). Geoid Undulations and Gravity Anomalies from T/P and ERS-1 Altimeter Data in the China Sea and Vicinity. *Chin. J. Geophys.* 42, 465–471. doi:10.3321/j.issn:0001-5733.1999.04.005

Zhang, Q. (2015). *Research on the Processing Methods of the Cross Point of Satellite Altimeter Data*. [master's thesis]. Qingdao: China University of Petroleum (East China).

Conflict of Interest: The authors declare that the research was conducted in the absence of any commercial or financial relationships that could be construed as a potential conflict of interest.

Publisher's Note: All claims expressed in this article are solely those of the authors and do not necessarily represent those of their affiliated organizations, or those of the publisher, the editors, and the reviewers. Any product that may be evaluated in this article, or claim that may be made by its manufacturer, is not guaranteed or endorsed by the publisher.

frontiers in Earth Science

ORIGINAL RESEARCH
published: 25 November 2021
doi: 10.3389/feart.2021.730513

Relationship Between Altimetric Quality and Along-Track Spatial Resolution for iGNSS-R Sea Surface Altimetry: Example for the Airborne Experiment

Zongqiang Liu[1,2†], Wei Zheng[1,2,3†], Fan Wu[2*†], Guohua Kang[1], Xuezhi Sun[2] and Qiang Wang[3]*

[1]School of Astronautics, Nanjing University of Aeronautics and Astronautics, Nanjing, China, [2]Qian Xuesen Laboratory of Space Technology, China Academy of Space Technology, Beijing, China, [3]School of Geomatics, Liaoning Technical University, Fuxin, China

OPEN ACCESS

Edited by:
Jinyun Guo, Shandong University of Science and Technology, China

Reviewed by:
Fan Gao, Shandong University, China
Lavinia Tunini, Istituto Nazionale di Oceanografia e di Geofisica Sperimentale, Italy

***Correspondence:**
Wei Zheng
zhengwei1@qxslab.cn
Fan Wu
wufan@qxslab.cn

[†]These authors have contributed equally to this work

Specialty section:
This article was submitted to Environmental Informatics and Remote Sensing, a section of the journal Frontiers in Earth Science

Received: *25 June 2021*
Accepted: *03 November 2021*
Published: *25 November 2021*

Citation:
Liu Z, Zheng W, Wu F, Kang G, Sun X and Wang Q (2021) Relationship Between Altimetric Quality and Along-Track Spatial Resolution for iGNSS-R Sea Surface Altimetry: Example for the Airborne Experiment. Front. Earth Sci. 9:730513. doi: 10.3389/feart.2021.730513

The altimetric quality and the along-track spatial resolution are the critical parameters to characterize the performance of interferometric global navigation satellite systems reflectometry (iGNSS-R) sea surface altimetry, which is closely related to each other through signal processing time. Among them, the quality of sea surface height (SSH) measurement includes precision and accuracy. In order to obtain higher altimetric quality in the observation area, a longer signal processing time is needed, which will lead to the loss of spatial resolution along the track. In contrast, higher along-track spatial resolution requires more intensive sampling, leading to unsatisfactory altimetric quality. In this study, taking the airborne iGNSS-R observation data as an example, the relationship between the altimetric quality and the along-track spatial resolution is analyzed from the perspectives of precision and accuracy. The results indicate that the reduction in the along-track spatial resolution will improve the altimetric quality. The accuracy range is 0.28–0.73 m, and the precision range is 0.24–0.65 m. However, this change is not linear, and the degree of altimetric quality improvement will decrease as the along-track spatial resolution worsens. The research results in this paper can provide a scientific reference for the configuration of parameters for future spaceborne iGNSS-R altimetry missions.

Keywords: interferometric global navigation satellite systems reflectometry (iGNSS-R), altimetric quality, along-track spatial resolution, airborne experiment, altimetric precision, altimetric accuracy

INTRODUCTION

As an effective and innovative bistatic radar remote sensing technology, the global navigation satellite system reflectometry (GNSS-R) can measure a series of physical parameters of the earth's surface by using GNSS reflected signals, including the sea surface wind speed (Garrison et al., 2002; Katzberg et al., 2006; Foti et al., 2015), the sea surface height (SSH) (Lowe et al., 2002; Rius et al., 2010; Cardellach et al., 2014; Gao et al., 2021) and the soil moisture (Masters et al., 2004; Rodriguez-Alvarez et al., 2009; Wu et al., 2021), etc. Among them, the height of the earth's reflecting surface relative to the reference ellipsoid can be obtained by measuring the path delay between the direct signal and the reflected signal (Martin-Neira, 1993). Since Martin-Neira first proposed the concept of Passive

Reflection and Interference System (PARIS) in 1993, this technology has been verified on various platforms such as ground (Martin-Neira et al., 2001; He et al., 2021), shipborne (Gao et al., 2020), airborne (Lowe et al., 2002; Ruffini et al., 2004; Cardellach et al., 2014), and satellite (Clarizia et al., 2016; Li et al., 2018; Cardellach et al., 2019). Compared with the traditional radar altimeter, GNSS-R altimetry has the advantages of low cost, multi-simultaneous observation, and high spatial coverage.

According to the signal processing method of obtaining path delay, cGNSS-R (conventional GNSS-R) and iGNSS-R (interferometric GNSS-R) are mainly used in GNSS-R sea surface altimetry at present. The cGNSS-R technology cross-correlates the locally generated replica of the transmission signal with the reflected signal for a certain time (typically 1 ms) after proper compensation of the Doppler frequency shift (Zavorotny et al., 2014). Therefore, cGNSS-R needs to use the GNSS signals with known structure, such as L1C, L2C, L5 of GPS, B1I, B1C, B2a of BDS-3 et al. However, the maximum bandwidth of the above signals can only reach 20.46 MHz, which limits the altimetric quality and the along-track spatial resolution (Cardellach et al., 2014). In order to overcome the bandwidth limitation, ESA proposed PARIS in-orbit demonstrator mission (PARIS IoD) in 2011 (Martin-Neira et al., 2010), which aimed to realize the signal interference processing originally proposed by Martin-Neira (Martin-Neira, 1993), i.e., iGNSS-R technology. The iGNSS-R technology makes complex cross-correlation between the direct signal and reflected signal, which can fully use the spectral components in the GNSS signal, and the bandwidth can reach 25 to 50 MHz. The sharper autocorrelation function can be obtained using the wider bandwidth, which will significantly improve the altimetric quality and the along-track spatial resolution (Li et al., 2016).

The altimetric quality and the along-track spatial resolution are the key indicators to characterize the iGNSS-R altimetry performance. It is worth noting that altimetric quality mainly includes precision and accuracy. Among them, the altimetric precision is mainly affected by zero-mean random error, and the altimetric accuracy is mainly determined by the total absolute measurement error affected by the additional random and deterministic errors (Li et al., 2019). The along-track spatial resolution represents the ability of spatial sampling along the orbit of iGNSS-R altimeter, which can be expressed as $R_{a\_t} = v_{SP} \cdot T_{coh} \cdot N_{incoh}$ (v_{SP} is the speed of the specular point along the ground track, T_{coh} is the coherent integration time and T_{incoh} is the number of samples incoherently averaged) (Cardellach et al., 2014). The along-track spatial resolution can be improved by reducing signal integration time. However, the decrease in the number of independent waveform samples will increase the impact of speckle noise, resulting in a loss in the signal-to-noise ratio (SNR), which will increase the uncertainty of the waveform retracking and ultimately make the altimetric quality poor. Currently, there is no iGNSS-R altimetry satellite in orbit. In contrast, ESA has released several iGNSS-R altimetry mission plans in recent years, such as the PARIS IOD (Martin-Neira et al., 2010), the GNSS reflectometry, radio occultation, and scatterometry onboard the International Space Station (GEROS-ISS) (Wickert et al., 2016), the "Cookie" constellation (Martín-Neira et al., 2016) and the GNSS Transpolar Earth Reflectometry exploriNg system (G-TERN) (Cardellach et al., 2018). The airborne experiment (as shown in **Figure 1**) is usually used as a pre-research technology for satellite missions. At present, some experimental flight campaigns have been carried out, among which the more typical are the two missions carried out by the Institut d'Estudis Espacials de Catalunya (IEEC) in the Baltic Sea, which are called PIRA (Cardellach et al., 2014) and SPIR (Ribo et al., 2017). Based on this observation, a series of researches on the altimetric quality and the along-track spatial resolution of iGNSS-R were carried out. In 2014, Cardellach et al. used the PIRA observation data to analyze the altimetric precision of cGNSS-R and iGNSS-R under different signal processing times, and simulated the low-orbit iGNSS-R altimetry performance. The results showed that increasing the signal processing time will significantly improve the altimetric precision (Cardellach et al., 2014). In 2017, Ribo et al. first published the SNR results of the SPIR waveform under multi-GNSS (Ribo et al., 2017). In the same year, Li et al. studied the altimetric precision of the SPIR with the signal processing time in 1, 10, and 100 s (Li et al., 2017). In 2019, Fabra et al. analyzed the altimetric accuracy of the SPIR mission when the signal processing time was 10 s. The results show that the altimetric accuracy ranges from 0.09 to 0.66 m according to different signal sources and elevation angles (Fabra et al., 2019). Nevertheless, there has not been a comprehensive study on the relationship between the iGNSS-R altimetric quality (i.e., altimetric precision and accuracy) and the along-track spatial resolution.

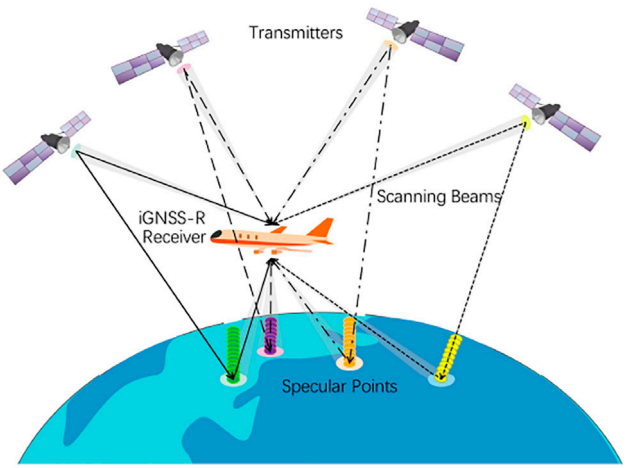

FIGURE 1 | Scheme of the airborne iGNSS-R altimeter theoretical method.

Different from previous studies, taking the experimental data of airborne interferometric GNSS-R provided by IEEC as an example, the altimetric precision and accuracy under different signal integration times are calculated in this paper. Then, through the relationship between the signal integration time and the along-track sampling, the relationship between the airborne iGNSS-R altimetric quality and the along-track spatial resolution is comprehensively analyzed from two

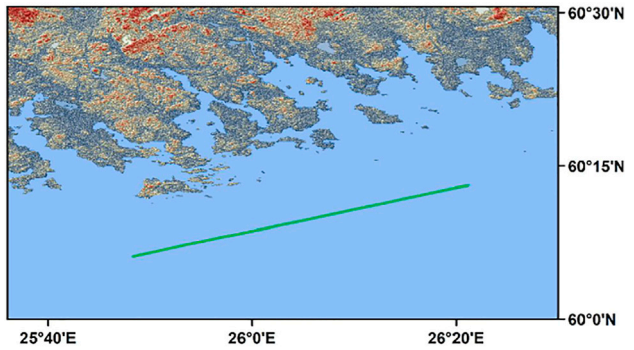

FIGURE 2 | Flight path of the experimental data over Baltic Sea used in this study.

aspects of the altimetric precision and accuracy. The purpose of this study is to provide a reference for the payload and orbit design of the future iGNSS-R altimetry satellites.

DATA SETS

In this study, we used the iGNSS-R airborne observation data, the DTU15 global mean sea surface model and the DTU global tide model. Among them, we used the iGNSS-R airborne observation data to retrieve the SSH, and the DTU15 global mean sea surface model and the DTU10 global ocean tide model to construct the SSH validation model.

iGNSS-R Airborne Experiment Campaign

The iGNSS-R observation data used in this study come from the airborne experimental campaign carried out by IEEC on December 3, 2015. The mission location is in the Baltic Sea near Helsinki, Finland (as shown in **Figure 2**). The critical point of this mission is using the new-generation iGNSS-R receiver developed by IEEC for the first time, which can collect primitive and complex GNSS reflection signals from 16 front-ends at a sampling rate of 80 MHz. The operating frequency band includes all commonly used GNSS L1, L2, and L5 bands (Fabra et al., 2019).

In this study, we used the observation data of GPS PRN01 in the L1 band with a time of 40001-40600 (GPS SOD, i.e., GPS seconds of day) for a total of 10 min.

Sea Surface Height Validation Model

In order to obtain the altimetric accuracy, it is necessary to compare the SSH retrieved by iGNSS-R observation with the measured SSH data. However, we used the validation model in this study due to the lack of measured SSH data.

In this study, we used the DTU15 MSS model and the DTU10 global tide model to construct the SSH validation model:

$$SSH_{\mathrm{ref}} = DTU15_{\mathrm{MSS}} + DTU10_{\mathrm{Tide}} \quad (1)$$

The DTU15 mean sea surface (MSS) is a global high-spatial resolution (2 arc-min) mean sea surface model released by the Technical University of Denmark (DTU) in December 2015. Compared with the previous version, the most significant improvement of DTU15 model is the use of improved Cryosat-2 LRM, SAR, and SAR-In data (Skourup et al., 2017).

The DTU also releases the DTU10 global tide model. The DTU10 considered the influence of wavelength and water depth of diurnal and semidiurnal tidal components, and uses the dynamic difference method based on depth to interpolate the correction value into the FES 2004. The load tide uses the calculation results of the FES 2004. The grid resolution is $7.5' \times 7.5'$ (Turner et al., 2013).

SIGNAL PROCESSING AND SEA SURFACE HEIGHT RETRIEVAL METHODS

In this section, we illustrate the theoretical method of the SSH inversion from the raw IF data, including the signal processing, the delay estimation and the SSH retrieval. **Figure 3** shows the whole process.

Signal Processing

Raw Signal Processing

After receiving the raw IF data through the zenith and nadir antennas, it needs further processing to obtain the complex waveforms. This research adopts the original data processing method provided in Fabra et al. (2019). First of all, the direct and reflected signals are combined through beamforming. After that, the direct and reflected signals are cross-correlated in the frequency domain, and a total of 6×10^5 complex waveforms (1 ms) $c(t, \tau)$ are obtained. Compared with the signal processing method of cGNSS-R, the main difference of iGNSS-R is the need for beamforming and the use of the observed direct signal as the correlation input.

Coherent Integration and Incoherently Averaged

In order to reduce the influence of thermal and speckle noise, and improve the SNR of the power waveform, it is necessary to perform coherent integration (T_{coh}) and a large number of incoherent averages (N_{incoh}) on the complex waveform (1 ms) (Zavorotny et al., 2014):

$$w(T_0 + N_{\mathrm{incoh}} \cdot T_{\mathrm{coh}}/2, \tau) = \frac{1}{N_{\mathrm{incoh}}} \sum_{n=0}^{N_{\mathrm{incoh}}-1} c(nT_{\mathrm{coh}}, \tau) \quad (2)$$

where T_0 is the start time of the signal processing.

The corresponding power waveform is:

$$W(T_0 + N_{\mathrm{incoh}} \cdot T_{\mathrm{coh}}/2, \tau) = |w(T_0 + N_{\mathrm{incoh}} \cdot T_{\mathrm{coh}}/2, \tau)|^2 \quad (3)$$

It is worth noting that waveform alignment is needed before the incoherent averages (Park et al., 2012). In this study, the coherent integration time is 1, 2, 5, and 10 ms, respectively, and the average number of incoherent is 1,000 (i.e., 1 s incoherent average time).

Delay Estimation

Accurate estimation of the delay at the specular point is the key to ensure the iGNSS-R altimetry quality. The initial delay can be

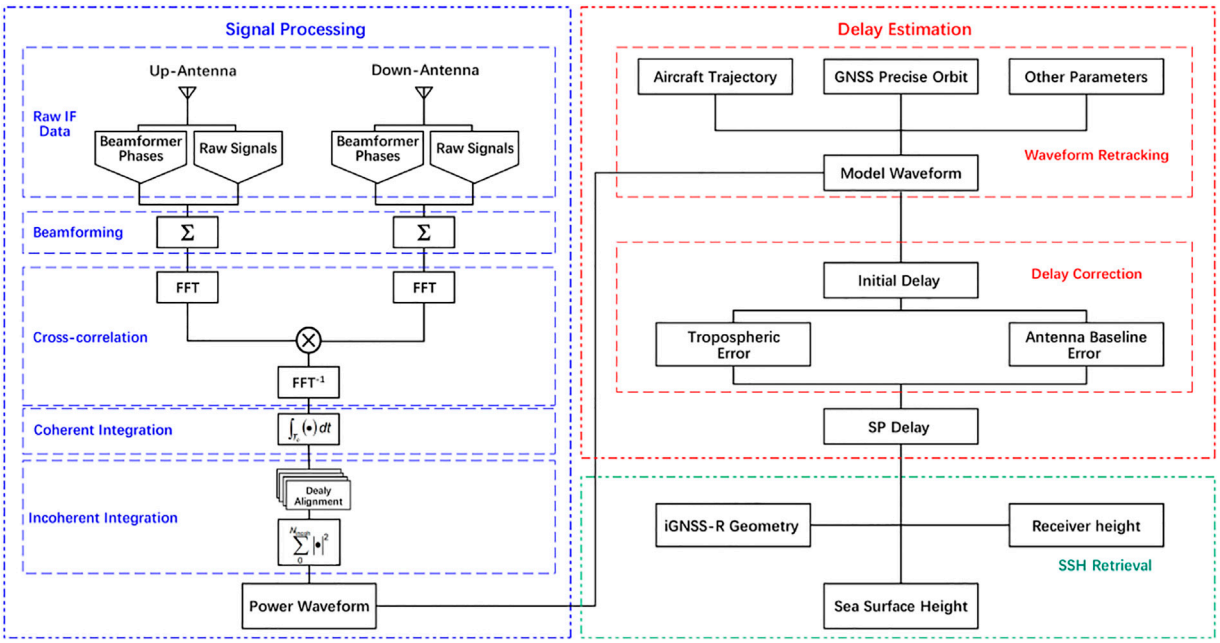

FIGURE 3 | Schematic flow chart of the process followed by SSH inversion from raw IF signals.

obtained through waveform retracking. In addition, the correction of delay errors is needed, such as the tropospheric delay and the zenith-nadir antenna baseline delay.

Waveform Retracking

The reflected waveform retracking is based on comparing measured and modeled waveforms (Li et al., 2019). The modeled waveform corresponding to each measured waveform in this paper is obtained through the Z-V model implemented in the "wavpy" GNSS-R open-source software (Fabra et al., 2017). Currently, the waveform retracker mainly includes HALF (the point at a fraction of the peak power), DER (the point with the maximum of waveform's first derivative), and FIT (fitting the waveform to its model) (Li et al., 2019). In this study, we used the DER to estimate the delay of the specular point along the waveform (Cardellach et al., 2014):

$$\tau_{\mathrm{sp}} = \tau_{\mathrm{DER}}^{\mathrm{obs}} + \left(\tau_{\mathrm{sp}}^{\mathrm{model}} - \tau_{\mathrm{DER}}^{\mathrm{model}}\right) \tag{4}$$

where $\tau_{\mathrm{DER}}^{\mathrm{obs}}$ is the delay corresponding to the maximum derivative point calculated from the measured waveform, $\tau_{\mathrm{sp}}^{\mathrm{model}}$ and $\tau_{\mathrm{DER}}^{\mathrm{model}}$ represent the specular point delay and derivative maximum point delay of simulation waveform respectively.

Delay Correction

The troposphere goes generally from the ground to 15 km altitude. Due to the high humidity of the sea surface and the different transmission paths of direct and reflected signals, the deviation caused by the troposphere to the airborne iGNSS-R delay estimation cannot be ignored. In this study, we used the model provided in Jin et al. (2014) to estimate the tropospheric delay:

$$\tau_{\mathrm{trop}} = 2\frac{2.3}{\sin\theta}\left(1 - e^{-H_{\mathrm{R}}/H_{\mathrm{trop}}}\right) \tag{5}$$

where θ is the elevation angle at the specular point, H_{R} represents the height of the iGNSS-R receiver. The H_{trop} is the height of the troposphere at the observation location (we take H_{trop} = 8,621 m).

The zenith-nadir antenna baseline delay τ_{antenna} is obtained by the path difference between the zenith antenna and the nadir antenna relative to the specular point.

Sea Surface Height Retrieval

After correcting the delay error of the specular point, the ellipsoidal height of the sea surface above the WGS84 reference ellipsoid can be obtained by the geometric relationship of the airborne iGNSS-R (Li et al., 2019):

$$SSH_{\mathrm{iGNSS-R}} = \frac{\tau_{\mathrm{sp}} - \left(\tau_{\mathrm{trop}} + \tau_{\mathrm{antenna}}\right)}{2\sin\theta} - H_{\mathrm{R}} \tag{6}$$

Altimetric Quality Standard

Altimetric Precision

The altimetric precision is affected by zero-mean random error, mainly due to the random nature of the received signals caused by thermal and speckle noise. The measured SSH sequence is subtracted from a fitted piecewise linear function to form zero mean, near white noise SSH residuals (Li et al., 2017). Therefore, we define the altimetric precision as:

$$\sigma_{\mathrm{p}} = SSH_{\mathrm{iGNSS-R}} - Fit\left(T_i\right) \tag{7}$$

where $Fit\left(\right)$ is the linear fitting equation based on the measured SSH, T_i is the epoch.

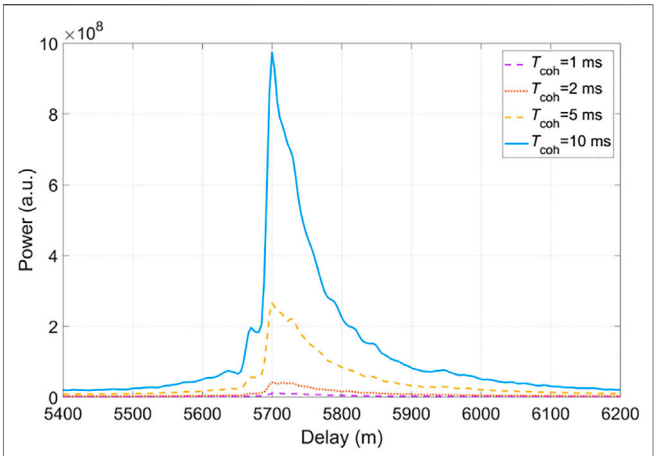

FIGURE 4 | Power waveform of airborne iGNSS-R under different signal processing time.

We define the average altimetric precision of N specular points as:

$$\bar{\sigma}_{\mathrm{p}} = \frac{\sum_{i=1}^{N} \left|\sigma_{\mathrm{p}}^{i}\right|}{N} \tag{8}$$

Altimetric Accuracy

In this study, we define the altimetric accuracy as the difference between the measured SSH and the validation SSH:

$$\sigma_{\mathrm{a}} = SSH_{\mathrm{iGNSS-R}} - SSH_{\mathrm{ref}} \tag{9}$$

We define the average altimetric accuracy of N specular points as:

$$\bar{\sigma}_{\mathrm{a}} = \frac{\sum_{i=1}^{N} \left|\sigma_{\mathrm{a}}^{i}\right|}{N} \tag{10}$$

RESULTS AND DISCUSSION

Power Waveform

The power waveform is the database for obtaining the iGNSS-R altimetric quality. Among them, the altimetric precision is directly related to the SNR of the waveform, and the acquisition of the altimetric accuracy requires the power waveform retracking to calculate the delay of the specular points. In this study, the coherent integration time is set to 1, 2, 5, and 10 ms, and the number of the incoherent average is 1,000, so the signal processing time is 1, 2, 5, and 10 s, respectively. Since a total of 10 min of airborne iGNSS-R observations are used, the corresponding number of the power waveform is 600, 300, 120, and 60, respectively.

Figure 4 presents the iGNSS-R power waveform results at different signal processing times. Although the longer of signal processing time will generate the greater noise amplitude, it will increase the amplitude of the waveform power more significantly.

In this study, we define the SNR of the waveform as (Lowe et al., 2002):

$$SNR_{\mathrm{wf}} = \frac{\max[W(\tau)] - A_{\mathrm{noise}}}{\sigma_{\mathrm{noise}}} \tag{11}$$

where A_{noise} is the average noise amplitude of the waveform, σ_{noise} is the standard deviation of noise amplitude. According to **Equation (11)**, the corresponding SNR of 1, 2, 5, and 10 s power waveforms is 8.69, 11.09, 14.82, and 17.04 dB, respectively.

Relationship between Altimetric Precision and Along-Track Spatial Resolution.

Based on the airborne iGNSS-R power waveform obtained by the signal processing, the altimetric precision corresponding to each specular point is calculated according to **Equation (7)**. The results (**Figure 5**) show a clear stable distribution of the altimetric precision with the increase of signal processing time, suggesting a significant role played by the SNR. According to **Equation (8)**, the average altimetric precision under different along-track spatial resolutions is calculated. The relationship between the average altimetric precision and along-track spatial resolution is intuitively presented in **Table 1** and **Figure 6**.

These results indicate that the altimetric precision of iGNSS-R gradually increases as the along-track spatial resolution decreases. However, this dependence is not linear. When the along-track spatial resolution changes in the range of 50 m–150 m, the altimetric precision changes sharply, and then the fluctuation of the altimetric precision becomes relatively weak with the increasing of the along-track spatial resolution, which is mainly due to the increase of signal processing time, and the SNR will tend to the stable state.

In order to estimate the performance of PARIS IOD, Martin-Neira et al. (2010) established a model of altimetric precision and SNR:

$$\sigma_{\mathrm{p}} = \frac{c}{2\sin\theta_{\mathrm{S}}\sqrt{N_{\mathrm{incoh}}}} \cdot \frac{W(0)}{W(0)'} \cdot \sqrt{\left(1 + \frac{1}{SNR}\right)^{2} + \left(\frac{1}{SNR}\right)^{2}} \tag{12}$$

where c is the speed of light in vacuum, $W(0)$ is the signal power at the specular point, $W(0)'$ is the first derivative value at the specular point. Based on the SNR results in *Section Power Waveform* and **Equation (12)**, the precision results under the model are calculated. The model precision results have an average deviation of 0.17 m from the results in **Figure 6**. We consider that the precision model does not take into account the correlation between power waveform and noise. The correlation between waveforms in the airborne scene is significantly stronger than that in the spaceborne scene (You et al., 2004), which leads to the precision estimation deviation using the model in the airborne scene.

Relationship Between Altimetric Accuracy and Along-Track Spatial Resolution

According to the iGNSS-R power waveform and the DER retracking algorithm, combined with **Equation (6)** and **Equation (9)**, the SSH and the altimetric accuracy are calculated. The results (**Figure 7**) demonstrate that the SSH

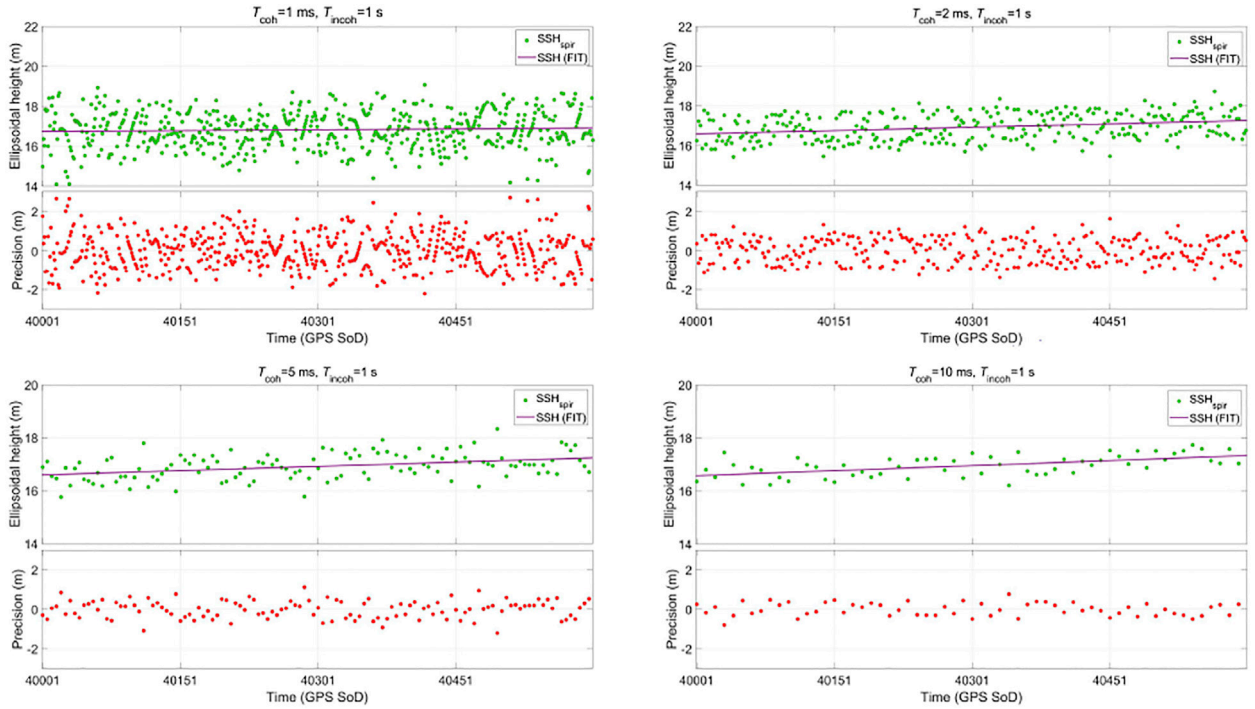

FIGURE 5 | Airborne iGNSS-R altimetric precision under different signal processing time.

TABLE 1 | The performance of the altimetric precision and the along-track spatial resolution.

Coherent integration time (ms)	Along-track spatial resolution (m)	Altimetric precision (m)
1	55.13	0.65
2	109.80	0.48
5	274.44	0.32
10	548.67	0.24

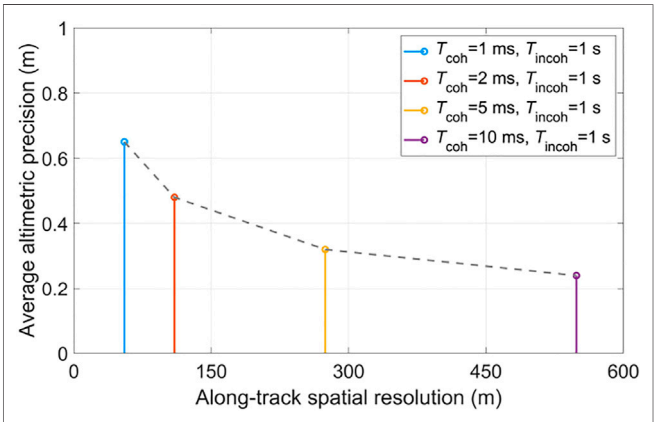

FIGURE 6 | Altimetric precision as a function of along-track spatial resolution under airborne scene.

inversed from the airborne iGNSS-R observations is in good consistency with the validation model. As the coherent integration time increases, the deviation between $SSH_{\text{iGNSS-R}}$ and SSH_{ref} gradually decreases. The main reasons for the deviation are as follows.

1) In this study, only the tropospheric delay and the zenith-nadir antenna baseline delay were considered in the altimetry retrieval, and other errors such as the aircraft positioning error and the flight altitude were not included in the SSH inversion.
2) The signal processing time ranges from 1 s to 10 s. Although the SNR of the reflected signal has been improved, there are still some speckle and thermal noise in the power waveform.
3) The validation model SSH_{ref} is obtained based on the inversion of observation from multiple remote sensing and gravity satellites for many years, which has good stability. However, the airborne experimental campaign only performed a single measurement at the observation area, and the results have certain randomness, which led to the deviations between the inversed SSH results and the validation model.

According to **Equation (10)**, the average altimetric accuracy under different along-track spatial resolutions is calculated, and the results are given in **Table 2** and **Figure 8**.

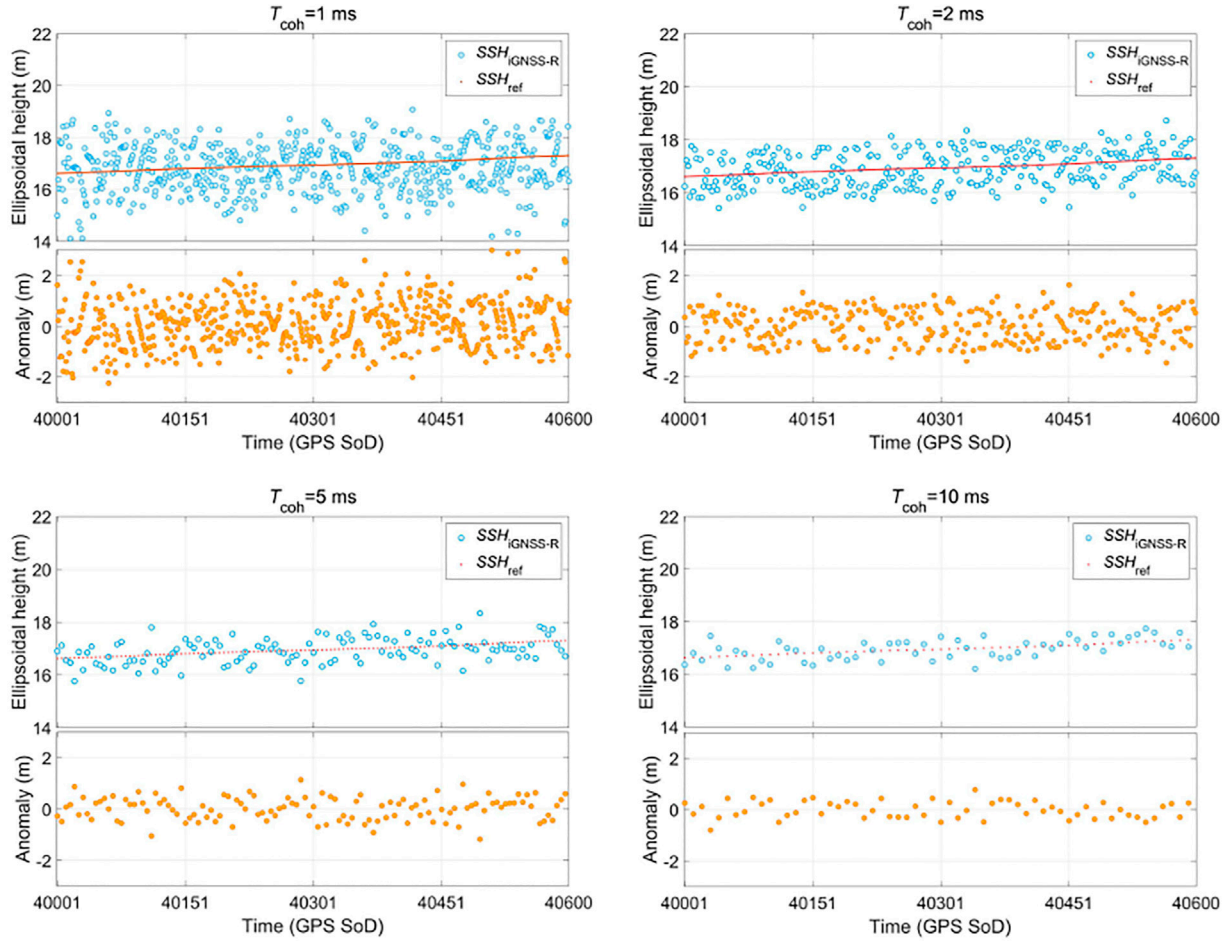

FIGURE 7 | Airborne iGNSS-R altimetric accuracy under different signal processing time.

TABLE 2 | The performance of the altimetric accuracy and the along-track spatial resolution.

Coherent integration time (ms)	Along-track spatial resolution (m)	Altimetric accuracy (m)
1	55.13	0.73
2	109.80	0.55
5	274.44	0.37
10	548.67	0.28

The result of the altimetric accuracy changes with the along-track spatial resolution is similar to that in *Section Relationship Between Altimetric Accuracy and Along-Track Spatial Resolution*. The altimetric accuracy increases as the along-track spatial resolution decreases due to the steeper lead-edge of the power waveform, thus improving the accuracy of the specular point delay estimation.

Advices for Future Spaceborne iGNSS-R Altimetry Missions

Combined with the airborne experimental results, in order to give more accurate suggestions for future iGNSS-R altimetry satellite missions, the altimetric precision is simulated based on the NASNRM model (Liu et al., 2019), SNR model of direct signal (Jin et al., 2014) and the precision model (Martin-Neira et al., 2010). Simulation parameters are shown in **Table 3**. Combined with the simulation results of spaceborne iGNSS-R altimetric quality and along-track spatial resolution, the advices for future spaceborne iGNSS-R altimetry missions as follows.

1) The future iGNSS-R sea surface altimetry satellites require high-gain zenith and nadir antennas. The iGNSS-R altimetric precision increases as the along-track spatial resolution decreases, mainly due to the increase in signal processing

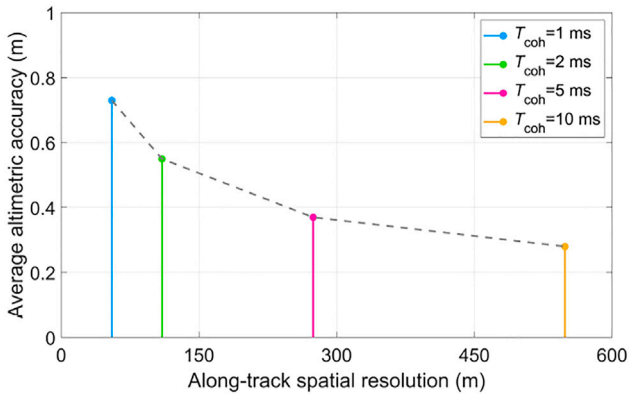

FIGURE 8 | Altimetric accuracy as a function of along-track spatial resolution under the airborne scene.

TABLE 3 | System and instrument parameters of the simulated spaceborne iGNSS-R altimeter.

Parameter	Value
GNSS-R Satellite Orbital Altitude (km)	635
Receiver Bandwidth (MHz)	30
Signal Bandwidth (MHz)	GPS L1 (Full Composite): 25
Signal Frequency (MHz)	1,575.42
EIRP (dBw)	34 (optimistic)
Antenna Equivalent Noise Temperature (K)	Zenith Antenna 500 Nadir Antenna 550
Antenna Radiation Efficiency (%)	100
U10 Wind Speed (m/s)	10
Wave Spectrum Model	Elfouhaily
Altimetry Sensitivities (m^{-1})	0.089

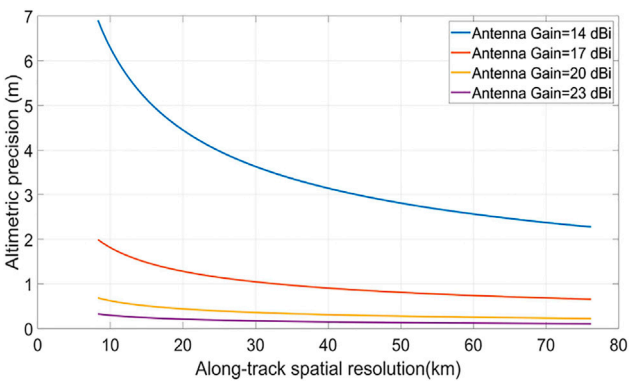

FIGURE 9 | Relationship between precision and spatial resolution under different antenna gains at elevation angle of 75 degrees in the spaceborne scene.

time that improves the SNR of the waveform. The increase in the antenna gain can also increase the SNR of the waveform, which can reduce the signal processing time and thereby improve the along-track spatial resolution. The performance of spaceborne iGNSS-R altimetry under

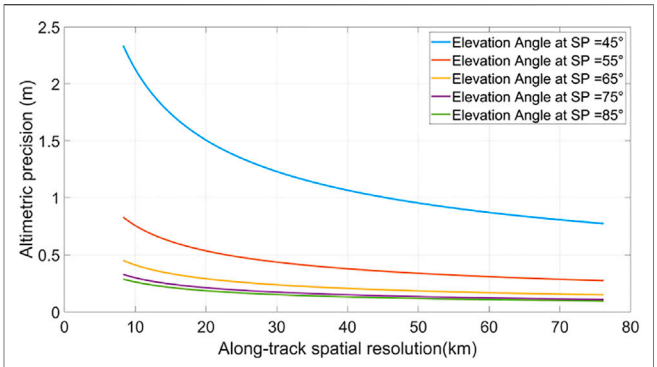

FIGURE 10 | Relationship between precision and spatial resolution under different elevation angle at antenna gains of 23 dBi the spaceborne scene.

different gains when the elevation angle is 75 degrees is presented in **Figure 9**. The results show that the amplitude of accuracy varies with spatial resolution becomes gentle with the increase of antenna gain. When the antenna gain is greater than 20 dBi, the altimetric precision can be better than 1 m at the spatial resolution of 10 km. Of course, the increase in gain will also improve the quality of the antenna, which needs to be considered in the design of the satellite system.

2) The future spaceborne iGNSS-R receiver should be designed for all available GNSS satellites. Gao et al. (2019) studied the distribution of specular reflections under different GNSS systems. Compared with only the GPS as the illuminator, the number of specular reflection events is 3.75 times higher when the transmitter is four-system GNSS (i.e., GPS, BDS, GALILEO, and GLONASS), which indicates that the geometric relationship of iGNSS-R under four-system GNSS is better than only GPS, and reflection events with higher elevation angles can be obtained. The spaceborne iGNSS-R altimetry at different elevation angles is simulated when the antenna gain is 23 dBi. As shown in **Figure 10**, the influence of elevation angle on iGNSS-R altimetry performance is significant. When the spatial resolution is 10 km, the altimetric precision is 2.20 m when the height angle is 45 degrees and 0.25 m when the height angle is 85 degrees. Therefore, it can be predicted that the increase in the number of signal sources will significantly improve the iGNSS-R altimetry performance.
3) The future iGNSS-R altimetry satellites need to use wider bandwidth signals. The signal bandwidth is one of the main factors limiting the performance of GNSS-R altimetry. The iGNSS-R technology breaks through the limitation that cGNSS-R technology can only use signals with known structure. In the future iGNSS-R satellites can use signals with a wider bandwidth than GPS L1, such as Galileo E5 Full. The signal bandwidth of Galileo E5 Full can reach 51 MHz, so the spectral spatial resolution of Galileo E5 Full can be 1.43 times higher than that of GPS L1 Full. In addition, the altimetry sensitivity of Galileo E5 Full signal in the spaceborne scene can reach 0.19 m^{-1}, so the altimetric precision of Galileo

E5 Full can be improved by 2.13 times compared with GPS L1 Full under the same SNR.

CONCLUSION

The altimetric quality and the along-track spatial resolution are critical parameters in the design of the spaceborne iGNSS-R altimetry missions. In order to reduce the error caused by the simulation, this research uses the airborne iGNSS-R altimetry experimental observation to analyze the relationship between the altimetric quality and the along-track spatial resolution from two perspectives precision and accuracy, in order to obtain more precise information of ocean activities under the condition of ensuring the altimetric quality. This study calculated the altimetric precision and accuracy under different along-track spatial resolutions by changing the signal processing time. The results indicate that the iGNSS-R altimetric quality increases with the decrease of the along-track spatial resolution. The range of altimetric precision is 0.24–0.65 m, and the altimetric accuracy is 0.28–0.73 m. However, this relationship is not linear, and the increase in altimetric quality gradually weakens as the along-track spatial resolution decreases, which is determined by the relationship between the power waveform characteristics and the signal processing time.

The estimated altimetry performance of spaceborne iGNSS-R altimeter is also discussed in this paper. The higher antenna gain and better GNSS observation geometry can obtain better altimetric quality with the same along-track spatial resolution. In addition, the GNSS signal under the new system will also bring available opportunities for the improvement of iGNSS-R altimetry. It is worth noting that we used the ideal instrument parameters in the simulation. Some errors generated in the practical application are not considered, such as the antenna efficiency, the power loss in the receiver channel, and phase error in beamforming. Of course, the increase of SNR can reduce the impact of the above errors on altimetry performance estimation.

This study verified the interdependence between the altimetric quality and the along-track spatial resolution, providing a theoretical reference for the balanced selection of the two parameters in the future spaceborne iGNSS-R altimetry missions.

In future research, due to the correlation between waveform and noise in signal processing, it is necessary to establish an optimization model of altimetric precision and effective coherent integration time to evaluate the optimal signal processing time.

DATA AVAILABILITY STATEMENT

The original contributions presented in the study are included in the article/Supplementary Material, further inquiries can be directed to the corresponding authors.

AUTHOR CONTRIBUTIONS

ZL: Conceived the experiments and wrote the paper. WZ and FW: Experiment design, project managment, review, and modification. GK: Provided suggestions for the experiments. XS and QW: Data collection. All authors contributed to the article and approved the submitted version. ZL, WZ, and FW contributed equally to this paper.

FUNDING

This work was supported by the National Natural Science Foundation of China under Grant (41774014, 41574014), the Liaoning Revitalization Talents Program under Grant (XLYC2002082), the Frontier Science and Technology Innovation Project and the Innovation Workstation Project of Science and Technology Commission of the Central Military Commission under Grant (085015), the Independent Research and Development Start-up Fund of Qian Xuesen Laboratory of Space Technology (Y-KC-WY-99-ZY-000-025), and the Outstanding Youth Fund of China Academy of Space Technology.

ACKNOWLEDGMENTS

We would like to thank Institute of Space Sciences (ICE, CSIC) and Institute for Space Studies of Catalonia (IEEC) for providing the raw data processing results of the air-borne experiment. We would also like to thank DTU for providing the DTU15 global mean sea surface model and the DTU10 global ocean tide model.

REFERENCES

Cardellach, E., Flato, G., Fragner, H., Gabarro, C., Gommenginger, C., Haas, C., et al. (2018). GNSS Transpolar Earth Reflectometry exploriNg System (G-TERN): Mission Concept. *IEEE Access* 6, 13980–14018. doi:10.1109/ACCESS.2018.2814072

Cardellach, E., Li, W., Rius, A., Semmling, M., Wickert, J., Zus, F., et al. (2020). First Precise Spaceborne Sea Surface Altimetry with GNSS Reflected Signals. *IEEE J. Sel. Top. Appl. Earth Observations Remote Sensing* 13, 102–112. doi:10.1109/JSTARS.2019.2952694

Cardellach, E., Rius, A., Martin-Neira, M., FabraNogues-Correig, F. O., Nogues-Correig, O., Ribo, S., et al. (2014). Consolidating the Precision of Interferometric GNSS-R Ocean Altimetry Using Airborne Experimental Data. *IEEE Trans. Geosci. Remote Sensing* 52, 4992–5004. doi:10.1109/tgrs.2013.2286257

Clarizia, M. P., Ruf, C., Cipollini, P., and Zuffada, C. (2016). First Spaceborne Observation of Sea Surface Height Using GPS-Reflectometry. *Geophys. Res. Lett.* 43, 767–774. doi:10.1002/2015GL066624

Fabra, F., Cardellach, E., Li, W., and Rius, A. (2017). "WAVPY: A GNSS-R Open Source Software Library for Data Analysis and Simulation," in Proceeding of the . IEEE Int. Geosci. Remote Sens. Symp. (IGARSS), Fort Worth, TX, USA, July 2017 (IEEE), 4125–4128. doi:10.1109/IGARSS.2017.8127908

Fabra, F., Cardellach, E., Ribó, S., Li, W., Rius, A., Arco-Fernández, J., et al. (2019). Is Accurate Synoptic Altimetry Achievable by Means of Interferometric GNSS-R? *Remote Sensing* 11, 5051–50519. doi:10.3390/rs11050505

Foti, G., Gommenginger, C., Jales, P., Unwin, M., Shaw, A., Robertson, C., et al. (2015). Spaceborne GNSS Reflectometry for Ocean Winds: First Results from

the UK TechDemoSat-1 Mission. *Geophys. Res. Lett.* 42, 5435–5441. doi:10.1002/2015GL064204

Gao, F., Xu, T., Meng, X., Wang, N., He, Y., and Ning, B. (2021). A Coastal experiment for GNSS-R Code-Level Altimetry Using BDS-3 New Civil Signals. *Remote Sensing* 13 (7), 1378. doi:10.3390/rs13071378

Gao, F., Xu, T., Wang, N., He, Y., and Luo, X. (2020). A Shipborne Experiment Using a Dual-Antenna Reflectometry System for GPS/BDS Code Delay Measurements. *J. Geod* 94, 88. doi:10.1007/s00190-020-01421-4

Gao, F., Xu, T., Wang, N., Jiang, C., Du, Y., Nie, W., et al. (2018). Spatiotemporal Evaluation of GNSS-R Based on Future Fully Operational Global Multi-GNSS and Eight-LEO Constellations. *Remote Sensing* 10, 67. doi:10.3390/rs10010067

Garrison, J. L., Komjathy, A., Zavorotny, V. U., and Katzberg, S. J. (2002). Wind Speed Measurement Using Forward Scattered GPS Signals. *IEEE Trans. Geosci. Remote Sensing* 40, 50–65. doi:10.1109/36.981349

He, Y., Gao, F., Xu, T., Meng, X., and Wang, N. (2021). Coastal Altimetry Using Interferometric Phase from Geo Satellite in Quasi-Zenith Satellite System. *IEEE Geosci. Remote Sensing Lett.* 99, 1–5. doi:10.1109/LGRS.2021.3068376

Huaizu You, H., Garrison, J. L., Heckler, G., and Zavorotny, V. U. (2004). Stochastic Voltage Model and Experimental Measurement of Ocean-Scattered GPS Signal Statistics. *IEEE Trans. Geosci. Remote Sensing* 42 (10), 2160–2169. doi:10.1109/TGRS.2004.834628

Jin, S., Cardellach, E., and Xie, F. (2014). *GNSS Remote Sensing: Theory, Methods and Applications; Remote Sensing and Digital Image Processing*. Dutch, The Netherlands: Springer

Katzberg, S. J., Torres, O., and Ganoe, G. (2006). Calibration of Reflected GPS for Tropical Storm Wind Speed Retrievals. *Geophys. Res. Lett.* 33, L18602-1–L18602-5. doi:10.1029/2006GL026825

Li, W., Cardellach, E., Fabra, F., Ribo, S., and Rius, A. (2020). Assessment of Spaceborne GNSS-R Ocean Altimetry Performance Using CYGNSS mission Raw Data. *IEEE Trans. Geosci. Remote Sensing* 58, 238–250. doi:10.1109/tgrs.2019.2936108

Li, W., Cardellach, E., Fabra, F., Ribó, S., and Rius, A. (2018). Lake Level and Surface Topography Measured with Spaceborne GNSS-Reflectometry from CYGNSS Mission: Example for the Lake Qinghai. *Geophys. Res. Lett.* 45, 13332–13341. doi:10.1029/2018GL080976

Li, W., Rius, A., Fabra, F., Cardellach, E., Ribo, S., and Martin-Neira, M. (2018). Revisiting the GNSS-R Waveform Statistics and its Impact on Altimetric Retrievals. *IEEE Trans. Geosci. Remote Sensing* 56, 2854–2871. doi:10.1109/tgrs.2017.2785343

Li, W., Rius, A., Fabra, F., Martín-Neira, M., Cardellach, E., Ribó, S., et al. (2016). The Impact of Inter-Modulation Components on Interferometric GNSS-Reflectometry. *Remote Sensing* 8, 10131–101311. doi:10.3390/rs8121013

Liu, Z. Q., Zheng, W., Wu, F., Kang, Q., Li, Z., Wang, Q., et al. (2019). Increasing the Number of Sea Surface Reflected Signals Received by GNSS-Reflectometry Altimetry Satellite Using the Nadir Antenna Observation Capability Optimization Method. *Remote Sensing* 11 (21), 2473. doi:10.3390/rs11212473

Lowe, S. T., LaBrecque, J. L., Zuffada, C., Romans, L. J., Young, L. E., and Hajj, G. A. (2002). First Spaceborne Observation of an Earth-Reflected GPS Signal. *Radio Sci.* 37, 71–128. doi:10.1029/2000RS002539

Lowe, S. T., Zuffada, C., Chao, Y., Kroger, P., Young, L. E., and LaBrecque, J. L. (2002). 5-cm-Precision Aircraft Ocean Altimetry Using GPS Reflections. *Geophys. Res. Lett.* 29, 1375. doi:10.1029/2002GL014759

Martin-Neira, M. (1993). A Passive Reflectometry and Interferometry System (PARIS): Application to Ocean Altimetry. *ESA J.* 17, 331–355

Martin-Neira, M., Caparrini, M., Font-Rossello, J., Lannelongue, S., and Vallmitjana, C. S. (2001). The PARIS Concept: an Experimental Demonstration of Sea Surface Altimetry Using GPS Reflected Signals. *IEEE Trans. Geosci. Remote Sensing* 39, 142–150. doi:10.1109/36.898676

Martin-Neira, M., D'Addio, S., Buck, C., Floury, N., and Prieto-Cerdeira, R. (2011). The PARIS Ocean Altimeter In-Orbit Demonstrator. *IEEE Trans. Geosci. Remote Sensing* 49, 2209–2237. doi:10.1109/tgrs.2010.2092431

Martín-Neira, M., Li, W., Andrés-Beivide, A., and Ballesteros-Sels, X. (2016). "Cookie": A Satellite Concept for GNSS Remote Sensing Constellations. *IEEE J. Sel. Top. Appl. Earth Observations Remote Sensing* 9, 4593–4610. doi:10.1109/JSTARS.2016.2585620

Masters, D., Axelrad, P., and Katzberg, S. (2004). Initial Results of Land-Reflected GPS Bistatic Radar Measurements in SMEX02. *Remote Sensing Environ.* 92, 507–520. doi:10.1016/j.rse.2004.05.016

Park, H., Camps, A., Valencia, E., Rodriguez-Alvarez, N., Bosch-Lluis, X., Ramos-Perez, I., et al. (2012). Retracking Considerations in Spaceborne GNSS-R Altimetry. *GPS Solut* 16, 507–518. doi:10.1007/s10291-011-0251-7

Ribó, S., Arco-Fernández, J., Cardellach, E., Fabra, F., Li, W., Nogués-Correig, O., et al. (2017). A Software-Defined GNSS Reflectometry Recording Receiver with Wide-Bandwidth, Multi-Band Capability and Digital Beam-Forming. *Remote Sensing* 9, 4501–45020. doi:10.3390/rs9050450

Rius, A., Cardellach, E., and Martin-Neira, M. (2010). Altimetric Analysis of the Sea-Surface GPS-Reflected Signals. *IEEE Trans. Geosci. Remote Sensing* 48, 2119–2127. doi:10.1109/tgrs.2009.2036721

Rodriguez-Alvarez, N., Bosch-Lluis, X., Camps, A., Vall-Llossera, M., Valencia, E., Marchan-Hernandez, J. F., et al. (2009). Soil Moisture Retrieval Using GNSS-R Techniques: Experimental Results Over a Bare Soil Field. *IEEE Trans. Geosci. Remote Sensing* 47, 3616–3624. doi:10.1109/TGRS.2009.2030672

Ruffini, G., Soulat, F., Caparrini, M., Germain, O., and Martín-Neira, M. (2004). The Eddy Experiment: Accurate GNSS-R Ocean Altimetry from Low Altitude Aircraft. *Geophys. Res. Lett.* 31. doi:10.1029/2004GL019994

Skourup, H., Farrell, S. L., Hendricks, S., Ricker, R., Armitage, T. W. K., Ridout, A., et al. (2017). An Assessment of State-of-the-Art Mean Sea Surface and Geoid Models of the Arctic Ocean: Implications for Sea Ice Freeboard Retrieval. *J. Geophys. Res. Oceans* 122 (11), 8593–8613. doi:10.1002/2017JC013176

Turner, J. F., Iliffe, J. C., Ziebart, M. K., and Jones, C. (2013). Global Ocean Tide Models: Assessment and Use within a Surface Model of Lowest Astronomical Tide. *Mar. Geodesy* 36, 123–137. doi:10.1080/01490419.2013.771717

Wickert, J., Cardellach, E., Martin-Neira, M., Bandeiras, J., Bertino, L., Andersen, O. B., et al. (2016). GEROS-ISS: GNSS Reflectometry, Radio Occultation, and Scatterometry Onboard the International Space Station. *IEEE J. Sel. Top. Appl. Earth Observations Remote Sensing* 9, 4552–4581. doi:10.1109/JSTARS.2016.2614428

Wu, X., Ma, W., Xia, J., Bai, W., Jin, S., and Calabia, A. (2021). Spaceborne GNSS-R Soil Moisture Retrieval: Status, Development Opportunities, and Challenges. *Remote Sensing* 13, 451–4521. doi:10.3390/rs13010045

Zavorotny, V. U., Gleason, S., Cardellach, E., and Camps, A. (2014). Tutorial on Remote Sensing Using GNSS Bistatic Radar of Opportunity. *IEEE Geosci. Remote Sens. Mag.* 2, 8–45. doi:10.1109/mgrs.2014.2374220

Conflict of Interest: The authors declare that the research was conducted in the absence of any commercial or financial relationships that could be construed as a potential conflict of interest.

Publisher's Note: All claims expressed in this article are solely those of the authors and do not necessarily represent those of their affiliated organizations, or those of the publisher, the editors and the reviewers. Any product that may be evaluated in this article, or claim that may be made by its manufacturer, is not guaranteed or endorsed by the publisher.

frontiers in Earth Science

ORIGINAL RESEARCH
published: 14 March 2022
doi: 10.3389/feart.2022.730551

Correction of Atmospheric Delay Error of Airborne and Spaceborne GNSS-R Sea Surface Altimetry

Zhengjie Yan[1,2†], *Wei Zheng*[1,2*†], *Fan Wu*[2*†], *Cheng Wang*[2], *Huizhong Zhu*[1] *and Aigong Xu*[1]

[1]School of Geomatics, Liaoning Technical University, Fuxin, China, [2]Qian Xuesen Laboratory of Space Technology, China Academy of Space Technology, Beijing, China

Improving the measurement accuracy is a necessary condition for sea surface altimetry using the Global Navigation Satellite System Reflectometry (GNSS-R). The ionosphere and troposphere delay the transmission of satellite signals, which directly affect the measuring accuracy. The influence of the atmospheric environment on GNSS-R altimetry differs from different platforms. By analyzing and sorting out the altimetry data of airborne and spaceborne platforms, this paper studies the variation law of signal delay in the altimetry process from the point of view of mathematical geometry, which provides an example for improving the precision of GNSS-R altimetry measurements. Firstly, in order to facilitate data analysis, this paper constructed an altimetry model with the GNSS satellite position, specular reflection point position, receiver position as nodes, classified direct signals, and reflected signals. Secondly, calculate ionospheric puncture point coordinates , and interpolate GIM products provided by IGS using time and puncture point coordinates to obtain the VTEC value in the vertical direction of the puncture point, which was converted into the path direction STEC by projection function, the ionospheric delay of each part was obtained in this way. The tropospheric delay of each part is considered for the along-path component and the geometric component, the delay of along-path component was calculated by the UNB3m model, and the delay of geometric component was calculated by the equation provided by Nikolaidou (Nikolaidou et al., 2021). Thirdly, by comparing the sea surface height inversion results with or without atmospheric delay correction with the mean sea surface height provided by DTU15, the measurement accuracy with atmospheric delay correction is obviously improved. The study results of the influence of atmospheric delay on the altimetry experiments precision error of airborne and spaceborne platforms show that the error magnitude is consistent with the existing literature. In the airborne experiment, the influence of the ionosphere is negligible and the troposphere has sub-meter influence on altimetry results, among which the tropospheric along-path delay component occupies a high proportion. The geometric delay component has a high correlation with the satellite elevation angle and its influence on the measurement accuracy decreases with the elevation angle increase. The effect of this factor can be effectively weakened by setting a high satellite cutoff angle. In the spaceborne experiment, the effect of atmospheric delay on altimetry results fluctuates in the range of 3~5 m when the satellite elevation angle is greater than 60°. In this paper, the method of calculating signal atmospheric delay through geometric relation to improving the

OPEN ACCESS

Edited by:
Jinyun Guo,
Shandong University of Science and Technology, China

Reviewed by:
Cheng Wang,
Beihang University, China
Thalia Nikolaidou,
Department of Natural Resources, Canada

***Correspondence:**
Wei Zheng
zhengwei1@qxslab.cn
Fan Wu
wufan@qxslab.cn

[†]*These authors have contributed equally to this work*

Specialty section:
This article was submitted to "Environmental Informatics and Remote Sensing", a section of the journal Frontiers in Earth Science

Received: *25 June 2021*
Accepted: *02 February 2022*
Published: *14 March 2022*

Citation:
Yan Z, Zheng W, Wu F, Wang C, Zhu H and Xu A (2022) Correction of Atmospheric Delay Error of Airborne and Spaceborne GNSS-R Sea Surface Altimetry. Front. Earth Sci. 10:730551. doi: 10.3389/feart.2022.730551

measurement accuracy can provide an example for the atmospheric delay correction of GNSS-R ocean altimetry with high precision and spatial resolution in future research.

Keywords: airborne GNSS-R, spaceborne GNSS-R, atmospheric delay, tropospheric delay, ionospheric delay, global navigation satellite system-reflectometry(GNSS-R) ocean altimetry

INTRODUCTION

Sea surface height (SSH) is the basic data for the study of ocean dynamics, meteorology, geodesy, geophysics, geodesy, and other fields. The worldwide SSH can be used to monitor global climate change, obtain geoid, determine ocean circulation, invert the ocean gravity field, establish ocean tidal models, and conduct research on mesoscale climate models (Liu et al., 2019; Zhang et al., 2020b). It is of great significance to monitor sea level changes. At present, the SSH can be obtained from the traditional ship surveys and tidal stations to the present medium resolution spectrometer imaging, synthetic aperture radar, radar altimeter, and other methods (Liu et al., 2019; Hang et al., 2020). However, ship survey and tidal station models are limited in space, inefficient at spatial sampling, and suitable for local observation, unable to achieve global ocean coverage. Synthetic aperture radar altimeter and radar altimeter can only measure the target height of the subsatellite point and their application conditions are limited. At present, the famous Jason-2 altimeter satellite is jointly developed by CNES, NASA, EUMETSAT and NOAA, which can achieve the measurement of centimeter-level of SSH. It plays a huge role in weather forecasting and climate monitoring but its revisiting period is 9.9156 days and its coverage is concentrated in the sea, due to its lack of mesoscale spatial resolution results in that the surface water information at this scale cannot be observed steadily for a long time and cannot meet the application requirements of new ocean observation (Ren et al., 2018; Liu et al., 2019; Liu, 2020).

Global Navigation Satellite System Reflectometry (GNSS-R) Remote Sensing Technology is a new generation of altimetry technology which uses the reflection of GNSS signals on the sea surface to achieve altimetry (Hu et al., 2020a; Zhang et al., 2020b). In GNSS navigation and positioning, the reflected signals as multi-path interference are generally considered harmful when receiving direct signals and need to be suppressed and eliminated. However, from the point of view of electromagnetic wave propagation theory, the reflected signals carry the physical characteristics information of the reflecting surface, which can be obtained by the parameters change of reflected signals such as waveform, polarization characteristics, amplitude, phase, and frequency (Yang and Zhang, 2011). Therefore, it is possible to estimate and invert the physical properties of the reflecting surface by accurately receiving and estimating the reflected signals. Based on this theory, in 1993, ESA scientist Martin-Neira first proposed and described the concept of PARIS (passive reflectometry and interferometry system) using sea surface reflected signals (Martin-Neira, 1993). The main idea is to use the GPS sea surface reflected wave as the ranging signal to measure the ocean altimetry. In 1994, French scientist Auber accidentally found that the receiver could receive GPS sea surface reflected signals through flight tests (Auber et al., 1994). The Langley Research Center of NASA in the United States concluded, through the series of experiments, that the GPS reflected signals need a special receiver (Liu et al., 2007). Martin-Neira designed bridgeⅠ, bridgeⅡand bridge Ⅲ tests of PARIS altimeter in Holland in September 1997, June 2001, and February 2003 respectively, and verified the possibility of GNSS-R altimetry by using the methods of C/A code phase delay and carrier phase measurement (Martin-Neira et al., 2001; Caparrini et al., 2003; Rivas and Martin-Neira, 2006; Liu et al., 2007). In 2003, the GNSS-R equipment carried by the UK-DMC satellite successfully obtained surface physical coefficients such as sea surface roughness. In 2014, the first GNSS-R satellite (TDS-1) was launched (Jin et al., 2017). These achievements have stimulated the interest of many researchers in GPS reflected signals and prompted countries, world-wide, to begin the exploration and research of GNSS-R technology, and thus, GNSS-R technology has been developed rapidly.

GNSS-R Remote Sensing Technology is a new and effective dual-base radar passive remote sensing technology, compared with the traditional remote sensing technology, and it has the advantage of rich signal sources, low cost, wide-coverage, low power consumption, all-weather, high spatio-temporal resolution, and other advantages. At present, GNSS-R has been widely used in ocean wind measurement, ocean altimetry, sea ice detection, ocean salinity detection, soil moisture detection, moving target detection, and other fields. GNSS-R ocean altimetry technology mainly includes five methods, which are code delay altimetry, carrier phase altimetry, carrier frequency variation altimetry, interference altimetry, delay-doppler map (DDM) altimetry, and signal-to-noise ratio (SNR) altimetry (Hu et al., 2020a).

The realization of GNSS-R ocean altimetry depends on the transmission of GNSS electromagnetic wave signals in space. Signal propagation in space will be affected by the ionosphere, troposphere, multipath, and more. These factors, as error terms, will affect the accuracy of GNSS sea surface measurement, so it is necessary to eliminate the influence of these errors as much as possible (Camps et al., 2014; Zhang et al., 2020b). Literature (Katzberg and Garrison, 2001) pointed out that the ionosphere on the satellite altimeter uses the high frequency signal of dozens of centimeters of distance error, single frequency altimeter is useful in a low electron concentration areas with the scientific research needed, high-precision ionospheric correction is inevitable, and double-frequency altimeters on the spacecraft will produce cost and problem complexity. The GNSS-R technique is proposed by the author to determine the ionospheric electron density near the satellite and analyze the possibility of this technique. The literature (Ruffini et al., 2001) also studied the feasibility of using spaceborne GNSS-R technology to study the ionosphere.

Through simulation experiments, the results showed that GNSS dual-frequency or multi-frequency signals could be used to estimate the ionospheric delay by GNSS-R technology and the dual-frequency pseudo-distance measurement and model prediction could be used to obtain the result that the measurement accuracy of 2 m could be improved after 1s integration. In terms of ionospheric detection, Chen Biyan proposed an improved ionization layer chromatography method which used the observation data of the ground GPS receiver to establish the regional ionospheric model and interpolated it to obtain sufficient TEC, and overcome the shortcomings of the empirical ionospheric model affected by spatial environment and distortion (Chen, 2012). Literature (Yan and Huang, 2016) proposed a method of using DDM to inversion the total electron content in the ionosphere over the ocean. The results are in good agreement with the IRI-2012 model. Based on the data of GPS, GLONASS, BDS and Galileo combined with MGEX network and IGS network, Ren Xiaodong established the ionospheric model based on the multi-system GNSS observation data and analyzed the accuracy of the model, and the results showed that the accuracy was similar to that of IGS products. At the same time, the un-difference ambiguity fixing technique is proposed to extract TEC. Compared with the traditional carrier phase smoothing pseudo distance, the accuracy of ionospheric TEC extracted by this method is significantly improved, which is of great value for the future extraction of TEC from short-period low-orbit satellite data (Ren, 2017). In other studies of GNSS-R application, researchers used models to correct atmospheric delay errors, which were divided into single-frequency navigation receivers using the global ionospheric model for correction, such as the Klobuchar model, and dual-frequency navigation receivers using a linear combination of carrier phase and pseudo-range code to eliminate ionospheric errors (Adriano et al., 2016). There is no systematic study on the variation law of atmospheric delay. In the study of the airborne GNSS-R reflected signal altimetry model, Zhang Yun only excluded the influence of the ionosphere on the experimental results theoretically but did not give the actual results in depth (Zhang et al., 2020b).

The troposphere is a non-dispersive medium. The delayed effect of the troposphere is only related to atmospheric refraction for electromagnetic wave signals and the delay effect is manifested as the propagation path increases and the propagation speed decreases. At present, the existing tropospheric delay correction models include the Saastamoinen model, the UNB3m model, the Hopfield model, and so on. In the application of GNSS-R, some scholars have noticed the influence of tropospheric delay and corrected it, but no specific algorithm or research has been presented. Nikolaidou explained the influence of the troposphere on experimental results for ground-based GNSS-R measurements in detail and showed the change of tropospheric delay from two components of the geometric and the along-path, which accounted for 50% each at low elevation angles, and with the increase of elevation angle, the proportion of the geometric component decreased and the proportion of the along-path component increased. Based on the variation of altimetry platform height and elevation angle, the atmospheric correction is shown as a function of satellite cutoff angle. (Nikolaidou et al., 2020a; Nikolaidou et al., 2020b; Nikolaidou, 2020c; Nikolaidou et al., 2021).

Unlike previous research, this article is from the math geometric point of view, to subdivide the signal path from the receiver, GPS satellite, and specular reflection point actual spatial changes to study the ionosphere and troposphere effect for the GNSS-R sea surface altimetry, and explore the relationship between the satellite elevation angle with atmosphere delay, based on an airborne experiment, and extend the study to the spaceborne platform to provide a possibility to improve the precision of the spaceborne GNSS-R altimetry.

MATERIALS AND METHODS

GNSS-R Ocean Altimetry Model

According to the geometric path of signal propagation, the geometric path delay model of GNSS-R altimetry can be established as shown in **Figure 1**.

Path delay refers to the distance that the reflected signal experiences more than the direct signal. As shown in **Figure 1**, the total path delay is: (Katzberg and Garrison, 1997; Yang and Zhang, 2011):

$$\Delta\rho = \rho_E = \rho_r - \rho_i \tag{1}$$

According to the geometric relationship, it can be concluded that: (Yang and Zhang, 2011; Wang et al., 2021):

$$2h = \frac{\Delta\rho}{\cos\left(\frac{\pi}{2} - \theta\right)} \tag{2}$$

$$h = \frac{\Delta\rho}{2\sin\theta} \tag{3}$$

Where, h represents the height from the receiving platform to the reflecting surface, and θ represents the satellite elevation angle at the mirror reflection point.

GNSS signals propagate through the ionosphere and troposphere in space, resulting in the atmospheric delay. Therefore, the distance relationship between the observed pseudo distance and the actual distance is:

$$\rho_e = \rho_p + \rho_{ion} + \rho_{tro} - c \cdot \delta t_i + c \cdot \delta t^j + \varepsilon \tag{4}$$

Among them, ρ_p represents the actual distance, ρ_{ion} represents the ionospheric delay, ρ_{tro} represents the tropospheric delay, ε represents other error terms, δt_i represents the receiver clock difference, δt^j represents the satellite clock difference, and c represents the speed of light. The path delay between the GNSS direct signal and the reflected signal is:

$$\begin{aligned}\Delta\rho &= \rho_e^r - \rho_e^d \\ &= \rho_p^r + \rho_{iono}^r + \rho_{tro}^r - c \cdot \delta t_i^r + c \cdot \delta t^{rj} + \varepsilon^r \\ &\quad -\rho_p^d - \rho_{iono}^d - \rho_{tro}^d + c \cdot \delta t_i^d - c \cdot \delta t^{dj} - \varepsilon^d \\ &= \Delta\rho_p + \Delta\rho_{iono} + \Delta\rho_{tro} - c \cdot \Delta\delta t_i + c \cdot \Delta\delta t^j + \Delta\varepsilon\end{aligned} \tag{5}$$

Among them, $\Delta\rho_{ion}$ represents the difference of the ionospheric delay between reflected signals and direct signals, $\Delta\rho_{tro}$ represents

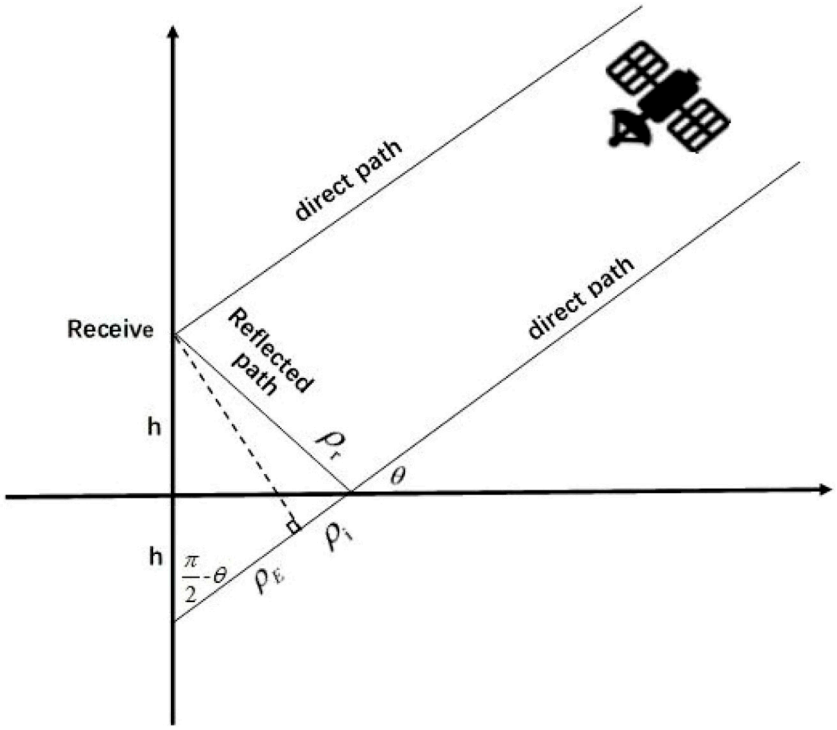

FIGURE 1 | Geometric path delay model of GNSS-R altimetry (Yang and Zhang, 2011).

the difference of the tropospheric delay between reflected signals and direct signals. Substitute **Eq. 5** into **Eq. 3** while only considering the atmospheric delay, and it can be expressed as:

$$h = \frac{\Delta\rho_p + \Delta\rho_{ion} + \Delta\rho_{tro}}{2sin\theta} \tag{6}$$

Among them, the latter two atmospheric delays are the terms that affect the height accuracy of inversion:

$$\Delta h = \frac{\Delta\rho_{ion} + \Delta\rho_{tro}}{2\sin\theta} \tag{7}$$

Ionospheric Delay Correction

The ionosphere is a dispersive medium in which electromagnetic waves of different frequencies have different propagation paths and velocities. This effect is called ionospheric delay. For GNSS signals, the distance difference of the electromagnetic wave propagation path caused by ionospheric refraction can reach a maximum of 50 m in the vertical gradient direction and 150 m in the horizontal gradient direction (Wang, 2008). According to the A-H (Appleton-Hartree) equation, without considering the higher-order terms, the refraction index of the ionosphere is: (Yuan, 2002; Dong et al., 2018):

$$n = 1 - \frac{k}{f^2}, k = 40.3N_e\left(Hz^2m^3\right) \tag{8}$$

Among them, N_e represents the electron density along the path of the signal. Carrier phase signal and code signal go through phase path and group path, respectively, in the ionospheric region and the corresponding delay is called phase lead and code delay. The phase refraction index is used respectively, n_p、group refraction index n_g combined with the mathematical equation, the TEC (Total Electron Content) indicates the total amount of electrons contained in the column per unit area of ionosphere, and it is generally representative 10^{16}~10^{17} electronic per square (Yuan, 2002; Camps et al., 2017; Taoufiq et al., 2018; Liu, 2020).

$$n_p = 1 - 40.3\frac{TEC_{f_i}}{f_i^2}, n_g = 1 + 40.3\frac{TEC_{f_i}}{f_i^2} \tag{9}$$

The phase lead caused by the ionospheric phase path is: (Yuan, 2002):

$$I = \int_{l1}^{l2}\left(n_p - 1\right)dl = -\frac{40.3}{f_i^2}TEC_{f_i} \tag{10}$$

The code delay caused by the ionospheric group path is: (Yuan, 2002):

$$I = \int_{l1}^{l2}\left(n_g - 1\right)dl = \frac{40.3}{f_i^2}TEC_{f_i} \tag{11}$$

The ionosphere contains the most electrons at a distance of 130–500 km from the ground. For the convenience of research, the ionosphere is regarded as a compressed layer 450 km from the ground, which is called the ionospheric single layer model. The intersection point where the GPS signal passes through the model

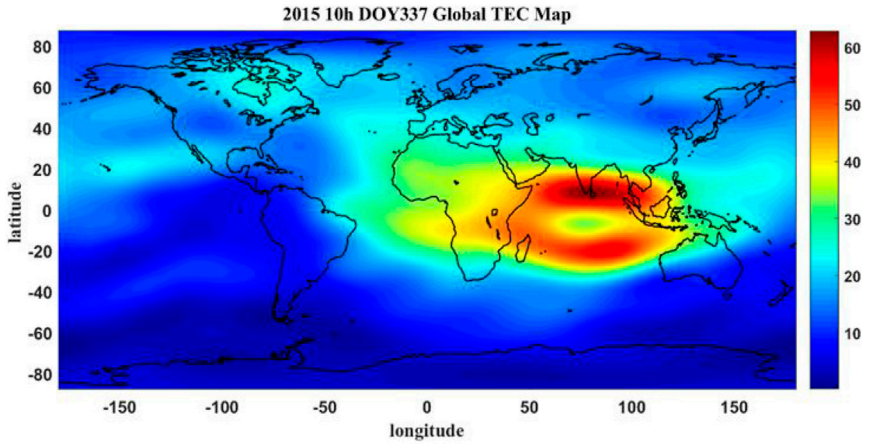

FIGURE 2 | Global ionospheric VTEC distribution.

is called the puncture point and the coordinates of this point can be obtained by the following equation: (Liu, 2020):

$$\gamma = \frac{\pi}{2} - \theta - \arcsin\left(\frac{R_e * \cos\theta}{R_e + h}\right)$$
$$\varphi_m = \arcsin\left(\sin\phi_n \cos\gamma + \cos\phi_n \sin\gamma + \cos A\right) \quad (12)$$
$$\lambda_m = \lambda_n + \arcsin\left(\frac{\sin\lambda \sin A}{\cos\varphi_m}\right)$$

Among them, φ_m, λ_m represents the longitude and latitude of the puncture point, φ_n, λ_n represents the latitude and longitude of the receiver, θ represents satellite elevation angle, A represents the azimuth of the satellite, Υ represents the angle of the center of the earth, R_e is the radius of the earth, h represents the ionospheric monolayer height.

In this work, the GIM (Grid Ionospheric Model) products published by IGS (International GNSS Services) are used to obtain the electron concentration information. The ionospheric grid model divides the space into several grids according to a certain longitude and latitude and the intersection point of each grid is called the ionospheric grid point. At present, IGS divides the world into 5,183 grids according to the longitude from −180°–180° with an interval of 5° and latitude from −87.5°–87.5° with an interval of 2.5°. By interpolating the coordinate values of ionospheric grid points, VTEC at any position can be obtained. Compared with other ionospheric models, GIM can provide a wide range of ionospheric data and is not limited by the environment of the base station. The ionospheric products of the CODE analysis center have high accuracy (Li et al., 2017; Hu et al., 2020b; Liu, 2020), so the ionospheric products provided by CODE is selected for this research. **Figure 2** shows the global ionospheric VTEC distribution map obtained from the GIM product provided by CODE at 10:00 on December 3, 2015.

In this work, the IDW (inverse distance weighting) method is used to interpolate the GIM to obtain the ionospheric VTEC value at the puncture point and then the STEC value in the signal path direction is calculated through the geometric relationship to obtain the ionospheric delay in the signal path direction.

The IDW method is based on the distance between the point to be solved and the surrounding known points, to determine the correlation degree between the point to be solved and the known points, to determine the weight coefficient, and to obtain the attribute value of the point to be solved (Wu et al., 2018). The closer the point to be solved is to the known point, the greater the weight. Using the IDW method, the expression of the zenith direction VTEC at the ionospheric puncture point is as follows: (Wu et al., 2018):

$$VTEC_{ion}^{j} = \begin{cases} \left(\sum_{i=1}^{n} \frac{VTEC_{ion}^{j}}{d_{ij}}\right) \Big/ \left(\sum_{i=1}^{n} \frac{1}{d_{ij}}\right), |d_{ij} < DR \\ VTEC_{ion}^{I}, |d_{ij} = 0 \end{cases} \quad (13)$$

Among them, $VTEC_{ion}^{j}$ represent the VTEC value of j at the ionospheric puncture point to be solved, $VTEC_{ion}^{i}$ represent the VTEC value at the ionospheric grid point i within the range of the ionospheric puncture point, d_{ij} represent the distance between the ionospheric puncture point j and the ionospheric grid point i, DR represent the distance threshold (Wu et al., 2018).

The value obtained through the above interpolate is the TEC in the zenith direction at the ionospheric puncture point, denoted as VTEC. In the calculation, the TEC along the propagation path of the signal is required, denoted as STEC. Usually, a projection function is used to convert STEC to VTEC. In this experiment, a single-layer projection function is used to convert VTEC to STEC. The projection function is as follows (Liu, 2020):

$$m(\xi) = \frac{1}{\cos\xi} = \frac{STEC}{VTEC}$$
$$\xi = \arcsin\left(\frac{R_e \times \cos\theta}{R_e + h}\right) \quad (14)$$

Among them, ξ represent the angle between VTEC and STEC at the ionospheric puncture point and the other values are consistent with the above.

In this work, we studied the process of the GNSS-R SSH measurement of atmospheric delay influence on measuring precision, and the VTEC at the ionospheric puncture point is obtained by interpolating the GIM production which is provided from IGS, which is then converted into the path direction STEC through the projection function. Finally, the corresponding ionospheric delay is obtained through **Eq. 15** (Yuan, 2002).

$$\rho_{iono} = \frac{40.3}{f^2} \times STEC \tag{15}$$

Tropospheric Delay Correction

From the ground to an altitude of about 60 km is the earth's atmosphere, of which about 8 km above the ground is the troposphere. When electromagnetic waves pass through the atmosphere, the signal propagation is delayed due to the change of medium density. About 80% of the atmospheric delay occurs in the troposphere, which is called the tropospheric delay. Nikolaidou has pointed out that delay caused by the troposphere is represented by signal velocity delay (linear refraction) and direction bending (angular refraction) (Nikolaidou et al., 2021). In the existing literature, the tropospheric delay for the direct and reflected paths above the receiving platform is offset. Nikolaidou believes this method has certain error defects and ignores the angular refraction delay of signal in space, and this delay will cause an additional atmospheric delay of geometric nature. Nikolaidou creatively analyzed the delay effect caused by signal angular refraction and pointed out that the along-path component and the geometric component must both, be considered in the calculation of tropospheric delay. The equation for the geometric component is as follows: (Nikolaidou et al., 2020a; Nikolaidou et al., 2020b; Nikolaidou, 2020c):

$$\rho_{tro}^{g} = 2H\delta\theta\cos\theta \tag{16}$$

The equation for the along-path component is as follows: (Nikolaidou et al., 2020a; Nikolaidou et al., 2020b; Nikolaidou, 2020c):

$$\rho_{tro}^{a} = 2HN_l \csc\theta' \tag{17}$$

Among them, θ represent the satellite elevation angle in the vacuum, θ' represent the satellite elevation angle in the presence of the atmosphere, H represent the height of the receiver (m), $\delta\theta$ represent the difference between the elevation angle in the presence of the atmosphere and the elevation angle in the vacuum;

The equation of the geometric delay component for atmospheric altimetry correction is also given in the literature (Nikolaidou et al., 2021):

$$\Delta H_g = H\delta\theta\cot\theta \tag{18}$$

This experiment adopted the UNB3m model from the University of New Brunswick to calculate tropospheric delay for along-path component. This model is composed of the Saastamoinen model, Niel mapping function, and annual mean and amplitude table of meteorological parameters. The advantage is that no measured meteorological parameters are needed. The tropospheric delay can be calculated only from the information of altitude, latitude, and annual date.

The calculation equation is as follows, ZHD and ZWD, respectively, represent dry and wet delay of troposphere zenith, m_d and m_h, respectively, represent mapping functions of dry delay and wet delay:

$$\rho_{tro}^{a} = ZHD \times m_d(\theta) + ZWD \times m_w(\theta) \tag{19}$$

$$ZHD = \frac{10^{-6}k_1R_dP_0}{g_m}\left[1 - \frac{\beta H}{T_0}\right]^{\frac{g}{R_d\beta}} \tag{20}$$

$$ZWD = \frac{10^{-6}\left(T_m k'_2 + k_3\right)R_d}{g_m\lambda' - \beta R} \times \frac{e_0}{T_0} \times \left[1 - \frac{\beta H}{T_0}\right]^{\frac{g\lambda'}{R_d\beta}-1} \tag{21}$$

Among them, g represent the acceleration of gravity, g_m represent the gravitational acceleration of the cylinder atmosphere, H represent the height of the station, R represent the dry air gas constant, T_m represent the average temperature of water vapor(K), $k_1, k_2^{'}, k_3$ represent the refraction coefficient, θ represent the elevation angle of satellite, meteorological parameter such as T_0, P_0, e_0, β, λ are calculated by the annual mean value table and amplitude table of meteorological parameter, as shown in (Leandro et al., 2006), which will not be discussed in this work.

Therefore, the total tropospheric delay is: (Nikolaidou et al., 2021):

$$\rho_{tro} = \rho_{tro}^{a} + \rho_{tro}^{g} \tag{22}$$

When substituting **Eq. 22** into **Eq. 7**, the influence of atmospheric delay on altimetry results can be expressed as:

$$\begin{aligned}\Delta h &= \frac{\Delta\rho_{iono}}{2\sin\theta} + \frac{\Delta\rho_{tro}^{a}}{2\sin\theta} + \frac{\Delta\rho_{tro}^{g}}{2\sin\theta} \\ &= \frac{\Delta\rho_{iono}}{2\sin\theta} + \frac{\Delta\rho_{tro}^{a}}{2\sin\theta} + H\delta\theta\cot\theta\end{aligned} \tag{23}$$

The last item is the influence value of the geometric component of tropospheric delay on altimetry results, which is consistent with the literature (Nikolaidou, 2020c).

EXPERIMENTAL DATA

Airborne GNSS-R Ocean Altimetry Experimental Data

The data were collected from an airborne experiment over the Baltic Sea of Finland by IEEE of Spain on December 3, 2015. During the experiment, the aircraft flew at an altitude of about 3 km and a flight speed of about 50 m/s (Li et al., 2018). The antenna collecting direct signals (RHCP, circularly polarized right hand) pointed to the zenith and the antenna collecting reflected

FIGURE 3 | Flight trajectory diagram.

signals (LHCP, circularly polarized left hand) pointed to the ground. The direct signals and reflected signals were obtained by an antenna array of eight components, respectively. The signal is converted down through the RF module to the 35 MHz IF signal and then quantized and stored at a rate of 80 MHz at 1bit, and through the direct signal and reflected signal cross-correlation output one-dimensional delay waveform. The instrument control and data recording system consists of an industrial computer running Linux. The original data recording is turned off when the aircraft turns, and the spectrum analysis of the signals collected during the interval cannot be performed (Ribó et al., 2017).

The airborne experimental data of GPS time was 384702–386364s, and to avoid the impact of the plane turned, the plane turned period of 385121–385542s was removed so only the data of straight flight of the aircraft was selected as the experimental analysis data. The flight trajectory of the aircraft is shown in **Figure 3**, and PRN1 was selected as the signal source. The elevation angle of the satellite varies from 62.62°–72.30° in this time interval.

Spaceborne GNSS-R Ocean Altimetry Data

The spaceborne data were derived from the products provided by the spaceborne GNSS-R satellite on June 27, 2019, and the satellite orbital altitude was 580 km. The data of different spaceboard platforms in different periods of the day were selected for analysis. The selected data creation time was 3: 33 and 20: 48 UTC on June 27, 2019 of spaceborne A platform and 3: 48 and 21: 03 UTC on June 27, 2019 of spaceborne B platform.

Validated Model

In this work, we adopted the method of DER tracking to obtain the delay of the reflected signal relative to the direct signal, so as to obtain the height h of the receiver platform relative to the reflected surface. After the height H of the platform relative to the reference ellipsoid is known, the SSH was obtained by the following equation:

$$h_{SSH} = H - h \tag{24}$$

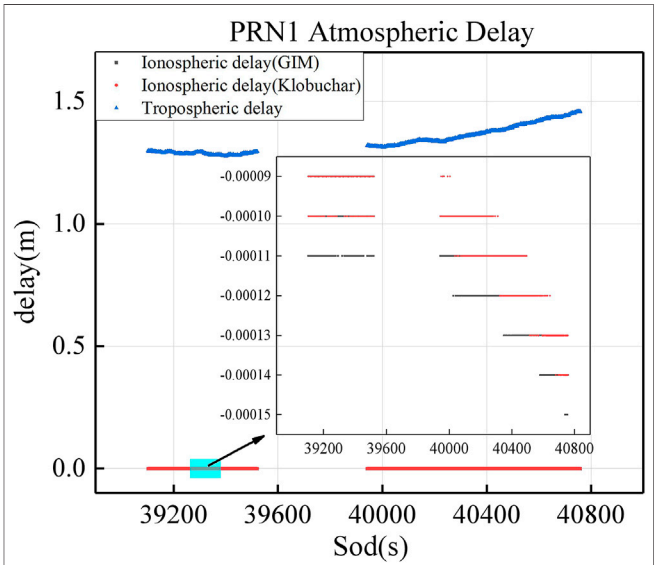

FIGURE 4 | Atmospheric delay of PRN1(Blue represent tropospheric delay, red represents the results of the Klobuchar model, and black represent. the results of GIM product).

Due to the lack of measured data, the accuracy of SSH inversion was determined by comparing the inversion with the validation model. In this work, the global mean sea surface model (DTU15 model) explored by the University of Denmark Technical was used as the validation model and compare the SSH inversion of considering the atmospheric delay or not, and to observe the results of atmospheric delay correction.

RESULTS AND DISCUSSION

Modified Results of Airborne Experiments

In the experiment of airborne GNSS-R sea surface altimetry, the spatial process of the signal can be divided into three parts.

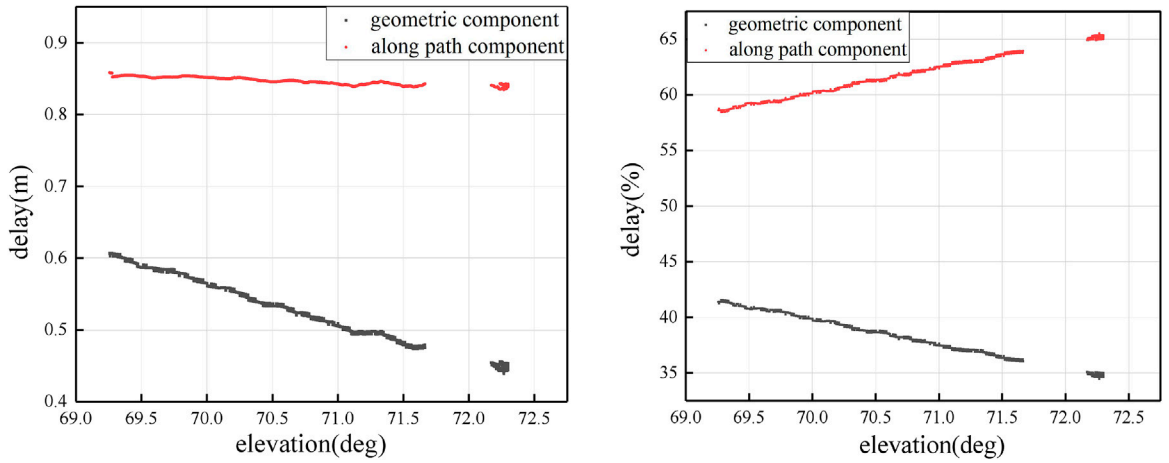

FIGURE 5 | atmospheric delay as a function of satellite elevation angle (left), relative contribution of each component to the total (right).

The first part is the path between the GPS satellite and the airborne receiver, which is the direct signal transmission path. During the transmission, the signal through the ionosphere and troposphere suffers from the ionospheric delay and tropospheric delay. The second part is the path between the GPS satellite and the specular reflection point. The signal through the ionosphere and troposphere. The third part is the path of the signal between the airborne receiver and the specular reflection point. As the altitude of the aircraft is only about 3km, the ionospheric delay and tropospheric delay are not considered at this stage.

In this work, the ionospheric delay of each part is calculated by the Klobuchar model and **Eq. 15**, the tropospheric delay geometric component of each part is calculated by **Eq. 16**, the tropospheric delay along-path component of each part is calculated by the UNB3m model, we then take the difference between the first part and the second part, and the result is the atmospheric delay experienced during the experiment, which is substituted into **Eq. 23** to obtain the influence of atmospheric delay on altimetry results.

Figure 4 shows the atmospheric delay obtained by PRN1 satellite as signal sources. The blue line represents the tropospheric delay, the red line represents the ionospheric delay calculated by the Klobuchar model, and the black line represents the ionospheric delay calculated by the GIM product. **Figure 5** shows the atmospheric delay as a function of satellite elevation angle (left) and the relative contribution of the two components to the total delay (right), the red line represents the delay component of along-path, and the black line represents the delay component of the geometric. **Figure 6** shows the SSH inversion results of PRN1, the black line represents the SSH provided by the DTU15 model, the red line represents the SSH inversion without considering atmospheric delay, and the blue line represents the SSH inversion which is considering atmospheric delay.

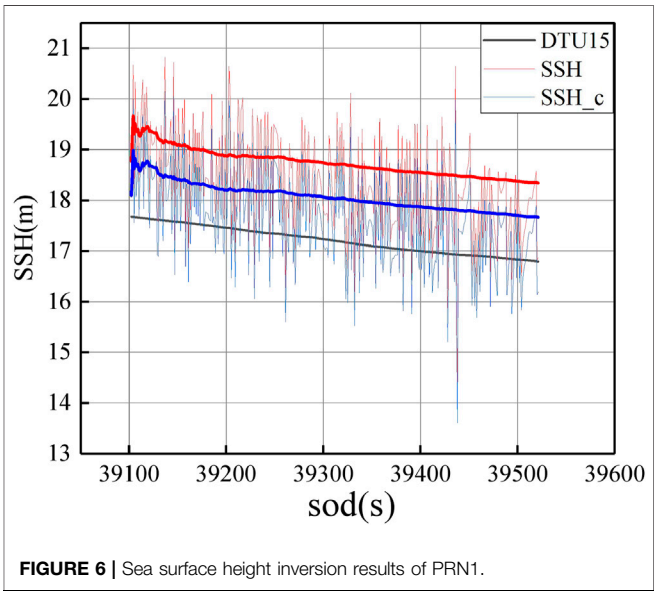

FIGURE 6 | Sea surface height inversion results of PRN1.

Modification Results of Spaceborne Experiments

In the spaceborne GNSSS-R altimetry experiment, the transmission path of electromagnetic wave signals is the same as that in the airborne experiment. The difference is that in the spaceborne experiment, since the receiver is carried on a satellite running at a height of 580 km, the direct signals travel only through the ionosphere and are not affected by the troposphere. The reflected signals travel not only through the ionosphere but also through the troposphere. **Figure 7** shows the relation between the atmospheric delay by different satellites and the satellite elevation angle at the specular reflection point in the experiments in each period above. The horizontal axis represents SOW (Second of the week), while the vertical axis represents

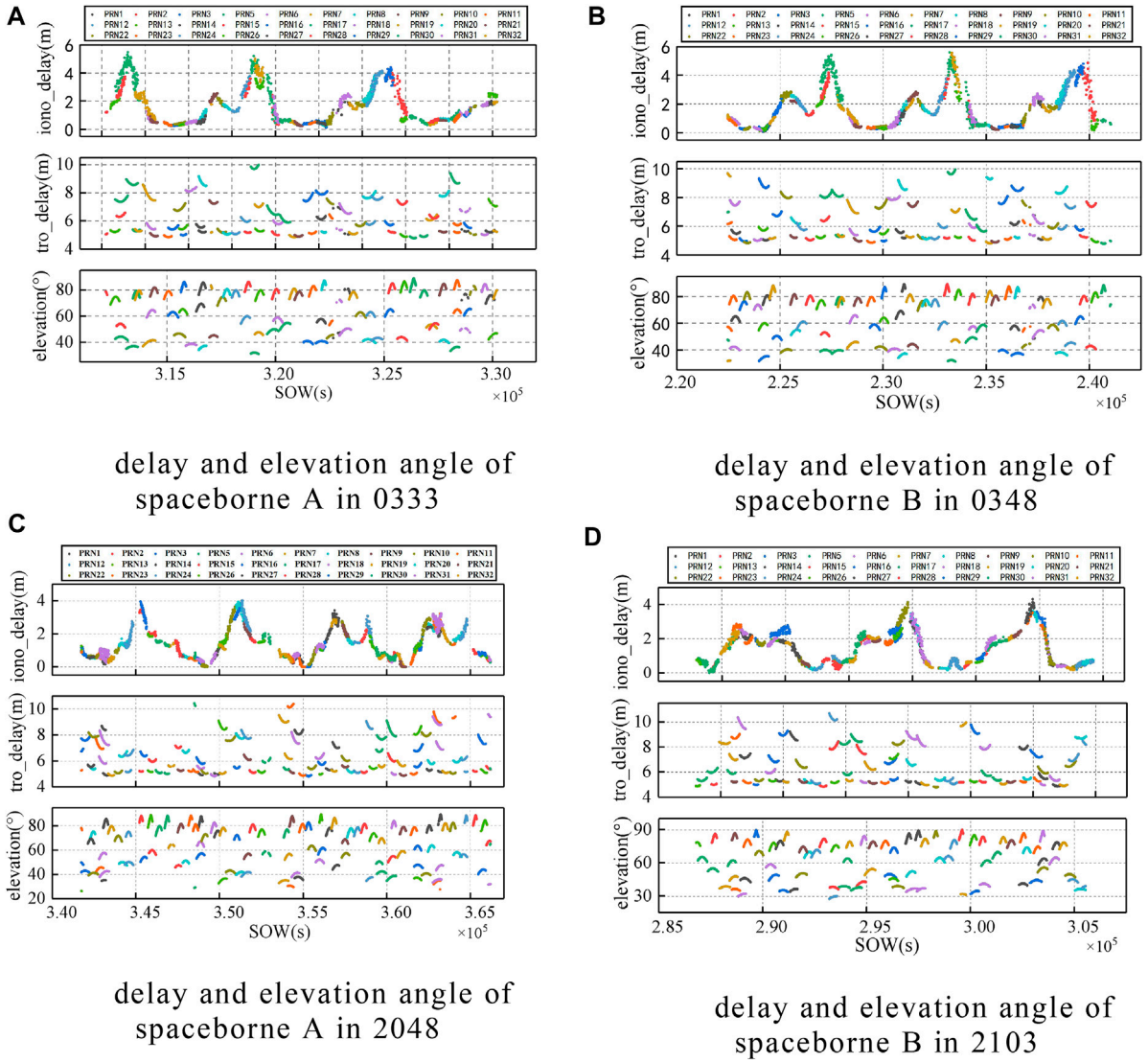

FIGURE 7 | Results of spaceborne experimental atmospheric delay: (numbers represent time, the subgraphs are ionospheric delay, tropospheric delay, and specular point elevation angle from top to bottom). Delay and elevation angle of **(A)** spaceborne A in 0333, **(B)** spaceborne B in 0348, **(C)** spaceborne A in 2048, **(D)** spaceborne B in 2103.

ionospheric delay, tropospheric delay, and satellite elevation angle from top to bottom.

DISCUSSION

By analyzing **Figure 4** to **Figure 6**, it is obvious that in the airborne platform GNSS-R altimetry experiment, the influence of the ionosphere on the altimetry is negligible, while the troposphere has a meter-level delay effect on the signal. At 69.5° elevation angles, the geometric delay component is almost 0.59 m which accounts for 41% of the total delay, the along-path delay component is almost 0.85 m which accounts for 59% of the total delay. At 71.5° elevation angles, the geometric delay component is almost 0.48 m which accounts for 36% of the total delay, the along-path delay component is almost 0.84 m which accounts for 64% of the total delay. And with the increase of the elevation angle, the proportion of the along-path component is increased and the proportion of the geometric component is decreased. The comparison with the DTU15 model shows that the accuracy of SSH inversion is higher after eliminating atmospheric delay error. In this work, mean absolute error (MAE) and Standard Deviations (STD) were taken as the evaluation criteria of the experiment. Meanwhile, **Eq. 25** was used to calculate the average value of the influence of tropospheric delay on the altimetry results in this period, which was represented by Mean, the calculation equation is as follows: (Zhang et al., 2021):

TABLE 1 | Results of airborne altimetry experimental data.

MAE/m	Along-path component	0.005
	Geometric component	0.041
STD/m	Along-path component	0.004
	Geometric component	0.026
MEAN/m	Along-path component	0.466
	Geometric component	0.264

TABLE 2 | The average statistical results of the influence of atmospheric delay.

	Elevation (°)	28–40	40–50	50–60	60–70	70–80	80–90
A-0333	Iono_mean/m	2.261	2.070	1.452	1.289	1.062	0.591
	Tro_mean/m	7.236	5.390	3.961	2.844	2.271	2.505
A-2048	Iono_mean/m	1.861	1.621	1.201	0.957	0.866	0.732
	Tro_mean/m	7.552	5.332	3.734	3.054	2.647	2.552
B-0348	Iono_mean/m	1.972	1.733	1.358	0.896	0.660	0.570
	Tro_mean/m	7.101	5.311	3.634	3.165	2.631	2.544
B-2103	Iono_mean/m	1.727	1.396	0.834	0.619	0.583	0.497
	Tro_mean/m	7.521	5.043	3.793	3.030	2.666	2.562

$$MAE = \frac{1}{n}\sum_{a=1}^{n}(|\tilde{x}_a - x_a|)$$
$$STD = \sqrt{\frac{1}{n}\sum_{a=1}^{n}(|\tilde{x}_a - x_a| - MAE)^2} \quad (25)$$
$$MEAN = \frac{1}{\mathrm{n}}\sum_{\mathrm{a}=1}^{\mathrm{n}}\frac{\tilde{x}_a}{2\sin\theta}$$

Among them, $\tilde{x}_a$ represent the tropospheric delay value, x_a represent average tropospheric delay, θ represent the elevation angle at the specular reflection point. **Table 1** shows data statistics of airborne experimental results.

For the results of the spaceborne experiment, the elevation angle of the specular reflection point is divided into 10° intervals in this work, and the average value of atmospheric delay on altimetry measurement influence is statistically calculated. The mean value of ionospheric influence is Iono-mean and the mean value of tropospheric influence is Tro-mean. The statistical results are shown in **Table 2**, and the naming rules are shown as above.

Zhang Qiuyang analyzed the corresponding ionospheric delay measurement values in eight different regions of the world in the spaceborne GNSS-R experiment (Zhang et al., 2020a), and the results showed a meter-level accuracy. Among them, the ionospheric delay at a place close to this experimental site shows a fluctuation of about 6 m. In the experiment, Zhang Yun used the international reference ionospheric model to conduct ionospheric correction on the spaceborne GNSS-R altimetry experiment and the delay error was about 15 m (Zhang et al., 2021). In the experiment of this work, by studying the spaceborne GNSS-R experiment data, it was found that the spaceborne GNSS-R altimetry is greatly affected by the ionosphere and the troposphere, and the order of magnitude results are the same as those in the above literature, which is an error term that must be considered to improve the measurement accuracy. Same as in the airborne experiment, the larger the elevation angle, the smaller the ionospheric delay and the tropospheric delay. As shown in **Figure 7**, when the elevation angle increases, the error effect caused by the ionosphere and troposphere decreases, the tropospheric delay mainly varies within the range of 4–10 m, and the ionospheric delay is generally less than 6 m. By choosing the suitable elevation angle and correcting the atmospheric delay error, the accuracy of GNSS-R ocean altimetry can be improved by 3~5 m.

CONCLUSION

As a new remote sensing measurement technology, GNSS-R has gradually attracted the attention of scholars at home and abroad. Land-based and space-based research and experiments have also achieved remarkable success. However, the research on the spaceborne platform is limited by hardware conditions and there is little research on it at home and abroad. It is not difficult to predict the development prospect of the GNSS-R application on a spaceborne platform. High precision measurement results are the key to the popularization of GNSS-R technology. Electromagnetic waves, as a signal transmission medium, are bound to be affected by the space environment. Therefore, it is necessary to deeply conduct study and exploration on atmospheric delay correction in the signal transmission process.

In this work, the influence of ionosphere and troposphere on the results of GNSS-R altimetry was analyzed by studying the variation of atmospheric delay. Research shows that:

1) In the airborne altimetry experiment, the accuracy of GNSS-R sea surface altimetry measurement can be improved effectively by atmospheric delay correction. Because the airborne platform is too low relative to the ionosphere, the influence of the ionosphere on altimetry can be ignored. The troposphere has a meter-level delay effect on the signal, at 69.5° elevation, the geometric delay component account for 41% of the total delay, the along-path delay component account for 59% of the total delay, at 71.5° elevation, the geometric delay component account for 36% of the total delay, the along-path delay component account for 64% of the total delay. With the decrease of the elevation angle, this effect also decreases. Compared with the DTU15 model, it can be seen that the accuracy of SSH inversion is significantly improved by about 0.7 m after eliminating atmospheric delay.
2) In the spaceborne altimetry experiments, the ionospheric delay and tropospheric delay are both error terms that must be corrected to improve the measurement accuracy. The direct signal is only through the ionosphere above the GNSS-R orbit, not through the troposphere. The reflected signal passes through the entire ionosphere once and the ionosphere below the GNSS-R orbit once, and passes through the troposphere twice. Through calculation, the atmospheric delay error in the spaceborne GNSS-R altimetry fluctuates within the range of 5–16 m and the influence on the altimetry precision is in the range of 3~5 m.

3) The SSH is a function of elevation angle and the path delay, and the atmospheric delay function is also associated with the elevation angle. Both airborne and spaceborne experiments also show that the atmospheric delay at a high elevation angle is less than that at low elevation angle. Therefore, increasing the altitude cutoff angle of the satellite can effectively improve the data quality in experimental collection.

DATA AVAILABILITY STATEMENT

The original contributions presented in the study are included in the article/Supplementary Material, further inquiries can be directed to the corresponding authors.

AUTHOR CONTRIBUTIONS

ZY scientific analysis and manuscript writing. WZ and FW experiment design, program management, review, and editing. All authors contributed to the article and approved the submitted version.

FUNDING

This work was supported by the National Nature Science Foundation of China (41774014, 41574014), the Liaoning Revitalization Talents Program under Grant (XLYC2002082), the Frontier Science and Technology Innovation Project and the Innovation Workstation Project of Science and Technology Commission of the Central Military Commission under Grant (085015), the Outstanding Youth Foundation of the China Academy of Space Technology, and the Independent Research and Development Start-up Fund of Qian Xuesen Laboratory of Space Technology (Y-KC-WY-99-ZY-000-025).

ACKNOWLEDGMENTS

We would like to thank the Institute of Space Sciences (ICE, CSIC) and the Institute for Space Studies of Catalonia (IEEC) for providing the raw data processing results of the airborne experiment. We would also like to thank IGS for providing SP3n precise orbit documents and thank CODE for providing the GIM product.

REFERENCES

Auber, J. C., Bibuat, A., and Rigal, J. M. (1994). "Characterization of Multipath on Land and Sea at GPS Frequencies," in Proceedings of the 7 th International Technical Meeting of the Satellite Division of the Institute of Navigation, Salt Lake City, September 20-23 1994, 1155–1171.

BelmonteRivas, M., and Martin-Neira, M. (2006). Coherent GPS Reflections from the Sea Surface. *IEEE Geosci. Remote Sensing Lett.* 3, 28–31. doi:10.1109/lgrs.2005.855617

Camps, A., Park, H., Sekulic, I., and Rius, J. (2017). GNSS-R Altimetry Performance Analysis for the GEROS Experiment on Board the International Space Station. *Sensors* 17, 1583. doi:10.3390/s17071583

Camps, A., Park, H., Valencia i Domenech, E., Pascual, D., Martin, F., Rius, A., et al. (2014). Optimization and Performance Analysis of Interferometric GNSS-R Altimeters: Application to the PARIS IoD mission. *IEEE J. Sel. Top. Appl. Earth Observations Remote Sensing* 7, 1436–1451. doi:10.1109/jstars.2014.2320873

Camps, A., ParkFoti, H., Foti, G., and Gommenginger, C. (2016). Ionospheric Effects in GNSS-Reflectometry from Space. *IEEE J. Sel. Top. Appl. Earth Observations Remote Sensing* 9, 5851–5861. doi:10.1109/jstars.2016.2612542

Caparrini, M., Ruffini, L., and Ruffini, G. C. (2003). "Parfait: GNSS-R Coastal Altimetry," in The 2003 Workshop on Oceanography with GNSS Reflection, Barcelona, Spain.

Chen, B. (2012). "Ionospheric Tomographic Technology and Applications,". [master's thesis] ([ChangSha]: Central South University).

Dong, D., Chen, J., and Wang, J. (2018). *GNSS High Precision Positioning Principle*. Bei Jing: China Science Publishing &Media Ltd, 40.

Hang, S., Zhang, Y., Li, B., Yang, S., and Han, Y. (2020). Feasibility of Coastal Phase Altimetry Using BeiDOU IGSO Satellite Reflected Signals. *Remote Sensing Inf.* 35, 73–81. doi:10.3969/j.issn.1000-3177.2020.01.009

Hu, Y., Chen, X., Gu, W., Zhong, L., and Liu, W. (2020a). Research Sea Surface Altimetry Status and Common Methods. *GNSS World of China* 45, 96–103. doi:10.13442/j.gnss.1008-9268.2020.03.017

Hu, Z., Fan, L., Wang, C., Wang, Z., Shi, C., and Jing, G. (2020b). More Reliable Global Ionospheric Maps Combined from Ionospheric Products of the Seven IGS Analysis Centers. *Results Phys.* 17, 103162–103797. doi:10.1016/j.rinp.2020.103162

Jin, S., Zhang, Q., and Qian, X. (2017). New Progress and Application Prospects of Global Navigation Satellite System Reflectometry (GNSS+R). *Acta Geodaetica et Cartographica Sinica* 46, 1389–1398. doi:10.11947/j.AGCS.20170282

Katzberg, S., and Garrison, J. (1997). *Utilizing GPS to Determine Ionospheric Delay over the Ocean*. Virginia: NASA Langley Technical Report Server.

Katzberg, S. J., and Garrison, J. L. (2001). Surface Reflected Signals from the Global Positioning System for Ionospheric Measurements: Experimental Results at Aircraft Altitudes. *Int. J. Remote Sensing* 22 (4), 663–689. doi:10.1080/01431160050505919

Leandro, R., Santos, M., and Langley, R. (20062006). *UNB Neutral Atmosphere Models Development and Performance*. Monterey, California, USA: Proc. IONNTM, Institute of Navigation, 564–573.January 18-20

Li, W., Rius, A., Fabra, F., Cardellach, E., Ribó, S., and Martín-Neira, M. (2018). Revisiting the GNSS-R Waveform Statistics and its Impact on Altimetric Retrievals. *IEEE Trans. Geosci. Remote Sensing* 56, 2854–2871. doi:10.1109/TGRS.2017.2785343

Li, Z., Wang, N., Li, M., Zhou, K., Yuan, Y., and Yuan, H. (2017). Evaluation and Analysis of the Global Ionospheric TEC Map in the Frame of International GNSS Services. *ChineseJ.Geophys.* 60, 3718–3729. doi:10.6038/cjg20171003

Liu, h. (2020). "Research on Global Ionospheric Modeling Based on Multi-Source Data Fusion,". [master's thesis] (Xi'an: Xi'an University of Science and Technology).

Liu, J., Shao, L., and Zhang, X. (2007). Advances in GNSS-R Studies and Key Technologies. *Geomatics Inf. Sci. Wuhan Univ.* 32, 955–960.

Liu, Z., Zheng, W., Wu, F., Kang, G., Li, Z., Wang, Q., et al. (2019). Increasing the Number of Sea Surface Reflected Signals Received by GNSS-Reflectometry Altimetry Satellite Using the Nadir Antenna Observation Capability Optimization Method. *Remote Sensing* 11 (21), 2473. doi:10.3390/rs11212473

Martin-Neira, M. (1993). A Passive Reflectometry and Interferometry System (PARIS): Application to Ocean Altimetry. *ESA J.* 17, 331–335.

Martin-Neira, M., Caparrini, M., Font-Rossello, J., Lannelongue, S., and Vallmitjana, C. S. (2001). The PARIS Concept: an Experimental Demonstration of Sea Surface Altimetry Using GPS Reflected Signals. *IEEE Trans. Geosci. Remote Sensing* 39, 142–150. doi:10.1109/36.898676

Martin-Neira, M., D'Addio, S., Buck, C., Floury, N., and Prieto-Cerdeira, R. (2011). The PARIS Ocean Altimeter In-Orbit Demonstrator. *IEEE Trans. Geosci. Remote Sensing* 49, 2209–2237. doi:10.1109/tgrs.2010.2092431

Nikolaidou, T. (2020c). "Atmospheric Delay Modelling for Ground-Based GNSS Reflectometry,". PhD dissertation (New Brunswick, Fredericton: Department of Geodesy and Geomatics Engineering, University of New Brunswick).

Nikolaidou, T., Santos, M. C., Williams, S. D. P., and Geremia-Nievinski, F. (2020b). Raytracing Atmospheric Delays in Ground-Based GNSS Reflectometry. *J. Geod* 94, 68. doi:10.1007/s00190-020-01390-8

Nikolaidou, T., Santos, M., Williams, S. D. P., and Geremia-Nievinski, F. (2020a). A Simplification of Rigorous Atmospheric Raytracing Based on Judicious Rectilinear Paths for Near-Surface GNSS Reflectometry. *Earth Planets Space* 72, 91. doi:10.1186/s40623-020-01206-1

Nikolaidou, T., Santos, M., Williams, S., and Geremia-Nievinski, F. Preprint (2021) Development and Validation of Comprehensive Closed Formulas for Atmospheric Delay and Altimetry Correction in Ground-Based GNSS-R. doi:10.36227/techrxiv.14345153

Ren, J., Zhang, Q., Jia, H., Liu, J., and Zhang, H. (2018). Research on Development of Space-Based Wide-Swath Imaging Altimetry Technology Systems. *Spacecraft Eng.* 27, 84–91. doi:10.3969/j.issn.1673-8748.2018.06.012

Ren, X. (2017). "Theory and Methodology of Ionospheric TEC Modelling and Differential Code Biases Estimation with Multi-GNSS,". [master's thesis] ([Wuhan]: Wuhan University).

Ribó, S., Arco-Fernández, J., Cardellach, E., Fabra, F., Li, W., Nogués-Correig, O., et al. (2017). A Software-Defined GNSS Reflectometry Recording Receiver with Wide-Bandwidth, Multi-Band Capability and Digital Beam-Forming. *Remote Sensing* 9, 450. doi:10.3390/rs9050450

Ruffini, G., Caparrini, M., Soulat, F., Martin-Neira, M., Silvestrin, P., and Sharman, K. (2001). *Using GNSS Reflections for Ionospheric Studies*.

Taoufiq, J., Mourad, B., Rachid, A., and Amory-Mazaudier, C. (2018). Study of Ionospheric Variability Using GNSS Observations. *Pos* 09, 79–96. doi:10.1236/pos.2018.9400610.4236/pos.2018.94006

Wang, F., Yang, D., Zhang, G., and Zhang, B. (2021). Measurement of Sea Surface Height Using Airborne Global Navigation Satellites System Reflectometry. *Acta Aeronautica et Astronautica Sinica*, 1–10. doi:10.7527/S1000-6893.2020.24852

Wang, J. (2008). "Monitoring and Application of GNSS Regional Ionospheric TEC,". [master's thesis] (BeiJing: Chinese Academy of Surveying and Mapping).

Wu, Y., Guo, C., and W, Y. (2018). "Comparison of Two Interpolation Algorithms in Grid Ionospheric Model," in The 9th China Satellite Navigation Academic Annual Conference Proceedings - S07 Satellite Navigation Enhancement Technology, Harbin, Heilongjiang, China, May 23-25, 2018. http://www.beidou.gov.cn/zt/dhnh/djjzgwxdhxsnh/.

Yan, Q., and Huang, W. (2016). *Retrieval of Ionospheric TEC over Oceans from GNSS-R Delay-Doppler Map*. Shanghai, China: MAT/IEEE oceans. doi:10.1109/OCEANSAP.2016.7485349

Yang, D., and Zhang, Q. (2011). *GNSS Reflected Signal Processing: Fundamentals and Applications*. Bei Jing: Publishing House of Electronics Industry, 129–142.)7-12

Yuan, Y. (2002). "Study on Theories and Methods of Correcting Ionosphere Delay and Monitoring Ionosphere Based on GPS,". [master's thesis] ([BeiJing: Chinese Academy of Sciences).

Zhang, Q., Liu, Y., and Xia, J. (2020a). Space-Borne GNSS-R Ionospheric Delay Error Elimination by Optimal Spatial Filtering. *Sensors* 20, 5535. doi:10.3390/s20195535

Zhang, Y., Ma, D., Meng, W., Zheng, Q., and Yang, S. (2021). Research on Sea Surface Altimetry Mode of GPS Reflected Signal Based on TechDemoSat-1 Satellite. *J. Beijing Univ. aeronautics astronautics*, 1–13. doi:10.13700/j.bh.1001-5965.2020.0357

Zhang, Y., Zhang, Y., Meng, W., Yang, S., and Han, Y. (2020b). Research on Sea Surface Altimetry Model of Airborne GNSS Reflected Signal. *HaiyangXuebao* 42, 149–156. doi:10.3969/j.issn.0253–4193.2020.03.015

Conflict of Interest: The authors declare that the research was conducted in the absence of any commercial or financial relationships that could be construed as a potential conflict of interest.

Publisher's Note: All claims expressed in this article are solely those of the authors and do not necessarily represent those of their affiliated organizations, or those of the publisher, the editors and the reviewers. Any product that may be evaluated in this article, or claim that may be made by its manufacturer, is not guaranteed or endorsed by the publisher.

Advantages of publishing in Frontiers

OPEN ACCESS
Articles are free to read for greatest visibility and readership

FAST PUBLICATION
Around 90 days from submission to decision

HIGH QUALITY PEER-REVIEW
Rigorous, collaborative, and constructive peer-review

TRANSPARENT PEER-REVIEW
Editors and reviewers acknowledged by name on published articles

Frontiers
Avenue du Tribunal-Fédéral 34
1005 Lausanne | Switzerland

Visit us: www.frontiersin.org
Contact us: frontiersin.org/about/contact

REPRODUCIBILITY OF RESEARCH
Support open data and methods to enhance research reproducibility

DIGITAL PUBLISHING
Articles designed for optimal readership across devices

FOLLOW US
@frontiersin

IMPACT METRICS
Advanced article metrics track visibility across digital media

EXTENSIVE PROMOTION
Marketing and promotion of impactful research

LOOP RESEARCH NETWORK
Our network increases your article's readership